

CARBON ALLOYS

NOVEL CONCEPTS TO DEVELOP CARBON
SCIENCE AND TECHNOLOGY

E. YASUDA, M. INAGAKI, K. KANEKO,
M. ENDO, A. OYA & Y. TANABE (EDITORS)

ELSEVIER

CARBON ALLOYS
Novel Concepts to Develop Carbon
Science and Technology

Elsevier Science Internet Homepage - <http://www.elsevier.com>

Consult the Elsevier homepage for full catalogue information on all books, journals and electronic products and services.

Related Journals/Products

Free specimen copy gladly sent on request. Elsevier Science Ltd, The Boulevard, Langford Lane, Kidlington, Oxford, OX5 1GB, UK

Applied Surface Science
Carbon
Chemical Physics
Chemical Physics Letters
Diamond and Related Materials
Journal of Power Sources
Surface and Coatings Technology
Surface Science
Thin Solid Films

Elsevier Titles of Related Interest

BURCHELL

Carbon Materials for Advanced Technologies
ISBN: 008-042683-2

DRESSELHAUS & DRESSELHAUS

Science of Fullerenes and Carbon Nanotubes: Their Properties and Applications
ISBN: 0122218205

INAGAKI

New Carbons – Control of Structure and Functions
ISBN: 008-043713-3

MARSH

Activated Carbon Compendium
ISBN: 008-044030-4

TANAKA, YAMABE & FUKUI

The Science and Technology of Carbon Nanotubes
ISBN: 008-042696-4

To Contact the Publisher

Elsevier Science welcomes enquiries concerning publishing proposals: books, journal special issues, conference proceedings, etc. All formats and media can be considered. Should you have a publishing proposal you wish to discuss, please contact, without obligation, the publisher responsible for Elsevier's materials chemistry programme:

| | |
|------------------------------|--|
| Iain Craig | |
| Publishing Editor | |
| Elsevier Science Ltd | |
| The Boulevard, Langford Lane | Phone: +44 1865 843631 |
| Kidlington, Oxford | Fax: +44 1865 843920 |
| OX5 1GB, UK | E-mail: i.craig@elsevier.com |

General enquiries, including placing orders, should be directed to Elsevier's Regional Sales Offices – please access the Elsevier homepage for full contact details (homepage details at the top of this page).

CARBON ALLOYS

Novel Concepts to Develop Carbon Science and Technology

Edited by

Ei-ichi YASUDA
Michio INAGAKI
Katsumi KANEKO
Morinobu ENDO
Asao OYA
Yasuhiro TANABE

2003



AMSTERDAM – BOSTON – LONDON – NEW YORK – OXFORD – PARIS
SAN DIEGO – SAN FRANCISCO – SINGAPORE – SYDNEY – TOKYO

ELSEVIER SCIENCE Ltd
The Boulevard, Langford Lane
Kidlington, Oxford OX5 1GB, UK

© 2003 Elsevier Science Ltd. All rights reserved.

This work is protected under copyright by Elsevier Science, and the following terms and conditions apply to its use:

Photocopying

Single photocopies of single chapters may be made for personal use as allowed by national copyright laws. Permission of the Publisher and payment of a fee is required for all other photocopying, including multiple or systematic copying, copying for advertising or promotional purposes, resale, and all forms of document delivery. Special rates are available for educational institutions that wish to make photocopies for non-profit educational classroom use.

Permissions may be sought directly from Elsevier Science via their homepage (<http://www.elsevier.com>) by selecting 'Customer support' and then 'Permissions'. Alternatively you can send an e-mail to: permissions@elsevier.com, or fax to: (+44) 1865 853333.

In the USA, users may clear permissions and make payments through the Copyright Clearance Center, Inc., 222 Rosewood Drive, Danvers, MA 01923, USA; phone: (+1) (978) 7508400, fax: (+1) (978) 7504744, and in the UK through the Copyright Licensing Agency Rapid Clearance Service (CLARCS), 90 Tottenham Court Road, London W1P 0LP, UK; phone: (+44) 207 631 5555; fax: (+44) 207 631 5500. Other countries may have a local reprographic rights agency for payments.

Derivative Works

Tables of contents may be reproduced for internal circulation, but permission of Elsevier Science is required for external resale or distribution of such material.

Permission of the Publisher is required for all other derivative works, including compilations and translations.

Electronic Storage or Usage

Permission of the Publisher is required to store or use electronically any material contained in this work, including any chapter or part of a chapter.

Except as outlined above, no part of this work may be reproduced, stored in a retrieval system or transmitted in any form or by any means, electronic, mechanical, photocopying, recording or otherwise, without prior written permission of the Publisher.

Address permissions requests to: Elsevier Science Global Rights Department, at the fax and e-mail addresses noted above.

Notice

No responsibility is assumed by the Publisher for any injury and/or damage to persons or property as a matter of products liability, negligence or otherwise, or from any use or operation of any methods, products, instructions or ideas contained in the material herein. Because of rapid advances in the medical sciences, in particular, independent verification of diagnoses and drug dosages should be made.

First edition 2003


Library of Congress Cataloging in Publication Data

A catalog record from the Library of Congress has been applied for.

British Library Cataloguing in Publication Data

A catalogue record from the British Library has been applied for.

ISBN: 0 08 044163 7

 The paper used in this publication meets the requirements of ANSI/NISO Z39.48-1992 (Permanence of Paper).
Printed in The Netherlands.

Contents

| | |
|---|------|
| <i>Preface</i> | xiii |
| Part 1. Introduction | |
| Chapter 1. Introduction | 3 |
| <i>Ei-ichi Yasuda and Michio Inagaki</i> | |
| 1 A Short History | 3 |
| 2 Carbon Family | 5 |
| 3 Carbon Alloys | 9 |
| References. | 11 |
| Part 2. Space Control in Carbon Alloys | |
| Chapter 2. Hybrid Orbital Control in Carbon Alloys | 15 |
| <i>Riichiro Saito</i> | |
| 1 Hybridization in a Carbon Atom | 15 |
| 2 Defect States and Modifications of the Hybridization | 27 |
| 3 Spectroscopies for sp^n Structure. | 33 |
| 4 Conclusions. | 38 |
| References. | 38 |
| Chapter 3. Structural Design and Functions of Carbon Materials by Alloying in Atomic and Molecular Scales | 41 |
| <i>Morinobu Endo, Takuya Hayashi, Yoong Ahm Kim, Hiroaki Ohta and Sung Wha Hong</i> | |
| 1. Introduction | 41 |
| 2. Intercalation Compounds | 42 |
| 3. Insertion of Li Ions into the Disordered Carbon Materials. | 44 |
| 4. Substitution of Heteroatoms | 46 |
| 5. Metal-doped Fullerenes | 49 |
| 6. Metal-doped Carbon Nanotubes | 50 |
| 7. Conclusions. | 54 |
| References. | 54 |
| Chapter 4. Surface and Hidden Surface-controlled Carbon Alloys | 57 |
| <i>Katsumi Kaneko</i> | |
| 1 Importance of Hidden Surfaces and Confined Spaces in Carbon Materials | 57 |
| 2 Carbon Structure of Superhigh Surface Area | 64 |
| 3 Design of Hidden Surfaces with Alloying | 65 |

| | | |
|--|---|-----|
| 4 | Properties of Hidden Surface- or Pore Space-alloyed Carbons. | 68 |
| 5 | Design of New Porous Carbon with Carbon Alloying Technique | 76 |
| | References. | 77 |
| Chapter 5. Control of Interface and Microstructure in Carbon Alloys. | | 83 |
| <i>Yasuhiro Tanabe and Ei-ichi Yasuda</i> | | |
| 1 | Introduction | 83 |
| 2 | Interface Control. | 85 |
| 3 | Microstructure Control | 89 |
| 4 | Conclusion | 93 |
| | References | 93 |
| Part 3. Typical Carbon Alloys and Processing | | |
| Chapter 6. Intercalation Compounds. | | 99 |
| <i>Noboru Akuzawa</i> | | |
| 1 | Introduction | 99 |
| 2 | Li-insertion into Carbon Materials | 100 |
| 3 | New Intercalation Compounds Prepared from Unique Host Carbon Materials | 103 |
| 4 | Host Effect on the Intercalation of Halogen Molecules and Alkali Metals | 104 |
| 5 | Physical Properties of MCl_2 -GICs and Alkyl Derivative of Boehmite with Layered Structure | 105 |
| 6 | Conclusion. | 105 |
| | References | 106 |
| Chapter 7. Porous Carbon | | 109 |
| <i>Takashi Kyotani</i> | | |
| 1 | Introduction | 109 |
| 2 | Control of Pore Structure | 110 |
| 3 | Performance of Advanced Porous Carbon | 118 |
| 4 | Conclusions | 123 |
| | References | 124 |
| Chapter 8. Polymer Blend Technique for Designing Carbon Materials | | 129 |
| <i>Asao Oya</i> | | |
| 1. | Introduction. | 129 |
| 2. | Porous Carbon Materials. | 129 |
| 3 | Preferential Support of Metal Particles on Pore Surface | 131 |
| 4 | Carbon Nanofibers and Carbon Nanotubes | 133 |
| 5 | Other Fibrous Carbon Materials with Unique Shapes. | 139 |
| 6 | Conclusions | 141 |
| | References | 141 |
| Part 4. The Latest Characterization Techniques | | |
| Chapter 9. Computer Simulations | | 145 |
| <i>Shinji Tsuneyuki</i> | | |
| 1 | Methods | 145 |

| | | |
|---|--|-----|
| 2 | Applications | 150 |
| 3 | Conclusions | 156 |
| | References | 156 |
| Chapter 10. X-ray Diffraction Methods to Study Crystallite Size and Lattice | | |
| | Constants of Carbon Materials | 161 |
| | <i>Minoru Shiraishi and Michio Inagaki</i> | |
| 1. | Introduction | 161 |
| 2 | Measurement Method (JSPS Method) | 162 |
| 3 | Characterization of Carbonized Materials Heat-treated at Low Temperatures | 170 |
| | References | 173 |
| Chapter 11. Pore Structure Analyses of Carbons by Small-Angle X-ray | | |
| | Scattering | 175 |
| | <i>Keiko Nishikawa</i> | |
| 1. | Introduction | 175 |
| 2. | Fundamentals of Small-Angle X-ray Scattering | 176 |
| 3 | Analyses | 180 |
| 4 | Examples of Structure Determination | 183 |
| | References | 187 |
| Chapter 12. XAFS Analysis and Applications to Carbons and Catalysts 189 | | |
| | <i>Hiromi Yamashita</i> | |
| 1 | Introduction | 189 |
| 2 | XAFS Analysis | 190 |
| 3 | Applications to Carbon Related Materials and Catalysts | 200 |
| 4 | XAFS in the Future. | 207 |
| | References | 207 |
| Chapter 13. X-Ray Photoelectron Spectroscopy and its Application to Carbon. 211 | | |
| | <i>Noboru Suzuki</i> | |
| 1 | Introduction and XPS | 211 |
| 2 | C1s Binding Energy. | 212 |
| 3 | Application to Carbon Materials | 212 |
| | References | 220 |
| Chapter 14. Transmission Electron Microscopy 223 | | |
| | <i>Hiroyasu Saka</i> | |
| 1 | Introduction | 223 |
| 2 | Materials Characterization by Means of TEM | 223 |
| 3 | Specimen Preparation by FIB | 231 |
| 4 | In-Situ Heating Experiment | 235 |
| | References | 238 |
| Chapter 15. Electron Energy-Loss Spectroscopy and its Applications to | | |
| | Characterization of Carbon Materials. | 239 |
| | <i>Hisako Hirai</i> | |
| 1 | Introduction | 239 |
| 2 | Basic Principles of EELS and Instrumentation. | 240 |

| | | |
|---|---|-----|
| 3 | The Energy-Loss Spectrum | 242 |
| 4 | Applications to Characterizing Carbon Materials | 249 |
| 5. | Conclusions: The Future of EELS. | 254 |
| | References | 255 |
| Chapter 16. Visualization of the Atomic-scale Structure and Reactivity of Metal Carbide Surfaces Using Scanning Tunneling Microscopy 257 | | |
| <i>Ken-ichi Fukui, Rong-Li Lo and Yasuhiro Iwasawa</i> | | |
| 1 | Introduction | 257 |
| 2 | Principle of Scanning Tunneling Microscopy (STM). | 259 |
| 3 | Preparation of Mo ₂ C Surfaces | 259 |
| 4 | Visualization of the Atomic-scale Structure and Reactivity of Molybdenum Carbide Surfaces by STM | 260 |
| 5 | Conclusions and Future Prospects. | 265 |
| | References | 266 |
| Chapter 17. Infra-Red Spectra, Electron Paramagnetic Resonance, and Proton Magnetic Thermal Analysis 269 | | |
| <i>Osamu Ito, Tadaaki Ikoma and Richard Sakurovs</i> | | |
| 1 | Infra-Red (IR) Spectra. | 269 |
| 2 | EPR | 276 |
| 3 | Proton Magnetic Resonance Thermal Analysis (PMRTA) | 281 |
| | References | 283 |
| Chapter 18. Raman Spectroscopy as a Characterization Tool for Carbon Materials. 285 | | |
| <i>Masato Kakihana and Minoru Osada</i> | | |
| 1 | Introduction | 285 |
| 2 | Raman Spectra of Carbon Materials | 288 |
| 3 | Remarks about Raman Measurements | 290 |
| 4 | Recent Raman Studies of Carbon Materials | 292 |
| | References | 297 |
| Chapter 19. Basics of Nuclear Magnetic Resonance and its Application to Carbon Alloys 299 | | |
| <i>Takashi Nishizawa</i> | | |
| 1 | Introduction | 299 |
| 2 | Apparatus | 299 |
| 3 | Basics of NMR for Spin 1/2 Nucleus | 300 |
| 4 | Characterization of Pitch. | 308 |
| 5 | Solid-state ⁷ Li-NMR | 313 |
| | References | 318 |
| Chapter 20. Gas Adsorption 319 | | |
| <i>Yohko Hanzawa and Katsumi Kaneko</i> | | |
| 1 | Adsorption, Absorption, Occlusion and Storage | 319 |
| 2 | Classification of Pores and Porosity | 320 |
| 3 | Selection of an Adsorbate Molecule. | 321 |
| 4 | Surface Structure and the Adsorption Isotherm | 324 |

| | |
|--|-----|
| References | 331 |
| Chapter 21. Electrochemical Characterization of Carbons and Carbon Alloys | 335 |
| <i>Tsuyoshi Nakajima</i> | |
| 1 Introduction | 335 |
| 2 Characterization Techniques | 336 |
| 3 Electrochemical Characterization of Carbon Alloys | 340 |
| 4 Conclusions | 349 |
| References | 349 |
| Chapter 22. Mechanical Probe for Micro-/Nano-characterization | 351 |
| <i>Mototsugu Sakai</i> | |
| 1 Introduction | 351 |
| 2 Theoretical Considerations | 353 |
| 3 Experimental Details | 360 |
| 4 Application to Carbon-related Materials | 364 |
| 5 Concluding Remarks | 380 |
| References | 382 |
| Chapter 23. Magnetism of Nano-graphite | 385 |
| <i>Toshiaki Enoki, Bhagvatula L.V. Prasad, Yoshiyuki Shibayama,</i> <i>Kazuyuki Takai and Hirohiko Sato</i> | |
| 1 Introduction | 385 |
| 2 Conversion from Diamond to Graphite in Nano-scale Dimension | 386 |
| 3 Nano-graphite Network | 389 |
| 4 Fluorinated Nano-graphite | 392 |
| References | 393 |
| Chapter 24. Magnetoresistance and its Application to Carbon and Carbon Alloys | 395 |
| <i>Yoshihiro Hishiyama</i> | |
| 1 Introduction | 395 |
| 2 Background for the Magnetoresistance Measurement | 395 |
| 3 Measurement of Magnetoresistance | 400 |
| 4 Application of Magnetoresistance Technique for Synthesis of High-Quality Graphite Film from Aromatic Polyimide Film | 403 |
| 5 Negative Magnetoresistance in Boron-doped Graphites | 409 |
| References | 413 |
| Part 5. Function Developments and Application Potentials | |
| Chapter 25. Applications of Advanced Carbon Materials to the Lithium Ion Secondary Battery | 417 |
| <i>Morinobu Endo and Yoong Ahm Kim</i> | |
| 1 Introduction | 417 |
| 2 Characteristics of Li-ion Secondary Battery | 420 |
| 3 Carbon and Graphite Host Materials | 420 |
| 4 Lithium/Graphite Intercalation Compounds | 421 |
| 5 Voltage Profiles of Carbon Electrodes | 424 |
| 6 Effect of Microstructure of Carbon Anode on the Capacity | 426 |

| | | |
|---|--|-----|
| 7 | Li Storage Model | 430 |
| 8 | Conclusions | 431 |
| | References | 432 |
| Chapter 26. Electrochemical Functions | | 435 |
| <i>Mikio Miyake</i> | | |
| 1 | Features of Carbon Materials as Electrodes | 435 |
| 2 | Electrochemical Reactions on Carbon | 436 |
| 3 | Electrochemical Behavior of Various Carbons | 439 |
| 4 | Application of Carbon Electrodes | 441 |
| | References | 444 |
| Chapter 27. Electric Double Layer Capacitors | | 447 |
| <i>Soshi Shiraishi</i> | | |
| 1 | Introduction | 447 |
| 2 | Influence of Pore Size Distribution of ACFs on Double Layer Capacitance | 449 |
| 3 | Double Layer Capacitance of Other Carbon Materials | 454 |
| 4 | Conclusion. | 456 |
| | References | 456 |
| Chapter 28. Field Electron Emissions from Carbon Nanotubes | | 459 |
| <i>Yahachi Saito, Koichi Hata and Sashiro Uemura</i> | | |
| 1 | Introduction | 459 |
| 2 | FEM Study of Nanotubes | 460 |
| 3 | Nanotube-based Display Devices | 465 |
| | References | 468 |
| Chapter 29. Gas Separations with Carbon Membranes | | 469 |
| <i>Katsuki Kusakabe and Shigeharu Morooka</i> | | |
| 1 | Properties of Carbon Membranes | 469 |
| 2 | Preparation of Carbon Membranes | 472 |
| 3 | Permeances of Molecular Sieving Carbon Membranes | 474 |
| 4 | Oxidation of Molecular Sieving Carbon Membranes | 478 |
| 5 | Separation Based on Surface Flow | 480 |
| 6 | Conclusions | 481 |
| | References | 481 |
| Chapter 30. Property Control of Carbon Materials by Fluorination | | 485 |
| <i>Hidekazu Touhara</i> | | |
| 1 | Introduction | 485 |
| 2 | Control of Carbon Properties by Fluorination | 486 |
| 3 | The Chemistry of Carbon Nanotubes with Fluorine and Carbon Alloying by Fluorination | 487 |
| | References | 497 |
| Chapter 31. Preparation of Metal-loaded Porous Carbons and Their Use as a Highly Active Catalyst for Reduction of Nitric Oxide (NO). | | 499 |
| <i>Kouichi Miura and Hiroyuki Nakagawa</i> | | |
| 1 | Introduction | 499 |
| 2 | Sample Preparation. | 500 |

| | | |
|--|---|-----|
| 3 | Carbonization Behavior of the Resins. | 501 |
| 4 | Characterization of Metal Loaded Porous Carbons | 502 |
| 5 | Nitric Oxide Decomposition on Metal Loaded Porous Carbons . . . | 504 |
| 6 | Conclusions | 512 |
| | References | 512 |
| Chapter 32. Formation of a Seaweed Bed Using Carbon Fibers | | 515 |
| <i>Minoru Shiraishi</i> | | |
| 1 | Introduction | 515 |
| 2 | Rapid Fixation of Marine Organisms | 515 |
| 3 | Food Chain Through a Carbon Fiber Seaweed Bed | 518 |
| 4 | Formation of an Artificial Bed of Seaweed Using Carbon Fibers. . . | 519 |
| | References | 521 |
| Chapter 33. Carbon/Carbon Composites and Their Properties | | 523 |
| <i>Tatsuo Oku</i> | | |
| 1 | Introduction | 523 |
| 2 | Carbon Fibers and Carbon Coils | 524 |
| 3 | Novel Materials and Control of Micro-structures | 527 |
| 4 | Improvement of Properties and Correlation Between Properties and Microstructures | 531 |
| 5 | Fracture and its Mechanism | 538 |
| 6 | Microstructure Observation | 542 |
| 7 | Concluding Remarks | 542 |
| | References | 543 |
| Chapter 34. Super-hard Materials | | 545 |
| <i>Osamu Takai</i> | | |
| 1 | Super-hard Materials | 545 |
| 2 | Diamond-like Carbon | 546 |
| 3 | Carbon Nitride | 552 |
| 4 | Boron Carbonitride (B _x C _y N _z). | 556 |
| 5 | Conclusion. | 557 |
| | References | 557 |
| <i>Contributing authors.</i> | | 559 |
| <i>Subject index.</i> | | 563 |

Preface

Carbon is a unique material having diversity of structure and property. The concept of “Carbon Alloys” was initiated in Japan as a national project and is now recognized internationally. Carbon Alloys are defined as being materials mainly composed of carbon materials in multi-component systems, the carbon atoms of each component having physical and/or chemical interactive relationships with other atoms or compounds. The carbon atoms of the components may have different hybrid bonding orbitals to create quite different carbon components. We hope that this book will be a major reference source for those working with carbon alloys.

The book is divided into five parts: (1) definitions and approaches to carbon alloys; (2) analyses of results in terms of controlling the locations of other alloying elements; (3) typical carbon alloys and their preparation; (4) characterization of carbon alloys; and (5) development and applications of carbon alloys.

Prior to the preparation of this book, and as a spin-off from the carbon alloy project, we published a *Carbon Dictionary* (in Japanese) with the collaboration of Professor K. Kobayashi, Professor S. Kimura, Mr. I. Natsume and Agune-shoufu-sha Co., Ltd.

The book is published with the support of a Grant-in-Aid for Publication of Scientific Research Results (145309), provided by the Japan Society for Promotion of Science (JSPS). All workers in this project are grateful for the receipt of aid from the Grant-in-Aid for Scientific Research on Priority Area (B) 288, *Carbon Alloys*. We are also grateful to the sixty-four researchers, eight project leaders and the evaluating members of the team who promoted the Carbon Alloys project (see overleaf). On a personal note, I would like to express my thanks to Ms. K. Marui, Ms. M. Kimura, Ms. Y. Hayashi, Ms. Y. Kobayashi and Ms. M. Sasaki for their secretarial roles. I must also thank Professor M. Inagaki for reviewing the manuscripts and Professor H. Marsh for correcting the English of all thirty-four chapters of this book. I thank Professor T. Iseki for his central role leading to the publication of the book. Finally, my sincere thanks go to Elsevier Science Ltd. for publishing this book and for editing the manuscripts prior to publication.

Ei-ichi Yasuda
*Professor of Materials and Structures Laboratory
Tokyo Institute of Technology*

Members of the Carbon Alloys Project supported by Grant-in-Aid for Scientific Research on Priority Area (B) 288:

Masahiko Abe (*Science Univ. of Tokyo*), Kazuo Akashi (*Science Univ. of Tokyo*), Noboru Akuzawa (*Tokyo Nat. College of Tech.*), Norio Arai (*Nagoya Univ.*), Yong-Bo Chong (*Res. Inst. for Applied Science*), Morinobu Endo (*Shinshu Univ.*), Toshiaki Enoki (*Tokyo Inst. of Tech.*), Mitsutaka Fujita (*Univ. of Tsukuba*), Hiroshi Hatta (*The Inst. of Space and Astronaut. Science*), Shojun Hino (*Chiba Univ.*), Hisako Hirai (*Univ. of Tsukuba*), Yoshihiro Hirata (*Kagoshima Univ.*), Yoshihiro Hishiyama (*Musashi Inst. of Tech.*), Masaki Hojo (*Kyoto Univ.*), Hideki Ichinose (*The Univ. of Tokyo*), Michio Inagaki (*Aichi Inst. of Tech.*), Hiroo Inokuchi (*Nat. Space Dev. Agency of Japan*), Masashi Inoue (*Kyoto Univ.*), Kunio Ito (*The Univ. of Tokyo*), Osamu Ito (*Tohoku Univ.*), Shigeru Ito (*Science Univ. of Tokyo*), Hiroshi Iwanaga (*Nagasaki Univ.*), Yasuhiro Iwasawa (*The Univ. of Tokyo*), Kiichi Kamimura (*Shinshu Univ.*), Katsumi Kaneko (*Chiba Univ.*), Tomokazu Kaneko (*Tokai Univ.*), Teiji Kato (*Utsunomiya Univ.*), Yoshiya Kera (*Kinki Univ.*), Masashi Kijima (*Univ. of Tsukuba*), Shiushichi Kimura (*Yamanashi Univ.*), Tokushi Kizuka (*Nagoya Univ.*), Kazuo Kobayashi (*Nagasaki Univ.*), Akira Kojima (*Gunma College of Tech.*), Yoza Korai (*Kyushu Univ.*), Shozo Koyama (*Shinshu Univ.*), Noriyuki Kurita (*Toyohashi Univ. of Tech.*), Katsuki Kusakabe (*Kyushu Univ.*), Takashi Kyotani (*Tohoku Univ.*), Koji Maeda (*The Univ. of Tokyo*), Takeshi Masumoto (*Tohoku Univ.*), Takashi Matsuda (*Kitami Inst. of Tech.*), Michio Matsushashi (*Tokai Univ.*), Yohtaro Matsuo (*Tokyo Inst. of Tech.*), Michio Matsushita (*Tokyo Metropol. Univ.*), Yoshitaka Mitsuda (*The Univ. of Tokyo*), Kouichi Miura (*Kyoto Univ.*), Mikio Miyake (*Japan Adv. Inst. of Science and Tech.*), Hiroshi Moriyama (*Toho Univ.*), Seiji Motojima (*Gifu Univ.*), Tsuyoshi Nakajima (*Kyoto Univ./Aichi Inst. of Tech.*), Yoshihiro Nakata (*Hiroshima Univ.*), Yusuke Nakayama (*Ehime Univ.*), Keiko Nishikawa (*Chiba Univ.*), Hirokazu Oda (*Kansai Univ.*), Zenpachi Ogumi (*Kyoto Univ.*), Kiyoto Okamura (*Osaka Pref. Univ.*), Tatsuo Oku (*Ibaraki Univ.*), Takehiko Ono (*Osaka Pref. Univ.*), Chuhei Oshima (*Waseda Univ.*), Asao Oya (*Gunma Univ.*), Riichiro Saito (*The Univ. of Electro-Commun.*), Hidetoshi Saitoh (*Nagaoka Univ. of Tech.*), Hiroyasu Saka (*Nagoya Univ.*), Mototsugu Sakai (*Toyohashi Univ. of Tech.*), Makoto Sasaki (*Muroran Inst. of Tech.*), Shiro Shimada (*Hokkaido Univ.*), Minoru Shiraiishi (*Tokai Univ.*), Takashi Sugino (*Osaka Univ.*), Kazuya Suzuki (*Yokohama Nat. Univ.*), Noboru Suzuki (*Utsunomiya Univ.*), Takashi Suzuki (*Yamanashi Univ.*), Osamu Takai (*Nagoya Univ.*), Yoshiyuki Takarada (*Gunma Univ.*), Yoshio Takasu (*Shinshu Univ.*), Tsutomu Takeichi (*Toyohashi Univ. of Tech.*), Hisashi Tamai (*Hiroshima Univ.*), Hajime Tamon (*Kyoto Univ.*), Yasuhiro Tanabe (*Tokyo Inst. of Tech.*), Takayuki Terai (*The Univ. of Tokyo*), Akira Tomita (*Tohoku Univ.*), Hidekazu Touhara (*Shinshu Univ.*), Norio Tsubokawa (*Niigata Univ.*), Shinji Tsuneyuki (*The Univ. of Tokyo*), Yasuo Uchiyama (*Nagasaki Univ.*), Kazumi Yagi (*Hokkaido Univ.*), Tokio Yamabe (*Kyoto Univ.*), Osamu Yamamoto (*Kanagawa Inst. of Tech.*), Takakazu Yamamoto (*Tokyo Inst. of Tech.*), Hiromi Yamashita (*Osaka Pref. Univ.*), Toyohiko Yano (*Tokyo Inst. of Tech.*), Eiichi Yasuda (*Tokyo Inst. of Tech.*).

Part 1

Introduction

Chapter 1

Introduction

Ei-ichi Yasuda^a and Michio Inagaki^b

^a*Materials and Structures Laboratory, Tokyo Institute of Technology, Midori-ku, Yokohama 226-8503, Japan*

^b*Aichi Institute of Technology, Yakusa, Toyota 470-0392, Japan*

Abstract: Carbon materials having a wide range of structure, texture and properties are classified according to their C–C bonding, based on sp , sp^2 or sp^3 hybrid orbitals. A short history of these carbon materials is divided into basic science, materials development and technology development. The carbon family is composed of diamond, graphite, the fullerenes and the carbynes, each member being unique in terms of structure and texture, and also their ability to accept foreign atoms/compounds into their structures. Based on these considerations, a new strategy for the development of carbon materials, called *carbon alloys*, has been implemented in Japan which has resulted in success for developments in carbon science and technology.

Keywords: Carbon materials, Classic carbons, New carbons, Carbon family, Carbon alloys.

1 A Short History

Carbon materials have attracted the attention of human beings from prehistoric times. Carbon materials include charcoals used as heat sources, diamond crystals used not only as jewels but also for cutting and abrasion, graphite as lubricants and electrical conductors, and carbon blacks as black printing inks. Graphite electrodes, essential for metal refining, are still produced in tonnage quantities. Carbon blacks of different sizes have many applications: the small ones for tyres and the large for wet suits, etc. Activated carbons are important materials for supporting our modern lifestyle. These three carbon materials (electrode graphites, carbon blacks and activated carbons) have a long history of usage and are called *classic carbon* materials, in contrast to newly developed carbon materials the so-called *new carbons*.

Carbon materials play a part in our daily lives in various ways, many not being that obvious. For example, among the *new carbons* there are carbon fibers for reinforcing rackets and fishing rods, activated carbons as filters for deodorization in refrigerators and for water purification, membrane switches for keyboards of computers and other electronic devices including electrical conductors for automatic pencils, etc.

Table 1

Topics related to carbon materials

| Year | Basic science | Materials development | Technology development |
|------|--|--|--|
| 1960 | Mesophase spheres | Polyacrylonitrile (PAN)-based carbon fibers; Pyrolytic carbons; Glass-like carbons | Electrode for electric discharge machining |
| 1965 | | Needle-like cokes; Mesophase-pitch-based carbon fibers | |
| 1970 | Biocompatibility of carbons | Vapor-grown carbon fibers | Carbon prostheses |
| 1975 | High conductivity of graphite intercalation compounds | | Mesocarbon microbeads |
| 1980 | <i>i</i> -carbon films | Isotropic high-density graphites | Carbon electrode for fuel cell |
| 1985 | Buckminsterfullerene C ₆₀ | Carbon fiber-reinforced concrete | First wall for fusion reactor |
| 1990 | Superconductivity of K ₃ C ₆₀ ; Carbon nanotube single-wall and multiwall; Proposal of the concept of "carbon alloys" | | Carbon anode for lithium ion rechargeable batteries |
| 1995 | Storage of hydrogen in carbon nanofilaments | | Clinging of microorganisms in water to carbon fibers. Large capacity for heavy oil sorption by exfoliated graphite |

It is interesting to note how *classic carbon* materials are further developed by researchers every four to five years, and are called *old but new materials* [1,2]. Table 1 lists some representative developments since 1960, grouped under the headings of basic science, materials development and technology applications.

The year 1960 saw the beginning of the era of new carbon materials, because of the development of carbon fibers from polyacrylonitrile (PAN), of pyrolytic carbons and of glass-like carbons. Carbon fibers, first prepared from polyacrylonitrile, were extremely attractive materials by reason of their high strength and flexibility. Developments of other carbon fibers, pitch-based and vapor-grown fibers, followed in the 1970s. Japanese researchers made significant contributions to the development of these carbon fibers: Shindo with PAN-based, Otani with pitch-based, and Koyama and Endo with vapor-grown carbon fibers. Today, these three types of carbon fibers are produced on an industrial scale and have wide applications. In contrast, glass-like carbon, a hard carbon showing conchoidal (glass-like) fracture surfaces with extremely low gas permeability, found various industrial applications. A Japanese group, represented by Yamada, was deeply involved with these glassy carbons. Pyrolytic carbons were produced by a non-conventional method, namely that of chemical vapor deposition (CVD). The strong anisotropy of these pyrolytic carbons

facilitated several applications, such as the use of highly oriented pyrolytic graphite (HOPG) as a monochromator in X-ray diffractometers.

In 1964, the formation of optically anisotropic spheres during pitch pyrolysis, the so-called mesophase spheres and their coalescence were demonstrated. The detailed studies which followed into the structure of these spheres, their growth and coalescence, and formation of bulk mesophase, promoted the industrial production of needle-like cokes essential for high-power graphite electrodes, as well as mesophase-pitch-based carbon fibers with high performance and the mesocarbon microbeads (MBMC) with several applications.

Around 1970, a good biocompatibility of carbon materials was found and various prostheses, such as heart valves, tooth roots, etc., were developed. In about 1980, industrial technology for producing isotropic high-density graphite materials, using isostatic pressure, was established. These found applications as jigs for the synthesis of semiconductor crystals and also electric discharge machining. In about 1985, a composite of carbon fibers with cement paste resulted in a pronounced reinforcement of concrete. Today, not only carbon fiber reinforced concrete but also carbon fibers themselves are used in various constructions, such as buildings and bridges.

The high electrical conductivity of the AsF_5 -graphite intercalation compound, higher than metallic copper, made a strong impact. In 1990, lithium-ion rechargeable batteries were developed, where intercalation of lithium ions into a graphite anode was the essential electrochemical reaction. Research currently continues to develop further practical uses of carbons as anode materials for lithium-ion rechargeable batteries. Electrical double layer capacitors were also developed using activated carbons with extremely high surface areas.

The discovery and synthesis of buckminsterfullerene C_{60} and the superconductivity of its potassium compound K_3C_{60} in 1984 and 1990, respectively, opened up a new world in carbon materials and created world-wide research activities. Large-sized fullerenes, such as C_{70} and C_{76} , some giant fullerenes such as C_{540} , multi-wall fullerenes followed. In 1991, Iijima found single-wall and multi-walled nanotubes which offered a very promising prospect for modern nanotechnology.

In the 1990s, marked developments in technology related to applications came about; Table 1 mentions just two, i.e., carbon fibers for water purification and exfoliated graphite for heavy oil recovery.

The proposal of the idea "Carbon Alloys" by the Japanese Carbon Group in 1992 promoted research activity not only into basic science but also the technology which was related to both material preparation and applications. Most of the results of this research are described in this book.

2 Carbon Family

It is established that carbon atoms have three different hybrid orbitals, sp^3 , sp^2 and sp , and have a variety of chemical bonds. This variety in chemical bonding facilitates the formation of an enormous number of organic compounds, and it is the extension of

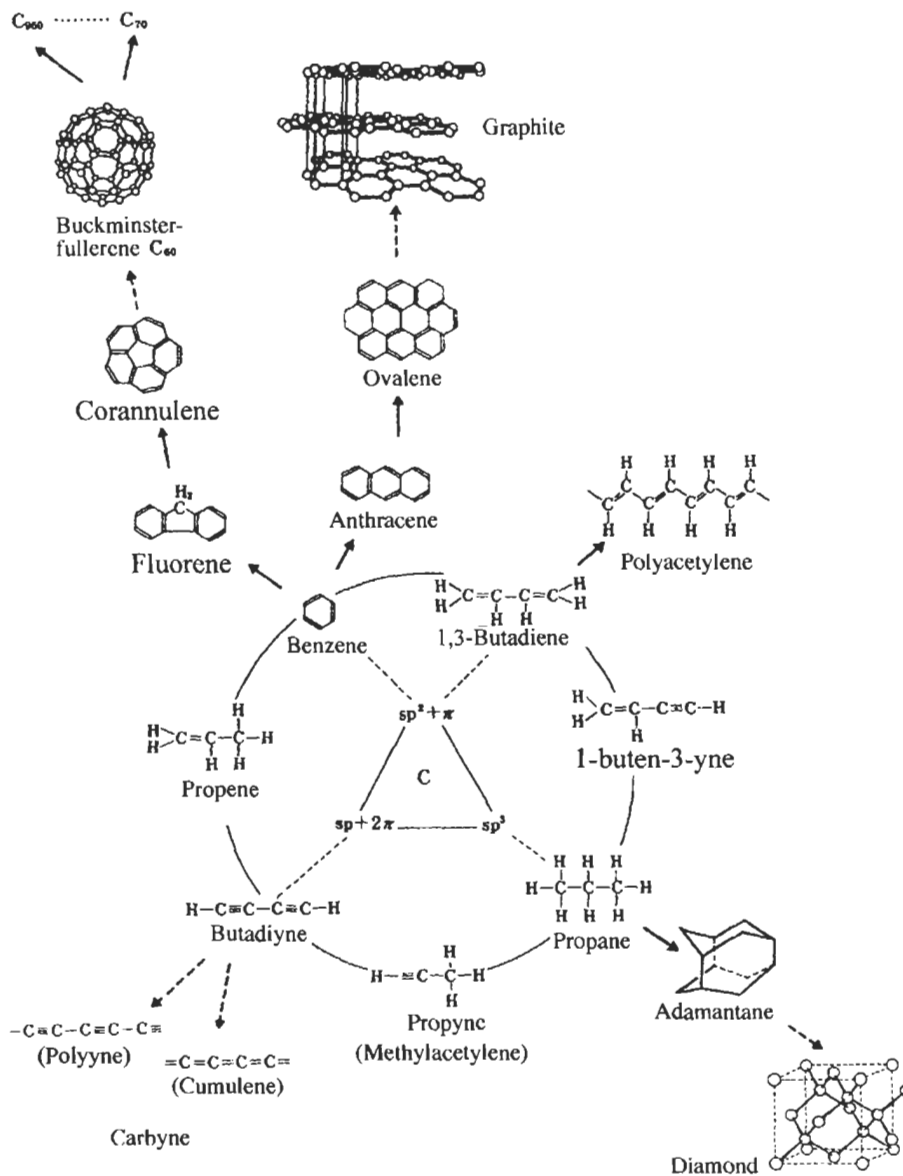


Fig. 1. Organic compounds based on carbon-carbon bonds using sp^3 , sp^2 and sp hybrid orbitals and inorganic carbon materials as their extension.

these considerations to carbon materials which is shown in Fig. 1 [1,2]. The C-C bonds using sp^3 and sp^2 hybrid orbitals result in diamond and graphite, respectively. The buckminsterfullerene C_{60} is an extension of sp^2 bonding with the carbynes utilizing sp bonding.

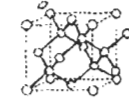
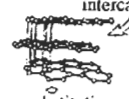
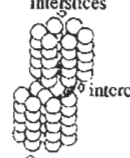

| Carbon family: | DIAMOND | GRAPHITE | CARBENE | FULLERENES |
|---|---|--|---|---|
| Dimensionality: | three-dimensional | two-dimensional | one-dimensional | zero-dimensional |
| Structural diversity: | cubic & hexagonal systems | hexagonal & rhombohedral systems | cumulene & polyene types | bucky-balls to nanotubes |
| | diamond-like carbon | diversity in structure graphitic to turbostratic diversity in texture | diversity in length & density of chains | single-wall & multiwalled |
| Possibility of accepting foreign species: | substitution  | intercalation  substitution | doping in interstices  intercalation substitution | doping in interstices  doping into sphere substitution addition |

Fig. 2. Carbon family, their dimensions, structural diversity and possibility to accept foreign species.

The family of inorganic carbon materials, the *carbon family*, consists of diamond, graphite, the fullerenes and carbynes [1,2]. Figure 2 summarizes the dimensions of the distinct structural units of each family member and indicates how heteroatoms can be added to each member.

Diamond consists of sp^3 hybrid orbitals with these covalent chemical bonds extending in three dimensions. As a result, diamonds are very hard, isotropic and electrically insulating. Long-range periodicity of these bonds gives the diamond crystal. Most diamond crystals are cubic, but some are hexagonal and so resemble zinc-blende and wurtzite, respectively, as in the compounds ZnS and BN. Where long-range periodicity is not attained, resulting from the introduction of either structural defects or hydrogen atoms, diamond-like carbon (DLC) with an amorphous structure is formed.

The family members with sp^2 bonding as represented by graphite, where the layers of carbon atoms, arranged hexagonally are stacked parallel to each other because of π -electron cloud interactions with a regularity of ABAB.... A rhombohedral ABCABC stacking also exists, belonging to the hexagonal crystal system, which occurs 'locally' by introducing stacking faults. Random stacking of imperfect layers is found in the carbons prepared at temperatures $< 1300^\circ\text{C}$. Here, the layers are small in size but where a small number of layers are stacked approximately parallel to each other, then these carbons are described as being *turbostratic*. On heating these carbons to temperatures of 3000°C , the size and number of stacked layers increase and also the regularity of stacking is improved. Hence, a wide range of structures can be obtained from the turbostratic to near-perfect ABAB graphitic stacking. Carbons of intermediate heat treatment temperatures contain variable ratios of turbostratic and graphitic stacking, with small and large crystallites, depending primarily on starting materials (precursors) and heat treatment conditions. The carbon materials

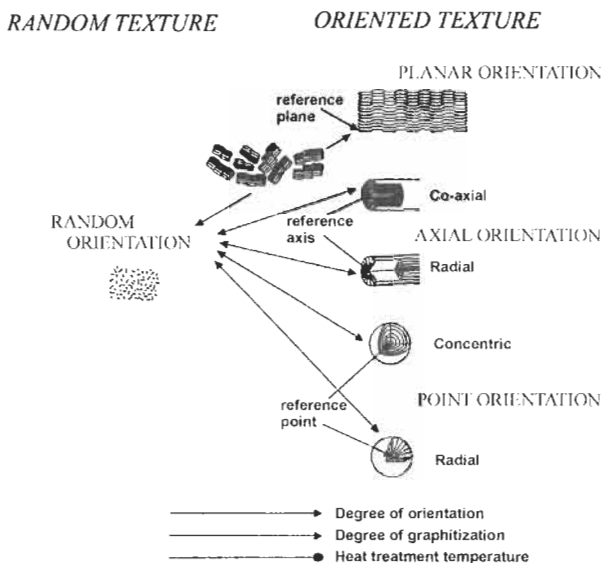


Fig. 3. Microtextures in carbon materials related to graphite.

belonging to this carbon family based on graphitic structure are electrically and thermally conducting and soft mainly because of the presence of π -electrons, in sharp contrast to diamond.

In this *graphite family* the basic structural unit is a layer of carbon atoms arranged hexagonally (not necessarily perfectly) giving these materials a strong anisotropy because the bonding in the layers is covalent and the bonding between the layers is van der Waals. The way these layers are arranged relative to each other gives diversity in texture (called *nanotexture*). A classification based upon a scheme of preferred orientation of anisotropic layers and its degree is proposed in Fig. 3. This scheme has been successfully adopted [3,4]. From the variety of nanotextures, the existence of various morphologies in carbon materials with sp^2 hybrid orbitals could be understood, for example flaky, fibrous and spherical particles.

A molecule of buckminsterfullerene C_{60} is made up of carbon atoms arranged as 12 pentagons and 20 hexagons, the C–C bondings being sp^2 hybrid orbitals. Increasing the number of hexagons beyond C_{60} separates further the pentagons leading to giant fullerenes. To separate two groups of six pentagons results in nanotubes. In this carbon family, the diversity in structure is mainly due to the number of carbon atoms existing as fullerene particles and the relative location of 12 pentagons. There are also variations in the number of layers so creating single-walled and multi-walled nanotubes.

Carbyne is made up of carbon atoms bound linearly by sp hybrid bonding, where two π -electrons resonate, giving two possibilities, namely an alternative repetition of single and triple bonds (polyne-type) or a simple repetition of double bonds

(cumulene-type). Its detailed structure is not yet clarified, but a proposed structural model is shown in Fig. 2. In this carbyne family, a diversity in structure is mainly due to the number of carbon atoms in a chain, i.e., the thickness of layers consisting of linear carbon chains, and the density of chains in a layer.

3 Carbon Alloys

Taking account of the fact that each carbon family has different structures and properties—with further diversity in structure and texture within a family—most industrial carbon materials consist of ‘blends’ of different carbons. Graphite electrodes are composites of filler coke particles of millimetre size connected with binder coke. The carbon/carbon composites are composed of carbon fibers with a fibrous morphology and micrometre-size diameter, within a matrix carbon. These are examples of combinations of carbon materials with different textures within the graphite-based family. Diamond-like carbon, however, is known to be composed of both sp^3 and sp^2 C–C bonds.

There are many possibilities for the substitution and intercalation of heteroatoms (foreign species) into the structures of each carbon family, so widening the range of possible applications. Each family has different possibilities, as summarized in Fig. 2. In diamond, only substitution by heteroatoms for carbon atoms is possible. In graphites, intercalation can occur of several species (ions, molecules and complexes), in addition to substitution by heteroatoms. In carbynes, intercalation between layers of carbon chains, doping into the space between carbon chains in a layer and also substitution are possible. The intercalation of either iron or potassium atoms is reported to stabilize the carbyne structure. In fullerenes, there are four possibilities: doping in the interstitial sites of fullerene particles, doping into the interiors of particles, substitution of foreign atoms and the adsorption (adduct) of organic radicals onto the surface of a molecule. For carbon nanotubes, the filling of the central hollow tube by metals has been attempted in order to synthesize metallic nanowires, in addition to substitution processes.

In addition to these combinations on the nanometric scale, various composite materials have been developed which have wide applications, e.g., carbon fiber-reinforced plastics and concrete and carbon materials coated by various ceramic films with oxidation resistance.

On the basis of these rapid new developments in carbon materials, with such a wide range of structures, textures and properties, and also because of the great demands on materials science from modern technology, a new concept or strategy for the development of carbon materials was needed. The Japanese Carbon Group proposed a new strategy, i.e., *carbon alloys* in 1992 [6].

The following definition of carbon alloys was tentatively suggested:

Carbon alloys are materials mainly composed of carbon atoms in multi-component systems, in which each component has physical and/or chemical interactions with each other. Here, carbons with different hybrid orbitals account as different components.

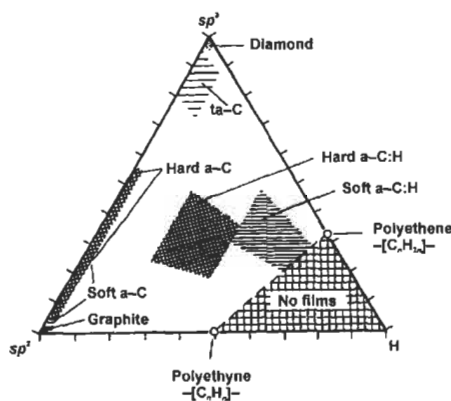


Fig. 4. Classification diagram for amorphous carbon films [7].

According to this definition, most carbon materials are carbon alloys (homo-atomic alloys), as mentioned above. The classification diagram proposed for amorphous carbon films in Fig. 4 [7] shows that such alloying gives variety in carbon materials. Amorphous carbons, which so far have been classified into one category, can be considered as carbon alloys using sp^3 and sp^2 hybrid orbitals, in addition to bonding with hydrogen. In this definition of carbon alloys, porous carbons can be understood as a combination of carbon atoms and nanospaces. In Japanese research projects (as explained later) special attention is given to 'hidden' surfaces which may give a bi-modal function to carbon materials.

Further, the concept of carbon alloys gives new possibilities for combination with other elements (hetero-atomic alloys) including combination with hydrogen (as shown in Fig. 4), for B-C-N compounds with either sp^2 , sp^3 bonds or their mixture, and a new understanding of combinations of metal carbide and carbon. In Fig. 5, the elements which have been used for alloying with carbon are marked in the Periodic Table.

Based on this concept, the Japanese Carbon Group (JCG) undertook a major research project with the Ministry of Education, Science, Sports and Culture, Grant-in-Aid for Scientific Research on Priority Areas, called "Carbon Alloys", over a period three years from 1997 with the participation of more than 60 researchers, mainly from universities. In this research project, carbon alloys were classified as follows: homo-atomic alloys, substitutional alloys, intercalation alloys, surface-and/or hidden surface controlled alloys, and microstructure controlled alloys. Special attention was paid to space control and function development by alloying with carbons. The formation of carbon alloys may be considered as the filling of space by carbon atoms with different hybrid orbitals and foreign atoms, because sp^3 carbon gives three-dimensional alignment, sp^2 carbon gives two-dimensional planar structures and sp carbon is linear. The incorporation of foreign atoms, either substitutionally or interstitially, may give strain in the structure due to the different

| | | | | | | | | | | | | | | | | | |
|----|----|----|----|----|----|----|----|----|----|----|----|----|----|----|----|----|----|
| H | | | | | | | | | | | | | | | | | He |
| Li | Be | | | | | | | | | | | B | C | N | O | F | Ne |
| Na | Mg | | | | | | | | | | | Al | Si | P | S | Cl | Ar |
| K | Ca | Sc | Ti | V | Cr | Mn | Fe | Co | Ni | Cu | Zn | Ga | Ge | As | Se | Br | Kr |
| Rb | Sr | Y | Zr | Nb | Mo | Tc | Ru | Rh | Pd | Ag | Cd | In | Sn | Sb | Te | I | Xe |
| Cs | Ba | La | Hf | Ta | W | Re | Os | Ir | Pt | Au | Hg | Tl | Pb | Bi | Po | At | Rn |
| Fr | Ra | | | | | | | | | | | | | | | | |
| | | La | Ce | Pr | Nd | Pm | Sm | Eu | Gd | Tb | Dy | Ho | Er | Yb | Lu | | |
| | | Ac | Th | Ra | U | Np | Pu | Am | Cm | Bk | Cf | Es | Fm | Md | Lr | | |

Fig. 5. The Periodic Table indicating the elements used for carbon alloys. Elements used for: direct interaction with carbon (red) and causing modifications to carbon materials (blue).

sizes of foreign atoms. In other words, the preparation of carbon alloys is the control of space by filling with carbon and foreign atoms, and, as a consequence of this space control, novel applications are hoped for. This research project has made significant advances in many areas.

This concept led to the formation of nano- and micro-sized spaces in different carbon alloys, and also to nano-sized carbon materials for various energy storage devices. Other research projects on “Creation of functional nano- and micro-sized spaces in carbon materials” and “Basic science and application of nanocarbons developed for advanced energy devices” were part of the Future Research Program of the Japan Society for the Promotion of Science for five years from 1996 and 1999, respectively. The main results of the former project are published in the journal *Synthetic Metals* as a special issue [8].

References

1. M. Inagaki and Y. Hishiyama, *New Carbon Materials*. Gihoudou Pub., 1994.
2. M. Inagaki, *New Carbons—Control of Structure and Functions*. Elsevier Science, 2000.
3. M. Inagaki, *Microtextures in carbon materials*. Tanso, 114–122, 1985.
4. Y. Hishiyama, Y. Kaburagi and M. Inagaki, Characterization of structure and microtexture of carbon materials by magnetoresistance technique. In: P. Thrower (Ed.), *Chemistry and Physics of Carbon*, Vol. 23. Marcel Dekker, pp. 1–68, 1991.
5. Y. Yamada and M. Inagaki, *Synthesis and structure of carbyne*. Tanso, 178: 122–127, 1997.
6. Y. Tanabe and E. Yasuda, *Carbon alloys*. Carbon, 38: 329–334, 1995.
7. P.K. Bachmann, *Ullman's Encyclopedia of Industrial Chemistry*, Vol. A26, pp. 72–25, 1996.
8. M. Inagaki (Ed.) *Creation of functional nano- and micro-sized spaces in carbon materials*. Special issue of *Synthetic Metals*, 125: 139–266, 2002.

Part 2

Space Control in Carbon Alloys

Chapter 2

Hybrid Orbital Control in Carbon Alloys

Riichiro Saito*

*Department of Electronic-Engineering, University of Electro-Communications, Chofu, Tokyo,
182-8585 Japan*

Abstract: The basic concept of sp^n hybridization for carbon atoms is discussed and an analytical expression for general sp^n hybridization is given. When a third chemical bond from two given chemical bonds is constructed in a general sp^3 hybridization, there is a forbidden region of directions for the third chemical bond. The sp^2 hybridization of graphite can be modified to sp^3 hybridization by doping with a halogen atom. Defect states induced by structural disorder, doping and a finite crystalline size are essential to control hybridization in carbon materials. This hybridization is characterized by experiment using Raman scattering, XPS and STM/STS techniques.

Keywords: Hybridization, Core level, XPS, Raman, Isomers, Fullerenes, Nanotubes.

1 Hybridization in a Carbon Atom

1.1 Introduction

Carbon is a unique element which has several hybridized forms of atomic orbitals in various carbon-based materials. Hybridization of atomic orbitals is defined by the mixing of atomic orbitals, which possess different angular momenta, s, p, \dots , so as to change the direction of the chemical bonds and to lower the total energy of the molecule. Because the number of chemical bonds for a carbon atom can be changed by constructing different hybridizations, there exist many carbon isomers possessing zero to three-dimensional solid structures. For example, fullerene, carbynes, graphite, and diamond are zero-, one-, two-, and three-dimensional carbon isomers respectively in which two, three, and four chemical bonds per carbon atom, known as σ bonds, are connected to the nearest-neighbor carbon atoms. Further, new forms of carbon, such as fullerenes and carbon nanotubes [1,2], are spherical-and tubular-shaped carbon isomers, in which three chemical bonds per carbon atom make a hexagonal network. These fullerenes and nanotubes are possible by placing twelve

Present address: Department of Physics, Tohoku University, Sendai, 780-8578, and CREST, JST, Japan.

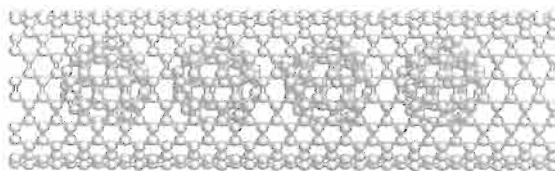


Fig. 1. Peapod: fullerenes encapsulated in a single wall carbon nanotube. Here four C_{60} molecules are encapsulated in the (10,10) armchair carbon nanotubes.

pentagonal rings into a hexagonal planar network, to create a closed surface. Photopolymerization of fullerenes is used to change the dimensionality of fullerenes by changing the hybridization and by connecting carbon atoms in different molecules [3–5]. Fullerenes, encapsulated in a single wall carbon nanotube (see Fig. 1), called a “peapod”, are a new concept for combining structures with different dimensions within a single molecule [6]. Hence, an understanding of hybridization of carbon atoms is essential for constructing new forms of carbon. This chapter discusses the hybridization of carbon atoms and shows that the directions of chemical bonds within a molecule cannot always be anticipated.

Another important issue of carbon materials is that the solid state properties of carbons depend strongly on defect concentration and crystallite size. Because of the high melting point of carbon, the crystallite size can be controlled by varying the heat treatment temperature (HTT), which can modify the properties of carbons significantly. For example, the surface area and the crystallite size of a carbon fiber is controlled by HTT from 700 to 1500°C [7–9]. The performance of carbon fibers by lithium doping in a secondary battery [7,10] and for gas absorption is better for carbons of lower HTT, which corresponds to a smaller crystallite size. Recently, the zigzag edge of a graphite crystal has been shown to have special electronic states, which appear as the Fermi energy [11]. Such states cannot be neglected in samples with relatively small crystallite size (2–3 nm) called “nano-graphite”. In amorphous carbons, on the other hand, the mixing of different hybridizations restricts the ordering of the crystal structure, in which the local geometry of the chemical bonds cannot be changed easily. Such materials are known to be very stiff and are called “hard carbons”. In the planar graphene structure, a pentagonal or a heptagonal ring can be a topological defect in the electronic structure. Here, a topological defect means that the hexagonal network cannot be divided into two sub-lattices by a pentagonal or a heptagonal defect, even though every carbon atom has three chemical bonds. Single-wall carbon nanotubes have not only an outer surface, but also an inner surface consisting of a hollow core. Because the cap of a single wall carbon nanotube can be opened by oxidation, the inner space can be considered as a new chemical reaction space. In fact, polymerizations of fullerenes occur in the “peapod”. In this way, new concepts for carbons have appeared in recent years. In this chapter we give an overview of the progress made in discovering new forms of carbon materials based on the keyword “hybridization”.

A variety of forms of hybridization thus generates many interesting carbon structures, each of which has its own special electronic and photon structure. This chapter introduces the basic idea of the hybridization of a carbon atom and gives an analytic formula for general sp^n hybridization. Then, a possible modification is presented of the planar sp^2 hybridization by doping the carbon with fluorine atoms. Finally the various spectroscopic techniques for observing sp^n hybridization are discussed.

1.2 Atomic Orbitals of Carbon Atoms

Carbon is the sixth element of the periodic table and is listed at the top of column IV. An electrically neutral carbon atom has six electrons which occupy $1s^2$, $2s^2$, and $2p^2$ atomic orbitals in the ground state. The $1s^2$ orbital contains two strongly bound electrons, called core electrons, whose one-electron energy is about 285 eV below the vacuum level. Four electrons occupy the $2s^2$ and $2p^2$ orbitals. Those electrons which contribute to the chemical bonding are called valence electrons. In the crystalline phase the valence electrons give rise to $2s$, $2p_x$, $2p_y$, and $2p_z$ orbitals which are important in forming covalent bonds in carbon materials.

Because the energy difference between the upper $2p$ energy level and the lower $2s$ level in carbon is relatively small (4 eV) compared with the energy gain in forming the chemical bonds, the electronic wavefunctions for these four electrons can mix with each other, thereby changing the occupation of the $2s$ and three $2p$ atomic orbitals to enhance the binding energy of the C atom with its neighboring atoms. In fact, in the free carbon atom, the excited state, $2s2p^3$, which is denoted by 3S , is 4.18 eV above the ground state 3P using the general notation for a multiplet of electrons. The mixing of a single $2s$ orbital with n ($=1,2,3$) $2p$ orbitals is defined by sp^n hybridization [12].

In carbon, three possible hybridizations occur: sp , sp^2 and sp^3 ; other group IV elements such as Si, Ge exhibit only sp^3 hybridization. Because there are inner p atomic orbitals for Si and Ge, electron–electron repulsions of electrons between the inner and outer electronic shells of an atom facilitate the directions for sp^3 hybridization. An example is the (1,1,1) direction for outer valence orbitals in which the inner p orbitals have charge densities along the x , y and z axes. Here, the axes are defined by each atom. On the other hand, there are no “difficult” directions for the hybridized orbitals in a carbon atom because a carbon atom has a spherical $1s$ orbital as an inner shell. This fact is so relevant to the existence of so many different carbon isomers.

The following shows how to mix atomic orbitals to produce sp , sp^2 and sp^3 orbitals. Regular solutions of sp , sp^2 and sp^3 hybridization give bond angles, respectively, of 180° , 120° , and 109.47° , which are obtained from $\cos^{-1}(-1/n)$, ($n=1,2,3$). However, in fullerenes and carbon nanotubes, a pentagonal ring gives a different sp^2 bonding from that for a hexagonal ring. Furthermore, the curvature in carbon nanotubes gives a modification to their sp^2 bonding as in a graphene sheet, and this affects their electronic structure, especially for small diameters of less than 1 nm. In amorphous carbon, the directions of the nearest neighbor carbon atoms are distorted from the

regular tetrahedral directions, (1,1,1), (-1,-1,1), (-1,1,-1) and (1,-1,-1). For amorphous carbon, it is not always possible to get four chemical bonding directions per C atom, and sp^2 and sp hybridization may appear in some cases of bonding to neighbor atoms. A general expression is presented here for sp^n hybridizations which describes the forbidden range of directions for a chemical bond.

1.3 sp Hybridization

In sp hybridization, a linear combination of the $2s$ orbital and one of the $2p$ orbitals of a carbon atom, for example $2p_x$, is formed. From these two atomic orbitals of a carbon atom, two hybridized sp atomic orbitals, denoted by $|sp_1\rangle$ and $|sp_2\rangle$, expressed by the linear combination of $|2s\rangle$ and $|2p_x\rangle$ wave functions of the carbon atom

$$\begin{aligned} |sp_1\rangle &= C_1|2s\rangle + C_2|2p_x\rangle \\ |sp_2\rangle &= C_3|2s\rangle + C_4|2p_x\rangle, \end{aligned} \quad (1)$$

where the C_i are coefficients. Using the ortho-normality conditions $\langle sp_i | sp_j \rangle = \delta_{ij}$, where δ_{ij} is either 1 or 0 depending on whether $i = j$ or $i \neq j$, respectively, we obtain the relationship between the coefficients C_i :

$$\begin{aligned} C_1C_3 + C_2C_4 &= 0, \quad C_1^2 + C_2^2 = 1 \\ C_3^2 + C_4^2 &= 1, \quad C_1^2 + C_3^2 = 1. \end{aligned} \quad (2)$$

The last equation is given because the sum of the squares of $|2s\rangle$ components in $|sp_1\rangle$ and $|sp_2\rangle$ is unity. An orthonormal solution of Eq. (2) is $C_1 = C_2 = C_3 = 1/\sqrt{2}$ and $C_4 = -1/\sqrt{2}$ so that

$$\begin{aligned} |sp_1\rangle &= \frac{1}{\sqrt{2}} (|2s\rangle + |2p_x\rangle) \\ |sp_2\rangle &= \frac{1}{\sqrt{2}} (|2s\rangle - |2p_x\rangle) \end{aligned} \quad (3)$$

Figure 2 shows a schematic view of the directed valence of the $|2s\rangle + |2p_x\rangle$ $|sp_1\rangle$ orbital. The shading denotes a negative amplitude of the wave function. Here, the radial wave function of the $2s$ orbitals has a node around $r = 0.2 \text{ \AA}$ (0.02 nm) because of the orthogonality with $1s$ orbitals, while that of the $2p$ orbitals has no nodes except for $r = 0$ in the radial direction. Figure 2 defines a positive amplitude of the $2s$ wave function for a given radius for $r > 0.2 \text{ \AA}$ for simplicity. The sign of the wave-function is not essential to physical properties as long as the definition of the sign is consistent within the discussion. In this definition, the wave function of $|2s\rangle + |2p_x\rangle$ is elongated in the positive direction of x (Fig. 2), while that of $|2s\rangle - |2p_x\rangle$ is elongated in the



Fig. 2. sp hybridization. The shading denotes the positive amplitude of the wave function. $|2s\rangle + |2p_x\rangle$ is elongated in the positive direction of x .

negative direction of x . Thus, when nearest-neighbor atoms are in the direction of the x axis, the overlap of $|sp_1\rangle$ with the wave function at $x > 0$ becomes larger compared with the original $|2p_x\rangle$ function, so giving rise to a larger binding energy. If $|2p_y\rangle$ for $|2p_x\rangle$ is selected, the wave function shows a valence in the direction of the y axis.

It is important to emphasize that the solution of Eq. (3) is not a unique solution of Eq. (2). Below we give a general solution of Eq. (2). Generality is not lost when $C_1 = \sin\theta_1$, $C_2 = \cos\theta_1$, $C_3 = \sin\theta_2$, and $C_4 = \cos\theta_2$, and use the orthogonal condition, $C_1C_3 + C_2C_4 = 0$ which becomes

$$\sin\theta_1 \sin\theta_2 + \cos\theta_1 \cos\theta_2 = \cos(\theta_1 - \theta_2) = 0, \quad (4)$$

and gives $\theta_1 - \theta_2 = \pm \pi/2$, so that we obtain $\sin\theta_2 = \pm \cos\theta_1$ and $\cos\theta_2 = \mp \sin\theta_1$. Thus, a general solution of sp hybridization is given by denoting θ_1 simply by θ in the relations

$$\begin{aligned} |sp_1\rangle &= \sin\theta|2s\rangle + \cos\theta|2p_x\rangle \\ |sp_2\rangle &= \mp \cos\theta|2s\rangle \pm \sin\theta|2p_x\rangle, \end{aligned} \quad (5)$$

where the sign is taken so that $|sp_2\rangle$ is elongated in the opposite direction to $|sp_1\rangle$. This general sp solution is a two-dimensional unitary transformation which belongs to the special orthogonal group (SO(2)) of $|2s\rangle$ and $|2p_x\rangle$. The angle θ and the signs in Eq. (5) are determined for each molecular orbital, so as to minimize the total energy of the molecule. The elongation and the asymmetric shape of the sp hybridized orbital become maxima for $\theta = \pm \pi/4$ which corresponds to Eq. (3). When the two nearest neighbor atoms are different elements, the coefficients are shifted from $\theta = \pm \pi/4$.

When an asymmetric shape of the charge density (see Fig. 2) is needed to form a chemical bond then a mixing of $2p$ orbitals with $2s$ orbitals occurs. The mixing of $2p$ orbitals, only, with each other gives rise to the rotation of $2p$ orbitals, because the $2p_x$, $2p_y$, and $2p_z$ orbitals behave as a vector (x, y, z) . The wave function $C_x|2p_x\rangle + C_y|2p_y\rangle + C_z|2p_z\rangle$, where $C_x^2 + C_y^2 + C_z^2 = 1$, is the $2p$ wave function whose direction of positive amplitude is the direction (C_x, C_y, C_z) . The $2p$ wave functions of Eq. (3) correspond to $(C_x, C_y, C_z) = (1, 0, 0)$ and $(C_x, C_y, C_z) = (-1, 0, 0)$, respectively.

A simple carbon-based material showing sp hybridization is acetylene, $\text{HC}\equiv\text{CH}$, where \equiv is used by chemists to denote a triple bond between two carbon atoms. The acetylene molecule $\text{HC}\equiv\text{CH}$ is a linear molecule with each atom having its

equilibrium position along a single axis and with each carbon atom exhibiting sp hybridization. The hybridized $|sp_1\rangle$ orbital for a carbon atom in the $\text{HC}\equiv\text{CH}$ configuration makes a covalent bond with the $|sp_2\rangle$ orbital for the other carbon atom, and this bond is called a σ bond. In a bonding molecular orbital, the amplitude of the sp wave functions has the same sign in the chemical bonding region between atoms, while there is a node for anti-bonding orbitals. The hybridization parameter θ of Eq. (5) for each C atom depends on the molecular orbital or on the energy. The $2p_y$ and $2p_z$ wave functions of each carbon atom are perpendicular to the σ bond, and the $2p_y$ and $2p_z$ wave functions form relatively weak bonds, called π bonds, with those of the other carbon atom. Thus, one σ bond and two π bonds yield the triple bond of $\text{HC}\equiv\text{CH}$. When the bond angle $\text{H}-\text{C}\equiv\text{C}$ of $\text{HC}\equiv\text{CH}$ is 180° , it is not possible for $2p_y$ and $2p_z$ to be hybridized with a $2s$ orbital. This point is discussed analytically in Section 1.7.

1.4 sp^2 Hybridization

In sp^2 hybridization, the $2s$ orbital and the two $2p$ orbitals, for example $2p_x$ and $2p_y$, are hybridized. An sp^2 hybridization in *trans*-polyacetylene, $(\text{HC}=\text{CH})_n$, is as shown in Fig. 3, where carbon atoms form a zigzag chain with an angle of 120° . All σ bonds shown in Fig. 3 are in an (xy) plane, and, in addition, a π orbital for each carbon atom exists perpendicular to the plane. Because the directions of the three σ bonds of the central carbon atom in Fig. 3 are $(0, -1, 0)$, $(\sqrt{3}/2, 1/2, 0)$, and $(-\sqrt{3}/2, 1/2, 0)$, the corresponding sp^2 hybridized orbitals $|sp_i^2\rangle$ ($i = 1, 2, 3$) are made from $2s$, $2p_x$, and $2p_y$ orbitals, as follows:

$$\begin{aligned} |sp_1^2\rangle &= C_1|2s\rangle - \sqrt{1-C_1^2}|2p_y\rangle \\ |sp_2^2\rangle &= C_2|2s\rangle - \sqrt{1-C_2^2}\left\{\frac{\sqrt{3}}{2}|2p_x\rangle + \frac{1}{2}|2p_y\rangle\right\} \\ |sp_3^2\rangle &= C_3|2s\rangle - \sqrt{1-C_3^2}\left\{-\frac{\sqrt{3}}{2}|2p_x\rangle + \frac{1}{2}|2p_y\rangle\right\} \end{aligned} \quad (6)$$

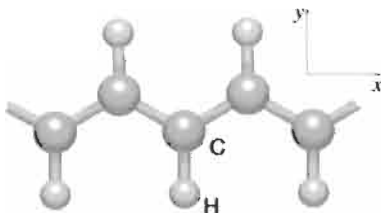


Fig. 3. *Trans*-polyacetylene, $(\text{HC}=\text{CH})_n$, where the carbon atoms form a zigzag chain with an angle of 120° , through sp^2 hybridization. All σ bonds shown are in the xy plane, and in addition, one π orbital per carbon atom exists perpendicular to the plane.

It is now possible to determine the coefficients C_1 , C_2 , and C_3 . From the orthonormality requirements of the $|sp_i^2\rangle$ and $|2s\rangle$, $|2p_{x,y}\rangle$ orbitals, three equations can be obtained to determine the coefficients, C_i ($i = 1, \dots, 3$):

$$\begin{aligned} C_1^2 + C_2^2 + C_3^2 &= 1 \\ C_1 C_2 &= \frac{1}{2} \sqrt{1 - C_1^2} \sqrt{1 - C_2^2} = 0 \\ C_1 C_3 &= \frac{1}{2} \sqrt{1 - C_1^2} \sqrt{1 - C_3^2} = 0, \end{aligned} \quad (7)$$

yielding a solution of Eq. (7) given by $C_1 = C_2 = C_3 = 1/\sqrt{3}$. The sp^2 orbitals thus obtained have a large amplitude in the direction of the three nearest-neighbor atoms, and these three-directed orbitals are denoted by *trigonal* bonding. There are two kinds of carbon atoms in polyacetylene, as shown in Fig. 3, denoting different directions for the nearest-neighbor hydrogen atoms. For the upper carbon atoms in Fig. 3, the coefficients of the $|2p_y\rangle$ terms in Eq. (6) are positive, but change to $-|2p_y\rangle$ for the lower carbon atoms in Fig. 3.

1.5 A Pentagonal Ring

For a pentagonal or heptagonal ring, sp^2 hybridization is constructed differently from the regular sp^2 hybridization of Eq. (7) as long as the ring exists within a plane. In general, the three chemical bonds do not always lie in a plane, such as for a C_{60} molecule, and thus a general sp^3 hybridization has to be considered. However, it is useful to consider the general sp^2 hybridization before showing the general sp^3 hybridization.

Here we consider the coefficients C_i for a carbon atom O at $(0,0,0)$ in a planar pentagonal ring, as shown in Fig. 4. The two nearest carbon atoms of the pentagonal ring are the atom A on the x axis and the atom B which is obtained by rotating the atom A by 108° around O . Further, a hydrogen atom H is considered in the plane of the three atoms whose direction is given by rotating atom A by -126° around O . With the substitutions $\beta = \cos 108^\circ$ and $\gamma = \cos 126^\circ$, it is possible to write:

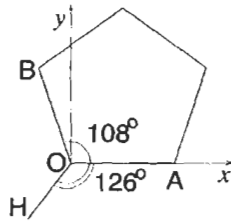


Fig. 4. A pentagonal ring. We will consider the sp^2 hybridization of the atom O , where A and B are nearest neighbor carbon atoms and H is a hydrogen atom.

$$\begin{aligned}
 |sp_1^2\rangle &= C_1|2s\rangle + \sqrt{1-C_1^2}|2p_x\rangle \\
 |sp_2^2\rangle &= C_2|2s\rangle + \sqrt{1-C_2^2}\{\beta|2p_x\rangle + \sqrt{1-\beta^2}|2p_y\rangle\} \\
 |sp_3^2\rangle &= C_3|2s\rangle + \sqrt{1-C_3^2}\{\gamma|2p_x\rangle + \sqrt{1-\gamma^2}|2p_y\rangle\}
 \end{aligned} \tag{8}$$

From the ortho-normality conditions, we obtain

$$\begin{aligned}
 C_1 &= \sqrt{\frac{\beta\gamma}{\alpha}} \\
 C_2 &= \sqrt{\frac{(\alpha-\beta\gamma)\beta}{\gamma+(\alpha-\beta\gamma)\beta}} \\
 C_3 &= \sqrt{\frac{(\alpha-\beta\gamma)\gamma}{\beta+(\alpha-\beta\gamma)\gamma}},
 \end{aligned} \tag{9}$$

in which α is given by

$$\alpha = \sqrt{(1-\beta^2)(1-\gamma^2)} \tag{10}$$

If we put $\beta = \gamma = \cos 120^\circ = -1/2$, we obtain $\alpha = 3/4$ and the regular sp^2 result of Eq. (6) for a hexagonal ring. For a heptagonal ring, the solution is given by using $\beta = \cos(180-360/7)^\circ$ and $\gamma = \cos(90+180/7)^\circ$. It is easy to extend this formula for an m membered ring ($m \geq 5$) and a solution can be found by taking $\beta = \cos(180-360/m)^\circ$ and $\gamma = \cos(90+180/m)^\circ$. In the limit of $m \rightarrow \infty$, $\beta = -1$, $\gamma = 0$, $\alpha = 0$ and $\gamma/\alpha \rightarrow -1/2$, we obtain $C_1 = C_2 = \sqrt{1/2}$ and $C_3 = 0$, which correspond to sp hybridization given by Eq. (3). It is to be noted that there is no real solution of Eq. (9) for $m = 3$ and $m = 4$. Thus, the present result is a general expression within a planar sp^2 hybridization.

1.6 sp^3 Hybridization

It is not possible for four chemical bonds to exist in a plane. If it were possible, then an axis perpendicular to the plane could be taken, for example the z axis, when there would be no component $|2p_z\rangle$, for the four chemical bonds, so giving an unphysical result that four chemical bonds could be constructed from three atomic orbitals. Thus, in sp^3 hybridization, four chemical bonds cannot be in a plane simultaneously. The carbon atoms in methane, (CH_4), provide a simple example of sp^3 hybridization through its tetrahedral bonding of the carbons to its four nearest neighbor hydrogen atoms which have a maximum spatial separation from each other. The four directions of the tetrahedral bonds from the carbon atom can be selected as $(1,1,1)$, $(-1,-1,1)$, $(-1,1,-1)$, $(1,-1,-1)$. In order to make elongated wave functions to these directions,

the $2s$ orbital and three $2p$ orbitals are mixed with each other, forming an sp^3 hybridization. Using equations similar to Eq. (6) but with four unknown coefficients, C_i , ($i = 1, \dots, 4$), and orthonormal atomic wave functions, the sp^3 hybridized orbitals can be obtained in these four directions:

$$\begin{aligned}
 |sp_1^3\rangle &= \frac{1}{2} \{ |2s\rangle + |2p_x\rangle + |2p_y\rangle + |2p_z\rangle \} \\
 |sp_2^3\rangle &= \frac{1}{2} \{ |2s\rangle - |2p_x\rangle - |2p_y\rangle + |2p_z\rangle \} \\
 |sp_3^3\rangle &= \frac{1}{2} \{ |2s\rangle - |2p_x\rangle + |2p_y\rangle - |2p_z\rangle \} \\
 |sp_4^3\rangle &= \frac{1}{2} \{ |2s\rangle + |2p_x\rangle - |2p_y\rangle - |2p_z\rangle \}
 \end{aligned} \tag{11}$$

When a crystal lattice is constructed in the sp^3 hybridized form, the resultant structure is diamond. All the valence chemical bonds are σ bonds and the material thus obtained is stable and has a large energy gap at the Fermi energy level. However, at the surface of the crystal, the dangling bonds generated by sp^3 hybridization do not have so much energy, so that the structure is deformed to a lower symmetry than Eq. (11) indicated, and this is known as surface reconstruction. As a result, the crystal growth of diamond becomes difficult at room temperature and ambient pressure where amorphous carbon or amorphous graphite are produced from the gas phase. This situation can be understood partially by the restrictions imposed on the direction of the chemical bonds for a general sp^3 hybridization. The next subsection considers a general solution to sp^3 hybridization.

1.7 General sp^3 Hybridization

When there are four nearest neighbor atoms, it is not always possible to construct general sp^3 covalent bonds by mixing $2s$ orbital with $2p$ orbitals. A clear example where four chemical bonds cannot be made occurs when three of four neighbor atoms are close to one another. In this case, correspondence of $2p$ orbitals in the direction of three carbon atoms from the original atom is not sufficient to contribute to the elongation of the wave functions at the same time. Here, an sp^3 hybridization cannot be made, but an sp^2 or sp hybridization may be possible.

Such a situation is investigated by specifying the conditions needed to form an sp^3 hybridization and is as follows. Here the original carbon atom O is put at $(0,0,0)$ and the four atoms A, B, C, D are placed in the directions of $\vec{a}, \vec{b}, \vec{c}, \vec{d}$ from O , respectively. Although the lengths of the four vectors are taken to be unity, the distances of the four atoms from O do not need to be unity. When we define $\vec{p} = (|p_x\rangle, |p_y\rangle, |p_z\rangle)$ and when we denote the coefficient $C_i = \sin\theta_i$, ($i = 1, \dots, 4$), the four hybridized orbitals are given by

$$\begin{aligned}
|sp_1^3\rangle &= \sin\theta_1|2s\rangle + \cos\theta_1(\vec{a}\cdot\vec{p}) \\
|sp_2^3\rangle &= \sin\theta_2|2s\rangle + \cos\theta_2(\vec{b}\cdot\vec{p}) \\
|sp_3^3\rangle &= \sin\theta_3|2s\rangle + \cos\theta_3(\vec{c}\cdot\vec{p}) \\
|sp_4^3\rangle &= \sin\theta_4|2s\rangle + \cos\theta_4(\vec{d}\cdot\vec{p})
\end{aligned} \tag{12}$$

where $(\vec{a}\cdot\vec{p}) = a_x|2p_x\rangle + a_y|2p_y\rangle + a_z|2p_z\rangle$ etc. and $0 < \theta_i < \pi$ is defined without losing generality. Now, seven unknown variables need to be considered, namely four θ_i , variables ($i = 1,4$) and 3 variables d_x , d_y , and d_z . Because we have six orthogonality conditions between the hybridized orbitals, we can write $\langle\varphi_i|\varphi_j\rangle = 0$ for $i \neq j$, and we have an additional equation that the length of \vec{d} is unity. The seven unknown variables are then expressed by the remaining variables, listed as the six orthonormal equations:

$$\begin{aligned}
\tan\theta_1 \tan\theta_2 &= -\vec{a}\cdot\vec{b} \\
\tan\theta_2 \tan\theta_3 &= -\vec{b}\cdot\vec{c} \\
\tan\theta_3 \tan\theta_1 &= -\vec{c}\cdot\vec{a} \\
\tan\theta_1 \tan\theta_4 &= -\vec{a}\cdot\vec{d} \\
\tan\theta_2 \tan\theta_4 &= -\vec{b}\cdot\vec{d} \\
\tan\theta_3 \tan\theta_4 &= -\vec{c}\cdot\vec{d}
\end{aligned} \tag{13}$$

where the inner product of $\vec{a}\cdot\vec{b}$, etc. corresponds to $\cos\angle AOB$, in which $\angle AOB$ is the bond angle between \vec{a} and \vec{b} . From the first three equations of Eq. (13) we obtain

$$\begin{aligned}
\tan^2\theta_1 &= -\frac{(\vec{a}\cdot\vec{b})(\vec{a}\cdot\vec{c})}{(\vec{b}\cdot\vec{c})} \\
\tan^2\theta_2 &= -\frac{(\vec{b}\cdot\vec{c})(\vec{b}\cdot\vec{a})}{(\vec{c}\cdot\vec{a})} \\
\tan^2\theta_3 &= -\frac{(\vec{c}\cdot\vec{a})(\vec{c}\cdot\vec{b})}{(\vec{a}\cdot\vec{b})}
\end{aligned} \tag{14}$$

In order to have real values for θ_i , ($i = 1,2,3$), the product of $(\vec{a}\cdot\vec{b})(\vec{a}\cdot\vec{c})(\vec{b}\cdot\vec{c})$ must be negative. This condition is satisfied when: (1) all three inner products are negative, or (2) two of the three inner products are positive and one is negative. In other words, sp^3

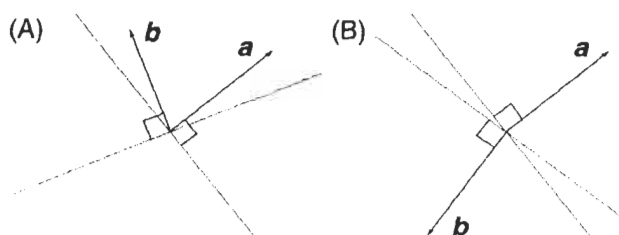


Fig. 5. The shaded region denotes the possible directions of \vec{c} for the cases: (A) $\vec{a} \cdot \vec{b} > 0$ and (B) $\vec{a} \cdot \vec{b} < 0$. The vector \vec{c} should satisfy the following relations for the cases (A) $(\vec{a} \cdot \vec{c})(\vec{b} \cdot \vec{c}) < 0$ and (B) $(\vec{a} \cdot \vec{c})(\vec{b} \cdot \vec{c}) > 0$, so as to get real solutions for Eq. (14). The figures A and B are seen from the direction perpendicular to the plane made by \vec{a} and \vec{b} .

hybridization is not possible when (a) all three inner products are positive, or (b) one of them is positive and two are negative.

Figure 5 shows the shaded regions in which \vec{c} is allowed for sp^3 hybridization for the cases (A) $\vec{a} \cdot \vec{b} > 0$ and (B) $\vec{a} \cdot \vec{b} < 0$. Here we see the three-dimensional shaded region from a direction perpendicular to the plane determined by \vec{a} and \vec{b} . When \vec{c} is not along a direction in the shaded region between two planes which are perpendicular to \vec{a} and \vec{b} , a real solution to Eq. (14) cannot be obtained.

When the bond angle between \vec{a} and \vec{b} is smaller than 90° (see Fig. 5A), the vector \vec{c} cannot exist in the region opposite to \vec{a} and \vec{b} . When the bond angle between \vec{a} and \vec{b} is larger than 90° , the vector \vec{c} exists only in a small region which bisects the bond angle made by \vec{a} and \vec{b} . The general solution of sp^2 hybridization is a special case of (B) in which \vec{a} , \vec{b} and \vec{c} are in a plane. Figure 5B shows that sp^2 hybridization is not possible when \vec{a} and \vec{b} are almost in opposite directions. The largest area possible for \vec{c} is obtained when \vec{a} and \vec{b} are perpendicular to each other. However, in this case, $\tan\theta_3$ diverges and thus there is no $2p$ component in $\{sp^3\}$.

When the three chemical bonds have a real solution, a fourth direction is obtained for this generalized sp^3 chemical bond. Using the next three equations of Eq. (13) we obtain

$$\vec{d} = -\tan\theta_4 \mathbf{A}^{-1} \vec{\theta} \quad \text{and} \quad \tan\theta_4 = \frac{1}{|\mathbf{A}^{-1} \vec{\theta}|} \quad (15)$$

where the matrix \mathbf{A} and the vector $\vec{\theta}$ are defined by

$$\mathbf{A} = \begin{pmatrix} a_x & a_y & a_z \\ b_x & b_y & b_z \\ c_x & c_y & c_z \end{pmatrix}, \quad \vec{\theta} = \begin{pmatrix} \tan\theta_1 \\ \tan\theta_2 \\ \tan\theta_3 \end{pmatrix} \quad (16)$$

When the inverse matrix of \mathbf{A} exists, the fourth direction of the general sp^3 bonds is given by the direction of three vectors and the values of θ_i ($i = 1, 2, 3$). The condition that the inverse matrix exists requires that the three vectors are not in a plane.

We conclude from the above discussion of general sp^3 hybridization that: (1) the third chemical bond does not always exist, or (2) the calculated fourth chemical bond does not always have a direction to the fourth neighbor atom, even though the directions to the four neighboring atoms have been selected. Furthermore, even when four chemical bonds are directed to the neighbor atoms, the chemical bond length, which is determined by θ_i , does not always fit the bond lengths for the four atoms simultaneously. In this way, the general sp^3 hybridization does not always work well, except for the symmetrical diamond structure. When four or three hybridized orbitals linked to a carbon atom cannot be obtained, the material becomes a carbon alloy in which sp^3 , sp^2 and sp hybridizations may co-exist. This may be a reason why amorphous materials exist. When we start giving a nucleus for a crystal where the nucleus is amorphous, we can expect that there would be no reason to recover the single crystal formation in the process of the crystal growth.

For fullerenes and carbon nanotubes, although the bond angle is distorted from 120° , all bond angles between any two chemical bonds are more than 90° which is the stable condition (B) for general sp^3 hybridization. A spherical C_{20} molecule is the minimum fullerene cage molecule, and C_{20} consists of only twelve pentagonal rings; its related hemisphere C_{10} is a minimum cap for a single-wall carbon nanotube at both ends. Even for this smallest fullerene case, all bond angles are more than 90° . Thus, fullerenes and carbon nanotubes are considered to be possible structures from a topological standpoint.

In Fig. 6 the s component for the fourth chemical bond in a general sp^3 hybridization is plotted as a function of the pyramidal angle in fullerenes. Here M in s^M corresponds to $1/n$ in sp^n . M becomes a maximum value of $1/3$ in the figure at the pyramidal angle of 109.47° (19.47° in the horizontal axis), and the s component quickly increases as a function of the pyramidalization angle shown in Fig. 6. Because the carbon atoms in fullerene molecules are not equivalent to each other, except for C_{60} , and because the fourth direction is not in the radial direction for the atom which is at the vertex of two hexagon and one pentagon rings, the pyramidalization angle is an averaged angle over the molecule. The diameters of C_{60} and C_{240} are 0.7 and 1.4 nm, respectively. Most fullerenes from C_{60} and C_{100} have M values from 0.05 to 0.1. Because a typical single wall carbon nanotube has a diameter of 1.4 nm which is the same as that of C_{240} , the corresponding M value is 0.02 at most. This means that the π bonding character is a good approximation in carbon nanotubes though some effects of s character may appear with small energy values less than 0.1 eV [1].

In general, for sp^n hybridization, $n+1$ electrons belong to a carbon atom in an occupied hybridized σ orbital and $4-(n+1)$ electrons are in the π orbital. For sp^3 hybridization, the four valence electrons occupy $2s^1$ and $2p^3$ states as σ bonding states. The excitation of $2s^1$ and $2p^3$ states in the solid phase from the $2s^2 2p^2$ atomic ground state requires an energy approximately equal to the energy difference between the $2s$ and $2p$ levels (~ 4 eV). However, the covalent bonding energy for σ orbitals is comparable (3–4 eV per bond) to the $2s-2p$ energy separation. Thus, the sp^3 hybridization of carbon to form diamond is not a thermodynamically stable structure

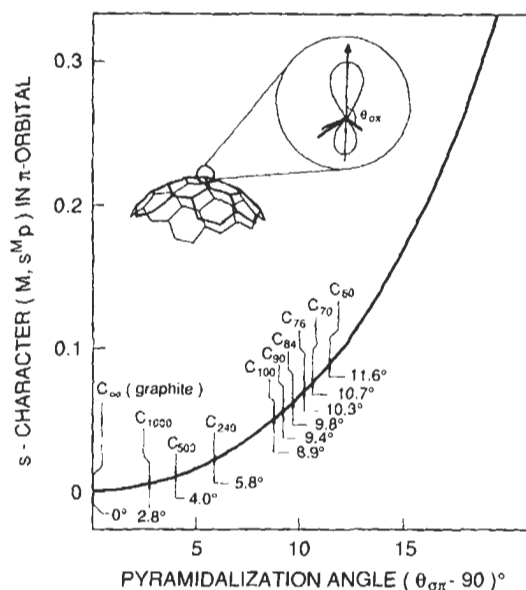


Fig. 6. The s component for the fourth chemical bond in the general sp^3 hybridization is plotted as a function of the pyramidal angle in fullerenes. Here M in $s^M p$ corresponds to $1/n$ in sp^n . M becomes a maximum value of $1/3$ in the figure at the pyramidalization angle of 109.47° (19.47° in the horizontal axis) [13].

at ambient pressure, and sp^2 graphite is the stable structure [14–16]. A simple explanation for the occurrence of sp^2 hybridization at ambient pressure is that the energy gain for forming the sp^3 structure is smaller than the energy loss for changing from sp^2 to sp^3 hybridization. In other words, the energy gain of π bonding becomes large (3–4 eV) when the C atoms form a honeycomb network, which is relevant to the fact that the radial wave function has no node for the $2p$ orbitals and that the overlap of $2p$ orbitals for nearest C atoms is large (~ 0.5). Thus, there is a need to consider π bonding for the molecular structure in some detail.

2 Defect States and Modifications of the Hybridization

As discussed in the previous section, a disordered structure may not give rise to an sp^3 hybridization of the carbon atom, so that a mixture of hybridizations would be expected for amorphous carbons. Furthermore, a substitutional impurity may change the hybridization and consequently the electronic properties. Because the lattice constant between carbon atoms is relatively small (1.40–1.55 Å), there are not many atoms which can form a substitutional impurity. For example, a boron atom can be substituted up to 2.35 at% boron concentration by heat treatment at 2300 K. Such boron addition enhances the lithium absorption performance [17,18] (see, e.g., Chapter 25). Another possible substitutional impurity is a nitrogen or phosphorus atom introduced by an arc method (see, for example, Chapter 21). Since the lattice

constant increases or decreases by B or N doping, respectively, the strain energy increases by substitutional doping. However, when we dope both B and N atoms from a pyridine–borane complex by heating at 1000°C for two hours in Argon gas, the solid solubility of B and N increases up to 28.6 at% [19]. The electronic structure calculation of the B–N–B complex in the graphene cluster shows a smaller Li absorbing energy [20]. It is because the lowest unoccupied molecular orbital (LUMO) for the B–N–B doped graphite cluster becomes close to the Fermi energy compared with the B doped graphite cluster and that the charge transfer of electrons from Li to the graphene cluster becomes relatively easy for the B–N–B doped graphite cluster [20]. It is noted that the B–N–B cluster has a planer structure unless the number of B–N–B is comparable to the number of carbon atoms.

However, following doping by other species, such as alkali metal atoms and acid molecules, the in-plane graphite structure does not change, but the interlayer spacing increases, the guest atoms being inserted (or intercalated) between the graphene layers, to form “graphite intercalation compounds (GICs)” [21]. Here, the valence electron of the alkali atom is transferred to the anti-bonding π band of the graphite structure, while in an acceptor type GIC, the π electrons are removed from the graphene sheet. This phenomenon is related to changing the Fermi energy of the π band and is not relevant to the modification of the sp^2 structure of carbon atoms. However, for a fluorine atom this makes a covalent bond in the graphitic plane by an sp^2 to sp^3 transformation. Below we show a calculated result for one or two fluorine atoms on a graphite cluster using a semi-empirical quantum chemistry calculation, from the MOPAC93 library, in which the lattice optimization is performed by “Parametric Method 3” (PM3) inter-atomic model functions, and the Hartree–Fock calculation is adopted for the determination of the electronic structure [22].

2.1 A Fluorine Atom on Nanographite

When a fluorine atom is placed near to an interior carbon atom, denoted by C_0 in a $C_{24}H_{12}$ cluster (Fig. 7a), the optimized position of the fluorine atom is not above the center of a hexagonal ring of carbon atoms, as is commonly observed in alkali-metal doped GICs, but above the carbon atoms, as shown in Fig. 7a, suggesting that a covalent bond forms between the carbon and halogen atoms. In fact, one-electron energy states of the $2s$ and $2p$ orbitals of the fluorine atoms exist in the energy region of the bonding σ orbitals. The formation of a σ bond between the fluorine atom with the re-hybridized sp^3 orbitals for the carbon atoms results in a large energy gain compared with charge-transfer ionic states, as is observed for the GICs. The sp^3 hybridization of the carbon atom can be seen from the following results: (1) the deformation of the lattice by fluorine doping, (2) the disappearance of the π component in the density of states (DOS) spectra for heavy fluorine doping, and (3) the increased width of the σ states in the DOS spectra, as shown below.

In the optimized F-doped cluster, the carbon atom, which is denoted by C_0 in Fig. 7a, forms an sp^3 hybridized structure by making a covalent bond with the fluorine

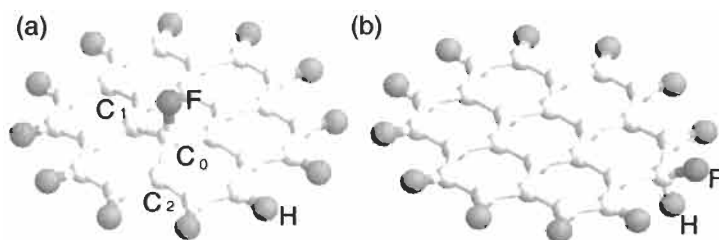


Fig. 7. A $C_{24}H_{12}$ cluster. (a) A fluorine atom is doped at the center of the cluster. (b) A fluorine atom is doped at the edge of the cluster [22].

atom. In fact, the bond angles of $F-C_0-C_1$ and $C_2-C_0-C_1$ are 107° and 112° , respectively. Here C_1 and C_2 are nearest neighbor carbon atoms to the C_0 atom at the inner and outer hexagonal rings, respectively (Fig. 7a). If the structure of the doped cluster is *not* optimized, the corresponding bond angles would be 90° and 120° , respectively. The optimized bond angles are, however, close to the sp^3 bond angle of 109.47° . The bond lengths from the C_0 atom to the F, C_1 , C_2 atoms are 1.388, 1.518, 1.520 Å, (0.1388, 0.1518, 0.1520 nm), respectively. The bond length between the carbon and fluorine atoms is close to the sum of the ionic radius of F (0.68 Å) and half of the C–C distance of graphite (0.71 Å), and the C_0-C_1 and C_0-C_2 distances of the sp^3 configuration are slightly smaller than the nearest-neighbor distance of diamond, 1.544 Å. Because the π electron is transferred to the F atom, the π bond between carbon atoms does not exist for the C_0 atom, and thus the C–C bond length becomes large in the honeycomb lattice. Thus, the formation of sp^3 bonding is more favorable, not only for reducing the strain energy, but for strengthening the chemical bond.

When fluorine atoms are replaced by a chlorine or bromine atom, the angles $X-C_0-C_1$ and $C_2-C_0-C_1$ ($X = \text{Cl}$ and Br), become (104° , 115°) and (98° , 118°), for Cl and Br, respectively. This shows that the deformation from the sp^2 to the sp^3 structure becomes smaller with increasing atomic number, which is consistent with the fact that the C_0-C_1 distance becomes 1.48 Å and 1.45 Å for Cl and Br atoms, respectively, closer to the graphite value of 1.42 Å. Also, the sp^3 deformation is sensitive to the ionic radius of the halogen ions. When the halogen ionic radius is relatively large compared with the carbon–carbon distance, considerable overlap occurs between the wave functions of the halogen atoms and the π orbitals of not only the C_0 carbon, but also of the neighboring C_1 and C_2 carbon atoms, when the nanographite plane is flat. Thus, a small deformation is energetically favoured for a large ionic radius compared with the formation of a single sp^3 σ bond with the halogen atom. A chemical bond between carbon and iodine atoms could not be obtained. Thus, C–I bonds are not to be expected on the graphene surface [23]. Miyajima and his coworker showed an enhancement of carbonization to lower temperatures ($<800^\circ\text{C}$) after iodine treatment [24] (see Chapter 5). Here, iodine atoms are coupled to the carbon atoms at the edge and form a charge transfer complex, and this causes the C–H bonding in the coal-tar pitch to weaken [24]. It is of interest that the weak coupling of the iodine atom

with carbon atoms has a catalytic role for carbon and hydrogen atoms in chemical reactions [23].

The calculated ionicities of F, Cl, and Br are -0.15 , -0.08 , and -0.22 , respectively, when the halogen atoms are put on the C_0 atom. The ionicity value for Br is comparable to the ionicity for most acceptor type GICs, which is about -0.3 . One reason why we get a smaller value for the ionicity of Cl (relative to the F, Cl, Br progression) arises from the one-electron energy of Cl atoms. For the Cl atom, the $2p$ orbital is only weakly coupled to the p_z and σ orbitals of carbon, and is clearly shown by the results for the partial density of states (PDOS) of halogen atoms. Because halogen atoms are present, their atomic levels could be seen if there was no hybridization between the halogen orbitals and the orbitals of the carbon atoms. If there was strong coupling between the halogen and the carbon orbitals, a component of the halogen orbitals would appear over a large part of the energy range of graphite.

In Figs. 8a and b are plotted the PDOS associated with the $2p_z$ and σ ($2s$, $2p_x$, and $2p_y$) orbitals of the C_0 atom (see Fig. 7a), respectively. In Figs. 8c and d are plotted the PDOS of the $2p_z$ and σ orbitals for all the carbon atoms in the cluster in units of states/eV/atom allowing for some broadening of the discrete molecular energies. The graphite π bands can be seen in Fig. 8c, while no corresponding levels at the same energy are found in Fig. 8a. The $2p_z$ levels of the C_0 atom appear at a lower energy region in which the $2p_z$ levels are mixed with the σ orbitals. This result indicates the local nature of sp^3 hybridization. In fact, the fluorine orbitals have energies that cover a wide range of carbon valence orbitals. As for the Cl and Br atoms, because the energy of the s orbital is widely separated from the p orbital, only the Cl and Br p orbitals are coupled to the carbon valence orbitals. Further, the PDOS for the Cl p orbital does not significantly couple with the carbon valence orbitals, so that the PDOS gives sharp spectra. It is for this reason that the ionicity of Cl is relatively small.

Once a fluorine atom is covalently bonded to a carbon atom, the movement of the fluorine atom from one carbon site to another may be difficult compared with GICs where the fluorine is ionically bonded. Activation energies for the fluorine motion

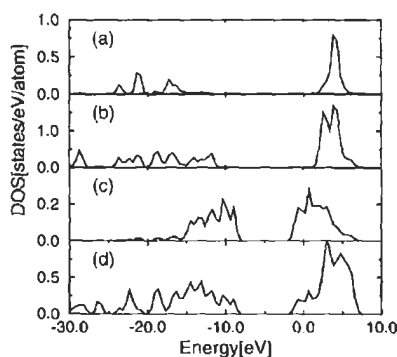


Fig. 8. Partial density of states for the (a) $2p_z$ and (b) σ ($2s$, $2p_x$, and $2p_y$) orbitals of the C_0 atom, and for the (c) $2p_z$ and (d) σ orbitals for all the carbon atoms of the $C_{24}H_{12}F$ cluster, as shown in Fig. 7 [22].

from a C_0 site to a C_1 site can be calculated from bond optimization calculations in which the relative positions of the F between two nearest neighbor carbon sites are fixed in the calculation. The lengths of the bonds between the fluorine and the two carbon atoms and the corresponding bond angle can be optimized in the calculation. The calculated activation energy for moving a fluorine atom from the C_0 site to a C_1 interior site is about 1.8 eV. This value is comparable with the formation energy of a fluorine atom on the nanocluster. Thus, movement of an F atom from a C_0 site to a C_1 carbon site is as difficult as desorbing the F atom.

When a fluorine atom is placed near to an edge carbon atom, as is shown in Fig. 7b, the hydrogen atom which moves out of the graphitic plane and the carbon atom at the edge form an sp^3 hybridization state to make a bond between the hydrogen and the fluorine atom. Although the bond angles, bond lengths and ionicity for an edge carbon atom are not so different from the corresponding parameters for the inner carbon atom, the total energy calculated for the fluorine atom attached to the edge carbon atom is 0.92 eV smaller than for an inner carbon atom. When we compare the contribution to the total energy from the electronic energy and the nuclear repulsion, the change of each contribution energy from that for non-doped cluster becomes very large, in the order of 100 eV, and therefore a large relaxation of the cluster occurs upon fluorine doping. Because the lattice relaxation is much easier for the edge sites, the fluorine atoms first attach themselves to the edge carbon atoms, and they then start to attach themselves to the inside of the cluster.

2.2 Two Fluorine Atoms in the Cluster

With two fluorine atoms in the cluster, differences are clearly found between the nanographite and acceptor-type GICs. For acceptor type GICs, the negative ions distribute themselves homogeneously between two graphite layers because of the electronic repulsion. However, for the fluorine atoms, the nearest neighbor carbon sites are the most energetically favored, because the unpaired spins of two fluorine atoms form spin singlet states ($S = 0$). There are two possibilities for the geometry of the two fluorine atoms adjacent to nearest neighbor carbon atoms: on the same plane and on staggered sides of the graphitic plane. When the total energy of the F_2 dimer on the same side and on opposite sides of the graphene plane are compared, it is found that an F_2 dimer on the same side at the edge is 0.043 eV more stable than when the two fluorine atoms are at opposite sides of the graphene cluster. The energy difference comes from the absence of F-F interactions for when the two fluorine atoms are on different sides of the graphene cluster. Further, when the two fluorine atoms are near a carbon atom and move a hydrogen atom to the nearest neighbor carbon site to keep the same $C_{24}H_{12}F_2$ stoichiometry, then the structure is 0.5 eV more stable than the same side configuration. This value cannot be directly compared with the same side geometry, since locating two hydrogen atoms at the end of the cluster produces a stable structure. However, it is understood that the closer the F-F distance, the more stable is the structure.

The calculated result shows that an F–F interaction is effective only when the two fluorine atoms are close to nearest-neighbor carbon atoms [22]. This result follows because the wave functions of the fluorine valence electrons are localized near fluorine atoms. However, it is found in the unrestricted Hartree–Fock (UHF) calculation that the spin triplet states ($S = 1$) are more stable for even number n th neighbor sites than the spin singlet states, while the spin singlet is more stable than the spin triplet with an odd number n th neighbor sites. This indicates a weak spin interaction compared with the difference between the total energy of two spins at fluorine atoms which is caused by carbon π electrons. In fact, for the singly occupied molecular orbital (SOMO), a spin density around the fluorine atom is localized on the graphene sheet. Further, even if the two fluorine atoms are in nearest neighbor locations, the interior region is not so stable for fluorine doping as compared with the edge fluorine sites.

From these results, the following picture of F-doping of a nanographite cluster emerges. First, consider the fluorine atom placed near to an edge carbon site. For an even number of fluorine atoms, the nearest neighbor sites are more stable for the singlet pair. Up to 12 fluorine atoms can be doped into the $C_{24}H_{12}$ cluster, because there are 12 carbon atoms at the edge. Then, if the hydrogen atoms are dissociated from the carbon atoms, the fluorine atoms can be substituted for the hydrogen atoms. By this substitution, 24 fluorine atoms can be doped at the edges. It is found from the heat formation of fluorine that the fluorine is still more stable at an edge site than at an interior carbon site. After all, if 12 carbon edge sites are terminated by 24 fluorine atoms, then 12 fluorine atoms can be placed near the 12 interior carbon atoms of the $C_{24}H_{12}$ cluster in a staggered way, so as to form an sp^3 structure. In this way the ratio of sp^3 to sp^2 hybridization can be changed by changing the fluorine concentration.

It is interesting to discuss the occurrence of unpaired spins in F-doped nanographite samples, as has been observed experimentally [25,26] (see Chapter 23 for details). According to experiment, when the ratio F/C is smaller than 0.4, the occurrence of unpaired spins is not large. This situation corresponds to fluorine atoms placed near to the edge atoms of carbon. When a fluorine atom is placed near the edge, the fluorine atom should be more subject to the inter-atomic potential as compared with the fluorine atom located in the interior region. Thus, it is easy to form an F_2 dimer near the edge with a spin singlet. In the case of $C_{24}H_{12}$ this corresponds to an F/C ratio of 1.0 or 0.5, depending on whether the hydrogen atoms are dissociated from the carbon atom or not, respectively. In the experimental situation, the diameter is around 30 Å and this roughly corresponds to C_{216} with 36 edge carbon atoms. When F/C = 0.4 is the stoichiometry for the C_{216} cluster and all the fluorine atoms are attached to the edge carbon atoms, and there are no hydrogen atoms, then 72 fluorine atoms are attached to the cluster.

When all of the fluorine edge atoms are terminated, the interior fluorine atoms can be added in a rather random way, so that an unpaired spin can be observed with some probability. When two fluorine atoms are at nearest neighbor carbon sites, the total number of electrons around the fluorine atoms becomes an even number. In this case

a spin-singlet state is expected, even though the two fluorine atoms are each located on opposite sides of the graphene plane.

It is to be noted that spin magnetism is also found in the zigzag edge of a non-doped graphene cluster in which there is a localized π electron states at the Fermi energy [11]. This spin magnetism is controlled by the HTT values determined from Curie magnetism at low HTTs (<1100°C) to metallic Pauli magnetism at higher (>1200°C) [27]. It will be interesting to study new inorganic, magnetic materials in which the interaction between the spins in a nanographite by fluorine doping can be controlled.

3 Spectroscopies for sp^n Structure

In order to characterize carbon materials, the availability of a variety of spectroscopic techniques is important to observe the electronic structure at the atomic level. Experimental results of Raman, X-ray photoelectron spectroscopy (XPS), scanning tunnelling microscope (STM) and scanning tunnelling spectroscopy (STS) observations of sp^n structures are introduced below. The detail of the experimental technologies are given by several authors in the chapter “The Latest Characterization Technologies”.

3.1 Raman Spectroscopy

Raman spectroscopy for graphite, diamond, fullerenes and carbon nanotubes is widely used for characterizations. In two-dimensional graphite, Raman spectra show a strong peak at approximately 1590 cm^{-1} associated with the E_{2g} mode or the G-band. The G-band Raman peak becomes strong when the crystalline size becomes large following heat treatment. For disordered graphites [28], activated carbon fibers [12] and carbon nanotubes [29], it is established that there is a broad Raman spectral feature around 1350 cm^{-1} which is assigned to a defect oriented Raman peak called the D-band [28]. Because of this defect, the phonon dispersion relations of graphite at the K point (corners of the hexagonal Brillouin zone) are folded to the Γ point for a $\sqrt{3} \times \sqrt{3}$ superstructure. Recent experiments show that the D-band Raman frequency shifts by $52\text{ cm}^{-1}/\text{eV}$ by changing the laser energy, and this is identified with a double resonance Raman effect [29,30]. When the optical absorption of an electron from the π band to the π^* band occurs, the phonon modes with corresponding k vectors are enhanced by about 10^3 , indicating a resonance Raman observation. This observation provides evidence for assigning the D-band to the K point phonon mode of graphite, since the D-band Raman frequency changes with changing the laser energy [29,30]. The 1350 cm^{-1} peaks are given by 2.54 eV laser light [29].

The intensity of the D-band becomes weak with increasing crystallite size of the graphite, and thus the ratio of the G-band to D-band intensity is a good measure of the degree of disorder of graphitic materials [28,31]. The amount of disorder in carbon fibers [12] and in graphite nano-clusters [32] can be controlled by the heat

treatment temperature (HTT) or by ion implantation [33]. Because the Raman frequency of crystalline diamond is 1333 cm^{-1} , we should be careful in identifying the Raman mode of diamond when both diamond and disordered graphite exist in the sample. See the review article by Zaitsev for optical values of the Raman and photoluminescence frequencies for various carbon materials [34].

In carbon nanotubes, the G-band is split into three Raman-active modes (A , E_1 and E_2) modes because of the lower symmetry of the cylindrical structure. Recent calculations show that there are in fact six Raman-active modes in the G-bands (two A , two E_1 and two E_2 modes) which come from the two branches of the phonon dispersion relationships associated with longitudinal and transverse optic (LO and TO) phonons [35]. Their relative intensities depend on the degree of helical geometry, as is defined by the chiral angle θ [35]. In carbon nanotubes there are strong Raman modes, including the radial breathing mode (RBM) in which the diameters of the nanotubes are oscillating [36]. Because the frequency of the RBM modes is inversely proportional to the diameter, $\omega_{\text{RBM}} = 248/d_i\text{ cm}^{-1}$ where d_i is the diameter of an isolated nanotube in nm units. A chirality can be assigned in terms of the (n,m) index [1,37] from the resonant Raman experiment of an individual carbon nanotube [38]. See the review articles by Dresselhaus [39] for further detail of Raman spectroscopy of carbon nanotubes.

In fullerenes, because of the high symmetry of the molecule, there exist special Raman-active modes of the molecule [37]. Group theory predicts that 10 ($2A_g + 8H_g$) of the 46 mode frequencies are Raman active as a first-order Raman process. Among the fullerene modes, the tangential A_g mode, the so-called pentagonal pinch mode at 1469 cm^{-1} , is known as a strong Raman-active mode. The RBM mode of C_{60} appears at 496 cm^{-1} . In the higher fullerenes, the number of Raman-active modes in the Raman signal becomes large because of the symmetry lowering from C_{60} , and all the 46 C_{60} modes and most of the Raman modes in higher fullerenes have been assigned by experiment [37].

In low-dimensional carbon materials, the polarization effect of light is important. When the incident and the scattered polarizations are parallel to each other, the symmetric A modes and other asymmetric modes, such as E_1 and E_2 or (H_g for C_{60}), are observed. When the incident and the scattered polarizations are perpendicular to each other, only the asymmetric phonon modes can be observed. Thus, we can see the symmetry of phonons by changing the polarization of the light. Another important effect on the Raman intensity, especially for carbon nanotubes, is the so-called antenna effect in which the light can absorb only when the polarization is parallel to the nanotube axis [40]. Because of the large anisotropy on the Raman intensity, this effect can be used to observe the alignment of nanotubes.

Doping with GICs changes the position of the Fermi energy. In GICs, the density of states at the Fermi energy $D(E_F)$ becomes finite, while $D(E_F)$ becomes zero in neutral graphite. In the presence of conduction electrons, the Raman discrete lines are coupled with the continuous, low energy excitation of electrons (plasmons) to form the Breit–Wigner–Fano (BWF) lines. The energy position of the BWF lines

becomes either higher or lower than the original phonon lines, depending on the sign of the interaction. Because the charge transfer of electrons depends on the density of states at the Fermi energy, the BWF frequency is a good measure of the density of states at the Fermi energy in GICs [41] and in carbon nanotubes. A single wall carbon nanotube is either metallic or semiconducting depending on its diameter and chirality [42,43]. In the metallic nanotube, the density of states at the Fermi energy in units of states per carbon atom is inversely proportional to the tube diameter [1], and thus the BWF frequencies become smaller with decreasing nanotube diameter. Typical BWF lines for a carbon nanotube with $d_t = 1.4$ nm appear around 1540 cm^{-1} [44], and are observed by laser energies of 1.55 eV and 1.85 eV for Stokes and anti-Stokes resonant Raman spectroscopy [45].

Recently, the Raman spectrum of an individual single walled nanotube was observed by surface enhanced Raman spectroscopy (SERS) [46] and confocal micro Raman spectroscopy (CMRS) [38] in which the laser is focused on an aligned bundle with a diameter of $1\text{ }\mu\text{m}$ and gold nano-particles were used for enhancement of the Raman intensity in SERS and where the resonant Raman effect is observed in CMRS. The characterization of Raman spectroscopy for carbon materials is progressing rapidly.

3.2 XPS Spectra

In X-ray photo-electron spectroscopy (XPS), the energy of a photo-electron is observed with the given energy of X-ray photon. As is discussed in the Introduction, carbon $1s$ core orbitals do not generally affect the solid state properties of carbon materials, because the energy position of the $1s$ core levels is 280 eV below the Fermi energy. The work function of graphite is 5 eV. Because of the small overlap between the $1s$ orbitals on adjacent atomic sites in the solid, the energy spectrum of the $1s$ core levels in carbon materials is sharp (~ 0.65 eV) and the core level energies lie close to that of an isolated carbon atom. Using XPS, the energy of the $1s$ core level is measured relative to the position of the vacuum level, and this energy difference is especially sensitive to the transfer of electric charge between carbon atoms. Specifically, the $1s$ core level shifts in energy relative to the vacuum level by an amount depending on the interaction with nearest-neighbor atoms or between a molecule and the carbon substrate, and this effect is known as the chemical shift of XPSs. For example, the XPS peaks at 284.6 ± 0.3 eV and 283.3 ± 0.1 eV are assigned, respectively, to the carbon $1s$ orbital for diamond and to a Si-C crystal [47]. From the relative intensity of the 284.6 eV to 283 eV features, the nucleation of diamond nuclei can be evaluated in the plasma chemical vapor deposition process. Other values for C $1s$ peaks are given in the literature of electron spectroscopy for chemical analysis (ESCA) [48]: Ti-C 281.6 eV, graphite 284.2 eV, C-C (CH_2) single bond 285 eV, CaCO_3 289.6 eV, BaCO_3 289.2 eV, and CF_2 292.5 eV. These values are useful for calibrating the vacuum level of the experimental setup. Similar values are to be found in the handbook by J.F. Moulder et al. [49].

Furthermore, XPS refers to the photo-electron spectroscopy (PES) process when the excitation photon is in the X-ray range and the electron excitation is from a core level. XPS spectra have been obtained not only for the vacuum levels but also for the unoccupied orbitals for a variety of fullerenes, which give a side band for the XPS spectra. For example, the spectrum for C_{60} shows well-defined peaks with an intense, narrow main line identified with the emission of a photo-excited electron from the carbon $1s$ state, and has a binding energy of 285.0 eV and a very small line width of 0.65 eV at half-maximum intensity [50]. The sharpest side-band feature in the down-shifted XPS spectrum is identified with an on-site molecular excitation across the HOMO–LUMO gap at 1.9 eV [50]. This side-band peak is sensitive to doping of the fullerene. Furthermore, at a lower energy, there are further peaks due to the photo-emission counterparts of electric dipole excitations seen in optical absorption, and which represent intra-molecular plasmon collective oscillations of the π and σ charge distributions. Plasma excitations are also prominently featured in core level electron energy loss spectra (EELS).

The $1s$ levels of a boron and a nitrogen atom are, respectively, 189.4 and 398.1 eV below the vacuum level [49]. The chemical shift of the $1s$ levels of nitrogen is relatively large (3–4 eV), depending on the different type of carbon-based molecule and other elements in the molecule. Typical values are NH_2 398.8 eV, NH_3 400.5 eV, NO 403.6 eV, and NO_2 405.5 eV [51] and NC_3 400.9 eV (see Chapter 21 on CN_x for further details.) These values are sensitive to the local hybridization and the geometry of the cluster.

3.3 STM/STS Measurements

STM/STS are recently developed experimental tools for observing the electronic structure with atomic resolutions and are members of the scanning probe microscope category. In the STM experiment, a tip is scanned on the surface of material by fixing the electric current which flows from the tip to the surface, in which the atomic resolution of the surface is observed as a function of the controlled height of the tip (constant current mode). In the STS experiment, on the other hand, when the bias voltage between tip and the surface, V , is changed by fixing the tip at a specified location, we get a tunnelling current I as a function of the bias voltage

$$I \propto \int_{E_f}^{E_f + eV} \rho(\mathbf{r}, E) dE \quad (17)$$

where $\rho(\mathbf{r}, E)$ is the local density of states at position \mathbf{r} with the energy E . The differential conductance dI/dV is relevant to $\rho(\mathbf{r}, E)$ which can be compared with theoretical calculations. Thus we can see the position of an atom by STM and its local electronic structure by STS, which is a standard technique for STM/STS experiment.

Graphite is used very often as a standard sample for an STM experiment, because the surfaces of graphene layers are flat and the electronic structure of graphite is well established. Because of the ABAB stacking of the graphene layers in graphite, the

Fermi energy consists of the Bloch function of the B atom, where the B atom does not have a carbon atom in the nearest neighbor layers in the direction perpendicular to the graphene plane. As a result, the STM images are obtained as a triangular lattice which consists of only B atoms in the surface.

In carbon nanotubes, STM measurements of a single-wall carbon nanotube provide a direct measurement of the chirality (n,m) , and STS experiments for the observed nanotube [52,53] show evidence that a metallic or semiconducting nanotube occurs, respectively, when $n - m = 3$ or when $n - m \neq 3$ for (n,m) nanotubes. STS also shows that the energy gap of semiconducting nanotubes is inversely proportional to the diameter [43]. A pentagonal ring becomes a topological defect in a graphitic cone whose STM images show a $\sqrt{3} \times \sqrt{3}$ superstructure relative to the original graphite lattice structure [54]. Kobayashi has shown by the calculation of STM images that the mixing of the molecular orbitals of A and B sites at the topological defect causes this superstructure [55].

A single impurity of a fluorine atom on a graphite cluster is observed by STM experiments in which the electronic structure of π bonds are modified locally around the fluorine atom. The STM images show that the π electrons are missing at the fluorine site (see the chapter by T. Enoki for more details). When the modifications caused by the fluorine atom are localized, the impurity effect on the ballistic conductance in carbon nanotubes is significant. A theoretical calculation of the Landauer conductance of a single-wall carbon nanotube shows that a single impurity destroys one of the two conductance channels of the carbon nanotube at the Fermi energy. Here a channel is defined by the sub-band in electronic structure which crosses the Fermi energy for the electronic conduction. In this case, the conductance becomes G_0 , where G_0 is a quantum of conductance and $1/G_0 = 12.9 \text{ k}\Omega$. The conductance is quantized in one dimension if there is no scattering in the conductance of a channel. However, two fluorine atoms are placed over A and B nearest sites, the two channels recover and the conductance becomes $2G_0$ in spite of the two impurities in the theoretical calculation [56,57]. Further, when the conductances were calculated for many impurity positions, three cases of quantized conductance, $2G_0$, G_0 and 0 were obtained depending on the impurity positions. The basic physics comes from the absence of back scattering [58] by impurities because of the geometrical phase factor of the scattered Bloch wave functions around the K point of the Brillouin zone which cancel each other for a time reversal pair of back scattering processes. Here, an example of a time reversal pair is $k \rightarrow k_1 \rightarrow k_2 \rightarrow -k$ and $k \rightarrow -k_2 \rightarrow -k_1 \rightarrow -k$ whose total scattering amplitudes are identical to each other but whose phase factors differ by π . The time reversal pair is possible only for back scattering processes. This geometrical phase factor generated around the degenerate point of the energy spectra is known as Berry's phase [59] and this degeneracy is an essential phenomena in the two-dimensional electronic structure of graphite. Thus, we can theoretically control the quantum conductance in the graphite or nanotube by putting fluorine atoms on the cluster and by changing local electronic structure to sp^3 hybridization (see details in the review by T. Ando [60]).

4 Conclusions

In conclusion, we have presented an analytical form for a general sp^n hybridization in which there is a strong correlation between the chemical bonds of an atom for elongating the hybridized orbitals, depending on the neighbor atom positions. A possible modification from an sp^2 to sp^3 configuration by fluorine-doping on the graphite plane is shown, in which the unpaired spin occurs on the graphitic plane. Raman, XPS, and STM/STS are informative techniques to observe the hybridization of carbon atoms in various materials and for studying the related solid state physics. The science of carbon materials will be directed in the future towards controlled hybridization and π electronic systems to design new structures and functions. By combining the dimensionality of the carbon isomers, we can construct new forms of carbon with many desirable functions.

Acknowledgement

The author would like to express his sincere gratitude to Professor Gene Dresselhaus and Professor Mildred S. Dresselhaus for collaborating on the research in this chapter for many years and for giving important advice on this chapter. The author acknowledges Professor Tadamasu Kimura, Professor Toshiaki Enoki, Professor Morinobu Endo, and many members of their groups for valuable discussions and for showing important experimental data before publication.

References

1. R. Saito, G. Dresselhaus and M.S. Dresselhaus, *Physical Properties of Carbon Nanotubes*. Imperial College Press, London, 1998.
2. R. Saito, T. Takeya, T. Kimura, G. Dresselhaus and M.S. Dresselhaus, *Phys. Rev. B*, 57: 4145, 1998.
3. A.M. Rao, P. Zhou, K.-A. Wang, G.T. Hager, J.M. Holden, Ying Wang, W.T. Lee, Xiang-Xin Bi, P.C. Eklund, D.S. Cornett, M.A. Duncan and I.J. Amster, *Science*, 259: 955, 1993.
4. A.M. Rao, M. Menon, K.A. Wang, P.C. Eklund, K.R. Subbaswamy, D.S. Cornett, M.A. Duncan and I.J. Amster, *Chem. Phys. Lett.*, 224, 106, 1994.
5. C. Yeretizian, K. Hansen, F.N. Diederich and R.L. Whetten, *Nature (London)*, 359: 44, 1992.
6. B.W. Smith, M. Monthieux and D.E. Luzzi, *Nature*, 396: 323, 1998.
7. K. Sato, M. Noguchi, A. Demachi, N. Oki and M. Endo, *Science*, 264: 556, 1994.
8. M. Endo, K. Takeuchi, S. Igarashi, K. Kobori, M. Shiraishi and H.W. Kroto, *J. Phys. Chem. Solids*, 54: 1841, 1994.
9. S. Yata, Y. Hato, H. Kinoshita, N. Ando, A. Anekawa, T. Hashimoto, M. Yamaguchi, K. Tanaka and T. Yamabe, *Synthetic Metals*, 73: 273, 1995.
10. M. Endo, K. Nishimura, T. Takahashi, K. Takeuchi and M.S. Dresselhaus, *ISIC 8: Conference Proceedings, Vancouver, BC, May 1995. J. Phys. Chem. Solids*, 57: 725, 1996.
11. K. Nakada, M. Fujita, G. Dresselhaus and M. S. Dresselhaus, *Phys. Rev.*, B54: 17954, 1996.
12. M.S. Dresselhaus, G. Dresselhaus, K. Sugihara, I.L. Spain and H. A. Goldberg, In: *Graphite Fibers and Filaments*, Springer-Verlag, Berlin, Vol. 5, 1988.

13. R.C. Haddon, *Accounts Chem. Res.*, 25: 127, 1992.
14. F.P. Bundy, *J. Geophys. Res.*, 85: 6930, 1980.
15. F.P. Bundy, In: S. Minomura (Ed.), *Solid State Physics under Pressure: Recent Advance with Anvil Devices*. D. Reidel, Dordrecht, 1985.
16. F.P. Bundy, W.A. Bassett, M.S. Weathers, R.J. Hemley, H.K. Mao and A.F. Goncharov, *Carbon*, 34: 141, 1996.
17. M. Endo, C. Kim, T. Karaki, Y. Nishimura, M.J. Matthews, S.D.M. Brown and M.S. Dresselhaus, *Carbon*, 37: 561, 1999.
18. S. Flandrois, B. Ottaviani, A. Derre and A. Tressaud, *J. Phys. Chem. Solid.*, 57: 741, 1996.
19. M. Sasaki, Y. Goto, M. Inagaki and N. Kurita, *Mol. Cryst. Liq. Cryst.*, 340: 499, 2000.
20. N. Kurita, *Mol. Cryst. Liq. Cryst.*, 340: 413, 2000.
21. M.S. Dresselhaus and G. Dresselhaus, *Adv. Phys.*, 30: 139, 1981.
22. R. Saito, M. Yagi, T. Kimura, G. Dresselhaus and M.S. Dresselhaus, *J. Phys. Chem. Solids*, 60: 715, 1999.
23. R. Saito, M. Yagi, T. Kimura, G. Dresselhaus and M.S. Dresselhaus, *Proceedings of ISIC-10. Mol. Cryst. Liq. Cryst.*, 340: 71, 2000.
24. N. Miyajima, T. Akatsu, T. Ikoma, O. Ito, B. Rand, Y. Tanabe and E. Yasuda, *Carbon*, 38: 1831, 2000.
25. K. Takai, private communication, 1998.
26. K. Takai, H. Sato, T. Enoki, N. Yoshida, F. Okino, H. Touhara and M. Endo, *Mol. Cryst. Liq. Cryst.*, 340: 289, 2000.
27. Y. Shibayama, H. Sato, T. Enoki and M. Endo, *Phys. Rev. Lett.*, 84: 1744, 2000.
28. F. Tuinstra and J.L. Koenig, *J. Chem. Phys.*, 53: 1126, 1970.
29. S.D.M. Brown, A. Jorio, G. Dresselhaus and M.S. Dresselhaus, *Phys. Rev.*, B64: 073403, 2001.
30. R. Saito, A. Jorio, A.G. Souza Filho, G. Dresselhaus and M.S. Dresselhaus, *Phys. Rev. Lett.*, 88: 027401, 2002; related papers therein.
31. P. Lespade, R. Al-Jishi and M.S. Dresselhaus, *Carbon*, 20: 427, 1982.
32. M.J. Matthews, X.X. Bi, M.S. Dresselhaus, M. Endo and T. Takahashi, *Appl. Phys. Lett.*, 68: 1078, 1996.
33. M.S. Dresselhaus and R. Kalish, *Ion Implantation in Diamond, Graphite and Related Materials*, Springer-Verlag; Springer Series in Materials Science, Vol. 22, Berlin, 1992.
34. A.M. Zaitsev, *Optical Properties*, In: L.K. Bigelow, M.A. Prelas and G. Popovici (Eds.), *Handbook of Industrial Diamonds and Diamond Films*, p. 227. Marcel Dekker, New York, 1998.
35. R. Saito, A. Jorio, J. Hafner, C.M. Lieber, M. Hunter, T. McClure, G. Dresselhaus and M.S. Dresselhaus, *Phys. Rev.*, B64: 085312, 2001.
36. A.M. Rao, E. Richter, S. Bandow, B. Chase, P.C. Eklund, K.W. Williams, M. Menon, K.R. Subbaswamy, A. Thess, R.E. Smalley, G. Dresselhaus and M.S. Dresselhaus, *Science*, 275: 187, 1997.
37. M.S. Dresselhaus, G. Dresselhaus and P.C. Eklund, *Science of Fullerenes and Carbon Nanotubes*. Academic Press, New York, NY, 1996.
38. A. Jorio, R. Saito, J. Hafner, C.M. Lieber, G. Dresselhaus and M.S. Dresselhaus, *Phys. Rev. Lett.*, 86: 1118, 2001; and M.S. Dresselhaus, G. Dresselhaus, A. Jorio, A.G. Souza Filho and R. Saito, *Carbon*, 40: 2043, 2002.
39. M.S. Dresselhaus and P.C. Eklund, *Adv. Phys.*, 49: 705, 2000.
40. H. Ajiki and T. Ando, *Physica B, Condensed Matter*, 201: 349, 1994.
41. I. Ohana, M.S. Dresselhaus and S.I. Tanuma, *Phys. Rev.*, B43: 1773, 1991.
42. R. Saito, M. Fujita, G. Dresselhaus and M.S. Dresselhaus, *Phys. Rev.*, B46: 1804, 1992.
43. R. Saito, M. Fujita, G. Dresselhaus and M.S. Dresselhaus, *Appl. Phys. Lett.*, 60: 2204, 1992.

44. S.D.M. Brown, A. Jorio, P. Corio, M.S. Dresselhaus, G. Dresselhaus, R. Saito and K. Kneipp, *Phys. Rev.*, B63: 155414, 2001.
45. S.D.M. Brown, P. Corio, A. Marucci, M.S. Dresselhaus, M.A. Pimenta and K. Kneipp, *Phys. Rev.*, B61: R5137, 2000.
46. K. Kneipp, H. Kneipp, P. Corio, S.D.M. Brown, K. Shafer, J. Motz, L.T. Perelman, E.B. Hanlon, A. Marucci, G. Dresselhaus and M.S. Dresselhaus, *Phys. Rev. Lett.*, 84: 3470, 2000.
47. P. Reinke and P. Oelhafen, *Phys. Rev.*, B56: 2183, 1997.
48. ESCA750. The values are taken from the manual of ESCA750, Shimazu. Co., Japan.
49. J.F. Moulder, W.D. Stickle, P.E. Sobol and K.D. Bomben, In: J. Chastain (Ed.), *Handbook of X-ray Photoelectron Spectroscopy*. Perkin-Elmer Co., Minnesota, 1992.
50. J.H. Weaver, J.L. Martins, T. Komeda, Y. Chen, T.R. Ohno, G.H. Kroll, N. Troullier, R.E. Haufler and R.E. Smalley, *Phys. Rev. Lett.*, 66: 1741, 1991.
51. K. Siegbahn et al., *ESCA*, Uppsala, 1967.
52. J.W.G. Wildöer, L.C. Venema, A.G. Rinzler, R.E. Smalley and C. Dekker, *Nature (London)*, 391: 59, 1998.
53. T.W. Odom, J.L. Huang, P. Kim and C.M. Lieber, *Nature (London)* 391: 62, 1998.
54. M. Ge and K. Sattler, *Chem. Phys. Lett.*, 220: 192, 1994.
55. K. Kobayashi, *Phys. Rev.*, B61: 8496, 2000.
56. M. Igami, T. Nakanishi and T. Ando, *J. Phys. Soc. Japan*, 68: 3146, 1999.
57. T. Ando, M. Igami and T. Nakanishi, *J. Phys. Soc. Japan*, 68: 3994, 1999.
58. T. Ando and T. Nakanishi, *J. Phys. Soc. Japan*, 67: 1704, 1998.
59. T. Ando, T. Nakanishi and R. Saito, *J. Phys. Soc. Japan*, 67: 2857, 1998.
60. T. Ando, *Sci. Technol.*, 15: R13, 2000.

Chapter 3

Structural Design and Functions of Carbon Materials by Alloying in Atomic and Molecular Scales

Morinobu Endo, Takuya Hayashi, Yoong Ahm Kim, Hiroaki Ohta and Sung Wha Hong

Faculty of Engineering, Shinshu University, Japan

Abstract: Carbon alloys with diverse structures, preparation methods and properties, are characterized and evaluated specifically from a microscopic point of view, where the structures of carbons and graphite are controlled and designed on an atomic scale. These carbon alloys have been prepared by doping heteroatoms into the hexagonal networks by diffusion, by intercalating into the interlayer space of graphite sheets as well as by turbostratic stacking, in addition to co-carbonizations with specific organic precursors. By such alloying methods, both the atomic and the electronic structures are modified, resulting in new properties and behaviors of the pristine materials. Structural modifications of fullerene and carbon nanotubes are also demonstrated.

Keywords: Doping, Intercalations, Polymer precursors, Fullerenes, Carbon nanotubes.

1. Introduction

Heteroatoms are inserted into carbon materials in order to improve their electrical, thermal, mechanical and chemical properties. The carbon alloy is studied extensively in one form or another in a variety of physical and chemical systems. In many of these applications, carbon materials are exposed to a wide range of operating conditions, such as concentrated additives to the host carbon materials, to superconductive materials, to anti-oxidant additives, to graphitization catalysts, and to improvements to the charge–discharge capacities of Li-ion rechargeable batteries. The concept of “carbon alloys” is used for almost all host carbons such as graphites, disordered carbons, carbon nanotubes and nanofibers, fullerenes, carbon fibers, activated carbons and carbon-carbon composites. In this chapter, the concept is focused at molecular and atomic levels as shown in Fig. 1. Carbon alloys, with structures designed on an atomic scale, provide modified atomic structures and modified resultant properties, which create and emphasize new functions to the host materials. In this

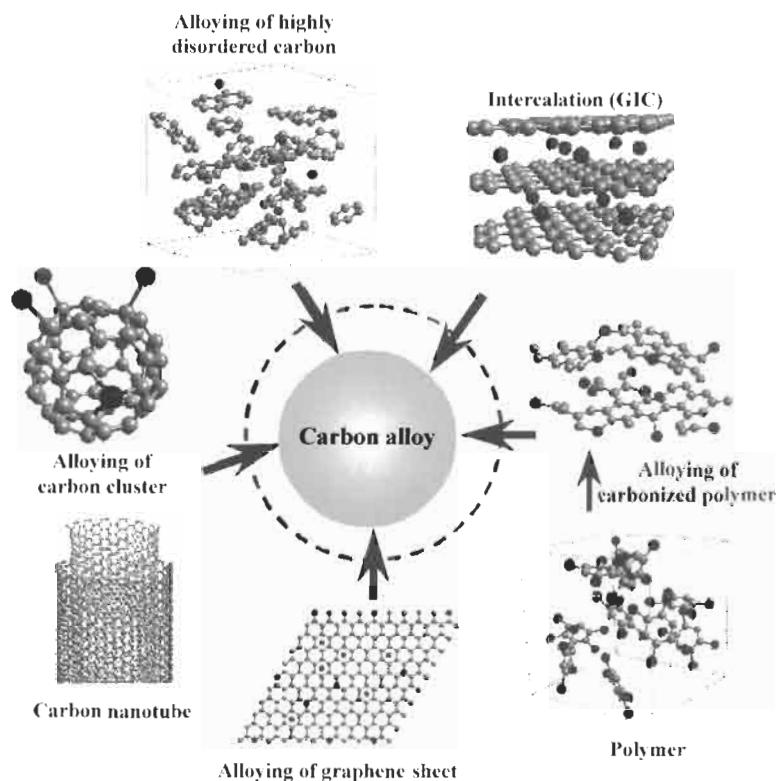


Fig. 1. Scheme for the carbon alloys designed in the microscopic level of molecules and atoms.

chapter, carbon alloys, whose structures are modified at the atomic level, are illustrated and discussed.

2. Intercalation Compounds

It has been established that heteroatoms, ions and molecules intercalate between the hexagonal layers of carbons and graphites. The intercalation of heteroatoms into the carbon materials is the process forming graphite intercalation compounds (GICs). GIC is a typical carbon alloys designed at the nanometer level, in which the structure and properties are drastically changed from the pristine carbon and graphite by intercalation. Figure 2 shows structural models for graphite intercalation compounds where the layered structure of the host graphite is maintained. Many atoms and compounds are intercalated into well-ordered graphite and even into some quite disordered carbon materials. Recently, carbonaceous and graphite materials doped with such heteroatoms as boron and phosphorus have been suggested for applications as anodes in Li-ion rechargeable batteries (LIB) [1,2], in which the charge and discharge efficiency as well as the capacity can be improved [3,4]. Lithium ions (Li^+)

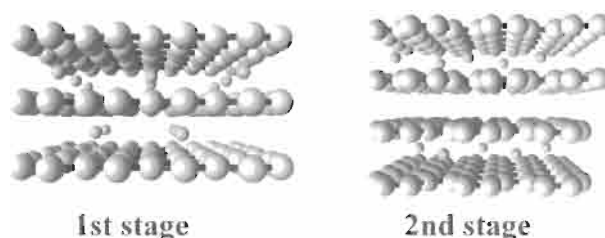


Fig. 2. Structural models for the graphite intercalation compound (Li-GIC first- and second-stage compound).

are intercalated and stored between the hexagonal networks of the carbon atoms, which can reversibly absorb and release the lithium ions at low electrochemical potentials. These electrochemical properties such as charge and discharge capacity are improved in the doped graphite system compared with pristine graphite, and are expected to have practical applications in high capacity LIB [4]. This is an interesting aspect of carbon alloys not only from the scientific point of view but also from application viewpoints.

Because of the weak van der Waals interlayer forces associated with the sp^2 bonding in graphite, anisotropically layered graphite-based intercalated compounds can, in principal, be synthesized. In the donor type GICs, mobile electrons are transferred from the donor type intercalate species (such as a layer of the alkali metal of potassium) into the graphite layers, thereby raising the Fermi level and increasing the electron concentration by two or three orders of magnitude. Leaving the intercalated layer positively charged, in part, results in lowering the mobility of conduction carriers in adjacent carbon layers by one order of magnitude. Conversely, for acceptor type GICs, conduction holes are generated by charge transfer by the intercalated species (which are usually molecules), and this results in a lowering of Fermi levels. Thus, enhanced electrical conduction in both types of GICs occurs predominantly in the graphene layers as a result of charge transfer. The electrical conduction between adjacent graphene layers (i.e., c -axis conduction) is much lower in acceptor compounds (especially in compounds where the graphene layer separation is relatively large) than in donor compounds.

Structures of intercalates (host materials) essentially control the formation of GICs and resultant properties. The structure of the carbon to be intercalated must be considered and so parent materials are of crucial importance. As is well established, chemical and physical structures of parent organic materials affect structures of resultant carbons and graphites via carbonization ($<1500^\circ\text{C}$) and graphitization ($2500\text{--}3000^\circ\text{C}$) processes by heat treatment. These have been intensively studied as graphitizable (soft) and non-graphitizable (hard) carbons. For soft and hard carbons, of equal heat treatment temperature, microstructures and intercalation phenomena are very different. Both types of carbon have been used as anode materials for LIB, and have different battery performances because of differences in GIC formation.

3 Insertion of Li Ions into the Disordered Carbon Materials

Non-graphitizable, disordered or glassy carbons, also called hard carbons, are produced by heat treatment of polymer resins and isotropic pitches. The glassy carbons referred to as a family of disordered amorphous carbon materials are characterized by broad profiles of 002 X-ray diffractions, although the basic structural units are known to be small carbon layers with hexagonally arranged carbon atoms. They have no three-dimensional A·B·A·B· stacking of graphene layers. They have a turbostratic structure consisting of small segments of defective carbon networks with relatively larger interlayer spacing of about 0.34 nm rather than the 0.3354 nm of graphite.

Because of the disordered nature of glassy carbons, their physical and chemical properties, especially electrochemical, are quite different from well-ordered graphite materials. The schematic model for the lithium insertion into a polyparaphenylene (PPP)-based carbon, that is a LiC_2 model, is shown in Fig. 3a. A side view of the LiC_2 model suggests that density of Li ions in PPP-based carbons is higher than that of LiC_6 (Fig. 3b). Endo et al. have extensively studied the electrochemical lithium insertion into PPP-based disordered carbons using NMR [5] and *in-situ* Raman spectroscopy [6]. The PPP-based carbon, heat treatment temperature 700°C, has a Li storage

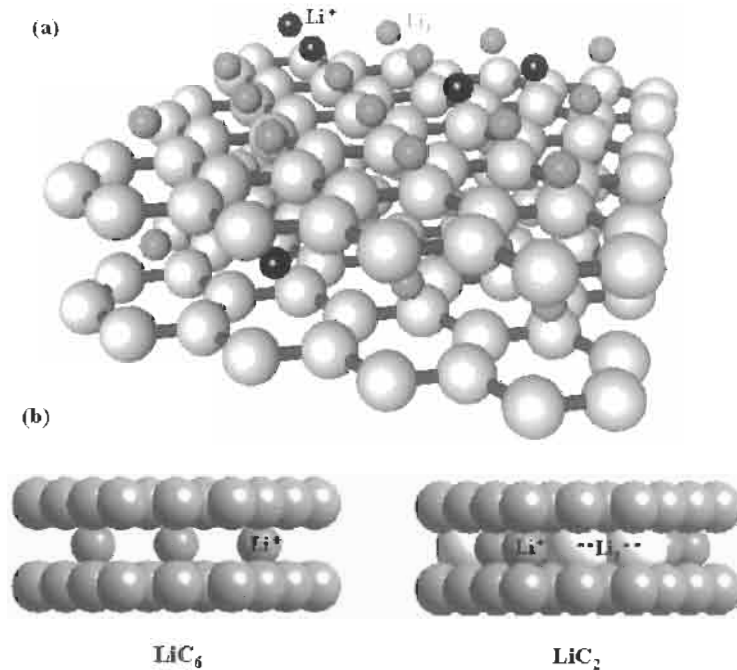


Fig. 3. A schematic model (LiC_2) for lithium insertion into the PPP-based carbons (a) and side view of a LiC_6 model is shown on the left while side view of LiC_2 model is shown on the right (b).

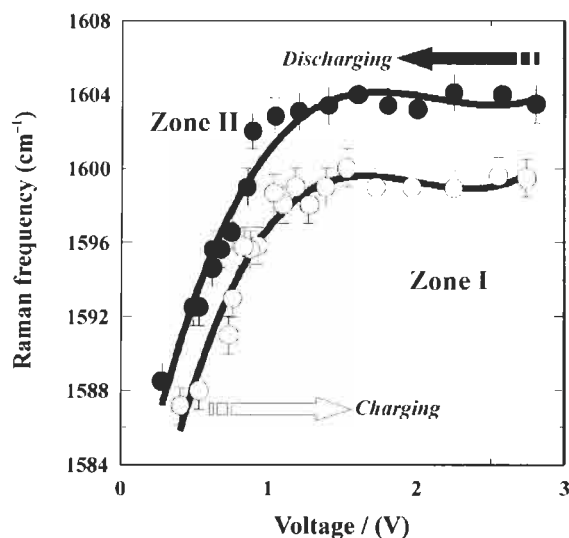


Fig. 4. The voltage dependence for the high frequency Raman modes of the PPP-based carbon anode in the lithium-ion battery. Heat treatment at 700°C and curves were obtained by fits to a Lorentzian line shape.

capacity of LiC_2 , which is three times higher than in graphite (LiC_6). The voltage dependence of the high frequency Raman modes of the PPP-based carbon, heat treatment temperature 700°C, for electrochemical insertion of Li ions is shown in Fig. 4 [6]. Lithium is taken up at a preferred binding site in PPP-based carbons in the high voltage range (2.8–1.0 V), denoted by Zone I, while Li insertion and release in the PPP-based carbon are accompanied by a shift of the peak wave number to the lower voltage range (1–0.04 V), denoted by Zone II. Raman results on PPP-based carbons suggest a charge transfer effect, following introduction of Li^+ ions, even in such a disordered material. Other kinds of disordered carbon show no change in Raman peaks. Raman experiments in highly ordered graphite exhibit a distinct peak change based upon the stage phenomena. The intensity changes of the Raman bands observed in PPP-based carbon correlate with the electrical conductivity associated with the lithium insertion and release. Inaba et al. reported an *in situ* Raman study on MCMC heat-treated at around 1000°C, and showed no change in 1580 cm^{-1} Raman peak [7]. These different results indicate that these charge and discharge mechanisms taking place especially in low temperature carbons, with super high Li storage capacity, differ carbon to carbon, being dependent upon the detail of structure within these carbons.

The above results are consistent with NMR studies of charge and discharge processes [5]. The lithium atoms in PPP-based carbon must occupy two different sites corresponding to bands A and B. Band C can be assigned to the by-product lithium carbonate. Band A has a Gaussian line shape with a chemical shift of 9.85 ppm and a half width of 11.6 ppm. Band B has a Lorentzian line shape with a chemical shift of

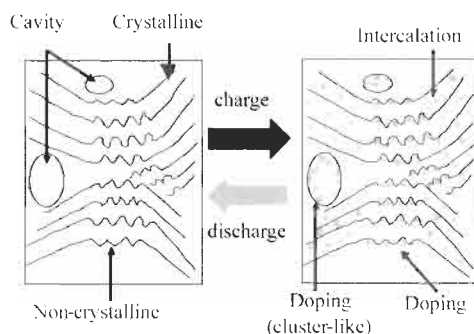


Fig. 5. A schematic model for the insertion of lithium into the internal surfaces of nanopores formed by single, bi- and tri-layer graphene sheets in glassy carbon materials.

−0.62 ppm and a half width of 8.9 ppm. The nature of band A can be understood from the doping of a lithium ion by PPP-based carbons. This is accompanied by electron occupation in the lowest unoccupied molecular orbital (LUMO) and gives rise to radical formation. The Gaussian line shape of band A is consistent with the ionic mechanism, where ${}^7\text{Li}$ nuclei are fixed and inhomogeneous broadening determines the line shape. Namely, site A can be considered as an ionic or GIC site. On the other hand, band B may result from the existence of molecular Li_2 in the PPP-based carbon. A small chemical shift for band B is consistent with a Li_2 molecule model. This model is also consistent with a Lorentzian line shape. As a result, this site is called a “covalent” site to be distinguished from the ionic site. Both lithium sites are schematically demonstrated in Fig. 3b.

The large Li storage capacity as LiC_2 in the PPP-based carbon is largely due to the formation of small flat pre-graphitic clusters with small diameters of several nanometres. The insertion of lithium into the disordered carbons obtained from a petroleum pitch [8], epoxy Novolac resin [9], and polyfurfuryl alcohol [10] has been extensively studied by measuring the voltage profiles for charging and discharging of Li ions, aiming for development of high capacity LIB. The voltage profiles of the glassy or disorder carbons show characteristic low voltage plateaux with relatively high charge–discharge capacities.

The storage sites of Li^+ ions with higher densities than in first-stage Li remain to be elucidated. Another model in which lithium is inserted and stored in the specific nanopores or surfaces of single layer graphene sheets [11,12] has been put forward, and is as shown schematically in Fig. 5. In disordered carbons, three types of Li storage mechanisms could be occurring depending upon the defective small carbon network structure.

4 Substitution of Heteroatoms

Many heteroatoms and molecules can be intercalated between the layers and or can reside at the edges of carbon “grains” and near to inter-cluster vacancies. However,

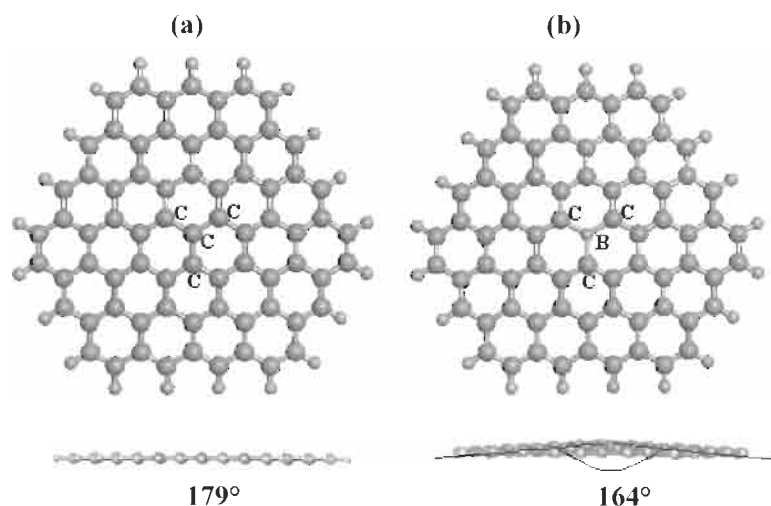


Fig. 6. A schematic model for (a) undoped and (b) boron-substituted graphene sheet. Side view of the graphene at the left is the undoped sheet, and at the right is the boron-doped sheet that has an apex angle of 164° .

such heteroatoms as boron (B) and nitrogen (N) can occupy carbon lattice sites substitutionally. In disordered carbons, nitrogen atoms have sp^3 bonding. Boron (B) atoms can substitute carbon atoms in the hexagonal basal planes of graphite to an extent of less than 2.5–3.0 at% [20]. The substituted boron atoms behave as an anti-oxidant, a graphitization catalyst and improve the charge–discharge capacity for Li-ion rechargeable batteries [13–18]. A schematic model for the boron-substituted graphene sheet based on the structure analysis obtained by STM of HOPG (highly oriented pyrolytic graphite) and calculated model is shown in Fig. 6, to be compared with that of pristine graphite sheet [19]. At a B-doped lattice site an electron is localized and an emphasized atomic image can be observed in the specific trigonal lattice of an STM image. Boron doping of graphitizable carbons can reach 2.5 at% [20] with electronic [19,21] as well as electrochemical changes [1,2].

Oxidation is a serious problem for carbon–carbon composites above 400°C , so limiting applications at high temperatures. It is established that substituted boron significantly improves the anti-oxidation behavior of a carbon–carbon composite [17,22]. Jones and Thrower proposed three possible mechanisms to explain the role of boron as an anti-oxidant of graphite [17].

1. Physical blockage of the surface active sites by a B_2O_3 barrier layer formed on the surface during oxidation.
2. Chemical inhibition via electron transfer between carbon and substitutional boron atoms on the internal graphite lattice sites, which increases the activation energy for the C-O_2 reaction.
3. Boron doping results in the improvement of graphite crystallinity, and thus decreases in the total number of accessible active surface sites for oxygen.

Both chemical features and electronic structures can be modified by B-doping. Boron doping has been reported for mesocarbon microbeads (MCMBs) [1] and carbon fibers [2], heat treatment temperature $>1800^{\circ}\text{C}$, by using metallic boron as a dopant, extents of substitution increasing with increasing HTT. An effect of boron doping is to accelerate the graphitization of carbon materials for HTT of $1800\text{--}2500^{\circ}\text{C}$. Electrochemical lithium intercalation takes place at a higher potential in boron-doped graphite than in undoped carbons presumably because the substitutional boron acts as an electron acceptor in the carbons and changes the electronic structure especially of Highest Occupied Molecular Orbital (HOMO) [23]. The interlayer spacing distances (d_{002}) as a function of heat treatment temperature and charge-discharge profiles for doped and undoped MCMBs heat treated at 2000°C are compared in Figs. 7a and b [1,2].

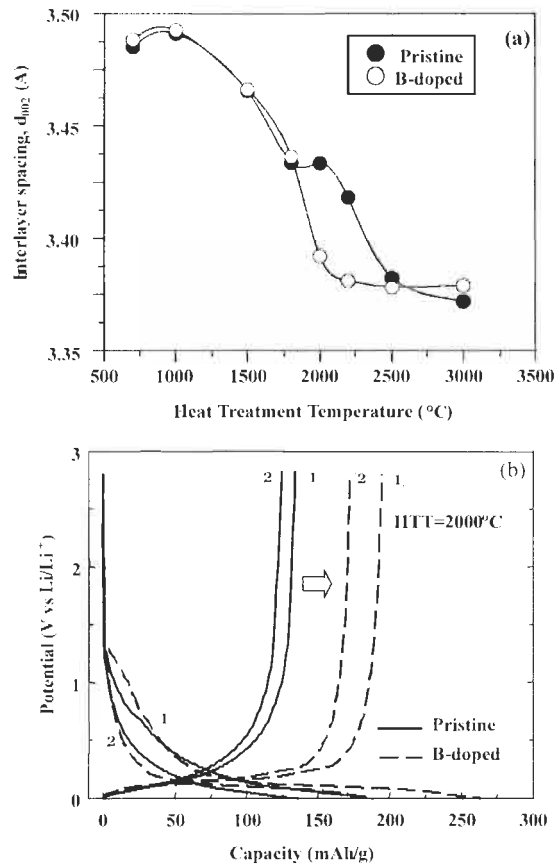


Fig. 7. The interlayer spacing distances (d_{002}) as a function of heat treatment temperatures (a) and charge-discharge profiles for doped and undoped MCMBs heat treated at 2000°C (b). First and second cycles are indicated in (b).

The carbon alloys obtained by doping with B, N and possibly with Si and P may modify the electronic, chemical and physical properties of graphene layers. Doping is one promising approach for alloying carbons, one which may widen applications of graphite and carbons.

5 Metal-doped Fullerenes

Fullerene-containing soot is synthesized using an arc discharge between graphite electrodes in approximately 200 torr of helium gas [24]. The soot contains about 13 wt% of C_{60} and 2% C_{70} . Doping is used to modify the electronic properties of the fullerene molecule and bulk crystals. Metal-doped fullerene, mainly *endohedral* doping, is where rare earth metals such as La, Y and Sc enter the interior of such cage molecules such as C_{60} , C_{66} and C_{82} [25]. The substitution of a heteroatom such as boron for a carbon atom on the cage molecule has also been known [26]. *Exohedral* doping, also called intercalation with doped species located between the cage molecules, is the most common method for doping fullerenes. Electrical conductivity of fullerenes increases considerably with exohedral doping [27] as in GIC. Alkali metals such as Li, Na, K, Rb, and Cs have been used as exohedral dopants for C_{60} crystalline solids. Structural models for endohedral and exohedral doping into the fullerenes are shown in Fig. 8. The most interesting electric property of the metal-doped fullerenes is the high temperature superconductivity at about 40 K [28]. Fullerenes doped with Cs at 40 K [29], Rb at 29 K [30], and K at 18 K [31] show superconductivity. Metal-

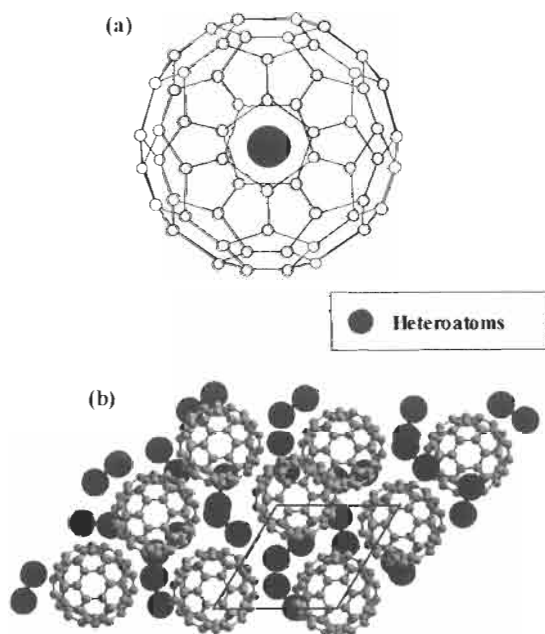


Fig. 8. The model structures for (a) endohedral and (b) exohedral doping into the fullerenes.

doping causes the lattice constant of the host crystals, based on C_{60} , to increase, the C_{60} – C_{60} coupling to decrease, and the electronic bandwidth derived from the LUMO level to narrow, and thereby the corresponding electronic density of states to increase. The strong dependence of the superconducting transition temperature T_c for various metal (M) compounds such as M_3C_{60} and $M_{3-x}M_3C_{60}$ on the lattice constant has been studied [31]. Enhancement in electrical conductivity and occurrence of superconductivity takes place by charge transfer phenomena after exohedral doping, very similar to the occurrence of superconductivity in GICs such as $C_4CsBi_{0.55}$ (4.05 K).

6 Metal-doped Carbon Nanotubes

The electrical resistivity of carbon nanotubes and fullerenes can be significantly improved by metal doping. Metal-doped carbon nanotubes can also be synthesized by a laser ablation method. Figure 9 shows the schematic model for a metal-doped carbon nanotube rope. Thess et al. report [32–34] that Ni/Co-doped carbon electrodes form bundles of single-walled carbon nanotube (SWCNT) through the laser ablation method, resembling a rope-like nanotube bundle. The electrical resistivity of the rope-like tube is $0.34 \times 10^{-4} \Omega\text{-cm}$ at 300 K, showing metallic behavior in the temperature dependence. It has an electron transport property of a nano-scale quantum wire at low temperatures. Doping with K or Br_2 brings about important changes in the overall resistivity-temperature behavior. Figure 10 the variation of resistivity with temperature for doped bulk SWNT samples [34]. After doping, the resistivity exhibits a more metallic behavior as observed in GICs.

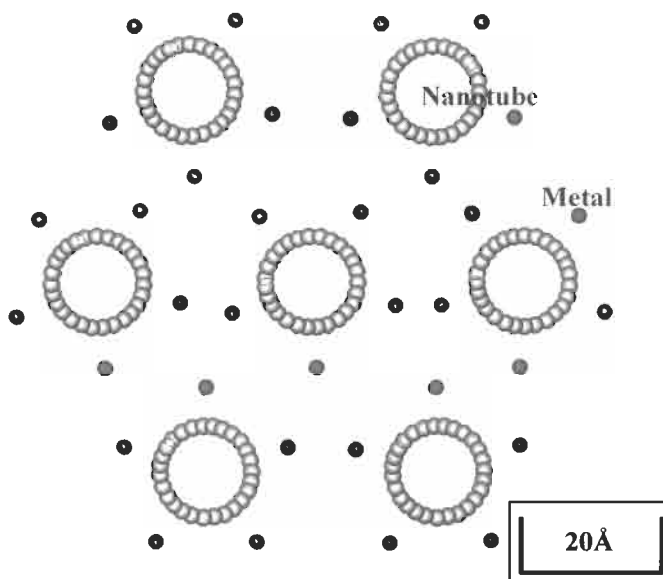


Fig. 9. A schematic model of the metal-doped carbon nanotube.

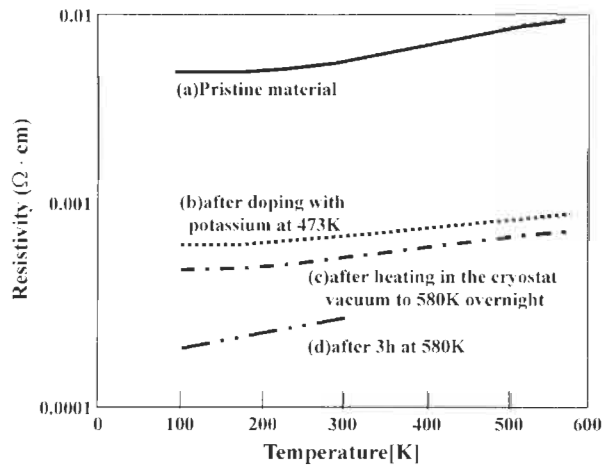


Fig. 10. Resistivity versus temperature for a bulk SWCNT sample [3]: (a) Pristine material; (b) after doping with potassium at 473 K; (c) after heating in the cryostat vacuum to 580 K overnight; (d) after 3 h at 580 K.

An ambitious approach, unique to SWNTs, would be to exploit the quantum phenomena observed at very low temperatures; doping-induced shifts in conductance peaks versus voltage should be directly related to the shift in Fermi energy of the tubes.

Another type of alloying of carbon nanotubes is doping by nitrogen atoms. This will change the electronic structure of carbon nanotubes to metallic so suggesting further applications. N-doped carbon nanotubes are prepared by several methods. One method is the pyrolysis of a solid organic precursor such as melamine using ferrocene as a catalyst [35]. SEM images of N-doped (CN_x) nanotubes obtained by the pyrolysis of solid organic precursor are shown in Fig. 11. The SEM images show well-aligned tubes. HRTEM images (Fig. 12a) show the bamboo-shaped morphology of CN_x tubes. The above SEM and HRTEM images suggest the schematic model of CN_x tubes as shown in Fig. 12b. Another method for preparing the CN_x nanotube is by spray pyrolysis [36,37].

Carbon nanotubes can be fluorinated as reported for carbon fibers [38,39]. The electronic state is that of a semiconductor [38,39] being dependent on the type of C-F bonding (covalent or ionic) and the location of the fluorine atoms within the carbon. The lubrication properties of fluorinated nanotubes and of nanofibers are better than for other CF_x systems. In Fig. 13, TEM images of fluorinated nanotubes at different resolutions are shown. These images show that the morphology of the fluorine-containing fibers is amorphous and defective and that this is caused by the presence of fluorine atoms within the graphene layers. This is very similar to that observed in bulk $(CF)_n$ [40]. The proposed model for ideal fluorination of a nanotube is shown in Fig. 14. In this model, the stoichiometry is CF_2 , but in the fluorinated nanotubes it is estimated, from the EELS spectra, that their fluorine content was ca. 1–8 at% [41]. It

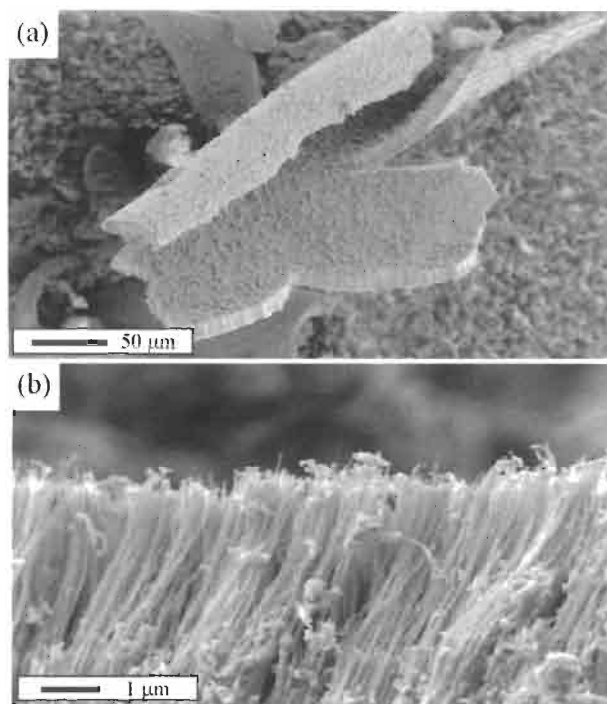


Fig. 11. SEM images of CN_x nanotubes at different resolutions.

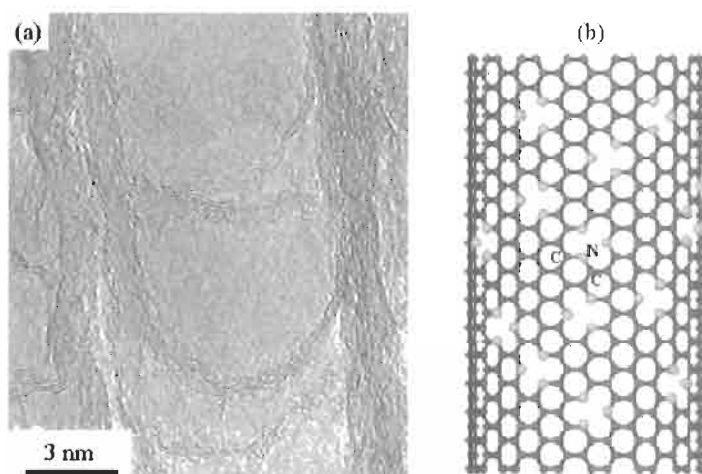


Fig. 12. TEM image (a) and schematic model (b) of CN_x tube. Bamboo shape morphology is clearly found in the image.

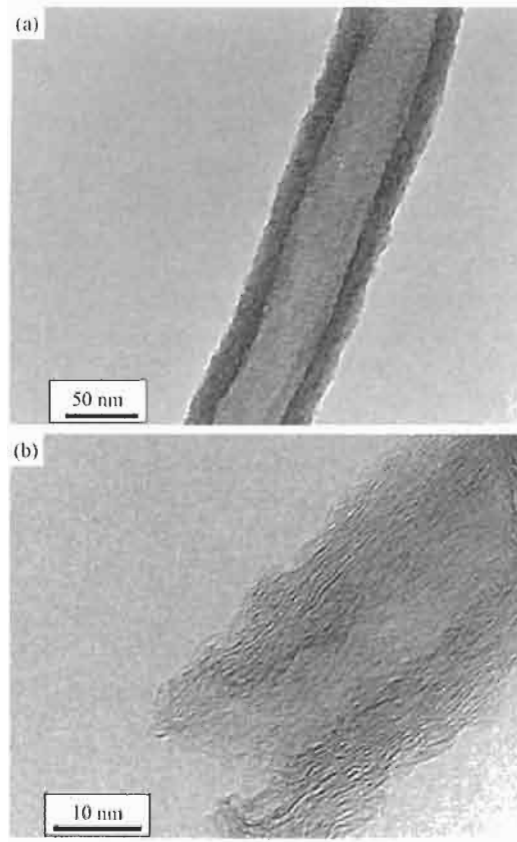


Fig. 13. TEM images of fluorinated carbon nanotubes at different resolutions. Disordered layer structure can be found.

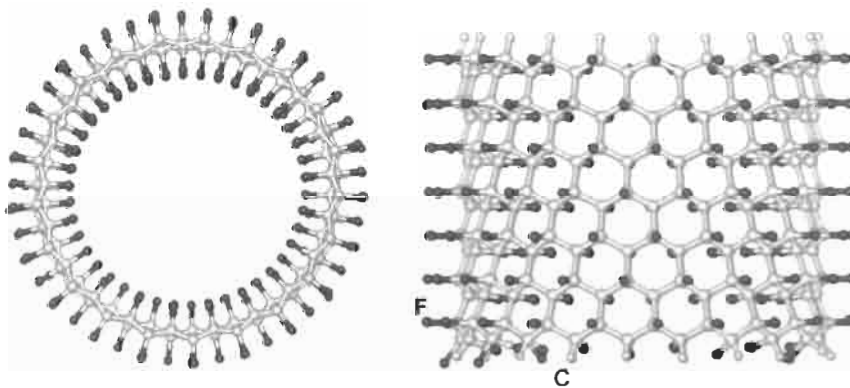


Fig. 14. Simulated model of CF_2 nanotube.

was also found that electron beam irradiation heating of fluorinated nanotubes, using UHVTEM, enhances the dissociation of fluorine atoms from the carbon network, resulting in the recovery of the layered structure of the undoped carbon nanotubes [41,42].

7 Conclusions

Research into carbon alloys by designing the structure at the both atomic and molecular levels for carbon nanotubes, fullerenes, fibers, glassy carbons, single crystal graphites and related materials, is still at an early stage in science and in practical application. Reaction mechanisms for alloying need further elucidation. However, carbon alloys may have important and promising industrial applications such as in electrical and electronic devices, space technologies, batteries and bioengineering. Large-scale production of carbon alloys is also an important target for the carbon industries. The nano-scale structure of carbon materials and their alloys may be a key factor to control and to design the physical and chemical properties of innovative applications of carbons, graphites and related materials

References

1. C. Kim, T. Fujino, K. Miyashita, T. Hayashi, M. Endo and M.S. Dresselhaus, *J. Electrochem. Soc.*, 147: 1257, 2000.
2. C. Kim, T. Fujino, K. Miyashita, T. Hayashi, M. Endo and M.S. Dresselhaus, *J. Electrochem. Soc.*, 147: 1265, 2000.
3. Sony's Catalog, Lithium ion rechargeable battery, ACG-4012-N-9707-P3-002, 1997.
4. M. Endo, C. Kim, T. Karaki, Y. Nishimura, M.J. Matthews, S.D.M. Brown and M.S. Dresselhaus, *Carbon*, 37: 561, 1999.
5. K. Sato, M. Noguchi, A. Demachi, K. Oki and M. Endo. *Science*, 264: 556, 1994.
6. M. Endo, C. Kim, T. Karaki, T. Fujino, M.J. Matthews, S.D.M. Brown and M.S. Dresselhaus, *Synthetic Metals*, 98: 17, 1998.
7. M. Inaba, H. Yoshida and Z. Ogumi, *J. Electrochem. Soc.*, 143: 2572, 1996.
8. N. Sonobe, M. Ishikawa and T. Iwasaki, 35th Battery Symposium in Japan, Extended Abstracts, 47, 1994.
9. Y. Liu, J.S. Xue, T. Zheng and J.R. Dahn, *Carbon*, 34: 193, 1996.
10. A. Omaru, H. Azuma, M. Aoki, A. Kita and Y. Nishi, 182nd meeting of the Electrochemical Society, Toronto, Canada, Extended Abstracts of Battery Division, 34, 1992.
11. A. Mabuchi, K. Tokumitsu, H. Fujimoto and T. Kasuh. *J. Electrochem. Soc.*, 142: 1041, 1995.
12. J.R. Dahn, T. Zheng, Y. Liu and J.S. Xue. *Science*, 270: 590, 1995.
13. B.M. Way, J.R. Dahn, T. Tiedje, K. Myrtle and M. Kasrai, *Phys. Rev.*, B46: 1897, 1992.
14. M. Endo, C. Kim, T. Karaki, T. Tamaki, Y. Nishimura, M.J. Matthews, S.D.M. Brown and M.S. Dresselhaus, *Phys. Rev.* B58: 8991, 1998.
15. J.R. Dahn, J.N. Reimers, A.K. Sleight and T. Tiedje, *Phys. Rev.* B45: 3773, 1992.
16. J.G. Naeni, B.M. Way, J.R. Dahn and J.C. Irwin, *Phys. Rev.* B54: 144, 1996.
17. L.E. Jones and P.A. Thrower, *Carbon*, 29: 251, 1991.
18. A. Agrawal, H. Yinnon, D.R. Uhlmann, R.T. Pepper, C.R. Desper, *J. Mat. Sci.*, 21: 3455, 1986.

19. M. Endo, T. Hayashi, S.W. Hong, T. Enoki and M.S. Dresselhaus, *J. Appl. Phys.*, 90: 5670, 2001.
20. C.E. Lowell, *J. Am. Ceram. Soc.*, 50: 142, 1967.
21. Y. Hishiyama, H. Irumano and Y. Kaburagi, *Phys. Rev.*, B63: 245406, 2001.
22. H. Murty, D. Beiderman and E. Herintz, *Fuel*, 56: 305, 1997.
23. N. Kurita, *Carbon*, 38: 65, 2000.
24. H.W. Kroto, J.R. Heath, S.C. O'Brien, R.F. Curl and R.E. Smalley. *Nature (London)*, 318: 162, 1985.
25. D.S. Bethune, R.D. Johnson, J.R. Salem, M.S. de Vries and C.S. Yannoni, *Nature (London)*, 366: 123, 1993.
26. M.S. Dresselhaus, G. Dresselhaus and P.C. Eklund, *J. Mat. Res.*, 8: 2054, 1993.
27. M.S. Dresselhaus and G. Dresselhaus, *Adv. Phys.*, 30: 139, 1991.
28. C.M. Lieber and C.C. Chen, In: *Solid State Physics*. Academic Press, New York, 109, 1994.
29. T.T.M. Palstra, O. Zhou, Y. Iwasa, P. Sulewski, R. Fleming and B. Zegarski, *Solid State Commun.*, 93: 327, 1995.
30. H.A. Hebard, *Phys. Today*, 45: 26, 1992, Nov. issue.
31. R.C. Haddon, A.F. Hebard, M.J. Rosseinsky, D.W. Murphy, S.J. Duclos and F.A. Thiel, *Nature (London)*, 350: 320, 1991.
32. A. Thess, R. Lee, P. Nikolaev, H. Dai, P. Petit, J. Robert, C. Xu, Y. H. Lee and S.G. Kim, *Science*, 273: 483, 1996.
33. J.E. Fischer, H. Dai, A. Thess, R. Lee, N.M. Hanjani, D.L. Dehaas and R.E. Smalley. *Phys. Rev.*, B55: R4921, 1997.
34. R.S. Lee, H.J. Kim, J.E. Fischer, A. Thess and R.E. Smalley. *Nature*, 388: 255, 1997.
35. M. Terrones, H. Terrones, N. Grobert, W.K. Hsu, Y.Q. Zhu, J.P. Hare, H.W. Kroto, D.R.M. Walton, Ph. Kohler-Redlich, M. Rühle, J.P. Zhang and A.K. Cheetham, *Appl. Phys. Lett.*, 75: 3932, 1999.
36. M. Mayne, N. Grobert, M. Terrones, R. Kamalakaran, M. Rühle, H.W. Kroto and D.R.M. Walton, *Chem. Phys. Lett.*, 338: 101, 2001.
37. M. Terrones, R. Kamalakaran, T. Seeger and M. Rühle, *Chem. Comm.*, 23: 2335, 2000.
38. G. Seifert, T. Kohler and T. Frauenheim, *Appl. Phys. Lett.*, 77: 1313, 2000.
39. K.N. Kudin, H.F. Bettinger and G.E. Scuseria, *Phys. Rev. B*, 6304: 5413, 2001.
40. M. Endo, M. Shikata, H. Touhara, K. Kadono, and N. Watanabe. *Trans. Inst. Elect. Eng. Japan*, 105-A: 329, 1985 (in Japanese).
41. T. Hayashi, M. Terrones, C. Scheu, Y.A. Kim, M. Rühle, T. Nakajima and M. Endo, *Nanoletters*, 1: 491, 2002.
42. T. Hayashi, M. Terrones, Y.A. Kim, T. Nakajima and M. Endo, In: *Nanotubes and Related Materials*, MRS, A14, 18, 2001.

Chapter 4

Surface and Hidden Surface-controlled Carbon Alloys

Katsumi Kaneko

Department of Chemistry, Faculty of Science, Chiba University, Inage, Chiba 263-8522, Japan

Abstract: The importance is emphasized of a new concept called a “hidden surface” to describe porosity in carbons; the necessity for this concept of a hidden surface is supported by molecular potential theory. Approaches to methods of alloying porous carbons and the merits of alloyed porous carbons are described. The alloying of hidden surfaces can be brought about by (a) introduction of mixed valencies into carbons, (b) doping by foreign atoms or clusters, (c) development of specific porosities, and (d) the tailoring of hidden surfaces with clusters and ultrafine particles. Space-alloying in porosity is further discussed in terms of alloying-induced pore space, control of pore space functions by alloying, and nanogeometry-controlled growth of foreign compounds. Several examples of alloyed porous carbons possessing new functions and properties are described.

Keywords: Micropore, Mesopore, Gas adsorption, Molecular potential calculation, Alloyed porous carbon.

1 Importance of Hidden Surfaces and Confined Spaces in Carbon Materials

Solid surfaces are never completely flat. Even the surface of a single crystalline solid has some roughness due to an irregular arrangement of the surface atoms. Solid surfaces have a roughness factor stemming from surface voids and pores. Although there is no rigorous distinction between surface voids and pores, the term “pore” is used for a void whose depth is larger than molecular sizes. Pores are classified into micropores ($w < 2$ nm), mesopores (2 nm $< w < 50$ nm), and macropores ($w > 50$ nm) according to IUPAC [1]. Here w is the pore width which is the slit width for slit-shaped pores or the diameter of cylindrical pores. Here this new concept of the hidden surface is used to stress differences from the concepts of established surface science. Pore-wall surfaces are called the hidden surfaces because they cannot be elucidated by ordinary surface-science investigative tools and because they have unique properties quite different from those of external surfaces.

Solid materials have a cohesive structure which depends on the interaction between primary particles. The cohesive structure leads indispensably to void spaces which are not occupied by such composite particles as atoms, ions, and fine particles.

Consequently, such voids or pores intensively depend on the cohesive forces. For carbons, diamond has very strong covalent sp^3 - sp^3 bonding, while graphite has both conjugated (sp^2 - sp^2) bonding in the graphene sheet and the weak inter-graphene sheet interactions which approximate to van der Waals interactions. The van der Waals interaction is associated with the interacting area. The inter-graphene sheet distance becomes larger with decreasing graphene sheet size. Thus, the pore structure depends on fundamental chemical bonding structures.

Carbon materials are classified into crystalline and less-crystalline materials. Graphite and diamond are representatives of well-crystalline (single crystal) carbon materials. Graphite is composed of stacked graphene sheets with the interlayer spacing almost coinciding with the thickness of the graphene sheet, owing to the above-mentioned bonding state. Consequently, graphite has no effective space between the graphene sheets for acceptance of foreign atoms and molecules. However, appropriate conditions produce what are called “intercalation compounds”. Atoms such as potassium atoms can be inserted between the graphene sheets. Thus, even graphite can have latent spaces in its structure. For diamond, the interatomic covalent bond is too strong to accept foreign atoms to form a new compound. Activated carbon is a representative porous solid. The fundamental structure is noncrystalline, and is composed of imperfect nanographitic units (these are designated “nanographites” here) with inter-nanographite-linkages of the sp^3 - sp^3 bonding nature to form the pore walls. The chemical bonding state of activated carbon is a mixed state of graphite and diamond. There is an abundance of pore space between pore walls. The surface areas of the pore walls and the external surface of activated carbon sample can be determined by nitrogen adsorption at 77 K with the aid of the subtracting pore effect (SPE) method [2,3]; this method will be described later. The surface area of pore walls of activated carbon is $> 1000 \text{ m}^2 \text{ g}^{-1}$, whereas that of the external surface is less than $\sim 50 \text{ m}^2 \text{ g}^{-1}$. Therefore, the pore spaces or intrapore surfaces are predominant compared with the external surface. Is there any difference between the hidden surfaces in the pore and external surfaces of carbon materials? Although the structures of actual activated carbons have a complexity inherent to the higher order structure of the precursor, the nano-level structure can be approximated by the basal plane of the graphite.

1.1 Differences between Hidden and External Surfaces based on Molecular Potential Theory

An explicit distinction for the hidden and external surfaces can be derived for the basal plane model using the following molecular potential theory. Two model cases will be shown: one is a graphite-slit pore model and the other is a single-wall nanotube open pore model. The graphite-slit pore model has been applied to activated carbon to explain the molecular adsorption properties. The latter model is applied to the single-wall carbon nanotube and single-wall carbon nanohorn.

The interaction of a molecule with the graphitic slit pore of the micropore model of activated carbon is expressed by use of the Lennard-Jones (LJ) potential and Steele potential. The interaction between a molecule and a surface atom as a function $\Phi(r)$ of the distance r between them can be expressed by the LJ potential

$$\Phi(r) = 4\varepsilon_{st}[(\sigma_{st}/r)^{12} - (\sigma_{st}/r)^6] \quad (1)$$

where ε_{st} and σ_{st} are the well depth and effective diameter for the molecule-graphitic carbon atom. These cross parameters are calculated according to the Lorentz-Berthelot rules, $\varepsilon_{st} = (\varepsilon_{ss} \varepsilon_{tt})^{1/2}$, $\sigma_{st} = (\sigma_{ss} + \sigma_{tt})/2$. Here, $(\sigma_{ss}, \varepsilon_{ss})$ and $(\sigma_{tt}, \varepsilon_{tt})$ are the Lennard-Jones parameters for a surface atom and a molecule, respectively. The interaction potential $\Phi(z)$ for a molecule and a single graphite slab is given by the Steele 10-4-3 potential [4]

$$\Phi(z) = 2\pi\rho_C \varepsilon_{st} \sigma_{st}^2 \Delta \{ (2/5)(\sigma_{st}/z)^{10} - (\sigma_{st}/z)^4 - \sigma_{st}^4 / [3\Delta(0.61\Delta + z)^3] \} \quad (2)$$

where z is the vertical distance of the molecule above the surface, Δ is the separation between graphite layers ($= 0.335$ nm), ρ_C is the number density of carbon atom in a graphite layer ($= 114/\text{nm}^3$). As the micropores of activated carbon can be approximated by the slit spaces between the predominant basal planes of nanographitic units, the whole interaction potential $\Phi(z)_p$ of a molecule with the micropore of an inter-graphite surface distance H can be given by Eq. (3):

$$\Phi(z)_p = \Phi(z) + \Phi(H - z) \quad (3)$$

Consequently, we can evaluate the potential profile of the molecule adsorbed in the graphitic micropore. Here H is not the effective pore width w determined by the adsorption experiment. The difference between H and w is a function of σ_{st} and σ_{tt} [5].

$$H - w = 0.85 \sigma_{st} - \sigma_{tt} \quad (4)$$

Figure 1 shows potential profiles of a nitrogen molecule with slit-shaped graphite pores of $w = 0.5$ and 1.2 nm using the one-center approximation. Here, the molecular position in Fig. 1 is expressed by a vertical distance z from the central plane between two pore-wall surfaces. The potential minimum for the flat surface is 1100 K, while the minima for $w = 0.5$ nm and 1.2 nm are 2250 K and 1200 K, respectively. The overlapping of the interaction potential from the opposite pore walls gives rise to a greater potential minimum for the slit pore. Also, the interaction potential profile for the $w = 0.5$ nm indicates that there are no sites localized on the pore-wall surface. The bottom of the potential profile is almost flat near the central position ($z = 0$) of the pore. On the other hand, the potential profile of $w = 1.2$ nm has distinct double minima on the pore-wall surface. Although the potential depth of $w = 1.2$ nm is greater than that of the flat surface, the potential profile indicates the localization of

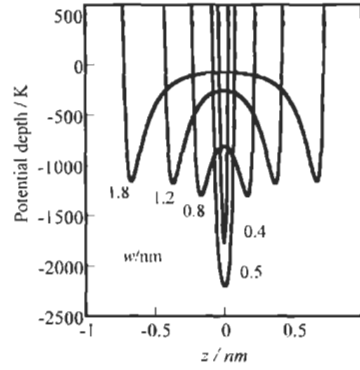


Fig. 1. The interaction potential profiles of an N_2 molecule with graphite slit pore as a function of pore width w .

nitrogen molecules on the pore walls. Accordingly, the potential profile of $w = 0.5$ nm is unique and it is indicative of the importance of the space concept inherent to the very narrow pores (ultra-micropores). The potential profile of the pore of $w = 0.4$ nm has the repulsive effect. The potential minimum of $w = 0.4$ nm is higher than that of $w = 0.5$ nm. Thus, the flat surface and the pore surface must be distinguished from the molecular potential theory. Also the external surface must be divided into the basal plane and the edge surface of actual graphite crystals. The molecule–surface interaction on the edge surface is different from that on the basal plane even without the presence of surface functional groups. The ideal structure of edge surfaces of graphite crystals should be surface terminated with hydrogen atoms, being completely different from the basal plane of the graphite. Fujita et al. [6] classified two types of the carbon–carbon structures at the edges of a graphene sheet as “armchair” and “zigzag” arrangements; the electronic structure sensitively depends on the structure. However, only differences between external and hidden basal planes will be discussed here.

For single-wall carbon nanotubes, the following equation for the molecule–pore wall interaction is used for calculation of the interaction potential profile [7].

Interaction potentials are evaluated below for molecules inside and outside a pore wall made of n -graphene rolled sheets by replacing the sum over atoms in each cylindrical shell by an integral. One will be left with a sum over shells of radii a_0, a_1, a_2, \dots , with $a_n = a_0 + n \times 0.34$ [nm]. Thus

$$U_{sf} = 4\epsilon_{sf}\rho_C \sum_n \int_{-\infty}^{\infty} dz' \int_0^{2\pi} a_n d\phi \left\{ \left(\frac{\sigma_{sf}}{r_{sf}} \right)^{12} - \left(\frac{\sigma_{sf}}{r_{sf}} \right)^6 \right\} \quad (5)$$

where ρ_C is the two-dimensional density of carbon and r is the distance of the adsorbate molecule from the axis of the cylinder and z' is the distance parallel to the pore axis. ϕ is the angle between a_0 and r . Equation (5) can be written as

$$U_{sf} = 4\varepsilon_{sf}\rho_C \left\{ \sigma_{sf}^{12} I_6 - \sigma_{sf}^6 I_3 \right\} \quad (6)$$

where

$$I_m = \int_{-\infty}^{\infty} dz' \int_0^{2\pi} \frac{a_n d\phi}{(z'^2 + a_n^2 + R^2 - 2a_n R \cos \phi)^m} \quad (m = 3 \text{ or } 6) \quad (7)$$

This integral can be expressed by a hypergeometric function using R and a_n . Here, R is the distance of the molecule from the center of the tube. Then the Steele smooth function for a molecule inside and outside the cylindrical pore can be analytically calculated. The detailed calculation procedures are reported elsewhere [8].

The interaction profiles of a nitrogen molecule with a nanotube of interatomic diameter $H = 2$ nm were calculated. The potential minimum inside the tube (1250 K) is deeper than that of the external position by more than 300 K. Thus, the difference of the molecule-pore wall interaction between the external and intrapore configurations is remarkable, compared with the slit-shaped pore of $H = 2$ nm (see Fig. 1). Hence, it is important to distinguish between the molecular states in the intrapore-space and on the external surface for molecular processes on the nano-order structures. This important feature on the inside and outside of pores can be extended to the macroscopic level. The Kelvin equation describes the dependence of the sign of the curvature of the surface of the condensate on the vapor pressure change of the condensate [9].

We need to introduce the concept of the hidden surface in order to stress the different nature of the pore-walls. In particular, the pores of nanometre ranges such as micropores and small mesopores require the concept of the hidden surface. Why do we use the term "hidden surface"? There are various kinds of advanced tools for surface science analyses using electrons such as X-ray photoelectron spectroscopy XPS, and scanning tunnelling microscopy STM. Unfortunately, these powerful surface science tools cannot be applied to elucidation of pore-wall structures and nano-order atomic or molecular systems in pores. Namely, the pore-wall structure and atomic or molecular system in pores are hidden from these surface science tools. Appropriate research methods to study hidden pore-wall structures and molecular systems confined in the pore need to be developed.

1.2 Confinement of Molecules in Carbon Micropore Spaces

The concept of a confined carbon space is important. A graphite slit-like pore of $w \leq 1$ nm has a deep potential well, as described above. Kaneko et al. elucidated the special function of such pores for molecules and atoms with *in situ* X-ray diffraction, *in situ* small angle X-ray scattering, low temperature magnetic susceptibility measurement, high resolution adsorption measurement, heats of adsorption measurements, and computer simulation using activated carbon fiber (ACF). ACFs have uniform

micropores. It is to be noted that pitch-based ACFs have fewer surface functional groups and ACFs of different w values are available. Typical examples of the confinement effect of molecules in the micropores of ACFs are given in the following.

The adsorption energy of a helium atom for the first layer with a graphite surface is 108 K (the energy is expressed in Kelvin) and even that of the second layer is 19 K, both of which are much greater than 4.2 K. Therefore, an enhanced bilayer adsorption occurs even on the graphite surface and carbon black at 4.2 K. Steele proposed a theoretical mechanism of enhanced bilayer adsorption [10]. This enhanced bilayer adsorption is particularly relevant for adsorption in carbon micropores at 4.2 K. This prediction is supported by the formation of a high density structure and marked uptake from an extremely low relative pressure P/P_0 [11,12]. A clear difference between the helium adsorption isotherm at 4.2 K and the nitrogen adsorption isotherm at 77 K of an ACF is observed; amounts of helium adsorption in the extremely low P/P_0 range ($<10^{-3}$) are much greater than those of nitrogen adsorption, indicating the presence of the enhanced bilayer adsorption of helium.

The critical and boiling temperatures of xenon are 289.6 K and 165.9 K at 101.32 kPa, respectively. The size of a spherical xenon molecule is 0.396 nm and the Xe–Xe interaction energy is 217 K, which is slightly smaller than the thermal energy at ambient temperature. Also the formation of xenon dimers of 0.2% was observed in the gas phase of 13 kPa at 190 K [13]. If we adsorb xenon atoms in carbon micropores, a considerable number of xenon dimers or clusters should be produced even near ambient temperature. As vapor can be coexistent with liquid, molecules in the vapor phase are associated with each other on the solid surface to induce a predominant physical adsorption. On the other hand, the intermolecular interaction of the supercritical gas is weaker than that of the liquid and thereby the formation of an adsorbed layer for the supercritical gas is quite difficult. The adsorption isotherm of supercritical xenon on ACF at 300 K is “Langmuirian” and extents of xenon adsorption are high regardless of the supercritical conditions, suggesting a special intermolecular interaction of xenon molecules such as the dimer and cluster formation. The simulated adsorption of supercritical xenon in a graphite slit at 300 K by the grand canonical Monte Carlo (GCMC) simulation is quite close to the observed isotherm. The cluster analysis of snapshots obtained by the GCMC simulation shows the presence of highly concentrated xenon clusters, which cannot be deduced from the bulk phase at 300 K. The calculated radial distribution functions from the snapshots for xenon molecules in the micropore of $w = 1.0$ nm at 76 kPa and 300 K give possible geometrical structures of the clusters; the association number of the clusters is widely distributed as twelve and triangle-based cluster structures are suggested [14]. If this cluster formation can be controlled, then supercritical xenon can be more efficiently adsorbed due to transformation from a supercritical gas to a vapor.

The critical temperature of NO is 180 K and hence it is quite difficult to adsorb supercritical NO at ambient temperatures. NO is a paramagnetic molecule and NO molecules form dimers in the condensed phase at low temperatures [15]. If this dimerization is enhanced with the aid of magnetic interactions, then NO should lose

its supercritical nature even at room temperature. The concentration of the NO dimers was determined for NO adsorbed in micropores of ACF by using magnetic susceptibility, because the NO monomer is paramagnetic and both the NO dimer and the ACF show diamagnetism. The magnetic susceptibility measurements determined the equilibrium constant K_d for the following dimerization reaction:



The K_d of NO adsorbed on pure ACF was determined at different temperatures, even though amounts of NO adsorption on pure ACF correspond to less than 0.2 of the fractional filling. The linear van 't Hoff plots of the K_d for the dimerization equilibrium lead the enthalpy of the NO dimer formation ΔH_d from the slope of the linear plot. The ΔH_d values obtained are in the range of 22 to 25 kJ mol⁻¹, being greater than that of the bulk phase by more than 10 kJ mol⁻¹. The NO dimers are stabilized in the micropores. The dimer concentration at 303 K is in the range of 92 to 98%. Thus, highly concentrated NO dimers are formed in the carbon micropores even at 303 K, although NO molecules are dimerized on the graphite surface at low temperature.

An alcohol molecule has both a hydroxyl and alkyl group and thereby the balance between inter-alkyl chain interaction and hydrogen bonding should be important in the adsorbed layer structure in micropores. The structures of alcohol molecules in carbon micropores were studied by adsorbed density and electron radial distribution function (ERDF) analyses of X-ray diffraction patterns [18–20]. The adsorbed densities from the micropore volume and the saturated adsorption of alcohol are summarized in Table 1. The bulk liquid and solid densities for alcohol are also shown in Table 1 for comparison. At the same time results using water are shown for comparison purposes. The adsorbed density of alcohol in micropores $w = 0.7$ nm is smaller than the bulk liquid density, whereas that of $w = 1.0$ nm is close to the bulk solid density. Accordingly, the adsorbed density data strongly suggest that the molecular structures of alcohol in micropores of $w = 0.7$ are less ordered than those of $w = 1.0$ nm and only molecular assemblies in micropores of $w = 1.0$ nm should be highly ordered. This prediction, however, does not agree with results from the ERDF

Table 1

Adsorbed density of alcohol and water in carbon micropores at 303 K (density unit: g/cm³)

| | $w = 0.7$ nm | $w = 1.1$ nm | Liquid | Solid |
|------------|--------------|--------------|--------|--|
| Methanol | 0.70 | 1.00 | 0.79 | 0.98(113 K) |
| Ethanol | 0.70 | 1.10 | 0.79 | 1.03(87 K) |
| 1-Propanol | 0.75 | 0.88 | 0.79 | 0.97 |
| Water | 0.86 | 0.81 | 0.996 | 0.92(I _h) 0.92(I _c) 1.17(I _{ll}) |

analysis. The ERDFs of methanol, adsorbed in micropores of $w = 0.7$ nm and $w = 1.0$ nm, have peaks at the same positions as bulk liquid methanol. Hence, the intermolecular structure of adsorbed methanol must be similar to liquid methanol. However, the amplitude of the adsorbed methanol is much higher than that of liquid methanol. The amplitude of methanol in $w = 0.7$ nm is more predominant than that in $w = 1.0$ nm. Here a greater amplitude of the ERDF peak means a more localization of molecules. Also, there is a shoulder on the peak at $r = 4.0$ nm, indicating the presence of contact orientation with the micropore wall. So, methanol molecules must form a highly ordered structure in micropores of $w = 0.7$ nm rather than $w = 1.0$ nm. This result contradicts the adsorbed density approach. However, the methanol molecules cannot fill effectively the highly restricted small space and the adsorbed density data do not necessarily contradict the concept of oriented structures. The peak position of ERDFs of ethanol and propanol adsorbed in micropores shifts to a smaller distance compared with the ERDF of the liquid ethanol and propanol. In particular, the shift of $w = 0.7$ nm is remarkable, indicating the presence of a dense packing structure. Also the peak amplitudes of adsorbed ethanol and propanol are much higher than those of liquid ethanol and propanol. The ordering limits of adsorbed ethanol and propanol are larger than those of liquid alcohol as noted from the damping of the amplitude. Therefore, ethanol and propanol both form highly oriented structures in the carbon micropores even in micropores of $w = 0.7$ nm, although the adsorbed density is smaller than that of bulk liquid. The ordered structures of alcohol on graphite surface at low temperature were studied by Morishige et al. [21]. They found that the molecular chain of an alcohol molecule is parallel to the (001) plane of graphite and those molecules are hydrogen-bonded to each other. Alcohol molecules form similar ordered structures in carbon micropores even at 303 K. This stems from the confinement effect due to the deep molecular potential well. Water is not adsorbed in graphitic micropores at low P/P_0 , but water molecules are adsorbed suddenly at the medium P/P_0 . In situ X-ray diffraction showed the ordered structure formation of water molecules in carbon micropores [22,23]. The ordered structure of water molecules in micropores of $w = 0.7$ nm does not change up to 140 K. Dipolar SO_2 molecules also form a dipole oriented structure in the carbon micropores [24,25].

Thus, carbon micropores accelerate formation of ordered structures for adsorbates and stabilize them. This confinement effect is the general effect which depends on the balance between the molecule–molecule and molecule–pore wall interactions. Then, the confinement accelerates pseudo-lattice formation of molecules.

2 Carbon Structure of Superhigh Surface Area

The theoretical upper limit of surface area for carbonaceous materials is $2630 \text{ m}^2 \text{ g}^{-1}$, which is calculated from an infinite single graphene layer. For a single wall carbon nanotube, the same upper limit applies. Carbons materials with surface areas greater than $2630 \text{ m}^2 \text{ g}^{-1}$ must, therefore, have unusual structures. However, X-ray diffraction

studies show that activated carbons consist of graphitic units whose stack width and stack height are about 2 nm and 1 nm, respectively. These nanographitic units are combined with each other to form the highly porous structure. For nanographitic units, contributions from edge surfaces, relative to the total surface area cannot be neglected and the surface area becomes larger than the limiting value. For example, nanographites of a trilayer structure of polyhexagons of carbon number = 56 and 71 have 3200 and 3100 $\text{m}^2 \text{g}^{-1}$ of the surface area, respectively. Therefore, if these nanographites are combined with each other to form the micropore wall without seriously losing contributions from the edge surface, activated carbon having the surface area = 2630 $\text{m}^2 \text{g}^{-1}$ can be expected [26]. Consequently, the great surface area can give a measure for the contribution by edge carbon atoms to molecular adsorption, in particular, for activated carbons having high surface areas close to the limiting value. An activated carbon having the surface area more than 2630 $\text{m}^2 \text{g}^{-1}$ is called a “super-high” surface area carbon, which is expected to exhibit characteristic physical properties [27,28]. At the same time, an overestimation of the surface area of the microporous carbon must be corrected. A routine BET analysis often provides an overestimation of about 50% for activated carbon whose pore width nearly corresponds to the thickness of the trilayer of nitrogen. This is because pores are filled in the P/P_0 range of 0.05 to 0.3 which is the best range of the validity of the BET equation. The enhanced molecule–pore wall interaction in micropores gives rise to completion of the monolayer formation below $P/P_0 = 10^{-3}$. Kaneko et al. [2,3,29] recommended a *subtracting pore effect (SPE) method* for an accurate evaluation of the surface area using the high resolution nitrogen adsorption isotherm over the wide P/P_0 range from 10^{-6} to 1. The SPE method uses the slope of the line passing through the origin and the amount of adsorption at $\alpha_x = 0.5$ for α_x -plot. The SPE surface area a_{SPE} is given

$$a_{\text{SPE}} = 2.14 \times (\text{slope of the line}) [\text{mg g}^{-1}] \quad (9)$$

Here, the amount of nitrogen adsorption is expressed by mg per g-adsorbent (mg g^{-1}). According to the SPE method, the enhanced adsorption can be removed from the upward swings below and/or above $\alpha_x = 0.5$. Hence, the difference between the SPE surface area and 2630 ($\text{m}^2 \text{g}^{-1}$) can be used as a measure of the edge surface contribution because the valency state of carbon atoms at the edge of nanographite is different from that of the inner carbon in the polyhexagon. The residual valence of the edge carbon atom should form an unpaired electron and a stable chemical bond with oxygen and hydrogen. Therefore, the SPE surface area may be a method for alloying.

3 Design of Hidden Surfaces with Alloying

Carbon materials having micropores and mesopores can be expected to possess excellent properties for such processes as adsorption, separation, and catalysis due to the inherent structures and natures described above. These functions are

indispensable to develop energy saving technologies, a comfortable society, and better medical technologies. Accordingly, it is desirable to control and improve the properties of carbon materials possessing micropores and mesopores. The concept of carbon alloys must be applied to these porous carbons. The alloying of porous carbons should be selectively applied to the hidden surfaces, external surfaces, and pore spaces. The key procedures for alloying hidden surfaces are as follows:

3.1 *Hidden Surface-Alloying*

(a) *Introduction of mixed valences*

As the main structure of porous carbon is composed of carbon atoms of sp^2 valence, the introduction of sp^3 or sp valence creates a mixed valence state, which alters the physical and chemical properties significantly. For the transition metal oxides, the introduction of mixed valence plays a key role in controlling electrical, magnetic, and optical properties.

(b) *Doping of foreign atoms or clusters*

Carbon and boron nitride share common allotropes; there are the hexagonal graphitic form and the cubic diamond one. However, there is a distinct difference between carbon and boron nitride in the nature of the interatomic bonding. Boron nitride has a polar character due to the boron–nitrogen bond ($-N^- - B^+ -$), while graphite and diamond have no polar character in the carbon–carbon bonding. Borek et al. [30] prepared a microporous boron nitride. Doping of foreign atoms having different valence and electron negativity in the graphitic frame can vary partially the bonding character, as shown by boron nitride. The doping of foreign atoms can be selectively done on the hidden and external surfaces in order to promote specific functions.

(c) *Development of pore structures*

An increase in surface area of carbon materials is accompanied with an increase in numbers of edge carbon atoms. The bonding state of the edge carbon atoms is different from that of the carbon atoms within a graphene sheet (see Section 2). Thus, activation processes inevitably bring about the alloying effect in carbon materials. If polymer precursor containing heteroatoms such as nitrogen are carbonized and activated, then heteroatom-imbedded hidden surfaces can be produced. A typical example is polyacrylonitrile-based activated carbon which contains nitrogen atoms in the carbon frame.

(d) *Tailoring hidden surface with clusters and ultrafine particles*

The graphitic nature of the predominant hidden surfaces is modified by dispersion of clusters and ultrafine particles which have properties different from the graphene surface. For example, the hydrophobic nature of the graphene surface can be changed into hydrophilic one by dispersion with ultrafine silica particles. The clusters and ultrafine particles are selectively dispersed on both hidden surfaces and external

surfaces. The dispersion of iron oxides in the micropores of ACF can be done as follows. The ACF evacuated in vacuo is immersed in the iron salt solution and ultrafine iron oxide particles can be formed on the external and hidden surfaces. Intensive washing removes the iron oxide particles from the external surface and so only hidden surfaces are modified with iron oxide particles. Dispersed iron oxide particles on ACF are characterized by FeK-edge XAFS [31]. For selective modification with metal oxides of the external surface, organometallic molecules whose diameter is greater than the micropore width can be used. Iron acetylacetonate $C_{15}H_{21}O_6Fe$ (diameter = 1.3 nm) is adsorbed on only the external surface of ACF. The decomposition of the adsorbed iron acetylacetonate leads to Fe_3O_4 on the external surface [32]. This external surface modification enhances NO adsorption.

3.2 Pore Space-Alloying

(a) Alloying-induced pore space

Graphite has no open pores, but intercalation of foreign atoms in graphite produces open spaces. However, the intercalated graphite is unstable under the ambient conditions except for a special case and it is difficult to produce effective pore spaces by intercalation. Hydrogen and alcohol molecules are adsorbed in the micropores produced by intercalation between the graphite sheets [33–35].

(b) Control of pore space function with alloying

Clusters and ultrafine particles are dispersed in pores. This modification procedure has been widely adopted to donate new surface functions to activated carbon. This control is not explicitly distinguished from the tailoring of hidden surfaces described above. In the case of mixed gas adsorption, the coexistent gas can affect the adsorption of a predominant component gas due to formation of a type of molecular clathrate compound. Water molecules in carbon micropores form an ordered structure, as described above. It tends to get guest molecules to form the hydrate compound structure [36–38]. This is an alloying effect.

(c) Nanogeometry-controlled growth of foreign compounds

Activated carbons have slit-shaped micropores, while carbon nanotubes have cylindrical micropores. Therefore, if we introduce reagents in micropores to grow a compound *in situ*, the geometry of the prepared compound is regulated by the pore geometry, providing the compound is of nanometre size. Hence, nano-order sheets and wires may be obtained using the slit-shaped and cylindrical micropores of carbon. This synthetic technique is often called template synthesis. This template synthesis using pore spaces has another merit. The reactant confined in nano-range pores is exposed to the strong molecule–pore interaction potential field, which induces a quasi-high pressure effect, described above. Accordingly, template synthesis provides new, special modification of the compound which is stable only at high pressure regardless of the reaction conditions of the sub-atmospheric pressure. Also the

synthetic reaction can be accelerated by the quasi-high pressure effect. There is clear evidence for such an acceleration effect for the disproportionation reaction of $(\text{NO})_2$ [39,40].

4 Properties of Hidden Surface- or Pore Space-alloyed Carbons

4.1 Alloying by introduction of mixed valences

Activated mesocarbon microbeads (a-MCMB) prepared from mesocarbon microbeads (MCMB) with oriented polycyclic aromatic layer structures have large surface areas, with structures of mixed sp^2 and sp^3 valencies. The conjugated sp^2 electrons lead to strong diamagnetism, whereas sp^3 dangling bonds of edge carbon atoms give paramagnetic properties. Hence, the magnetic susceptibility χ at a low temperature should be helpful to elucidate the mixed valence state of porous carbons. According to the preceding studies, a-MCMB shows spin glass or mictomagnetism. The χ -T curve with the heating has a maximum at 4.2 K, whereas with cooling increases the χ -T curve with lowering of temperature. This is a characteristic of spin glass, which originates from highly isolated spins. The isolated spins should be mainly associated with sp^3 dangling bonds. Hence, the systematic examination of the χ -T relation at a low temperature range is requested for the mixed valence state of a-MCMB. However, the preceding a-MCMB was activated by KOH using a stainless equipment and thereby it contains slight magnetic impurities such as Fe [27]. Accordingly it is necessary to prepare a-MCMB by KOH activation using nonmagnetic equipment [28]. The a-MCMB was prepared with KOH activation using a platinum crucible at 1173 K for 1 h under an air or nitrogen atmosphere as a function of the KOH quantity. The KOH activated MCMB is denoted an a-Mx. Here x is the weight ratio of KOH to MCMB. The samples after the KOH activation were washed with distilled water and 0.1 N HCl to remove the residual KOH and metallic potassium.

The nitrogen adsorption isotherms of a-MCMB activated using different amounts of KOH are basically of Type I, indicating that predominant pores are micropores. The adsorption isotherm of a-MCMB other than a-M1 has a vertical jump near $P/P_0 = 0$ and a wide plateau above $P/P_0 = 0.4$. The wide pressure range isotherm from $P/P_0 = 10^{-6}$ shows clear differences. The SPE analysis gives the pore structural parameters. The surface area increases from 410 to 1470 $\text{m}^2 \text{g}^{-1}$ with the increase of x of 1 to 4, while the micropore volume augments from 0.22 to 1.02 ml g^{-1} . The pore width w increases from 1.1 to 1.4 nm. Consequently, the amount of KOH controls the microporosity nicely.

Figure 2 shows the χ -T curves of a-M2 in the low temperature region. The χ values increase for the field cooling conditions with decreasing temperature. However, there is a maximum at 3.5 K in the zero-field cooling curve. This is the spin glass behavior published before [27]. This indicates the presence of magnetically interacted spins, which probably are assigned to sp^3 electrons. The dangling bonds of sp^3 should be associated with each other near to the edge of the nanographites. Consequently, the

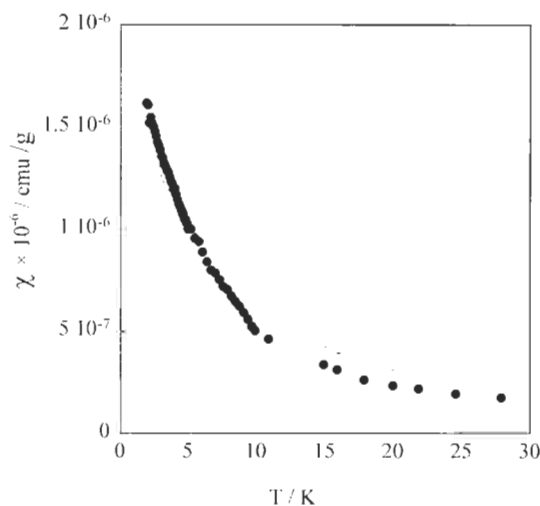


Fig. 2. Temperature dependence of magnetic susceptibility of activated MCMB (a-M2) at low temperature range: (O) heating; (●) cooling.

activated MCMB should have a mixed valence structure of sp^2 and sp^3 . However, a spin at the defect in the graphene layer is possible. Contributions by sp^2 and sp^3 carbon atoms must be separated by future research. Relationships between mixed valence states and the potential field must also be elucidated further.

4.2 Foreign Atom- or Cluster-doped Porous Carbons

4.2.1 Hidden Surface Fluorinated ACF

ACF was fluorinated by reaction with fluorine gas of 101 kPa at 373 K after drying by Touhara and his colleagues [41]; the fluorinated ACF is denoted as F-ACF. The chemical composition of F-ACF was $C_{1.4}F$ from gravimetric measurements and hence about one third of the carbon atoms are fluorinated. The XPS spectra of C1s and F1s were measured for F-ACF. The C1s of F-ACF had three peaks, which stem from the graphitic, $(CF)_n$, and $(C_2F)_n$ (graphite fluoride) structures. The peak position of XPS F1s of F-ACF was close to that of $C_7F_{15}COONa$, being far from that of LiF; the C-F bonding is not ionic, but covalent. On the other hand, the shape of nitrogen adsorption isotherm of F-ACF was of Type I; fluorination seriously decreases the surface area and pore volume, but pore widths do not change significantly. The porosity data are given in Table 2. Hence, fluorination partially reduces the high order structure of the nanographitic walls to decrease the effective porosity. Fluorination brought about a major change in water adsorption. The pristine ACF showed the representative Type V isotherm of water which has a steep uptake near $P/P_0 = 0.5$, whereas no water was adsorbed on F-ACF below $P/P_0 = 0.8$ irrespective of

Table 2
Micropore structures of F-alloyed and pristine ACFs

| Samples | Surface area (m ² /g) | Micropore volume (ml/g) | Pore width (nm) |
|---------|-------------------------------------|----------------------------|--------------------|
| F-ACF | 340 | 0.14 | 0.83 |
| ACF | 1220 | 0.51 | 0.85 |

sufficient numbers of micropores and the isotherm had no steep rise even above $P/P_0 = 0.8$ [41–43]. As water molecules cannot be adsorbed in carbon mesopores but in micropores [44,45], the fluorination brings about an intensive hydrophobicity.

4.2.2 Carbon Nanotube with Selectively Fluorinated Hidden Surface

Kyotani et al. [46] succeeded in preparing aligned carbon nanotubes by the template carbonization technique using anodic aluminum oxide films which have uniform and straight channels with a diameter of ca. 20 nm. The template carbonization technique also allows the preparation of uniform open-ended nanotubes whose length, width and thickness are accurately controlled. Only the hidden surfaces of the tube can be fluorinated using the template coating, described as follows.

Aluminum oxide films used as templates were prepared by anodic oxidation of aluminum plates at 20 V cell voltage in a 20 wt% sulphuric acid solution at 273–278 K for 2 h. The thickness of this film was about 75 μm , the diameter of the straight channels being about 30 nm. The chemical vapor deposition on the templates was carried out at 1073 K using propylene and a nitrogen flow to produce the carbon-coated anodic aluminum oxide composite films (C-Al₂O₃ films). Fluorination was performed by direct reaction of C-Al₂O₃ films with elemental fluorine in the temperature range from 323 to 473 K under 101 kPa of fluorine gas in the nickel reactor. The fluorinated C-Al₂O₃ films were washed with an excess amount of 46% HF solution at room temperature to dissolve the Al₂O₃ template. Thereby, fluorinated carbon nanotubes were obtained in the form of an insoluble fraction.

High resolution TEM examination of the nanotubes, with fluorinated hidden surfaces, showed slight perturbation of the 002 lattice fringe image at the inner area of the pore-wall, indicating selective fluorination. Also high resolution EDX showed the distribution of fluorine at the hidden surface. The surface energy of the fluorinated hidden surfaces of nanotubes is lower than that of nonfluorinated surfaces and based on a detailed analysis of nitrogen adsorption isotherms on the fluorinated and pristine nanotubes at 77 K. The fluorinated nanotubes show characteristic electrochemical behavior with flat and stable discharge potentials at ca. 2.4 V and a high capacity of 620 Ah kg⁻¹ as a cathode material for lithium cells [47–49].

4.2.3 Carbon Aerogel of Ce-Zr Oxide-doped Hidden Surfaces

Carbon aerogels (CAs) are a special class of low-density foams synthesized by organic reactions that proceed through sol-gel transitions [50]. CAs are mesoporous materials with high surface areas and few micropores, formed for example during the pyrolysis of resorcinol (R)-formaldehyde (F) aerogels. The mesopores of CA are very uniform. Accordingly, CAs have strong possibilities for technological applications. Hanzawa et al. [51,52] introduced microporosity to the mesoporous CAs by activation with carbon dioxide. Recently, it has been shown that addition of Ce and Zr nitrate salts to the resorcinol-formaldehyde aqueous solution gives highly microporous materials [53-55]. This demonstrates an extended possibility for control of the pore structure of carbon aerogels. The interest in Ce and Zr as doping elements stems from the high oxygen storage capacity and redox behavior of the mixed Ce-Zr oxides [56,57]. Ce-containing compounds show an excellent catalytic activity [58]. Thus, the preparation of Ce-Zr oxide doped carbon aerogels is an important target of the carbon alloy project.

The experimental approach for formation of carbon aerogels is as follows. An aqueous solution of resorcinol and formaldehyde has a fixed R/F mole ratio of 1:2. $\text{Ce}(\text{NO}_3)_3$ and $\text{Zr}(\text{NO}_3)_2$ are added to the solution (Ce/Zr mole ratio was approximately 1:1). The initial pH was adjusted for the sample prepared at pH = 3 or 7. Typically, gelation occurs in several hours for solution with a pH = 3 and it starts on the next day with a solution of pH = 7. The gel was washed with acetone until water is completely exchanged, then it is dried with supercritical carbon dioxide ($T_c = 304 \text{ K}$, $P_c = 7.4 \text{ MPa}$) and carbonized at 1323 K for 3 h under nitrogen.

The Ce-Zr-doped CAs obtained at pH = 7 and pH = 3 show different morphologies using TEM. The aerogel prepared at pH = 7 shows structures similar to a typical CA, being composed of loosely bonded particles about 20 nm in diameter. Doped metals are distributed homogeneously throughout the material in the form of nanosized particles and no aggregation is found. This observation suggests that the doped elements are anchored to the carbon structure preventing their migration and growth. The pH = 3 aerogel consists of spherical particles with a diameter of about 3 μm . The space between the primary particles is in the range of a large macropore. Also, no particles of doped substances were detected for this sample. As for the Ce-Zr doped CA prepared pH = 7, XPS analyses indicated the presence of Zr^{4+} on the surface. Cerium cations were not detected, suggesting that the Cerium is probably covered with carbon.

The sample obtained at pH = 7 exhibits a nitrogen adsorption isotherm of Type IV with hysteresis H3. This feature of the isotherm is similar to that for pure CA [52]. However, the doped CAs reveal adsorption isotherms with higher plateaux at the initial stage due to the presence of micropores with the hysteresis not being predominant when compared with that of pure CAs. In contrast, a Type-I nitrogen adsorption isotherm, representative of microporous materials, is observed for the doped CAs prepared at pH = 3. Figure 3 shows the nitrogen adsorption isotherms of

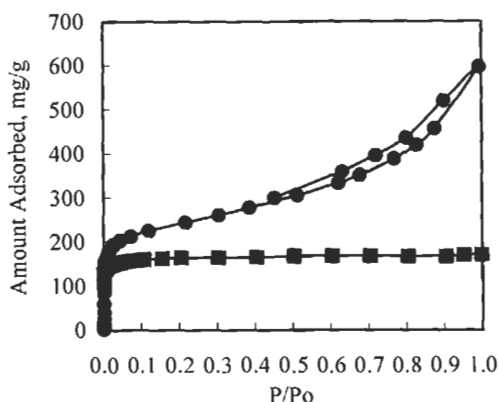


Fig. 3. Adsorption isotherms of N_2 on carbon aerogels prepared at: (●) pH = 3, and (■) pH = 7.

Ce-Zr doped CAs at 77 K prepared at pH = 3 and 7. The amounts of doped Ce and Zr are 0.22–0.25% and 0.15%, respectively. The SPE analysis of the nitrogen adsorption isotherms gives a better illustration of the effect of the initial pH on the aerogel structure. The surface areas of Ce-Zr-doped CAs at pH = 3 and 7 are 500 and 800 $m^2 g^{-1}$, respectively. Although the doped CA at pH = 7 has mesopores, the microporosities of both samples are almost identical despite a remarkable morphology difference (micropore volume 0.17–0.20 $ml g^{-1}$, and micropore size 0.7 nm).

4.2.4 External Surface-aminated Activated Carbon

A coconut shell activated carbon was vacuum-dried at 373 K for 24 h and treated with hydrogen at 373 K. Nitration was carried out using acetic anhydride, concentrated sulphuric acid, and nitric acid [59]. After nitration, the nitrate groups were reduced to amino groups (NH_2-) using aqueous ammonia and sodium hydrosulphite. The addition of amino groups (1.6% nitrogen) was confirmed by XPS analysis. The amination does not change the surface area and pore volume. However, adsorption of supercritical NO is enhanced remarkably by the amination.

4.3 Development of New Porous Carbon

Activation of carbon materials is one of several alloying processes, as described in Section 3.3.

4.3.1 Activated Carbon Film of Nitrogen-embedded Hidden Surface

Inagaki et al. [60,61] studied structures and physical properties of carbon films by carbonizing polyimide films. Hatori et al. [62] introduced macropores into the carbon

Table 3

Bulk and surface chemical compositions

| | C | H | O | N |
|-------------------------------|----|-----|-----|------|
| Bulk composition Kapton film* | 22 | 10 | 4.4 | 2.3 |
| Surface composition | 22 | 2.0 | 2.1 | 0.53 |
| Activated carbon film | 22 | – | 0.7 | 0.5 |

*Ideal composition of Kapton film: $C_{22}H_{10}O_5N_2$.

film. The polyimide film, carbonized and activated at 1173 K in carbon dioxide, was heated in argon at 1323 K [63,64]. An XPS examination of the resultant carbon film showed the presence of nitrogen atoms in the carbon frame. The bulk and surface chemical compositions are in Table 3. Nitrogen and oxygen are both contained within the film. The surface concentration of nitrogen and oxygen is lower than the bulk concentration. The high resolution nitrogen adsorption at 77 K shows the presence of micropores of pore width $w \leq 0.5$ nm and $0.6 \leq w \leq 0.9$ nm. A cross-section surface of the activated carbon film was studied by atomic force microscopy. The stacking structure of particles along the thickness direction was monitored, suggesting the presence of folded sheets which are bent at the predominant face of the carbon film.

4.3.2 Highly Porous Carbon Cryogels

Although carbon aerogels were initially produced through supercritical drying of resorcinol–formaldehyde aerogels, Tamon et al. [65] recently developed a freeze-drying technique for preparation of carbon aerogels. They named these new carbon aerogels the “carbon cryogels”. The carbon cryogels have high surface areas > 800 m² g⁻¹ and large mesopore volumes > 0.55 ml g⁻¹.

4.4 Tailoring Hidden and External Surfaces of Activated Carbon with Clusters or Ultrafine Particles

There are many examples of hidden and/or external surfaces tailored with clusters or ultrafine particles. Although supercritical NO cannot be adsorbed predominantly on activated carbon near room temperature, tailoring the external or hidden surface of ACF with ultrafine iron oxide enhances remarkably the NO adsorptivity at 303 K; the saturated amount of adsorption at 101 kPa of NO is greater than 0.3 g g⁻¹ [66,67]. Recent examples are described below.

4.4.1 Tailoring Hidden Surfaces of ACF with Nitrogen-containing Units

Yang and Kaneko modified the hidden surfaces of ACF with nitrogen-deposition by chemical vapor deposition of pyridine at 1273 K for 1 h after heating ACF at 1273 K in

Table 4
Micropore structures of N-alloyed and pristine ACFs

| Samples | Surface area (m ² /g) | Micropore volume (ml/g) | Pore width (nm) |
|---------|-------------------------------------|----------------------------|--------------------|
| N-ACF | 1280 | 0.64 | 0.89 |
| ACF | 2000 | 0.99 | 1.0 |

argon, a method originally developed by Kawabuchi et al.[68]. The resultant ACF is described as N-ACF. The electronic states of doped nitrogen atoms were determined using XPS; depth profiles of nitrogen atoms were measured with argon etching. The composition of N-ACF was C_{57.1}N. The content of doped nitrogen atoms in graphitic skeletons is < 1.8 at%. The peak of the broad XPS spectrum of N1s was observed at 401 eV, and is assigned to quaternary nitrogen. The peak of N1s, for pyridinic nitrogen, was not observed at 398 eV. Therefore, the nitrogen atoms in “graphitic” units appear to be deposited on the hidden surfaces and have effective positive charges.

The N-deposition procedure does not change the features of the nitrogen adsorption isotherm, suggesting that N-ACF is highly microporous. Table 4 summarizes the pore structures of these ACF samples. N-ACF has a surface area > 1000 m² g⁻¹ regardless of the CVD treatment at 1273 K with pore widths becoming slightly smaller after N-alloying. Some pores should be blocked by the CVD deposition treatment on preparation of N-ACF. The nitrogen deposition enhances water and ethanol adsorptivities of ACF due to the introduction of the polar sites [69,70].

4.4.2 Clustered TiO₂-embedded ACF from an Ionized Cluster Beam Method

Yamashita et al. [71] prepared an ACF impregnated with ultrafine TiO₂ particles using the ionized cluster beam method. The method deposits ultrafine TiO₂ clusters on the external surface of ACF without blocking the micropores. The composite effects arising from the micropores of ACF and the deposited TiO₂ induce excellent photocatalysis properties. This ACF is efficient for the photocatalytic degradation of 1,2-dichloroethane diluted in water. The concentrated 1,2-dichloroethane in micropores of ACF from the solution is effectively decomposed by the photocatalysis of TiO₂ on external surfaces.

4.5 Function of Pore Space Alloyed with Clusters and Fine Particles

Alloying the pore space is not clearly distinguishable from alloying the hidden surfaces, as mentioned in Section 2. From the many examples available, a few are described below.

4.5.1 Ambient Temperature Reduction of NO to N₂ by Metal-tailored Carbon Micropores

Ru or Pt fine particles exhibit a high catalytic activity for the reduction of NO. Ultrafine Pt or Ru particles are dispersed in the carbon micropores of ACF by reduction with hydrogen at 623 K of a dried metal salt after immersion of the evacuated ACF in metal salt solution. XPS shows the formation of metal particles with small amounts of oxide. The tailored amounts of metal particles are in the order of 0.2–0.5% of carbon atoms, by XPS analysis. Accordingly, the microporosity of ACF does not markedly vary due to the tailoring. N₂O from the concentrated NO dimer in the micropores is reduced to nitrogen very quickly even at 303 K [72]. The NO reduction finishes within 7 min. The first-order plot for the initial reaction gives a half-life of 3 min. No CO₂ is observed at 303 K, whereas small amounts of N₂O (0.005 N₂O/N₂) are formed. However, raising the reaction temperature to 423 K lowers the reaction rate and leads to production of CO₂ (CO₂/N₂ = 0.08). Mass analysis indicated the formation of nitrogen corresponding to a yield of 0.77. Thus, NO is rapidly reduced to nitrogen over Ru- or Pt-ACF at 303 K. In this case, NO is removed by both reduction and adsorption; the total removal ratio of NO at 303 K is 0.96 which is greater than the nitrogen yield. As no oxygen is observed, the oxygen of the system must be chemisorbed on the ACF.

This formation of nitrogen stems from the quasi-high pressure effect of the strong molecular potential field [73]. As molecules confined in micropores have a highly dense structure, as if they were compressed by high pressure, the confined molecular assembly exhibits a special reactivity. For NO, almost all NO molecules adsorbed in carbon micropores are dimerized even at 303 K because the adsorbed layer forms the low temperature liquid-like phase. This quasi-high pressure effect assists the catalysis of NO reduction by ultrafine Ru and Pt metals.

4.5.2 Morphology Controlled Nanocrystal Formation in Pore Space of Carbon Tubes

Kyotani et al. prepared carbon nanotubes using the template of anodic aluminum oxide film containing straight pores by chemical vapor deposition of propylene. Their method is illustrated in Fig. 4. They then introduced material by metal-organic chemical vapor deposition or by reduction of impregnated metal ions to the carbon-coated nanochannels of the anodic aluminium oxide film [74–76]. As the inner diameter of the carbon tube is ca. 20 nm, low dimensional crystals were obtained. They prepared nickel oxide nanobelts, iron oxide nanoparticles, and platinum nanorods.

The preparation method of nickel oxide nanobelts is as follows. The carbon-coated anodic aluminium oxide film was subject to metal-organic chemical vapor deposition of nickelocene at 548 K using a mixed gas flow of the nickelocene (0.6 kPa) with hydrogen diluted with nitrogen. The aluminium oxide was dissolved with 10 M NaOH solution at 423 K in an autoclave. TEM images showed the formation of a single nanobelt 500 nm in length, within the carbon tube. Selected area electron diffraction

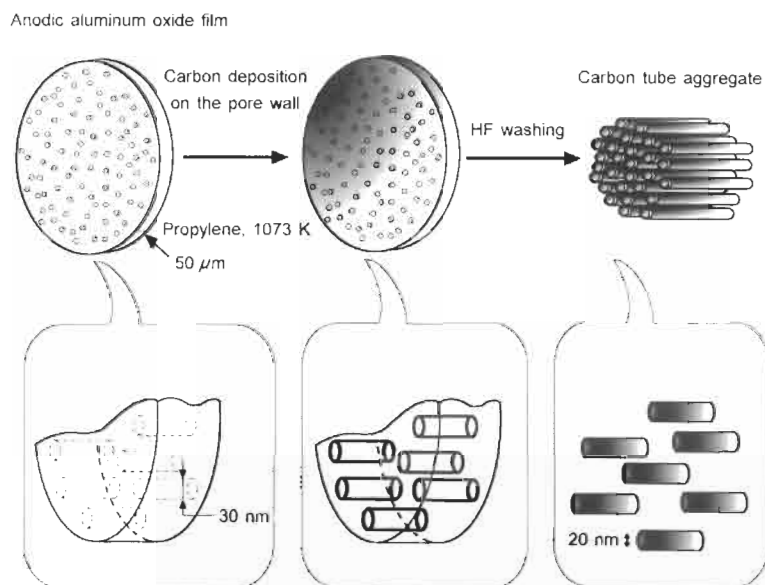


Fig. 4. Template carbonization method using anodic oxide film for preparation of carbon tube of inner diameter of 20 nm.

indicated the formation of a crystalline nickel oxide. Further, iron oxide nanoparticles and platinum nanorods, as nanodimensional crystals, were formed in the carbon tubes and characterized by TEM, selected area electron diffraction and X-ray diffraction. These nanodimensional crystal-tailored nanotubes are expected to show a new catalysis and special physical properties.

5 Design of New Porous Carbon with Carbon Alloying Technique

Possible applications for porous carbons with hidden and external surfaces modified with alloying are discussed above. However, the separation of molecular processes on hidden and external surfaces is not straightforward. It is considered that carbon nanotubes are ideal absorbents having regular cylindrical intrapores. Nevertheless, carbon nanotubes have an aggregate structure which promotes the existence of micropores and mesopores. Hence, it is not straightforward to distinguish between molecular processes on hidden and external surfaces. Inoue et al. attempted to distinguish between these two processes using multi-wall carbon nanotubes [77]. Recently, Murata et al. [8,78] succeeded in distinguishing between these processes using the single wall carbon nanohorn; they experimentally demonstrated a pure molecular process within the intrapores of a carbon nanohorn. Hopefully, this experimental result will stimulate further theoretical studies of molecular behavior in carbon nanotubes [79,80] and so give a new direction to the design of carbon nanomaterials.

Further developments of porous carbons could be based on the use of this alloying technique which can use the different concepts of related scientific fields. For example, the surface science of carbon materials has an intimate relationship with carbon pore space science. Iwasawa et al. [81] studied the surface structure and changes of transition metal carbides with low energy electron diffraction and scanning tunnelling microscopy. Their studies are helpful in the design of new alloying methods of hidden surfaces of porous carbon. Also Takasu et al. [82] studied the interfacial behavior of transition metal oxides on graphite surfaces with an electrochemical technique. This study also suggested the tailoring of hidden surfaces making use of transition metal oxides. Currently, experimental techniques available to elucidate the nature of molecular assemblies or dispersed particles confined in carbon pores are not as powerful as those of surface science. Hence, the sciences of hidden surfaces and materials confined in carbon pore spaces require further significant improvements based on a variety of expertises [82–86].

Acknowledgement

Dr. H. Inokuchi suggested the importance of the hidden surface concept.

References

1. K.S.W. Sing, D.H. Everett, R.A.W. Haul, L. Moscou, R.A. Pierotti, J. Rouquerol and T. Siemieniowska, Reporting physisorption data for gas/solid systems with special reference to the determination of surface area and porosity. *Pure Appl. Chem.*, 57: 603–619, 1985.
2. K. Kaneko and C. Ishii, Superhigh surface area determination of microporous solids. *Colloids Surfaces*, 67: 203–212, 1992.
3. N. Setoyama, T. Suzuki and K. Kaneko, Simulation study on relationship between high resolution α_s -plot and pore size distribution for activated carbon. *Carbon*, 36: 1459–1467, 1998.
4. W.A. Steele, The physical interaction of gases with crystalline solids. *Surface Sci.*, 36: 317–352, 1973.
5. K. Kaneko, R. Cracknell and D. Nicholson, Nitrogen adsorption in slit pores at ambient temperature. *Langmuir*, 10: 4606–4609, 1994.
6. K. Wakabayashi, M. Fujita, H. Ajiki and M. Sigrist, Electronic and magnetic properties of nanographite ribbons. *Phys. Rev.*, B59: 8271–8282, 1999.
7. K. Murtata, K. Kaneko, W.A. Steele, F. Kokai, K. Takahashi, D. Kasuya, K. Hirahara, M. Yudasaka and S. Iijima, Molecular potential structures of heat-treated single-wall carbon nanohorn assemblies. *J. Phys. Chem.*, in press.
8. K. Murata, K. Kaneko, W.A. Steele, F. Kokai, K. Takahashi, D. Kasuya, M. Yudasaka and S. Iijima, External and internal nanospaces of single wall carbon nanohorn aggregates. *Nanoletters*, 1: 197–199, 2001.
9. R. Defay, I. Prigogine, A. Bellemans and D.H. Everett. *Surface Tension and Adsorption*, Chap. 1. Longman, London, 1966.
10. W.A. Steele, Concerning a theory of multilayer adsorption with particular reference to adsorbed helium. *J. Chem. Phys.*, 25: 819–823, 1956.

11. N. Setoyama, K. Kaneko and F. Rodriguez-Reinoso, Ultramicropore characterization of microporous carbons at low temperature helium adsorption. *J. Phys. Chem.*, 100: 10331–10336, 1996.
12. N. Setoyama and K. Kaneko, Density of He adsorbed in micropores at 4.2 K. *Adsorption*, 1: pp.1–9, 1995.
13. R.E. Leckenby and E.J. Robbins, The observation of double molecules in gases. *Proc. Roy. Soc. (London)*, A291: 389–412, 1966.
14. M. Aoshima, T. Suzuki and K. Kaneko, Molecular association-mediated micropore filling of supercritical Xe in a graphite slit pore by grand canonical Monte Carlo simulation. *Chem. Phys. Lett.*, 310: 1–7, 1999.
15. C.E. Dinerman and G.E. Ewing, Infrared spectrum, structure, and heat of formation of gaseous (NO)₂. *J. Chem. Soc.*, 100: 6948–631, 1978.
16. K. Kaneko, N. Fukuzaki and S. Ozeki, The concentrated NO dimer in micropores above room temperature. *J. Chem. Phys.*, 87: 776–777, 1987.
17. K. Kaneko, Nanospace geometry sensitive molecular assembly. *Supramolecular Sci.*, 5: 267–273, 1998.
18. T. Ohkubo, T. Iiyama, K. Nishikawa, T. Suzuki and K. Kaneko, Pore width-dependent ordering of C₂H₅OH molecules confined in graphitic slit nanospaces. *J. Phys. Chem.*, 103: 1859–1863, 1999.
19. T. Ohkubo, T. Iiyama and K. Kaneko, Organized structures of methanol in carbon nanospaces at 303 K with *in situ* X-ray diffraction. *Chem. Phys. Lett.*, 312: 191–195, 1999.
20. T. Ohkubo and K. Kaneko, Oriented structures of alcohol hidden in carbon micropores with ERDF analysis. *Colloid Surfaces*, 187–188: 177–185, 2001.
21. K. Morishige, K. Kawamura and A. Kose, X-Ray diffraction study of the structure of a monolayer methanol adsorbed on graphite. *J. Chem. Phys.*, 93: 5267–5270, 1990.
22. T. Iiyama, K. Nishikawa, T. Otowa and K. Kaneko, An ordered water molecular assembly in a slit-shaped carbon nanospace. *J. Phys. Chem.*, 99: 10075–10076, 1995.
23. T. Iiyama, K. Nishikawa, T. Suzuki and K. Kaneko, Study of the structure of a water molecular assembly in a hydrophobic nanospace at low temperature with *in situ* X-ray diffraction. *Chem. Phys. Lett.*, 274: 152–158, 1997.
24. Z.M. Wang and K. Kaneko, Effect of pore width on micropore filling mechanism of SO₂ in carbon micropores. *J. Phys. Chem.*, 102: 2863–2868, 1998.
25. T. Ohkubo, C.-M. Yang, E. Raymundo-Pinero, A. Linares-Solano and K. Kaneko, High-temperature treatment effect of microporous carbon on ordered structure of confined SO₂. *Chem. Phys. Lett.* 329: 71–75, 2000.
26. K. Kaneko, C. Ishii, M. Ruike and H. Kuwabara, Origin of superhigh surface area and microcrystalline graphitic structures of activated carbon. *Carbon*, 30: 1075–1088, 1992.
27. C. Ishii and K. Kaneko, Surface and magnetic properties of microporous carbon spheres. *Prog. Organic Coatings*, 31: 147–152, 1997.
28. Y. Higaonna, C. Ishii and K. Kaneko, Magnetic properties and pore structures of KOH-activated mesocarbon microbeads. In preparation
29. K. Kaneko, C. Ishii, H. Kanoh, Y. Hanzawa, N. Setoyama, T. Suzuki, Characterization of Porous Carbons with High Resolution α -analysis and low temperature magnetic susceptibility. *Adv. Colloid Interface Sci.*, 295: 76–77, 1998.
30. T.T. Berek, W. Ackerman, D.W. Hua, R.T. Raine and D.M. Smith, Highly microporous boron nitride for gas adsorption. *Langmuir*, 7: 2844–2846, 1991.
31. K. Kaneko, N. Kosugi and H. Kuroda, Characterization of iron oxide dispersed activated carbon fibers with water adsorption and Fe K-edge XANES and EXAFS. *J. Chem. Soc. Faraday Trans.*, 85: 869–881, 1989.
32. A. Matsumoto and K. Kaneko, Micropore filling of supercritical NO on external surface

- modified microporous carbons. *J. Chem. Soc. Faraday Trans.*, 85: 3437–3450, 1989.
33. H. Inokuchi, N. Wakayama, T. Kondow and Y. Mori, Activated adsorption of hydrogens on aromatic–alkali–metal charge transfer complexes. *J. Chem. Phys.*, 46: 834–842, 1967.
 34. H. Sakuno, A. Ogawa, N. Akuzawa and Y. Takahashi, Adsorption of organic molecules on alkali metal–graphite intercalation compounds. *Tanso*, 238–243, 1990.
 35. N. Akuzawa, M. Murakami, M. Nakano, Y. Soneda, R. Matusmoto and Y. Takahashi, Host effect on the properties of AM-GICs. *Mol. Cryst. Liq. Cryst.*, 340: 59–64, 2000.
 36. K. Fujie, S. Minagawa, T. Suzuki and K. Kaneko, NO/H₂O clathrate formation in sub-nano graphitic slit space. *Chem. Phys. Lett.*, 236: 427–430, 1995.
 37. J. Miyawaki, T. Kanda, T. Okui, M. Saito, T. Suzuki and K. Kaneko, Macroscopic evidence of enhanced formation of methane nanohydrates in hydrophobic nanospaces. *J. Phys. Chem.*, 102: 2187–2192, 1998.
 38. J. Miyawaki and K. Kaneko, Hysteresis-associated pressure shift water adsorption in carbon micropores. *Langmuir*, 17: 664–669, 2001.
 39. J. Imai, M. Soma, S. Ozeki, T. Suzuki and K. Kaneko, Reaction of dimerized NO_x ($x = 1$ or 2) with SO₂ in a restricted slit-shaped micropore space. *J. Phys. Chem.*, 95: 9955–9960, 1991.
 40. K. Kaneko, Specific intermolecular structures of gases confined in carbon nanospace. *Carbon*, 38, pp.287–303, 1999.
 41. N. Setoyama, G. Li, K. Kaneko, F. Okino, R. Ishikawa, M. Kanda and H. Touhara, Nitrogen adsorption on fluorination activated carbon fiber. *Adsorption*, 2: 293–297, 1996.
 42. G. Li, K. Kaneko, S. Ozeki, F. Okino and H. Touhara, Water rejective nature of fluorinated microporous carbon fibers. *Langmuir*, 11: 716–717, 1995.
 43. K. Kaneko, T. Ohkubo, T. Iiyama, C. Yang and H. Touhara, Cluster mediated filling of water and alcohol on microporous carbon alloys, In: D.D. Do (Ed.), *Adsorption Science and Technology*, pp. 1–5. World Scientific, Singapore, 2000.
 44. Y. Hanzawa and K. Kaneko, Lack of a predominant adsorption of water on carbon mesopores. *Langmuir*, 13: 5802–5805, 1997.
 45. K. Kaneko, Y. Hanzawa, T. Iiyama, T. Kanda and T. Suzuki, Cluster-mediated water adsorption on carbon nanospaces. *Adsorption*, 5: 7–13, 1999.
 46. T. Kyotani, L. Tsai and A. Tomita, Preparation of ultrafine carbon tubes in nanochannels of anodic aluminum oxide film. *Chem. Mater.* 8: 2109–2113, 1996.
 47. Y. Hattori, Y. Watanabe, S. Kawasaki, F. Okino, B.K. Pradham, T. Kyotani, A. Tomita and H. Touhara, Carbon-alloying of the rear surfaces of nanotubes by direct fluorination. *Carbon*, 37: 1033–1038, 1999.
 48. H. Touhara, Potential use of carbon nanotube as anode materials for lithium batteries. *Ouyou Butsuri (Applied Physics)*, 69, 3–37, 2000.
 49. H. Touhara and F. Okino, Property control of carbon materials by fluorination. *Carbon*, 38: 241–267, 1999.
 50. R.W. Pekala. *J. Matter. Sci.*, 24: 3221–3227, 1989.
 51. Y. Hanzawa and K. Kaneko, Activated carbon aerogels. *Langmuir*, 25: 6167–6169, 1996.
 52. Y. Hanzawa, K. Kaneko, R.W. Pekala and M.S. Dresselhaus, The pore structure determination of carbon aerogels. *Adsorption*, 2: 187–196, 1998.
 53. E. Bekyarova and K. Kaneko, Microporous nature of Ce, Zr-doped carbon aerogels. *Langmuir*, 15: 7119–7121, 1999.
 54. E. Bekyarova and K. Kaneko, Structure and physical properties of tailor-made Ce, Zr-doped carbon aerogels. *Adv. Mater.*, 12: 1625–1628, 2000.
 55. E. Bekyarova, K. Kaneko and E. Bekyarova, Adsorption of supercritical N₂ and O₂ on pore-controlled carbon aerogels. *J. Colloid Interface Sci.*, 238: 357–361, 2001.
 56. P. Fornasiero, R. Di Monte, G. Ranga Rao, J. Kaspar, S. Meriani, A. Trovarelli and M.

- Graziani, Rh-Loaded CeO₂-ZrO₂ solid solutions as highly efficient oxygen exchanges. *J. Catal.* 151: 168–177, 1995.
57. G. Balducci, J. Kaspar, P. Fornasiero, M. Graiani and M. Saiful Islam, J. Gale, Computer simulation studies of bulk reduction and oxygen migration in CeO₂-ZrO₂ solid solution. *J. Phys. Chem. B*, 101: 1750–1753, 1997.
 58. M. Haneda, T. Mizushima and N. Kakuta, Behavior of oxygen species adsorbed of Al₂O₃-supported cerium oxide catalysts for methane oxidation. *J. Chem. Soc. Faraday Trans.*, 91: 4459–4465, 1995.
 59. M. Abe, K. Kawashima, K. Kozawa, H. Sakai and K. Kaneko, Amination of activated carbon and adsorption characteristics of its aminated surface. *Langmuir*, 16: 5059–5063, 2000.
 60. M. Inagaki, K. Sakamoto and Y. Hishiyama, Carbonization and graphitization of polyimide upilex. *J. Mater. Res.*, 6: 1108–1113, 1991)
 61. Y. Hishiyama, A. Yoshida and Y. Kaburagi, Graphite films prepared from carbonized polyimide films. *Carbon*, 30: 333–337, 1992.
 62. H. Hatori, Y. Yamada and M. Shiraishi, Preparation of macroporous carbon films from polyimide by phase inversion method. *Carbon*, 30: 303–304, 1992.
 63. M. Sato, H. Isobe, H. Yamamoto, T. Iiyama and K. Kaneko, Oriented micrographitic carbon film of high surface area. *Carbon*, 33: 1347–1350, 1995.
 64. M. Nozaki, Y. Nishi, T. Iiyama and K. Kaneko, Alloyed-nitrogen induced pore-gate control of nanostructure oriented carbon film. *Langmuir*, to be submitted.
 65. H. Tamon, H. Ishizaka, T. Yamamoto and T. Suzuki, Preparation of mesoporous carbon by freeze drying. *Carbon*, 37: 2049–2055, 1999.
 66. K. Kaneko, Effect of temperature on micropore filling of supercritical NO on Fe₂O₃ dispersed activated carbon fibers. *Colloid Surf.*, 37: 329–338, 1989.
 67. Z.M. Wang, T. Suzuki, N. Uekawa, K. Asakura and K. Kaneko, Mixed valence oxide dispersed induced micropore filling of supercritical NO. *J. Phys. Chem.*, 96: 10917–10922, 1992.
 68. Y. Kawabuchi, C. Sotowa, M. Kishino, S. Kawano, D.D. Whitehurst and I. Mochida, Chemical vapor deposition of heterocyclic compounds over activated carbon fiber to control its porosity and surface function. *Langmuir*, 13, 2314–2317, 1997.
 69. C.-M. Yang, M. El-Merraoui and K. Kaneko, Characterization of nitrogen-alloyed activated carbon fiber. *Langmuir*, 17: 675–680, 2001.
 70. C.-M. Yang and K. Kaneko, Adsorption properties of nitrogen-alloyed activated carbon fibers. *Carbon*, 39: 1075–1082, 2001.
 71. H. Yamashita, M. Harada, A. Tanii, M. Honda, M. Takeuchi, Y. Ichihashi, M. Anpo, N. Iwamoto, N. Itoh and T. Hirao, Preparation of efficient titanium oxide photocatalysts by an ionized cluster beam method and their photocatalytic reactivities for the purification of water. *Catalysis Today*, 223: 1–7, 2000.
 72. Y. Nishi, T. Suzuki and K. Kaneko, Ambient temperature reduction of NO to N₂ in Ru-tailored carbon subnanospace. *J. Phys. Chem.*, 101: 1937–1938, 1997.
 73. K. Kaneko, Control of supercritical gases with solid nanospaces. *Studies Surf. Sci. Catal.*, 120B: 635–658, 1998.
 74. T. Kyotani, L.F. Tsai and A. Tomita, Formation of platinum nanorods and nanoparticles in uniform carbon nanotubes prepared by a template carbonization method. *Chem. Commun.*, 701–702, 1997.
 75. B.K. Pradhan, T. Toba, T. Kyotani and A. Tomita, Inclusion of crystalline iron oxide nanoparticles in uniform carbon nanotubes prepared by a template carbonization method. *Chem. Mater.*, 10: 2510–2515, 1998.
 76. B.K. Pradhan, T. Kyotani and A. Tomita, Nickel nanowire of 4 nm diameter in the cavity of carbon nanotubes. *Chem. Commun.*, 1317–1318, 1999.

77. K. Murata, K. Kaneko, F. Kobori, K. Takahashi, M. Yudasaka and S. Iijima, Pore structure of single-wall carbon nanohorn aggregates. *Chem. Phys. Lett.*, 331: 14–20, 2000.
78. S. Inoue, N. Ichikuni, T. Suzuki, T. Uematsu and K. Kaneko, Capillary condensation of N_2 on multi-wall carbon nanotube. *J. Phys. Chem.*, 102: 4689–4691, 1998.
79. G. Stan, M.J. Bojan, S. Curtarolo, S.M. Gatica and M.W. Cole, Uptake of gases in bundles of carbon nanotubes. *Phys. Rev. B*, 62: 2173–2180, 2000.
80. S.M. Gatica, M.W. Cole, G. Stan, J.M. Hartman and V.H. Crespi, Momentum distribution of helium and hydrogen in nanotubes. *Phys. Rev. Biol.*, 6: 9989–9991, 2000.
81. K. Fukui, L. Rong-Li, S. Otani and Y. Iwasawa, Novel selective etching reaction of carbon atoms on molybdenum carbide by oxygen at room temperature visualized by scanning tunneling microscopy. *Chem. Phys. Lett.*, 325: 275–280, 2000.
82. Y. Takasu, T. Ohnuma, W. Sugimoto and Y. Murakami, Pseudocapacitance of molybdenum oxide particles highly dispersed on glassy carbon surface. *Electro Chemistry*, 67: 1187–1188, 1999.
83. K. Kaneko, Nanodimensional magnetic assembly of confined O_2 , In: J. Schwarz and C. Contescue (Eds.), *Surfaces of Nanoparticles and Porous Materials*, pp. 635–658, Marcel Dekker, New York, 1998.
84. T. Iiyama, T. Ohkubo and K. Kaneko, *In situ* X-ray diffraction studies on micropore filling, In: Kanellopoulos (Ed.), *Recent Advances in Gas Separation by Microporous Membranes*, pp. 35–66, Elsevier Science, Amsterdam, 2000.
85. N. Miyajima, T. Akatsu, T. Ikoma, O. Ito, B. Rand, Y. Tanabe and E. Yasuda, A role of charge-transfer complex with iodine in the modification of coal tar pitch. *Carbon*, 38: 1832–1838, 2000.
86. K. Nishikawa, K. Fukuyama and T. Nishizawa, Structure change of glass-like carbon with heat treatment, studied by small angle X-ray scattering: I. Glass-like carbon prepared from phenolic resin. *Jpn. J. Appl. Phys.*, 37: 6486–6491, 1998.

Chapter 5

Control of Interface and Microstructure in Carbon Alloys

Yasuhiro Tanabe and Ei-ichi Yasuda

*Materials and Structures Laboratory, Tokyo Institute of Technology, Midori, Yokohama
226-8503, Japan*

Abstract: Graphite-related materials are actually alloys consisting of three types of carbon having the different sp^1 , sp^2 and sp^3 bonding, and also of other elements. Graphite consists of sp^2 bonding, is the stable phase of carbon at ambient temperature and pressure, and shows strong anisotropy dependent on its covalent and van der Waals bonding. This strong anisotropy gives wide variations to the properties of graphite-related materials. Alloying techniques can be applied to modify the structures, and, as a consequence, their properties. The following are introduced as examples of alloying: surface treatments of carbon fibers in order to modify the bonding and structures of interfaces with carbon matrices, as well as precursor modification to change microstructures of resultant carbon products. Although detailed mechanisms for modification of interfaces are still not clarified, oxygen-, amino- and amine-groups on carbon fibers do change the structures of interfaces, and the properties of their composites. Chemical modifications of precursors modify structures in resultant carbons.

Keywords: Interface, Microstructure, Anisotropy, Surface treatment, Composite.

1 Introduction

As mentioned in Chapter 1, carbon materials consisting of sp^1 , sp^2 and sp^3 bondings are carbene, graphite and diamond, respectively. The thermodynamically stable phase at the ambient pressure and temperature is graphite. Depending on the hybrid orbital structure of sp^2 , graphite crystals show a strong anisotropy being covalent within the hexagonal basal planes (graphene layers) with van der Waals bonding in the direction normal to the planes.

Elastic moduli, C_{11} and C_{33} , of a graphite crystal are 1060 GPa and 36 GPa, respectively. Graphite-related materials are normally agglomerations of imperfect graphite crystals/crystallites. Young's modulus of the graphite crystal in off-axis can be expressed as a function of inclined stressing angle, θ ($\phi = \cos\theta$), to the c -axis as follows [1,2]:

$$1/E = S_{11}(1 - \phi^2)^2 + S_{33}\phi^4 + (2S_{13} + S_{44})\phi^2(1 - \phi^2) = C(\phi) \quad (1)$$

The compliance of the graphite crystal in off-axis is shown together with each term of $(2S_{13} + S_{44})$, S_{33} and S_{11} in Fig. 1. The compliance between 0 and 25° is governed by S_{33} , that above 25° by shear modulus of $(2S_{13} + S_{44})$, and only between 88° and 90° does S_{11} control the stiffness. The crystallites have to be aligned within ca. $\pm 2^\circ$ to the fiber direction to give a high modulus of the fiber. Young's modulus of general polycrystalline graphite materials can be expressed as in the following equation:

$$1/E_{\text{calc}} = \sum \{C(\phi) \cos^m \phi / \int \cos^m \phi d\phi\} \quad (2)$$

The measured Young's moduli of selected carbon fibers are plotted in Fig. 2 [3] against the Young's moduli estimated from Eq. (2).

The thermal expansion coefficients of a graphite crystal also show large anisotropy in different directions: $\alpha_a = -1.8 \times 10^{-6} \text{ K}^{-1}$ and $\alpha_c = 27 \times 10^{-6} \text{ K}^{-1}$ at ambient temperature. Thermal expansion coefficients of polycrystalline graphites can also be estimated from the same equation as for the Young's modulus.

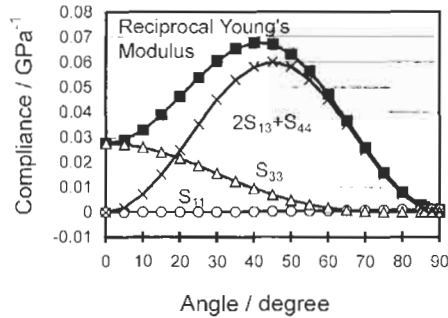


Fig. 1. Young's modulus of graphite crystal in off-axis angle.

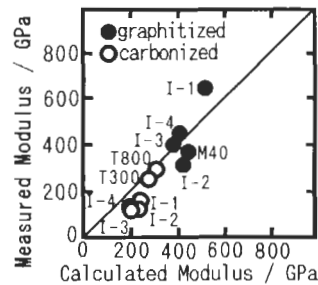


Fig. 2. Measured Young's modulus of some carbon fibers versus calculated modulus from Eq. (2) [3].

Highly Orientated Pyrolytic Graphite (HOPG) has the highest thermal conductivity of 5000 W/(m·K) along the layer planes at about 100 K [4]. Because the phonon conduction is predominant in graphite-related materials, thermal conductivity (κ) is expressed as a product of density (ρ), heat capacity (c), phonon velocity (v) and the mean free path length (l) of the phonon as indicated in Eq. (3):

$$\kappa = 1/2 \rho \cdot c \cdot v \cdot l \quad (3)$$

Considering the form of the equation, large thermal conductivities result from high phonon velocity and large mean free path length as exist in graphitizable and graphitic carbons.

Thermosetting resin precursors generally produce hard carbons, i.e., non-graphitizable carbons. However, they give graphite-like structures when in the matrix form of composites with fibers [5]. The mechanism of the graphitization is attributed to “stress graphitization” [6]. However, the carbon derived from furan resin could be graphitized using only low stress values or even no stress above 1000°C, when it was compressed during carbonization to about 2 MPa [7]. Transmission electron microscope (TEM) observations reveal that orientations of carbon hexagonal layers in the carbon matrix existed on heat treatment temperatures (HTT) to 1100°C the graphitic structure appearing at 2400°C irrespective of the matrix precursor [8]. Interactions between fibers and matrix affect the graphitization and the orientation of the layers. Further, graphitization of the matrix in carbon fiber reinforced carbon matrices ((C/C) composites) could be changed by surface treatment of the carbons fibers [9]. Microstructure modification by surface treatment of fibers has been observed in composites using a pitch precursor for the matrix [10]. Surface treatment of carbon fibers changed the mechanical properties not only of CFRPs [11] but also C/C composites [9]. It is reported that induced surface roughness of fibers affected bonding/adhesion with matrix resins including precursors [12] and could change mechanical properties.

In this chapter chemical ways to control microstructures and interfaces within C/C composites are reviewed.

2 Interface Control

Surface treatments and sizing treatments of carbon fibers affect matrix microstructures and the mechanical properties of C/C composites [9]. Non-surface-treated carbon fibers result, during carbonization, in a large size of matrix domains in the composites as observed using optical microscopy (matrix domains) with small bulk shrinkage of the composites normal to the fiber axis. Carbonized C/C composites prepared from fibers without surface treatment show pseudo-plastic fracture behavior with a high breaking strength, whilst carbonized C/C composites from surface-treated fibers were brittle and had low strength. However, after graphitization, composites with non-surface-treated fibers had lower strengths compared to those with surface-

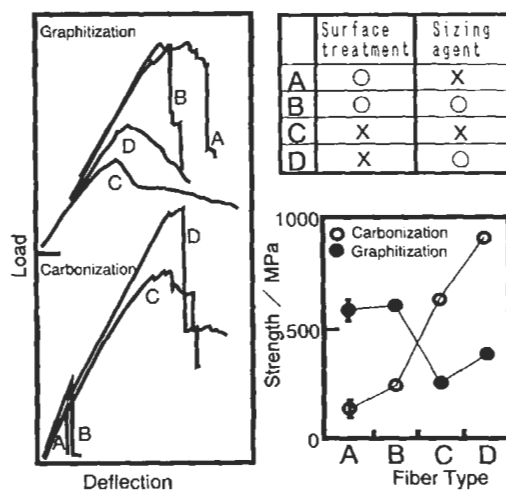


Fig. 3. Stress-strain, load-deflection, diagrams of various C/C composites using carbon fibers with or without surface treatment and sizing treatment [9].

treated fibers. In composites with non-surface-treated fibers, the domains of graphite-like structure in the matrix were large, interfacial bonding was weak and the interface could not transfer forces between fibers and matrix effectively. The relevant stress-strain (load-deflection) diagram is as Fig. 3.

Surface-treated carbon fibers caused large bulk shrinkages of the composites with many closed cracks being initiated in the matrix so making impregnation treatments difficult. On the other hand, the degree of graphitization was affected by the size and aspect ratio of fillers: larger size and aspect ratios increased the degree of graphitization [13].

To study the effects of surface treatment on interfacial bonding, i.e., the shear strength, PAN- and Pitch-based carbon fibers were heat treated at 2600° before ozone treatment; functional groups on as-received fibers were removed by this treatment [10]. Furfuryl alcohol condensate was selected as the matrix precursor. All of the processing was carried out in 25 mm diameter graphite tubes containing 40 vol% of unidirectionally aligned fiber. After oxidation of the fiber in the tube at 110°C for 0 to 8 h, furfuryl alcohol condensate was impregnated, carbonized and graphitized. With increasing oxidation periods, the density increased from 1.4 to 1.55 g cm⁻³, and the open porosity decreased from 25 to 8%. The shear strength is shown in Fig. 4. This shows that for fibers without surface treatment a low shear strength of 7 MPa exists increasing to 20 MPa gradually with increasing extents of oxidation [14].

Interfacial shear strengths of CFRP with epoxy resin correlated well with polarities of fiber surfaces as calculated using advancing contact angles rather than receding contact angles [15]. This indicates that infiltration of resin affects interfacial strength as well as wettability. The polarity of fibers increased with increasing oxidation treatment. In the electrochemical treatment of carbon fibers in 0.1 N NaOH for 28 s,

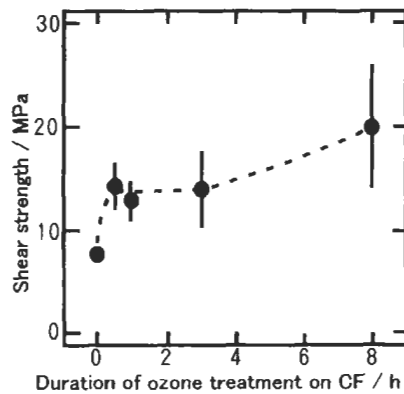


Fig. 4. Shear strength of furan resin derived UD C/C composites with a surface treatment of the carbon fiber by ozone treatment [14].

increases in electric current density decreased in nanometre steps (step-like features) in fibers, and mild structural heterogeneity of fibers was obtained [16]. Surface functional groups introduced by the surface treatment were localized on edges of graphite-like crystallites.

Introduction of amino-groups to surfaces of carbon fibers resulted in no degradation of the fibers but with increased interfacial bonding to an epoxy resin [17]. The amino-groups increased the wettability of fibers to epoxy resins and reacted with the hardening agent of the resins. Amine-groups on the fiber surfaces also increased wettability between fibers and epoxy resins [18]. Treatment of fibers with 14.7 Am^{-2} resulted in no STM image due to a loss of electrical conductivity between the fibers and the tip of the STM equipment. It indicates that carbon surfaces were covered with non-conductive material.

Direct fluorination of carbon fibers introduces stable hydrophilic groups to their surfaces at room temperature but decreased the degradation of fibers compared with anodic oxidation of fibers [19]. In anodic oxidation, numbers of micro/meso pores less than 5 nm in diameter decreased and those over 5 nm increased.

Surfaces of commercially available carbon fibers contain larger amounts of nitrogen compared with surfaces of non-oxidized fibers. Bulk nitrogen diffuses to the fiber surfaces by the oxidation treatment. XPS analysis revealed that the fibers were bound to the matrix by covalent bonding [20]. Functional groups produced by surface treatment enhanced bonding because the sizing agent did not cover all of the surfaces of the fibers.

The domain sizes of matrix microstructure became smaller when fine graphite particles were mixed into pitch and thermosetting resin matrix precursors [21,22]. Surface treatment of carbon fibers affected the microstructure following the addition of graphite powder, i.e., non-surface-treated fibers resulted in much finer domains than surface-treated fibers. However, surface-treatment of fibers had no significant

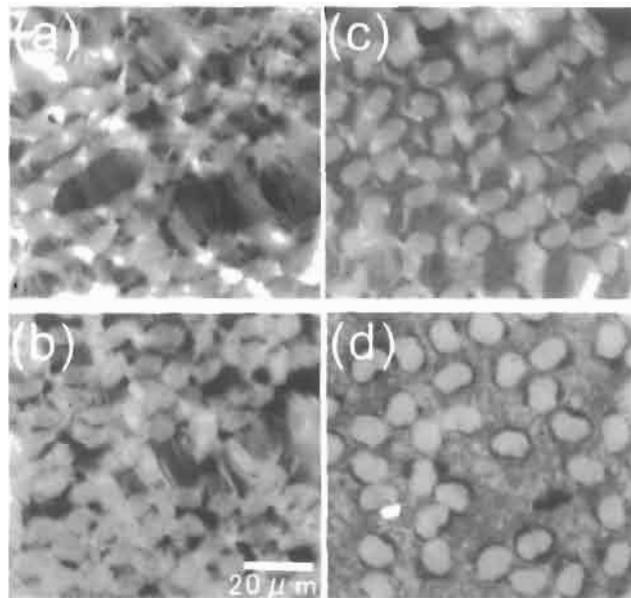


Fig. 5. Microstructures in various graphitized C/C composites. (a) With surface-treated fiber without graphite powder, (b) with surface-treated fiber with graphite powder, (c) non-surface-treated fiber without graphite powder, and (d) non-surface-treated fiber with graphite powder [9].

effects on carbons derived from thermosetting resins [21], as shown in Fig. 5. Small-sized graphite powder mixed in sizing agent effectively decreased the size of the matrix domains, i.e., < 1 wt% addition effectively decreased the domain size in pitch-derived matrix carbon [23].

In C/C composites, oxidation is initiated at the interface between fibers and matrix [24]. Hence, strong bonding at the interface would be effective in enhancing oxidation resistance [25]. Surface treatments should therefore be made on carbon fibers. In C/C composites using surface-treated fibers, an interface region between fibers and matrix consisted of amorphous carbon which degraded the mechanical properties of the composites. In a CFRP with oxidized carbon fibers, an interface layer that differed from the matrix resin was detected by dynamic visco-elastic measurements [26]. This layer in CFRPs could become the amorphous region following carbonization of C/C composites. However, no detailed information on functional groups and sizing agents for the phase change are currently available.

When matrix precursors were impregnated into composites after high temperature heat treatment of the composites, i.e., graphitization, weak interfaces between the original matrix and the impregnated matrix appeared. This is because amounts of covalent bonding decreased due to the development of the graphite-like structure by heat treatment to high temperatures [27]. Such phenomena were also observed in different combinations of two different matrices, especially after heat treatment to high temperatures [28].

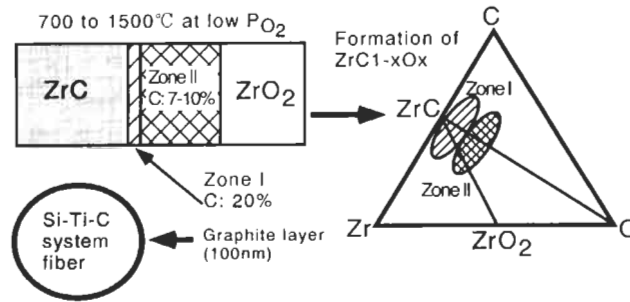


Fig. 6. Schematics of a layered structure of oxidized carbide at a low pressure of oxygen.

An interesting result concerning the interface of carbon fibers is that residual carbons in a Si-Ti-C-O fiber system were deposited on the surfaces as a homogeneous carbon/graphite layer and this layer acted as a sliding layer in the composites [29]. As a result, this layer changed the fracture behavior of the composites from brittle to pseudo-plastic. At low oxygen pressures, metal carbides were transformed into a layered structure consisting of graphite and metal oxides [30]. The schematics of this are illustrated in Fig. 6. In composites using Si-Ti-C-O-system fibers the same phenomena took place and a graphite layer was formed.

Ion implantation techniques are used as surface treatments of carbon-related materials [31]. Metal ions were implanted in a thin layer of the surface and the layer became amorphous with a dose of 10^{16} to 10^{17} with 150 keV acceleration. Annealing treatment tended to enrich the ions on surfaces and the metal ions became stable. It was thought that amorphous carbon on the surfaces of the implanted carbons would improve their performance as electrodes. Therefore, they can be used as special electrodes [31].

3 Microstructure Control

As mentioned above, thermal conductivity of graphitic materials is strongly affected by their microstructure. A typical example is demonstrated in a C/C composite. Figure 7 shows thermal conductivity k of a UD-C/C composite for a thermosetting resin derived matrix. Thermal conductivity increased significantly with increasing HTT. This change coincides with increases in the crystallite size (110 diffraction band), which coincides with the mean free path length of phonons calculated from Eq. (3) as seen in Fig. 8 [32].

Generally, precursors with a large molecular weight gave smaller domain sizes in carbon products than those having a small molecular weight [22]. The former precursors are of high viscosity at low temperatures, with the latter showing low char yields and melting during carbonization at atmospheric pressure. To change the microstructure of carbon products, ratios of small to large molecules were controlled [22] and additions of small amounts of fine graphite/carbon particles were found to be

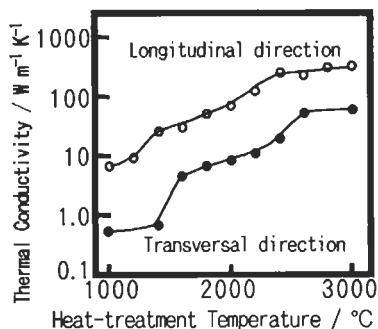


Fig. 7. Change of thermal conductivity of UD C/C composite as a function of heat treatment temperature [32].

effective [33]. However, it is quite difficult to control the viscosity of carbonizing systems. Therefore, it is preferable to use low molecular weight precursors and then polymerize them at low temperatures in order to produce a high char yield. Dehydration and/or cross-linking by air-oxidation and treatments with chlorine at about 200°C were found to be effective in stabilizing precursors during carbonizations. Some disadvantages of these treatments are that air-oxidation took a long time at the relatively high temperature of above 250°C and chlorine treatment caused localized reactions resulting in heterogeneous structures.

Recently, it was found that iodine treatment at ca. 100°C for coal-tar-pitch, softening point 103°C, resulted in a decreased benzene-soluble fraction, an increasing pyridine-insoluble fraction in the pyrolyzed pitch, an increasing char yield to 75 wt% and a decreasing domain size in the resultant carbon [34]. Detailed studies [35,36] revealed that iodine formed a charge transfer complex with pitch molecules, and that the complex increased char yield and also viscosity during carbonization. Condensed aromatic rings consisting of molecules having ca. 14 benzene rings were suitable for complex formation. A structural model for the complex was produced. Iodine affected dehydration and polymerization of the pitch during its pyrolysis, with

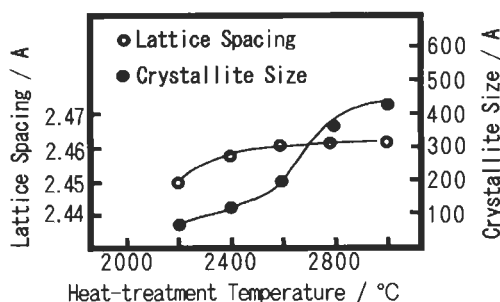


Fig. 8. Crystallite size of (110) plane in resin derived composite [32].

polymerizations taking place at a temperature 200°C lower than for the original pitch. This low temperature polymerization brought about the high char yield.

An interesting phenomenon has been observed with a glassy carbon. On heat treatment, a surface layer, only 20 to 30 nm deep, is graphitized, the interior remaining more or less unchanged [37]. Surfaces themselves have an important role in the determination of crystal structure.

New types of carbon alloys with interesting properties have appeared as a result of the project "Carbon Alloys". For example, activated carbons with controlled pore size(s) have been produced from a mixture of a standard resin with an ion-exchanged resin containing different cations, as well as hard carbons with nitrogen alloying, and semiconductor carbons [38].

The concept of Carbon Alloys can be extended to ceramic materials containing carbons [39]. For example, the synthesis of fine carbide powders through a sol-gel route employed a mixture of resin precursors and metal alkoxides. In this process, homogeneous structures with small quantities of doping additives in resultant carbons can be easily achieved. Ultra-fine particles of ceramics were also synthesized at low temperatures.

For PAN fibers mixed with fine particles of Fe or Ni dispersed in the carbon, reaction rates were accelerated at 1250 K including the evolution of nitrogen gas resulting in low nitrogen contents and high carbon yields from the PAN fibers [40].

An interesting effect of alloying on the oxidation of resin-derived carbon was found. Additions of small amounts, <1 wt% of Ta or Ti, into a resin precursor enhanced the oxidation resistance of the resultant carbons [41]: in a typical case, oxidation rates decreased by a factor of ten. Detailed mechanisms still await clarification. The number of the active sites in the carbon decreases and oxidation rates were lower than the desorption rates of CO and CO₂ [42].

For amorphous films of hydrogenated carbon nitride formed by a CVD process, the hardness of the films depended upon amounts of hydrogen that terminated the

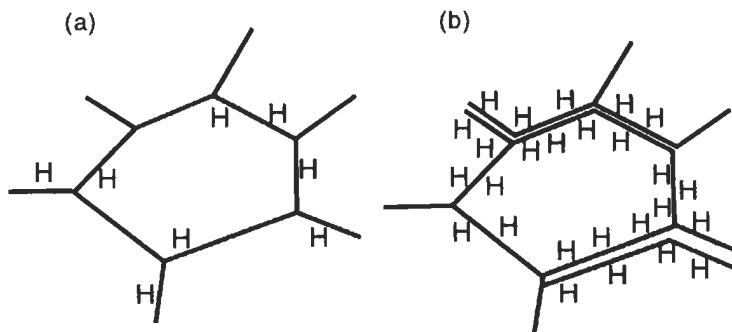


Fig. 9. Cluster models for amorphous hydrogenated carbon nitride. Each hexagon indicates a cluster consisting of carbon and nitrogen network. Hydrogen atoms terminate the networks. (a) Relatively small amount of hydrogen and the boundary is mechanically strong, and (b) relatively large amount of hydrogen and the boundary is weak [43].

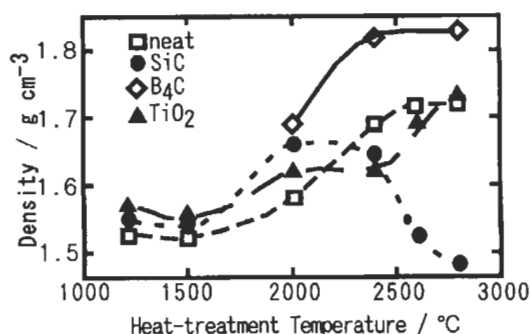


Fig. 10. Density change of inorganic powder contained composites [44].

clusters. The model in Fig. 9 indicates hardness increases with hydrogen content [43]. The hexagons indicate clusters of amorphous hydrogenated carbon nitride with carbon and nitrogen networks being terminated by hydrogen.

As the shear strength of the graphene layer planes of HOPG is as low as 3 MPa, then the high orientation of graphite crystals in the matrix has to be restrained. To make high shear strength materials, a fine microstructure is required, achieved when fine particles were added to the precursor. In general terms, density, grain size, and orientation of both the crystallite in the grains and the grains themselves mainly control the mechanical properties of ceramics. The density of the composites mixed with fine particles is plotted against HTT, as in Fig. 10. The densities of the composite, except for SiC-doped composites, increased with increasing HTT. However, the density of SiC-doped composites decreased dramatically above 2400°C. The phase diagram of the silicon–carbon system indicates the incongruent melting of SiC at about 2550°C, the vapor pressure of the molten silicon being well above this temperature [44].

The (002) diffraction profiles of a furan-resin derived C/C composite were asymmetric, the profile being composed of three peaks, from the fiber, from the glass-like matrix carbon and from the partially graphitized matrix. Peak separation was carried out by computer using a Pierson-VII type function. Composites with added B₄C had the smallest interlayer d_{002} spacings reaching the value of single crystal graphite of 0.336 nm at 2400°C. Doping with TiO₂ accelerated the graphitization at above 2600°C of composites [44].

Shear strengths of selected composites, measured by the DNC method, are shown in Fig. 11. Although some additives affected strength, additions of tantalum, effective as an anti-oxidant, had little effect on shear strength even for composites with high HTT. Shear strengths of composites without additives have much higher values than reported values, until now. The shear strength of a UD C/C composite made using a short curing period was about 30 MPa (HTT 1000°C) [14], this being about 40% lower than that of a fully cured composite [45]. In resin-derived matrix composites the curing process is quite important in determining the properties of composites.

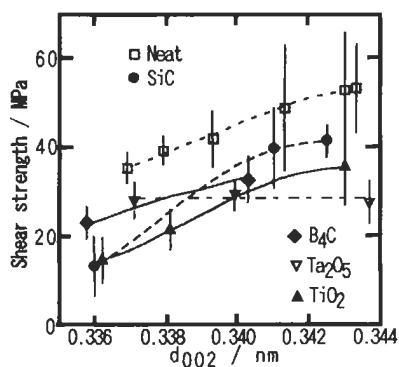


Fig. 11. Shear strength as a function of interlayer spacing of graphite component in the matrix (Neat, SiC, B₄C, Ta₂O₅, TiO₂) [45].

4 Conclusion

Interactions or reactions between carbon/graphite and metals are observed directly by TEM at temperatures from 1200 to 1500°C [38]. However, the detailed mechanisms of alloying for surface treatments and microstructural arrangements, on both nano- and meso-scales, remain to be elucidated. Alloying of some elements to precursors is effective in modifying structures and properties of both precursors and resultant carbon products. Although the concept of carbon alloys is novel, in general terms, carbons are actually alloys consisting not only of carbon atoms but also other elements. However, many complicated phenomena observed with conventional carbons may be resolved based on the carbon alloys concept.

References

1. B.T. Kelly, *Physics of Graphite*. Applied Science, London, pp. 62–266, 1986.
2. L. Hull, *Introduction to Composite Materials*. Cambridge University Press, London, pp. 102–125, 1981.
3. Y. Tanabe, E. Yasuda, K. Yamaguchi, M. Inagaki and Y. Yamada, *Tanso*, 147: 66–73, 1991.
4. Y. Touloukian, R.W. Powell, C.Y. Ho and P.G. Klemens, *Thermal Conductivity. Thermophysical Properties of Matter series, Vol. 2*. IFI/Plenum, New York, p. 41, 1970.
5. Y. Hishiyama, M. Inagaki, S. Kimura and S. Yamada, *Carbon*, 12: 249–258, 1974.
6. M. Inagaki and R.A. Meyer, *Chemistry and Physics of Carbon, Vol. 26*. Marcel Dekker, New York, pp. 149–244, 1999.
7. Y. Tanabe, E. Yasuda and S. Kimura, *Ext. Abstracts the 18th Biennial Conference on Carbon*, pp. 241–242, Worcester, USA, 1987.
8. G.S. Rellick and P.M. Adams, *Carbon*, 32 (1): 127–144, 1994.
9. L.M. Manocha, E. Yasuda, Y. Tanabe and S. Kimura, *Carbon*, 26: 333–337, 1988.
10. E. Yasuda, Y. Suzuki, Y. Inoue, H. Izawa, O. Ebato, S. Takano, K. Kihara, A. Kondou, M. Ookawa, T. Hiraoka, M. Shimada, M. Kume, K. Niiya, Y. Aiba and K. Takeuchi, *Tanso*, 170: 247–254, 1995 (in Japanese).

11. N. Tsujioka, Z. Maekawa, H. Hamada and M. Hojo, *J. Soc. Mater. Science, Japan*, 42: 163–169, 1997.
12. F. Nakao and H. Asai, *Sen-I Gakkai-Shi*, 49 (1): 18–25, 1993 (in Japanese).
13. Y. Tanabe, K. Hoshi, M. Ishibashi, T. Akatsu and E. Yasuda, *Carbon*, 39: 294–296, 2000.
14. E. Yasuda, J. Ariyoshi, T. Akatsu and Y. Tanabe, *Composites '95, Proc. Japan-US CCM-VII, Kyoto*, pp. 159–166, 1995.
15. F. Nakano, *J. Adhesion Soc. Jpn.*, 28 (8): 315–323, 1992 (in Japanese).
16. J.-B. Donnet, S.-J. Park and W.-D. Wang, *Polymer for Advanced Technologies*, 5: 395–399, 1994.
17. K. Kawashima, H. Takahashi, M. Shimazaki, T. Kohno, H. Sakai, K. Nishiyama and M. Abe, *Tanso*, 195: 336–340, 2000 (in Japanese).
18. A.N. Netravali and Y.K. Kamath, *Proceedings of the ASME Materials Division*, 69 (1): 785–798, 1995.
19. Y.-B. Chong, H. Ohara and N. Watanabe, *Sen-I Gakkai-Shi*, 49 (3): 111–116, 1993 (in Japanese).
20. M.J. Reis, A.M. Bothlho Do Rego, J.D. Lopes Da Silva and M.N. Soares, *J. Mater. Sci.*, 30: 118–126, 1995.
21. E. Yasuda, Y. Tanabe, L.M. Manocha and S. Kimura, *Carbon*, 26: 225–227, 1988.
22. S. Kimura, E. Yasuda, K. Yasuda, Y. Tanabe, K. Kawamura and M. Inagaki, *Tanso*, (125): 62–68, 1986.
23. E. Yasuda, Y. Tanabe and M. Takabatake, *Tanso*, (140): 310–313, 1989 (in Japanese).
24. E. Yasuda, S. Kimura and Y. Shibusa, *Trans. JSCM*, 6: 14–23, 1980.
25. P.A. Thrower and L.R. Radovic, *AFRL-SR-BL-TR-98-0150*, 1998.
26. S. Ide and T. Takahashi, *Polymer Preprints Japan*, 37 (9): 2630–2632, 1988 (in Japanese).
27. E. Fitzer and L.M. Manocha, In: *Carbon Reinforcements and Carbon/Carbon Composites*. Springer-Verlag, Berlin, pp. 179–185, 1998.
28. P.W.M. Peters, G. Luedenbach, R. Pleger and R. Weiss, *J. European Ceramic Soc.*, 13: 561–569, 1994.
29. K. Matsunaga, T. Ishikawa, S. Kajii, T. Hogami and Y. Kohtoku, *J. Ceram. Soc. Jpn.*, 103 (3): 288–292, 1995.
30. S. Shimada, *J. Ceramic. Soc. Jpn.*, 109: S33–42, 2001.
31. K. Takahashi, K. Yoshida and M. Iwaki, *J. Chem. Soc. Jpn.*, 6: 1055–1063, 1985.
32. S. Kimura, E. Yasuda and Y. Tanabe, *J. Ceramic Soc. Jpn.*, 93 (2): 89–95, 1985 (in Japanese).
33. S. Kimura, K. Yasuda, E. Yasuda and Y. Tanabe, *Tanso*, 128: 30–37, 1987 (in Japanese).
34. E. Yasuda, H. Kajiura and Y. Tanabe, *Tanso*, 170: 286–289, 1995.
35. N. Miyajima, T. Akatsu, T. Ikoma, O. Ito, B. Rand, Y. Tanabe and E. Yasuda, *Carbon*, 38: 1831–1838, 2000.
36. N. Miyajima, T. Akatsu, O. Ito, R. Sakurovs, S. Shimizu, M. Sakai, Y. Tanabe and E. Yasuda, *Carbon*, 39: 647–653, 2001.
37. Y. Tanabe, J. Yamanaka, K. Hoshi, H. Migita and E. Yasuda, *Carbon*, 39: 2343–2349, 2001
38. Presented in the final report of Grant-in-Aid for Scientific Research “Carbon Alloys”, 2000 (in Japanese); some of the topics are presented in this book.
39. N. Narisawa, Y. Okabe, M. Iguchi, K. Okamura and Y. Kurachi, *J. Sol-Gel Sci. Technol.*, 12: 143–152, 1998.
40. T. Watanabe, Y. Ohtsuka and Y. Nishiyama, *Carbon*, 32: 329–334, 1994.
41. E. Yasuda, S. Park, T. Akatsu and Y. Tanabe, *J. Mater. Sci. Lett.*, 13: 378–380, 1994.
42. Y. Tanabe, M. Utsunomiya, M. Ishibashi, T. Kyotani Y. Kaburagi and E. Yasuda, *Carbon*, 40: 2295–2301, 2002.

43. H. Saitoh, K. Yatsui, H. Ito and S. Ohshio, Final report of the Carbon Alloys Projects, pp. 239–244, 2000.
44. E. Yasuda, Y. Hotta, T. Akatsu and Y. Tanabe, Proc. 2nd Int. Meeting of Pacific Rim Ceramic Societies (PacRim 2), 1996.
45. Y. Tanabe, Y. Hotta, T. Akatsu, S. Yamada and E. Yasuda, *J. Mater. Sci.*, 16: 557–559, 1997.

Part 3

Typical Carbon Alloys and Processing

Chapter 6

Intercalation Compounds

Noboru Akuzawa

Tokyo National College of Technology, 1220-2 Kunugida, Hachioi-shi, Tokyo 193-0997, Japan

Abstract: The science and technology of intercalation compounds developed in the project “Carbon Alloys” are summarized in this chapter. The subjects are: lithium insertion into carbon materials, new intercalation compounds prepared from unique host carbon materials, and host effects following the intercalation of halogen molecules and alkali metals. Several carbons are examined as possible anodes of lithium-ion batteries and the origins of large capacities of less graphitized carbons are debated. Theoretical approaches are proposed for the analysis and design of anode materials with high performances. Effects of heteroatoms introduced into carbons have been extensively investigated by experiment and by calculation. The electronic and magnetic properties of diamond-derived nanographite and its derivatives formed by the intercalation of potassium and halogen molecules are investigated. It was found that edge-inherited non-bonding π -electron states play an essential role in characterizing the electronic structure of nanographite. The intercalation of potassium into nanographite diminishes the contribution of the edge-states due to charge transfer from the potassium atom. Evidence of charge transfer from nanographite to iodine, absent in bulk-graphite, is identified. The charge transfer fraction, per carbon atom f_c , follows the order of potassium > bromine > iodine. Intercalation of cesium into carbon materials with different heat-treatment temperatures (HTT) was carried out and the resultant carbon alloys were characterized by XRD, ESR, Raman spectroscopy and molecular sorption techniques. Increases in carbon–carbon interlayer spacings due to intercalation by cesium were observed even for less-graphitized carbons of $\text{HTT} < 1273 \text{ K}$. The compound CsC_{24} was able to sorb molecules such as hydrogen, although almost no shift of the Raman peak (G-band) was observed, suggesting weak interactions between the cesium and carbon layers.

Keywords: GIC, Intercalation, Lithium-ion battery, Host–guest reaction, Nanographite, Host effect.

1 Introduction

Intercalation modifies the structure of graphite and carbon materials. The resulting compounds consist of carbon and intercalate layers. They show unique properties such as high electrical conductivity, catalysis in chemical reactions, molecular sorption, etc. The possibilities for application of graphite intercalation compounds

Table 1

Possible applications of graphite intercalation compounds

| | |
|---|---|
| 1. Highly conductive materials | HNO ₃ , AsF ₅ , etc. |
| 2. Electrode materials in batteries | |
| primary cell | F, CoCl ₂ , etc. |
| secondary batteries | Li, H ₂ SO ₄ , Ni(OH) ₂ , etc. |
| thermocell | Br ₂ , HNO ₃ |
| 3. Catalyst for organic synthesis | Li, K, Br ₂ , etc. |
| 4. Materials for storage and isotope-separation of hydrogen | K, Rb, Cs |
| 5. Others | |
| exfoliation of graphite | H ₂ SO ₄ , HNO ₃ , K-THF, etc. |
| thermal energy storage | MnCl ₂ -NH ₃ |
| electrochromic | Li-DMSO |

are summarized in Table 1 [1]. Ten years ago, the idea of using carbon materials as the anode of Li-ion batteries had not been realized. Practical applications were limited to carbon fluoride as cathodes of a primary cell and Li-insertion compounds for Li-ion secondary batteries, as well as exfoliated graphite for use as gaskets.

In the Carbon Alloys project, various topics concerning intercalation compounds were investigated from fundamental levels to practical applications. This chapter describes the results with special reference to lithium-insertion into carbons, new intercalation compounds prepared from unique host carbons, host effects on intercalation of alkali metals and halogen molecules. The topics described in this chapter are summarized in Fig. 1.

2 Li-insertion into Carbon Materials

Carbon materials have been used as anode electrodes in commercial Li-ion secondary batteries for portable electronic devices. This battery system has several advantages over conventional aqueous batteries, including: (1) higher energy densities (up to 135 Wh kg⁻¹, 300 Wh l⁻¹); (2) higher cell voltages (up to 4.0 V); and (3) longer shelf-life (5–10 years) and cycle life (1000–3000 cycles) [2]. Several carbons ranging from non-graphitizable carbon to graphite were examined. Further improvements are required and the results of this Carbon Alloys project are summarized in Part 5. This section focuses on the Li-intercalation (and de-intercalation) properties of these carbon materials.

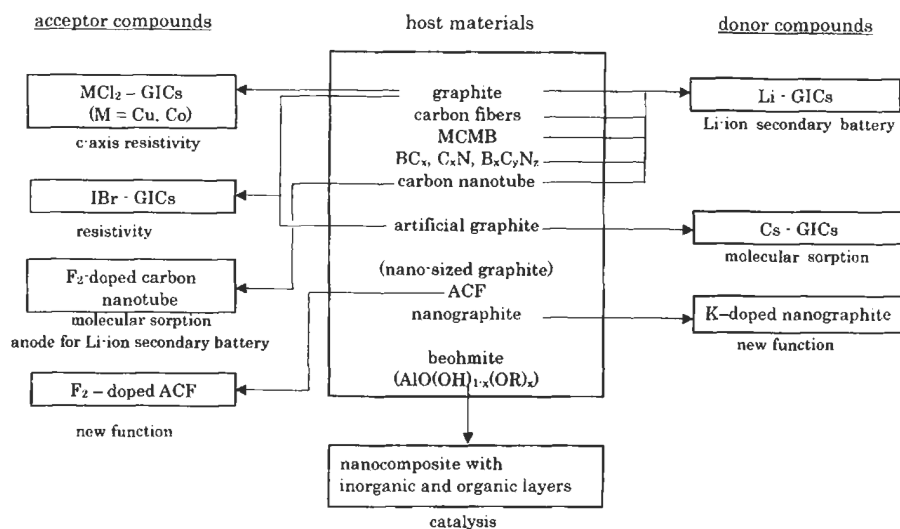


Fig. 1. Schematic representation of the intercalation compounds investigated in the Carbon Alloys project.

Milled mesophase pitch-based carbon fibers (mMPCFs) were developed to enhance cell performance in terms of specific capacity and coulombic efficiency, carbons having excellent anode performances [3]. The effects of boron doping in mMPCFs were also examined [4,5]. The electrochemical Li-insertion into boron doped mMPCFs, at a concentration of 2.7 at% (2.4 wt%), took place at a voltage about 40 mV higher than in the original mMPCFs. It is considered that substitutional boron acts as an electron acceptor in the graphite lattice.

Carbon alloys containing boron and/or nitrogen were prepared by chemical vapor deposition (CVD) or arc-discharge techniques, and the electrochemical Li-insertion behavior was examined [6–11]. C_xN , BC_x and $B_xC_yN_z$ soots prepared by arc-discharge were composed of fine particles, diameters of 20–100 nm, the electrode potentials increasing linearly with increasing lithium-ion deintercalation, accompanied by a large irreversible capacity. On the other hand, carbon, BC_x and $B_xC_yN_z$ cathode deposits produced simultaneously with the above soots and consisting mainly of nanotubes with diameters of ca. 20 nm and nanoparticles with diameters < 100 nm, showed similar charge–discharge behavior to that of natural graphite, although the reversible capacity was less. It was also shown that for C_xN -coated graphite, prepared by CVD, the electrode potential was low and gradually increased during the final stages of deintercalation of lithium. The reversible capacity was $\sim 397 \text{ mAh g}^{-1}$, larger than $\sim 365 \text{ mAh g}^{-1}$ for carbon-coated graphite and 334 mAh g^{-1} for heat-treated C_xN soot.

Molecular orbital calculations on stable structures and on electronic and lithium-adsorption properties of several polyaromatic hydrocarbon sheets substituted by boron, nitrogen, etc. were performed to understand the large capacities of boron-

substituted disordered carbon materials [12–16]. A semi-empirical molecular orbital calculation on model structures (polyaromatic hydrocarbons such as $C_{24}H_{12}$, $B_2C_{22}H_{12}$, $N_2C_{22}H_{12}$, etc.) gave the following results. The substitution of boron into carbon networks creates an electron acceptor level in a energy region lower than that for pristine carbon. This lower level accepts electrons from the adsorbed lithium atoms more easily, resulting in the stabilization energy by lithium adsorption being larger than for pristine carbon. On the other hand, for the nitrogen-substituted carbon networks, the electron acceptor level is almost the same. The effects of B-N-B-unit substitution on the electronic properties of $C_{54}H_{18}$ were also examined. Substitution is preferred at the periphery of the $C_{54}H_{18}$ sheet, so creating electron acceptor levels in a lower energy region than that for $C_{54}H_{18}$. This level accepts electrons from the adsorbed lithium atoms more easily, so that the lithium adsorption energy for B-N-B-substituted sheet is larger than that for the pristine sheet. The adsorbed lithium atoms are stabilized near boron atoms to be far from nitrogen atoms, indicating that nitrogen atoms may have a negative effect in the enhancement of lithium storage of B-N-B-substituted carbon sheets.

The same calculations were applied to the system of a lithium-doped graphite cluster with dangling bonds (C_{54} , C_{96}) and to hydrogen terminations at the edges of the cluster ($C_{54}H_{18}$, $C_{96}H_{24}$) [17,18]. Negative ion states for lithium atoms were found in a graphite cluster heavily doped with lithium. These calculations identified a quasi-stable site near the terminated hydrogen atoms for a negative lithium ion, and this site was stabilized by Coulomb interactions between the lithium ions. The origin of the negative ions comes from the finite size effects of the graphite cluster. The negatively charged lithium sites are energetically unstable compared with the positively charged lithium sites. Thus, if there is only a single lithium atom on the cluster, then a positive lithium ion will always result. The total charge transfer from lithium ions to the cluster does not depend on the number of lithium atoms but rather on the relative geometries of the doped lithium atoms on the cluster.

The *ab initio* molecular orbital method applied to lithium doped pyrene ($C_{16}H_{10}$) and ovalene ($C_{32}H_{14}$) showed the following [19]:

1. There exist not only ionic but also covalent characters between Li and the carbon sheet; the covalent character originates from the overlap between lithium 2p and carbon π -atomic orbitals, and is prominent at the edge sites.
2. The energy barrier for a Li to travel from one site to another is very small at room temperature.
3. Substitution of a hydrogen atom by a hydroxyl group stabilizes a Li dopant, with substitution by methyl groups having little effect.

Lithium insertion into fluorinated open-ended nanotubes embedded in an Al_2O_3 template was investigated [20] showing a large irreversible capacity ($> 1000 \text{ mAh g}^{-1}$) in the first charge-discharge cycle, similar to MWNT [21] and SWNT [22]. The efficiency, however, increases sharply after the second cycle. The reversible capacity of the second cycle is 501 mAh g^{-1} , much larger than the theoretical value of 372 mAh g^{-1} for the graphite intercalation compound, LiC_6 .

In situ calorimetry of mesocarbon microbeads (MCMBs) heat-treated to 973, 1273 and 2073 K was carried out during electrochemical Li-insertions and Li-extractions [23]. The MCMBs with HTTs of 973 and 1273 K showed hysteresis in the voltage profiles and exhibited large heat evolution over the plateau regions at ~ 0 V in the Li-insertion process and at ~ 1 V for Li-extraction. Otherwise, an MCMB, HTT 2073 K, showed a small heat evolution attributable mainly to the entropy change. An observed large heat evolution for MCMBs with HTTs of 973 and 1273 K is due to the existence of two Li-sites in the carbon materials, i.e. intercalation sites and bonding sites [24].

3 New Intercalation Compounds Prepared from Unique Host Carbon Materials

Diamond nanoparticles (grain size 4–6 nm) were converted to graphitic nano-sized clusters by heat-treatment to high temperatures. The onset temperature for the diamond–graphite transition is ~ 1473 K with complete conversion to graphitic structures at around 1873 K [25,26]. Their intercalation compounds with potassium, bromine and iodine were prepared [27,28]. The staging phenomenon observed in bulk-graphite intercalation compounds was absent, as is to be expected for a finite size host–guest system. K-intercalated samples contained a small fraction of neutral potassium clusters. Raman scattering measurements indicated the absence of charge transfer from nanographite to iodine, also absent in bulk-graphite. The charge transfer fraction per carbon atom f_c followed the order of potassium > bromine > iodine, which is similar to the trends observed in bulk-graphite intercalation compounds.

Activated carbon fibers (ACFs), with a three-dimensional network of nano-sized graphites of size 2–3 nm, provided micropore space available for the accommodation of guest species through intercalation or inclusion processes. The effect of doping with fluorine or iodine on the electrical properties and magnetic properties was studied [29–32]. For iodine molecules, charge transfer took place from nanographite to iodine giving a nanographite–iodine intercalation system in metallic ACFs (ACFs with HTT > 1273–1473 K), similar to the system of diamond-derived nanographite with iodine. For insulating ACFs (ACFs with HTT < 1273–1473 K), the presence of accommodated iodine species modified the electron conduction process between the nanographite domains. The introduction of fluorine brought about the formation of sp^3 defects having dangling bonds with localized magnetic moments accompanied with local lattice distortion. In nanographites, the electronic state of the dangling bonds associated with formed C–F bonds extended in the wide region, resulting in the shrinkage of π -electron wave functions. A semi-empirical quantum calculation supported those features [33,34]. By adding fluorine atoms singly to the $C_{24}H_{12}$ cluster, fluorine atoms first terminated at the edge sites of the cluster, and then the interior carbon atoms were doped by the fluorine atoms by breaking the π -bonds between a carbon atom and its neighboring carbon atom.

Control of properties of carbons by fluorination was extensively investigated [35–39]. Carbon nanotubes prepared by pyrolytic carbon deposition onto anodic

aluminum oxide films were fluorinated in the temperature range 323–473 K [35–38]. Fluorine atoms were covalently bonded to carbon atoms on the internal surfaces (hidden surfaces) of the tubes. The pristine and fluorinated nanotubes embedded in the template (aluminum oxide films) adsorbed nitrogen within the tubes. Amounts of nitrogen adsorbed by the fluorinated tubes were less than for the pristine tubes. Analysis of the isotherms suggested that fluorination of the internal surfaces of the nanotubes provided a low surface energy for the cylindrical mesopore systems of the tubes. Fluorination of C_xN at temperatures 300–573 K yielded intercalation compounds consisting of mixtures of several stages or mixtures with the unreacted phase [39]. The reason why the substituted nitrogen of C_xN made the intercalation of fluorine easier was considered as follows. Nitrogen substitution induces electron localization, and hence carbon atoms bound to nitrogen are positively charged. However, second or third neighboring carbon atoms are usually considered to be negatively charged. The increase in the electron density is favourable for fluorination.

Monolayers of Yb, Cu or Ag were successfully intercalated beneath a monolayer of graphite adsorbed on a Ni (111) substrate [40]. Surface phonon dispersion was determined before and after intercalation. The phonon dispersion relationships of the monolayer of graphite on Ni(111) system and those of the Yb-intercalated were characterized by graphite-like phonon modes which were softened by strong interactions with the Ni substrate. For Cu- or Ag-intercalated material, the dispersion curves were very similar to those of bulk graphite. The stiffening observed after Cu or Ag intercalation was caused by a weaker interaction of the graphite monolayer with the Ni substrate.

4 Host Effect on the Intercalation of Halogen Molecules and Alkali Metals

Electrical resistivities of a graphite (graphene) sheet and anisotropic materials derived from petroleum cokes, with HTT 1273 to ~3073 K were determined during IBr doping at room temperature [41]. Considerable changes in resistivity were observed for graphite and carbon materials, HTT > 2273 K. The relative resistances, R/R_0 , defined as the resistance of IBr-doped material divided by that of the pristine material, were as follows: 0.095 (graphite sheet), 0.116 (HTT 3073 K), 0.117 (HTT 2673 K), 0.167 (HTT 2473 K), 0.269 (HTT 2273 K), 0.862 (HTT 2023 K) and 0.838 (HTT 1273 K). IBr molecules did not intercalate with carbon materials of HTT < 2273 K, but reduced the resistivity somewhat by surface adsorption. However, they intercalated into carbon materials with HTTs > 2273 K and reduced the resistivity considerably through charge transfer between intercalated IBr molecules and carbon layers. This result is in good agreement with the observations of X-ray diffraction measurements and Raman spectroscopy of the carbon materials. Both the d_{004} (XRD parameter) and R -value (Raman parameter) changed significantly at ~2273 K. The heat treatment of the IBr-doped carbon materials yielded stable residue compounds. The resistivity value of a residue compound was about half that of the corresponding host carbon.

Intercalation of cesium into the carbons (the same as used in the IBr doping) was done to understand any host effects on the structure and properties of the resulting compounds [42]. CsC₂₄ absorbed hydrogen at 77 K, irrespective of HTT of the host carbons, although a stepwise increase of the absorbed amount was observed at HTT ~ 2273 K. The G-band of Raman spectra of CsC₂₄ prepared from carbon materials with HTT > 2023 K shifted from 1580 cm⁻¹ (host carbon) to 1602 cm⁻¹. On the other hand, almost no shift was observed for CsC₂₄ prepared from materials with HTTs < 2023 K. However, expansion of C–C interlayer spacings of CsC₂₄ was detected by X-ray diffraction. Those facts suggest that nanospaces were created by intercalation of cesium even for less graphitized material, HTT 1273 K, but that well-organized nanospaces were created from the more graphitized materials. A similar host effect was seen in the intercalation of potassium [43].

5 Physical Properties of MCl₂-GICs and Alkyl Derivative of Boehmite with Layered Structure

The *c*-axis resistivities of Stages 1 and 2 MCl₂-GICs (M = Cu, and Co) were determined under magnetic fields [44]. The *c*-axis resistivity of Stage 1 (CuCl₂-GIC) showed a typical angular dependent magnetoresistance oscillation, as commonly observed in several quasi two-dimensional electron systems with a periodically warped cylindrical Fermi surface. This indicated a band conduction along the *c*-axis. On the other hand, both band conduction and incoherent interlayer hopping took place for stage 2 CuCl₂-GIC and Stage 1 CoCl₂-GIC, with only incoherent interlayer hopping for Stage 2 CoCl₂-GIC.

The reaction of aluminum alkoxide in straight-chain primary alcohols at elevated temperatures yielded the alkyl derivatives of boehmite [AlO(OH)_{1-x}(OR)_x], a class of intercalation compound where moiety of guests were covalently bonded to the host boehmite layers [45,46]. A composite alumina/carbon was prepared by calcination of the glycol derivatives of boehmite [AlO(OH)_x(O(CH₂)_nOH)_y] (*x* + *y* = 1) in an inert atmosphere. The activity of a Co-Mo catalyst supported on this composite for desulphurization of thiophene was excellent.

6 Conclusion

Topics relating to intercalation compounds in the Carbon Alloys project are described. Li-insertion into a variety of carbon materials is of interest, mainly because of practical applications. Both experiments and calculations showed that there are two kinds of site for lithium atoms (i.e., two kinds of electronic states of Li) in carbons composed of small “crystallites”. A diamond-derived carbon (nanographite) has a unique electronic state due to edge effects. The charge transfer from nanographite to iodine was confirmed, this not having been recognized in bulk-graphite. The effects of degree of graphitization of host carbons on the properties of the intercalation compounds were also studied.

References

1. M. Inagaki, Application of graphite intercalation compounds. *J. Mater. Res.*, 4: 1560–1568, 1989.
2. T. Zheng and J.R. Dahn, Applications of carbon in lithium-ion batteries, In: T.D. Burchell (Ed.), *Carbon Materials for Advanced Technologies*, p. 341. Pergamon, Amsterdam, 1999.
3. M. Endo, C. Kim, T. Karaki, T. Kasai, M.J. Matthews, S.D.M. Brown, M.S. Dresselhaus, T. Tamaki and Y. Nishimura, Structural characterization of milled mesophase pitch-based carbon fibers. *Carbon*, 36: 1633–1641, 1998.
4. M. Endo, C. Kim, Y. Nishimura, M.J. Matthews, S.D.M. Brown and M.S. Dresselhaus, Anode performance of a Li ion battery based on graphitized and B-doped milled mesophase pitch-based carbon fibers. *Carbon*, 37: 561–568, 1999.
5. M. Endo, C. Kim, Y. Nishimura, T. Fujino and K. Miyashita, Recent development of carbon materials for Li ion batteries. *Carbon*, 38: 183–197, 2000.
6. M. Koh and T. Nakajima, Synthesis of well crystallized boron–carbon filament by chemical vapor deposition using a nickel catalyst. *Carbon*, 36: 913–920, 1998.
7. M. Koh and T. Nakajima, Electrochemical behavior of carbon alloy BC_x and of BC_x -coated graphite prepared by chemical vapor deposition. *Electrochimica Acta*, 44: 1713–1722, 1999.
8. T. Nakajima and M. Koh, Synthesis of high crystalline carbon–nitrogen layered compounds by CVD using nickel and cobalt catalysts. *Carbon*, 35: 203–208, 1997.
9. M. Koh, T. Nakajima and R. N. Singh, Synthesis and electrochemical behavior of carbon alloy C_xN . *Mol. Cryst. Liq. Cryst.*, 310: 341–346, 1998.
10. T. Nakajima, M. Koh and M. Takashima, Electrochemical behavior of carbon alloy C_xN prepared by CVD using a nickel catalyst. *Electrochimica Acta*, 43: 883–891, 1998.
11. T. Nakajima, M. Koh and T. Katsube, Structure, chemical bonding and electrochemical behavior of heteroatom-substituted carbons prepared by arc discharge and chemical vapor deposition. *Solid State Sci.*, 2: 17–29, 2000.
12. N. Kurita, Molecular orbital calculations on lithium-absorption in boron or nitrogen substituted disordered carbon. *Tanso*, 1998: 266–271, 1998 (in Japanese).
13. N. Kurita, Molecular orbital calculations on electronic properties and lithium storage of substituted disordered carbons. *Mol. Cryst. Liq. Cryst.*, 340: 413–418, 2000.
14. N. Kurita, M. Sasaki and Y. Goto, Electronic and Li-absorption properties of boron and nitrogen substituted graphite sheets. *Hyomen*, 38: 10–19, 2000 (in Japanese).
15. N. Kurita, Molecular orbital calculations on lithium absorption in boron- or nitrogen- substituted disordered carbon. *Carbon*, 38: 65–75, 2000.
16. N. Kurita and M. Sasaki, Molecular orbital calculations on stable structures, electronic and lithium-absorption properties of BNB-substituted graphite sheets. *Tanso*, 347–352, 2000 (in Japanese).
17. M. Nakadaira, R. Saito, T. Kimura, G. Dresselhaus and M.S. Dresselhaus, Excess Li ions in a small graphite cluster. *J. Mater. Res.*, 12: 1367–1375, 1997.
18. M. Yagi, R. Saito, T. Kimura, G. Dresselhaus and M.S. Dresselhaus, Electronic states in heavily Li-doped graphite nanoclusters. *J. Mater. Res.*, 14: 3799–3804, 1999.
19. H. Ago, M. Kato, K. Yahara, K. Yoshizawa, K. Tanaka and T. Yamabe, *Ab initio* study on interaction and stability of lithium-doped amorphous carbons. *J. Electrochem. Soc.*, 146: 1262–1269, 1999.
20. H. Touhara, Application of carbon nanotubes to lithium battery. *Ouyobuturi*, 69: 33–37, 2000 (in Japanese).
21. E. Frackowiak, S. Gautier, H. Gaucher, S. Bonnamy and F. Beguin, Electrochemical stor-

- age of lithium multiwalled carbon nanotubes. *Carbon*, 37: 61–69, 1999.
22. B. Gao, A. Kleinhammes, X. P. Tang, C. Bower, L. Fleming, Y. Wu and O. Zhou, Electrochemical intercalation of single-walled carbon nanotubes with lithium. *Chem. Phys. Lett.*, 307: 153–157, 1999.
 23. M. Inaba, M. Fujikawa, T. Abe and Z. Ogumi, Calorimetric study on the hysteresis in the charge–discharge profiles of mesocarbon microbeads heat-treated at low temperatures. *J. Electrochem. Soc.*, 147: 4008–4012, 2000.
 24. T. Zhen, W.R. McKinnon and J.R. Dahn, Hysteresis during lithium insertion in hydrogen-containing carbons. *J. Electrochem. Soc.*, 143: 2137–2145, 1996.
 25. O.E. Andersson, B.L.V. Prasad, H. Sato, T. Enoki, Y. Hishiyama, Y. Kaburagi and S. Bandow, Structure and electronic properties of graphite nanoparticles. *Phys. Rev. B*, 58: 16387–16395, 1998.
 26. B.L.V. Prasad, H. Sato, T. Enoki, Y. Hishiyama, Y. Kaburagi, A.M. Rao, P.C. Eklund, K. Oshida and M. Endo, Heat-treatment effect on the nanosized graphite π -electron system during diamond to graphite conversion. *Phys. Rev. B*, 62: 11209–11218, 2000.
 27. B.L.V. Prasad, H. Sato, T. Enoki, Y. Hishiyama and Y. Kaburagi, Nano-graphites and their potassium intercalated compounds: structural and electronic properties. *Mol. Cryst. Liq. Cryst.*, 340: 793–798, 2000.
 28. B.L.V. Prasad, H. Sato, T. Enoki, Y. Hishiyama and Y. Kaburagi, A.M. Rao, G.U. Sumanasekera and P.C. Eklund, Intercalated nanographite: structure and electronic properties. *Phys. Rev. B*, 64 (24) 235407–235416, 2001.
 29. K. Takai, H. Sato, T. Enoki, N. Yoshida, F. Okino, H. Touhara and M. Endo, Fluorine-induced sp^3 -carbon sites in a nano-sized π electron system and their effects on the electrical properties. *Mol. Cryst. Liq. Cryst.*, 340: 289–294, 2000.
 30. Y. Shibayama, H. Sato, T. Enoki, X.-X. Bi, M.S. Dresselhaus and M. Endo, Novel electronic properties of a nano-graphite disordered network and their iodine doping effects. *J. Phys. Soc. Japan*, 69: 754–767, 2000.
 31. Y. Shibayama, H. Sato, T. Enoki, M. Endo and N. Shindo, Magnetic properties of activated carbon fibers and their iodine-doping effect. *Mol. Cryst. Liq. Cryst.*, 310: 273–278, 1998.
 32. T. Enoki, K. Takai, Y. Shibayama, N. Kobayashi, A. Nakayama, H. Sato, N. Yoshida and H. Touhara, Host–guest systems in microporous carbons. *Mat. Res. Symp. Proc.*, 548: 3–14, 1999.
 33. R. Saito, M. Yagi, T. Kimura, G. Dresselhaus and M. S. Dresselhaus, Electronic structure of fluorine doped graphite nanoclusters. *J. Phys. Chem. Solids*, 60: 715–721, 1999.
 34. R. Saito, M. Yagi, T. Kimura, G. Dresselhaus and M.S. Dresselhaus, Chemical reaction of intercalated atoms at the edge of nano-graphene cluster. *Mol. Cryst. Liq. Cryst.*, 340: 71–76, 2000.
 35. H. Touhara and F. Okino, Property control of carbon materials by fluorination. *Carbon*, 38: 241–267, 2000.
 36. Y. Hattori, Y. Watanabe, S. Kawasaki, F. Okino, B.K. Pradham, T. Kyotani, A. Tomita and H. Touhara, Carbon-alloying of the rear surfaces of nanotubes by direct fluorination. *Carbon*, 37: 1033–1038, 2000.
 37. Y. Hattori, K. Kobayashi, S. Kawasaki, F. Okino, K. Yanagiuchi, A. Tsuyoshi, M. Nakayama, K. Nakajima, K. Kimura and H. Touhara, Direct thermal fluorination of DLC surfaces. *Carbon*, 36: 1399–1401, 1998.
 38. Y. Hattori, K. Kaneko, F. Okino, H. Touhara, T. Kyotani and A. Tomita, Adsorptive properties of designed fluorinated carbon nanotubes in D.D. Do (Ed.), *Adsorption Science and Technology*: pp. 309–313, World Scientific, Singapore, 2000.
 39. M. Koh, H. Yumoto, H. Higashi and T. Nakajima, Fluorine intercalation in carbon alloy C_3N . *J. Fluorine Chem.*, 97: 239–246, 1999.

40. D. Farias, K.H. Rieder, A.M. Shikin, V.K. Adamchuk, T. Tanaka and C. Oshima, Modification of the surface phonon dispersion of a graphite monolayer absorbed on Ni(III) caused by intercalation of Yb, Cu and Ag. *Surface Sci.*, 454–456: 437–441, 2000.
41. N. Akuzawa, K. Kaneko, N. Miyata, Y. Soneda and Y. Takahashi, Doping of IBr into graphite and carbon materials with different graphitization degree. *Tanso*, 229–232, 1999.
42. N. Akuzawa, T. Tajima, M. Watanabe, Y. Soneda and Y. Takahashi, Sorption of molecules by alkali metal–carbon alloys. *Proc. Eurocarbon 2000*, Vol. 2, pp. 827–828, 2000.
43. N. Akuzawa, M. Murakami, M. Nakano, Y. Soneda, R. Matsumoto and Y. Takahashi, Host effect on the properties of AM-GICs. *Mol. Cryst. Liq. Cryst.*, 340: 59–64, 2000.
44. H. Sato, O.E. Andersson, T. Enoki, I.S. Suzuki and M. Suzuki, Dimensional crossover and angular dependent magnetoresistance of magnetic graphite intercalation compounds; MCl_2 GIC's ($M=Cu$ and Co). *J. Phys. Soc. Jpn.*, 69 (4): 1136–1144, 2000.
45. M. Inoue and M. Kimura, Alkyl derivatives of boehmite having the second stage structure. *Mol. Cryst. Liq. Cryst.*, 341: 431–436, 2000.
46. M. Inoue, M. Kimura and T. Inui, Alkoxyalumoxanes. *Chem. Mater.*, 12: 55–61, 2000.

Chapter 7

Porous Carbon

Takashi Kyotani

*Institute of Multidisciplinary Research for Advanced Materials, Tohoku University, Katahira,
Sendai 980-8577, Japan*

Abstract: The porous material group of Scientific Research on Priority Areas “Carbon Alloys” project had two subjects to consider: (1) the development of methodologies for precise control of carbon pore structure, and (2) the development of novel utilization procedures for porous carbons. The concern of the first subject was the control of micro- and meso-porosity in carbons. For this purpose, several methods and techniques were proposed. Research into the second subject showed that advanced porous carbons of this project could be used as high performance membranes, adsorbents and catalyst supports. This chapter describes the results of individual research groups.

Keywords: Micropore, Mesopore, Template carbonization, Carbon nanotube, Molecular sieving carbon, Adsorption, Catalyst support.

1 Introduction

Porous carbons or activated carbons have been used for thousands of years and are now versatile materials of major industrial significance. They are characterized by their highly developed surface areas and porosities. The development of micro- and meso-pores is of importance because only such pores allow carbons to adsorb large quantities of chemicals from gas and liquid phases. For pore development, these carbons usually have been activated, that is gasification with an oxidizing gas or by reaction with a suitable chemical reagent. The complexity of carbon structure, however, prevents these conventional activation processes from preparing carbons with specific pore structures. Current environment problems and the recent development of industrial technology provide new applications for porous carbons and, at the same time, they require carbons to have desired pore structures. To meet such requirements, novel approaches to control pore structure were proposed under “Carbon Alloys”. Furthermore, it was demonstrated that such porous carbons have outstanding performances in several novel applications. Thus, in this chapter, special emphasis has been placed on two issues: (a) the development of methodologies for precise control of pore structures of carbons and (b) the development of novel utilization areas for porous carbons.

2 Control of Pore Structure

2.1 Control of Micropores

Porous carbons are characterized by their highly developed micro- and meso-pore structures, micropores being essential for adsorption of small molecules. Efforts to control structure in carbons are particularly relevant to the molecular sieving carbons (MSC). The porosity of MSC consists of uniform pores of nanometre size. Such unique pore structures of MSC separate molecules in terms of either size or shape. It is established that zeolites possess molecular sieve properties because of their regular three-dimensional porosity. In comparison with zeolites, MSC have other attractive features such as excellent shape selectivity for planar molecules, a high hydrophobicity, a high heat-resistance and a high corrosion-resistance. Thus, it is suggested that MSC can be used in applications unsuitable to zeolites.

There are two main methods to prepare MSC; one is synthesis by pyrolysis of a suitable carbon precursor(s) and the other is the modification of existing porosity of a suitable porous carbon. For the first method, Miura et al. [1] proposed the use of an ion-exchange resin as the precursor. The ion-exchange resin was a spherical polystyrene-based resin with sulphonic acid groups as ion exchangeable sites. The resins were ion-exchanged with several types of cations and carbonized at 500 to 900°C. Figure 1 shows accumulated pore volume distributions of the resultant carbons with metal additions at different loadings. The metal and its loading (mol kg⁻¹ of resin) are denoted by the symbol of the element followed by a number. Although the starting resin materials were very similar, the pore size distribution curves differed considerably. Carbons prepared from resins with di- or tri-valent cations (Ca, Fe, Ni, Cu and Zn) have larger micropore volumes than those with uni-valent cations (H, Na and K). The average pore diameter of the former resins varied 0.38 to 0.45 nm, depending on the multivalent cation. This suggests that micropore sizes are controllable by changing the cation. Miura et al. [1] put forward the following explanation for such behavior. The metal sulphides and/or the metals formed in the

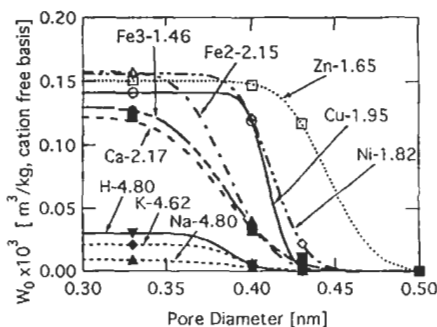


Fig. 1. Pore volume distribution curves of MSCs prepared from the ion-exchange resins with a different metal cation. (Reprinted from Ref. [1], Copyright (1999) with permission from Elsevier Science).

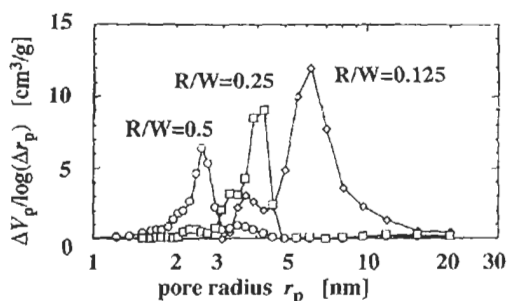


Fig. 2. Effect of resorcinol/water ratio on pore distributions of the carbon aerogels. (Reprinted from Ref. [4], Copyright (2000) with permission from Elsevier Science).

decomposition of the sulphonate groups with di- or tri-valent metal cations behave as pillars standing between the carbon layers, the presence of such pillars preventing collapse of micropores during carbonizations.

From a practical point of view, this method is very promising, because waste ion-exchange resins can be converted to MSC by this method. In fact, Miura et al. [1] carbonized waste resins containing calcium ions and confirmed the formation of uniform micropores as seen in Fig. 1 [2].

Chemical modification of micropore walls may give porous carbons some novel properties and functions. Kaneko et al. [3] introduced nitrogen into the pores of activated carbon fibres. They carried out pyridine CVD over pitch-based activated carbon fibres, HTT 700 to 1000°C. The CVD experiments at 700 and 1000°C gave activated carbon fibres alloyed with nitrogen and with their original micropore structures almost unchanged. XPS analyses showed that the nitrogen exists either as pyridinic or quaternary nitrogen. These alloyed carbons showed higher adsorption capacities for water and ethanol because of the presence of nitrogen atoms on the pore wall.

2.2 Control of Mesopores

For adsorbates of large molecular size, such adsorbates as polymers, dyes or vitamins and bacteria, as well as electric double-layer capacitors, mesopores are needed within adsorbents for such adsorbates. Thus, the design and control of mesoporosity is desirable both for improvements of performance of activated carbons and for the development of new applications. Details of these methods are reviewed by Kyotani [4]. Some of the methods, especially those within the Carbon Alloys project, are introduced below.

2.2.1 Catalytic activation

Catalytic activation of carbon is the most common method [5–10]. Tamai et al. [11] demonstrated that porous carbons, having extremely large mesoporosities, were

formed when organo-rare-earth metal complexes were used as an additive. Complexes such as $Y(acac)_3$ (Y acetylacetonate) or $Ln(C_2H_5)_3$ ($Ln = Y, Sm, Tb, Yb, Lu$) were mixed with petroleum pitch in THF. After removing the solvent, the mixture was pre-oxidized with air at $360^\circ C$ and then activated in steam at $930^\circ C$. The pore structure of the resulting carbons was examined. Both BET and BJH analyses of nitrogen isotherms at $-196^\circ C$ gave total and mesopore surface areas, respectively, and the ratio of these two surface areas was used as a measure of mesopore ratio. It was found that, although the BET surface areas of these carbons were rather low ($200\text{--}400\text{ m}^2\text{ g}^{-1}$), the mesopore ratio reached 70–80% by additions of metal complexes. To obtain both mesoporosity and high surface area, Tamai et al. [12,13] applied a method similar to the preparation of mesoporous carbon fibres. When they used $Y(acac)$ as an additive, they obtained mesoporous carbon fibres with a surface area as high as $1200\text{ m}^2\text{ g}^{-1}$. The mechanism of such mesopore formation using metal complexes is not fully understood. Probably, migration of metal-containing nano-particles in the carbon matrix during the steam activation caused the development of mesopores, as Tomita et al. [5] and Yoshizawa et al. [14] have pointed out.

2.2.2 Carbonization of mesoporous aerogel

Mesoporous carbon can also be prepared by carbonizing mesoporous organic aerogels prepared by a sol-gel reaction. The preparation of organic aerogels and their carbonizations were originally carried out by Pekala et al. [15], who found that the resultant carbon aerogels had high porosities ($> 80\%$) and high surface areas ($400\text{--}900\text{ m}^2\text{ g}^{-1}$). However, the details of their porous structures were not fully examined. Tamon et al. [16–18] analyzed the porous structure of carbon aerogels and attempted to control the pore size distributions.

Briefly, the preparation procedure adopted by Tamon et al. [16–18] is as follows. A basic aqueous solution of resorcinol (R) and formaldehyde (F) was prepared and kept in a glass vial at $20^\circ C$. During this period, polycondensation of R and F, cluster formation and gelation took place. To preserve the network structure of the aerogel and to minimize the shrinkage during drying, the gel was subject to a supercritical drying using carbon dioxide. The resultant organic aerogel was then carbonized at $1000^\circ C$. Figure 2 shows pore distribution curves of the carbon aerogels prepared with different ratios of R to water [19]. All the carbon aerogels have a narrow pore distribution in the mesopore range without microporosity. The mesoporosity of the carbon aerogels could be ascribed to a network structure that was inherited from the original organic aerogel. It should be noted that the pore size and the pore volume can be controlled by changing the ratio of R to water. Tamon et al. [16–18] thoroughly investigated the effect of preceding sol-gel conditions (i.e. amounts of R, F, water and catalyst) on final pore-size distributions. Also provided were empirical equations to estimate mesopore sizes and volumes from the amounts of R, F, water and catalyst in the sol-gel reaction. According to Tamon et al. [16–18], strict control of mesopore size is possible in the range of 2.5–9.2 nm. Recently, they examined the applicability of

freeze-drying instead of supercritical drying [20], because the former drying process is more cost-effective than the latter. They prepared organic cryogels from R and F using freeze-drying with *t*-butanol and indicated the formation of mesoporous carbons even from such organic cryogels.

Kaneko et al. prepared Ce, Zr-doped carbon aerogels as the catalyst support for NO conversion [21]. A serious problem of the carbon support is carbon consumption by oxidation during the NO reduction. Ceria has a high capacity for oxygen storage and the reducibility of ceria is enhanced by mixing with ZrO₂. Thus, a Ce–Zr-doped porous carbon could be a new catalyst for the NO conversion. Kaneko et al. [21] successfully doped Ce and Zr in carbon aerogels using the sol–gel polycondensation of resorcinol with formaldehyde with additions of Ce and Zr nitrate salts, followed by carbonization at 1050°C and then activation with carbon dioxide. The doped carbon aerogels were found to be highly microporous and have a monolith form as with the non-doped mesoporous aerogel. Such characteristics of the resultant doped carbons are suitable as catalyst supports.

2.2.3 Carbonization of polymer blends

Another approach for the production of mesoporous carbons is to carbonize a polymer blend, of a physical or chemical mixture, of more than two different types of polymers. Because a polymer blend (including block and graft copolymers) possesses properties more attractive than each constituent polymer, such blends are now used as important industrial raw materials as well as a highly functional material. The interactions between each constituent polymer in a polymer blend determine its morphology, that is, whether it has a homogenous or phase-separated structure. The phase separation phenomena of a polymer blend provide a selection of microdomain structures with sizes at the nanometre to millimetre level, depending on blend ratio and the compatibility of constituent polymers. The concept of polymer blend carbonizations was interpreted by Ozaki et al. [22] as follows. Two types of polymers with different degrees of thermal stability were employed. One becomes a carbon matrix with its original shape unchanged following high temperature treatment while the other carbonizes to gaseous products. If such a polymer blend has a phase-separated structure, its carbonization would lead to the formation of a porous structure, because the thermally unstable polymer (pore-former polymer) would decompose to leave pores in the carbon matrix formed from the stable polymer (carbon-precursor polymer).

Hatori et al. adapted this method to prepare mesoporous carbon films [23]. They used two different types of polymer; poly(diphenylene pyromellitimide) (PP) and poly(ethylene glycol) (PEG) as carbon precursor and pore former polymers, respectively. The polymer blend film prepared from PP and PEG was imidized at 200°C and then carbonized at 600°C. An analysis of the nitrogen adsorption isotherm of the resultant carbon showed that 55% of the total pore volume was made up of mesopores with pore entrances of about 4 nm.

Ozaki et al. prepared mesoporous carbon fibres using the polymer blend carbonization method [22]. The carbon precursor and the pore-forming polymers were a Novolac-type phenol resin and poly(vinyl butyral), respectively. These two polymers were mixed in methanol, followed by removal of the solvent, the spinning of the polymer blend and finally carbonization at 900°C. The introduction of poly(vinyl butyral) resulted in the development of some mesopores. Ozaki et al. prepared Pt-loaded carbon fibres by using Pt-containing poly(vinyl butyral) as a pore forming polymer when most of platinum particles were present on the pore wall [24].

Not only mesoporous but also macroporous carbon can be synthesized by the polymer blend method, as Takeichi et al. demonstrated [25]. They prepared poly(urethane-imide) films in which polyimide (carbonizing polymer) and polyurethane (pyrolyzing polymer) were phase-separated. They thermally treated the films at 350–400°C, followed by carbonization at 900°C. The SEM studies of the carbon films showed the formation of macropores of 1.5 μm diameter.

The microdomain size of phase separated structures in a polymer blend is controllable at nanometre to millimetre levels, the domains having the shape of spheres, rods or lamellae. Such flexibility in size and shape makes for an attractive carbonization method based on polymer blends. It is noteworthy that this method does not require an activation process.

2.3 Porous Carbon Prepared by Template Carbonization

A template carbonization method consists of the carbonization of an organic compound in the nanospace of a template inorganic substance and the subsequent liberation of the resultant carbon from the template. Such spatial regulation of a carbonization field by the nanospace makes it possible to control the structure of a carbon at nanometre level by changing either the size or the shape of the nanospace. So far, several unique carbons have been synthesized using this method. For example, the groups of Kyotani and Tomita prepared ultra-thin graphite films from the carbonization of organic polymers in the two-dimensional openings between the lamellae of a layered clay such as montmorillonite and taeniolite [26–28]. The template carbonization technique also allows the preparation of mesoporous carbon, when a porous inorganic material is used as a template. For example, Knox et al. [29,30] impregnated silica gel or porous glass with phenol resin and then carbonized the resin, followed by the removal of the template. The resultant carbon was mesoporous and it is commercially available as a column-packing material for liquid chromatography. Kamegawa et al. used a similar method to prepare mesoporous carbons and found that the porous carbons showed swelling phenomenon when kept in contact with organic vapors [31]. Han et al. used silica nanoparticles as a template for the production of mesoporous carbons [32–34].

Kyotani et al. prepared mesoporous carbon from a nano-composite of polyfurfuryl alcohol/silica gel produced by a sol-gel process [35]. At first, silica sol was prepared by stirring the mixture of TEOS, ethyl alcohol, de-ionized water and HCl at 80°C for 3 h.

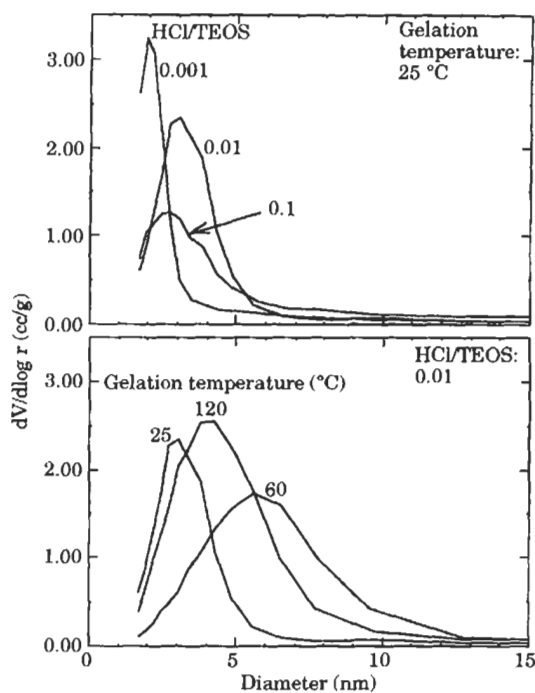


Fig. 3. Pore size distribution curves for mesoporous carbons prepared by the sol-gel method with different HCl/TEOS ratios and gelation temperatures. (Reprinted from Ref. [4], Copyright (2000) with permission from Elsevier Science).

After cooling the mixture in an ice bath, furfuryl alcohol (FA) was added to the silica sol. This mixture was poured into a dish and then heated for 2 h at temperatures up to 120°C. During this treatment, both the gelation of TEOS and the polymerization of FA took place. Then, the polyfurfuryl alcohol/silica gel film was further heat-treated at 800°C to carbonize the polymer in the film. The resultant carbon/silica composite film was washed with HF to extract carbon from the silica framework. Figure 3 shows pore size distribution curves for the carbons prepared at different sol-gel reaction conditions. All the curves have a peak in the range of 2–6 nm, and their peak position and broadness change with the sol-gel reaction conditions. At low HCl/TEOS ratios, the pore size is about 2 nm and its distribution looks sharp. The size and the broadness become larger with increasing HCl/TEOS ratios. The gelation temperature also influences resultant pore sizes quite considerably.

As well as silica gel and porous glass, zeolites are attractive templates because of their regular porous structure. If the nano channels in zeolites are completely filled with carbon and the carbon is extracted from the zeolite framework, then formation of a porous carbon can be expected. Using this concept, Kyotani et al. used a USY zeolite as a template to prepare new types of porous carbons [36]. They used the CVD method to introduce carbon into the zeolite channels. The CVD used propylene at

Table 1

Effect of carbon deposition conditions on pore structure of the CVD-carbons prepared in zeolite channels

| Deposition temperature (°C) | Propylene conc. (% in N ₂) | Deposition period (h) | BET surface area (m ² g ⁻¹) | Micropore volume (cc g ⁻¹) | Mesopore volume (cc g ⁻¹) |
|-----------------------------|--|-----------------------|--|--|---------------------------------------|
| 800 | 2.5 | 1 | 1320 | 0.54 | 0.42 |
| 800 | 2.5 | 3 | 1720 | 0.69 | 0.71 |
| 800 | 2.5 | 6 | 1510 | 0.55 | 0.64 |
| 800 | 2.5 | 12 | 1430 | 0.57 | 0.52 |
| 800 | 1.3 | 12 | 2060 | 0.82 | 0.75 |
| 800 | 1.3 | 15 | 2200 | 0.88 | 0.83 |
| 800 | 1.3 | 18 | 1790 | 0.72 | 0.62 |
| 700 | 2.5 | 12 | 1660 | 0.66 | 0.79 |
| 700 | 2.5 | 18 | 2260 | 1.11 | 0.76 |

700 or 800°C and the carbon was liberated from the zeolite framework by acid washing. A SEM examination found that the appearance of the carbon was similar to that of the zeolite; not only did both consist of fine particles, but also the surface features of each particle were similar. This surprising similarity in micro-morphology meant that the presence of carbon in the zeolite channels occurred without serious carbon deposition on the external surface of the zeolite. Table 1 contains BET surface area, micropore and mesopore volumes for the carbons prepared under different CVD conditions. The results indicate that all of the carbons are highly porous with some surface areas exceeding 2000 m² g⁻¹. The porosity of these carbons originates from the porous structure of the USY zeolite. It is to be noted that the porosity consists not only of micropores but also of considerable amounts of mesopores. Mallouk et al. and Rodriguez-Mirasol et al. also reported the formation of similar types of porous carbon by using zeolites Y and β as templates [37,38]. Recently, two Korean research groups independently obtained mesoporous carbon with an ordered structure based on mesoporous silica (MCM-48) as the template [39,40]. Kyotani et al., by using a two-step method for the filling of carbon into the channels of zeolite Y template, prepared an ordered microporous carbon that retained the structural regularity of zeolite Y [41]. They carbonized polyfurfuryl alcohol in the nano-channels in zeolite Y and then deposited carbon from the propylene CVD on the zeolite. It was found that the resultant microporous carbon has a periodicity of 1.4 nm, the same as the spacing of (111) plane of zeolite Y. This method therefore has good possibilities because of the variety of zeolites which are available.

2.4 Synthesis of Carbon Nanotubes

Carbon nanotubes are nanometre-wide needle-like cylindrical tubes of concentric graphitic sheets, and have attracted much attention because of their unusual structure, their potential applications, and interest in their fundamental properties. Carbon nanotubes were discovered in 1991 by Iijima when he investigated material deposited on a cathode used for the arc-evaporation synthesis of fullerenes [42]. Later, Ebbesen et al. found the optimum arc-evaporation conditions for the production of carbon nanotubes in bulk quantities [43]. Apart from the arc-discharge method, several other methods have been proposed, e.g. catalytic pyrolysis of hydrocarbons [44–46] and condensation of a laser-vaporized carbon–catalyst mixture [47]. In the Scientific Research on Priority Areas, “Carbon Alloys”, the following novel techniques for the production of carbon nanotubes have been proposed.

Kyotani et al. prepared carbon nanotubes by the template method using pyrolytic carbon deposition on the inner walls of the nanochannels of an anodic aluminum oxide film [48,49]. They then liberated the carbon from the film by dissolving away the template. A striking feature of their method is the production of monodisperse carbon tubes with uniform length, diameter and wall thickness. Furthermore, with this template technique, perfect encapsulation of other materials into the cavities of carbon nanotubes could easily be achieved when encapsulation was carried out before the dissolution of the template material. Other materials do not stick onto the outer surface of the carbon nanotubes; this is because there is no other space for the materials to be loaded except within the nanochannels of the carbon-coated anodic oxide film. With this filling technique, Kyotani et al. [50–54] prepared Pt, Ag, Fe and Ni-filled carbon nanotubes in which the metal or metal oxide was present as nanorods, nanoparticles, nanocrystals or nanoribbons, as shown in Fig. 4. It was found that the morphology of such nano-metal compounds formed in the tubes is significantly influenced by the method of metal loading, i.e., whether it was done by chemical vapor deposition, wet impregnation or ion-exchange loading. In other words, loading methods and conditions control the morphology of nano-metal compounds in the nanotubes.

By using a polymer blend as a carbon precursor, Oya et al. successfully prepared carbon nanotubes with outer diameters of 200–300 nm [55]. Figure 5 is a schematic drawing of their preparation method. Initially, fine particles of polyethylene, coated with phenol resin layer, were dispersed in polyethylene matrix. The whole system was spun and phenol resin tubes with a core of polyethylene were formed in the matrix. Then, after stabilization and carbonization, carbon nanotubes were formed, because the polyethylene cores and matrix decomposed whilst the phenol resin tubes remained as carbon material. The preparation scheme of Fig. 5 shows that a rigorous control is possible of tube diameter and tube wall thickness by changing the size of the original polyethylene particles and the skin thickness of the phenol resin. Furthermore, this simple preparation method facilitates the production of carbon nanotubes on a large scale. The establishment of mass production methods is indispensable for future applications of carbon nanotubes.

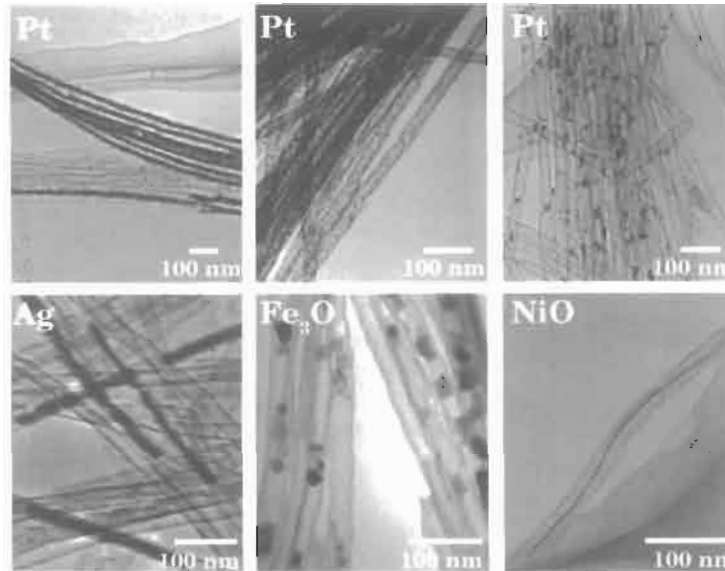


Fig. 4. TEM images of nano metal compounds in carbon nanotubes prepared by the template method.

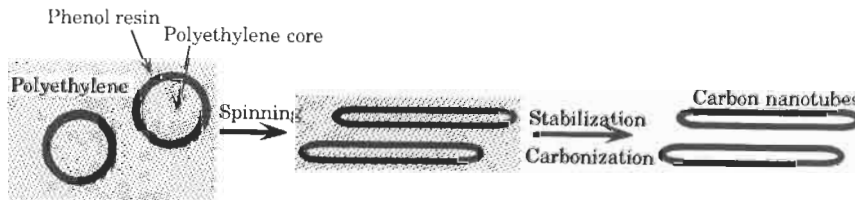


Fig. 5. Schematic drawing of the production process of carbon nanotubes by the polymer blend method.

3 Performance of Advanced Porous Carbon

3.1 Adsorption and Separation Processes

The molecular sieving carbons of powdery, granular or fibrous form are utilized as adsorbents for pressure-swing adsorption processes and/or as shape-selective catalyst supports. In addition, MSCs with a film morphology shape have applications as inorganic membranes for gas separation. A comprehensive study of MSC membrane has been undertaken by Morooka and Kusakabe [56–58]. A typical preparation procedure is as follows. A polyamic acid was synthesized from 3,3',4,4'-biphenyltetracarboxylic dianhydride (BPDA) and 4,4'-oxydianiline (ODA). The polyamic acid film was coated on the outer surface of a porous-alumina support tube by a dip-coating

method and then imidized at 300°C. This coating-imidization cycle was repeated two or three times to provide a pinhole-free BPDA-ODA membrane. Finally, the membrane on the support tube was carbonized at 500–900°C. The permeances of selected gases for the carbonized membranes were found to be in the order $\text{He} > \text{CO}_2 > \text{N}_2 > \text{CH}_4 > \text{C}_2\text{H}_6$, which was in agreement with the order of kinetic diameters, indicating molecular sieving effects in these carbon membranes. It was found that the membrane carbonized at 650–700°C exhibited a much higher gas permeance than the original polymer membrane. Thus, Kusakabe et al. concluded that carbonization is an effective way to increase gas permeance without serious reduction in permselectivity [57]. For further improvement of permeance, they modified carbon membranes by oxidation by oxygen at 300°C for 3 h [57]. Figure 6 shows the permeances of several gases for the carbon membranes with and without oxidation. The oxidation treatment increased each permeance with no observable change in permselectivity. This suggests that the micropore volume increased following oxidation with pore size distributions remaining almost unchanged. Furthermore, Kusakabe et al. prepared carbon membranes from a condensed polynuclear aromatic (COPNA) resin film and found that it functioned as a MSC membrane [58]. Because COPNA resin can form films more easily than the polyimide, even in the presence of metal cation, then an easier incorporation of metal fine particles into the carbon membrane is possible. Such metal-containing membranes would be expected to have not only separation capabilities but also catalytic functions.

As well as gas phase separations, those in the liquid phase are also of commercial importance. Oda et al. removed electrolytes from dilute aqueous solutions using several porous carbons [59]. The apparatus they used consisted of an electric double layer capacitor allowing an aqueous solution to flow through the capacitor cell, to which was applied a given voltage. Thus, during the flow of the solution, metal ions

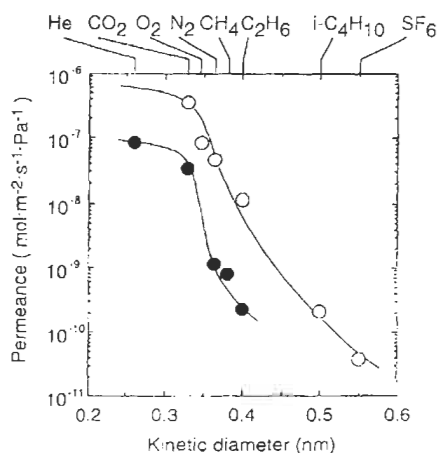


Fig. 6. Effect of oxidation on permeance at 65°C: (●) as formed; (○) oxidized in oxygen at 300°C for 5 h. (Reprinted with permission from Ref. [57], Copyright (1997) American Chemical Society).

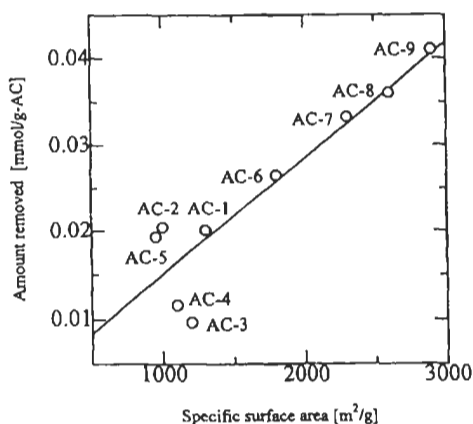


Fig. 7. Relationship between amounts of metal cation removed and the BET surface area of the porous carbon electrodes (Na_2SO_4 : 1 mmol l^{-1} , Flow rate: 1.0 ml min^{-1} , Applied voltage: 1.0 V , Run time: 80 min). (Reprinted with permission from Ref. [59], Copyright (2000) The Carbon Society of Japan).

were collected by the carbon electrode and so removed from the solution. The extent of ion removal increased with increasing voltage and with increasing BET surface area of porous carbon, as shown in Fig. 7. Under optimum conditions, as much as 90% removal of metal ions from dilute aqueous solutions was achieved.

The above two workers demonstrated the effective use of micropores in porous carbon for separation of small gas molecules and metal ions. On the other hand, the adsorption of giant molecules is possible only in mesopores. Tamai et al. studied adsorptions of vitamins, humic acids and cyclodextrin on mesoporous carbon fibres prepared by the catalytic activation method using rare-earth metals. They verified that the fibres show excellent adsorption characteristics for these large molecular adsorbates [13,60,61]. As an example, Fig. 8 shows the adsorption isotherms of Direct Black 19, Direct Yellow 50 and Direct Yellow 11 on the mesoporous carbon fibre (Y-ACF) prepared with steam activation using yttrium complex as an additive. Figure 8 indicates that amounts of each dye adsorbed on Y-ACF are higher amounts on A-20 (activated carbon fibre prepared with no metal additive). Although the BET surface area of Y-ACF is smaller ($1500 \text{ m}^2 \text{ g}^{-1}$) than that of A-20 ($1990 \text{ m}^2 \text{ g}^{-1}$), the mesoporosity of Y-ACF is much higher than that of A-20 and the average pore diameter of Y-ACF is larger than the molecular sizes of the dyes.

3.2 Chemical Reaction Process

As well as for adsorption and separation, porous carbons are used as catalyst supports. This section illustrates the effective use of porous carbons of the Carbon Alloys Project as catalyst supports.

The effective degradation of organic toxic compounds diluted in aqueous solutions is an important subject from an environmental point of view. Considerable attention

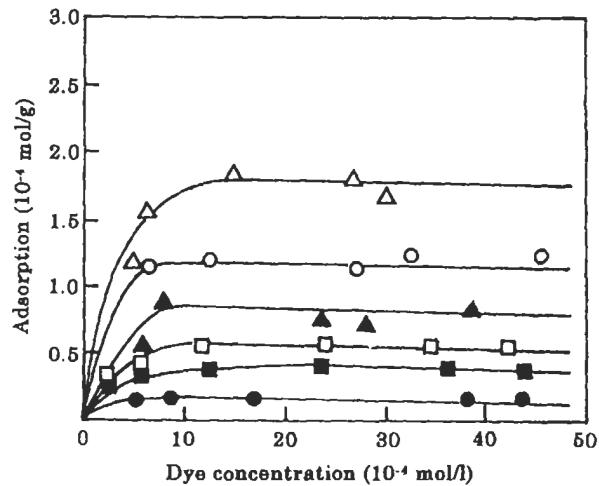


Fig. 8. Adsorption isotherms of Direct Black 19 (○,●), Direct Yellow 50 (△,▲) and Direct Yellow 11 (□,■) at 25°C. Open symbols: mesoporous Y-ACF; closed symbols: activated carbon fibres A-20. (Reprinted from Ref. [61], Copyright (1999) with permission from Elsevier Science).

has been given to photocatalytic degradation using UV irradiated TiO₂ powder photocatalysts. The design of TiO₂ photocatalysts anchored or embedded onto a large surface area support such as porous carbon is preferable, because such a support has a role in the condensation of dilute polluted substances, resulting in a higher efficiency. Furthermore, with such a support the filtration and suspension of small photocatalyst particles can be avoided. The sol-gel method is usually used to prepare TiO₂ thin-film photocatalysts. However, this method is a wet process and, consequently, it requires a calcination treatment at high temperatures, when carbon supports are easily gasified. Yamashita et al. [62,63] used the Ionized Cluster Beam (ICB) method to prepare active titanium oxides on support materials under mild and dry conditions. The advantages of using the ICB method are: (1) contamination by impurities can be minimized because the processes are performed in a high vacuum chamber; and (2) highly crystalline TiO₂ films can be prepared without any calcination at high temperatures. Thus, with this technique, porous carbon can be used as a catalyst support for TiO₂ photocatalyst. Yamashita et al. successfully prepared TiO₂ catalysts loaded on active carbon fibre by the ICB method and used the catalyst for the photocatalytic degradation of 1,2-dichloroethane diluted in water [62,63]. Figure 9 shows the degradation profiles using several types of catalysts including that prepared by the ICB method. It is evident that the presence of TiO₂ is essential to obtain high photocatalytic reactivity. Furthermore, the ICB method gave higher activity than the conventional wet impregnation method. These results suggest that, by using the ICB method, highly crystalline anatase TiO₂ particles can be prepared with both the microporous structure and adsorption properties of the ACF supports remaining unchanged.

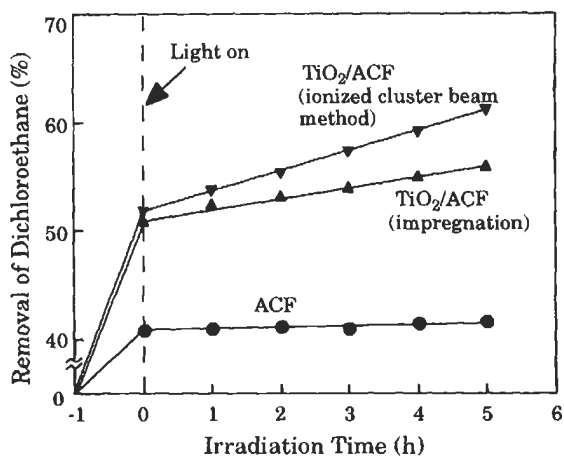


Fig. 9. Reaction time profiles of the photocatalytic degradation of 1,2-dichloroethane diluted in water on TiO₂/ACF photocatalysts prepared by the ICB method and the impregnation method using (NH₄)₂TiO(C₂O₄)₂ (Ti content: 3 wt% as Ti, calcination: 250°C).

The minimization of NO_x emission is another important and urgent subject for study. Miura et al. utilized Ni-containing porous carbons, prepared from a cation-exchange resin, as catalysts for the NO decomposition reaction [64]. The ion-exchange resin was a weak acid-type resin (M-type resin) with carboxylic groups. The resin was ion-exchanged with nickel cation in ammoniacal aqueous solution and then carbonized at temperatures of 500–900°C. These Ni-containing porous carbons catalysed the NO decomposition reaction. Figure 10 shows the reaction behavior of NO at 300°C with the time on stream for several types of metal-containing carbons prepared from the M-type resin. Among these carbons, Ni-500 (ion-exchanged with Ni-cation and carbonized at 500°C) gave almost complete conversion of NO throughout the entire reaction period with conversion to nitrogen being about 70%. On the

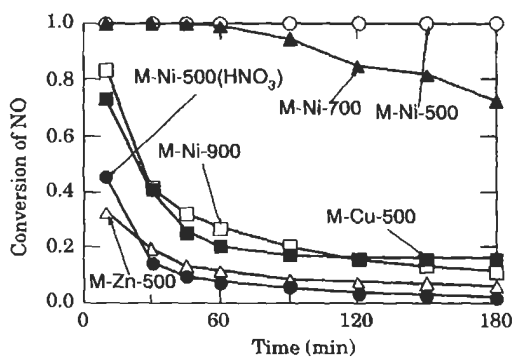


Fig. 10. NO conversion profiles of several carbon supported metal catalysts at 300°C under a flow of NO (500 ppm).

other hand, the Cu- and Zn-loaded carbons exhibited very poor activity. Noting that the active Cu-ZSM-5 NO decomposition catalyst converts NO to nitrogen by only 60%, even at 400°C, Miura et al. concluded that Ni-500 is a very active and promising catalyst for NO decomposition [64]. Because the Ni-free sample prepared from Ni-500, with HNO₃ washing, had a low activity, the presence of nickel was essential for catalytic activity. The results in Fig. 10 suggest that the carbonization of the Ni-exchanged resin at higher temperatures (Ni-700 and Ni-900) reduces activity. Because the Ni-loaded carbons, with different carbonization temperatures (Ni-500, Ni-700 and Ni-900), were found to have similar micropore structures, differences in activities could be ascribed to differences in the dispersion state of nickel species in the carbon matrices.

Porous carbons, especially activated carbon fibres, have now been applied in our normal lives as well as industrial applications. Thus, the effect of pore structure of carbons on the human body has to be examined from a physiological point of view. Koyama [65] investigated a time course change in blood immune-responded lymphocytes on mice that had been implanted subcutaneously with activated carbon fibres of different porosities over a six-month period. It was found that the activated carbon fibres act as foreign materials for animals. However, when micropore volumes and the surface areas increased, immunological reactions *in vivo* became less and cell survival and/or proliferation *in vivo* were maintained. They concluded that an optimum parameter for cell survival depends on the pore size of materials implanted.

4 Conclusions

The presence of micro- and meso-pores is essential for the production of high performance porous carbons. This chapter introduced several aspects of the Carbon Alloys Project to study pore structure control. The techniques the researchers used are unique and useful. The carbonization of metal-cation-exchanged resin gave MSC with uniform microporosities. For the production of mesoporous carbons, the methods of catalytic activation, polymer blend carbonization and organic gel carbonization were effective. The latter method related to the formation of controlled macropores. The template carbonization technique allows the preparation not only of unique porous carbons but also of uniform carbon nanotubes. It was shown that porous carbons exhibit outstanding properties in adsorption and separation processes, i.e., effective gas separations using MSC membrane, the removal of electrolytes from dilute aqueous solutions and giant molecule adsorption. Moreover, these carbons were excellent as catalyst supports for chemical reactions, especially for the chemical removal of environmental pollutants such as organic toxic compounds and NO_x. In addition, the effects of pore structure of carbons on the human body were examined from a physiological point of view. It is concluded that in the Carbon Alloys Project most of the researchers achieved their aims. Such fruits of research are the results of the work of individuals and of collaborations.

References

1. H. Nakagawa, K. Watanabe, Y. Harada and K. Miura, Control of micropore formation in the carbonized ion exchange resin by utilizing pillar effect. *Carbon*, 37: 1455–1461, 1999.
2. K. Miura, H. Nakagawa and K. Watanabe, Production of porous carbon from ion exchange resin waste. *Tanso*, 186: 25–29, 1999.
3. C.-M. Yang and K. Kaneko, Adsorption properties of nitrogen-alloyed activated carbon fiber. *Carbon*, 39: 1075–1082, 2001.
4. T. Kyotani, Control of pore structure in carbon. *Carbon*, 38: 269–286, 2000.
5. H. Marsh and B. Rand, The process of activation of carbons by gasification with CO₂. II. The role of catalytic impurities. *Carbon*, 9: 63–77, 1971.
6. A. Tomita, Y. Yuhki, K. Higashiyama, T. Takarada and Y. Tamai, Physical properties of Yallourn char during the catalyzed steam gasification. *Nenryo Kyokaishi (Journal of the Fuel Society of Japan)*, 64: 402–408, 1985.
7. A. Oya, S. Yoshida, J. Alcaniz-Monge and A. Linares-Solano, Formation of mesopores in phenolic resin-derived carbon fiber by catalytic activation using cobalt. *Carbon*, 33: 1085–1090, 1995.
8. K. Shimazaki, Preparation of polyacrylonitrile based activated carbon fiber (PAN-ACF) having high mesopore volume. *Nippon Kagaku Kaishi (Journal of Chemical Society of Japan)*: 807–812, 1993.
9. J.J. Freeman, F.G.R. Gimblett, R.A. Roberts and K.S.W. Sing, Studies of activated charcoal cloth. I. Modification of adsorptive properties by impregnation with boron-containing compounds. *Carbon*, 25: 559–563, 1987.
10. J.J. Freeman, F.G.R. Gimblett, R.A. Roberts and K.S.W. Sing, Studies of activated charcoal cloth. III. Mesopore development induced by phosphate impregnants. *Carbon*, 26: 7–11, 1988.
11. H. Tamai, T. Kakii, Y. Hirota, T. Kumamoto and H. Yasuda, Synthesis of extremely large mesoporous activated carbon and its unique adsorption for giant molecules. *Chem. Materials*, 8, 454–462, 1996.
12. H. Tamai, S. Kojima, M. Ikeuchi, J. Mondori, T. Kanata and H. Yasuda, Preparation of mesoporous activated carbon fibers and their adsorption properties. *Tanso*, 175: 243–248, 1996.
13. H. Tamai, M. Ikeuchi, S., Kojima and H. Yasuda, Extremely large mesoporous carbon fibers synthesized by the addition of rare earth metal complexes and their unique adsorption behaviors. *Advanced Materials*, 9: 55–58, 1997.
14. N. Yoshizawa, Y. Yamada, T. Furuta, M. Shiraishi, S. Kojima, H. Tamai and H. Yasuda, Coal-based activated carbons prepared with organometallics and their mesoporous structure. *Energy Fuels*, 11: 327–330, 1997.
15. R.W. Pekala, C.T. Alviso, F.M. Kong and S.S. Hulsey, Aerogels derived from multifunctional organic monomers. *J. Non-Cryst. Solids*, 145, 90–98, 1992.
16. H. Tamon, H. Ishizaka, M. Mikami and M. Okazaki, Porous structure of organic and carbon aerogels synthesized by sol-gel polycondensation of resorcinol with formaldehyde. *Carbon*, 35: 791–796, 1997.
17. H. Tamon, H. Ishizaka, T. Araki and M. Okazaki, Control of mesoporous structure of organic and carbon aerogels. *Carbon*, 36: 1257–1262, 1998.
18. H. Tamon and H. Ishizaka, Porous characterization of carbon aerogels. *Carbon*, 36: 1397–1409, 1998.
19. H. Tamon, personal communication.
20. H. Tamon, H. Ishizaka, T. Yamamoto and T. Suzuki, Preparation of mesoporous carbon by freeze drying. *Carbon*, 37: 983–989, 1999.

21. E. Bekyarova and K. Kaneko, Microporous nature of Ce, Zr-doped carbon aerogels, *Langmuir*, 15: 7119–7121, 1999.
22. J. Ozaki, N. Endo, W. Ohizumi, K. Igarashi, M. Nakahara, A. Oya, S. Yoshida and T. Iizuka, Novel preparation method for the production of mesoporous carbon fiber from a polymer blend. *Carbon*, 35: 1031–1033, 1997.
23. H. Hatori, T. Kobayashi, Y. Hanzawa, Y. Yamada, Y. Iimura, T. Kimura and M. Shiraishi, Mesoporous carbon membranes from polyimide blended with poly(ethylene glycol). *J. Appl. Polym. Sci.*, 79: 836–841, 2001.
24. J. Ozaki, W. Ohizumi, N. Endo, A. Oya, S. Yoshida, T. Iizuka, M. C. Roman-Martinez and A. Linares-Solano, Preparation of platinum loaded carbon fiber by using a polymer blend. *Carbon*, 35: 1676–1677, 1997.
25. T. Takeichi, Y. Yamazaki, M. Zuo, A. Ito, A. Matsumoto and M. Inagaki, Preparation of porous carbon films by the pyrolysis of poly(urethane-imide) films and their pore characteristics. *Carbon*, 39: 257–265, 2001.
26. T. Kyotani, N. Sonobe and A. Tomita, Formation of highly orientated graphite from polyacrylonitrile by using a two-dimensional space between montmorillonite lamellae. *Nature*, 331: 331–333, 1988.
27. N. Sonobe, T. Kyotani and A. Tomita, Formation of graphite thin film from polyfurfuryl alcohol and polyvinyl acetate carbons prepared between the lamellae of montmorillonite. *Carbon*, 29: 61–67, 1991.
28. T. Kyotani, T. Mori and A. Tomita, Formation of a flexible graphite films from poly(acrylonitrile) using a layered clay film as template. *Chem. Materials*, 6: 2138–2142, 1994.
29. M.T. Gilbert, J.H. Knox and B. Kaur, Porous glassy carbon, A new columns packing material for gas chromatography and high-performance liquid chromatography. *Chromatographia*, 16: 138–146, 1982.
30. J.H. Knox, B. Kaur and G.R. Millward, Structure and performance of porous graphitic carbon in liquid chromatography. *J. Chromatogr.*, 352: 3–25, 1986.
31. K. Kamegawa and H. Yoshida, Preparation and characterization of swelling porous carbon beads. *Carbon*, 35: 631–639, 1997.
32. S. Han and T. Hyeon, Novel silica–sol mediated synthesis of high surface area porous carbons. *Carbon*, 37: 1645–1647, 1999.
33. S. Han and T. Hyeon, Simple silica–particle template synthesis of mesoporous carbons. *Chem. Commun.*, 1955–1956, 1999.
34. S. Han, K. Sohn and T. Hyeon, Fabrication of new nanoporous carbons through silica templates and their application to the adsorption of bulky dyes. *Chem. Materials*, 12: 3337–3341, 2000.
35. D. Kawashima, T. Aihara, Y. Kobayashi, T. Kyotani and A. Tomita, Preparation of mesoporous carbon from organic polymer/silica nano-composite. *Chem. Materials*, 12: 3397–3401, 2000.
36. T. Kyotani, T. Nagai, S. Inoue and A. Tomita, Formation of new type of porous carbon by carbonization in zeolite nanochannels. *Chem. Materials*, 9: 609–615, 1997.
37. S.A. Johnson, E.S. Brigham, P.J. Olivier and T.E. Mallouk, Effect of micropore topology on the structure and properties of zeolite polymer replicas. *Chem. Materials*, 9: 2448–2458, 1997.
38. J. Rodriguez-Mirasol, T. Cordero, L.R. Radovic and J.J. Rodriguez, Structural and textural properties of pyrolytic carbon formed within a microporous zeolite template. *Chem. Materials*, 10: 550–558, 1998.
39. R. Ryoo, S.H. Joo and S. Jun, Synthesis of highly ordered carbon molecular sieves via template-mediated structural transformation, *J. Phys. Chem. B*, 103: 7743–7746, 1999.

40. J. Lee, S. Yoon, T. Hyeon, S.M. Oh and K.B. Kim, Synthesis of a new mesoporous carbon and its application to electrochemical double-layer capacitors. *Chem. Commun.*, 2177–2178, 1999.
41. Z. Ma, T. Kyotani and A. Tomita, Preparation of a high surface area microporous carbon having the structural regularity of Y zeolite. *Chem. Commun.*, 2365–2366, 2000.
42. S. Iijima, Helical microtubules of graphitic carbon. *Nature*, 354: 56–58, 1991.
43. T.W. Ebbesen and P.M. Ajayan, Large-scale synthesis of carbon nanotubes. *Nature*, 358: 220–222, 1992.
44. M. Endo, K. Takeuchi, K. Kobori, K. Takahashi, H. W. Kroto and A. Sarka, Pyrolytic carbon nanotubes from vapor-grown carbon fibers. *Carbon*, 33, 873–881, 1995.
45. W.Z. Li, S.S. Xie, L.X. Qian, B.H. Chang, B.S. Zou, W.Y. Zhou, R.A. Zhao and G. Wang, Large-scale synthesis of aligned carbon nanotubes. *Science*, 274: 1701–1703, 1996.
46. M. Terrones, N. Grobert, J. Olivares, J.P. Zhang, H. Terrones, K. Kordatos, W.K. Hsu, J.P. Hare, P.D. Townsend, K. Prassides, A.K. Cheetham, H.W. Kroto and D.R.M. Walton, Controlled production of aligned-nanotubes bundles. *Nature*, 388: 52–55, 1997.
47. A. Thess, R. Lee, P. Nikolaev, H. Dai, P. Petit, J. Robert, C. Xu, Y. H. Lee, S.G. Kim, A.G. Rinzler, D.T. Colbert, G.E. Scuseria, D. Tománek, J.E. Fischer and R.E. Smalley, Crystalline ropes of metallic carbon nanotubes. *Science*, 273: 483–487, 1996.
48. T. Kyotani, L. Tsai and A. Tomita, Formation of ultrafine carbon tubes by using an anodic aluminum oxide film as a template. *Chem. Materials*, 7: 1427–1428, 1995.
49. T. Kyotani, L. Tsai and A. Tomita, Preparation of ultrafine carbon tubes in nanochannels of an anodic aluminum oxide film. *Chem. Materials*, 8: 2109–2113, 1996.
50. T. Kyotani, L. Tsai and A. Tomita, Formation of platinum nanorods and nanoparticles in uniform carbon nanotubes prepared by template carbonization method. *Chem. Commun.*: 701–702, 1997.
51. B.K. Pradhan, T. Toba, T. Kyotani and A. Tomita, Inclusion of crystalline iron nanoparticles in uniform carbon nanotubes prepared by a template carbonization method. *Chem. Materials*, 10: 2510–2515, 1998.
52. B.K. Pradhan, T. Kyotani and A. Tomita, Nickel nanowires of 4 nm diameter in the cavity of carbon nanotubes. *Chemical Commun.*: 1317–1318, 1999.
53. T. Kyotani, B.K. Pradhan and A. Tomita, Synthesis of carbon nanotube composites in nanochannels of an anodic aluminum oxide film. *Bull. Chem. Soc. Jpn.*, 72: 1957–1970, 1999.
54. K. Matsui, B.K. Pradhan, T. Kyotani and A. Tomita, Formation of nickel oxide nanoribbons in the cavity of carbon nanotubes. *J. Phys. Chem. B*, 105: 5682–5688, 2001.
55. D. Hulicova, K. Okabe, F. Sato, A. Oya and M. Koishi, Thin carbon tubes prepared by polymer blend method. The 27th Annual Meeting of the Carbon Society of Japan, Kitakyushu, pp. 296–297, 2000.
56. J. Hayashi, M. Yamamoto, K. Kusakabe and S. Morooka, Simultaneous improvement of permeance and permselectivity of 3,3',4,4'-biphenyltetracarboxylic dianhydride-4, 4'-oxydianiline polyimide membrane by carbonization. *Ind. Eng. Chem. Res.*, 34: 4364–4370, 1995.
57. J. Hayashi, M. Yamamoto, K. Kusakabe and S. Morooka, Effect of oxidation on gas permeation of carbon molecular sieving membranes based on BPDA-pp'ODA polyimide. *Ind. Eng. Chem. Res.*, 36: 2134–2140, 1997.
58. K. Kusakabe, S. Gohgi and S. Morooka, Carbon molecular sieving membranes derived from condensed polynuclear aromatic (COPNA) resins for gas separations. *Ind. Eng. Chem. Res.*, 37: 4262–4266, 1998.
59. N. Mitui, T. Tomita and H. Oda, Removal of electrolytes from dilute aqueous solutions using activated carbon electrodes. *Tanso*, 194: 243–247, 2000.

60. H. Tamai, S. Kojima, M. Ikeuchi, J. Mondori, T. Kanata and H. Yasuda, Preparation of mesoporous activated carbon fibers and their adsorption properties. *Tanso*, 175: 243–248, 1996.
61. H. Tamai, T. Yoshida, M. Sasaki and H. Yasuda, Dye adsorption on mesoporous activated carbon fiber obtained from pitch containing yttrium complex. *Carbon*, 37: 983–989, 1999.
62. H. Yamashita, M. Harada, A. Tanii and M. Anpo, Preparation of titanium oxide/activated carbon fiber photocatalysts using an ionized cluster beam method. *Tanso*, 185: 296–298, 1998.
63. H. Yamashita, M. Harada, A. Tanii, M. Honda, M. Takeuchi, Y. Ichihashi, M. Anpo, N. Iwamoto, N. Itoh and T. Hirao, Preparation of efficient titanium oxide photocatalysts by an ionized cluster beam (ICB) method and their photocatalytic reactivities for the purification of water. *Catal. Today*, 63: 63–69, 2001.
64. K. Miura, H. Nakagawa, R. Kitaura and T. Satoh, Low temperature conversion of NO to N₂ by use of a novel Ni loaded porous carbon. *Chem. Eng. Sci.*, 56: 1623–1629, 2001.
65. S. Koyama, Review of possible biomedical applications of carbon alloy—it's biological significance. *Tanso*, 191: 49–61, 2000.

Chapter 8

Polymer Blend Technique for Designing Carbon Materials

Asao Oya

Faculty of Engineering, Gunma University, Kiryu, Gunma 376-8515, Japan

Abstract: Selection and modification of carbon precursors are important in controlling structure and properties of resultant carbons. A technique using polymer blends as precursors was developed several years ago and could be used widely as a unique method for preparing porous and non-porous carbons with special shapes. Studies using polymer blend techniques are reviewed.

Keywords: Carbon precursor, Polymer blend, Carbon structure, Design.

1. Introduction

The polymer blend technique is used widely in the polymer materials field to improve properties and to develop functionality [1]. The technique is also used effectively for carbons; in fact, trial studies of the carbon were started several years ago and interesting results are already available, some of which are introduced in Chapter 7. In this chapter, carbons prepared by using the polymer blend technique are introduced in more detail and the potential of the technique is elaborated upon.

2. Porous Carbon Materials

A polymer blend consisting of two kinds of polymers is used as an example. Suppose two polymers, A and B, which form a graphitizable and a non-graphitizable carbon respectively, are blended and used as the precursor. The resulting carbon has a polymer blend texture as shown in Fig. 1, i.e., consisting of a graphitizable carbon matrix in which non-graphitizable carbon is dispersed. The polymer blend technique is usually used to prepare porous carbon materials as described below.

Two kinds of polymers, with and without a carbon residue after heating in an inert atmosphere, are used to prepare a polymer blend. These are called carbonizing and pyrolyzing polymers in Chapter 7 and correspond to Polymers A and B in Fig. 1,

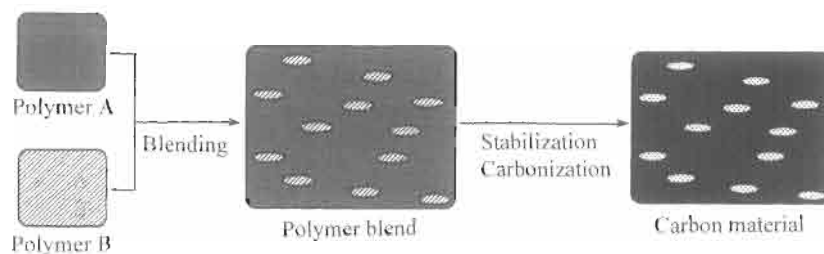


Fig. 1. A schematic illustration for the design of carbon materials by using polymer blend technique.

respectively. When such a polymer blend of carbonizing and pyrolyzing polymer is carbonized, pores are left in the carbon matrix of the carbonizing polymer following the volatilization of the pyrolyzing polymer. Pore sizes and volumes in the resultant carbons are controlled by the fineness of polymer blend texture and the blending ratio of the component polymers [1].

It is emphasized that the texture of a polymer blend is changed severely during such moulding processes such as spinning and casting. Consequently, it is the texture after moulding which determines the porous structure in the resultant carbon. Shrinkage of pores, which occurs during carbonization, also has to be considered when designing precise porous structures. As porous carbon films are discussed by Hatori et al. [2,3] and Takeichi et al. [4,5] in Chapter 7, a unique porous carbon fiber, only, is described below.

It is important to control the blending ratio between the carbonizing polymer and pyrolyzing polymer, e.g., a polymer blend with carbonizing/pyrolyzing polymer > 1 must be used for the preparation of porous carbon fibers. With a ratio of carbonizing polymer/pyrolyzing polymer < 1 is used carbon nanofibers are obtained.

Polystyrene microbeads (PS) of ca. $10\ \mu\text{m}$ diameter, as a pyrolyzing polymer, were dispersed uniformly in Novolac-type phenolic polymer (PF), as carbonizing polymer, with a blending ratio of PF/PS = 70/30 by weight. The polymer blend was subjected to melt-spinning, stabilization in an acid solution and finally carbonization at 900°C for 1 h [6,7]. Figure 2a is a SEM photograph of the cross-section of a stabilized fiber. The arrowed small spots are thinly extended PS fibers which disappear during carbonization resulting in porous carbon fibers.

Figures 2b–d are SEM photographs of a cross-section and a side-view of the carbonized fiber. Round pores, $< 1\ \mu\text{m}$ diameter, are seen on the cross-section of the fiber. These pores extend along the fiber axis as seen in the side-view (Fig. 2d). They were formed by the volatilization of the PS component which was elongated in the PF matrix as a result of the spinning process. These pores are isolated from the fiber surface so they are not available for adsorption.

As described above, porous structures prepared by using polymer blends depend strongly on the moulding process. A question arises: is it possible to prepare a carbon fiber with open pores without activation? So far, it has not been completed

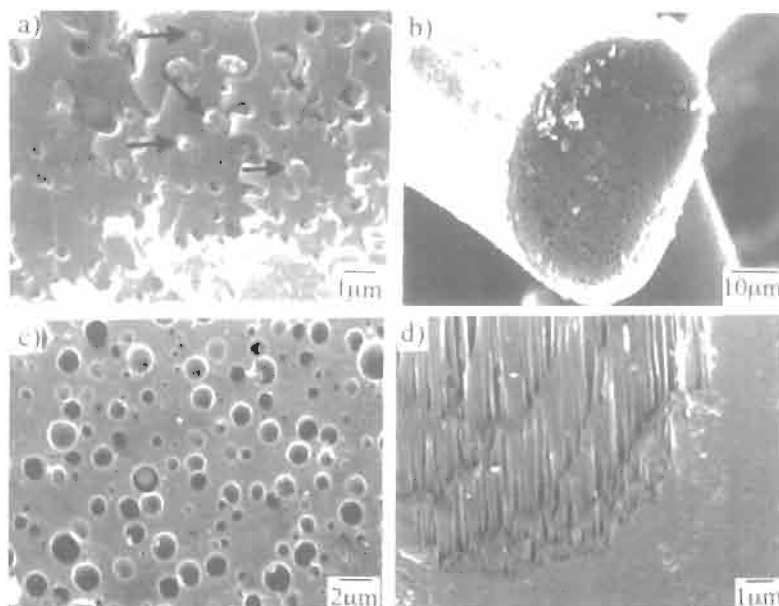


Fig. 2. SEM photographs of the polymer blend fiber (PF/PS = 70/30) before and after carbonization: (a) cross-section of stabilized fiber; (b) and (c) cross-section of carbonized fiber; (d) side-view of carbonized fiber.

successfully. However, the preparation of carbon particles with open pores may be prepared by this technique when polymer blend particles prepared by a spray-drying method are carbonized.

3 Preferential Support of Metal Particles on Pore Surface

The procedure for supporting metal particles was briefly described in Chapter 7. Here the validity of the technique is shown through the loading of platinum particles.

The materials used were PF and maleinic acid-modified polyethylene (m-PE) as carbonizing and pyrolyzing polymer, respectively; Pt-acetylacetonate (Pt-acac) was used as a precursor of Pt particles. Initially, m-PE containing finely dispersed Pt-acac was prepared, followed by blending with PF with heating (m-PE/PF = 20/80 by weight). When a precursor of metal particles has a low affinity for a pyrolyzing polymer but has a high affinity for a carbonizing polymer, the precursor diffuses from the pyrolyzing polymer into the carbonizing polymer during the blending process, using a kneader with heating. The metal particles are found finally in the matrix carbon derived from the carbonizing polymer. This is why Pt-acac was selected as a precursor compound for Pt particles [8]. To test this, a coarse blend texture of m-PE and PF was prepared hopefully to form large pores, as shown in Fig. 3 as a SEM micrograph. Electron probe X-ray microanalysis (EPMA) is not available for observation of the state of distribution of platinum particles in this narrow area. The

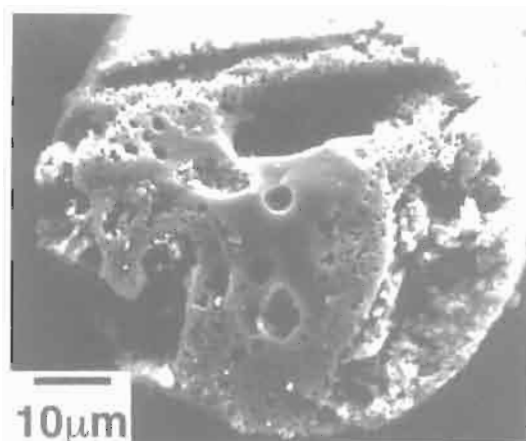


Fig. 3. SEM photograph of cross-section of porous carbon fiber supporting platinum particles.

polymer blend was subjected to spinning, stabilization and carbonization at 900°C [6,7].

Figure 4 shows SEM photographs and EPMA maps of platinum distributed within a stabilized fiber and the 900°C carbonized fibers. During carbonization the m-PE volatilized leaving pores as seen in Fig. 4, the resulting pore surface being covered with fine platinum particles identified by EPMA analyses. There were no platinum particles in the matrix carbon. Thus, the polymer blend technique can be used not only for pore formation but also for preferential support of metal particles on the pore surface.

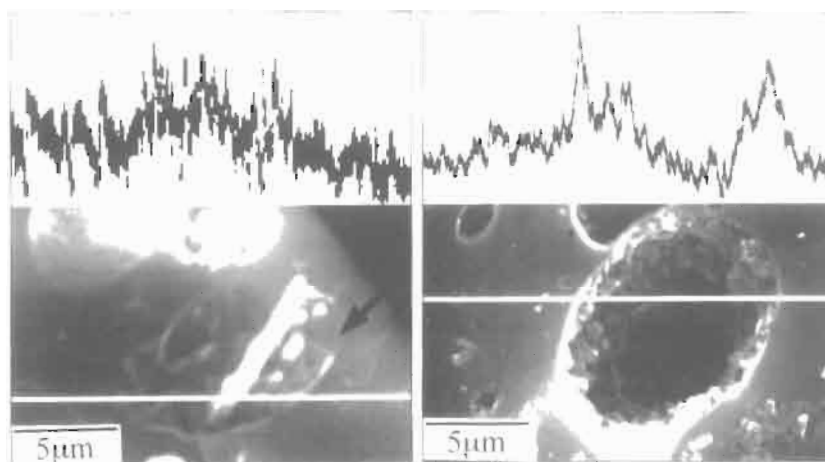


Fig. 4. SEM photographs and platinum distribution maps of the cross-sections of stabilize fiber (left) and carbonized fiber (right).

4 Carbon Nanofibers and Carbon Nanotubes

4.1 Carbon Nanofibers

When a polymer blend of carbonizing polymer/pyrolyzing polymer < 1 is used as a precursor, fine carbon fibers are left instead of thin and long pores, as seen in Fig. 2 following the loss of the pyrolyzing polymer matrix. For the preparation of thinner carbon fibers, smaller carbonizing polymer particles with a high elongation ability should be used as a precursor.

PF and PE (PF/PE = 30/70 by weight) were dissolved in acetone and warmed toluene, respectively. The acetone solution of PF was sprayed into the warmed toluene solution of PE with stirring. Fine PF particles were precipitated in the toluene solution of PE. Most of the precipitated particles were submicrometre. After evaporation of toluene under reduced pressure, PE containing the finely dispersed PF particles was obtained. Mechanical kneading was applied to the PE so obtaining a homogeneous dispersion of the particles. The polymer blend was then subject to spinning, stabilization and carbonization at 600°C for 1 h [9].

Figure 5 (top) shows a cross-section of the stabilized fiber. Thin PF fibers (arrowed) and fine pores are seen in cross-section; the latter supposedly were formed after the thin fibers were pulled out. The stabilized fiber resulted in a bundle of

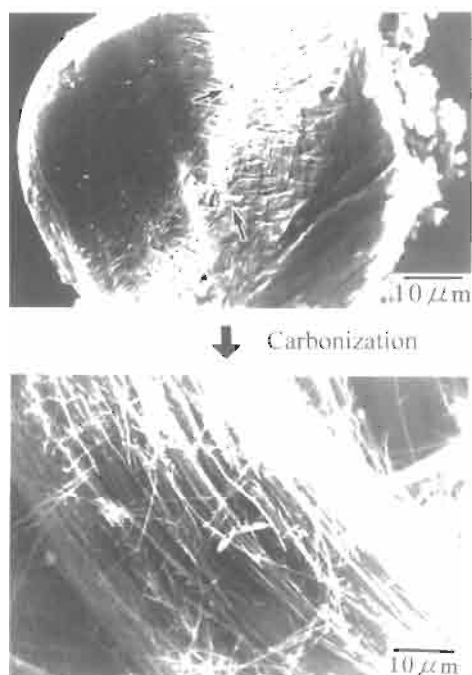


Fig. 5. SEM photograph of a cross-section of polymer blend fiber (PF/PE = 30/70) after stabilization (top) and the resulting bundle of carbon nanofibers (bottom).

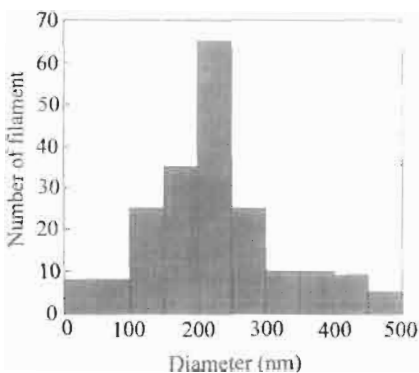


Fig. 6. Histogram of a carbon nanofiber cross-section.

carbon nanofibers after the loss of the PE matrix during carbonization (Fig. 5 (bottom)). The bundle was easily separated into individual filaments, just by touching. As the blend ratio of PF/PE was reduced, so the carbon nanofiber bundle became loose.

As can be seen from the histogram in Fig. 6, the nanofiber diameter ranged from 50 to 500 nm with a maximum at 200–250 nm. Figure 7 is a selection of TEM micrographs of carbon nanofibers after heating to 900 and 3000°C. The 900°C-fiber has a characteristic irregular surface and consists of fine carbon crystallites. After graphitization at 3000°C, the carbon crystallites developed and the surface became

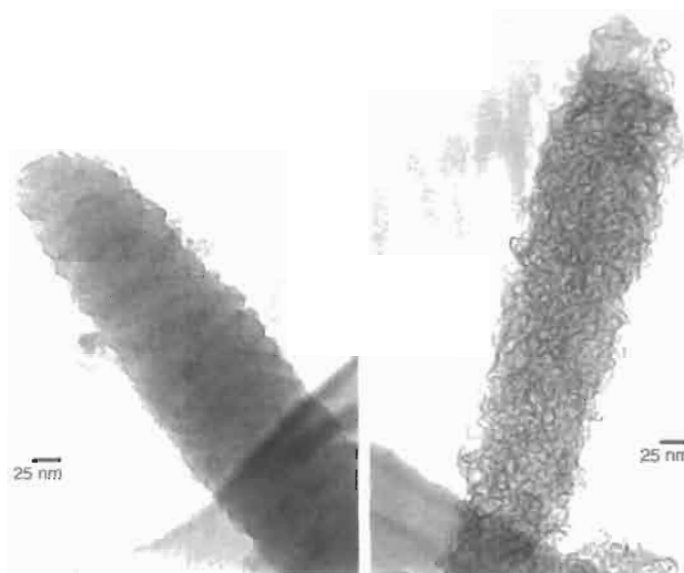


Fig. 7. TEM photographs of carbon nanofibers heated at 900°C (left) and 3000°C (right).

more irregular. It is clear from the micrographs that the carbon nanofibers have the structure of a non-graphitizable carbon.

Several preparation methods are available for carbon nanofibers which are usually prepared via gas phase reactions. Compared with these, the present method using polymer blends has advantages such as: (i) suitability for bulk-production, (ii) possibility to prepare long filaments, (iii) no formation of carbons as particles and plates, (iv) no metal catalysts, and (v) easy control of macro- and microstructures of nanofibers. However, some problems remaining to be solved include: (i) how to decrease the carbon nanofiber diameter, and (ii) how to prepare a graphitizable carbon nanofiber with a smooth surface.

4.2 Carbon Nanotubes

The concept of the preparation method is shown in Chapter 7 (Fig. 5). This method is sufficiently different from previous methods for carbon nanotube (CNT) preparation that it will be described in detail [10]. The most important process for preparation of fine carbon nanotubes involves the production of fine core/shell particles with a high elongation performance when spinning. Figure 8 shows a preparation process of the particles [10].

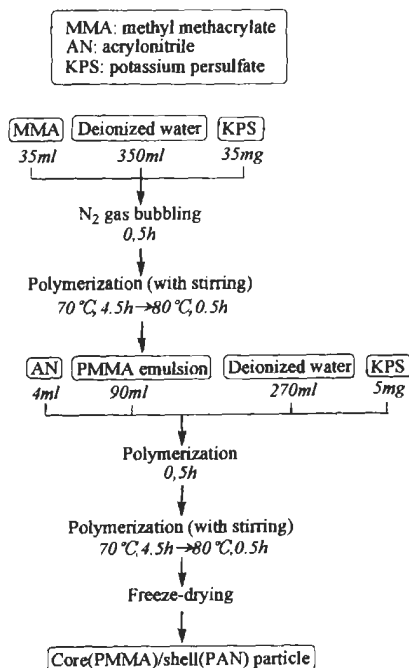


Fig. 8. Preparation process of Core(PMMA)/shell(PAN) particles.

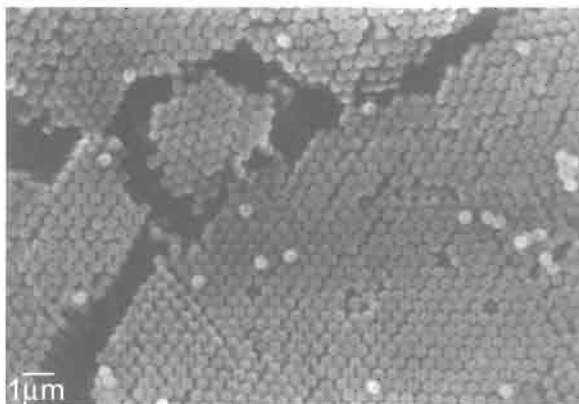


Fig. 9. SEM photograph of core(PMMA)/shell(PAN) particles.

Fine polymethylmethacrylate (PMMA) core particles were synthesized by polymerizing methylmethacrylate (MMA) in water at 70–80°C for 5 h using potassium persulphate (KPS) as a radical initiator. Acrylonitrile (AN) and KPS were added to the resulting PMMA emulsion and the AN polymerized at 70–80°C for 5 h to coat the core PMMA particles with polyacrylonitrile (PAN). Four ml of AN was added to 90 ml of the PMMA emulsion (corresponding to 8 ml of starting MMA). The PMMA decomposed at ca. 450°C without a carbon residue and the PAN had ca. 40 wt% carbon yield after heating to 1000°C in nitrogen. The resulting emulsion of core/shell particles was freeze-dried. Figure 9 shows the formation of uniform core(PMMA)/shell(PAN) particles with ca. 400 nm diameter. Figure 10 is a TEM photograph of a cross-section of the particles after coating the PAN shell with OsO₄ vapor. The core diameter and the shell thickness were 300–370 nm and 40–50 nm, respectively.

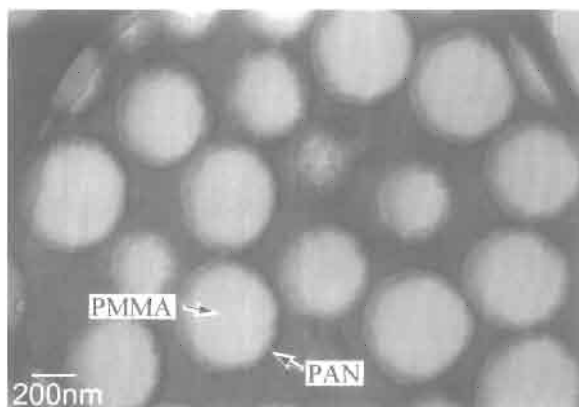


Fig. 10. TEM photograph of cross-sections of core(PMMA)/shell(PAN) particles coated with OsO₄ vapor.

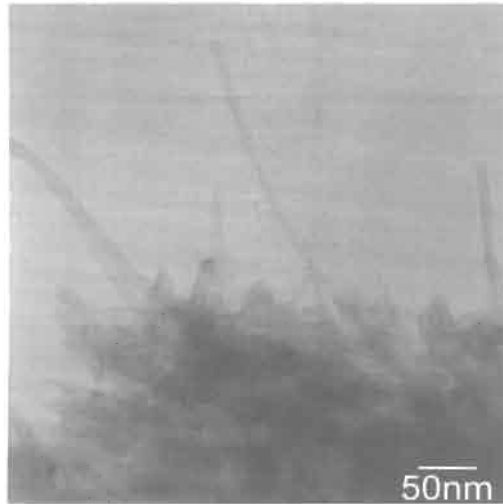


Fig. 11. TEM photograph of carbon nanotubes prepared from core(PMMA)/shell(PAN) particles.

The water emulsion of the core/shell particles was mixed with a water emulsion of PMMA particles, as a matrix, prepared in advance under sonication for 30 min. The PMMA particles prevent coalescence of the core/shell particles during the spinning process. The mixing ratio of the core/shell and the PMMA particles was 60/40 by weight. The emulsion mixture was freeze-dried and the resulting polymer blend was continuously melt-spun at 310–320°C using a conventional apparatus [6,7], followed by stabilization of the PAN in dry air at 250°C for 5 h, and finally by carbonization at 1000°C for 1 h in nitrogen.

A low magnification TEM photograph of CNTs from the particles after carbonizing at 1000°C is shown in Fig. 11. The diameter of CNTs ranged from 10 nm to 20 nm. CNTs thinner than 10 nm were rarely observed. The PMMA matrix in the spun fiber fused during carbonization to roll up by surface tension. The elongated shells were deformed together with the PMMA matrix, resulting in an entangled structure of the CNTs as seen at the bottom of Fig. 11. Carbon nanofibers and other morphological contamination carbons were entirely absent in this region.

Figure 12 is a high resolution TEM (HRTEM) image of the CNTs from the core/shell particles after carbonizing at 1000°C. CNTs consisting of highly oriented multi-walls are observed. The wall thickness and the hollow diameter of the CNT (arrowed) at the center of Fig. 12 are ca. 7 nm (stacking of ca. 20 graphene sheets) and 1.4 nm, respectively. Figure 13 shows a cap of CNT found in the same specimen. The cap is made of stacks of graphene sheets extending continuously from the tube wall. Because pentagonal carbons can close a tube tip, so such carbons must exist at the bent sites (arrowed) of the graphene sheets. A similar structure of the end cap was observed in CNTs synthesized by conventional methods in which CNTs were assembled from carbon fragments in the gas phase [11]. In contrast, CNTs by our



Fig. 12. TEM photograph of carbon nanotubes prepared from core(PMMA)/shell(PAN) particles.

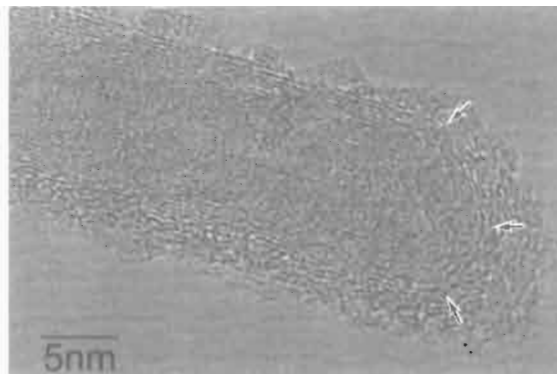


Fig. 13. TEM photograph of cap of a carbon nanotube prepared from core(PMMA)/shell(PAN) particle.

method were formed through a different route, i.e., the thermal degradation of PAN in a solid phase. It is interesting that both methods result in CNTs with quite similar CNT structures.

In order to avoid the formation of entangled CNTs, it is suggested that the ratio of PAN component to the PMMA component in the polymer blend must be as large as possible. So, the core(PMMA)/shell(PAN) particles were further thinly coated with PMMA. The resulting three-layered core/shell particles singly, without PMMA particles, were subject to melt-spinning, stabilizing and carbonizing at 1000°C. Figure 14 shows the resultant CNTs which were straight and long with diameters of 10–20 μm without formation of entangled CNTs.

A further consideration is whether a narrower CNT with a thinner wall can be prepared by this method. To do this, a finer core/shell particle with a thinner shell and a propensity for higher elongation must be used for spinning. A thinner PAN shell can



Fig. 14. TEM photograph of carbon nanotubes prepared from three-layered core/shell particles (PMMA/PAN/PMMA).

be prepared by controlling the amounts of PAN, so leading to the formation of thinner CNTs with thinner walls.

A second consideration is whether bulk production of CNTs is possible using this method. Because the method uses spinning already used by industry, it is more suitable for bulk production than other methods. Also, metal particles and morphological contamination by carbons were totally absent from these CNTs, leading to the elimination of a subsequent purification process.

A third consideration is why highly developed and oriented graphene sheets were formed at the low carbonization temperature of 1000°C. A similar structure has been observed in PAN-based carbon fiber heated to 2000°C [12]. It is supposed that severe stretching of the core/shell particle during the spinning process resulted in preferred orientation of PAN molecules along the fiber axis, the memory of which remained in the CNT after carbonization. Such a technique is being used to prepare PAN-based high performance carbon fibers [13]. The crystalline state of CNT can be also controlled through the selection of the carbon precursor polymer. Therefore, the present method may be suitable for the preparation of CNTs with a wide variety of crystalline structures and textures.

5 Other Fibrous Carbon Materials with Unique Shapes

In addition to the carbon materials described above, other fibrous carbon materials with unique shapes may be prepared using the polymer blend technique [14].

Figure 15 is a schematic of cross-sections of two types of microcapsules. First consider carbon materials formed from microcapsules through spinning, stabilizing

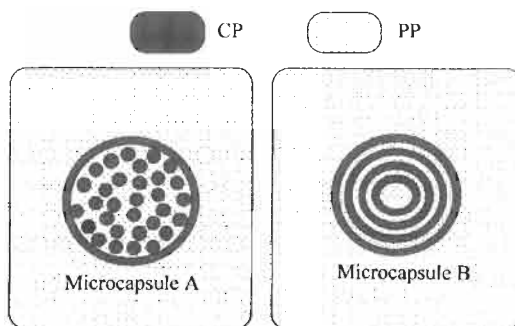


Fig. 15. Cross-section of microcapsules resulting in fibrous carbon with unique shape.

and carbonizing. The carbon in Fig. 16 must be derived from the microcapsule A, i.e, a large number of carbon nanofibers being included in a carbon sheath. However, such microcapsules cannot really be prepared so another technique must be used instead. Hence, a polymer blend of pyrolyzing PE matrix including fine PF particles was spun and stabilized according to the procedures for carbon nanofiber preparation. The resulting fibers were passed through a methanol solution of PF, dried to coat the fibers with the PF, stabilized again and then finally carbonized at 1000°C. The carbon material shown in Fig. 16 was thus prepared.

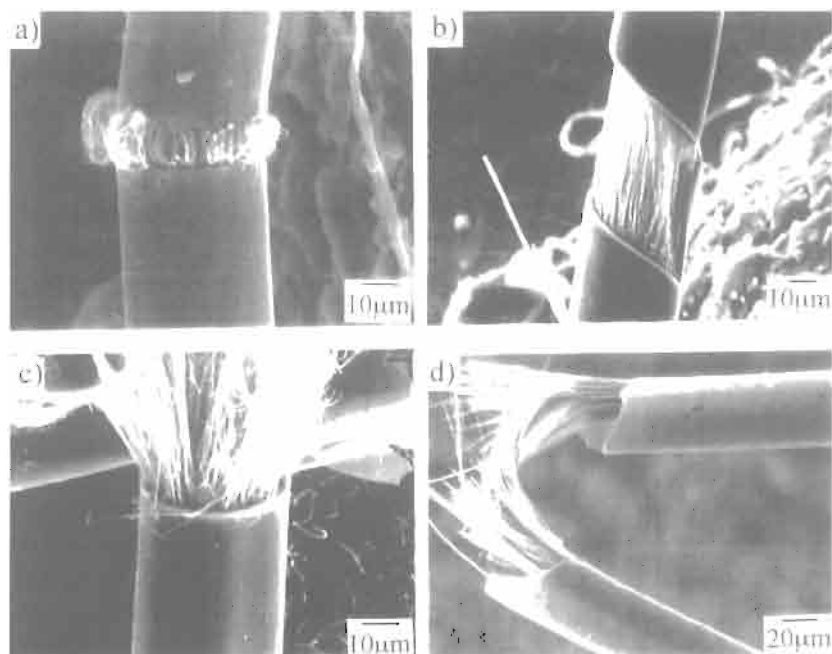


Fig. 16. SEM photographs of carbon tubes including carbon nanofibers.

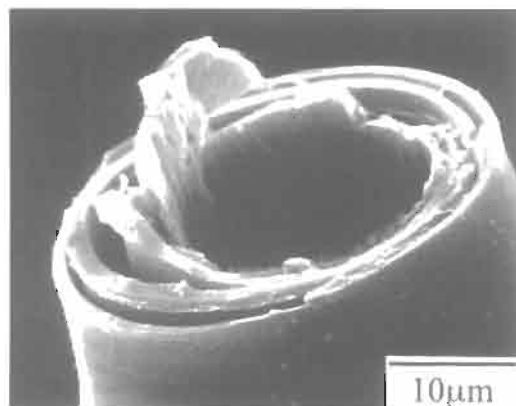


Fig. 17. SEM photograph of multi-walled carbon tube.

The carbon material derived from the microcapsule B is also unique, it being a multi-wall carbon tube. A problem here was the difficulty of preparing this type of microcapsule. An alternative technique was used in which a very thin vinylon fiber, used as a core pyrolyzing polymer, was coated with PF and PE, progressively, by using their solutions, and then subject to the conventional procedures described above. Figure 17 is a SEM photograph of the cross-section of the resulting multi-walled carbon tube.

6 Conclusions

Trial studies on the use of polymer blend techniques for the precise and controlled preparation of carbon materials began only several years ago and so only limited data are currently available. Nevertheless, this technique has expectations for use in the field of carbon materials, in particular the design of fine carbon materials.

References

1. D.R. Paul and C.B. Bucknall (Ed.), *Polymer Blends*, Vol. 1: Formulation; Vol. 2: Performance. John Wiley, New York, Chichester, 2000.
2. N. Yoshizawa, H. Hatori and Y. Yamada, Porous carbon materials—Preparation of mesoporous materials. *Hyomen (Surface)*, 35: 32–39, 1997 (in Japanese).
3. H. Hatori, T. Kobayashi, Y. Hanzawa, Y. Yamada, Y. Iimura, T. Kimura and M. Shiraishi, Mesoporous carbon membranes from polyimide blended with poly(ethylene glycol). *J. Appl. Polym. Sci.*, 179: 836–841, 2001.
4. T. Takeichi and Y. Yamazaki, Preparation and properties of porous polyimide films prepared from a polymer blend of polyol and poly(amide acid). *J. Photopolym. Sci. Technol.*, 13: 333–338, 2000.
5. T. Takeichi, Y. Yamazaki, M. Zuo, A. Ito, A. Matsumoto and M. Inagaki, Preparation of porous carbon films by the pyrolysis of poly(urethane-imide) Films and their pore characteristics. *Carbon*, 39: 257–266, 2001.

6. S. Otani, On the carbon fiber from the molten pyrolysis products. *Carbon*, 3: 31–38, 1965.
7. A. Oya, S. Yoshida, Y. Abe, T. Iizuka and S. Makiyama, Antibacterial activated carbon fiber derived from phenolic resin containing silver nitrate. *Carbon*, 31: 71–73, 1993.
8. Y. Horie, S. Shiraishi and A. Oya, Preferential supporting of platinum particles on pore surface by using a polymer blend technique. *J. Mater. Sci. Lett.*, 20: 105–106, 2001.
9. A. Oya and N. Kasahara, Preparation of thin carbon fiber from phenol-formaldehyde polymer micro-beads dispersed in polyethylene matrix. *Carbon*, 38: 1141–1144, 2000.
10. D. Hulicova, K. Hosoi, S. Kuroda, H. Abe and A. Oya, Multi-wall carbon nanotubes prepared from polymer core/shell microspheres. *Molec. Cryst. Liquid Cryst.*, 387: 107–112, 2002.
11. M. Terrones, W.K. Hsu, H.W. Kroto, D.R.M. Walton, Nanotubes: A revolution in materials science and electronics. *Topics Curr. Chem.*, 199: 189–234, 1999.
12. L.H. Peebles, *Carbon Fibers—Formation, Structure and Properties*. CRC Press, Boca Raton, Florida, pp. 7–25, 1995.
13. J.B. Donnet and R.C. Bansal, *Carbon Fibers; International Fiber Science and Technology*, Basel Series 3. Marcel Dekker, New York, pp. 51–105, 1984.
14. N. Patel, K. Okabe and A. Oya, Designing of carbon materials with unique shapes by use of polymer blending and coating techniques. *Carbon*, 40: 315–320, 2002.

Part 4

The Latest Characterization Techniques

Chapter 9

Computer Simulations

Shinji Tsuneyuki

Department of Physics, Graduate School of Science, The University of Tokyo, Tokyo, Japan

Abstract: Recent developments in computers and theoretical approaches have facilitated the use of several simulation methods to study carbon alloys in terms of system size, and the accuracy and reliability needed, as well as the computer resources available. This chapter provides a brief summary of methodologies and some of their applications to carbon alloys, especially focusing on electronic states.

Keywords: Electronic structure, Molecular dynamics, Density functional theory, Car–Parrinello method, Graphite–diamond transformation, Heterodiamond.

1 Methods

Prediction of structures and properties of materials from a knowledge of their chemical composition has been a longstanding problem in materials science. So far, many inventions with associated improvements have been made. Now, thanks to the development of computers, the most suitable methods can be applied to each problem. Atomistic simulations of materials are broadly classified into two categories. One is the treatment of structure and dynamics of atoms within Newtonian dynamics and/or classical statistics. The other is to study electronic structure using quantum mechanics. State-of-the-art simulation techniques are often a mixture of the two categories.

In this chapter, several simulation methods are introduced together with their abbreviated names and references. These methods are quite general and are not necessarily related to carbon alloys.

1.1 Classical Simulation of Atoms

It is possible to solve Newton equations of motion of atoms if the forces acting on each atom are known as a function of positions of atoms. The method is called Molecular Dynamics (MD) [1]. If there is no interest in dynamics or temperature dependence but only in the most stable structure, structural optimization can be performed using the same forces (Molecular Mechanics, MM). Another method to study classical distributions of atoms is the Monte Carlo method (MC), in which a description of the total energy is needed but not the forces acting on the atoms.

When a virtually infinite system such as a crystal is being studied, the periodic boundary condition to minimize finite size effects is adopted. The finite size effects caused by the existence of surfaces are thus eliminated. On the other hand, the artificial periodicity introduced here sometimes brings a fatal influence to the system such as symmetry restriction to some structural transformations. To minimize such influences, the shape of the simulation cell is allowed to change so that internal stress balances with external pressures. This method, first introduced by Parrinello and Rahman [2], is often called the variable cell-shape algorithm or the constant-pressure (isobaric) algorithm.

Structural properties of materials often depend on temperature. The simplest way to control temperature during an MD simulation is to scale velocities of the atoms so that the average of the kinetic energy of each atom is equal to $(3/2)k_B T$, where k_B is the Boltzmann constant. An arbitrary scaling procedure, however, does not reproduce statistically definite ensembles. Nosé proposed a Lagrangian including a variable for scaling “time”, by which the canonical ensemble is reached automatically [3]. The method has been slightly modified by Hoover and is now widely used for constant-temperature simulations [4].

The number of atoms simulated using the above method is typically several hundreds to several tens of thousands, though simulations of millions or billions of atoms have been reported recently. Application of the methods to such huge systems is *not* straightforward and needs major improvements and inventions of the algorithms [5], although the detailed description is beyond the scope of this chapter.

The most essential ingredient in methods to describe characteristics of systems is the interatomic potential which determines the forces acting on each atom. Typical examples are the Lennard-Jones potential for rare gases, Morse potentials for covalent bonding and Born–Mayor-type potential for ionic materials. These potentials depend on interatomic distances. For directional interactions like sp^3 bonding in diamond, directional potential should be used depending on the position of more than two atoms or angles between two chemical bonds. Such examples are Stillinger–Weber potential for silicon [6] and Tersoff potential for silicon and carbon [7]. Unfortunately, however, it is hopeless to find good interatomic potentials applicable to all situations, that is, to arbitrary chemical compositions or to insulating and metallic phases of the same materials. Experimental information is needed for the system before simulation and if there exists a need to simulate completely unknown systems, then, somehow, more *ab initio* methods should be used, as set out below. This often happens when carbon alloys are studied.

1.2 Quantum Simulations of Electrons

Forces acting on each atom are in principle determined by the electronic structure of the system. Although there are no ways of solving many-body Schrödinger equations exactly by a computer, a number of approximate ways have been proposed.

A simple and intuitively understandable way is the molecular orbital (MO) methods, the simplest versions of which are the famous Hückel's method for π orbitals and the extended Hückel method for all electrons. These methods are called empirical MO methods because the parameters in the Hamiltonian (site energies and transfer integrals) are determined empirically. The tight-binding (TB) model used by physicists for treating solids is of the same level as regards approximations, where many-body electron–electron interactions are considered to be included in the renormalized parameters in the one-body Hamiltonian.

A method that goes beyond the one-body approximation is the Hartree–Fock self-consistent-field (HF-SCF) method [8]. The many-body wave-function of electrons is approximated to by single Slater determinants of MOs (HF approximation) and the MOs are determined so that the expectation value of the Hamiltonian is minimized. This is achieved by solving self-consistently a set of Schrödinger-like equations for one electron under a mean field. The mean-field potential has two terms: the Hartree term which describes Coulomb repulsion between electron charge density and the exchange term which is caused by the Pauli principle stating that two electrons cannot occupy the same state and makes up for the overestimated repulsion by the Hartree term. Because evaluation of these terms needs two-electron integrals that cost both computational time and memory, in the early days some of the integrals were neglected or estimated semi-empirically. Such semi-empirical methods are Complete Neglect Differential Overlap (CNDO), Intermediate Neglect of Differential Overlap (INDO), Modified INDO (MINDO), etc. [8]

Full consideration of the two-electron integrals by numerical integration is made possible if we adopt Gaussian-type atomic orbitals as a basis set for expanding the molecular orbitals. The method is called the *ab initio* HF-SCF method and is widely used as a standard method for calculating electronic states of molecules [8].

Within the HF approximation, electrons with opposite spins move around without correlation, resulting in some serious problems. Common examples are failure in estimating formation (cohesive) energy or excitation energy of molecules and the dip of the electron density of states at the Fermi level in metals. The Configuration Interaction (CI) method is a remedy for taking into account the electron correlation and is used for calculation of the ground state and low-lying excited states of molecules [8]. However, the computer resources necessary for the method diverges rapidly with the size of the system, so that the method is not useful for solids. Instead, electronic-structure/total-energy calculations based on the Density Functional Theory (DFT) has been developed and used for solids [9].

DFT is quite different from CI in that it basically deals with electron charge density instead of many-body wave functions. This means that the number of degrees of freedom to be tackled in computers is much fewer. The key point is that the ground-state energy of the system is a functional of the electron charge density, as proved by Hohenberg and Kohn [10]. This was followed by Kohn and Sham's prescription to find one-electron orbitals ψ_i , of which the electron charge density is written as a squared sum [11]. A set of self-consistent equations for determining the

ground-state electron charge density $n(\vec{r})$ and the total energy E_{total} are written as follows:

$$\begin{aligned}
 E_{\text{total}}[n] = & \sum_i \varepsilon_i - \int d^3 r v(\vec{r}) n(\vec{r}) \\
 & + \int d^3 r v_{\text{ext}}(\vec{r}) n(\vec{r}) \\
 & + \frac{e^2}{2} \iint d^3 r d^3 r' \frac{n(\vec{r}) n(\vec{r}')}{|\vec{r} - \vec{r}'|} \\
 & + E_{\text{xc}}[n],
 \end{aligned} \tag{1}$$

$$\left\{ -\frac{\hbar^2}{2m} \Delta + v(\vec{r}) \right\} \psi_i(\vec{r}) = \varepsilon_i \psi_i(\vec{r}), \tag{2}$$

$$v(\vec{r}) = v_{\text{ext}}(\vec{r}) + e^2 \int d^3 r' \frac{n(\vec{r}')}{|\vec{r} - \vec{r}'|} + \mu_{\text{xc}}(\vec{r}), \tag{3}$$

$$n(\vec{r}) = \sum_i |\psi_i(\vec{r})|^2, \tag{4}$$

$$\mu_{\text{xc}}(\vec{r}) = \frac{\delta E_{\text{xc}}[n]}{\delta n(\vec{r})}. \tag{5}$$

Because $n(\vec{r})$ in Eq. (2) is written by ψ_i , the eigenvalue problem in Eqs. (2)–(5) has to be solved self-consistently. This is done by using basis functions for expanding the one-electron orbital ψ_i . If plane waves are adopted for the basis functions, then Fast Fourier Transformations (FFT) can be fully utilized to solve the equations and to systematically improve the accuracy by increasing the cut-off energy corresponding to the maximum wave number of the plane waves. The forces acting on each atom are calculated by the Hellman–Feynman theorem very easily. Moreover, dynamical diagonalization by the Car–Parrinello method [12] (see below) or the conjugate-gradient method [13] dramatically reduce the memory size and CPU time necessary for the solution. To omit localized core-electron-orbitals, for which plane-wave expansion is not efficient, several types of pseudo-potentials (PP) are proposed, such as norm-conserving PP [14], soft PP [15] and ultra-soft PP [16]. Localized basis functions are also used for explicitly treating localized valence orbitals for which the force calculation is quite cumbersome. Korrington–Kohn–Rostoker method (KKR) [17], Linear Augmented Plane Wave method (LAPW) [18] and Linear Muffin Tin Orbital method (LMTO) [19] are such examples.

In the above, E_{xc} is a functional of $n(\vec{r})$ and the functional form is determined by many-body perturbation theories or based on quantum Monte Carlo simulation of electron gas. In the simplest approximation, E_{xc} is assumed to be a function (not the

functional) of $n(\vec{r})$. This is called Local Density Approximation (LDA) and has been successfully used for various systems. To go beyond LDA, it was proposed recently to include gradients of $n(\vec{r})$ in the expression of E_{xc} (Generalized Gradient Approximation, GGA) [20,21] and is widely used nowadays. It is often said that GGA gives better cohesive energy than does LDA.

LDA and GGA have been used not only for structural optimization but also for band-structure calculations, considering the fact that the one-electron energy ϵ_i of the occupied state in Eq. (2) gives the energy for taking out an electron from the system [22]. It is known, however, that LDA and GGA give much smaller estimations of the band-gap energy of semiconductors (almost 50% in the case of Si), and so predict the metallic ground state for some small-gap semiconductors and highly correlated electronic systems like Mott insulators. Many attempts have been made from various viewpoints to overcome this difficulty, such as the Self-Interaction Correction (SIC) [23], the GW method [24,25] or the exact exchange method (EXX) [26].

Total energy and electronic-structure calculations by DFT are often called first-principles calculation. The results of DFT, however, depend on which expression of E_{xc} is used and the choice has to be supported by comparison with experimental results. At this point, some kind of empiricism gets into this “first-principles” calculation. In order to calculate total energy of solids more precisely and more non-empirically, Quantum Monte Carlo methods (QMC) for sampling many-body wave functions have been proposed [27].

So which method should we use? It all depends on the system, the accuracy or reliability needed, and also the computer resources available. If there is a need to study small clusters, *ab initio* HF-SCF calculation using a commercial program package Gaussian9* gives quite good starting point. If there is no need for either excitation energy or an accuracy of 100 meV, probably there is no need to go beyond HF-SCF. When the system gets larger and includes more than 100 atoms, HF-SCF is too tough but the empirical methods using program package MOPACK, for example, are still useful. DFT is more accurate and can tackle 100 atoms, though the necessary memory and CPU times are orders of magnitude larger than those for the empirical methods. Therefore, practically, it is recommended to use different methodologies if possible: that is to use empirical methods for large systems and first-principles methods for small systems for testing the reliability of the empirical calculation.

1.3 Simultaneous Simulation of Atoms and Electrons

In 1985, Car and Parrinello [12] suggested the use of MD of atoms and the DFT calculation for electrons, simultaneously, using a Lagrangian:

$$L = \sum_i \frac{\mu}{2} \int |\dot{\psi}_i(r;t)|^2 d^3r + \sum_n \frac{1}{2} M_n \dot{R}_n^2 - E[\{\psi_i(r;t)\}, \{R_n\}] \quad (6)$$

where M_n and R_n are the mass and position of atoms, ψ_i is the one-electron wave function (Kohn–Sham orbital), $\dot{\psi}_i$ is its time derivative, μ is an effective mass for the motion of ψ_i , and E is the electronic part of the total energy calculated within DFT. The Euler–Lagrange equations of this lead to coupled equations for atoms and wave functions and the latter becomes identical to the Kohn–Sham equation (2) when the motion of ψ_i is quenched. Note that this time-dependence is fictitious and not related to the wave packet dynamics by time-dependent Schrödinger equation. By this method the motion of atoms can be simulated by calculating forces by DFT with much less CPU time and memory than is needed to solve Eqs. (2)–(5) self-consistently at each MD step. This revolutionary method is now called the Car–Parrinello (CP) method or First-Principles Molecular Dynamics method (FPMD). The essence of the method is that the electronic state is dynamically (iteratively) diagonalized, so that the equation of motion for ψ_i is sometimes replaced by the Conjugate-Gradient method (CG) nowadays [13].

2 Applications

2.1 Simulations of Carbon-Related Materials

Recent discoveries of fullerenes and carbon nanotubes have undoubtedly accelerated attempts to simulate, investigate, and predict electronic and structural properties of carbon-related materials. As the system size is necessarily large, empirical treatments of the electronic states keep to the mainstream, although first-principles calculations are also performed for relatively small systems like perfect crystals made of fullerenes [28].

This section briefly summarizes the results of recent simulations of carbon-related new materials with DFT. Throughout these studies the constant-pressure FPMD method [29,30] is used to optimize efficiently structures under pressure. Calculations of electronic states are based on the density functional formalism within LDA. Norm-conserving soft pseudo-potentials [15] are used with a plane wave basis set to expand the electronic wave function. A correction to the energy functional is introduced to retain a constant energy cutoff for the basis irrespective of a change in the unit-cell volume [30,31].

2.2 Graphite–Diamond Transformation

Graphite transforms into diamond at high pressure. This is not only an important process for synthesizing diamond in industry but also is an interesting starting point to understand structural and chemical properties of carbon. From the viewpoint of computer simulation, the transformation is a difficult problem because (a) chemical bonds of carbon atoms change from sp^2 to sp^3 , and (b) the crystal changes from a semi-metal to an insulator.

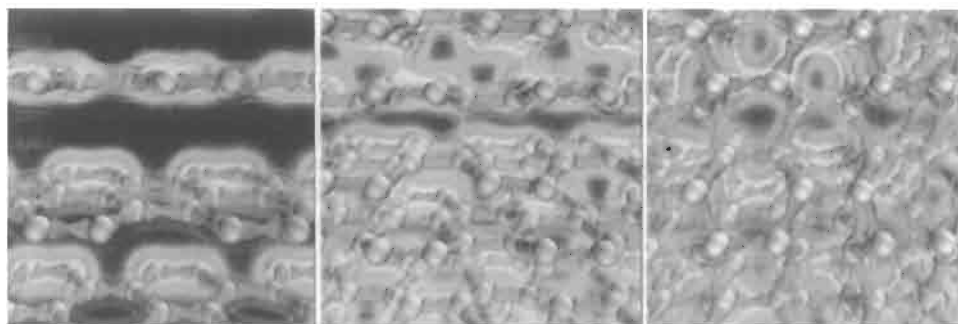


Fig. 1. Snapshots of graphite to hexagonal diamond transformation obtained by FPMD.

Scandolo et al. [32] first reported a constant-pressure FPMD simulation of this transformation. The number of atoms in the simulation was 48 to 64 with temperatures of 200–2000 K and with pressures reaching ~ 110 GPa. They found that the transformation path proceeds through a sliding of graphite planes (graphene sheets) into an unusual orthorhombic stacking, from which an abrupt collapse and buckling of the planes leads to both cubic and hexagonal forms of diamond in comparable proportions. Figure 1 comprises snapshots of the transformation (graphite to hexagonal diamond) reproduced by a similar FPMD simulation by our own code, where carbon nuclei are shown by spheres (with exaggerated radius) and higher electron densities are shown in brighter colours. Planar sp^2 bonds are distinguished between atoms as they change into three-dimensional sp^3 bonds. It should be noted that the intermediate phase (the center panel in Fig. 1) is energetically unstable and appears as a transient state for a few femto-seconds only.

Hexagonal diamond, which is rarely seen in nature, is only slightly more unstable than a cubic phase. A few experiments have shown that it is formed when well-crystallized graphite is compressed at low temperatures. So, the activation barriers were investigated going from graphite (G) to hexagonal diamond (HD) and from graphite to cubic diamond (CD) anticipating that the former will be smaller than the latter. The result was, surprisingly, the reverse and the difference was rather large (at 20 GPa, 0.22 eV/atom from G to HD and 0.15 eV/atom from G to CD) [30], even though the deformation of the bond angle is quite similar at both of the transition points.

Currently, it is our opinion that the nucleation process at the commencement of the structural change is important for HD formation at low temperatures [30].

2.3 BCN Heterodiamond

BCN heterodiamonds have attracted significant interest as a candidate for super-hard materials or wide band-gap semiconductors with high electron mobility and high thermal conductivity. Because they are ternary compounds with a large number of

structural freedoms, they are expected to show a variety of properties greater in number than those obtained from binary semiconductors, but only if their atomic composition and arrangement could be controlled.

Experiments have tried to synthesize BCN by shock wave compression or static compression and the heating of graphitic BC₂N prepared by chemical vapor deposition, but with only a few reports of successful syntheses [33]. This is probably because BCN compounds are less stable than the separated phases of diamond and cubic BN at high pressures. Also, apart from an investigation on (110) superlattices of diamond and cubic BN [34], there have been few theoretical reports of BCN heterodiamonds. Recently, energetically favourable structures of BC₂N heterodiamonds have been looked into including their synthesis paths using the FPMD method with constant-pressure formalism. The high-pressure synthesis of a class of BCN heterodiamonds utilizing diffusionless structural transformations at low temperatures has been proposed [35]. In order to explore applications to electronic devices, the electronic states of such probable structures using first-principles band calculations were studied [36].

The total energy calculation of several candidate structures of BC₂N revealed that a bond-counting rule holds in the B–C–N system. The rule is that more stable structures have more C–C and B–N bonds but have no B–B or N–N bonds. This is consistent with the tendency towards the phase separation observed experimentally. Thus, BN/C₂ (111) the superlattice as shown in Fig. 2b and called β-BC₂N by Tateyama et al. [35], is more stable than the (110) superlattice proposed previously [34] and energetically is the most favoured of the atomically mixed structures of BC₂N hetero-diamond. The bulk modulus of BN/C₂ (111) superlattice is calculated to be 438 ± 14 GPa, which is just between that of diamond and of c-BN. As for the synthesis of this superlattice, it may be difficult to make a well-crystallized sample by ordinary epitaxial growth methods, because island growth is expected to be predominant due to the bond-counting rule. On the other hand, when starting with a proper material, a desired sample may be made by a high pressure synthesis route from layered structures at a temperature low enough to suppress atomic diffusion. From this viewpoint, it is proposed that a graphitic superlattice (gr-BN/C₂) consisting of alternate stacking of graphite and hexagonal BN monolayers as shown in Fig. 2a is compressed at low

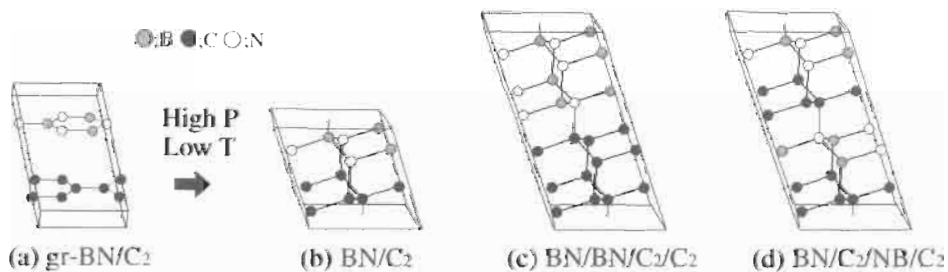


Fig. 2. Energetically favourable BC₂N heterodiamond (111) superlattices investigated in this work [35]. They could be synthesized using compression of graphitic superlattices at low temperatures.

temperatures so that atomic diffusion or phase separation is suppressed [35]. Because gr-BN/C₂ is energetically very stable and free from orientational disorder as well as intra-layer defects, it is a more promising route to a well-crystallized sample. The calculated pressure dependence of the enthalpies indicate that gr-BN/C₂ can transform into the BN/C₂ (111) superlattice with compression to ~16 GPa, suggesting that this synthesis route is experimentally feasible [35].

The results for the structural stability of BC₂N imply that the synthesis of BN/C₂ hetero-diamond (111) superlattices, with different stacking orders of diamond and cubic BN, may be possible using compression of graphitic structures. The structures shown in Figs. 2b and c are those of 1+1 (BN/C₂) and 2+2 (BN/BN/C₂/C₂) superlattices, respectively. The structure shown in Fig. 2d is also 1+1 superlattice, but with the BN orientation, in alternating BN layers, being reversed (BN/C₂/NB/C₂). This type of structure may appear locally as a stacking fault.

The band structures calculated using optimized structures in Figs. 2b–d are shown in Fig. 3. All these band structures can be roughly explained as a folding of diamond or cubic BN, as known for (110) superlattices [34], with the band gap being indirect in all cases. However, there are differences in the band edge states. The conduction band

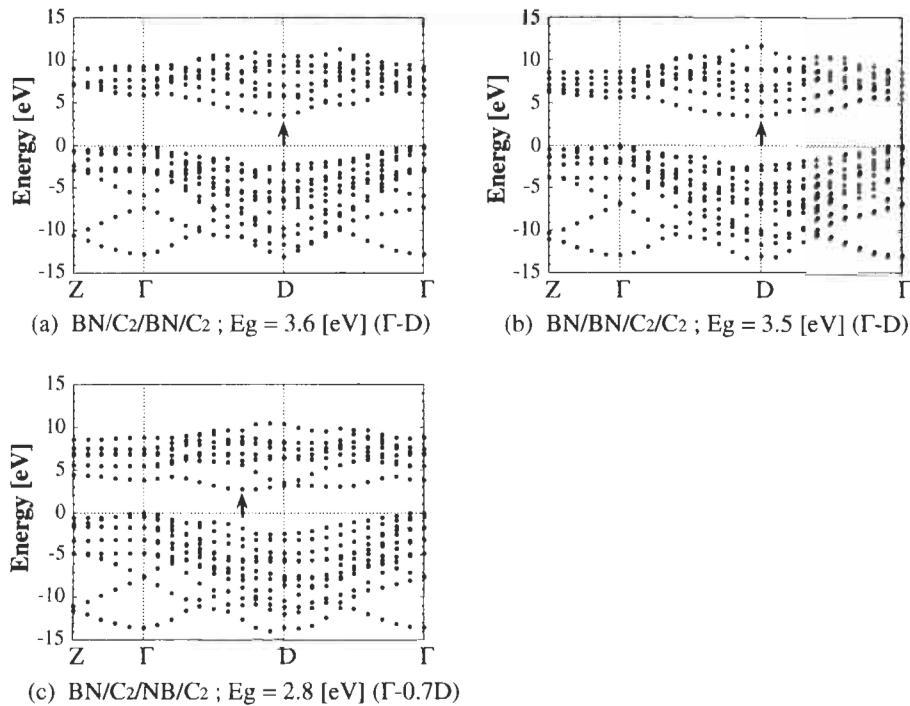


Fig. 3. The band structures of (a) BN/C₂/BN/C₂, (b) BN/BN/C₂/C₂ and (c) BN/C₂/NB/C₂ in a rhombohedral cell (space group R3m). The Z-Γ, Γ-D, D-Γ lines correspond (ΓL/4)-Γ, Γ-X, L-Γ in the fcc first Brillouin zone, respectively. Each arrow indicates the conduction band minimum in each structure. The band gaps (E_g) are calculated within LDA.

minima (CBM) of BN/C_2 and $\text{BN}/\text{BN}/\text{C}_2/\text{C}_2$ are located at the D-point which corresponds to the X-point in the fcc first Brillouin zone, at which the CBM of cubic BN is located. On the other hand, the CBM of $\text{BN}/\text{C}_2/\text{NB}/\text{C}_2$ is located at the 0.7 D-point on the Γ -D line, which is similar to that of diamond. The LDA band gaps are also different: those of BN/C_2 and $\text{BN}/\text{BN}/\text{C}_2/\text{C}_2$ are 3.6 and 3.5 eV, respectively, while that of $\text{BN}/\text{C}_2/\text{NB}/\text{C}_2$ is 2.8 eV. At the valence band maximum (VBM), a difference is also found in the splitting energy from triply degenerated p -like states into a p_z -like single state in the [111] direction and doubly degenerated states perpendicular to it. The spatial distribution of the CBM and VBM wave functions also show dramatic differences. The CBM states of BN/C_2 and $\text{BN}/\text{BN}/\text{C}_2/\text{C}_2$ spread throughout the entire crystal, while that of $\text{BN}/\text{C}_2/\text{NB}/\text{C}_2$ is localized in a carbon layer, which is sandwiched between the two N-layers.

Besides these superlattices, several types of stacking sequences have been studied to find systematic changes in their band gap and stability. Unfortunately, all of the structures investigated were found to have indirect band gaps so that application of BCN hetero-diamond to optoelectronic devices might be difficult. Nevertheless, it is good news that band-gap engineering appears to make sense in these systems.

2.4 Li-encapsulated Diamond

Cohesion of carbon atoms in graphite occurs in two ways: in a single graphite (graphene) layer, carbon atoms are tightly connected with each other via sp^2 covalent bonds, with interactions between the layers being attributed to the weak van der Waals forces. The weak interlayer coupling allows various elements or molecules to be intercalated between the graphite layers accompanied by ionization of the intercalate. Graphite intercalation compounds (GIC) is a generic term for compounds obtained in this way.

Because the graphite structure is well retained in the monolayer of GICs, it is expected that, at high pressures, GIC may undergo structural transformation into the diamond-like structure, if the intercalate is small enough to be encapsulated in a diamond cage. A candidate for such a small impurity is lithium, which is introduced into diamond by ion implantation [37,38]. Thus, Li-GICs were starting materials and the stabilities of lithium-doped diamonds, $\text{LiC}_6(\text{D})$ and $\text{LiC}_{12}(\text{D})$ were investigated, as expected from Stage-1 and Stage-2 Li-GICs, respectively [39]. These were called hypothetical diamonds or “Li-encapsulated diamonds”.

Stage-1 Li-GIC ($\text{LiC}_6(\text{G})$) has A- α -A- α ... stacking, where α layer is a $\sqrt{3} \times \sqrt{3}$ triangular lattice of Li atoms located at the center of facing hexagons in adjacent graphite layers. For the Stage-2 Li-GIC ($\text{LiC}_{12}(\text{G})$), the stacking structure is reported to be A- α -A-A- α -A... [40]. The diamond structure, naively expected from these graphite-layer stackings, is hexagonal diamond with the same c -axis orientation as the GICs. The Li atoms are expected to reside in the interstitial site, keeping the triangular lattice in the ab plane. The structures of hypothetical $\text{LiC}_{12}(\text{D})$ at 60 GPa are illustrated in Fig. 4.

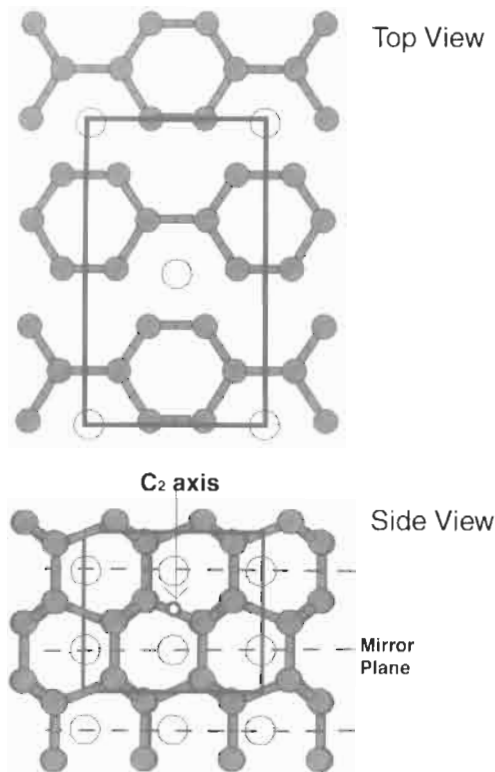


Fig. 4. Atomic configuration of $\text{LiC}_{12}(\text{D})$ at 60 GPa obtained by FPMD simulation. Grey circles and open circles denote carbon and lithium atoms, respectively. C–C bonds longer than 16 nm are not shown. The upper panel is the top view seen from the c -axis of starting $\text{LiC}_{12}(\text{G})$.

Structural optimization was performed of these Li-encapsulated diamonds without symmetry restriction by means of the CP-FPMD method. The unit cell for calculation contains twelve carbon atoms and one or two lithium atoms.

It was found that both $\text{LiC}_6(\text{D})$ and $\text{LiC}_{12}(\text{D})$ are stable at high pressure (40 GPa). At ambient pressure $\text{LiC}_6(\text{D})$ spontaneously collapses into a GIC phase. $\text{LiC}_{12}(\text{D})$ is quenchable at ambient pressure, at least at the low temperature limit, if it is once formed. The C–C bond-length in $\text{LiC}_{12}(\text{D})$ is elongated to 0.160 to 0.163 nm in the diamond cage encapsulating a lithium atom, while it remains as 0.152 to 0.154 nm elsewhere. The system contains an odd number of electrons in the unit cell and is metallic.

Because of the large lattice distortion, $\text{LiC}_{12}(\text{D})$ is less stable than GIC at low pressures, whereas it may be stabilized, more than GIC, at ultra-high pressures as with pure diamond. Therefore, this exotic material might be obtained by compression, if phase separations leading to carbide or lithium segregation are prohibited at low temperatures.

If intercalates larger than lithium are used, it may be that the diamond cage cannot be preserved. Even so, for higher-stage GIC, it is likely that thin diamond layers will be formed as ‘sandwich intercalate’ layers. If such a structure does exist, the dangling bonds at the interface will be passivated by the electrons transferred from the intercalates. Another possibility is that a three-dimensional network of sp^2 covalent bonds is formed just as in the high-pressure phase of silicide, or it may be that some carbon dimers form carbide locally. In any case, low-temperature compression of GICs would result in novel structural transformations and new high-pressure phases worthy of detailed investigation. Differences in layer stacking, intercalates and stage structure of the intercalates in the starting materials would result in useful variations of resultant materials.

3 Conclusions

In this chapter, several methods for computational simulation of materials are briefly explained to give some idea of the extent of approximations used in treating many-body problems of atoms and especially electrons. Among them, FPMD combining DFT with MD is one of the most powerful methods for investigating novel materials when experimental information is sufficient. Two examples of FPMD study of new carbon-related materials are presented.

An obvious merit of empirical methods is that it is easy to repeat trial and error experiments changing chemical composition or initial configuration of the system. This is especially useful for studying complicated and experimentally unknown structures such as a granular graphite in Li-ion batteries [41,42]. Another important merit of the empirical method with one-body approximation is that physical properties like optical properties, conductivity, magnetic field effects, etc. are easily discussed within the scheme [43,44]. On the other hand, first-principles methods are useful for quantitative prediction of the atomic/electronic structure of materials. The point is that theorists should use the best affordable methods for each problem.

References

1. W.G. Hoover, *Molecular Dynamics*. Lecture Notes in Physics Vol. 258. Springer-Verlag, Berlin, 1986.
2. M. Parrinello and A. Rahman, Polymorphic transitions in single crystals: A new molecular dynamics method. *J. Appl. Phys.*, 52: 7182–7190, 1981.
3. S. Nosé, A unified formulation of the constant temperature molecular dynamics methods. *J. Chem. Phys.*, 81: 511–519, 1984.
4. W.G. Hoover, Canonical dynamics: Equilibrium phase-space distributions. *Phys. Rev. A*, 31: 1695–1697, 1985.
5. P. Deuffhard, J. Hermans, B. Leimkuhler, A.E. Mark, S. Reich and R.D. Skeel, *Computational Molecular Dynamics: Challenges, Methods, Ideas*. Springer-Verlag, Berlin, 1999.
6. F.H. Stillinger and T.A. Weber, Computer simulation of local order in condensed phases of silicon. *Phys. Rev. B*, 31: 5262–5271, 1985.

7. J. Tersoff, New empirical model for the structural properties of silicon. *Phys. Rev. Lett.*, 56: 632–635, 1986; Empirical interatomic potential for carbon with applications to amorphous-carbon. *Phys. Rev. Lett.*, 61: 2879–2882, 1988.
8. See textbooks of quantum chemistry, e.g. A. Szabo and N.S. Ostlund, *Modern Quantum Chemistry: Introduction to Advanced Electronic Structure Theory*. McGraw-Hill, New York, 1989.
9. S. Lundqvist and N.H. March (Eds.), *Theory of the Inhomogeneous Electron Gas*. Plenum Press, New York, 1983.
10. P. Hohenberg and W. Kohn, Inhomogeneous electron gas. *Phys. Rev.*, 136: B864–B871, 1964.
11. W. Kohn and L.J. Sham, Self-consistent equations including exchange and correlation effects. *Phys. Rev.*, 140: A1133–A1138, 1965.
12. R. Car and M. Parrinello, Unified approach for molecular dynamics and density-functional theory. *Phys. Rev. Lett.*, 55: 2471–2474, 1985.
13. M. Payne, M.P. Teter, D.C. Allan, T.A. Arias and J.D. Joannopoulos, Iterative minimization techniques for *ab initio* total-energy calculations: molecular dynamics and conjugate gradients. *Rev. Mod. Phys.*, 64: 1045–1097, 1992.
14. G.B. Bachelet, D.R. Hamann and M. Schlüter, Pseudopotentials that work: From H to Pu. *Phys. Rev.*, B26: 4199–4228, 1982.
15. N. Troullier and J.L. Martins, Efficient pseudopotentials for plane-wave calculations. *Phys. Rev.*, B43: 1993–2006, 1991.
16. D. Vanderbilt, Soft self-consistent pseudopotentials in a generalized eigenvalue formalism. *Phys. Rev.*, B41: 7892–7895, 1990.
17. J. Korrington, On the calculation of the energy of a block wave in a metal. *Physica*, 13: 392–400, 1947; W. Kohn and N. Rostoker, Solution of the Schrödinger equation in periodic lattices with an application to metallic lithium. *Phys. Rev.*, 94: 1111–1120, 1954.
18. O.K. Andersen, Linear methods in band theory. *Phys. Rev.*, B12: 3060–3083, 1975; E. Wimmer, H. Krakauer, M. Weinert and A.J. Freeman, Full-potential self-consistent linearized-augmented-plane-wave method for calculating the electronic structure of molecules and surfaces: O₂ molecule. *Phys. Rev.*, B24: 864–875, 1981.
19. H.L. Skriver, *The LMTO Method: Muffin-tin Orbitals and Electronic Structure*. Springer-Verlag, Berlin, 1984; V. Kumar, O.K. Andersen and A. Mookerjee (Eds.), *Lectures on Methods of Electronic Structure Calculations*. World Scientific, Singapore, 1994.
20. J.P. Perdew and Y. Wang, Accurate and simple density functional for the electronic exchange energy: Generalized gradient approximation. *Phys. Rev.*, B33: 8800–8802, 1986; J.P. Perdew, Density-functional approximation for the correlation energy of the inhomogeneous electron gas. *Phys. Rev.*, B33: 8822–8824, 1986; J.P. Perdew, Erratum: Density-functional approximation for the correlation energy of the inhomogeneous electron gas [*Phys. Rev. B*, 33: 8822, 1986], *Phys. Rev. B*, 34: 7406, 1986.
21. A.D. Becke, Density-functional exchange-energy approximation with correct asymptotic behavior. *Phys. Rev. A*, 38: 3098–3100, 1988.
22. C.-O. Almbladh and U. von Barth, Exact results for the charge and spin densities, exchange-correlation potentials, and density-functional eigenvalues. *Phys. Rev. B*, 31: 3231–3244, 1985.
23. J.P. Perdew and A. Zunger, Self-interaction correction to density-functional approximations for many-electron systems. *Phys. Rev. B*, 23: 5048–5079, 1981.
24. L. Hedin and S. Lundqvist, Effects of Electron–electron and electron–phonon interactions on the one-electron states of solids. *Solid State Phys.*, 23: 1–181, 1969.
25. X. Zhu and S.G. Louie, Quasiparticle band structure of thirteen semiconductors and insulators. *Phys. Rev. B*, 43: 14142–14156, 1991.

26. J.A. Majewski, P. Vogl and A. Göling, Exact Kohn–Sham exchange potential in semiconductors. *Phys. Rev. Lett.*, 79: 2089–2092, 1997; M. Städele, M. Moukara, J.A. Majewski, P. Vogl and A. Göling, Exact exchange Kohn–Sham formalism applied to semiconductors. *Phys. Rev. B*, 59: 10031–10043, 1999.
27. W.M.C. Foulkes, L. Mitás, R.J. Needs and G. Rajagopal, Quantum Monte Carlo simulations of solids. *Rev. Mod. Phys.*, 73: 33–83 (2001).
28. S. Saito and A. Oshiyama, Cohesive mechanism and energy bands of solid C₆₀. *Phys. Rev. Lett.*, 66: 2637–2640, 1991.
29. R.M. Wentzcovitch, J.L. Martins and G.D. Price, *Ab initio* molecular dynamics with variable cell shape: Application to MgSiO₃. *Phys. Rev. Lett.*, 70: 3947–3950, 1993.
30. Y. Tateyama, T. Ogitsu, K. Kusakabe and S. Tsuneyuki, Constant-pressure first-principles studies on the transition states of the graphite–diamond transformation. *Phys. Rev. B*, 54: 14994–15001, 1996.
31. M. Bernasconi, G.L. Chiarotti, P. Focher, S. Scandolo, E. Tosatti and M. Parrinello, First-principle-constant pressure molecular dynamics. *J. Phys. Chem. Solids*, 56: 501–505, 1995.
32. S. Scandolo, M. Bernasconi, G. L. Chiarotti, P. Focher, and E. Tosatti, Pressure-induced transformation path of graphite to diamond. *Phys. Rev. Lett.*, 74: 4015–4018, 1995.
33. A.R. Badzian, Cubic boron nitride–diamond mixed crystals. *Mat. Res. Bull.*, 16: 1385–1393, 1981; Y. Kakudate et al., in: Proceedings of the 3rd IUMRS International Conference on Advanced Materials, Tokyo, 1993; S. Nakano, M. Akaishi, T. Sasaki and S. Yamaoka, Segregative crystallization of several diamond-like phases from the graphitic BC₂N without an additive at 7.7 GPa. *Chem. Mater.*, 6: 2246–2251, 1994; E. Knittle, R.B. Kaner, R. Jeanloz and M.L. Cohen, High-pressure synthesis, characterization, and equation of state of cubic C–BN solid solutions. *Phys. Rev. B*, 51: 12149–12156, 1995.
34. W.E. Pickett, Thin superlattices and band-gap discontinuities: The (110) diamond–boron nitride interface. *Phys. Rev. B*, 38: 1316–1322, 1988; W.L.R. Lambrecht and B. Segall, Electronic structure of (diamond C)/(sphalerite BN) (110) interfaces and superlattices. *Ibid*, 40: 9909–9919, 1990; W.L.R. Lambrecht and B. Segall, Anomalous band-gap behavior and phase stability of c–BN–diamond alloy. *Ibid*, 47: 9289–9296, 1993.
35. Y. Tateyama, T. Ogitsu, K. Kusakabe, S. Tsuneyuki and S. Itoh, Proposed synthesis path for heterodiamond BC₂N. *Phys. Rev. B*, 55: R10161–R10164, 1997.
36. Y. Tateyama, K. Kusakabe, T. Ogitsu and S. Tsuneyuki, Proc. of Int. Conf. on Silicon Carbide, III-nitrides and Related Materials—1997. Stockholm, Sweden, 1997.
37. G. Braunstein and R. Kalish, Damage and lattice location studies in high-temperature ion-implanted diamond. *Appl Phys. Lett.*, 38, 416–418, 1981.
38. S.A.Kajihara, A. Antonelli, J. Bernholc and R. Car, Nitrogen and potential n-type dopants in diamond. *Phys. Rev. Lett.*, 66: 2010–2013, 1991.
39. S. Tsuneyuki, T. Ogitsu, Y. Tateyama, K. Kusakabe and A. Kikuchi, Possible Synthesis of Heavily Doped Diamond from Li Intercalated Graphite, In: S.K. Sikka et al. (Eds.), *Advances in High Pressure Research in Condensed Matter*. National Institute of Science Communication, New Delhi, India pp. 104–108, 1997.
40. K.C. Woo, W.A. Kamitakahara, D.P. DiVincenzo, D.S. Robinson, H. Mertwoy, J.W. Milliken and J.E. Fischer, Effect of in-plane density on the structural and elastic properties of graphite intercalation compounds. *Phys. Rev. Lett.*, 182: 182–185, 1983 and references therein.
41. N. Kurita, Molecular orbital calculations on electronic properties and lithium storage of substituted disordered carbons. *Molec. Cryst. Liquid Cryst.*, 340: 413–418, 2000.
42. M. Yagi, R. Saito, T. Kimura, G. Dresselhaus and M.S. Dresselhaus, Electronic states in heavily Li-doped graphite nanoclusters. *J. Mater. Res.*, 14: 3799–3804, 1999; R. Satio, M.

- Yagi, T. Kimura, G. Dresselhaus and M.S. Dresselhaus, Chemical reaction of intercalated atoms at the edge of nano-graphene cluster, liquid crystal and molecular crystals. *Molec. Cryst. Liquid Cryst.*, 340: 71–76, 2000.
43. R. Saito, G. Dresselhaus and M.S. Dresselhaus, *Physical Properties of Carbon Nanotubes*. Imperial College Press, London, 1998.
 44. R. Saito, T. Takeya, T. Kimura, G. Dresselhaus and M.S. Dresselhaus. Finite size effect on the Raman spectra of carbon nanotubes. *Phys. Rev. B*, 59: 2388–2392, 1999; S. Roche and R. Saito, Effects of magnetic field and disorder on electronic properties of carbon nanotubes. *Phys. Rev. B*, 59, 5242–5246, 1999.

Chapter 10

X-ray Diffraction Methods to Study Crystallite Size and Lattice Constants of Carbon Materials

Minoru Shiraishi^a and Michio Inagaki^b

^aTokai University, School of High-technology for Human Welfare, Department of Material Science and Technology, Numazu, Shizuoka, 410-0395 Japan; ^bAichi Institute of Technology, Toyota, 470-0392 Japan

Abstract: The measurement of crystallite sizes (L_a and L_c) and lattice constants (a_0 and c_0) is described using X-ray diffraction profiles for graphitizable carbons during graphitization. The method is called the JSPS method and is based on the use of an internal standard of silicon crystal and thin sample (0.2 mm) with several corrections of observed intensity being applied. Crystallite size distributions are obtained from diffraction profiles for carbons heat-treated to relatively low temperatures.

Keywords: X-ray diffraction, Carbon materials, Crystallite size, Lattice constant, Crystallite size distribution, JSPS method.

1. Introduction

X-ray diffraction has been used for structural analyses of solids for quite some time. X-ray diffractometers use powder samples as well as single-crystal materials. X-ray diffraction is used to study mechanisms of graphitization and the characterization of non-graphitic carbon. Excellent reviews are available [1–3]. Modern computer technology makes numerical analyses much easier.

X-ray diffraction profiles of a petroleum coke (PC30) and a phenol-formaldehyde resin char (PF20), HTT 3000 and 2000°C, respectively, are shown in Fig. 1. Diffraction peaks from the petroleum coke correspond closely to diffraction lines from graphite crystal. However, for the phenol-formaldehyde resin, although a few diffraction profiles match closely those of graphite for position, they are much broader and are asymmetrical. Structures of PC30 and PF20 are thus quite different and X-ray diffractions can go some way in identifying these differences.

In graphitizable carbons, the 00 l diffractions are sensitive to the heat treatment temperatures (HTT) some 004 X-ray diffraction profiles being shown in Fig. 2. The

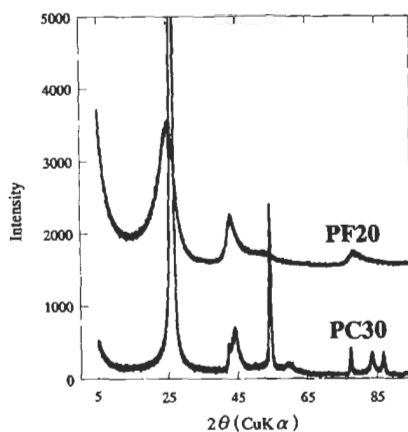


Fig. 1. Typical X-ray diffraction profiles of petroleum coke (PC30) heat-treated at 3000°C and phenol-formaldehyde resin carbon (PF20) heat-treated at 2000°C.

diffraction profiles sharpen and move to the high angle side with increasing HTT. The profile shape, position and width at half-maximum intensity (FWHM) are used in the characterization of carbons. There is a need, however, for all researchers to use identical procedures for (a) the measurement of the profile (peak) position, (b) the FWHM of the carbon, and (c) calculating (assessment) of stacking sizes from profile analysis of low-temperature carbons.

2 Measurement Method (JSPS Method)

In Japan, the X-ray diffraction method for carbons is the so-called JSPS method (Japan Society for the Promotion of Science) and has been used since 1963 [4]. Samples for these measurements are powdered carbons at various stages of the graphitization process. This method specifies the measurement condition for X-ray diffraction and analysis procedures. These features are summarized as follows:

1. Crystalline powders of high purity silicon are used as an internal standard.
2. The thickness of sample is limited to 0.2 mm.
3. Measurements of each diffraction line, 002, 004, 110 and 112 peaks, are based on the use of $\text{Cu } K_{\alpha}$ X-ray radiation.
4. Each diffraction profile is corrected for unwanted intensity factors, such as absorption and Lorenz-polarization.
5. A single procedure is adopted to determine the position and FWHM of each peak.
6. Lattice constants and apparent “crystallite sizes” are calculated by the same mathematical procedures.

X-ray diffraction profiles contain components arising from such effects as Lorenz-polarization factors, absorption factors, doubling of K_{α} radiation and

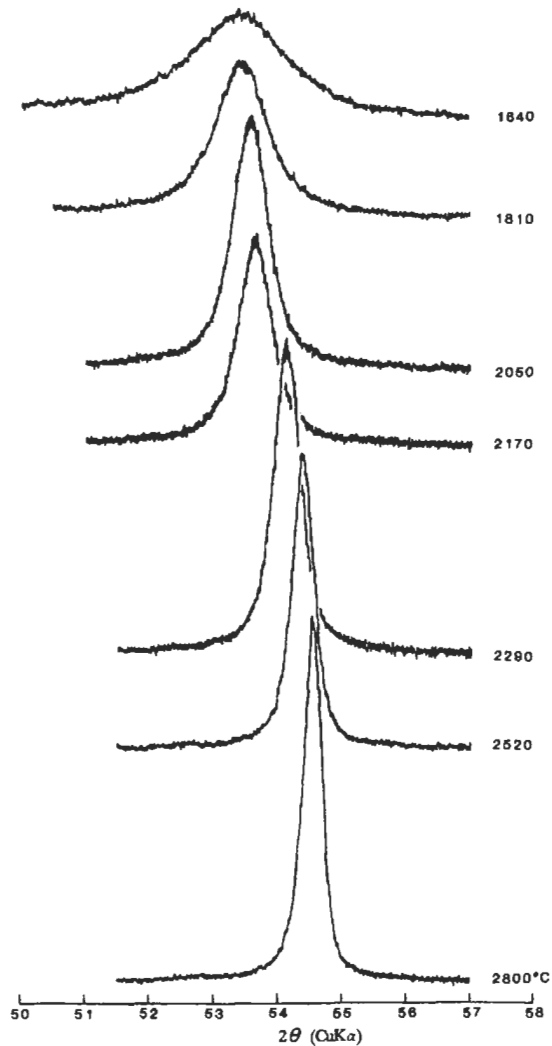


Fig. 2. Peak shift of 004 diffraction of graphitizable carbon with heat-treatment temperature.

instrumental broadening. The dependence of the atomic scattering factor of carbon on $\sin \theta/\lambda$ affects the profile, particularly the 002 band at low diffraction angles, θ . It is necessary to correct for these factors to obtain a more meaningful crystallite size from the profiles. Crystallite sizes thus calculated, however, still contain effects caused by lattice distortions in carbon structures. Therefore, it is recommended to regard the crystallite sizes obtained as “apparent” crystallite sizes, L_a and L_c .

In the JSPS method, observed diffraction intensities are corrected for the following factors as set out below.

2.1 Absorption Factors

As carbon is a light element, X-rays penetrate deep inside a thick sample and are diffracted/scattered there. The diffracted intensity is strengthened at the low-angle side, and the profile broadens. Therefore, observed profiles of carbons need to be corrected for absorption more than for other materials such as metals and metal compounds. Because X-ray scattering intensities, as measured by the diffractometer, are based on X-rays scattered from that part glanced from the detection counter within an irradiated sample volume, the change of the sample volume irradiated by X-rays at a diffraction angle has to be as small as possible. Hence, for low absorption coefficients and keeping small change of the irradiated sample volume during measurement of each diffraction line, the sample thickness is specified as being 0.2 mm. To correct for absorption, the absorption factor, A , in the following equation is used in the JSPS method [5]:

$$A = \left(1 - \frac{1}{2\mu'w \cos \theta}\right) \left(1 - \exp(-2\mu't \cos \theta)\right) + \frac{2t \cos \theta}{w} \exp(-2\mu't \cos \theta) \quad (1)$$

where θ is the diffraction angle, w is the width of X-ray radiation on the sample surface and μ' is the linear absorption coefficient of the carbon material mixed with a silicon standard for K_{α} . When the bulk density of the X-ray sample μ' is 1.0, the value of μ' is calculated to be 10 for the sample mixed with 10 wt% Si and 16 with 20 wt% Si, because mass absorption coefficients μ/ρ of carbon and silicon are $(\mu/\rho)_c = 4.219$ and $(\mu/\rho)_{si} = 65.32$, respectively.

2.2 Profile broadening due to K_{α} doublet

Because K_{α} radiation consists of $K_{\alpha 1}$ and $K_{\alpha 2}$ with small differences in wavelength (0.54056 and 0.154439 nm, respectively), all diffraction lines must be composed of two lines with small differences in diffraction angles. For the lines observed at high angles, two separated diffraction lines are observed, but only broadened profiles without apparent separation are observed at low angles. Jones [6] illustrated angular separation curves as a function of 2θ and proposed a separation procedure by assuming that the two profiles for $K_{\alpha 1}$ and $K_{\alpha 2}$ radiations have the same shape and breadth, but differ in height by a factor of two and a shift by Δ in 2θ . His procedure is employed in the JSPS method, the software for which is available in all commercially available X-ray diffractometers.

2.3 Instrumental Broadening

Diffraction profiles are broadened depending on the instrumental and optical conditions used, the instrumental broadening being related to the breadth of the X-ray source, flat specimen surface and axial divergence of the X-ray beam [7]. The

peak width of the silicon (internal standard) shows the instrumental broadening of the X-ray diffractometer, because of its high crystallinity. Jones [6] corrected observed profiles for instrumental broadening by applying a Fourier analysis to a sample which causes broadening due to a small crystal size as well as a standard material which does not show broadening because of its large crystal size and showing only instrumental broadening. Klug and Alexander [7] provided correction curves to the widths of X-ray diffractions arising from instrumental broadening under different conditions. The JSPS method adopts their curves for high-resolution low-angle reflection conditions.

2.4 Lorentz–Polarization Factor and Atomic Scattering Factor of Carbon

As the Lorentz factor (L) and polarization factor (P) change with diffraction angle, corrections are necessary to obtain a correct profile, particularly for broad profiles. In the JSPS method, corrections of the L and P factors are made for the profiles with FWHMs larger than 0.5° , according to the following equations:

$$L = \frac{1}{\sin^2 \theta \cdot \cos \theta} \quad (2)$$

$$P = \frac{1}{2} (1 + \cos^2 2\theta) \quad (3)$$

$$P = \frac{1 + \cos^2 2\theta \cdot \cos^2 2\theta'}{1 + \cos^2 2\theta'} \quad (4)$$

Equations (2) and (3) are used when a nickel filter is used, and Eqs. (2) and (4) for a graphite counter monochromator. In Eq. (4), $2\theta'$ is the diffraction angle of graphite, that is 26.56° .

Because atomic scattering factors decrease with increasing diffraction angle, it is necessary to correct the diffraction profiles of carbons using the square of the atomic scattering factor of carbon (f_c), given by the following equation [8]:

$$f_c = 2.26069 \exp(-22.6907 \times s^2) + 1.56165 \exp(-0.656665 \times s^2) \\ + 1.05075 \exp(-9.75618 \times s^2) + 0.839259 \exp(-55.5949 \times s^2) + 0.286977 \quad (5)$$

$$s = \sin \theta / \lambda$$

2.5 Practical Procedures

2.5.1 Correction of observed X-ray intensity

The observed X-ray intensity (I_{obs}) is given by

$$\begin{aligned}
 I_{\text{obs}} &= KLPAG^2 |F|^2 \\
 &= KLPAG^2 f_c^2 |F_g|^2
 \end{aligned}
 \tag{6}$$

in which K is a constant, L = Lorentz factor, P = polarization factor, G = Laue function, F = structure factor of graphite, f_c = atomic scattering factor of carbon, and F_g = geometrical structure factor of graphite. The factor that relates to the size of crystallites in the carbon is G^2 . To determine apparent crystallite sizes and lattice constants of carbon, the profile of G^2 has to be obtained first, this being achieved by correction of the observed profile using the factors, L , P , A and f_c^2 . Then the peak positions and FWHM can be determined.

In the JSPS method, the corrected profile is obtained by dividing the observed intensity by the factors $LPAf_c^2$ for each diffraction angle. Because values of $LPAf_c^2$ decrease monotonously, relative values of $LPAf_c^2$ which make $2\theta = 30^\circ$ to be unity for 002 diffractions and $2\theta = 57^\circ$ for 004 diffractions are used. These relative values (*FCT*) were calculated for a sample thickness of 0.2 mm mixed with 10 or 20 wt% silicon and approximated by the following series:

$$FCT = C_1 + C_2 \cdot (2\theta) + C_3 \cdot (2\theta)^2 + C_4 \cdot (2\theta)^3 + C_5 \cdot (2\theta)^4 + C_6 \cdot (2\theta)^5
 \tag{7}$$

Values of the coefficients C_1, C_2, C_3, \dots in Eq. (7) are listed in Table 1. The diffraction profile has to be further corrected by a levelling of the background.

Table 1

Coefficient of correction Eq. (7) for 002 and 004 diffraction intensities

| | Ni filter | | Counter monochromator | |
|------------------------|-----------------------------|-----------------------------|-----------------------------|-----------------------------|
| | Si 10% | Si 20% | Si 10% | Si 20% |
| 002 Diffraction | | | | |
| C_1 | 0.1062200×10^3 | 0.8902088×10^2 | 0.9350447×10^2 | 0.7836853×10^2 |
| C_2 | -0.1493785×10^2 | -0.1223796×10^2 | -0.1316116×10^2 | -0.1078659×10^2 |
| C_3 | 0.8948090×10^0 | 0.7201680×10^0 | 0.7921825×10^0 | 0.6383320×10^0 |
| C_4 | $-0.2796578 \times 10^{-1}$ | $-0.2217635 \times 10^{-1}$ | $-0.2491818 \times 10^{-1}$ | $-0.1980132 \times 10^{-1}$ |
| C_5 | 0.4500046×10^{-3} | 0.3521847×10^{-3} | 0.4038340×10^{-3} | 0.3170086×10^{-3} |
| C_6 | $-0.2956388 \times 10^{-5}$ | $-0.2285659 \times 10^{-5}$ | $-0.2672795 \times 10^{-5}$ | $-0.2074537 \times 10^{-5}$ |
| 004 Diffraction | | | | |
| C_1 | 0.1229242×10^3 | 0.9028824×10^2 | 0.4067178×10^2 | 0.3747529×10^2 |
| C_2 | -0.7458276×10^1 | -0.5160503×10^1 | -0.1807844×10^1 | -0.1656186×10^1 |
| C_3 | 0.1753749×10^0 | 0.1142502×10^0 | 0.2791991×10^{-1} | 0.2550629×10^{-1} |
| C_4 | $-0.1876302 \times 10^{-2}$ | $-0.1149098 \times 10^{-2}$ | $-0.1476100 \times 10^{-3}$ | $-0.1346840 \times 10^{-3}$ |
| C_5 | 0.7662217×10^{-5} | 0.4401877×10^{-5} | | |

2.5.2 Determination of lattice constants (c_0 and a_0)

As shown in Fig. 3, the diffraction angle $2\theta_{\text{obs}}$ is obtained from the position of middle point of the segment divided by the profile on the line parallel to the background at a position of $2/3$ height from the background. From the diffraction angle of the standard silicon ($2\theta_{\text{obs}}\text{Si}$) and that of carbon, ($2\theta_{\text{obs}}\text{C}$), the corrected diffraction angle, ($2\theta_{\text{cor}}\text{C}$) of the carbon is obtained from the following equation:

$$\begin{aligned} (2\theta_{\text{cor}})_\text{C} &= (2\theta_{\text{obs}})_\text{C} - \{(2\theta_{\text{obs}})_\text{Si} - (2\theta_{\text{cor}})_\text{Si}\} \\ &= (2\theta_{\text{cor}})_\text{Si} - \delta(\text{Si}-\text{C}) \end{aligned} \quad (8)$$

where $(2\theta_{\text{cor}})_\text{Si}$ are the diffraction angles calculated from the lattice constant (0.543073 nm) of the silicon crystal. Lattice constants along the c -axis (c_0) and a -axis (a_0) are calculated from the diffraction angles $(2\theta_{\text{cor}})_\text{C}$ of either 002, 004 or 006 lines and from the 110 line, respectively.

2.5.3 Determination of apparent crystallite size (L_c and L_d)

Apparent crystallite sizes are obtained from the Scherrer equation using FWHM of the profile corrected for instrumental broadening and the K_α doublet. The width of profile at the $1/2$ position (half-peak width) of the maximum intensity from the background, namely FWHM, is measured at the angle unit, as shown in Fig. 3. When the profiles do not show apparent separation of the K_α doublet, FWHM makes the correction on K_α doublet by using the curves shown in Fig. 4, which are referred to the profiles intermediate in shape between Gaussian and Cauchy [6]. This curve is approximated by the following equation:

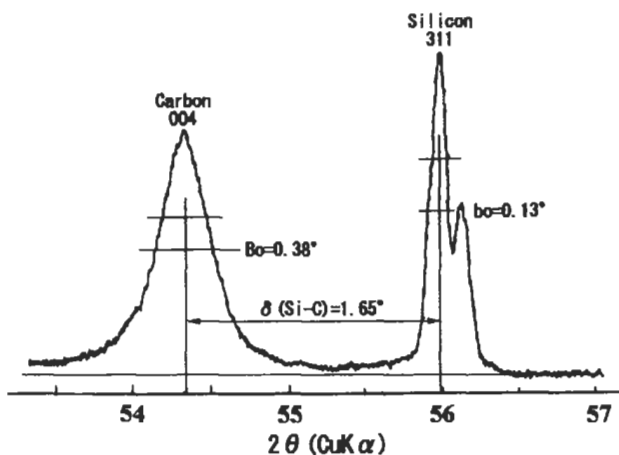


Fig. 3. Measurement example of diffraction angle and width.

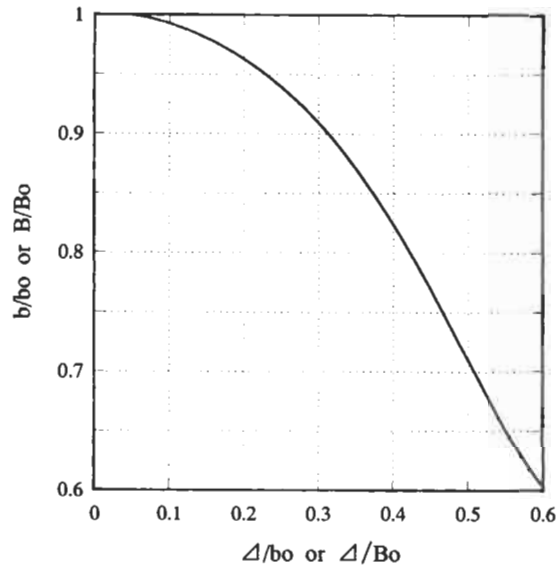


Fig. 4. Correction curve for angular separation of K_{α} doublet.

$$B/B_0 \text{ or } b/b_0 = 0.9991090 + 0.1180823 \cdot u - 2.447168 \cdot u^2 + 8.254356 \cdot u^3 - 20.96720 \cdot u^4 + 17.34026 \cdot u^5 \quad (9)$$

where B_0 is the experimental FWHM for the carbon, b_0 is the observed FWHM for the silicon standard, and Δ is the angular separation of the K_{α} doublet given in Table 2, and u is either Δ/B_0 or Δ/b_0 . From the curve of Fig. 4 or Eq. (9), are obtained FWHMs corrected for K_{α} doublet for carbon and silicon, that is B and b , respectively. When the profiles show apparent separation due to the K_{α} doublet, the procedure written above is applied and the FWHM values of B and b are measured from the profile of $K_{\alpha 1}$ radiation of sample carbon and standard silicon, respectively.

Table 2

Δ value of each diffraction peak

| Carbon | | Silicon | |
|--------|--------------------|---------|--------------------|
| hkl | $\Delta(^{\circ})$ | hkl | $\Delta(^{\circ})$ |
| 002 | 0.067 | 111 | 0.072 |
| 004 | 0.147 | 311 | 0.152 |
| 110 | 0.229 | 331 | 0.224 |
| 112 | 0.255 | 422 | 0.275 |
| 006 | 0.271 | | |

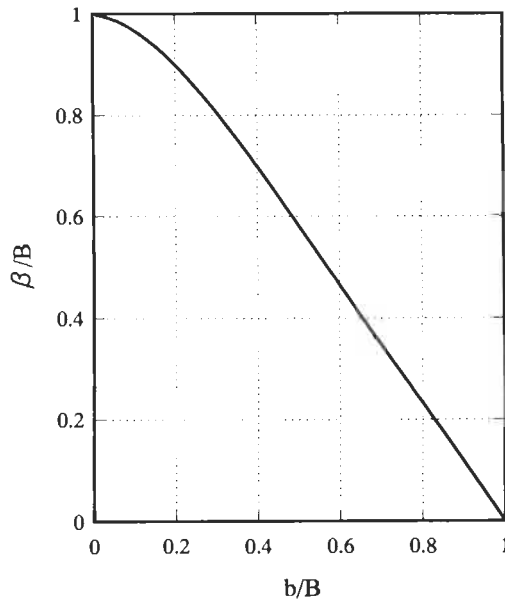


Fig. 5. Correction curve for instrumental broadening.

In the next step, the following approximation (Eq. (10)) is used for the instrumental broadening correction (Fig. 5):

$$\beta / B = 0.9981266 - 0.0681532 \cdot v - 2.592769 \cdot v^2 + 2.621163 \cdot v^3 - 0.9584715 \cdot v^4 \quad (10)$$

where $v = b/B$, and β is the corrected FWHM for the carbon being studied. The corrected FWHM β is obtained by multiplying B .

Apparent crystallite sizes are calculated using the following equations from β of each diffraction profile, as derived from the Scherrer equation using parameters appropriate to each diffraction line and also by assuming the shape factor to be 1.00.

$$\begin{aligned} L_c(002) &= 91 / \beta \\ L_c(004) &= 99 / \beta \\ L_a(110) &= 113 / \beta \\ L_c(112) &= 41 / \beta \end{aligned} \quad (11)$$

$L_c(002)$ and $L_c(004)$ are the *apparent* crystallite thickness along the c -axis, perpendicular to the hexagonal carbon layers stacked in parallel irrespective of whether a stacking order exists or not, as obtained from the 002 and 004 diffraction profiles, respectively. Both values are not always coincident, the existence of the lattice strain in the crystallites accounting for the difference. $L_a(110)$ is an apparent crystallite

width along the a -axis obtained from 110 diffraction, and $L_c(112)$ corresponds to the thickness of crystallites having three dimensional graphite stacking order, and obtained by converting the crystallite size along 112 direction into the c -axis direction.

Software which automatically or interactively deals with these procedures has been developed and uses diffraction intensity data downloaded into a personal computer. In addition, processing software that enhances accuracy has been recently developed by Fujimoto [9].

3 Characterization of Carbonized Materials Heat-treated at Low Temperatures

For carbons such as carbonaceous mesophase and coke heat-treated to comparatively low temperatures, it is more useful to analyze the form of diffraction profiles rather than to determine peak positions and FWHMs as performed by the JSPS method. By applying Fourier transformations of the 002 band and least-squares fitting of the 11 band using the Hirsch and Diamond method, the distribution and average values of L_c and L_a were measured and discussed for coals, pitches and their carbon products [10–12]. Figure 6 shows the layer size histogram for coal-tar pitch, as obtained from the 11 band by the Diamond method [13]. The fraction of amorphous matter (A) was about 9 wt% with an average layer size of 0.89 nm. The histogram of stack heights in the carbonaceous mesophase produced by the heat-treatment of a coal-tar pitch for 16 h at 430°C is shown in Fig. 7. The average number of layers per stack is 3.3 and the average layer spacing is 0.345 nm.

X-ray scattering intensities from a group of carbon layers stacked in parallel and having various sizes of L_a and L_c , were theoretically deduced by Warren et al. [14], as follows:

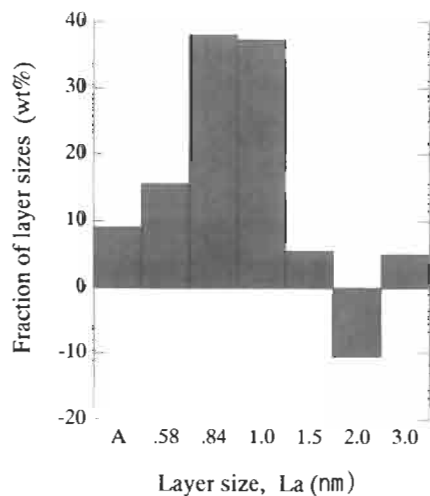


Fig. 6. Size histogram of carbon layers constituting coal-tar pitch.

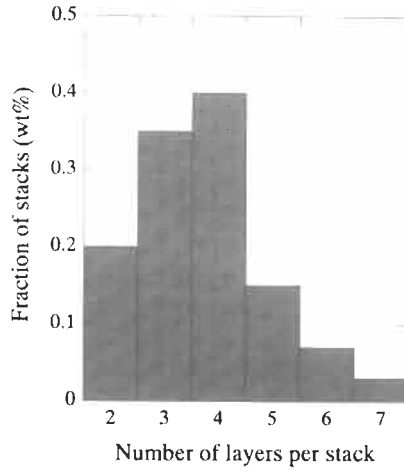


Fig. 7. Histogram of stack heights in carbonaceous mesophase.

$$I_{\text{coh}}(s) = \frac{1_{\text{cu}}(s)}{MN} = \frac{1}{N} \sum_i \sum_j f_c^2(s) \frac{\sin 2\pi s r_{ij}}{2\pi s r_{ij}} + 2 \sum_p f_c^2(s) \left(1 - \frac{p}{M}\right) i(p)$$

$$i(p) = \frac{0.2427}{s} \int_{pd_{002}}^{r_m} (\arccos u - u(1-u^2)^{1/2}) \sin 2\pi s r dr \quad (12)$$

$$r_m = (L_a^2 + (pd_{002})^2)^{1/2}$$

$$s = 2 \sin \theta / \lambda$$

where I_{coh} is the coherent scattering intensity from layered stacking groups, and M , N , 2θ , λ , f_c , r_{ij} are the number of layer planes per stack, the number of carbon atoms per single layer, and diffraction angle, X-ray wave length, atomic scattering factor of carbon and distance between two carbon atoms in the stack, respectively. The scattering profiles for the groups with various layer sizes and their stacking thicknesses, including a single layer plane, are calculated from the theoretical equation, Eq. (12). Then the optimum fitting between the observed profile and the assembly of the weighted theoretical scattering profile is explored making square root deviation minimum. The solution of this fitting process gives an structure image which is believed to be closer to the actual structure than the conventional method which shows only average values. This convenient analysis method using a personal computer was developed by Fujimoto et al. [15]. For samples of low crystallinity such as low-temperature cokes, incoherent scattering (I_{inc}) has to be subtracted from the observed intensity to obtain the coherent scattering intensity I_{coh} .

As an example of results obtained, the observed intensity and the theoretical intensity of the mesocarbon microbeams (MCMB) HTT of 1000°C are shown in Fig. 8.

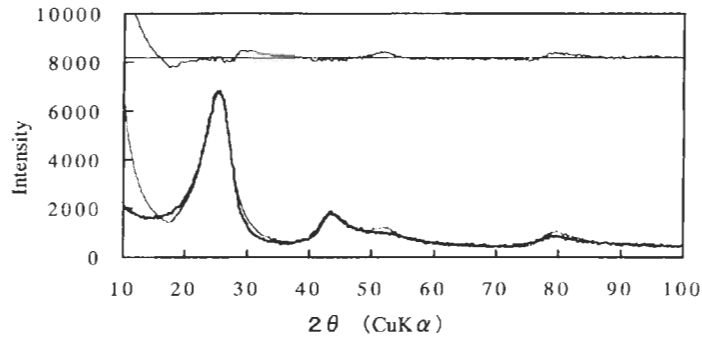


Fig. 8. The least square refinement of X-ray diffraction profile of MCMB (mesocarbon microbeads) heat-treated at 1000°C. Bold and thin lines denote observed and fitted profile, the upper part showing the residual curve with 6.51 of R-factor.

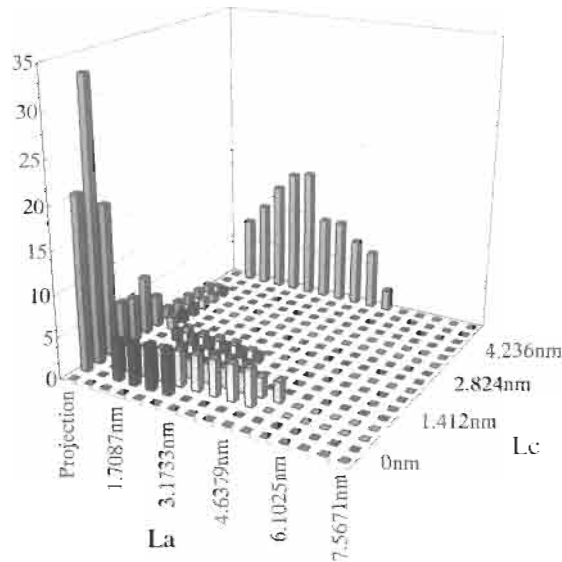


Fig. 9. Two-dimensional crystallite size distributions of MCMB heat-treated at 1000°C.

A notched thick curve is the observed profile and the thin curve is the theoretical profile calculated by assuming the distributions shown in Fig. 9. The two curves show good coincidence, although the deviation increases at the low-angle side, as shown in the upper part of the figure. The distribution of crystallites sizes in Fig. 9 shows that L_a varies over 4 nm, having a peak at about 1.7 nm, and there are two peaks in 2–4 and 6–8 layers in L_c . These results give useful information on the development of crystallites in MCMB.

References

1. S. Ergun, X-ray Studies of Carbon, In: P.L. Walker (Ed.), Chemistry and Physics of Carbon, Vol. 3. Marcel Dekker, New York, pp. 289–288, 1968.
2. W. Ruland, X-ray Diffraction Studies on Carbon and Graphite, In: P.L. Walker (Ed.), Chemistry and Physics of Carbon, Vol. 4. Marcel Dekker, New York, pp. 1–84, 1968.
3. J. Maire and J. Mering, Graphitization of Soft Carbons, In: P.L. Walker (Ed.), Chemistry and Physics of Carbon, Vol. 6. Marcel Dekker, New York, pp. 125–190, 1970.
4. Japan Society for the Promotion of Science (JSPS) 117 Committee, Measurement Method of Lattice Constants and Crystallite Sizes on Artificial Graphite. Tanso, 25–28, 1963.
5. M.E. Milberg, Transparency factor for weakly absorbing samples in X-ray diffractometry. J. Appl. Phys., 29: 64–65, 1958; M. Shiraishi and K. Kobayashi, On absorption correction for X-ray intensity. Tanso, 49–50, 1973.
6. F.W. Jones, The measurement of particle size by the X-ray method. Proc. Roy. Soc. (London), 166A: 16–43, 1938.
7. H.P. Klug and L.E. Alexander, X-ray diffraction procedures for polycrystalline and amorphous materials. John Wiley & Sons, pp. 290–311, pp. 640–640, 1973.
8. A.J.C. Wilson and E. Prince (Ed.), International Tables for Crystallography, Vol. C (2nd Edn.). Kluwer Academic, Dordrecht, pp. 572, 1999.
9. H. Fujimoto, Examination of “measurement method of crystallite sizes and lattice constants of artificial graphite” using the profile fitting method on Windows95/98. Japan Society for the Promotion of Science (JSPS), 117 Committee meeting 117-255-C1, Tokyo, 2000.
10. R.E. Franklin, The interpretation of diffuse X-ray diagrams of carbon. Acta Crystallogr., 3: 107–121, 1950.
11. P.B. Hirsch, X-ray scattering from coals. Proc. Roy. Soc., A226: 132–169, 1954.
12. R. Diamond, A least-squares analysis of the diffuse X-ray scattering from carbons. Acta Crystallogr., 11: 129–138, 1958.
13. M. Shiraishi and K. Kobayashi, An X-ray study of coal tar pitch. Bull. Chem. Soc. Japan, 46: 2575–2578, 1973.
14. B.E. Warren and P. Bodenstein, The diffraction pattern of fine particle carbon blacks. Acta Crystallogr., 18: 282–286, 1965.
15. H. Fujimoto and M. Shiraishi, Characterization of unordered carbon using Warren–Bodenstein’s equation. Carbon, 39: 1753–1761, 2001.

Chapter 11

Pore Structure Analyses of Carbons by Small-Angle X-ray Scattering

Keiko Nishikawa

*Division of Diversity Science, Graduate School of Science and Technology, Chiba University,
Yayoi, Inage-ku, Chiba 263-8522, Japan*

Abstract: Small-angle X-ray scattering (SAXS) is a powerful investigative tool used to analyze both open and closed porosity within materials. The fundamental concepts of SAXS are outlined below, with special reference to carbons. As an example for the determination of size, shape and fractal features of pores, a recent study by SAXS is described.

Keywords: Small-angle X-ray scattering, Pore structure, Porous carbon, Gyration radius, Fractal.

1. Introduction

Carbons are characterized by their varied form and function. The variety is understood in terms of their structure, by considering, for example, if the carbons are porous and what is the form and distribution of any porosity. This variety in properties of carbons and their various applications relates directly to their porosities. Analyses of porosities have lagged behind structural analyses of carbon substance because of the emphasis on the crystallinity of carbons. It is equally important to characterize pore structures to understand the functions of carbons. To this end, small-angle X-ray scattering (SAXS) is a useful experimental approach in association with adsorption methods. Unlike adsorption methods, the merit of the SAXS method is that it can be applied whether or not the porosity is open or closed.

SAXS patterns from a selection of carbons are shown in Fig. 1. The scattering intensities and their patterns differ considerably, being dependent on the carbons studied. Information within scattering patterns is closely dependent on the size, shape and distribution of pores. The purpose of this chapter is to introduce the fundamentals of SAXS methods and to give examples of their applications to carbons.

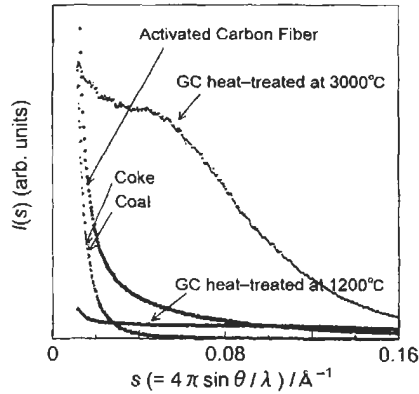


Fig. 1. Various patterns of small-angle X-ray scattering from carbon materials.

2. Fundamentals of Small-Angle X-ray Scattering

2.1 Scattering Parameter

First, we introduce the scattering vector s or the scattering parameter s , these being critical parameters to all scattering phenomena. Structural studies based on X-ray scattering phenomenon depend closely on an analysis of the interference of scattered X-rays from the carbons. That is, the key point of analyses of diffraction methods is to describe mathematically these phase differences which occur between scattered X-rays.

Consider the interference of X-rays scattered by particles positioned at O and A in a direction as shown in Fig. 2. Because the effective scatterers are electrons for X-ray scattering, the two particles are electrons. X-rays are scattered by the electrons at O and A with the same wavelength as the incident beam. The unit vectors which show the direction of incident X-ray and scattered X-ray are defined by e_i and e_s ,

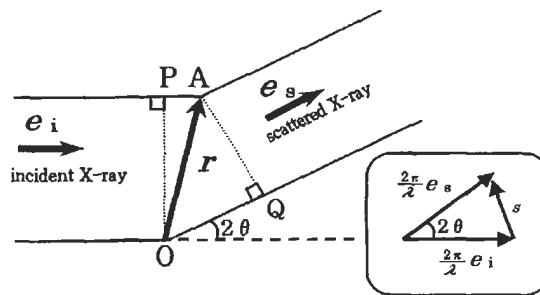


Fig. 2. Scattering vector s and scattering parameter s . The phase difference of X-rays scattered at point A and Point O becomes $(-r \cdot s)$, where r is the position vector of A from O.

respectively, and the position vector from O to A is denoted by r . The path difference d for the X-rays scattered at the two points is given by

$$\begin{aligned} d &= \overline{PA} - \overline{OQ} \\ &= r \cdot e_i - r \cdot e_s \\ &= -r \cdot (e_s - e_i) \end{aligned} \quad (1)$$

When we replace the path difference with the phase difference, p , this is given by

$$p = 2\pi d/\lambda = -2\pi r \cdot (e_s - e_i)/\lambda = -r \cdot s \quad (2)$$

where λ is the wavelength of X-ray and s is called a scattering vector and is given by

$$s = 2\pi(e_s - e_i)/\lambda \quad (3)$$

The direction of s is parallel to $(e_s - e_i)$ as shown in Fig. 2, and the magnitude is given by $4\pi\sin(\theta)/\lambda$, where 2θ is a scattering angle. The parameter s is mainly used for carbons because information on a three-dimensional structure is lost due to the disorder or orientation average. All scattering or diffraction experiments refer to the measurement of the scattering intensities in s or s space.

2.2 Three Principles of Small-angle X-ray Scattering

Books dedicated to SAXS are available which set out detailed explanations and applications [1–3]. Three important and fundamental concepts are listed below to aid the understanding and analyses of SAXS data.

2.2.1 Inverse Relation of Real Space and Reciprocal Space

Real space corresponds to the space where the scatterers exist and reciprocal space is the s or s space. The characteristic dimension to the real space is length, which describes the positional relation of particles. The dimension of reciprocal space is inverse of length. The information on a larger scale in real space appears in the smaller s -region and *vice versa*. SAXS is the scattering which occurs in a small s -region, when X-rays pass through a particle of 1 to ~ 10 nm in size or a substance which has non-homogeneous regions of electron density of equal size.

2.2.2 Small-angle Scattering Refers to Rough Observation

In contrast to SAXS, normal X-ray scattering to determine the structure of crystals or molecules is called wide-angle X-ray scattering (WAXS). The observed s -regions for

SAXS and WAXS are usually $0 < s < 0.2 \text{ \AA}^{-1}$ and $0.3 < s < 18 \text{ \AA}^{-1}$, respectively. Let us compare WAXS and SAXS for looking at cloth. If we focus our eyes to observe cloth at a short distance or with a microscope, we can distinguish individual fibers. If we do not focus our eyes on the cloth, its detailed structure disappears and we recognize it as a homogeneous substance with constant density. The former refers to WAXS and the latter to SAXS. Namely, specific structures for a small region are revealed by WAXS and diffuse structures, ranging over a larger region are revealed by SAXS. SAXS is a method which provides information of 'general' structure on a larger scale. For carbon materials, carbon matrix is considered to be homogeneous with a constant electron density throughout. It is the differences in electron density between the carbon matrix and the porosity which generate the SAXS intensities.

2.2.3 The Babinet Theorem

The SAXS intensity from a particle with n electrons is proportional to n^2 and that from the particles in the medium is written as:

$$I \propto N (\Delta\rho V)^2 \quad (4)$$

where $\Delta\rho$ is the difference between the average electron density of the particle and that of the medium, V is the volume of a particle and N the number of particles. A complementary system is shown in Figs. 3a and b. For (a), particles are in the medium, the electron density of the former being $\Delta\rho$ higher than the latter; for (b) *vice versa* is the case. For both, the shape, size and distribution of the particles are the same. The SAXS intensities from (a) and (b) become the same except for when the scattering value of $s = 0$, because

$$I_a(s) \propto N (\Delta\rho V)^2,$$

and

$$I_b(s) \propto N (-\Delta\rho V)^2. \quad (5)$$

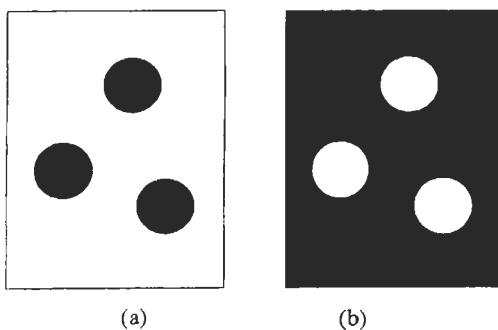


Fig. 3. Complementary system.

This equality of scattering intensities for the complementary system is called the Babinet theorem. For carbon materials, the black region in Fig. 3 refers to the carbon matrix with an average electron density ρ and the white region refers to pores or voids where the electron density is zero. Namely, it is permitted for the sake of convenience to say that the scatterers are pores as for case in Fig. 3b.

2.3 Dividing Reciprocal Space into Three Regions

Different types of structural information are contained within SAXS intensities, being dependent on the magnitude of the scattering parameter s . It is convenient to divide the SAXS intensity curve into three regions as shown in Fig. 4. The corresponding real spaces are also shown. As described in Section 2.2.1 information on the larger scale in real space appears in the smaller s -region and *vice versa*. Information on the size of a particle, namely gyration radius R_g (see Section 3.1) is obtained from the analysis of the scattering intensity of Region I. This region ranges from 0 to about $1/R_g$ in s value and is called the Guinier region. The information on the shape of the scatterer appears in Region II. Analyses to determine the shape are effective in this region, where, for example, a cross-sectional plot is applicable to a cylindrical structure and a thickness plot to a disk-like structure. The information on roughness of the surface of a particle or a boundary of two substances with different electron densities is obtained from Region III. This region is often called the Porod region.

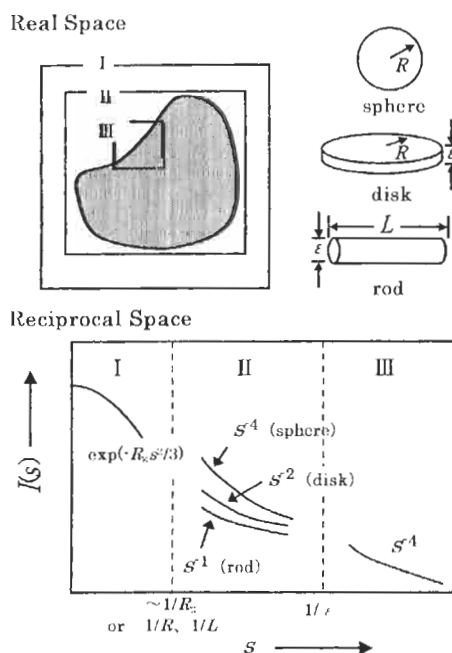


Fig. 4. Three regions in small-angle scattering curves and information obtained from them.

From an analysis of this region can be estimated a surface fractal dimension which indicates self-similarity of roughness on the surface or boundary. The boundary of Region II and III is at about $s = 1/r_{\min}$, where r_{\min} corresponds to the minimum value of the characteristic length of the particle.

3 Analyses

The several kinds of structural information included in the SAXS intensities interweave with each other. In analyses of SAXS data, it is important to keep in mind what information is needed and which analyses or approximations are adequate. Below, typical analyses of SAXS data are presented.

3.1 Gyration Radius: The Guinier Plot

The gyration radius of a particle [1] is defined by

$$R_g^2 = \frac{\int \rho(r)r^2 dV}{\int \rho(r)dV} = \frac{\int \rho(r)r^2 dV}{n} \quad (6)$$

where n is the total number of electrons in the particle and the integral is performed over the volume of the particle. Namely, nR_g^2 is equal to the second moment of the particle with the weight of electron density $\rho(r)$. For a homogeneous particle in which $\rho(r)$ is assumed to be constant ρ , Eq. (6) is rewritten by

$$R_g^2 = \frac{\rho \int r^2 dV}{n} \quad (7)$$

The relations between shape parameters of the particle and gyration radius are shown in Table 1. For a spherical particle, the radius R becomes

$$R = \sqrt{\frac{5}{3}} R_g \quad (8)$$

Table 1

Shape parameters and gyration radius (R_g)

| Shape | Shape parameter | Relation |
|----------------------------|-------------------------|-------------------------------|
| Sphere | radius R | $R_g^2 = (3/5)R^2$ |
| Cylinder | radius R , height L | $R_g^2 = R^2/2 + L^2/12$ |
| Ellipsoid | aces $2a, 2a, 2va$ | $R_g^2 = a^2(2 + v^2)/5$ |
| Rectangular parallelepiped | $2a, 2b, 2c$ | $R_g^2 = (a^2 + b^2 + c^2)/3$ |

In the Guinier region (Region I in Section 2.3), the scattering intensity from a particle is approximated to

$$I(s) = I_0 n^2 \exp\left(-\frac{R_g^2}{3} s^2\right) \quad (9)$$

where I_0 is a constant which includes the intensity of the incident X-rays, and the scattering power of an electron. For a system in which there are N particles with the same volumes and shapes and which, moreover, are separated from each other so as to have no structural correlation, Eq. (9) becomes

$$I(s) = NI_0 n^2 \exp\left(-\frac{R_g^2}{3} s^2\right) \quad (10)$$

By taking logarithms, the following relationship is obtained

$$\ln(I) = \ln(NI_0 n^2) - \frac{R_g^2}{3} s^2 \quad (11)$$

Namely, when a plot of $\ln(I)$ versus s^2 becomes a straight line, we obtain a value of R_g from the gradient. This analysis is called the Guinier plot.

This is the most popular and simplest analysis of SAXS data [1]. However, care must be taken in its application because Eq. (10) or Eq. (11) is valid only when the following assumptions or conditions are realized:

1. The region where the plot is performed must be in the Guinier region, namely $0 < s < 1/R_g$.
2. The scatterers (particles) are distributed in a medium and are separated from each other so as to have no structural correlation.
3. The shape and the volume of the scatterers are identical.

If the concentration of the scatterers becomes high, waves are observed on the scattering curve. For example, the curve of Fig. 1 is for GC (glass-like carbon) of HTT = 3000°C [4].

3.2 Determination of Shape

Information on the shape of scatterers is contained in Region II as mentioned in Section 2.3. Consider now the limiting cases for shape, i.e., a sphere, a rod with infinite length and a disk with an infinite area. If $\ln(I(s))$ for each particle is plotted against $\ln(s)$, the plot forms a straight line in Region II, the slope of which is listed in Table 2. For a long and slender scatterer such as a column, the cross-sectional plot, given by Eq. (12), is effective [3,5]:

$$\ln(I(s)s) = \ln(I(0)s) - R_c^2 s^2/2 \quad (12)$$

Table 2

Limiting law for particle scattering

| Shape | Slope |
|--------------------------|-------|
| Sphere | -4 |
| Rod with infinite length | -1 |
| Disk with infinite area | -2 |

where R_c is a gyration radius of the bottom of the column. This plot corresponds to cancelling the effect of s^{-1} on scattering intensity from the length of a slender particle as shown by the power law (Table 2). Values of R_c of the particle can be estimated from the slope if the plot of $\ln(I(s)s)$ versus s^2 is a straight line. Further, there is the following relation between R_c and radius of the column bottom R ,

$$R = \sqrt{2}R_c \quad (13)$$

We can estimate the gyration radius of the thickness of a disk (R_t) with a large area, by the thickness plot given by [6]:

$$\ln(I(s)s^2) = \ln(I(0)s^2) - R_t^2 s^2 \quad (14)$$

The thickness of the disk (t) is related to R_t by:

$$t = \sqrt{12}R_t \quad (15)$$

3.3 Distance Distribution Function

The real space is mathematically connected to the reciprocal space by way of the Fourier transform. The distance distribution function $P(r)$ [2] is introduced as an example of Fourier transform analyses. The function is given by:

$$P(r) = \frac{2}{\pi} \int_0^{\infty} I(s)sr \sin(sr) \exp(-Bs^2) ds \quad (16)$$

where B is the damping factor to remove the termination errors of the Fourier transform. The function $P(r)/4\pi r^2$ is a value proportional to the probability that we can put two points with the distance r in the region with the same electron density. The function $P(r)/4\pi r^2$ corresponds to the radial distribution function which is familiar in descriptions of liquid structures. In a usual liquid, the distribution of molecules around a given molecule is discussed. Because the particles are larger in systems

treated by SAXS, a given particle is included in the discussion of the radial distribution function as the distance distribution function. For porosity in carbons, the size of a given pore is usually discussed with the distance distribution function.

The gyration radius, R_g , can also be obtained from the distance distribution function from

$$R_g^2 = \frac{\int_V r^2 P(r) dr}{2 \int_V P(r) dr} \quad (17)$$

3.4 Surface Fractal Dimension

For porous materials, the surfaces of pores are often rough. If the roughness has a self-similarity, it can be described by the concept of a surface fractal. SAXS intensities at relatively large s -region (Region III in Section 2.3) contain information of the fractal features of scatterers. Bale and Schmidt indicate how surface fractal dimensions can be obtained from the SAXS intensities [7,8]. According to Bale and Schmidt, the surface fractal dimension D_s is given by

$$D_s = \alpha + 6 \quad (18)$$

where α is the gradient when the plot of $\ln(I)$ versus $\ln(s)$ forms a straight line.

4 Examples of Structure Determination [9]

As an example of the application of the SAXS method to carbons, a pore structure determination is presented below for carbon fibers prepared by the polymer blend technique [9]. The technique is a novel one to make porous carbon fibers without activation. It uses a polymer blend of a carbon precursor resin that forms the matrix by carbonization and a pore-forming resin that disappears during pyrolysis [10,11]. Different types of fibers depending on the combination of polymers can be produced by this method. Moreover, pore sizes and their distributions can be designed by controlling the composition of pore-forming resin and their contents in the blends. Overall, structural determinations of porosity in carbons is difficult, because several factors interweave with each other. The following factors need to be considered: (a) adsorption of molecules into the open pores [12,13]; (b) the variation of pore size and shape in carbons; and (c) a structural correlation of pores. The example given below is a standard SAXS procedure in which the above troublesome factors (a) to (c) are removed to give reliable information of pore sizes and distributions.

The polymer blend of this study was made up of a mixture of phenol-formaldehyde resin as carbon precursor and polystyrene (10 wt%, grain size 20 nm) as the pore-forming resin. This polymer blend was spun, stabilized and carbonized into carbon fibers. Two different carbons, HTT 500 and 1000°C, Carbons A and B respectively,

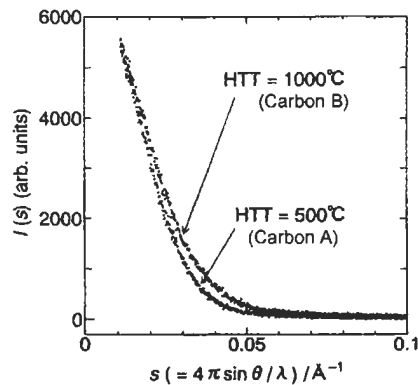


Fig. 5. The scattering patterns of Carbon A (500°C) and Carbon B (1000°C).

were prepared and studied. This combination of resins produced carbons with closed pores. The diameter of the fibers was ~ 0.1 mm, this size not affecting the small-angle X-ray scattering intensities in the measurable region used.

The SAXS patterns are shown in Fig. 5. Initially, an analysis of the intensity, $I(s)$, is in arbitrary units but is then normalized to the scattering intensity from the same number of carbon atoms. The scattering intensity of Carbon B is stronger than that of Carbon A overall, with the scattering patterns almost overlapping each other in the lower and higher s -regions. An analysis of the pore structure was tried initially using the Guinier analysis. It was noted that the Guinier analysis was effective in the region of $s = 0 - (1/R_g) \text{ \AA}^{-1}$ (the Guinier region). Therefore, regression lines were drawn to fit the experimental data of the lower s^2 region, as shown in Fig. 6. From the gradients of the lines, we obtained values of R_g of 71 \AA (7.1 nm) for Carbon A and 69 \AA (6.9 nm) for Carbon B, respectively. The s^2 -values corresponding to $(1/R_g)^2$ are shown by broken lines. The linearity of the Guinier plots, in the Guinier region, provides 71 \AA and 69 \AA as acceptable R_g values.

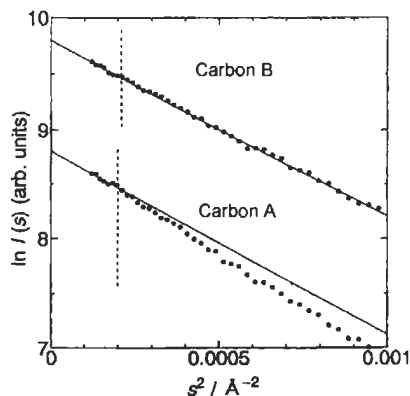


Fig. 6. Guinier plots; the plot for Carbon B is displaced by +1 unit for clarity.

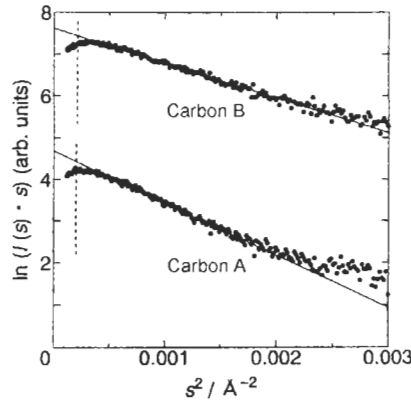


Fig. 7. Cross-section plots. The plot for Carbon B is displaced by +3 unit for clarity.

The R_g values of both carbons are almost identical. However, the Guinier plots differ from each other as shown in Fig. 6. The experimental points for Carbon A deviate only slightly from the regression line in s^2 -region, with the experimental points for Carbon B being on the regression line over a wider range. This fact shows that the shapes of the pores for the two samples are different. The information on the shape of pores is included in the scattering pattern in the larger region than in the Guinier region (Region II in Section 2.3). Useful analyses of the cross-section plots are described in Section 3.2 with results of the cross-section plots being shown in Fig. 7. The plots form two straight lines in respective regions, from whose gradients were obtained 50 \AA for Carbon A and 41 \AA for Carbon B for R_c values. The s^2 -values corresponding to $(1/R_g)^2$ are shown as dotted lines. Figure 7 shows that the cross-sectional plots of the both carbons show linearity in this region. It is reasonable to assume that the grains of the pore-forming resin, polystyrene, are deformed to a narrower shape by spinning from the spherical starting shape. It is assumed that the deformed shape is column-like with the long axis along the direction of spinning. From the R_c values and Eq. 13, values of the radius of column bottom R for Carbons A and B become 71 \AA and 58 \AA , respectively. For the column with the radius R and height L , the gyration radius R_g is given by

$$R_g^2 = \frac{R^2}{2} + \frac{L^2}{12} \quad (19)$$

From Eq. (19), we can determine values of L as 174 \AA (17.4 nm) for Carbon A and 192 \AA (19.2 nm) for Carbon B. The structure parameters of the two samples are summarized in Table 3. For Carbon B, the ratio of the diameter ($2R$) and the height (L) becomes about 1:1.66. It is known that for a column with a ratio of 1:1.65 the Guinier plot shows linearity in the wide region [1]. This is because the Guinier plot for Carbon B is more linear in the wider region than in the Guinier region (Fig. 6).

Table 3

Structure parameters for Carbon A (500°C) and Carbon B (1000°C). R_g^a is the gyration radius obtained from the Guinier plot. R_g^b is the one from the distance distribution function. R_c is the one of the cross section plot. R and L are radius and height of column, respectively.

| Carbon | $R_g^a/\text{\AA}$ | $R_c/\text{\AA}$ | $R/\text{\AA}$ | $L/\text{\AA}$ | $R_g^b/\text{\AA}$ |
|--------|--------------------|------------------|----------------|----------------|--------------------|
| A | 71 ± 3 | 50 ± 1 | 71 ± 2 | 174 | 72 |
| B | 69 ± 3 | 41 ± 1 | 58 ± 1 | 192 | 67 |

Secondly, R_g values were obtained by using the distance distribution function (Eqs. (16) and (17)), because here the Guinier regions are narrow in the measurable region due to the relatively large values of R_g for these carbons. The distance distribution functions for Carbons A and B are shown in Fig. 8. The calculated R_g values from the obtained $P(r)$ s and Eq. (5) become 72 \AA for Carbon A and 67 \AA for Carbon B, agreeing with those obtained from the Guinier analysis. The r values at which the $P(r)$ curve crosses the 0 line correspond to the longest distance of the pore. From Fig. 8, the longest distances refer to 226 \AA for Carbon A and 230 \AA for Carbon B. We assume that the shapes of the pores are columns and the sizes are determined by the R_g value from the Guinier plots and the cross-section plots. From these values, the longest distances become 225 \AA for Carbon A and 224 \AA for Carbon B, which are also consistent with results from the analysis of the distance distribution function. In order to study the pore structure of the carbon fiber, two different analyses were made, i.e. (the Guinier analysis) + (the cross-section one) and the Fourier transform analysis to give the distance distribution function. These results are consistent with each other and show that the structure determination can be performed with high reliability.

The plots of $\log(I(s))$ versus $\log(s)$ are shown in Fig. 9. The slopes of both regression lines are -4.0 in the Porod region (Region III), indicating that the surfaces of the pores are relatively smooth and have no fractal features.

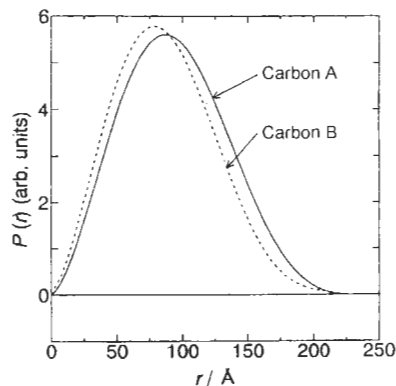


Fig. 8. The distance distribution functions $P(r)$ of Carbon A (500°C) and Carbon B (1000°C).

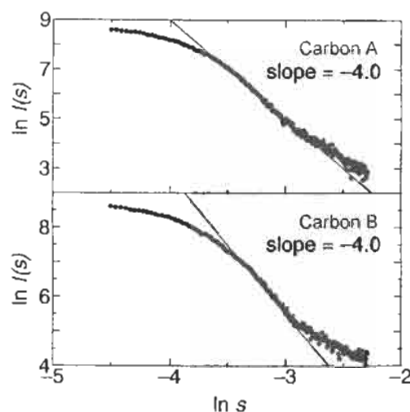


Fig. 9. The plots of $\ln(I(s))$ vs. $\ln(s)$.

There have been several reports of analyses of pore structure of carbon fibers as studied by SAXS measurements. The above study is considered as being quite successful for pore structure determinations. This is because (a) the pores are closed so that they are free from the influence of adsorbing molecules, and because (b) the pores are uniform in shape and size by controlling the sizes of the particles of the pore-forming resin and their concentrations.

References

1. A. Guinier and G. Fournet (translation by C.B. Walker), *Small-angle Scattering of X-rays*. Wiley, New York, 1955.
2. O. Glatter and O. Kratky (Eds.), *Small Angle X-ray Scattering*. Academic Press, London, 1982.
3. G.W. Taylor (Ed.), *Structure Analysis by Small-angle X-ray and Neutron Scattering*. Plenum Press, New York, 1987.
4. K. Nishikawa, K. Fukuyama and T. Nishizawa, Structure change of glass-like carbon with heat treatment, studied by small angle X-ray scattering (I). Glass-like carbon prepared from phenolic resin. *Jpn. J. Appl. Phys.*, 37: 6486–6491, 1998.
5. A. Mittelbach, Zur Röntgenkleinwinkelstreuung verdünnter kolloider systeme. *Acta Physica Austriac*, 19: 53–102, 1964.
6. H. Matsuoka, *Small-angle Scattering in Colloid Science IV*. Chemical Society of Japan (ed.), Tokyo Kagaku Dozin, Tokyo, 1996 (in Japanese).
7. H.D. Bale and P.W. Schmidt, Small-angle X-ray scattering investigation of submicroscopic porosity with fractal properties. *Phys. Rev. Lett.*, 53: 596–599, 1984.
8. P.W. Schmidt, Use of scattering to determine the fractal dimension, In: D. Avnir (Ed.), *The Fractal Approach to Heterogeneous Chemistry*. Wiley, New York, 1989.
9. K. Fukuyama, Y. Kasahara, N. Kasahara, A. Oya and K. Nishikawa, Small-angle X-ray scattering study of pore structure of carbon fibers prepared from a polymer blend of phenolic resin and polystyrene. *Carbon*, 39: 287–290, 2001.
10. J. Ozaki, N. Endo, W. Ohizumi, K. Igarashi, M. Nakahara, A. Oya, S. Yoshida and T. Iizuka, Novel preparation method for the production of mesoporous carbon fiber from a polymer blend. *Carbon*, 35: 1031–1033, 1997.

11. A. Oya and N. Kasahara, Preparation of thin carbo fibers from phenol-formaldehyde polymer micro-beads dispersed in polyethylene matrix. *Carbon*, 38: 1141–1144, 2000.
12. K. Kaneko, Y. Fujiwara and K. Nishikawa, The micropore swelling of activated carbon fibers with water adsorption studies by use of in situ small-angle X-ray scattering. *J. Colloid Interface Sci.*, 127: 298–299, 1989.
13. Y. Fujiwara, K. Nishikawa, T. Iijima and K. Kaneko, Simulation of small-angle X-ray scattering behavior of activated carbon fibers adsorbing water. *J. Chem. Soc. Faraday Trans.*, 87: 2763–2768, 1991.

Chapter 12

XAFS Analysis and Applications to Carbons and Catalysts

Hiromi Yamashita

Department of Applied Chemistry, Osaka Prefecture University, Sakai, Osaka 599-8531, Japan

Abstract: X-ray absorption fine structure (XAFS) analysis, i.e., EXAFS (Extended X-ray Absorption Fine Structure) and XANES (X-ray Absorption Near Edge Structure), provides quantitative information about such structural parameters as atomic distances and coordination geometry. XAFS analysis is associated with the synchrotron radiation technique. In this chapter, interactions between X-rays and materials, the fundamental principles of XAFS, measurement procedures, analyses of data from EXAFS/XANES, and applications of XAFS analysis to carbons and catalysts are presented. XAFS analysis has several advantages in the analyses of materials. These include: (1) liquid and gas samples and amorphous materials can be analyzed; (2) non-destructive experimentation is possible and measuring conditions can be selected freely; (3) *in-situ* measurements under experimental conditions are possible; (4) local structures can be analyzed for each element even in mixtures; and (5) analyses of elements at low concentrations are possible. Recently, such new measuring techniques as time-resolved XAFS measurements have become available, with *in-situ* measurement techniques being developed. With these benefits, XAFS analysis is a very powerful tool to elucidate local structures in carbons and catalysts.

Keywords: X-ray absorption, XAFS, EXAFS, XANES, Carbon material, Catalyst.

1 Introduction

Since the discovery of X-rays by Röntgen in 1895, the analysis technique using X-rays as a probe has developed further with the understanding of how X-rays interact with materials. Recent remarkable progress in synchrotron radiation analysis enables the use of powerful X-rays for the analyses of materials. As a useful means of giving quantitative information about local structure of materials, the analysis using X-ray absorption fine structure (XAFS) techniques has moved rapidly to wider research fields related to such materials as catalysts, metals, semiconductors and metal complex compounds [1]. X-ray diffraction studies are not useful to analyze materials without structural long range ordering such as amorphous materials and ultra-fine particles; however, analysis by XAFS, i.e. EXAFS (Extended X-ray Absorption Fine

Structure) and XANES (X-Ray Absorption Near Edge Structure), does give quantitative information about local structure such as atomic distance and coordination geometry. XAFS analysis has developed with the progress of synchrotron radiation techniques and has been utilized successfully [2–8].

In this chapter, an outline of the interactions between X-rays and materials is given, followed by some examples of applications of XAFS, fundamental principals, measurement procedures, and analyses of data of EXAFS/XANES which give quantitative information on atomic distances and coordination numbers.

2 XAFS Analysis

2.1 Interaction between X-rays and Materials

X-rays are electromagnetic waves with wavelengths of 0.1 to several 10 nm and energies of 0.1–100 keV (Fig. 1). X-rays with the shorter wavelengths are called hard X-rays and have a high transmission ability, while X-rays with the longer wavelengths

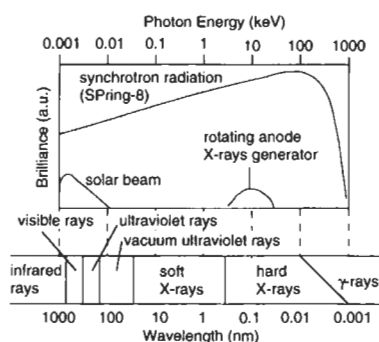


Fig. 1. Wavelength and brightness of X-rays in synchrotron radiation emissions.

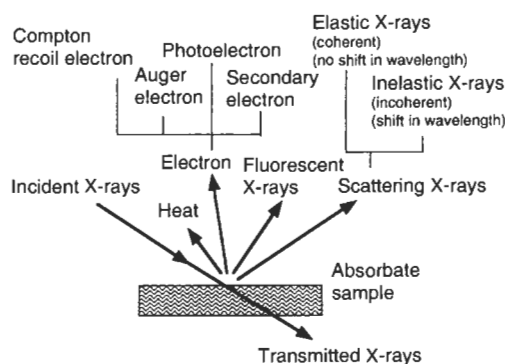


Fig. 2. Interaction between X-rays and materials.

are called soft X-rays. Usually, X-rays are generated by the collision of thermoelectrons accelerated in a high voltage field onto a metallic target. Such X-rays have a continuous spectrum of energies and the characteristic X-rays have a line spectrum. Recently, synchrotron radiation systems have been developed with an intense source of X-rays generated with a wide spectrum of energies. When X-rays irradiate materials, such phenomena as absorption, scattering and release of secondary waves occur with emissions of transmitted X-rays, scattered X-rays, fluorescent X-rays, photoelectrons and Auger electrons as well as heat (Fig. 2). In XAFS measurements, an absorption coefficient is obtained by monitoring the incident X-rays, the transmitted X-rays, fluorescent X-rays, or secondary electrons.

2.2 EXAFS/XANES Principles

EXAFS/XANES measures extents of absorption of X-rays by materials. Using a continuous range of X-ray energies, intensities of incident X-rays (I_0) and transmitted X-rays (I) are measured. Figure 3 is an X-ray absorption spectrum showing the variation of absorption coefficients of samples with energy of the X-rays ($\mu t = \ln(I_0/I)$, (t : thickness of samples, μ : total absorption coefficient). When the energy of X-rays is large enough to cause an electron to jump from a K level or L level (absorption edge), X-rays are absorbed and photoelectrons are emitted as a spherical wave. Oscillation (fine structure) is generated in the absorption spectrum by interference between the wave scattered from surrounding atoms (scattering atoms) and the direct wave being emitted from the absorption atom.

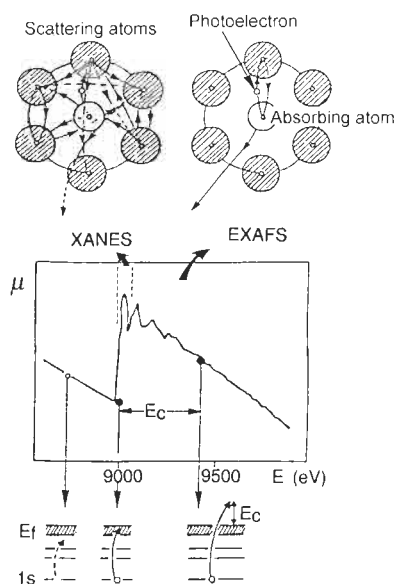


Fig. 3. Mechanism of XANES and EXAFS formation.

The oscillation (fine structure) observed in the energy region, ~ 50 to 1000 eV higher than the absorption edge, is called an EXAFS oscillation and is expressed as a function of wave number k ,

$$\chi(k) = \sum A_j(k) \sin(2kR_j + \phi_j(k)) \quad (1)$$

in which $A_j(k)$ is the amplitude intensity and the oscillation structure of EXAFS is shown in terms of a sine function. The amplitude part, $A_j(k)$, can be approximated to

$$A_j(k) = N_j / (kR_j^2) F_j(\pi, k) \exp(-2\sigma_j^2 k^2) \exp(-2R_j/\lambda) S(k) \quad (2)$$

where N_j is the number of scattering atoms located at the atomic distance of R_j , $F_j(\pi, k)$ is the back-scattering amplitude, $\exp(-2\sigma_j^2 k^2)$ is the decay attributed to the thermal atomic vibration and the structural distortion (σ_j : Debye-Waller factors), $\exp(-2R_j/\lambda)$ is the decay due to the inelastic scattering during the electron movement (λ : mean free path), and $S(k)$ is a term related to the lifetime of a relaxation process from the excited state generated by an electron transition from an inner shell.

Figure 4 shows EXAFS spectra at the K-edge of iron, nickel and copper metal foils. Although the energy regions of these spectra are different, both nickel and copper show similar spectra because they have face-centered cubic structures. On the other hand, iron with a body-centered cubic structure has a spectrum which completely differs from the spectra of nickel and copper. Thus, EXAFS spectra elucidate specific structures of materials [6].

From the procedures used for extraction of EXAFS oscillations, and the procedures of Fourier transformations and curve-fitting of measured signals to theoretical equations, then distances between absorption atoms and scattering atoms can be calculated from the oscillation frequencies. Further, coordination numbers can be determined quantitatively from amplitude intensities.

XANES measures strong oscillations observed within the region of 50 eV, from an absorption edge. Here, because of its small kinetic energy, a photoelectron receives

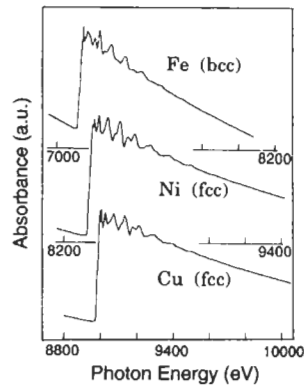


Fig. 4. X-ray absorption spectra of Fe, Ni and Cu foils.

strong perturbations from surrounding atoms when interactions between the direct wave and the multi scattering wave become important. Because the multi-scattering wave is affected not only by atomic distance but also by the coordination geometry of surrounding atoms, XANES is very sensitive to these structural factors. XANES corresponds to the process of excitation of an inner shell electron to a vacant level across to the Fermi level, the information relating to the electronic state (valence number) of an absorption atom being included.

Figure 5 shows K-edge XANES spectra of iron oxide (FeO), nickel oxide (NiO), and zinc ferrite (ZnFe_2O_4). These spectra consist of a pre-edge peak, an edge peak and post-edge peaks. Although the line features of FeO and NiO, which have the crystal structure of rock salt, are similar to each other, the spectrum of ZnFe_2O_4 , which has a crystal structure of an inverse spinel type, is considerably different from the others so reflecting the differences in crystal structure. The small absorption peak, before the edge absorption ($1s \rightarrow 4p$ transition), is called a pre-edge peak and is assigned to a $1s \rightarrow 3d$ transition. Although this $1s \rightarrow 3d$ transition is dipole prohibited with an isolated atom, a small peak due to the $1s \rightarrow 3d$ transition can be observed with solid samples accompanied by a decrease in the coordination symmetry. The pre-edge peak increases its intensity reflecting the decrease in the symmetry and increases in the vacancy of $3d$ orbits ($\text{Ni} < \text{FeO} < \text{ZnFe}_2\text{O}_4$). The splitting in the pre-edge peak of FeO and ZnFe_2O_4 is attributed to the crystal field splitting of d -orbitals (t_{2g}, e_g) [6,9]. In this way, from the positions and features of a XANES spectrum, the electronic state and coordination geometry (symmetry) of an absorption atom can be qualitatively estimated. In terms of experimentation, XANES requires high resolution X-rays to provide accurate peak positions and fine structures; EXAFS requires high intensity X-rays to provide spectra with high S/N ratios to analyze decayed EXAFS oscillations.

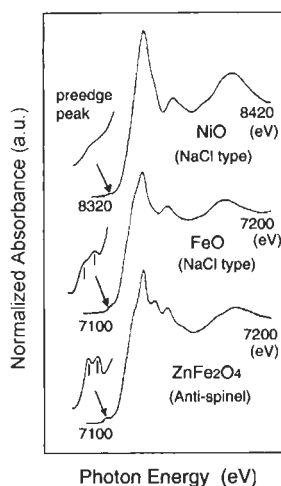


Fig. 5. XANES spectra of NiO, FeO and ZnFe_2O_4 .

2.3 Advantages and Disadvantages of XAFS Analysis

XAFS analysis offers specific advantages in the analyses of materials.

1. Liquid and gas samples and solids such as amorphous materials and ultra-fine particles can be analyzed, because long-range structural ordering is not a pre-requisite.
2. Non-destructive experiments are possible and measuring conditions are not critical ranging from temperatures of liquid helium (4 K to $\sim 1000^{\circ}\text{C}$, and pressures from nPa to 10 MPa).
3. *In-situ* measurements under reaction conditions are possible.
4. Because absorption edge energies are characteristic of an atom, local structures for each element of a mixture can be analyzed.
5. Analyses of elements at low concentrations are possible. Concentrations of ~ 500 ppm and about 0.5 wt% of a particular element can be analyzed using the fluorescence and transmission modes, respectively.

On the other hand, there are several disadvantages:

1. When a sample is made up of several different phases containing the same element, an observed XAFS spectrum is an average of spectra from the different phases. Hence, it is difficult to identify materials from a mixture of phases by XAFS.
2. In order to gain information of local structures, a complicated procedure for spectral analysis has to be gone through.
3. Structural information in three dimensions and long-distance ordering cannot be obtained from XAFS, unlike X-ray crystal structural analysis using XRD.

2.4 Instruments and Measurement Procedures

Because X-rays of high intensity in the wide wavelength (energy) region are indispensable for the rapid measurement of accurate XAFS spectra, synchrotron radiation is used. The process consists of several steps, namely the generation of X-rays, production of monochromatic X-ray radiation, irradiation of samples by X-rays, and the measurement of absorption coefficients by monitoring the incident X-rays and transmitted X-rays.

2.4.1 Utilization of X-rays from Synchrotron Radiation

Synchrotron radiation is a powerful electromagnetic wave emitted in a direction tangential to the synchrotron orbit. The movement in the directions of the electrons or positrons, and acceleration to velocities near to the speed of light, led to the accumulative storage ring, are then changed by a magnetic field under vacuum [10]. Characteristics of synchrotron radiation are (1) light of strong intensity, (2) continuous light, (3) light with strong direction, (4) pure light as generated under an ultra-high vacuum, (5) polarized light, and (6) pulse light. The synchrotron radiation

is a powerful continuous light in the region from hard X-rays to soft X-rays where it is usual for XAFS measurements to be made.

2.4.2 Monochromatic radiation

X-rays emitted from a synchrotron need to be monochromatized. To do this crystals of Si(111) and Si(311) are used for hard X-rays ($> \sim 5$ keV) and crystals of Ge(111) and InSb(111) are used for soft X-rays ($< \sim 4$ keV).

2.4.3 Measurement of X-ray absorption coefficients

Methods of measurement depend on whether transmitted X-rays, fluorescent X-rays, or photoelectrons are monitored when the sample is irradiated with incident X-rays.

(a) *Transmission mode*: This method offers the highest rewards from measurements using hard X-rays. Figure 6 shows that intensities of primary incident X-rays (I_0) and of transmitted X-rays (I) are measured using ionization chambers. Special attention is given to the thickness, thickness homogeneity and contamination of samples.

(b) *Fluorescence mode*: XAFS can be also observed from the fluorescent X-rays emitted by X-ray absorption of specified atoms. This approach is particularly effective for XAFS measurement using dilute samples and for surface adsorption situations (Fig. 7). The sensitivity of a fluorescence mode measurement is extremely high when compared with transmission mode measurements.

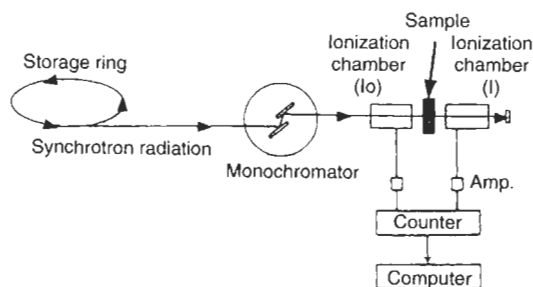


Fig. 6. System for XAFS measurements in the transmittance mode using synchrotron radiation.

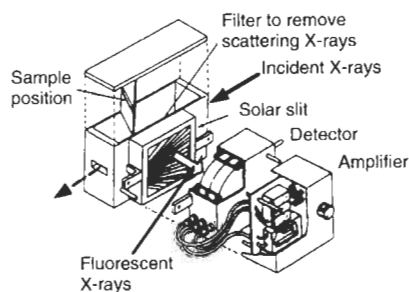


Fig. 7. Detector for XAFS measurements in the fluorescence mode (Lytle box).

(c) *Total electron yield method*: XAFS can be observed by measuring the total yield of Auger electrons and secondary electrons emitted following absorption of X-rays by atoms. Because the escape depth of an electron is very shallow, XAFS of surface structures (< 5.0 nm) can be detected. Measurements have to be made under vacuum.

2.5 *New Measurement Techniques*

New techniques to measure XAFS have recently been developed.

(a) *Total-reflection XAFS*: Surface sensitive XAFS spectra can be monitored by this total-reflection fluorescence technique [11]. When the incident angle of the X-rays is below the critical angle, then total reflection occurs. Under these conditions, as the penetration depth of the incident beam is less than about several nanometers and the X-ray scattering is low, then surface sensitive fluorescence XAFS signals result. Because X-ray radiation from a synchrotron is polarized and brilliant, a combination of the polarization and total reflection fluorescence methods enables anisotropic or asymmetric surface structures to be studied.

(b) *Microprobe XAFS*: In this technique, the X-ray beam is focused using two curved crystal mirrors in both parallel and normal directions or using two-dimensional focusing optics [12]. With the sample at the focus point, XAFS from selected portions of the sample from small spot sizes are seen. Current instruments have a beam diameter of about $1 \mu\text{m}$.

(c) *Time-resolved XAFS*: If XAFS measurements can be made on a short time scale then structural changes within a dynamic process, as chemical reactions, can be studied [12,13]. Time-resolved XAFS are recorded using intense white X-rays focused by a curved polychromator crystal and an energy dispersed monitor using a position sensitive semiconductor detector. Time-resolved XAFS spectra can be measured with resolutions of 10 ms to $100 \mu\text{s}$.

(d) *Laboratory XAFS*: Because synchrotrons are extremely expensive and access time is limited the need exists for the development of laboratory XAFS [14]. To do this a laboratory XAFS system uses a rotating anode X-ray generator, a curved crystal monochromator with Rowland circle geometry and a sensitive semiconductor detector (Fig. 8).

2.6 *Sample Preparation and In-situ Cell*

For measurements in the transmission mode, special attention is paid to sample thickness, homogeneity, and contamination. Although small amounts of general contaminants can be tolerated, small amounts of contamination by an element which absorbs within several hundreds eV of the absorption edge of the studied atom must be prevented. With the fluorescence mode, a correction is sometimes necessary, because the intensity of the fluorescent X-rays is not always proportional to the X-ray absorption coefficient with a thick sample and a sample with high concentrations of the studied atom.

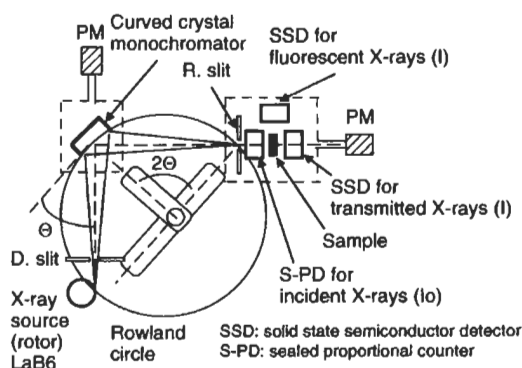


Fig. 8. Laboratory XAFS apparatus system with curved crystal monochromator.

Because non-destructive measurements of XAFS are possible, *in-situ* measurements are made under vacuum, high pressure, and high and low temperatures. Special *in-situ* measurement cells have been developed. The transmission ratio of window materials for the X-rays of the system must be considered. Currently, windows made from Kapton thin film with high transmission ratios are used. Because of the high transmissions by hard X-rays, a thin glass plate can be used as a window in the high energy region.

2.7 Analyses of EXAFS Spectra

An analysis of EXAFS spectrum is carried out as follows (Fig. 9) [8]. Because the EXAFS is observed as a modulation of absorption of about several percent of the

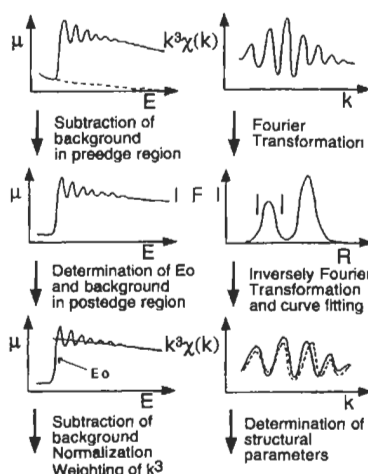


Fig. 9. Procedures for EXAFS analysis.

total absorption in the high energy region of the absorption edge, an analysis of EXAFS should be performed carefully.

2.7.1 Extraction of EXAFS oscillation $\chi(k)$

The EXAFS oscillation $\chi(k)$ can be extracted by a removal of background and by normalization as in the following procedures:

(i) Subtraction of background in the pre-edge region: Note that the absorption coefficient $\mu(k)t = -\ln(I(k)/I_0(k))$, obtained by measuring X-rays intensities (I_0, I) recorded at the front and back of the sample, includes a background from absorption by other elements and edges. These backgrounds can be subtracted by fitting of the spectra in the pre-edge regions to a Victoreen type multinomial expression ($C^*E^{-3} + D^*E^{-4}$), or a McMaster type multinomial expression and by extrapolating into the higher energy regions.

(ii) Determination of absorption edge energy (E_0): Because the EXAFS function $\chi(k)$ is a function of the wave-number of the kinetic energy of a photoelectron,

$$k = 2\pi\sqrt{2m/(h^2(h\nu - E_0))},$$

then the origin of a photoelectron must be decided upon for any method. Usually, absorption edge energy (E_0) is used. This E_0 is conveniently defined as the energy which gives the maximum value in the differentials of absorption spectra. This value is one of several variable parameters in the curve-fitting procedures.

(iii) Subtraction of background in the post-edge region: For the extraction of EXAFS oscillation $\chi(k)$, the absorption curve $\mu_s(k)t$, due to a free isolated atom and the background $\mu_0(k)t$ which cannot be removed by the previous procedure, should be estimated and removed. The smooth background curve, $\mu_0(k)t$, is estimated using the cubic spline technique or a polynomial determined by a least square curve fitting technique (Fig. 10).

(iv) Normalization: Thus obtained, EXAFS oscillations are normalized by the parameter (μ_s) as shown in the following equation:

$$\text{EXAFS function: } \chi(k) = (\mu(k) - \mu_0(k))/\mu_s(k) \quad (3)$$

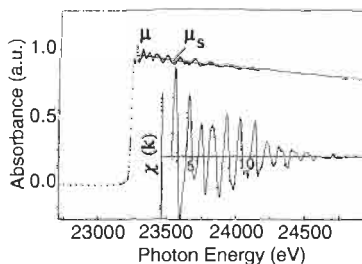


Fig. 10. EXAFS spectrum after subtraction of the background.

Here, $\mu(k)$ is the experimentally recorded absorption coefficient of this edge, the parameter (μ_s) is the absorption by a free isolated atom, and μ_0 is the contribution from the backgrounds. The parameter (μ_s) is estimated by fitting the absorption around the edge neighborhood by a Victoreen relational expression and the tabulated McMaster's relational expression. If an ideal spectrum is obtained, μ_0 can be substituted for μ_s .

2.7.2 Fourier Transformation of EXAFS to *r*-space

The extracted EXAFS function $\chi(k)$ is weighted by k^1 or k^3 . k^3 -Weighting is often used for the analysis of EXAFS. The k^3 -weighting compensates for a reduction in the EXAFS oscillation in the high k -region and diminishes effects of edge jump and ambiguity of E_0 . Fourier transformation of EXAFS function $\chi(k)$ to r -space uses Eq. (4):

$$F(R) = \sqrt{(1/2\pi)} \int (k^3 \chi(k) \exp(-2ikR)) dk \quad (4)$$

The amplitude of $F(R)$ is roughly proportional to the coordination number. The peak position corresponds to the bond distance, when it is shifted to the shorter distance (about 0.3–0.6 Å) by the phase shift $\phi_j(k)$. Depending on a condition of a spectrum, the k range is taken to be ~ 3 – 16 \AA^{-1} . This absolute value $|F(R)|$ reflects a pseudo-radial distribution function in the one dimension of a surrounding atom. The practical atomic distance is evaluated from the following curve-fitting processes.

2.7.3 Optimization of structural parameters

In order to know the accurate atomic distance (R_j) and coordination numbers (N_j), it is necessary to know the inverse Fourier transformation and the curve-fitting procedures.

(i) Inversely Fourier transformation of a specific $F(R)$ peak: By the inverse Fourier transformation to k -space of the selected $F(R)$ peak, the EXAFS oscillations $\chi_j(k)$ due to a group- j of scattering atoms which built up this selected $F(R)$ peak can be extracted. For this reason, this operation is called a Fourier filtering.

(ii) Least square curve fitting: As obtained EXAFS oscillations $\chi_j(k)$ are fitted by a least square curve fitting method to the theoretical oscillations synthesized using the theoretical equation (1) (2) with changing structural parameters of N_j , R_j , σ_j^2 . From these procedures optimized structural parameters can be obtained. At the same time, values of ϕ_j , $F_j(k)$ will be known already from analyses of model compounds having established local structures, the model compounds having structures and electronic states similar to the sample under investigation. When there is no appropriate model compound then theoretical values calculated by Teo and Rehr [15,16] can be used for ϕ_j , and $F_j(k)$, but with these the theoretical values of N_j , R_j , σ_j^2 cannot be decided upon absolutely.

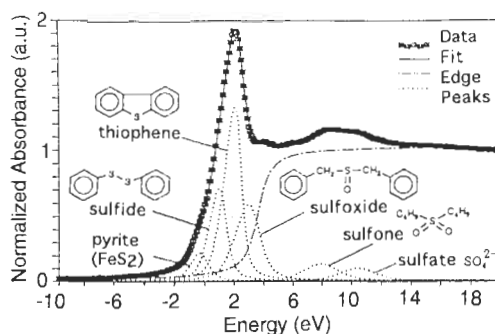


Fig. 11. Least-squares fit of the S K-edge XANES spectra of sulfur compounds included with in coal.

2.8 Analyses of XANES Spectra

Because the amplitude of a XANES spectrum is large enough to be measured even with dilute samples, the electronic state and the coordination geometry of an absorption atom are obtained from the position and fine structures of a XANES spectrum. A normalized XANES spectrum is deconvoluted into a continuum expressed by an arctangent function and a number of peaks expressed by Gaussian or Lorentzian functions and fitted by a non-linear least-squares method. By deconvoluting the XANES spectrum, contents of each atomic element in a mixture can be estimated (Fig. 11) [17].

3 Applications to Carbon Related Materials and Catalysts

XAFS analyses have been used for various materials, even bio-materials, with several studies of carbons, carbon related materials, coal, and catalysts being reviewed below.

3.1 Carbon

Several C K-edge XANES spectra have been studied for aromatic hydrocarbon compounds, in particular π -conjugated polynuclear aromatics (PNA) hydrocarbons, because these compounds give rise to characteristic features in the C 1s $\rightarrow \pi^*$ regions of XANES spectra reflecting their aromatic structures. These C K-edge XANES spectra help understand local structures in such complex carbon materials as carbon fibers, carbons deposited on catalysts and their precursors. The C K-edge XANES spectra are monitored by the total electron yield method.

Figure 12 shows C K-edge XANES spectra of PNA compounds and a spent catalyst with coke depositions in the zeolite cavities [18]. The sharp peaks at about 285 eV are assigned to the transition of C 1s electrons to unoccupied π^* antibonding orbitals (π^* resonance) of aromatic hydrocarbons, while the broad peaks above

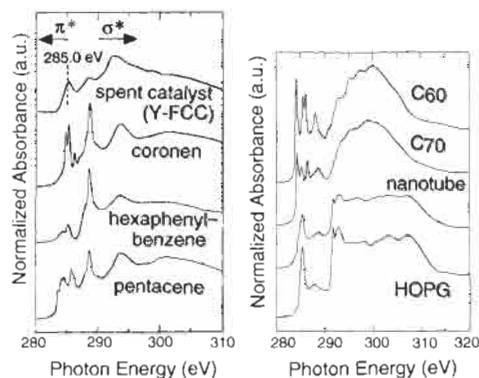


Fig. 12. C K-edge XANES spectra of PNA compounds, HOPG, fullerenes and carbon nanotubes.

290 eV are assigned to transitions mainly to C–C σ^* states (σ^* resonance). The assignment of the peaks between 285 and 290 eV is unclear, because both aromatic π^* resonance and C–H π^* resonance give rise to peaks in this region. By comparing these spectra, the structures of cokes (carbons) deposited on catalysts have been identified [18].

Figure 12 also shows XANES spectra of multi-wall carbon nanotubes, fullerenes and highly oriented pyrolytic graphite (HOPG) [19]. The XANES of carbon nanotubes exhibits a sharp intense peak at 284.5 eV with two broad peaks at 287.7 and 288.7 eV. The peak at 284.5 eV can be assigned to $1s \rightarrow \pi^*$ transitions. The latter two peaks cannot be assigned to the $1s \rightarrow \pi^*$ transition but are assigned to interlayer bands with σ -symmetry by analogy to HOPG. These nanotubes have a concentric multilayer tubular structure consisting of six-membered rings only. The almost infinitely long graphite structure yields a high degeneracy of π^* bands, resulting in a $1s \rightarrow \pi^*$ XANES feature analogous to HOPG. All carbon atoms in the fullerene C_{60} have electronically equivalent environments: each carbon atom is located at the intersection of two six-membered rings and one five-membered ring. The large splitting of the π^* band is ascribed to the presence of five-membered rings as well as six-membered ring. On the other hand, C_{70} contains the intersections of three six-membered rings together with the C_{60} -type intersections resulting in five types of carbon atom with different electronic environments. This feature makes the spectrum of C_{70} more complicated than C_{60} .

3.2 Compounds Dispersed on Carbon Materials

Identification of metal compounds and heteroatom compounds when highly dispersed in carbon-based materials such as fullerenes, graphite, coal, and the clarification of their local structure can be carried out easily by XAFS analysis, because the absorption coefficient of carbon is very small.

3.2.1 Minerals and Catalysts on Coal

The understanding of catalyst performance in coal processing is indispensable to exploration of the future technology of coal conversion, coal pyrolysis, liquefaction and gasification. Much attention should be directed toward a qualitative and quantitative determination of functionalities of catalysts, especially their structure. XAFS is an excellent method to investigate the local structure of a specific element in coal, such as in coal minerals and in catalysts. Compounds at extremely low concentrations (\sim ppm) or compounds in an amorphous state, detected by XRD, can be easily analyzed by XAFS. Various elements diluted in coal, such as Na, Mg, S, Cl, K, Ca, V, Fe, Mo, Sn, Hg, etc., have been investigated [17,20–27]. Usually, the XAFS of light elements such as Na, Mg, etc. is recorded using the total electron yields method, that of elements such as K, Ca, V, etc. is recorded using the fluorescent method and that of the heavy atom elements such as Mo, Sn, etc. using the transmission method, respectively.

Minerals in coal

XAFS is a powerful tool for analyses of mineral matter dispersed in coal. For example, quantitative analyses of all sulfur forms in coal [17], both organic and inorganic, have been carried out by a least-square analysis of the XANES spectrum into a series of peaks of $1s \rightarrow np$ photoelectron transition peaks and resonance scattering peaks, and arctangent step functions representing the transition of the photoelectron to the continuum (Fig. 11). Because the major sulfur forms in coal (pyrite, organic sulfide, thiophene, sulfoxide, sulfone, and sulfate) have characteristic $s \rightarrow p$ transition energies, the relative peak areas are converted to weight percentages of the sulfur form using calibration constants derived from XANES of standard compounds. Such sulfur K-edge XAFS analysis is a non-destructive method to determine sulfur forms in coal.

Figure 13 shows XANES spectra of vanadium minerals contained in coal and coal liquefaction residues [27]. The spectra of V-silicalite zeolite and vanadium compounds are also shown. The most significant difference in the features of these various spectra is a pre-edge peak, assigned to absorptions of the $1s \rightarrow 3d$ transition, appearing at the lower energy region of the edge absorption due to a $1s \rightarrow 4p$ transition. The $1s \rightarrow 3d$ dipole transition is forbidden for a transition metal atom in octahedral symmetry but the weaker quadrupole transition is allowed. For tetrahedral complexes, the lack of a center of inversion permits a dipole transition between the $1s$ and $3d$ character T_2 orbitals, and gives rise to the strong pre-edge peak. With the following compounds, VO (O_h symmetry), V_2O_3 (C_3), V_4O_7 and V_2O_4 (C_1), and V_2O_5 (C_s), local environments around the central vanadium atom lack a center of inversion and the stronger pre-edge peaks are observed. From the intensity and position of the pre-edge peak, identification of vanadium samples is possible [9,26,28]. V-silicalite zeolite has a spectrum similar to $VO(OiPr)_3$, indicating the

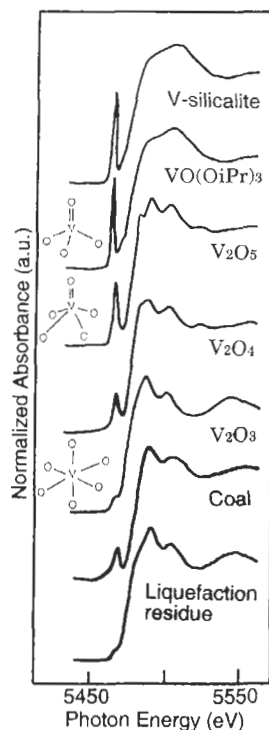


Fig. 13. XANES spectra of vanadium compounds and vanadium species included in coal and coal liquefaction residues.

presence of terminal mono-oxo $(V=O)O_3$ tetrahedra with C_{3v} symmetry. A detailed analysis by the curve-fitting of EXAFS suggests that this $(V=O)O_3$ moiety has perturbations from the neighboring surface OH groups in their electronic state [28]. For vanadium minerals in coal, it was found that vanadium exists in several environments where the vanadium is coordinated to oxygen atoms. There was no evidence for vanadium in nitrogen (porphyrin) or sulfide environments. Coal contains a mixture of vanadium oxide species, which have coordination geometries similar to those of V_2O_3 , V_2O_4 and V-silicalite. It was also found that the vanadium environments in the raw coal did not survive unchanged in a liquefaction process. In the liquefaction residue and the heavy fraction, vanadium species have a coordination similar to that of V_2O_3 , that is, V^{3+} in octahedral oxygen coordination.

The XANES spectra of a Ti-oxide catalyst at the Ti K-edge show several well-defined pre-edge peaks related to the local structures surrounding the titanium atom [27–31]. Also, the relative intensities of the pre-edge peaks provide information on the coordination number surrounding the titanium atom. Bulk powdered anatase and rutile TiO_2 catalysts exhibit three characteristic small pre-edge peaks attributable to the transitions from the 1s core level of titanium to three different molecular orbitals ($1t_{1g}$, $2t_{2g}$, and $3e_g$). On the other hand, tetrahedrally coordinated titanium such as

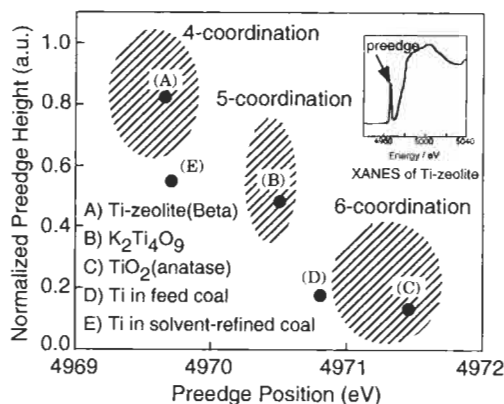


Fig. 14. Plots of normalized height vs energy position of the pre-edge peak in Ti K-edge XANES spectra showing the values observed with titanium compounds and titanium species in coal.

$\text{Ti}(\text{OPr})_4$ was found to exhibit an intense single pre-edge peak because a regular tetrahedron structure lacks an inversion center. From the intensities of pre-edge peaks and their peak positions observed in Ti K-edge XANES spectra (Fig. 14), titanium minerals in coal consist of a mixture of oxides having octahedral and tetrahedral coordination geometry, respectively [27–31].

Catalysts for coal conversion

The chemical form and coordination geometry of catalysts for gasification, pyrolysis and liquefaction of coal have been investigated using XAFS, especially for potassium [32], sodium [23], calcium [24] and iron [20–22,25]. Of the catalysts, iron is an active and cheap catalyst for gasification and liquefaction of coal. To make use of its maximum activity, it is important to know the relationship of the iron catalyst structure to its catalytic activity. The combined use of XAFS and Mössbauer spectroscopy indicates that the structure of iron catalysts, during devolatilization and steam gasification of brown coal impregnated with $\text{Fe}(\text{NO}_3)_3$, depended on catalyst loading, heat-treatment temperature, and extents of char conversion [20–22]. During devolatilization, the chemical form of the iron species changed stepwise with increasing heat-treatment temperature to include atomically dispersed iron species, ultrafine particles of FeOOH , $\gamma\text{-Fe}$ and crystalline species such as $\alpha\text{-Fe}$, Fe_3C , FeO and Fe_3O_4 . Ultrafine particles are too small to be detected by X-ray diffraction, but large enough to exhibit Fe–Fe coordination in the Fourier transforms of EXAFS spectra (FT-EXAFS). At lower iron loadings, the temperature of the above transformation increases. Figure 15 shows the FT-EXAFS of Fe K-edge spectra of iron catalysts during steam gasification of iron-loaded brown coal. In the initial stages of steam gasification, atomically dispersed iron species such as ultrafine FeOOH and $\gamma\text{-Fe}$, transform to ultrafine FeOOH ; other crystalline species transform to Fe_3O_4 . The proportion of the ultrafine FeOOH was higher at low char conversion in the coal with

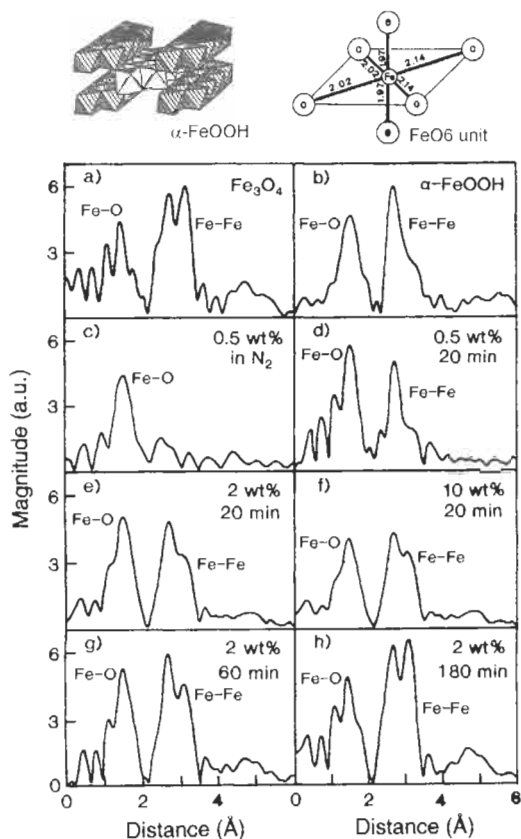


Fig. 15. Fourier transforms of EXAFS spectra with iron catalysts during steam gasification of iron-loaded coal char and the coordination geometry of FeOOH clusters.

a low loading. Ultrafine FeOOH is most likely to be the active component in steam gasification because the reactivity of the system closely follows the contents of ultrafine FeOOH. It was also found that interactions between the elements and oxygen-containing surface-functional groups on carbon are important to keep elements present in a high state of dispersion [20–25].

It is established that calcium is an active catalyst for gasification of carbon by carbon dioxide. Changes in the chemical nature of calcium species during the devolatilization of calcium-loaded coal in nitrogen and the initial stages of gasification by carbon dioxide have been determined by XAFS [24]. Relationships between the chemical form of the calcium species and the precursor salt, coal type, calcium-loading method, and heat treatment temperature are clarified (Fig. 16). In the calcium-loaded coal, calcium species exist in two chemical forms, as atomically dispersed calcium or as an amorphous calcium salt. The content of the former is high when impregnation or iron-exchange methods are used. The content of the latter species is high when large amounts of calcium are loaded or a high-rank coal is used.

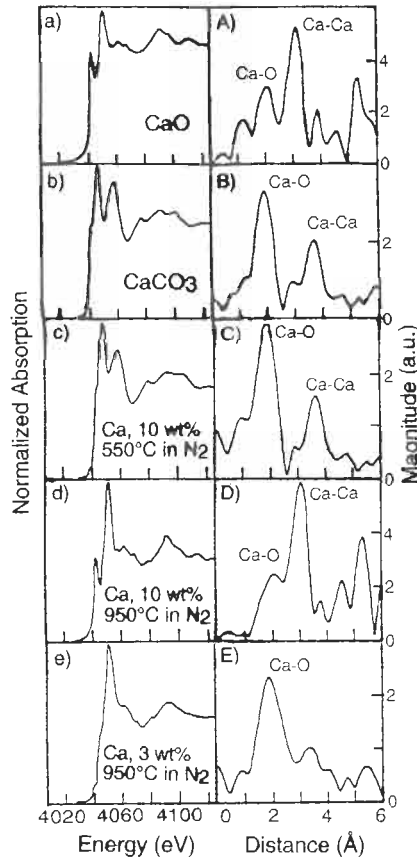


Fig. 16. XANES and Fourier transforms of EXAFS spectra with calcium catalysts after the devolatilization of calcium-loaded brown coal.

The local structure around a highly dispersed calcium atom was partly maintained even at high heat-treatment temperature, but with some calcium atoms having aggregated to form CaO. The amorphous salt aggregated and changed to CaCO₃ at relatively low heat-treatment temperatures. During gasification by carbon dioxide at 650°C, highly dispersed calcium species and CaCO₃ were detected; the former is probably the active species during gasification because catalytic activity closely correlates with content of atomic calcium.

3.2.2 Catalyst Supported on Carbon

The use of carbon as a catalyst support has several advantages such as stability in different reaction media and a high versatility of chemical and physical properties. Especially Pt/carbon and PtSn/carbon catalysts are widely used for various reactions. As catalysts for fuel cells, researchers have focused on studies of these metal-

supported carbon catalysts. The influence of support surface chemistry and metal precursor species on the properties of Pt/carbon and PtSn/carbon catalysts has been analyzed by XAFS measurements [33,34]. The effects of oxidation on the carbon support surface and preparation procedures on interactions of platinum with the support and/or with tin atoms have been clarified. In dried samples, when the carbon surface is pre-oxidized, then interactions of the platinum species with the support are stronger. The two-step impregnation approach, compared with the co-impregnation method, improves platinum-support interactions. The strength of these interactions determines the distribution of the active phase on the carbon support. The structure of the metallic phase after reduction is quite different for systems prepared with oxidized and non-oxidized carbon supports, and is also dependent on preparation procedures. The presence of bimetallic Pt/Sn alloy phases, pure Pt clusters and Pt–O–Sn species was established by XAFS analyses. The relative proportions of these structures in the catalysts and their distribution on the supports, which depend critically on the surface chemistry of the carbon supports, determine catalytic activity.

3.2.3 Metal Fullerenes

The coordination geometry of the metal ions (Ce, Rb, etc.) contained in carbon nanotubes and fullerenes (C_{60} , C_{70}), such as MC_{60} has been investigated by XAFS [35]. The distance between the metal atom (Rb) and the neighboring carbon atoms, determined by XAFS, shows that the metal atom is inside the C_{60} cage and is located off-center.

4 XAFS in the Future

Synchrotron radiation and laboratory XAFS equipment is more widely available now and XAFS (EXAFS/XANES) experimentation has become one of the most powerful of analytical tools. Various new measuring techniques such as time resolved XAFS measurement have been developed and improved, and *in-situ* measurements have provided a new insight into chemical compositions. For the development of new functional materials, new molecular systems must be designed specifically. Expectations of XAFS analysis are high.

References

1. F.W. Lytle, The EXAFS family tree. *J. Synchrotron Rad.*, 6: 123–134, 1999.
2. B.K. Teo, EXAFS: Basic Principles and Data Analysis. Springer, Berlin, 1986.
3. D.C. Koningsberger and R. Prins, X-ray Absorption: Principles, Applications, Techniques of EXAFS, SEXAFS and XANES. Wiley, New York, 1988.
4. Y. Iwasawa, X-ray Absorption Fine Structure for Catalysts and Structure. World Science, Singapore, 1996.
5. Y. Udagawa, X-ray Absorption Fine Structure: XAFS Measurement and Analysis. Gakkai Pub. Center, Tokyo, 1993.

6. T. Tanaka and S. Yishida, Fundamentals of X-ray absorption spectroscopy. In: T. Onishi (Ed.), *Analysis of Solid Surface I*. pp. 149-195, Kodansha, Tokyo, 1995.
7. H. Yamashita and A. Tomita, Structural analysis using X-rays: XRD, XAFS. *J. Jpn. Inst. Energy*, 73: 1199-1206, 1992.
8. H. Yamashita and M. Anpo, Structural Analysis by EXAFS/XANES measurement. *Shikizai*, 69: 266-281, 1996.
9. S. Yoshida and T. Tanaka, Metal oxide catalysts. In: Y. Iwasawa (Ed.), *X-ray Absorption Fine Structure for Catalysts and Structure*. pp. 304-325. World Science, Singapore, 1996.
10. S. Ichimura, Y. Hatano and H. Iguchi, *Synchrotron Radiation*. Kodansha, Tokyo, 1991.
11. M. Shirai and Y. Iwasawa, Total-reflection XAFS. In: Y. Iwasawa (Ed.), *X-ray Absorption Fine Structure for Catalysts and Structure*. pp. 332-344. World Science, Singapore, 1996.
12. H. Oyanagi, XAFS using high brilliance photon sources. In: Y. Iwasawa (Ed.), *X-ray Absorption Fine Structure for Catalysts and Structure*. pp. 383-391. World Science, Singapore, 1996.
13. B.S. Clausen and H. Topsoe, Combined EXAFS/XRD methods. In: Y. Iwasawa (Ed.), *X-ray Absorption Fine Structure for Catalysts and Structure*. pp. 345-353. World Science, Singapore, 1996.
14. Y. Udagawa, Laboratory XAFS. In Y. Iwasawa (Ed.), *X-ray Absorption Fine Structure for Catalysts and Structure*. pp. 131-145. World Science, Singapore, 1996.
15. B.K. Teo and P.A. Lee, *Ab initio* calculations of amplitude and phase functions for extended X-ray absorption fine structure spectroscopy. *J. Am. Chem. Soc.*, 110: 2815-2832, 1979.
16. J.J. Rehr, J.M. Leon, S.I. Zabinsky and R.C. Albers, Theoretical X-ray absorption fine structure standards. *J. Am. Chem. Soc.*, 113: 5135-5140, 1991.
17. G.P. Huffmann, S. Mitra, F.E. Huggins, N. Shah, S. Vaidya and F. Lu, Quantitative analysis of all major forms of sulfur in coal by X-ray absorption fine structure spectroscopy. *Energy Fuels*, 5: 574-581, 1991.
18. H. Shimada, M. Imamura, N. Matsubayashi, T. Saito, T. Tanaka, T. Hayakawa and S. Kure, Characterization of coke deposited on catalysts by carbon K-edge near edge X-ray absorption fine structure spectroscopy. *Topics Catal.*, 10: 265-271, 2000.
19. M. Imamura, H. Shimada, H. Matsubayashi, M. Yumura, K. Uchida, S. Oshima, Y. Kuriki, Y. Yoshimura, T. Sato and A. Nishijima, XANES study on the electronic states of carbon nanotube and related materials. *Physica B*, 208 & 209: 541-543, 1995.
20. H. Yamashita, EXAFS studies on structure of catalyst for coal conversion. *Bull. Inst. Chem. React. Sci. Tohoku Univ.*, pp. 1-22, 1992.
21. H. Yamashita, Y. Ohtsuka, S. Yoshida and A. Tomita, Local structures of metals dispersed on coal. 1. Change of local structure of iron species on brown coal during heat-treatment. *Energy Fuels*, 3: 686-692, 1989.
22. H. Yamashita, Y. Ohtsuka, S. Yoshida and A. Tomita, Local structures of metals dispersed on coal. 2. Ultrafine FeOOH as active iron species for steam gasification of brown coal. *Energy Fuels*, 5: 52-57, 1991.
23. H. Yamashita, S. Yoshida and A. Tomita, Local structures of metals dispersed on coal. 3. Na K-edge XANES studies on structure of sodium gasification catalyst. *Ind. Eng. Chem. Res.*, 30: 1651-1655, 1991.
24. H. Yamashita, M. Nomura and A. Tomita, Local structures of metals dispersed on coal. 4. Local structure of calcium species on coal after heat treatment and CO₂ gasification. *Energy Fuels*, 6: 656-661, 1992.
25. H. Yamashita and A. Tomita, Local structures of metals dispersed on coal. 5. Effect of coal rank and anion on structure of iron species during heat-treatment and steam gasification. *Ind. Eng. Chem. Res.*, 32: 409-415, 1993.

26. D.H. Maylotte, J. Wong, R.L. St. Peters, F.W. Lytle and R.B. Gregor, X-ray absorption spectroscopic investigation of trace vanadium sites in coal. *Science*, 214: 554–556, 1981.
27. F. Farges, G.E. Brown and J.J. Rehr, Coordination chemistry of Ti(IV) in silicate glasses and melts: 1. XAFS study of titanium coordination in oxide model compounds. *Geochim. Cosmochim. Acta*, 60: 3023–3038, 1996.
28. H. Yamashita, J. Zhang, M. Matsuoka and M. Anpo, Design of efficient photocatalysts incorporated within zeolite cavities and frameworks: titanium, vanadium, chromium oxides. In: M. Anpo (Ed.), *Photofunctional Zeolites: Synthesis, Characterization, Photocatalytic Reactions, Light Harvesting*. pp. 129–168. NOVA Sci., New York, 2000.
29. H. Yamashita, S. Kawasaki, Y. Ichihashi, M. Harada, M. Anpo, G. Stewart, M.A. Fox, C. Louis and M. Che, Characterization of titanium-silicon binary oxide catalysts prepared by the sol-gel method and their photocatalytic reactivity for the liquid phase oxidation of 1-octanol. *J. Phys. Chem. B.*, 102: 5870–5875, 1998.
30. H. Yamashita, K. Ikeue, T. Takewaki and M. Anpo, *In situ* XAFS studies on the effects of the hydrophobic-hydrophilic properties of Ti-Beta zeolites in the photocatalytic reduction of CO₂ with H₂O, *Topics Catal.*, 18: 95–100, 2002.
31. D.R. Sandstrom, R.H. Filby, F.W. Lytle and R.B. Gregor, Study of Ti in solvent-refined coal by X-ray absorption spectroscopy. *Fuel*, 61: 195–197, 1982.
32. G.P. Huffman, F.E. Huggins, R.G. Jenkins, A. Piotrowski, F.W. Lytle and R.B. Gregor, Investigation of alkali and alkaline earth coal gasification catalysts by EXAFS spectroscopy. *Fuel*, 65: 1339–1345, 1986.
33. M.C. Martinez, D. Cazorla-Amoros, A. Linares-Solano, C. Salinas-Martinez de Lecea, H. Yamashita and M. Anpo, Metal-support interaction in Pt/C catalysts. Influence of the support surface chemistry and the metal precursor. *Carbon*, 33: 3–15, 1995.
34. M.C. Roman-Martinez, D. Cazorla-Amoros, H. Yamashita, S. de Miguel and O.A. Scelza, XAFS Study of dried and reduced PtSn/C catalysts. Nature and structure of the catalytically active phase. *Langmuir*, 16: 1123–1131, 2000.
35. Y. Kubozono, K. Mimura, Y. Takabayashi, H. Maeda, S. Kashino, S. Emura, Y. Nishihata, T. Uruga, T. Tanaka and M. Takahashi, XAFS study on RhC₆₀. *J. Synchrotron Rad.*, 6: 564–566, 1999.

Chapter 13

X-Ray Photoelectron Spectroscopy and its Application to Carbon

Noboru Suzuki

Utsunomiya University, Utsunomiya 321-8585, Japan

Abstract: X-ray photoelectron spectroscopy (XPS) is a modern technique used for surface analysis of solid materials such as organic compounds, polymers and inorganic carbon materials as well as carbon alloys. In this chapter, the principles and features of XPS are summarized and applications to carbon-containing materials including carbon alloys are described.

Keywords: X-ray photoelectron spectroscopy (XPS), Chemical shift, Surface functionalities, Heteroatoms, Valence band spectrum.

1 Introduction and XPS

X-ray photoelectron spectroscopy (XPS) is a technique for surface analyses. XPS is interchangeably called electron spectroscopy for chemical analysis (ESCA). The applications of XPS are extensive because almost all solid materials are stable in the ultra-high vacuum chamber. Thus, the technique is applicable to metals, semiconductors, inorganic materials and organic materials and to the fields of material science, catalysis, electronics, tribology, corrosion, painting, cosmetics, food, etc. In this article, the principles and features of XPS and applications to carbon materials are discussed.

The physics of XPS is a photoemission process, as illustrated schematically in Fig. 1. When the atoms in the surface region are irradiated with photons from an X-ray source, the core level electrons are emitted from atoms by the photoelectric effect, and then travel to and escape from the surface. Thus, the basics of this process are described by Einstein's equation:

$$E_{\text{kin}} = h\nu - E_{\text{b}} \quad (1)$$

where E_{kin} is the kinetic energy of the photoelectron, $h\nu$ the X-ray photon energy irradiated to the sample surface ($\text{Mg K}\alpha = 1253.6 \text{ eV}$ or $\text{Al K}\alpha = 1486.6 \text{ eV}$ are

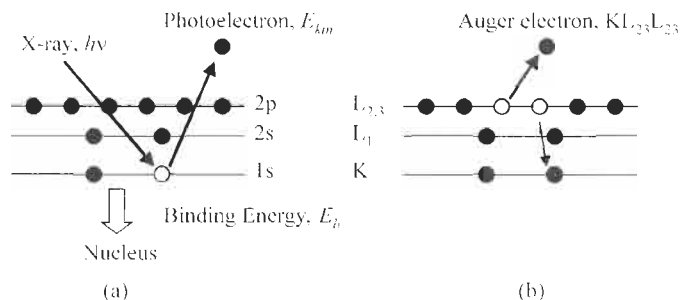


Fig. 1. (a) Photoemission process; electrons are bound to the atom by the positively charged nucleus. (b) The relaxation process after the photoemission (Auger process).

usually used) and E_b the electron binding energy. When $h\nu$ is known and E_{kin} is measured by the spectrometer, values of E_b are easily determined. As each element has its own series of electron binding energies, one can identify the elements in the surface region and determine their concentrations. As shown in Fig. 1, an electron from an outer level falls into the vacancy created by the photoemission process, and then another electron is emitted (Auger process). The Auger peaks also appear in the XPS spectra and are useful to confirm the identity of an element. The binding energies of photoelectrons vary slightly with the chemical nature of the element, i.e. with the valence state or electron structure. This change in binding energy is called *chemical shift*, which is the advantage of XPS analyses. Furthermore, the sophisticated measurements and analyses of XPS spectra give considerable information, as shown in Table 1. Some matters that require attention are listed in Table 2. The principles, apparatus, sample preparation and handling and analytical techniques are described in several books [1–3].

2 C1s Binding Energy

The most important factor for carbon materials is the binding energy of respective chemical states. Table 3 shows a list of C1s binding energies of organic and inorganic materials and functionalities (functional groups). Note that these values are approximate and that different researchers report slightly different values. Information from other analytical techniques, such as IR, UV, temperature programmed desorption (TPD), elemental analysis, etc. is used for a rigorous analysis of the XPS spectrum.

3 Application to Carbon Materials

3.1 Chemical Shift of C1s by Surface Functionalities

XPS is widely used for surface analysis of carbon materials including carbon alloys. The surface functionalities of carbon materials are the most important of surface characteristics. Viswanathan et al. [22] used XPS for studies of oxidized carbon fiber

Table 1

Information from XPS analysis

Common information

- (a) Qualitative identification of elements (except for H and He) in the surface region. The minimum concentration for that is $\sim 0.1\%$.
- (b) Quantitative analysis of elements.
 - Surface concentration of respective element using reference materials.
 - Surface elemental composition or atomic concentration using sensitivity factors of respective peaks.
 - The uncertainty will vary with the absolute concentration and the measuring conditions.
 - These quantitative analyses will give correct values in case the surface is homogeneous up to the thickness of 10–20 nm and give approximate values for an inhomogeneous surface.
- (c) Identification of the chemical nature (chemical state) of an element by the chemical shift. Note that the shift is not sufficient or has no linearity with the oxidation state for some elements (see some handbooks and databases). A two-dimensional plot, with the kinetic energy of the Auger electron on the ordinate and the binding energy of the photoelectron on the abscissa, of various chemical states of an element is very useful for some elements, such as Cu, Zn, Ag, Sn, etc.
- (d) The information of surface structure of single crystals by X-ray photoelectron diffraction based on the scattering by the neighboring atoms [4].

For inhomogeneous surfaces

- (a) Nondestructive determination of layered structure by angular resolved XPS (ARXPS) [5–7].
- (b) Nondestructive determination of in-depth atomic profile (distribution) using the quantitative analysis of peak intensity and peak shape including the inelastic peak (Tougaard method) [8,9].
- (c) Destructive determination of depth distribution of elements by argon ion etching into up to depths of 100 nm or more from the surface.
- (d) Two-dimensional imaging with the resolution of $\leq 2 \mu\text{m}$ by parallel imaging method and $\leq 10 \mu\text{m}$ by scanning X-ray method.

Table 2

Attentions necessary when making XPS measurements and analyses

- (a) Surface contamination (accidental contamination) will occur not only during exposure of a sample to the ambient atmosphere but may also take place during measurement even in ultra high vacuum chamber by adsorption.
- (b) Some materials, especially the organic ones, may be surface damaged (degradation, desorption or change in chemical state) during XPS measurement [10–13].
- (c) Differential charging in plane and/or in depth caused by the photoelectron emission may produce an artificial peak or induce peak deformation in the case of insulator or the materials containing it [14].
- (d) Argon ion etching generally causes an increase in the peak width [15] and may cause a change in surface morphology or roughening [16,17]. Also one must be careful for the preferential etching.
- (e) Surface roughness should be taken into account in the analysis.

surfaces and identified the functionalities (shown in Table 3) by the fitting of the C1s spectrum. They showed that, besides graphitic carbon, bridged structures and β -carbon atoms attached to oxidized carbon atoms, as shown in Fig. 2, are the main

Table 3

C1s binding energies [1–3, 18–22]. Some values are corrected so that the C1s binding energy of adventitious hydrocarbon (accidental hydrocarbon, contaminated hydrocarbon or contaminant) is set at 284.8 eV. This value was determined by the measurement of C1s on Au or Cu surface exposed to the laboratory environment [3]

| Organic compounds | | Inorganic Compounds | |
|--|------------------|--|-------------|
| Benzene | 284.7 | Carbides | 280.8–283.9 |
| Parafine | 284.8 (expected) | TiC | 281.3–281.6 |
| (–CH ₂ CHOH–) _n | 286.1 | Mo ₂ C | 282.7 |
| (–CH ₂ CH ₂ O–) _n | 286.1 | SiC | 282.7 |
| (CH ₃ CH ₂) ₂ O | 286.5 | WC | 282.8 |
| –CH ₂ CHCl–) _n | 286.5 | Fe ₃ C | 283.9 |
| CH ₃ CN | 287.2 | Graphite | 284.3–284.6 |
| (–CH ₂ CH ₂ CO–) _n | 287.4 | K ₃ Fe(CN) ₆ | 283.9 |
| CH ₃ COONa | 288.2 | BaCO ₃ | 289.4 |
| CH ₃ COOH | 289.3 | CaCO ₃ | 289.5–289.6 |
| CF ₃ COOC ₂ H ₅ | 290.4 | | |
| (–CF ₂ CF ₂ –) _n | 292.2–292.4 | | |
| CF ₃ COOC ₂ H ₅ | 292.9 | | |
| π–π* shake-up | 289–293 | | |
| Functionalities (functional groups) of organic materials | | Surface functionalities (surface groups) on carbon materials | |
| C–H, C–C | 284.8 | β-Carbon (see text) | 285.3 |
| C–N | 285.8 | C–O–H | 286.1 |
| C–O–H, C–O–C | 286.3 | C–O–C | 286.1 |
| C–Cl | 286.3 | C=N | 286.1 |
| C–F | 287.6 | Bridged structure | 286.6–286.9 |
| C=O | 287.8 | C=O | 287.7–288.2 |
| N–C=O | 288.0 | COOH | 288.8–289.1 |
| O–C=O | 288.8 | COOR | 288.8–289.1 |
| CO ₃ (Carbonate) | 290.1 | π–π* shake-up | 290–292 |
| –CF ₃ | 293–295 | | |

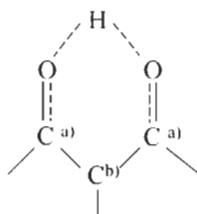


Fig. 2. (a) Bridged structure and (b) β-carbon (after Viswanathan et al. [22]).

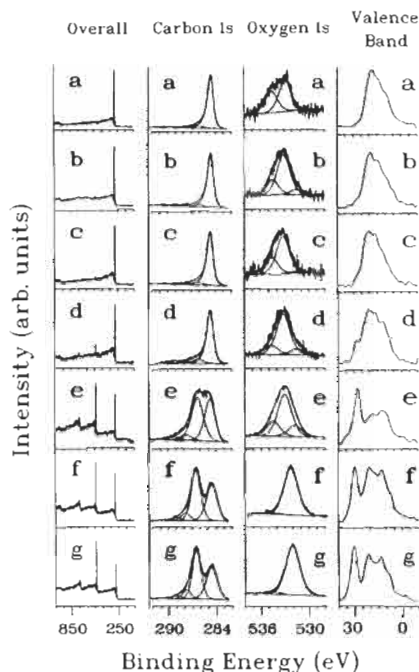


Fig. 3. XPS data for a high modulus pitch based carbon fiber before and after electrochemical treatment for 20 min in 1 M nitric acid. (a) Untreated; (b) immersed; (c) 1.0 V (SCE); (d) 1.5 V (SCE); (e) 2.0 V (SCE); (f) 2.5 V (SCE); (g) 3.0 V (SCE). (Reproduced from Sherwood [23] by permission of Elsevier Science.)

components of the C1s spectrum. A monochromatic X-ray source is used to identify the functionalities because the energy resolution is better. Curve fitting results for C1s and O1s peaks and valence band spectra are published by Sherwood [23]. Figure 3 contains results for electrochemically treated carbon fiber, showing that the intensity of higher energy side peaks attributed to oxygen-containing functionalities increases with the voltage.

3.2 Substitution Reaction (Labeling) of Surface Functionalities

The surface functionalities are sometimes difficult to identify because of small differences between binding energies. For the identification and quantification, it is useful to change to other functionalities containing other atoms absent from the original surface. This method is called tagging, derivatization or labeling [24]. Some such reactions are listed in Table 4 with many substitution reactions used for the XPS analysis being summarized [24,25]. Reactants containing fluorine or metal atoms have been used because their photo-ionization cross-sections (or sensitivity factors) are high. One must be careful, however, for the reaction stoichiometry, the possibility of cross-reactions with other functionalities, the stability of the products, parts of the reactant which remain, etc. [26].

Table 4

Chemical reactions of surface functionalities

| Surface functionality | Reagent | Product |
|-----------------------|---|------------------------------------|
| C-OH | $(CF_3CO)_2O$ | C-OCOCF ₃ |
| COOH | CF ₃ CH ₂ OH | COOCH ₂ CF ₃ |
| | TIOC ₂ H ₅ | COOTI |
| C=O | C ₆ F ₅ NHNH ₂ | CNNHC ₆ F ₅ |
| -NH ₂ | C ₆ F ₅ CHO | -NCHC ₆ F ₅ |

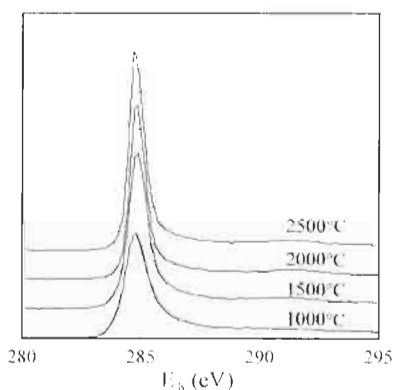


Fig. 4. C1s spectra of ultra-thin carbon film after the pyrolysis and heat-treatment of polyimide thin film prepared by the Langmuir-Blodgett method.

3.3 Peak Shift and FWHM Change of C1s Peak

Figure 4 shows the C1s spectra of an ultra-thin carbon film heat-treated to various temperatures. As temperature increases, so the C1s peak shifts to slightly lower binding energies although this may also be caused by a decrease in amounts of adsorbed contaminants coming from the atmosphere. Also, the full width at half maximum (FWHM) decreases with temperature due to a decrease in the types of component carbon. Kakiuchi et al. [27] reported that the C1s peak of diamond-like carbon (DLC) shifted toward the position of graphitic C1s peak after ion implantation of B, C, N and P, indicating an increase in the fraction of sp^2 carbon atom following ion implantation.

3.4 XPS of Other Elements in Carbon Alloys

Curve fitting of the O1s peak is very difficult for carbon materials due to the small chemical shift (except for many metal oxides), the overlapping of spectra [23] and the

possibility of adsorbed oxygen. However, the area of the O1s peak and/or the peak components is sometimes useful for the relative quantification of oxygen atoms, such as the ratio of O1s/C1s [21].

Boron-doped carbonaceous materials are widely studied for their electronic properties (e.g., anode performance of Li-ion batteries), the promotion of graphitization and for oxidation protection [28]. Konno et al. [28,29] studied nitrogen incorporation into a boron-doped graphite and the formation of B–N bonding. As shown in Fig. 5, boron-doped graphite showed a N1s peak with the peak intensity increasing with boron content, although no trace of N1s peak was observed in the XPS spectra of the undoped sample. The binding energies of the B1s and N1s peaks in high-resolution spectra were at 190.2–190.5 eV and 398.5–399.0 eV, respectively, indicating the formation of boron nitride.

Kim et al. [30] measured XPS spectra of B1s and N1s of boron-doped samples prepared by mixing petroleum cokes with 3 wt% of B_4C and then heat-treating at 2800°C in argon. They observed three peaks in the B1s spectra at 185.6, 187.7 and

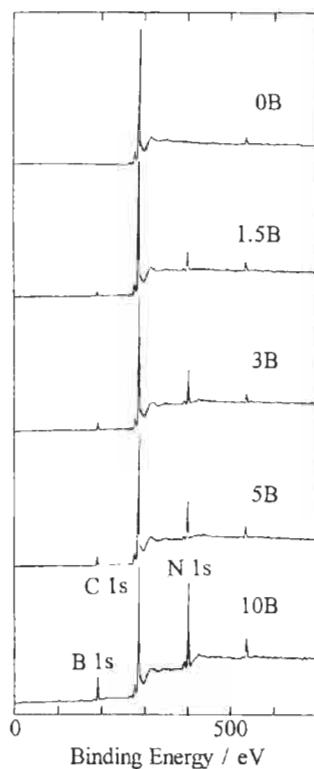


Fig. 5. XPS wide scan spectra of undoped and boron doped graphite samples. Numbers in the sample code, 0B to 10B, describe the boron content (mass %) in the initial mix of pitch coke and boron carbide. (Reproduced from Inagaki et al. [28,29] by permission of Elsevier Science.)

189.8 eV which were assigned to boron in boron carbide (B_4C), boron in a boron cluster (B) and boron bound to incorporated nitrogen atoms (BN), respectively. In the N1s spectra, a peak corresponding to nitrogen in boron nitride (BN) was observed at ~ 398 eV. Kim et al. [30] found that the electrochemical introduction of lithium ions took place at a potential ~ 40 mV higher for the boron-doped sample compared with the undoped sample.

Nitrogen is another attractive element in carbon materials. Konno et al. studied the state of nitrogen in carbon materials derived from nitrogen-containing polymers [31–33]. Figure 6 shows the change in the C1s and N1s spectra of polyimide Kapton with carbonization temperature up to 2000°C [31]. They used $Au4f_{7/2}$ peak of gold particles (sputter deposited) on the samples as the reference of binding energy (84.0 eV). The C1s peak at ~ 284 – 285 eV sharpened with increasing carbonization temperature and the binding energy of 284.5 remained at temperatures above 1000°C . This binding energy of 284.5 eV coincides with that of graphite. The peak at 288.4 eV for the original is assigned to carbonyl in a Kapton molecule. This peak disappears above 600°C with evolution of carbon monoxide and carbon dioxide. On the other hand, a broad peak appears at ~ 290 eV above 800°C which is assigned to a shake-up satellite peak due to the π – π^* transition in graphite. The main N1s peak of original Kapton at 400.5 eV develops a shoulder at the lower binding energy side. Increasing the heat treatment temperature develops a new peak at 398.8 eV at 600°C , and is assigned to pyridine-type nitrogen. Above this temperature, the binding energy of 400.5 eV gradually increases to 401.0 eV. This final peak is assigned to pyrrole-type nitrogen, as shown in Fig. 7.

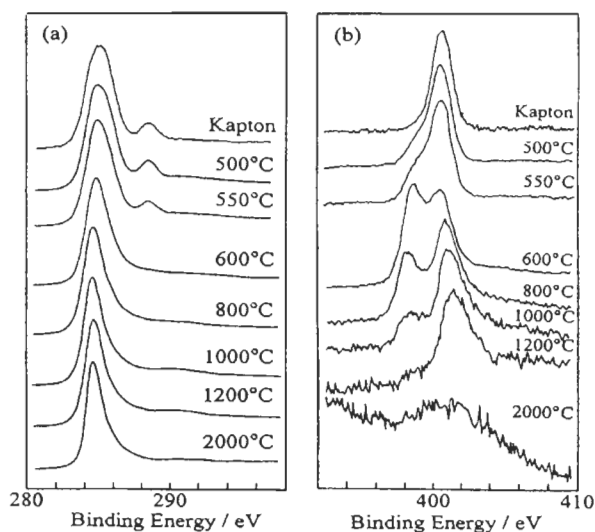


Fig. 6. Changes of C1s (a) and N1s (b) spectra of polyimide Kapton with carbonization temperature. (Reproduced from Konno et al. [31] by permission of Elsevier Science.)

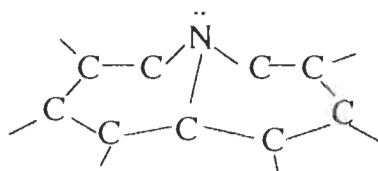


Fig. 7. A structure model for pyrrole-type nitrogen in carbon [31,32].

For a quantitative analysis, the peak intensity ratios of $I_{\text{N}1s}/I_{\text{C}1s}$ for every component of nitrogen (399, 401 and 403 eV), the relative intensity of pyridine- and pyrrole-type nitrogen and the atomic fraction of nitrogen, $[\text{N}]/([\text{N}]+[\text{C}])$, are useful [31,34]

The chemical state of bromine and iodine atoms in coal-tar pitches treated with those elements and their effects upon carbonization processes have been studied by Miyajima et al. [35]. Figure 8 shows the Br3d and I3d spectra of bromine- and iodine-treated pitches, respectively. As shown in Fig. 8a, the Br3d peak consists of two peaks at ~ 70.4 (major) and ~ 68 eV (minor), the former being assigned to the covalently bonded bromine and the latter to ionic bromine. Also the I3d5/2 peaks are divided into I_3^- (~ 620.6 eV) and I_5^- (~ 618.6 eV), which are assigned to charge transfer complexes. These differences in the states of bromine (covalent bond) and iodine (charge transfer complex) are related to the carbonization process.

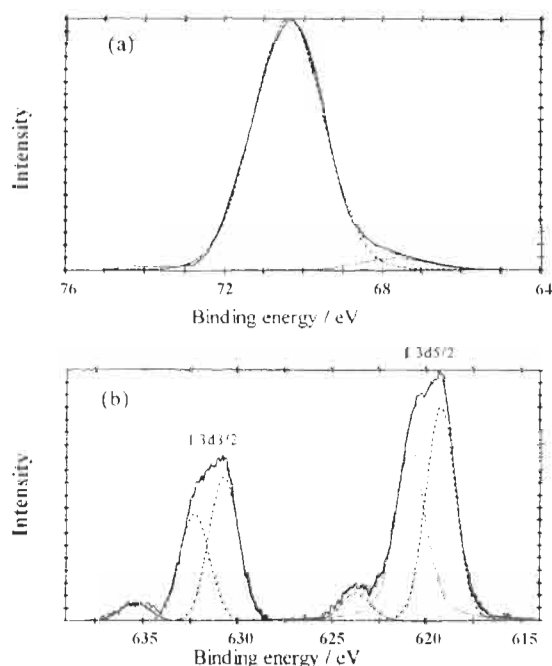


Fig. 8. Br3d (a) and I3d (b) spectra of bromine- and iodine-treated coal-tar pitches. (Reproduced from Miyajima et al. [35] by permission of The Carbon Society of Japan.)

Koh et al. [36] investigated fluorine intercalation into nitrogen-substituted carbon C_xN and measured XPS spectra of C1s, F1s and N1s. They assigned C1s peaks at 288.0 eV and ~290.7 eV to semi-ionic and covalent C–F bonds, respectively. Also, the main peak at 686.9 eV in F1s spectra were assigned to semi-ionic C–F bonds.

3.5 Valence Band Spectra

Ultraviolet photoelectron spectroscopy (UPS), using low energy photons (normally He^I, 21.2 eV, and He^{II}, 40.8 eV), is useful to study the valence band structures and electronic properties of many materials and to confirm the results of band structure calculations. Although UPS has a high energy resolution (< 0.1 eV), the spectrum is the convolution of valence (filled) band and conduction (empty) band states, the latter of which are due to the photoexcitation of valence electrons into the conduction band. On the other hand, XPS reveals true density of states, so that the valence band spectra of XPS are easy to understand and have been measured recently in many fields even if the energy resolution is not so high.

As already shown in Fig. 3, the valence band spectra of pitch-based carbon fibers have been measured before and after electrochemical oxidation, and compared with the calculations of model compounds [23]. By comparison, –C–O–C– and –OH functionalities have been identified and this is something which cannot be done from the C1s peak.

The fingerprinting capacity of valence band spectra is also useful to distinguish between different polymer materials. Although low density polyethylene, polypropylene and polybutene give identical C1s spectra, their valence band spectra are different [37]. By using valence band spectra, Endo et al. [38] examined surface damages of nitrocellulose and polytetrafluoroethylene samples after X-ray irradiation. Comparing the spectra at the beginning and after 120 min of X-ray irradiation with molecular orbital (MO) calculations using model molecules, it was concluded that NO₂ groups of the nitrocellulose cleave mainly during the XPS measurements. Valence band spectra of many polymers are available in handbooks [3,39].

References

1. D. Briggs and M.P. Seah (Eds.), Practical Surface Analysis, 2nd Edn., Vol. 1: Auger and X-ray Photoelectron Spectroscopy. Wiley, Chichester, 1990.
2. J.C. Veckerman (Ed.), Surface Analysis. Wiley, Chichester, 1997.
3. J.F. Moulder, W.F. Stickle, P.E. Sobol, K.D. Bomben and J. Chastain, Handbook of X-ray Photoelectron Spectroscopy. Physical Electronics, Eden Prairie, Minnesota, 1992.
4. C.S. Fadley, S. Thevuthasan, A.P. Kaduwela, C. Westphal, Y.J. Kim, R. Ynzunza, P. Len, E. Tober, F. Zhang, Z. Wang, S. Ruebush, A. Budge and M.A. Van Hove, Photoelectron diffraction and holography: Present status and future prospects. J. Electron Spectr. Rel. Phenomena, 68: 19–47, 1994.

5. L.B. Hazell, A.A. Rizivi, I.S. Brown and S. Ainsworth, The use of X-ray photoelectron take-off-angle experiments in the study of Langmuir–Blodgett films. *Spectrochim. Acta*, 40B: 739–744, 1983.
6. L.B. Hazell, I.S. Brown and F. Freisinger, A model for determining the composition of layer structured samples using XPS electron take-off angle experiments. *Surf. Interface Anal.*, 8: 25–31, 1986.
7. N. Suzuki, K. Iimura, S. Satoh, Y. Saito, T. Kato and A. Tanaka, Model for analysis of XPS electron take-off angle experiments in layer-structured samples: Determination of attenuation lengths in a well-characterized Langmuir–Blodgett film. *Surf. Interface Anal.*, 25: 650–659, 1997.
8. S. Tougaard, Surface nanostructure determination by X-ray photoemission spectroscopy peak shape analysis. *J. Vac. Sci. Technol. A*, 14: 1415–1423, 1996.
9. S. Tougaard, Accuracy of the non-destructive surface nanostructure quantification technique based on analysis of the XPS or AES peak shape. *Surf. Interface Anal.*, 26: 249–269, 1998.
10. G. Beamson and D. Briggs, *High Resolution XPS of Organic Polymers*. Wiley, Chichester, 1992.
11. N. Suzuki, T. Sakamoto, T. Isano, K. Iimura, T. Kato, H. Tohma, T. Maruyama, K. Miura and Organic Materials Group of SASJ, Surface damage of organic materials during XPS analysis (2). *J. Surf. Anal.*, 5: 224–227, 1999.
12. T. Maruyama, N. Suzuki, H. Tohma, K. Miura and Organic Materials Group of SASJ, A method of evaluating sample damage in XPS using nitrocellulose as a standard for organic materials. *J. Surf. Anal.*, 6: 59–65, 1999.
13. N. Suzuki, T. Isano, T. Sakamoto, T. Saino, K. Iimura and T. Kato, Degradation of organosilane monolayer during XPS measurement. *Surf. Interface Anal.*, 30: 301–304, 2000.
14. J.E. Fulghum, Practical aspects of charge compensation in X-ray photoelectron spectroscopy. *J. Surf. Anal.*, 6: 13–21, 1999.
15. N. Fukumoto, B.Q. Li and I. Kojima, Comparison of XPS spectra of inorganic materials with various kinds of pre-treatment methods. *J. Surf. Anal.*, 5: 200–203, 1999.
16. Y. Homma, Formation mechanism of indium microcrystals on ion-bombarded InP surfaces. *J. Surf. Anal.*, 3: 641–645, 1997.
17. T. Ogiwara, S. Tanuma, Y. Nagasawa and N. Ikeo, Auger depth profiling analysis of InP/GaInAsP multilayer thin films. *Microbeam Anal.*, 2: 133–138, 1993.
18. D.T. Clark, D.B. Adams, A. Dilks, J. Peeling and H.R. Thomas, Some aspects of shake-up phenomena in some simple polymer systems. *J. Electron Spectr. Rel. Phenom.*, 8: 51–60, 1976.
19. K.-S. Yu, J. W. Lee, M. M. Sung, S.-B. Lee and Y. Kim, Surface analysis of cubic SiC thin films prepared by high vacuum chemical vapor deposition using 1,3-disilabutane. *J. Surf. Anal.*, 5: 308–311, 1999.
20. G. Nanse, E. Papirer, P. Fioux, F. Moguet and A. Tressaud, Fluorination of carbon blacks: An x-ray photoelectron spectroscopy study: I. A literature review of XPS studies of fluorinated carbons. XPS investigation of some reference compounds. *Carbon*, 35: 175–194, 1997.
21. C.L. Weitzsacker, M. Xie and L.T. Drzal, Using XPS to investigate fiber/matrix chemical interactions in carbon-fiber-reinforced compounds. *Surf. Interface Anal.*, 25: 53–63, 1997.
22. H. Viswanathan, M.A. Rooke and P.A. Sherwood, X-ray photoelectron spectroscopy studies of carbon-fiber surfaces. 21. Comparison of carbon fibers electrochemically oxidized in acid using achromatic and monochromatic XPS. *Surf. Interface Anal.*, 25: 409–417, 1997.

23. P.M.A. Sherwood, Surface analysis of carbon and carbon fibers for composites. *J. Electron Spectr. Rel. Phenom.*, 81: 319–342, 1996.
24. C.D. Batich, Chemical derivatization and surface analysis. *Appl. Surf. Sci.*, 32: 57–73, 1988.
25. In Ref. [1], pp. 450–454.
26. In Ref. [2], pp. 88.
27. H. Kakiuchi, T. Kobayashi and T. Terai, *Nucl. Instrum. Methods Phys. Res., Sect. B*, 166–167: 415–419, 2000.
28. H. Konno, T. Nakahashi, M. Inagaki and T. Sogabe, Nitrogen incorporation into boron-doped graphite and formation of B–N bonding. *Carbon*, 37: 471–475, 1999.
29. M. Inagaki, T. Nakahashi, H. Konno and T. Sogabe, Nitrogen incorporation into boron-doped graphite. *Carbon*, 35: 1994–1995, 1997.
30. C. Kim, F. Fujino, T. Hayashi, M. Endo and M.S. Dresselhaus, Structural and electrochemical properties of pristine and B-doped materials for the anode of Li-ion secondary batteries. *J. Electrochem. Soc.*, 147: 1265–1270, 2000.
31. H. Konno, T. Nakahashi and M. Inagaki, State analysis of nitrogen in carbon film derived from polyimide Kapton. *Carbon*, 35: 669–674, 1997.
32. T. Nakahashi, H. Konno and M. Inagaki, Chemical state of nitrogen atoms in carbon films prepared from nitrogen-containing polymer films. *Solid State Ionics*, 113–115: 73–77, 1998.
33. J. Mittal, H. Konno, M. Inagaki and O.P. Bahl, Denitrogenation behavior and tensile strength increased during carbonization of stabilized PAN fibers. *Carbon*, 36: 1327–1330, 1998.
34. H. Saito, T. Inoue and S. Ohshio, Solid solubility of nitrogen in amorphous carbon films deposited in electron cyclotron resonance plasma. *Jpn. J. Appl. Phys.*, 37: 4983–4988, 1998.
35. N. Miyajima, E. Yasuda, B. Rand, T. Akatsu, K. Kameshima and Y. Tanabe, Comparison of bromine-treatment and iodine-treatment in the carbonization of pitches. *Tanso*, 2000: 405–409.
36. M. Koh, H. Yumoto, H. Higashi and T. Nakajima, Fluorine intercalation in carbon alloy C_xN. *J. Fluorine Chem.*, 97: 239–246, 1999.
37. In Ref. [1], pp. 448.
38. K. Endo, S. Maeda, H. Miura, K. Ohmori, K. Miura, H. Tohma, T. Maruyama and Organic Materials Group of SASJ, Surface damage of organic materials during XPS analysis (3). *J. Surf. Anal.*, 6: 54–58, 1999.
39. B.V. Crist, *Handbook of Monochromatic XPS Spectra*, 2: Polymers and Polymers Damaged by X-rays. Wiley, Chichester, 2000.

Chapter 14

Transmission Electron Microscopy

Hiroyasu Saka

Department of Quantum Engineering, Nagoya University, Nagoya 464-8603, Japan

Abstract: Material characterization by means of transmission electron microscopy is reviewed. A novel technique for specimen preparation, a focused ion beam technique, is described. Emphasis is placed on the significance of *in-situ* heating experiments. The formation of silicon carbide by reaction of solid silicon with graphite at temperatures above 1673 K is presented as an application.

Keywords: Transmission electron microscopy, Focused ion beam, *In-situ* heating experiment, Silicon carbide.

1 Introduction

Transmission electron microscopy (TEM) is well established and widely used to characterize materials [1–5]. It provides information on morphology, structure, chemistry and even the nature of bonds. A serious problem associated with material characterization by TEM, in the past, has been the preparation of thin foil specimens. However, a novel specimen-preparation technique, that is a focused ion beam (FIB) technique, has recently been developed [6–10]. Furthermore, the technique of *in-situ* electron microscopy makes it possible to observe, in a real-time mode and at high resolution, phenomena which are taking place at high temperatures. This approach is of special significance for the analyses of carbon alloys. An *in-situ* observation of formation of silicon carbide by reaction of solid silicon and graphite at a temperature of 1673 K is described as an example of the application of *in-situ* heating experiments to the study of carbon alloying.

2 Materials Characterization by Means of TEM

2.1 Mechanism of Contrast Formation

Consider an incident electron beam as it enters a single crystalline thin foil specimen (Fig. 1a). Some of the incident electrons pass through the specimen without any

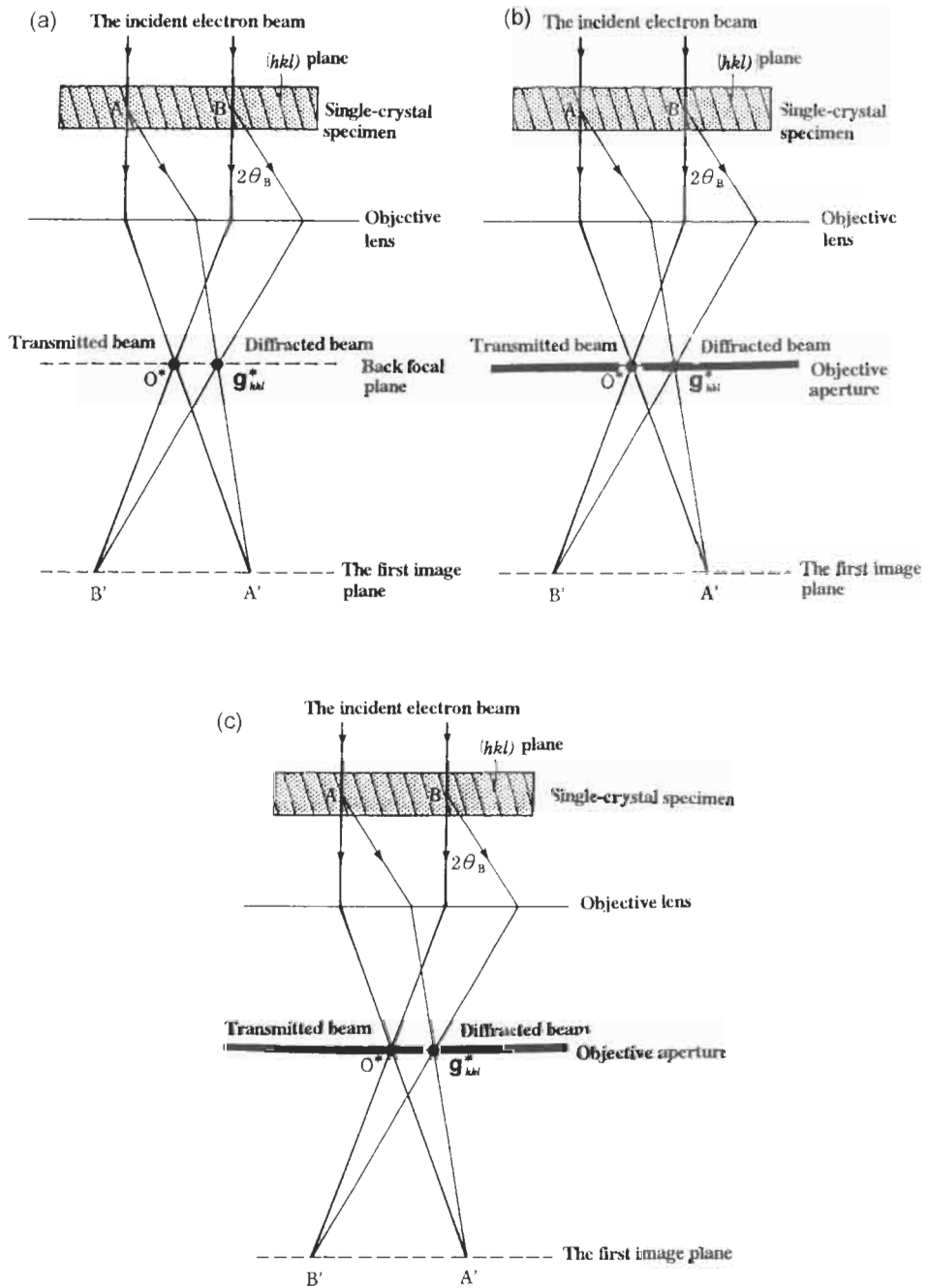


Fig. 1. Ray diagram illustrating the formation of: (a) a diffraction pattern and an image; (b) a bright-field (BF) image; and (c) a dark-field (DF) image [5].

interaction and reach the exit surface of the specimen. Other electrons are diffracted by a set of crystallographic planes, say, (hkl) planes, the angle between the transmitted beam and the diffracted beam being $2\theta_B$, where θ_B is the Bragg angle. Transmitted and diffracted beams are deflected by the objective lens. The transmitted beam is brought to the origin of the back focal plane, and the diffracted beam to a spot denoted by g . The transmitted and diffracted beams form an inverted image of the specimen in the first image plane. When a film is placed at the position of this back focal plane a diffraction pattern is obtained. With a film placed at the position of the first image plane, a magnified image of the specimen is obtained. The actual procedure is to adjust the focal length of the diffraction lens which is placed under the first image plane.

The objective aperture is inserted at the back-focal plane so that only the transmitted beam contributes to the electron image and a bright field (BF) image is obtained (Fig. 1b). If the objective aperture is moved to allow only the diffracted beam to pass, a dark field (DF) image is obtained (Fig. 1c). Contrast appears only

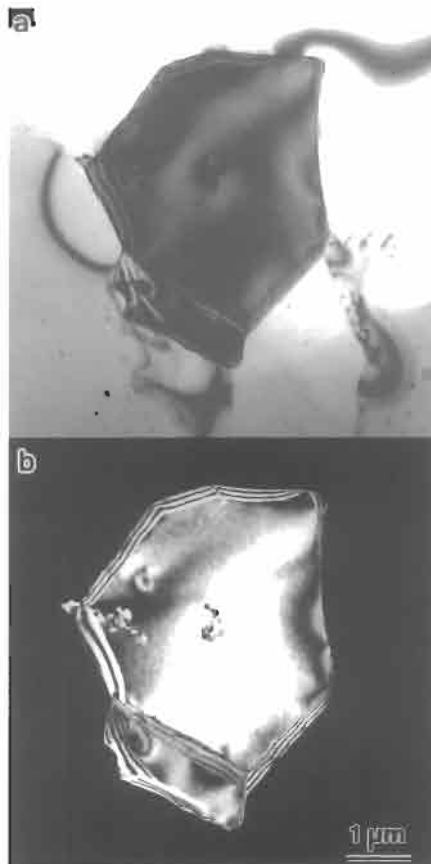


Fig. 2. Examples of (a) BF image, and (b) DF image.

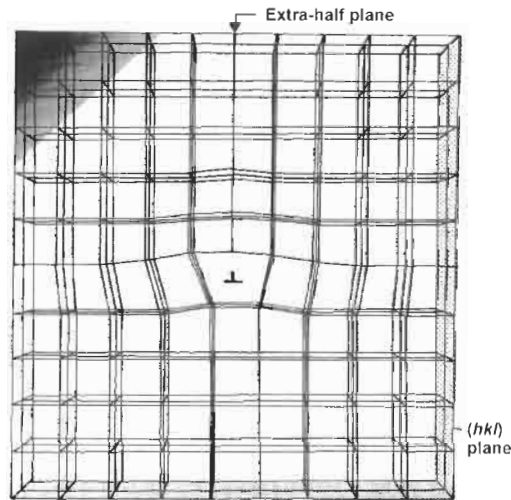


Fig. 3. Schematic illustration of an edge dislocation [5].

when the extents to which the Bragg condition are satisfied differ from one position to another within a specimen and this is called diffraction contrast. Deviation from an exact Bragg condition may be caused by different crystal orientations and/or crystal structure and by elastic bending of the crystal lattices around defects. Figures 2a and b are examples of BF and DF images of a crystallite which satisfies the Bragg condition exactly with the surrounding crystallites deviating substantially from the Bragg condition.

A dislocation can be imaged because the lattice near the core of the dislocation is bent elastically. Figure 3 shows schematically an edge dislocation. Extents of bending increase with decreasing distance from the dislocation core. Suppose a set of lattice planes (hkl), of an undistorted matrix, remote from a dislocation, slightly deviates from the Bragg condition, the angle between the incident electron beam and the lattice plane θ being larger than θ_B by $\Delta\theta$. Then, at a region near to the core of a dislocation, where the lattice is bent more strongly, Bragg conditions are satisfied locally and this will lead to diffraction contrast of the dislocation. If $\Delta\theta$ is large, that region where the Bragg condition is satisfied is very narrow and close to the core of the dislocation. That is, the image taken under these conditions is sharp and close to the real position of the dislocation. Usually the DF imaging mode is employed for such imaging. This technique is called the weak-beam (WB) technique [11]. Figures 4a and b show a conventional BF image and the WB image of a dislocation. It is evident that the WB image is much sharper and details of the dislocation configuration can be identified.

When both the transmitted and diffracted beams pass through a large aperture, interference takes place between the transmitted and diffracted beams, leading to one-dimensional lattice fringes of the (hkl) plane, which is responsible for the Bragg

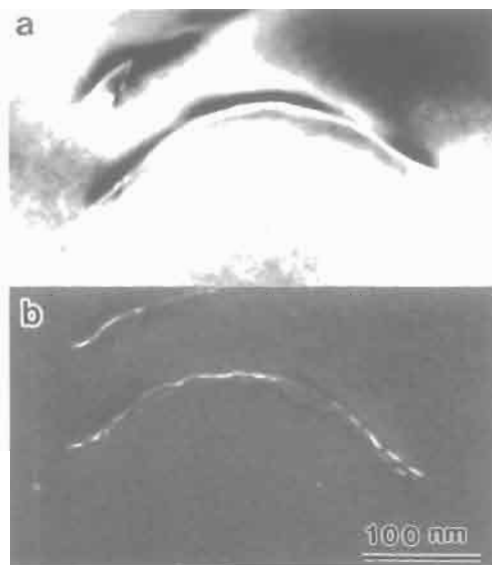


Fig. 4. A conventional BF image (a) and the WB image (b) of a dislocation.

diffraction. Figure 5 is an example of one-dimensional lattice fringes [12]. When further diffracted beams pass through, then two-dimensional lattice fringes are obtained, and under some conditions the observed image corresponds well to the real crystal structure. This kind of image is called the structure image. Figure 6 shows an example of such a high-resolution image of Si_3N_4 .

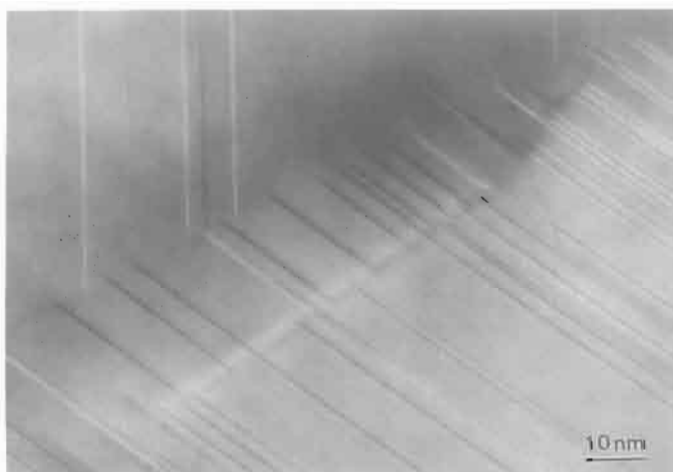


Fig. 5. One-dimensional lattice fringes in a shape memory alloy.

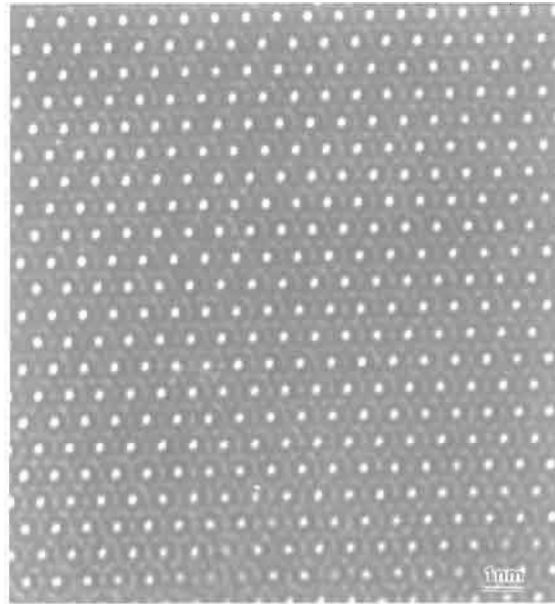


Fig. 6. HREM image of Si_3N_4 .

2.2 Diffraction patterns

When the diffraction lens is focused on the back focal plane of the objective, a diffraction pattern is magnified and displayed. When the spacing of an (hkl) plane, responsible for the Bragg diffractions, is d and the distance R , on the film is between the diffracted beam, i.e., diffraction spot and the transmitted beam, i.e., the direct spot, then the following relationship holds:

$$L\lambda = Rd$$

where λ is the wavelength of the electron beam, and L is a constant called the camera length. Using a selected-area aperture, placed at the first image plane, an area can be selected from which the diffraction pattern is taken. If the selected area contains polycrystalline grains, the diffraction pattern consists of Debye rings (Fig. 7a). If only a single grain is included in the selected area aperture, a network of diffraction spots is obtained (Fig. 7b).

The shape of a diffraction spot depends on the outer dimension of the specimen such that the half-peak width of the spot is roughly inversely proportional to the dimension of the specimen. Thus, diffraction spots from a needle-like specimen are elongated perpendicularly to the axis of the needle.

When a thick specimen is used, Kikuchi lines—a pair of black–white lines—appear in addition to, or instead of, diffraction spots (Fig. 8). Each of the Kikuchi lines

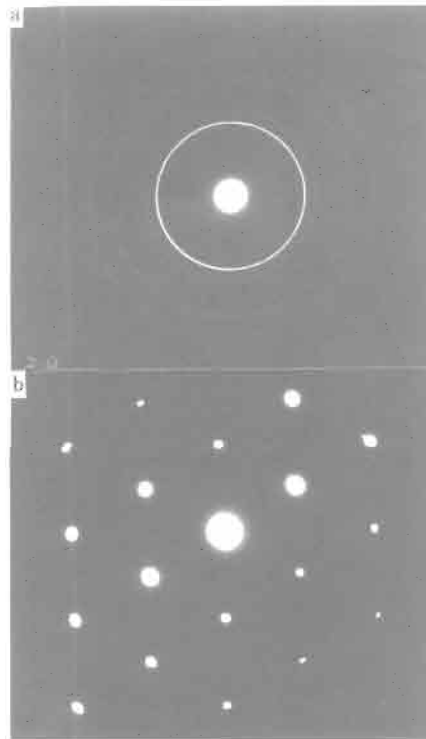


Fig. 7. (a) Debye rings, and (b) a network of diffraction spots.

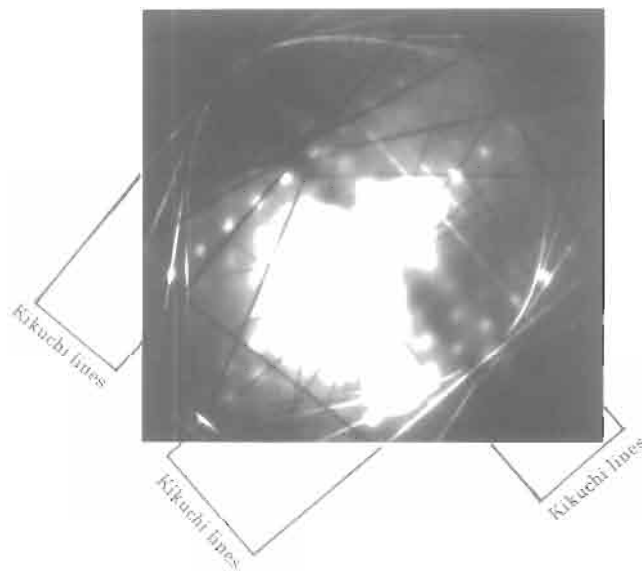


Fig. 8. Kikuchi pattern.

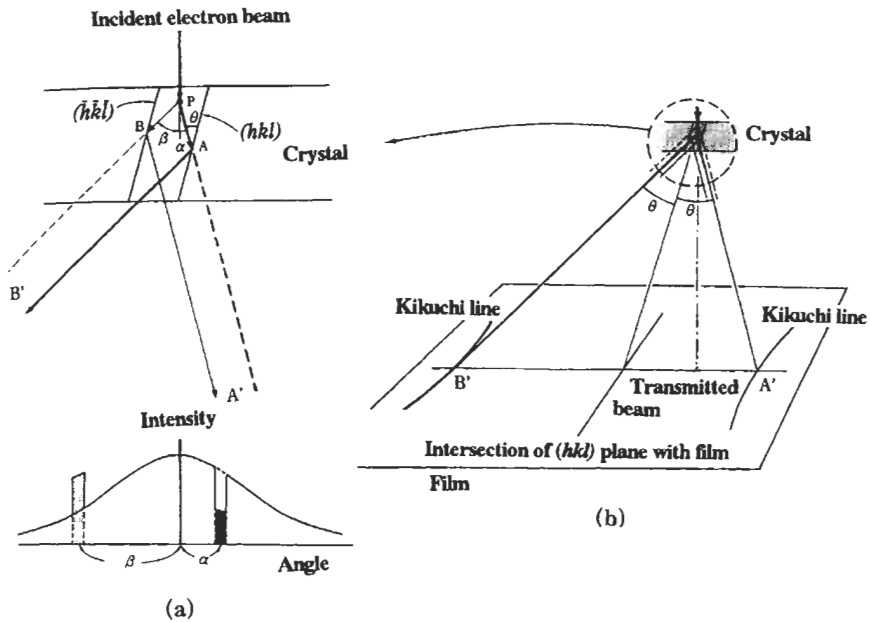


Fig. 9. Geometry of a lattice plane and the Kikuchi lines [5].

corresponds to the diffraction spot, and can be so indexed. Indeed, the mid-line of a Kikuchi pair of (hkl) plane corresponds to the intersection of the extension of the (hkl) plane with the film (Fig. 9). A slight tilting of the specimen, and hence of the (hkl) plane, results in a shift of the Kikuchi lines. Thus, the crystallographic orientation of the specimen and deviations from the exact Bragg condition can be determined accurately.

2.3 Elemental Analysis

X-Rays are generated when electrons interact with matter. With high energy incident electrons, inner shell electrons are ejected with characteristic energies and characteristic X-rays are emitted. The energy loss electrons and the characteristic X-rays are used to identify the elements which are interacting with the incident electrons.

Figure 10 shows an example of elemental mapping by means of characteristic X-rays. A stacking fault (SF) lies end-on in a Cu-Si alloy, and the line analysis across the stacking fault indicates that copper is segregated onto the stacking fault [13]. This segregation of solute atoms onto the SF was predicted theoretically by Suzuki in 1956 and has been called the Suzuki effect.

Elemental analysis using energy loss of the electrons (EELS) is discussed in detail in the following chapter.

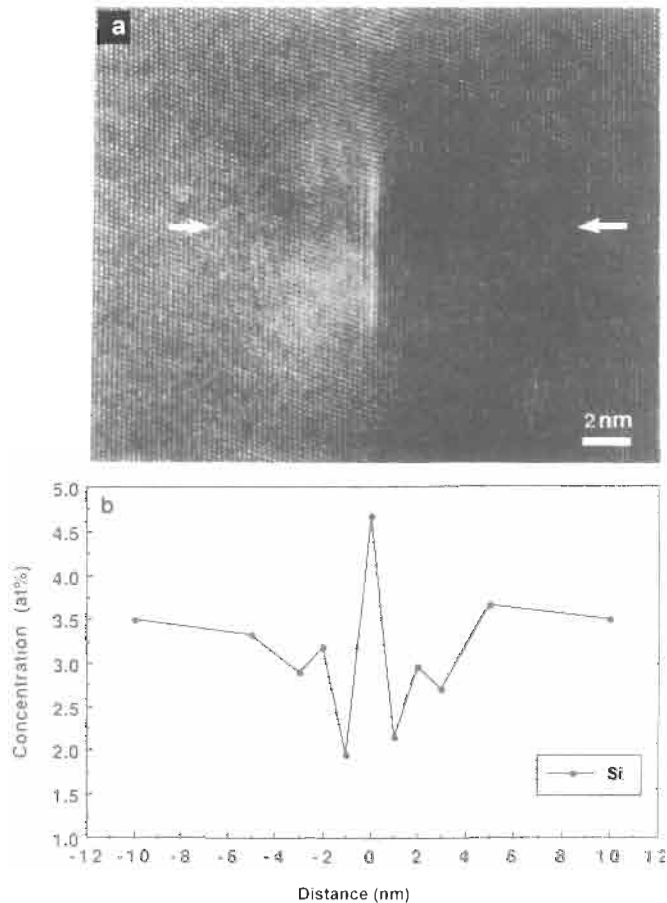


Fig. 10. Elemental mapping by means of characteristic X-rays. The stacking fault lies end on in a Cu–Si alloy.

3 Specimen Preparation by FIB

Preparation of thin foil specimens for TEM is a time-consuming and slow procedure. However, the technique of focused ion beam (FIB) milling is receiving attention as a new technique to prepare TEM specimens [6–10].

Figure 11 shows a schematic diagram of the FIB system. Gallium ions are emitted from a liquid gallium source. They are accelerated with a 30 kV high voltage and deflected to bombard the surface of the sample from which a thin foil specimen for TEM is to be prepared. Gallium ions sputter the sample and reduce thicknesses to those of thin foils. At the same time, secondary ions are emitted by the bombardment with gallium. The final shape of the specimen is shown in Fig. 12. Two trenches are produced, leaving behind a very thin wall which is electron transparent when tilted by 90°.

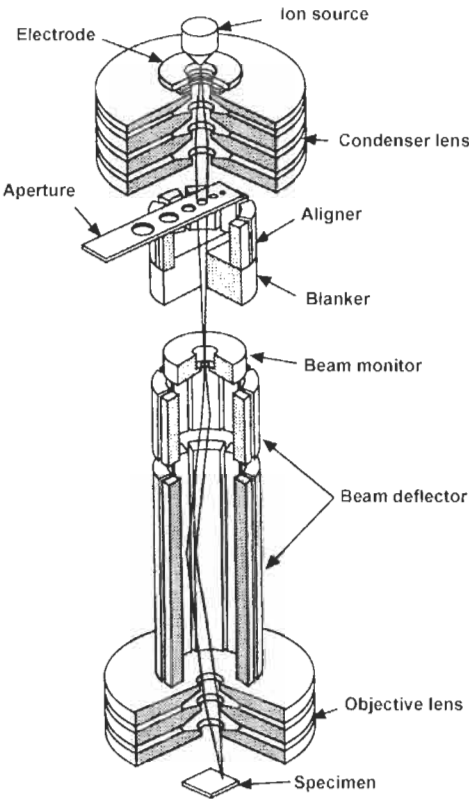
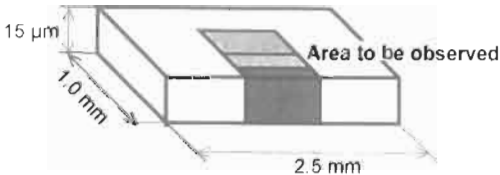


Fig. 11. Schematic diagram of the FIB system.

Mechanical polishing



FIB fabrication

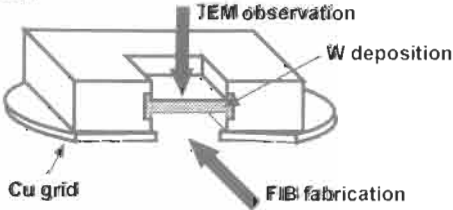


Fig. 12. The final shape of the specimen fabricated by a FIB system.

There are at least two advantages in using FIB to prepare TEM specimens. One is that it is possible to prepare a TEM specimen with pin-point accuracy from a pre-selected area. The other is that a TEM specimen can be easily prepared from coated materials or multilayered structures composed of different substances with quite different physical and/or chemical properties.

3.1 Pin-pointing specimens

One of the most successful applications of FIB to pin-pointing is the observation of a crack by TEM [14–17]. To carry out TEM observations of a crack, a thin foil specimen must be prepared. It can be extremely difficult to prepare such a specimen from a pre-selected region containing a crack tip.

Figure 13 is an electron micrograph of a crack formed by indentation on the (001) surface of silicon. The following features are evident.

1. Within the indent the crystal is deformed severely (P) and some dislocations (denoted by A) have glided out of the indent.
2. Near the indent, cracks piercing the foil are observed. There are two types of cracks. One is almost parallel to the foil surface, i.e., (001) plane (L_1, L_2, L_3, L_4, L_5) and has a tendency to lie on the $\{111\}$ plane. The other type is perpendicular to the foil surface and lies on the $\{110\}$ plane (H_v).
3. On both sides of the indent and underneath the indent, fringe contrasts can be observed (denoted by H_v). The areas with fringe contrast can be considered to contain cracks. The fringes can be explained by moire fringes which result from the crystal being separated into two regions by the crack.

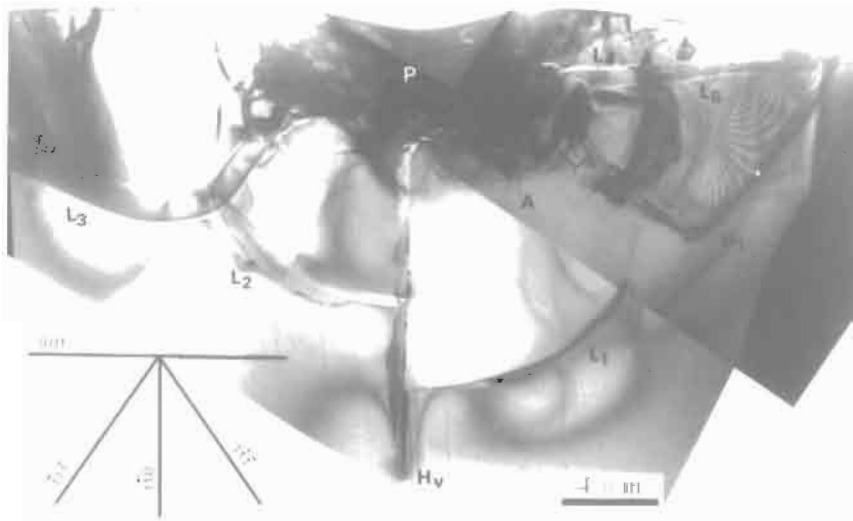


Fig. 13. Cross-sectional electron micrograph of a crack formed on a (001) surface of silicon.

3.2. Diamond coating on Si_3N_4 [18]

Diamond coating is used as a cutting tool. The performance of such a tool is governed mostly by the microstructure of the interface between diamond and the substrate. To characterize such an interface a cross-sectional TEM study would be informative. However, because diamond is very hard, it is very difficult to prepare a cross-section for a TEM examination using the traditional techniques. The FIB technique can be used to prepare such a cross-section.

Figure 14 is an example of a cross-sectional TEM micrograph of microstructure near the interface between diamond and Si_3N_4 . The coating Si_3N_4 was made using a chemical vapor deposition (CVD) method. The microstructures of diamond, of the Si_3N_4 and of the interface between them are clearly seen.



Fig. 14. Cross-sectional TEM micrograph of microstructure near an interface between diamond and Si_3N_4 .

4 In-Situ Heating Experiment [19]

4.1 Heating Holder

Figure 15 is a schematic diagram of a heating holder developed especially for use with a side-entry type goniometer of a transmission electron microscope. The heating element used is a fine wire (diameter 20–30 μm) of a refractory metal such as tungsten. The heating element is bridged across a gap of the holder and heated by direct current from dry batteries. The use of a dry battery as a power source is essential, because it provides a very stable current without any fluctuations which would affect the temperature of the sample and, consequently, the quality of a TEM image.

The temperature of the heating element is calibrated either using an optical pyrometer outside the microscope or observing the melting of a pure metal such as gold or aluminum inside the microscope. Figure 16 gives an example of a calibration curve. Temperatures as high as 1800 K can be achieved with a current as small as 250 mA as the thermal mass of the heating element is small. Because of this small thermal mass, the drift of a specimen due to instability of temperature during heating is also small. This permits the recording of an image in the high-resolution electron microscope (HREM) on an ordinary film even when the specimen is at a high temperature.

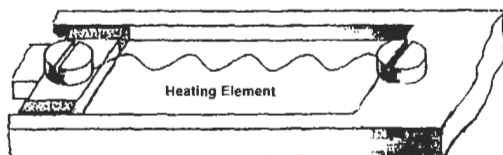


Fig. 15. Schematic diagram of the heating holder. Samples are directly mounted onto the heating element.

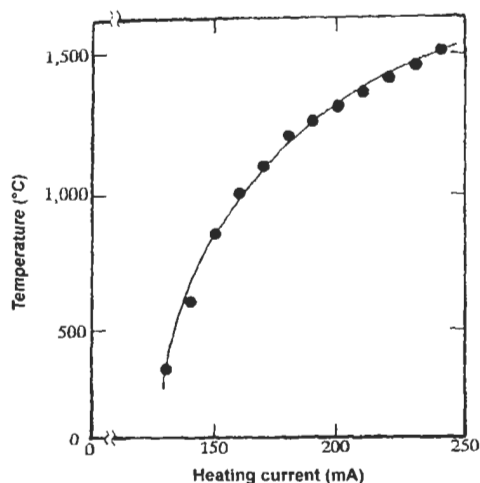


Fig. 16. Temperature versus heating current curve.

After mounting a mixture of fine particles of reactants, in this case graphite and Si, directly onto the heating element, excess reactant was blown away so that only attached particles were transferred into the electron microscope.

4.2 Results and Discussion

Figure 17a shows a low magnification micrograph, taken at room temperature, of a silicon particle attached to a particle of graphite itself attached to the heating element (not shown in the figure). Figure 17b was taken 5 min after the temperature had reached 1673 K. It can be seen that particle S, which was originally a single crystal of silicon, has now fragmented into many small particles. At the same time, the area denoted by SC in Fig. 17b, which is the same area denoted by C in Fig. 3a, became darker.

Figures 18a and b are diffraction patterns taken at room temperature and at 1673 K, respectively. Before heating (Fig. 18a), a typical diffraction pattern from a single crystal of silicon and typical Debye rings from graphite were observed. At 1673 K (Fig. 18b), extra Debye rings are seen in addition to those of the graphite. The lattice spacing of the extra Debye rings corresponded to cubic β -SiC.

These changes in diffraction patterns during the *in-situ* heating experiment show definitely that at 1675 K silicon atoms diffuse into graphite and react with carbon to form SiC. Furthermore, examination of the Debye rings of Figs. 18a and b shows that the spacing of the c-planes of graphite did not change during the reaction.

Figure 19 reproduces a sequence of HREM images showing the process of formation of SiC. In Fig. 19a a silicon particle is in the left bottom corner of the micrograph and has partially reacted with graphite to form SiC (indicated by arrow). However, most of the graphite remained unchanged. In Fig. 19c, which was taken 2 min after Fig. 19a, almost the whole region, of what had been graphite, had reacted with silicon to form SiC crystals. Figure 19b, taken 1 min after Fig. 19a, is an example of the stage between these two extremes showing a decrease in the contrast of lattice fringes of graphite.

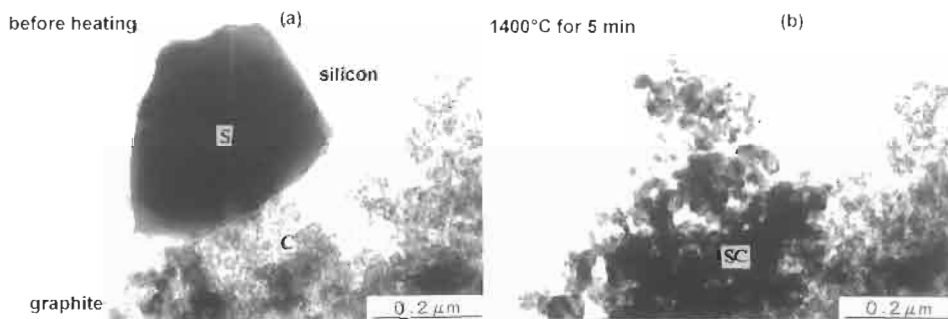


Fig. 17. (a) TEM image of a single crystalline silicon particle (denoted by S) sitting on graphite (denoted by C) before heating. (b) The same location as (a) but heated for 5 min at 1673 K.

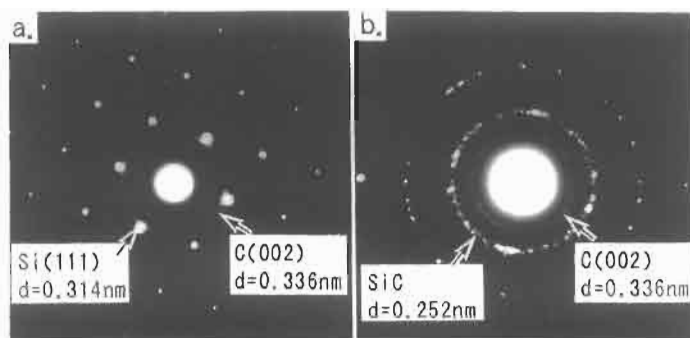


Fig. 18. Diffraction patterns taken (a) before heating, and (b) at 1673 K.

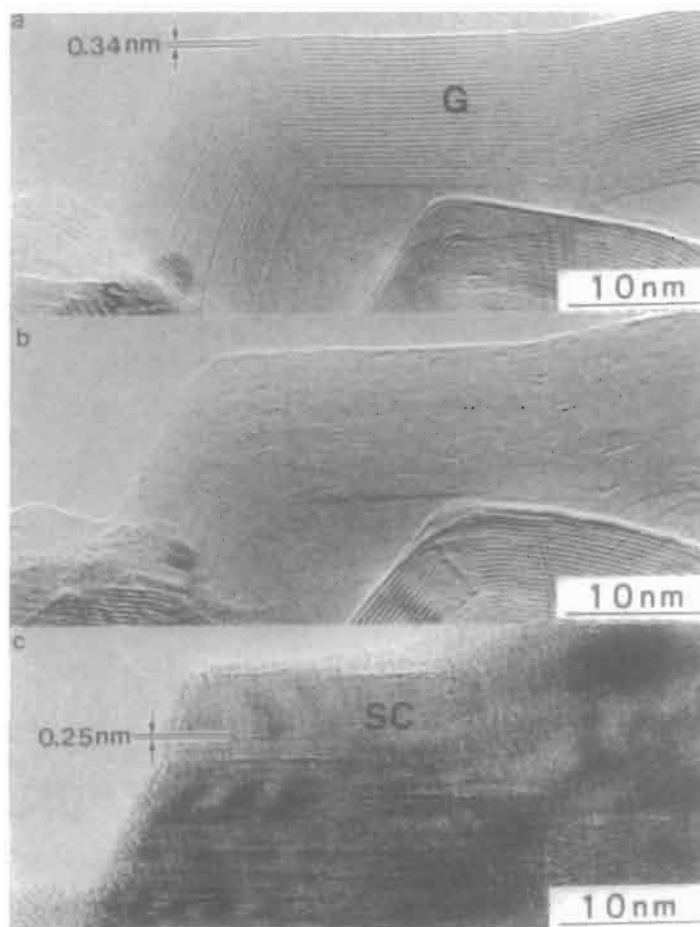


Fig. 19. A sequence of reactions between solid silicon and graphite observed at near-atomic resolutions.

References

1. P.B. Hirsch, A. Howie, R.B. Nicholson, D.W. Pashley and M.J. Whelan, *Electron Microscopy of Thin Crystals*. Butterworths, London, 1965.
2. M.H. Loretto and R.E. Smallman, *Defect Analysis in Electron Microscopy*. Chapman and Hall, London, 1975.
3. D.B. Williams and C.B. Carter, *Transmission Electron Microscopy*. Plenum Press, New York & London, 1996.
4. B. Howe and J.M. Howe, *Transmission Electron Microscopy and Diffractometry of Materials*. Springer, Berlin, 2001.
5. H. Saka, *Electron Microscopy of Crystals*. Uchidarokakuho, Tokyo, 1997 (in Japanese)
6. R.J. Young, E.C.G. Kirk, D.A. Williams and H. Ahmed, Fabrication of planar and cross-sectional TEM specimens using a focused ion beam. *Mater. Res. Soc. Symp. Proc.*, 199: 205–215, 1990.
7. K-H. Park, Cross-sectional TEM specimen preparation of semiconductor devices by focused ion beam etching, *Mater. Res. Soc. Symp. Proc.*, 199: 271–280, 1990.
8. T. Ishitani and T. Yaguchi, Microsc. Cross-sectional sample preparation by focused ion beam. *Res. Tech.*, 35: 320–333, 1996.
9. H. Saka, Transmission electron microscopy observation of thin foil specimens prepared by means of a focused ion beam. *J. Vac. Sci. Technol. B*, 16: 2522–2527, 1998.
10. T. Ishitani, Y. Taniguchi, S. Isakozawa, H. Kioke, T. Yaguchi, H. Matsumoto and T. Kamino, Proposals for exact-point transmission electron microscopy using focused ion beam specimen-preparation technique. *J. Vac. Sci. Technol. B*, 16: 2532–2537, 1998.
11. D.J.H. Cockayne, I.L.F. Ray and M.J. Whelan, Investigations of dislocation strain fields using weak beams. *Phil. Mag.*, 20: 1265–1270, 1969.
12. T. Katata and H. Saka, High-resolution electron-microscopic in situ observation of the motion of intervariant interfaces in Cu-Zn-Al thermoelastic martensite. *Phil. Mag.*, A: 59: 677–687, 1989.
13. T. Kamino, Y. Ueki, H. Hamajima, K. Sasaki, K. Kuroda and H. Saka, Direct evidence for Suzuki segregation obtained by high-resolution electron microscopy. *Phil. Mag. Lett.*, 66: 27, 1992.
14. H. Saka and G. Nagaya, Plan-view transmission electron microscopy observation of a crack tip in silicon. *Phil. Mag. Lett.*, 72: 251–255, 1995.
15. H. Saka and S. Abe, FIB/HVEM observation of the configuration of cracks and the defect structure near the cracks in Si. *J. Electron Microsc.*, 46: 45–57, 1997.
16. Suprijadi and H. Saka, On the nature of a dislocation wake along a crack introduced in Si at the ductile–brittle transition temperature. *Phil. Mag. Lett.*, 78: 435–443, 1998.
17. A. Muroga and H. Saka, Analysis of rolling contact fatigued microstructure using focused ion. *Scripta Met.*, 33: 151, 1995.
18. K. Kuroda, M. Takahashi, H. Itoh, H. Saka and S. Tsuji, Application of focused ion beam milling to cross-sectional TEM specimen preparation of industrial materials including heterointerfaces. *Thin Solid Films*, 319: 92, 1998.
19. T. Kamino, T. Yaguchi and H. Saka, *In situ* study of chemical reaction between silicon and graphite at 1400°C in a high resolution/analytical microscope. *J. Electron Microsc.*, 43: 104–110, 1994.

Chapter 15

Electron Energy-Loss Spectroscopy and its Applications to Characterization of Carbon Materials

Hisako Hirai

Institute of Geoscience, University of Tsukuba, Tsukuba, Ibaraki 305-8571, Japan

Abstract: Electron energy-loss spectroscopy (EELS) is an analysis of the distribution of electron energy emergent from a thin specimen due to inelastic interactions. An EELS spectrum contains a great deal of information about the specimen atoms not only what they are chemically but also their electronic structures, their bonding states, nearest neighbor distributions, coordination numbers, dielectric constants, and band gaps. These characteristics are observed in different energy regions depending on the energy lost. The fundamental principles of EELS and instrumentation are briefly described, and procedures to obtain atomic and electronic properties from the EELS spectrum are explained. An EELS analysis was used to characterize a new form of amorphous diamond, its sp^3 fraction, band gap, inter-band transition, and density of state. This analysis showed that the amorphous diamond consists of almost 100% sp^3 -bonded carbon close to crystalline diamond, as compared with other highly sp^3 -bonded amorphous carbons.

Keywords: EELS, Amorphous carbon, Amorphous diamond, Band gap, sp^3 fraction, Dielectric function.

1 Introduction

Electron energy-loss spectroscopy (EELS) is the analysis of the energy distribution of electrons that have interacted inelastically with the atoms of the specimen. These inelastic interactions provide a wealth of information about the electronic structure of the specimen atoms, their bonding and nearest neighbor distributions, and their dielectric response. Carbons exhibit a wide variety of forms involving crystalline and noncrystalline forms because of its various bonding states. In the noncrystalline forms, especially, not only is there pure sp^1 , sp^2 and sp^3 bonding, but also there is modified bonding (deformed from a pure bonding state) or combined bonding (i.e. more than two bonding states are included in a material). These exist because there is less constraint compared with a structure with long-range order. Studies of relationships between the topology of coordination and resultant physical properties are currently of major interest. An EELS analysis, therefore, is a powerful technique to

describe carbons in terms of their bonding states, atomic configurations, and physical properties. The principles and backgrounds of EELS analyses are described in detail by Egerton [1] with concepts and analytical procedures being described by Williams [2,3].

In this chapter, the principle of EELS analysis and the information obtained from the spectra are first briefly reported, after which the applications of EELS analysis to characterize an amorphous carbon material are described.

2 Basic Principles of EELS and Instrumentation

Fast electrons incident in thin specimens lose energy by several processes. The four most common energy loss processes, in order of increasing energy loss, are phonon excitation, inter- and intra-band transitions, plasmon excitation, and inner-shell ionization (Fig. 1). The two major parameters of any inelastic scattering are the energy loss E and the scattering semiangle θ ; typical values are summarized in Table 1. The probability of a specific scattering event occurring is expressed by the

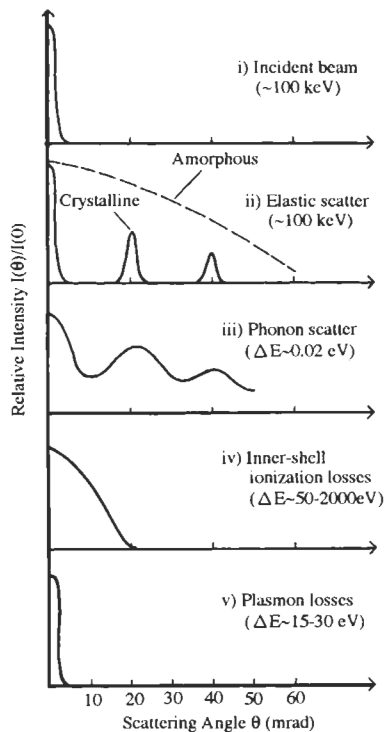


Fig. 1. Relative intensities of several scattering processes as a function of scattering angle θ : (i) incident beam, (ii) elastic scatter, (iii) photon scatter, (iv) inner-shell ionization losses, (v) plasmon losses. After Williams (1984) [3].

Table 1

Characteristics of the principal energy-loss processes. After Williams and Carter (1996) [2].

| Process | Energy loss (eV) | θ_E (m rads) |
|------------------------------|------------------|---------------------|
| Phonon excitation | ~0.02 | 5–15 |
| Inter/intra-band transitions | 5–25 | 5–10 |
| Plasmon excitation | ~5–25 | < ~0.1 |
| Inner-shell ionization | ~30–1000 | 1–5 |

scattering cross-section. When the energy loss is E , and the change of wave number vector is $q = k - k_0$, the elastic scattering cross-section is given by

$$\delta^2 \sigma / \delta E \delta \Omega = (1/\pi^2 a_0^2 e^2) (1/q^2) \text{Im}[-1/\epsilon(q, E)] \quad (1)$$

where a_0 is Bohr radius, σ is total scattering cross section, and Ω is solid angle [1,2]. This is the most fundamental equation of EELS, showing that several optical constants can be derived from an EELS spectrum. For instance, the term in Eq. (1), $\text{Im}[-1/\epsilon(q, E)]$, is called a loss function and is the relationship between the dielectric response of electrons and the EELS spectrum. The term is expressed by a real and ideal part of the dielectric function $\epsilon = \epsilon_1 + i\epsilon_2$.

$$\text{Im}[-1/\epsilon(q, E)] = \epsilon_2 / (\epsilon_1^2 + \epsilon_2^2) \quad (2)$$

EELS equipment is an electron spectrometer unit and detection unit. Currently, two types of commercial spectrometers are manufactured: one is the magnetic prism spectrometer (Gatan), and the other is the omega filter (Zeiss (now LEO)). The magnetic prism is designed with energy spectrometry as its primary function, and the omega filter is used mainly for energy-filtered imaging although spectra can be obtained. The recently designed Gatan Imaging Filter (GIF) combines both spectral and imaging capabilities. The magnetic prism is a simple but highly sensitive device with resolving power of approximately 1 eV even when the energy of the incident electron beam is as high as 400 keV. A schematic diagram of the spectrometer optics is shown in Fig. 2. Electrons are selected using a variable entrance aperture. The electrons travel down a “drift tube” through the spectrometer and are deflected through $\geq 90^\circ$ by the surrounding magnetic field. Electrons with greater energy loss (dashed line) are deflected further than those suffering zero loss (solid line). A spectrum is thus formed in the dispersion plane, which consists of a distribution of electron counts (I) versus energy loss (E). As shown in Fig. 2, electrons suffering the same energy loss but traveling in both on-axis and off-axis directions are also brought back to a focus in the dispersion plane of the spectrometer, which thus acts as a magnetic lens. The object plane of the spectrometer is usually set at the back focal of the projector lens.

There are two ways for acquiring the spectrum, serial-acquisition EELS (SEELS) and parallel-acquisition EELS (PEELS). PEELS gathers the whole energy spectrum

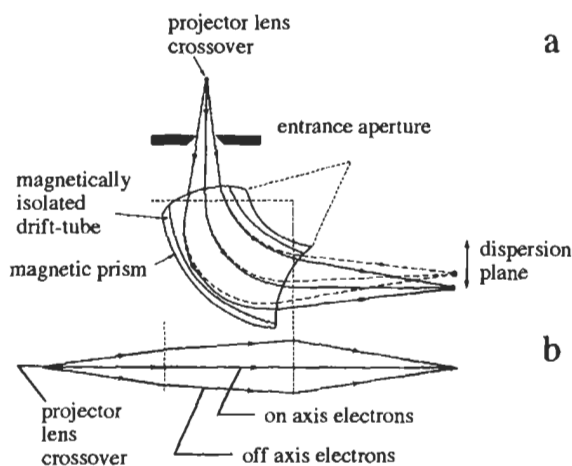


Fig. 2. Ray paths through a magnetic prism spectrometer: (a) dispersion and focusing of the electrons; (b) the lens-focusing action in the plane normal to the spectrometer. After Williams and Carter (1996) [2].

simultaneously and is more efficient than SEELS. PEELS comprises a YAG scintillator coupled via fiber optics to a semiconductor photodiode array in the dispersion plane of the spectrometer, as shown in Fig. 3a. The spectrum accumulates across the whole energy range simultaneously. After integration, the whole spectrum is read out via an amplifier through an A/D converter and into a multi-channel analyzer system. Spectra with sufficient intensity can be acquired in a fraction of a second, making PEELS imaging a practical reality. For the energy-filtered imaging, as described later, the detection system is composed of a two-dimensional slow scan CCD array detector rather than a single line of diodes (Fig. 3b).

3 The Energy-Loss Spectrum

An energy-loss spectrum contains three distinct groupings of spectral peaks, the first being the zero-loss peak, the second the low energy-loss (predominantly plasmon) peaks and the third the high energy-loss (ionization loss) peaks. Figure 4 shows a schematic EELS spectrum and the various processes of electron excitation in each energy region.

3.1 The Zero Loss Peak

The predominant peak of the spectrum is the zero-loss peak. As the name implies, this peak consists mainly of electrons that have retained the incident beam energy E_0 . Such electrons may be forward scattered in a relatively narrow cone within a few milliradians of the optic axis and constitute the 000 spot in the diffraction pattern, i.e. the direct beam. Strictly speaking, the peak is not just “zero-loss” electrons but contains electrons which have suffered very low energy-loss processes such as

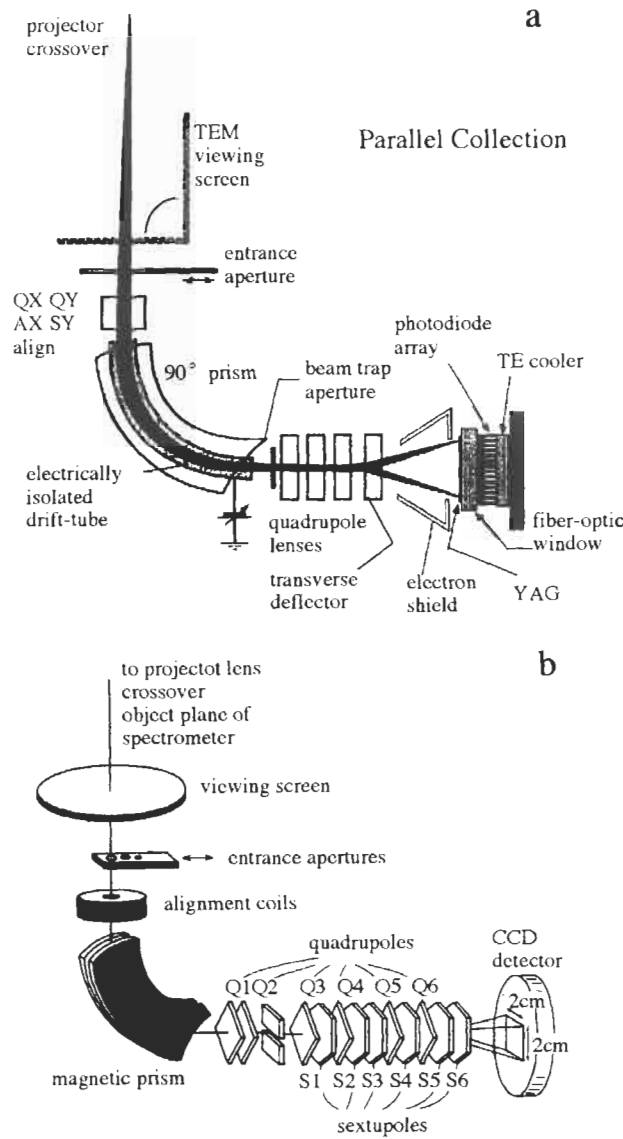


Fig. 3. (a) A representative EELS acquisition mode, parallel collection. (b) Gatan Imaging Filter using CCD detector. Courtesy of Gatan Inc.

excitation of phonons. The zero-loss peak contains no useful micro-analytical information, but the FWHM (full width at half maximum) of the zero-loss peak is commonly used as a definition of the resolution of the EELS system. The combination of the inherent resolution of the spectrometer and the energy resolution of the beam produces a finite width of zero-loss peak. In a well-aligned magnetic prism spectrometer, the best resolution is ~ 0.3 eV, but is ~ 1 eV in conventional use.

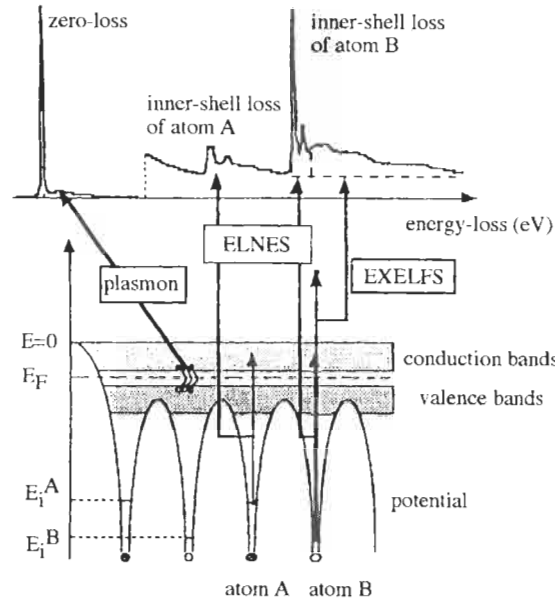


Fig. 4 An energy-loss spectrum and the related energy levels of electrons surrounding adjacent atom A and atom B. The zero-loss peak is above the Fermi energy E_F , the plasmon peak is at the energy level of the conduction/valence bands, and the critical ionization energy required to eject specific inner-shell electrons are shown.

3.2 Low-Loss Spectrum

3.2.1 Plasmon

The term “low-loss” is used to describe the energy-loss of electrons in the range up to about 50 eV. In this part of the spectrum, electrons, which have plasmon oscillations or have generated inter- or intra-band transitions, are observed. Plasmon is made up of longitudinal wave-like oscillations of weakly bonded electrons. The oscillations are rapidly damped, typically having a lifetime of about 10^{-15} seconds and so are quite localized to <10 nm. The plasmon peak is the second most dominant feature of the energy-loss spectrum after the zero-loss peak. The energy E_p lost by the beam electron when it generates a plasmon of frequency ω_p is given by

$$E_p = (\hbar/2\pi)\omega_p = (\hbar/2\pi)(n e^2/\epsilon_{0m})^{1/2} \quad (3)$$

where \hbar is Planck's constant, e and m are the electron charge and mass, respectively, ϵ_0 is the dielectric constant of free space, and n is the free-electron density. Typical values of E_p are in the range 5–25 eV. Spectra from unknown specimens are compared with stored library standards. A collection of low-loss spectra for all elements has been compiled in an EELS Atlas [4] and helps identify unknown specimen atoms.

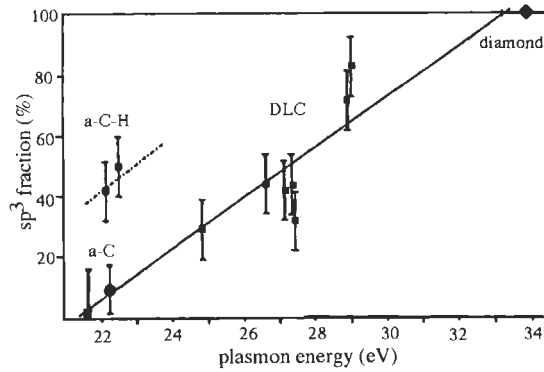


Fig. 5. The fraction of sp^3 bonding as a function of the bulk plasmon energy, modified from Fallon and Brown (1993) [5]. The sp^3 fraction was measured from the carbon k-edge $1s$ to π^* transition.

As seen in Eq. (3), E_p is affected by n , the free-electron density. Interestingly, n may change with the chemistry or bonding state of the specimen. So, in principle, measurement of the plasmon energy loss can give indirect semi-quantitative (microanalytical) information. The principle of plasmon-loss semi-quantitative analysis is based on empirical observations of shifts in the plasmon peak position (E_p) with composition C , giving an expression of the form:

$$E_p = E_p(0) \pm C(dE_p/dC) \quad (4)$$

where $E_p(0)$ is the plasmon energy loss for the pure component. By creating a series of binary systems of known composition, a working curve can be developed to be used to calibrate either E_p or C . This analysis can estimate sp^2/sp^3 ratios within amorphous carbons [5–8]. Similarly, using the relative intensity of $1s$ to π^* transition, observed close to the K-shell ionization peak (described below) the sp^2 fraction of amorphous carbon is estimated [5,7,9]. Figure 5 shows an empirically obtained relationship between the plasmon energy and fractions of sp^3 bonding that were measured from the $1s$ to π^* transition [5], showing a close relationship between the two.

3.2.2 Inter- and intra-band transitions

An electron in the beam may transfer sufficient energy to a core electron to cause it to change its orbital state, for example, to a Bohr orbital of higher quantum number. These events are called “a single electron interaction” and they result in energy losses of up to ~ 25 eV. Interactions with molecular orbitals such as π orbitals produce characteristic peaks in this low-energy region of the spectrum. It is possible to use the intensity variation in this part of the spectrum to identify a particular electronic state of the specimen. However, details of the spectrum intensity variations due to single electron interactions are not well understood.

3.2.3 Dielectric-constant determination and band gap

The energy-loss process can be considered as the dielectric response of electrons of the specimen to the passage of a fast electron. As a result, the energy-loss spectrum contains information about the dielectric constant (ϵ). The single-scattering spectrum intensity $I(l)$ is related to ϵ by the expression:

$$I(l) = I_0(t/k) \text{Im}(-1/\epsilon) \ln[1 + (\beta/\theta_E)^2] \quad (5)$$

where I_0 is the intensity in the zero-loss peak, t is the specimen thickness, and k is a constant incorporating the electron momentum and Bohr radius [1]. In order to extract the real part of the dielectric constant from the imaginary part (Im) in Eq. (5), a Kramers–Kronig analysis is used. In this analysis, because a single-scattering spectrum is necessary, a deconvolution has to be carried out.

The advantage of EELS for this kind of work is the improvement in spatial resolution over that of the electromagnetic radiation technique. Also, the frequency range which is available is more extended. The low-energy plasmon part of the energy-loss spectrum to about 20 eV is of most interest and corresponds to an optical analysis of the dielectric response from the visible to the ultraviolet.

In the region of the spectrum immediately after the zero-loss peak, and before the rise in intensity preceding the plasmon peak, a region of low intensity is observed. If this intensity approaches the dark noise of the detector, then there are no electron–electron energy transfers occurring. This effect implies that there is a forbidden transition region, which is simply the band gap between the valence and conduction bands in materials. This technique and concept have been adopted to measure band gap and dielectric constants of semiconductors such as silicon and insulators such as Al_2O_3 . Recently, the authors estimated band gap and dielectric properties of an amorphous diamond using this technique [10].

3.3 High-loss Spectrum

3.3.1 Inner-shell ionization

The high-loss part of the spectrum above 50 eV contains information from inelastic interactions with the inner or core shells.

When an electron beam transfers sufficient energy to a K, L, M, N, or O shell electron to move it outside the attractive field of the nucleus, then the atom is ionized. The decay of the ionized atom back to its ground state may produce a characteristic X-ray, or an Auger electron. So the processes of inner-shell ionization loss, that is EELS and X-ray energy-dispersive spectroscopy (XEDS), are different aspects of the same phenomenon. The process of ionization loss is characteristic of the atom involved and so the signal is a direct source of elemental information, as are the

characteristic X-rays. The ionization-loss signal is called an “edge” in EELS analysis. Detection of the beam electron that ionized the atom is independent of whether the atom emits an X-ray or an Auger electron. EELS is not affected by the fluorescence-yield limitation that restricts light-element X-ray analysis.

Inner-shell ionization is generally a high-energy process (Fig. 4). For example, the lightest solid element, Li, requires an input of ≥ 55 eV to eject a K-shell electron, and so the loss electrons are usually found in the “high-loss” region of the spectrum, above ~ 50 eV. In a case dealing with high-Z atoms, K-shell electrons require much more energy, so other lower-energy ionizations, such as the L and M edges, are searched for. Compared with plasmon excitation, which requires much less energy, the ionization cross-sections are relatively small and the mean-free paths relatively large. As a result, the ionization edge intensity in the spectrum is much smaller than the plasmon peak, and becomes even smaller as the energy loss increases. In Fig. 4 the intensities of the inner-shell loss are exaggerated.

3.3.2 *ELNES and EXELFS*

The energy resolution of the magnetic prism spectrometer is very high, which means that the energy-loss spectrum contains a great deal of information in addition to basic elemental chemistry. Most of this chemical information is contained in the fine-detailed intensity variations at the ionization edges in the core-loss spectra and is termed energy-loss near-edge structure (ELNES) and extended energy-loss fine structure (EXELFS) (Fig. 4). From this fine structure can be obtained information on the bonding of ionized atoms, the coordination of the atom, and the density of states. Furthermore, the distribution of other atoms around the ionized atom can be studied, i.e. the radial distribution function (RDF). Figure 6a shows a representative high-loss spectrum. The ionization edges are superimposed on a rapidly decreasing background intensity from electrons that have undergone random, plural inelastic scattering events (Fig. 6b). The edge shape may also contain fine structure (ELNES) immediately after the edge (Fig. 6c), which is due to bonding effects. More than 50 eV after the edge, small intensity oscillations (EXELFS) may be detectable (Fig. 6d), which is due to diffraction effects from the atoms which are neighbors to the ionized atom. EXELFS is analogous to extended X-ray absorption fine structure (EXAFS) in X-ray spectra.

3.3.3 *Energy filtered and spectrum imaging*

Intensities in any part of an EELS spectrum can be selected and used to form an image. A variety of images, not just elemental images, but dielectric-constant images, valence-state images and thickness images are formed by using selected energies and have several advantages over conventional TEM and STEM images. Figure 7 shows a bright field TEM image and a series of energy-filtered images revealing the Si, C, and O elemental distribution (Figs. 7b–d) and also the “bonding-state maps” of carbon

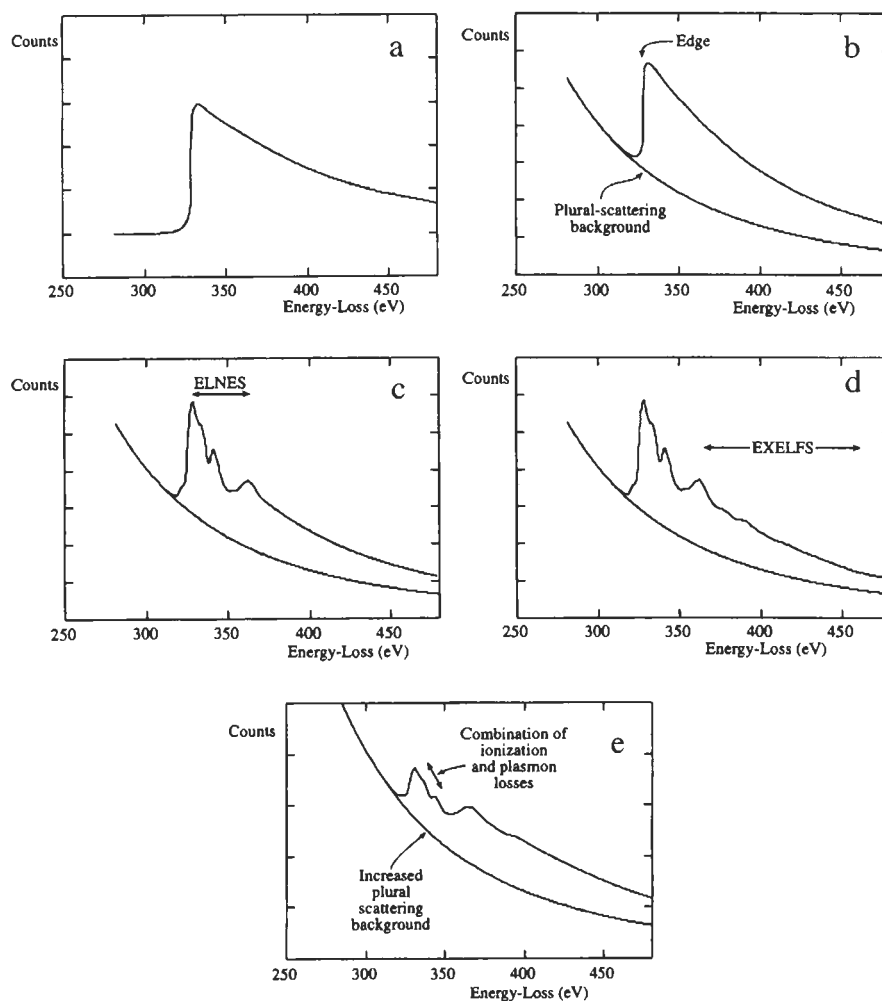


Fig. 6. The characteristic features of an inner-shell ionization edge: (a) idealized saw-tooth edge; (b) the edge superimposed on the background arising from plural inelastic scattering; (c) ELNES; (d) EXELFS; (e) in a thick specimen plural scattering, such as the combination of ionization and plasmon losses, distorts the post-edge structure. After Williams and Carter (1996) [2].

(Figs. 7e,f) for a diamond-like carbon film deposited on a silicon substrate. In the oxygen-rich interface layer carbon atoms exhibit a double layer of π bonds, while the carbon film itself is predominantly σ bonded, indicating a high degree of diamond-like character [2].

The strong forward-scattered EELS signal, combined with a detection efficiency close to 100%, shows that EELS imaging has considerable advantages over thin-film X-ray mapping. This makes EELS imaging an extremely attractive technique, by integrating enormous number of signals available in the EELS spectrum.

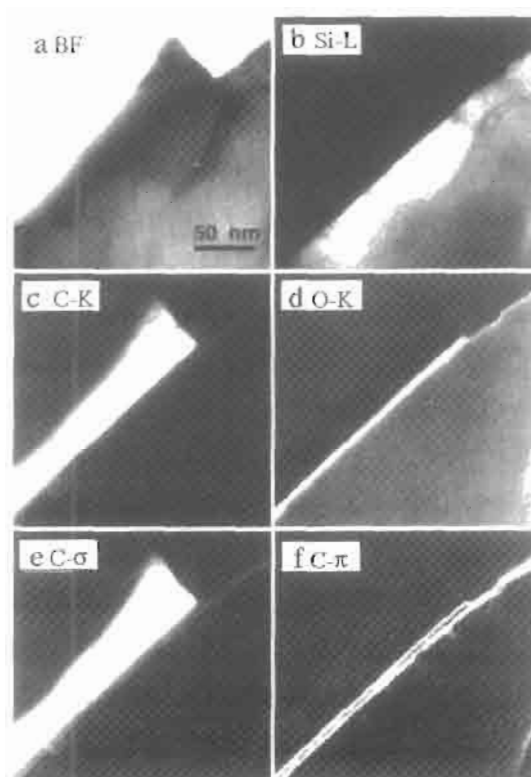


Fig. 7. TEM bright field image (a) and a series of the energy-filtered images (b) to (f) for a diamond-like carbon film on a Si substrate. After Williams and Carter (1996) [2].

4 Applications to Characterizing Carbon Materials

4.1 Estimation of Band Gap of an Amorphous Diamond

A series of characterizations of a unique carbon material in terms of its band gap, fraction of sp^3 , and density of state (DOS), as well as the plasmon and the inner-shell ionization, is described below. The sample material used in the study was a new form of transparent amorphous diamond, which was synthesized from C_{60} fullerenes by a shock-compression and rapid-quenching technique [11,12,13]. X-ray and electron diffractometry revealed that the material was amorphous in long-range order, and plasmon spectra of EELS showed it to be identical to diamond (Figs. 8 and 9) [11]. In addition, the structure in short-range order, determined by RDF analysis, demonstrated the characteristic configuration of carbon atoms [14]. The tetrahedra of carbon atoms were arranged in the same manner as those of crystalline diamond within a region of unit-cell size; in other words, this material consisted of randomly arranged unit-cell-sized diamond.

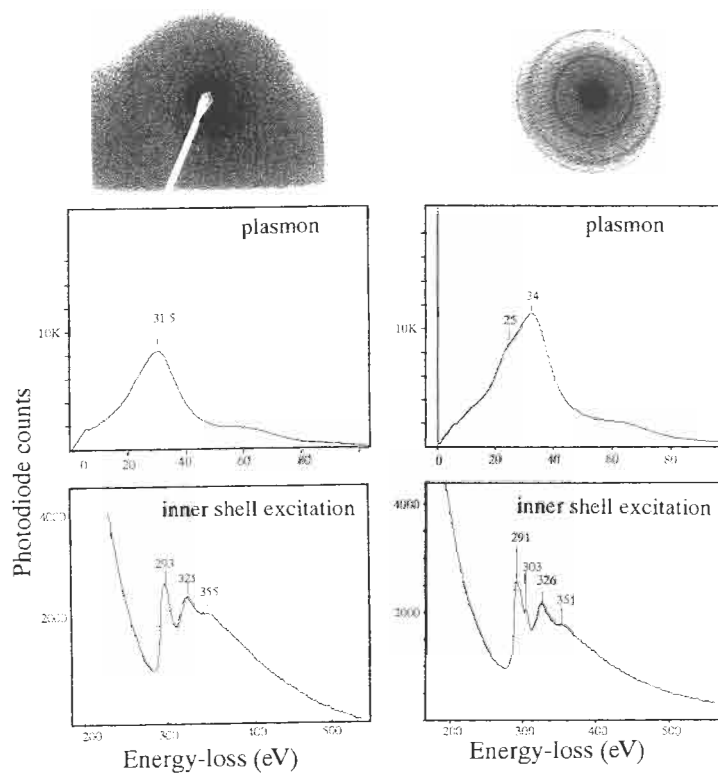


Fig. 8. Electron diffraction patterns, plasmon loss, and inner-shell excitation spectra for the amorphous diamond (left) and nanocrystalline diamond (right).

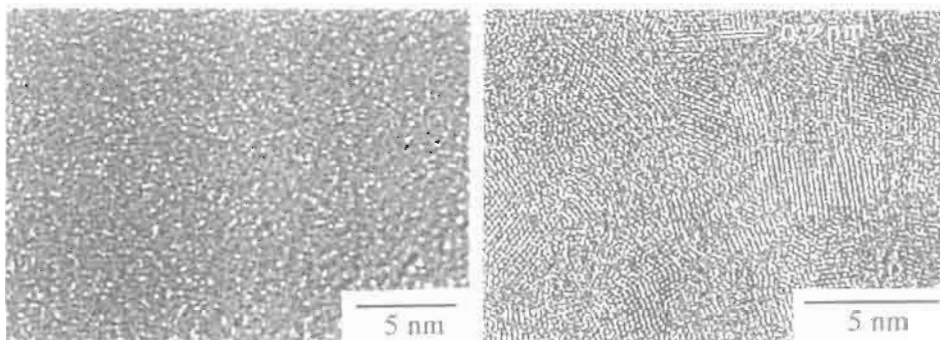


Fig. 9. Lattice images for the amorphous diamond (left) and nanocrystalline diamond (right).

An optical absorption method directly gives the imaginary part of the dielectric function, ϵ_2 , associated with a single electron excitation of an interband transition. An EELS spectrum does not directly give ϵ_2 . However, an EELS spectrum is related to the dielectric function by Eq. (5) [1], so that the real and the imaginary parts of the

dielectric function, ϵ_1 and ϵ_2 , can be obtained by a Kramers–Kronig analysis of the loss function ($\text{Im}[-1/\epsilon]$) obtained from the EELS spectrum. For this analysis, a high-energy-resolution EELS spectrum is required, so a specified spectrometer based on a TEM was used [15]. The energy-resolution of that measurement was 0.2 eV. To confirm the applicability of the technique to carbon materials, a natural crystalline diamond was examined.

Representative high-resolution EELS spectra for C_{60} fullerene, amorphous diamond, and natural crystalline diamond in the plasmon region (0–50 eV) and in the inner-shell excitation region (280–298 eV) are shown in Fig. 10a(top) and Fig. 10b(top), respectively. For the C_{60} fullerene, the peaks around 6.5 eV and 285 eV

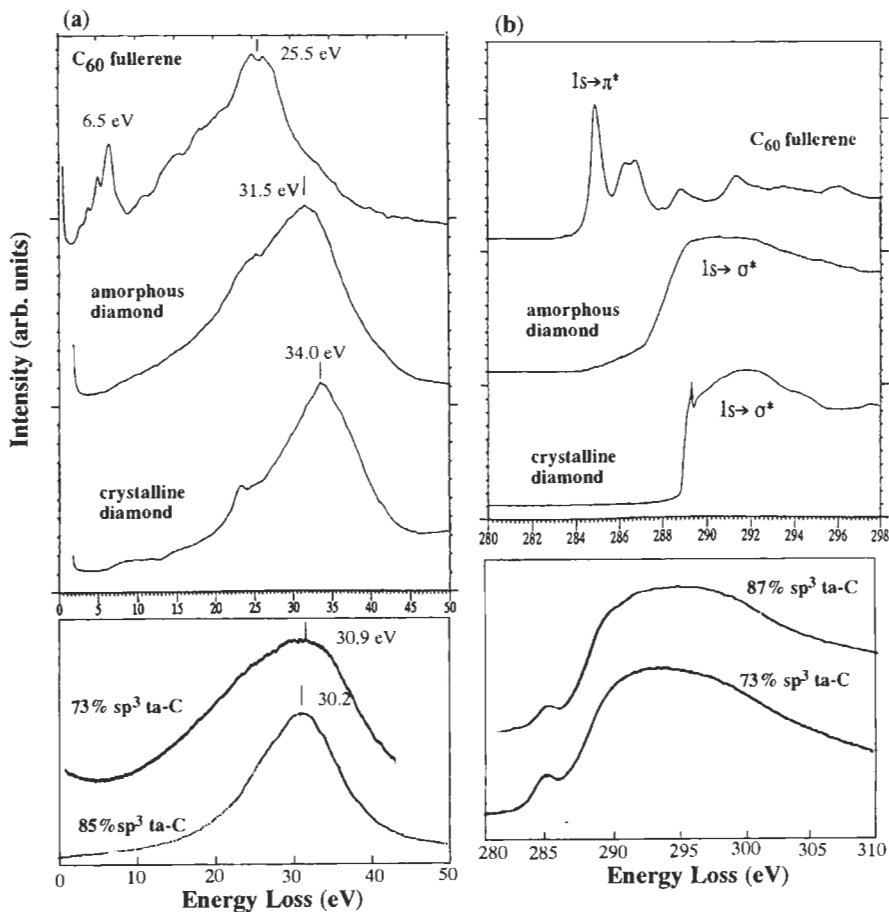


Fig. 10 High-resolution EELS spectra of (a) plasmon region and (b) inner shell excitation region, k-edge of carbon, for C_{60} fullerene, the present amorphous diamond, crystalline diamond. For comparison, plasmon spectra for 73% sp^3 [7] and for 85% sp^3 [8], and k-edge spectra for 87% sp^3 [9] and 73% sp^3 [7] are shown (each bottom). A sharp peak observed in the k-edge spectrum for the crystalline diamond is assigned to exciton.

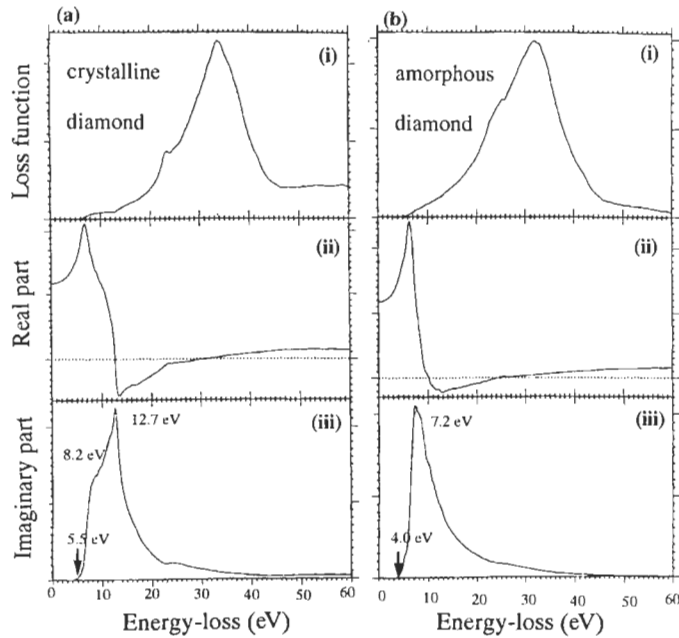


Fig. 11. Loss function (i), the real part (ii) and imaginary part (iii) of the dielectric function for natural crystalline diamond (a) and for amorphous diamond (b). For the amorphous diamond, the magnitude of 4.0 eV is approximately middle value among the sample fragments measured.

were attributed to $\pi \rightarrow \pi^*$ transition [15] and $1s \rightarrow \pi^*$ transition, respectively. These peaks were completely absent for the amorphous diamond. The σ -plasmon peak for the amorphous diamond was 31.5 eV. Figure 11 shows the loss function ($\text{Im}[-1/\epsilon]$), the real part (ϵ_1), and the imaginary part (ϵ_2) of the dielectric function calculated from Fig. 10a for the crystalline and the amorphous diamond. The loss function was obtained by removing contributions from multiple scattering using the Fourier-log deconvolution method and by using the refractive index, $n = 2.42$, of crystalline diamond. The dielectric function was derived from the loss function using Kramers–Kronig analysis. For the crystalline diamond, the onset energy of the spectrum (the band gap energy) was 5.5 eV (Fig. 11a(iii)), in excellent agreement with the established band gap of diamond (5.5 eV). Two peaks appeared at 8.2 and 12.7 eV in the ϵ_2 spectrum and were assigned to interband transitions at the Γ point and at the X and L points, respectively [16]. For the amorphous diamond, the intensity increase at the onset was broader than that of the crystalline diamond (Fig. 11b(iii)), indicating a broader DOS. The onset energy varied from 3.5 to 4.5 eV with the sample fragments. A prominent peak was observed at 7.2 eV, which may correspond to the Γ -point transition (Fig. 11b(iii)). Very little of the structure corresponding to the X and L points transition was seen. This characteristic phenomenon can be reasonably explained by the short-range structure mentioned above. Inner-shell excitation spectrum and ϵ_2 spectrum reflect the distribution of the electron density. Assuming

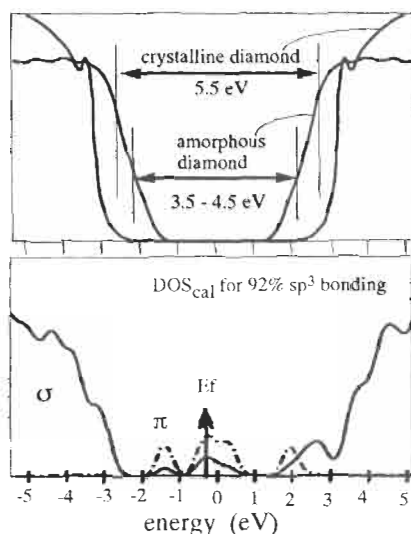


Fig. 12. Schematic illustration of hypothetical DOS for the amorphous diamond and for crystalline diamond (top). A theoretically calculated DOS for 92% sp^3 -bonded material by Robertson (1997) [17] is shown for comparison (bottom).

the inner-shell spectrum to be measured as the distribution of electrons in the conduction band, a hypothetical DOS was drawn for the amorphous diamond and crystalline diamond (Fig. 12).

4.2 Comparison with Other sp^3 Amorphous Materials

In investigations of diamond-like carbon, one aim is to fabricate highly sp^3 -bonded amorphous carbon with properties comparable to those of crystalline diamond. Thus, several highly sp^3 -bonded materials, having more than 80% sp^3 , were obtained with, for instance, 92% sp^3 material [18], 87% sp^3 [9], 85% sp^3 [19] and 83% sp^3 [20]. For 87% sp^3 [9] and 73% sp^3 [7] materials, the $1s \rightarrow \pi^*$ transition peak was clearly observed (Fig. 10b(bottom)), while the present amorphous diamond does not exhibit this peak. Further, in the plasmon region, the peaks of 85% sp^3 [19] and 73% sp^3 [7] material are 30.2 and 30.9 eV, respectively (Fig. 10a(bottom)), while the peak of the amorphous diamond is 31.5 eV.

Figure 13a shows a summary of the optical (band) gaps of amorphous carbon materials as reported above. The magnitude of the band gap of the present material was 3.5 to 4.5 eV. The variation was probably due to temperature distribution in the sample. In any case, the band gap measured was larger than any other sp^3 material reported before (Fig. 13a) [7,20–22]. An sp^3 fraction is usually estimated from the plasmon peak energy [5–7]. The plasmon peak energy of the present material, 31.5 eV, is the highest of the sp^3 materials. Figure 13b shows the variation of density with sp^3 fraction for some carbons [6,9,18,22,23]. The density of the amorphous diamond

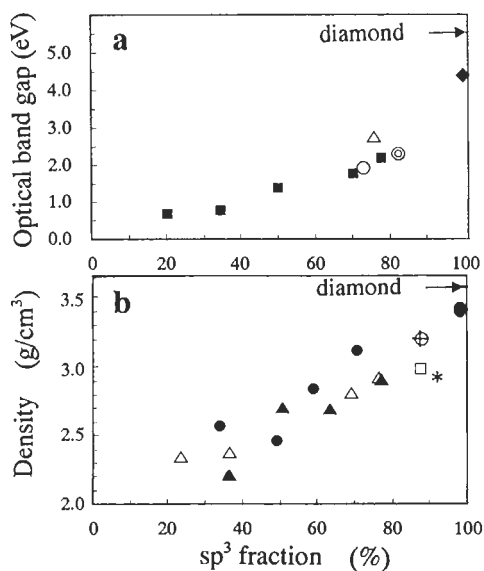


Fig. 13. (a) Variation of optical (band) gap versus the sp^3 fraction for amorphous carbon materials. Solid rhombus: the present amorphous diamond; open circle: Merkulov (1998) [7]; solid square: Lee (1998) [21]; double circles; Chhowalla (1997) [20]; open triangle: Weiler (1996) [22]. (b) The variation of density versus the sp^3 fraction for ta-C materials. solid rhombus: the present amorphous diamond; cross-hatched circle: Ravi (1996) [9]; Open square: Pharr (1996) [6]; open triangle: Weiler (1996) [22]; solid triangle: Fallon (1993) [23]; solid circle and asterisk: Mckenzie (1991) [18].

measured by a floating method was higher than 3.3 g cm^{-3} . Comparing the plasmon peak energies, which depend on electron density, for the amorphous diamond (31.5 eV) and the crystalline diamond (34.0 eV), the true density may be in the range 3.3 to 3.5 g cm^{-3} . The value of 3.3 g cm^{-3} , in spite of being the smallest estimation, is higher than those of other sp^3 materials (Fig. 13b). The largest band gap, up to 4.5 eV, the highest plasmon energy, 31.4 eV, and a density higher than 3.3 g cm^{-3} is associated with almost 100% sp^3 bonding within the amorphous diamond. These properties were confirmed by the short-range structure analysis using RDF.

5. Conclusions: The Future of EELS

Both the experimental techniques and the theoretical treatment of EELS are still developing. However, EELS analysis provides indispensable information to understanding carbons. Furthermore, the developed energy-filtering technique and imaging technique exhibit many advantages over conventional TEM and STEM images, because they display not just elemental images, but electronic-state images. Therefore, these techniques, as well as fine structure analysis (ELNEL, EXELFS), will find wider applications to carbons.

References

1. R.F. Egerton, *Electron Energy-Loss Spectroscopy in the Electron Microscope*, 2nd Edn. Plenum Press, New York, 1996.
2. D.B. Williams and C.B. Carter, *Transmission Electron Microscopy Vol. I: Basis; Vol. IV: Spectroscopy*. Plenum Press, New York, 1996.
3. D.B. Williams, *Practical Analytical Electron Microscopy in Materials Science*, 2nd Edn. Philips Electron Optics Publishing Group, Mahwah, New Jersey, 1984.
4. C.C. Ahn and O.L. Krivanek, *EELS Atlas*. Gatan Inc. Pennsylvania, 1983.
5. P.J. Fallon and L.M. Brown, Analysis of chemical-vapour-deposited diamond grain boundaries using transmission electron microscopy and parallel electron energy loss spectroscopy in a scanning transmission electron microscope. *Diamond and Relat. Mater.*, 2: 1004–1011, 1993.
6. G.M. Pharr et al., Hardness, elastic modulus, and structure of very hard carbon films produced by cathodic-arc deposition with substrate pulsed biasing. *Appl. Phys. Lett.*, 68: 779–781, 1996.
7. V.I. Merkulov, D.H. Lowndes, G.E. Jellison, A.A. Puretzky and D.B. Geohegan, Structure and optical properties of amorphous diamond films prepared by ArF laser ablation as a function of carbon ion kinetic energy. *Appl. Phys. Lett.*, 73: 2591–2593, 1998.
8. S.D. Berger, D.R. McKenzie and P.J. Martin, EELS analysis of vacuum arc-deposited diamond-like films. *Phil. Mag. Lett.*, 57: 285–290, 1988.
9. S. Ravi et al., Nanocrystallites in tetrahedral amorphous carbon films. *Appl. Phys. Lett.*, 69: 491–493, 1996.
10. H. Hirai, M. Terauchi, M. Tanaka and K. Kondo, Band gap of essentially four-fold coordinated amorphous diamond. *Phys. Rev. B*, 60: 6357–6361, 1999.
11. H. Hirai, K. Kondo, N. Yoshizawa, and M. Shiraiishi, Amorphous diamond from C60 fullerene. *Appl. Phys. Lett.*, 64: 1797–1799, 1994.
12. H. Hirai and K. Kondo, Modified phases of diamond formed under shock compression and rapid quenching. *Science*, 253: 772–774, 1991.
13. H. Hirai and K. Kondo, Changes in structure and electronic state from C60 fullerene to amorphous diamond. *Phys. Rev. B*, 51: 15555–15558, 1995.
14. H. Hirai, Y. Tabira, K. Kondo, T. Oikawa and N. Ishizawa, Radial distribution function of a new form of amorphous diamond shock induced from C60 fullerene. *Phys. Rev. B*, 52: 6162–6165, 1995.
15. R. Kuzuo, M. Terauchi, M. Tanaka, Y. Saito, and H. Shinohara, Electron-energy-loss spectra of crystalline C84. *Phys. Rev. B*, 49: 5054–5057, 1994.
16. R.A. Roberts and W.C. Walker, *Phys. Rev.*, 161: 7730, 1967.
17. J. Robertson, Electronic structure of diamond-like carbon. *Diamond Relat. Mater.*, 6: 212–218, 1997.
18. D.R. McKenzie, D. Muller and B.A. Pailthorpe, Compressive-stress-induced formation of thin-film tetrahedral amorphous carbon. *Phys. Rev. Lett.*, 67: 773–776, 1991.
19. C. Ronning, E. Dreher, J.-U. Thiele, P. Oelhafen and H. Hofsass, Electronic and atomic structure of undoped and doped-ta-films. *Diamond Relat. Mater.*, 6: 830–834, 1997.
20. M. Chhowalla, Y. Yin, G.A.J. Amaratunga, D.R. McKenzie and T. Frauenheim, Boronated tetrahedral amorphous carbon. *Diamond Relat. Mater.*, 6: 207–211, 1997.
21. J. Lee, R.W. Collins, V.S. Veerasamy and J. Robertson, Analysis of the ellipsometric spectra of amorphous carbon thin films for evaluation of the sp^3 -bonded carbon content. *Diamond Relat. Mater.*, 7: 999–1009, 1998.
22. M. Weiler et al., Preparation and properties of highly tetrahedral hydrogenated amor-

- phous carbon. *Phys. Rev. B*, 53: 1594–1608, 1996.
23. P.J. Fallon et al., Properties of filtered-ion-beam-deposited diamond-like carbon as a function of ion energy. *Phys. Rev. B*, 48: 4777–4782, 1993.

Chapter 16

Visualization of the Atomic-scale Structure and Reactivity of Metal Carbide Surfaces Using Scanning Tunneling Microscopy

Ken-ichi Fukui, Rong-Li Lo and Yasuhiro Iwasawa*

Department of Chemistry, Graduate School of Science, The University of Tokyo, Tokyo 113-0033, Japan

Abstract: Recent studies on atomic-scale structures and reactivity of metal carbide surfaces by scanning tunneling microscopy (STM) are reviewed. The structure of an α - $\text{Mo}_2\text{C}(0001)$ surface varies depending on surface coverage by carbon atoms which can be regulated by annealing temperature and reaction time. By careful control of the preparation procedures, well-ordered C-terminated surfaces with $(\sqrt{3} \times \sqrt{3})\text{R}30^\circ$ -honeycomb structure and $c(2 \times 4)$ -zigzag row structure were successfully prepared and imaged by STM. Each carbon atom inside the structures was visualized as a shallow sombrero protrusion at low tunneling resistances of less than $1 \text{ M}\Omega$. A novel selective etching reaction of the surface carbon atoms by oxygen gas occurred even at room temperature. On a C-terminated $\text{Mo}_2\text{C}(0001)$ surface with both $(\sqrt{3} \times \sqrt{3})\text{R}30^\circ$ -honeycomb and $c(2 \times 4)$ -zigzag row structures, the etching reaction selectively occurred on the $c(2 \times 4)$ -zigzag structure, leading to exposure of an underlying (1×1) molybdenum layer.

Keywords: Scanning tunneling microscopy, Electronic density of states, Tunneling resistance, Molybdenum carbide, Layered metal carbon alloy, Surface carbon atoms.

1 Introduction

Since the findings of Boudart et al. [1] that early transition metal carbides behave like noble metals rather than the native transition metals in surface catalysis, this class of material has been of considerable interest as potential substitutes for precious noble metals in catalyst applications [2]. The materials show high activities for hydrodesulfurization and hydrodenitrogenation of hydrocarbons [3]. These reactions are relevant in environmental catalysis. Also, transition metal carbides have attracted attention in both basic and applied research laboratories [4]. The transition metal carbides of Groups 4–6 have unique properties combining those of both metal and ceramics; they are good electrical and thermal conductors typical of metals, and they possess ultra-hardness, very high melting points, and stable sub-stoichiometry typical

of ceramics. The bonding mode is thought to be a combination of covalent, ionic and metallic bonds. Practically, they have been used as hard coating materials, as field electron emitters and have been proposed for first-wall materials for nuclear fusion reactors [5]. Studies with model carbide surfaces prepared by modification of metal single crystals have been undertaken [6]. However, little has been published about the composition of the single crystal surfaces of the chemically active transition metal carbides at an atomic scale resolution which is necessary to understand these unique catalytic abilities.

A few examples have been reported describing the surface structures of transition metal carbides by scanning tunneling microscopy (STM). The (110) surface tends to be faceted and such faceted structures have been observed on TaC(110) [7,8] and NbC_{0.865}(110) [9]. In the latter case, atoms at the ridge were resolved. On NbC_{0.75}(100) [9], the coexistence of a square lattice region and a hexagonal lattice region was detected, showing the complexity of the surface structure of these materials. Most of the (111) faces of transition metal carbides in Groups 4 or 5 are terminated by a metal layer [4], but co-existence with a C-terminated ($\sqrt{3} \times \sqrt{3}$)R30° structure was proposed from a STM study on VC_{0.8}(111) [10].

Molybdenum carbides are representative of metal carbides with good catalytic performances. α -Mo₂C is a stable crystalline form which has an orthorhombic crystal structure [11]. Hexagonal notation is used here, because the arrangement of molybdenum atoms is a slightly distorted hcp (hexagonal closest packed structure). Carbon atoms occupy half of the lattice octahedral voids. The (0001) surface in the hexagonal system is equivalent to the (100) surface in the orthorhombic system. The bulk-truncated structure of α -Mo₂C(0001) is shown in Fig. 1. Mo-terminated structure and C-terminated structures are possible. However, a recent study of the surface by low energy electron diffraction (LEED) and STM revealed that neither of the bulk-truncated structures is exposed but the surface is always reconstructed depending on the stoichiometry at the surface [12]. It is reported that the activity and selectivity of molybdenum carbide catalysts are very sensitive to their surface composition [13]. By careful control of the preparation procedure, well-ordered C-terminated surfaces can be prepared on Mo₂C(0001) [12], in contrast to other transition metal carbides [4,9,14].

This chapter reviews recent STM studies on Mo₂C(0001) with atomic-scale resolution [12,15,16]. Well-ordered C-terminated surfaces of the ($\sqrt{3} \times \sqrt{3}$)R30° surface and the c(2×4) surface were observed on Mo₂C(0001) and each carbon atom inside the structures was successfully visualized at low tunneling resistances. A novel selective etching reaction by oxygen of carbon atoms on the surface of Mo₂C(0001) was found to occur at room temperature (RT). This process was visualized by STM which discriminates between each surface carbon atom. On a well-defined C-terminated surface composed of ($\sqrt{3} \times \sqrt{3}$)R30°-honeycomb and c(2×4)-zigzag row structures, the etching reaction selectively occurred on the latter structure, leading to exposure of an underlying (1×1) molybdenum layer. This may be the first step to understand, on an atomic scale, the unique and high catalytic specificity of molybdenum carbide.

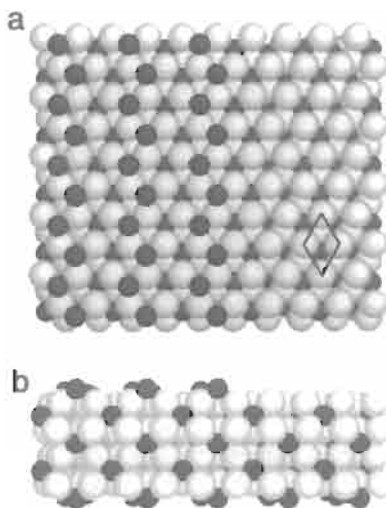


Fig. 1. Model of a bulk-truncated structure of an α - $\text{Mo}_2\text{C}(0001)$ surface. Larger and smaller spheres represent Mo and C atoms, respectively. Both of a Mo-terminated structure (right half) and a C-terminated structure (left half) are shown; (a) top view and (b) side view.

2 Principle of Scanning Tunneling Microscopy (STM)

After the initial observation of metal-vacuum-metal tunneling by Young et al. [17,18], Binnig et al. [19,20] demonstrated in 1981 the first successful combination of vacuum tunneling with a piezoelectric drive system attached to an STM. A conducting sample and a sharp metal tip, which acts as a local probe, were brought within nanometer distances of each other, to result in significant overlap of the electronic wavefunctions. With an applied bias voltage (V_s , typically between 10 mV and 4 V), a tunneling current (I_t , typically between 10 pA and 10 nA) flows from the occupied electronic states near the Fermi level of one electrode into unoccupied states of the other electrode. By using a piezoelectric XYZ-drive system for the tip and a feedback loop, a map of the surface topography can be obtained. Under favorable conditions, a vertical resolution of tens of nanometers and a lateral resolution of picometers can be obtained. As a result, STM provides real-space images of surfaces of conducting material with atomic resolutions. In contrast to other electron microscopes and surface analytical techniques using electrons, STM can be operated in air, liquid, vacuum, and *in situ* reaction conditions because no free electrons are involved.

3 Preparation of Mo_2C Surfaces

An α - Mo_2C single crystal was grown by the floating zone method [21], then cut and polished to expose a (0001) surface. The polished surface, $\text{Mo}_2\text{C}(0001)$, was cleaned by Ar^+ sputtering (at 2–3 keV for 10–20 min) and annealed to elevated temperatures

for 30–60 min while keeping the pressure in the 10^{-8} Pa range. X-ray photoelectron spectroscopy (XPS) measurements of the $\text{Mo}_2\text{C}(0001)$ surface indicated that the concentration of carbon at the surface increases with high-temperature annealing [22]. At least three phases were observed by LEED after annealing at temperatures above 840 K for 60 min after Ar^+ sputtering [12]. Surface structures of $\text{Mo}_2\text{C}(0001)$ surfaces varied depending on the annealing processes and these determine carbon concentrations at the surfaces [12].

4 Visualization of the Atomic-scale Structure and Reactivity of Molybdenum Carbide Surfaces by STM

4.1 Atomic-scale Visualization of Surface Structures of Carbon-terminated $\text{Mo}_2\text{C}(0001)$ Surfaces

Annealing a sputtered $\text{Mo}_2\text{C}(0001)$ surface between 840 and 960 K, a $(\sqrt{3} \times \sqrt{3})\text{R}30^\circ$ structure brings about a well-ordered structure. Figure 2 is an STM image of the $(\sqrt{3} \times \sqrt{3})\text{R}30^\circ$ structure with a corresponding LEED pattern, after annealing at 950 K for 1 h [15]. Relatively large terraces have developed on the surface. The height differences between the terraces were multiples of 0.232 ± 0.006 nm, in agreement with the thickness of a single Mo-C bilayer of Mo_2C crystal parallel to the (0001) face (0.236 nm) [11]. Further examination of the structure of the terraces indicates ordered dark depressions with honeycomb structures for tunneling conditions typical for metallic surfaces [12] but without bright spots. The distance between two neighboring depressions on the terrace was 0.522 ± 0.002 nm close to 0.520 nm, i.e. $\sqrt{3}$ times the (1×1) unit cell constant. Hence, the depressions of the honeycomb

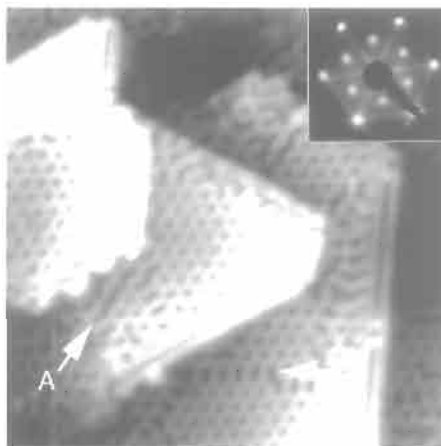


Fig. 2. STM topograph of a $\text{Mo}_2\text{C}(0001)$ - $(\sqrt{3} \times \sqrt{3})\text{R}30^\circ$ honeycomb structure which was measured after annealing an Ar^+ sputtered surface at 950 K for 1 h. $V_t = -100$ mV, $I_t = 0.5$ nA, 19.4×19.4 nm². Two types of domain boundaries are indicated by A and B with arrows. Inset is the corresponding LEED pattern recorded with a primary electron energy of 60 eV.

structure make the lattice of the $(\sqrt{3}\times\sqrt{3})R30^\circ$ structure. The terraces have hexagonal shapes surrounded by straight steps which are parallel to the direction of close packing in a molybdenum layer. One unit cell vector of the $(\sqrt{3}\times\sqrt{3})R30^\circ$ structure is always rotated from the step direction by 30° . In each terrace, there are several domains which are separated by two types of domain boundaries; a zigzag row of depressions (A type) and an array of elliptical depressions (B type). These boundaries are indicated by arrows in Fig. 2. Hammer et al. [10] also found a $(\sqrt{3}\times\sqrt{3})R30^\circ$ -honeycomb structure on $VC_{0.8}(111)$ and considered that a carbon atom was missing at the dark depression and that there was one carbon atom in each corner of the honeycomb skeleton. Each dark depression in the honeycomb structure corresponds to a carbon atom in the $Mo_2C(0001)-(\sqrt{3}\times\sqrt{3})R30^\circ$ structure, as explained below.

Each surface carbon atom located at the honeycomb hole is imaged by decreasing the tunneling resistance by shortening the separation distances from tip to surface [15]. Figure 3a is a high resolution STM topograph of the $(\sqrt{3}\times\sqrt{3})R30^\circ$ structure

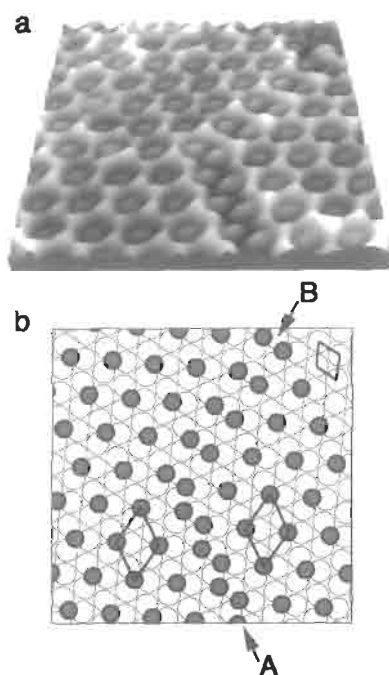


Fig. 3. (a) High resolution STM topograph ($4.4\times 4.3\text{ nm}^2$) of the $Mo_2C(0001)-(\sqrt{3}\times\sqrt{3})R30^\circ$ honeycomb structure which was imaged with a small tunneling resistance of $0.86\text{ M}\Omega$ ($V_s = +3\text{ mV}/I_t = 3.5\text{ nA}$). Each carbon atom adsorbed on the (1×1) Mo layer is visualized as shallow sombrero protrusions. This image includes two domains which are separated with two types of domain boundaries (A type and B type). (b) A schematic model of the $(\sqrt{3}\times\sqrt{3})R30^\circ$ structure corresponding to (A). Large empty circles and shaded circles represent Mo atoms and C atoms, respectively. A bulk-truncated Mo-terminated surface is postulated as the substrate (top right area with the (1×1) unit cell), but the layers under the Mo layer are not shown here to simplify the model.

with a tunneling resistance of $0.86 \text{ M}\Omega$ ($V_s = +3 \text{ mV}/I_t = 3.5 \text{ nA}$), which is much smaller than that in Fig. 2 ($200 \text{ M}\Omega$ ($V_s = -100 \text{ mV}/I_t = 0.5 \text{ nA}$)). This image has two $(\sqrt{3} \times \sqrt{3})\text{R}30^\circ$ domains separated by A-type and B-type domain boundaries seen in Fig. 2 as a zigzag row of depressions and an array of elliptic depressions, respectively. The corrugations of the atoms in the honeycomb structure and in the domain boundaries are 0.010 nm and 0.021 nm , respectively. The image contrast with positive bias voltages was slightly sharper than that of negative bias voltages. At an intermediate tunneling resistance of $6.67 \text{ M}\Omega$ ($V_s = +10 \text{ mV}/I_t = 1.5 \text{ nA}$), carbon atoms in dark depressions were imaged only at the domain boundaries. The STM image in Fig. 3a and the corresponding model in Fig. 3b show that carbon atoms at the boundaries occupy sites equivalent to those in either domain. Figure 3b shows a proposed model of the $(\sqrt{3} \times \sqrt{3})\text{R}30^\circ$ structure based on the assumption that each carbon atom occupies a three-fold hollow site of the (1×1) -hexagonal layer of molybdenum. This is supported from STM images taken near to a step edge of the $(\sqrt{3} \times \sqrt{3})\text{R}30^\circ$ surface, where the bright protrusions coincide with a unit cell of a (1×1) lattice of the bulk-truncated molybdenum layer[15]. Each bright protrusion could correspond to an exposed molybdenum atom in the outermost bilayer of the substrate without the $(\sqrt{3} \times \sqrt{3})\text{R}30^\circ\text{-C}$ layer. A STM observation of the $(\sqrt{3} \times \sqrt{3})\text{R}30^\circ$ surface, after exposure to carbon monoxide, indicated that carbon monoxide adsorbs preferentially on a step edge which has exposed molybdenum atoms. If the (1×1) unit mesh of the exposed molybdenum atoms is extended to the $(\sqrt{3} \times \sqrt{3})\text{R}30^\circ$ domain, dark depressions of the honeycomb correspond to three-fold hollow sites. Thus, the carbon atoms are considered to occupy a three-fold hollow site of the (1×1) molybdenum layer. The carbon atoms appear as dark depressions at high tunneling resistances and as shallow ‘sombbrero’ bumps at low tunneling resistances. The coverage of carbon on the $(\sqrt{3} \times \sqrt{3})\text{R}30^\circ$ -honeycomb structure is 0.33. It seems that carbon atoms float upon a calm sea of electronic states near the Fermi level.

The coverage of carbon on the surface increased by further annealing. The $(\sqrt{3} \times \sqrt{3})\text{R}30^\circ$ -honeycomb structure changed to being a $c(2 \times 4)$ -zigzag row as shown in Fig. 4a. The model in Fig. 4b locates carbon atoms at the folding points of a zigzag row having the same dimension as the A-type domain boundary in Fig. 3a. The coverage of carbon on the $c(2 \times 4)$ -zigzag row structure is 0.5. The $c(2 \times 4)$ structure does not cover the entire surface because the $(\sqrt{3} \times \sqrt{3})\text{R}30^\circ$ -honeycomb structure is always present.

4.2 Visualization of a Novel Selective Etching Reaction of Surface Carbon Atoms of C-terminated $\text{Mo}_2\text{C}(0001)$ Surfaces by Oxygen

When studying, by STM, the oxidation of C-terminated $\text{Mo}_2\text{C}(0001)$ surfaces by oxygen at room temperature a selective etching of surface carbon atoms occurred [16]. The oxygen was admitted to the microscope chamber through a variable leak valve to a pressure of $3.3 \times 10^{-4} \text{ Pa}$. Figure 5a shows an STM image before exposure to oxygen, where the $(\sqrt{3} \times \sqrt{3})\text{R}30^\circ$ -honeycomb structure and the $c(2 \times 4)$ -zigzag row

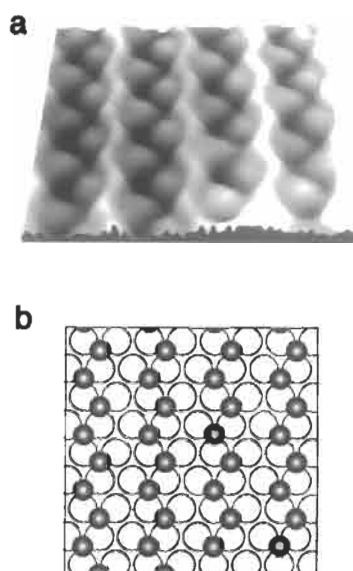


Fig. 4. (a) High resolution STM topograph ($2.3 \times 2.3 \text{ nm}^2$) of a $c(2 \times 4)$ -zigzag row structure on $\text{Mo}_2\text{C}(0001)$ (V_s : +10 mV, I_s : 2.0 nA). Coverage of surface C atoms is 0.5 ML. (b) A schematic model of the $c(2 \times 4)$ structure corresponding to (a). Large empty circles and shading circles represent Mo atoms and C atoms, respectively. A bulk-truncated Mo-terminated surface is postulated as the substrate.

structure co-exist and each carbon atom is imaged. Figure 5b, after reaction, shows several areas with higher concentrations of atoms, ordered in a hexagonal symmetry and with a separation distance of 0.30 nm to form the (1×1) lattice of the molybdenum substrate. Following further reaction with oxygen, these (1×1) regions spread to eventually coalesce (Figs. 5c and d). Figure 5d shows that most of the honeycomb structures remained, the areas of the zigzag row structures being selectively reduced. The position of newly formed atomic protrusions is imaged in Fig. 5e, derived from Fig. 5c. With a (1×1) mesh over the (1×1) region, all of the carbon atoms in the $(\sqrt{3} \times \sqrt{3})R30^\circ$ -honeycomb and $c(2 \times 4)$ -zigzag row structures are in the centers of the triangles, i.e. in the three-fold hollow sites of the (1×1) molybdenum layer as mentioned above. Thus, the (1×1) region results from exposure of the (1×1) molybdenum layer or by adsorbed species placed on top of the (1×1) molybdenum layer. It is unlikely that the (1×1) region is formed by adsorbed oxygen atoms or by a mixture of oxygen and carbon atoms adsorbed on top sites because previous structural studies of atomic adsorbates on metal surfaces suggest that they occupy sites with a higher coordination [23]. If atomic adsorbates form the (1×1) region, they should have preferred three-fold hollow sites to top sites. Therefore, it was concluded that the carbon atoms were etched by oxygen causing the molybdenum layer to appear. The reaction products, carbon monoxide and carbon dioxide, were not detected by mass spectrometry because of resolution limits. The surface in Fig. 5e is modeled in Fig. 5f.

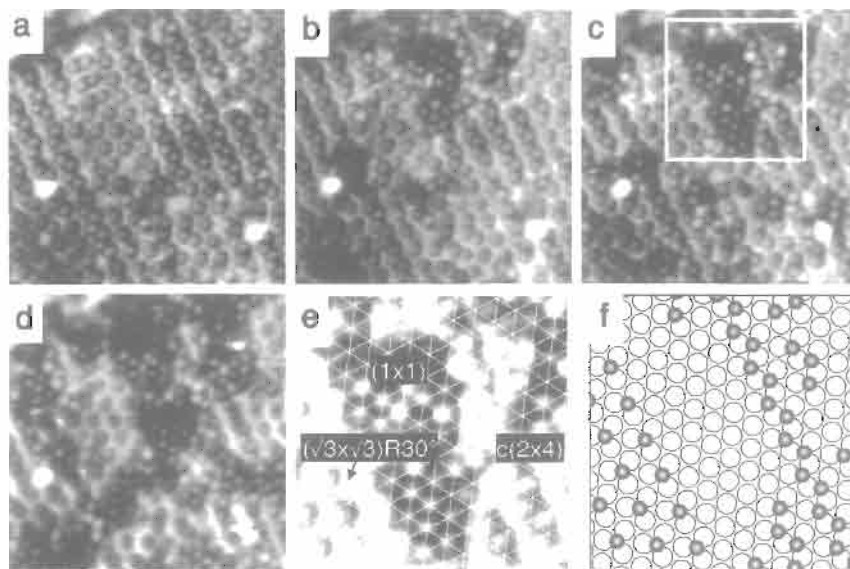


Fig. 5. Selective etching reaction of surface C atoms by exposing to O_2 gas (1.3×10^{-4} Pa) at RT in the same area visualized by STM; (a) 0 L (before exposure, I_t : 2.0 nA, V_t : 10 mV); (b) 2.5 L (I_t : 3.0 nA, V_t : 20 mV), (c) 5.0 L (I_t : 3.0 nA, V_t : 20 mV), (d) 10.0 L (I_t : 2.0 nA, V_t : 20 mV). 7.3×7.3 nm². The STM tip was retracted during exposure to oxygen gas. Each image was measured under UHV without oxygen ambient. (e) A magnified image of the square region in (c) with lines of the (1×1) lattice. 3.6×3.6 nm². (f) Model structure of (e). Empty circles and shaded circles represent Mo and C atoms, respectively.

Figure 5d indicates that 100 carbon atoms were etched by $\sim 2.3 \times 10^3$ molecules of oxygen impinging on the area.

Etching of the surface carbon atoms by oxygen at room temperature is unexpected because both carbon and oxygen atoms are strong adsorbates on molybdenum metal surfaces. The carbon and oxygen atoms could not be removed from the molybdenum surfaces below 1200 K, when adsorbed as a single element [24,25]. If carbon and oxygen atoms co-exist on molybdenum metals, they desorb as carbon monoxide at temperatures of ~ 1000 K [24,25]. An air-exposed Mo_2C catalyst desorbs carbon monoxide and carbon dioxide at temperatures above 800 K [26]. Thus, stable adsorbed oxygen atoms cannot etch carbon atoms on a $Mo_2C(0001)$ surface. On the other hand, a dissociative adsorption of O_2 on Al(111) [27] or Pt(111) [28] produces ‘hot’ oxygen atoms with translational energies parallel to the surface. Thermo-induced or photo-induced ‘hot’ oxygen atoms on Pt(111) react with adsorbed carbon monoxide to form carbon dioxide at temperatures below 150 K [29]. Such energetically excited oxygen atoms formed on the surface should be responsible for the etching reactions reported above.

The STM tip does not contribute to the etching reaction. The tip was retracted from the tunneling region during exposure to oxygen gas. Each frame of Fig. 5 is a sequential STM image measured under ultra-high-vacuum (UHV) conditions. The etched area was unchanged in the sequential images.

The etching reaction does not occur homogeneously but starts from specific points and expands the (1×1) areas. Energetic oxygen atoms migrate and react with the carbon atoms at the edges of the ordered domains. The reaction rates (collision efficiency) are lower for carbon atoms at the edges of the $(\sqrt{3} \times \sqrt{3})R30^\circ$ -honeycomb domains and at the $c(2 \times 4)$ -zigzag row domains. Thus, preferential etching is probably due to different adsorption energies of carbon atoms in the two structures, i.e. the adsorption energy of carbon atoms in the $(\sqrt{3} \times \sqrt{3})R30^\circ$ -honeycomb domain is higher than that of carbon atoms in the $c(2 \times 4)$ -zigzag row domains.

Certain atomic protrusions were found in the $(\sqrt{3} \times \sqrt{3})R30^\circ$ -honeycomb region after exposure to oxygen. Consecutive STM imaging showed that they occupied three-fold hollow sites at the center of the triangles formed by three carbon atoms, and movement (hopping) between equivalent sites, frame by frame, was observed, assigned to oxygen atoms. On the other hand, such oxygen atoms were not found on the (1×1) and the $c(2 \times 4)$ -zigzag row regions, suggesting high mobility of oxygen atoms in those regions rendering them invisible to STM. This contrasts with immobile oxygen atoms on molybdenum metal surfaces. The high mobility of oxygen atoms explains the high etching rate of carbon atoms on the surface.

A mild oxygen treatment of Mo_2C or WC catalysts improves their catalytic activities [1,13,30,31], probably because of the formation of oxycarbide phases. Other oxide phases formed by more extensive oxidation inhibit catalysis.

5 Conclusions and Future Prospects

STM is a powerful tool to image atomic arrangements of metal carbide surfaces. Each surface carbon atom of C-terminated $\text{Mo}_2\text{C}(0001)$ surfaces can be identified as a shallow sombrero protrusion using a low tunneling resistance less than $1 \text{ M}\Omega$. Imaging of surface carbon atoms by STM elucidates chemical reactions on metal carbide surfaces. The etching by oxygen of surface carbon atoms of C-terminated $\text{Mo}_2\text{C}(0001)$ surfaces was observed. This etching reaction selectively occurs on the $c(2 \times 4)$ -zigzag row structure even at room temperature, leading to exposure of the underlying (1×1) molybdenum layer. This reaction may be an important intermediate in the understanding of improvements to catalytic activity of Mo_2C or WC catalysts by mild oxidation treatments.

STM images indicate the local electronic density of states near to the Fermi level of a surface and relate to applied bias voltages between the tip and the surface. Local mapping of the electronic states of metal carbide surfaces is essential to the understanding of their physical properties and chemical reactivities. STM images indicate that molybdenum atoms in the $(\sqrt{3} \times \sqrt{3})R30^\circ$ -honeycomb structure and the $c(2 \times 4)$ -zigzag row structure have continuous electronic states near to the Fermi level and that the (1×1) molybdenum atoms without carbon atoms have localized electronic states. Combinations of high resolution STM mapping with scanning tunneling spectroscopy (STS) should clarify the causes of high activities of Mo_2C compared with noble metal catalysts.

References

1. R.B. Levy and M. Boudart, Platinum-like behavior of tungsten carbide in surface catalysis. *Science*, 181: 547–549, 1973.
2. S.T. Oyama, Introduction to the chemistry of transition metal carbides and nitrides. In: S.T. Oyama (Ed.), *The Chemistry of Transition Metal Carbides and Nitrides*, pp. 1–27. Blackie Academic and Professional, Glasgow, 1996.
3. S. Ramanathan and S.T. Oyama, New catalysts for hydroprocessing: transition metal carbides and nitrides. *J. Phys. Chem.*, 99: 16365–16372, 1995.
4. L.I. Johansson, Electronic and structural properties of transition metal carbide and nitride surfaces. *Surf. Sci. Rep.*, 21: 177–250, 1995.
5. A.T. Santhanam, Application of transition metal carbides and nitrides in industrial tools. In: S.T. Oyama (Ed.), *The Chemistry of Transition Metal Carbides and Nitrides*, pp. 28–52. Blackie Academic and Professional, Glasgow, 1996.
6. J.G. Chen, Carbide and nitride overlayers on early transition metal surfaces: preparation, characterization and reactivities. *Chem. Rev.*, 96: 1477–1498, 1996.
7. J.-K. Zuo, R.J. Warmack, D.M. Zehner and J.F. Wendelken, Periodic faceting on TaC(110): Observations using high-resolution low-energy electron diffraction and scanning tunneling microscopy. *Phys. Rev. B*, 47: 10743, 1993.
8. J.-K. Zuo, D.M. Zehner, J.F. Wendelken, R.J. Warmack and H.-N. Yang, TaC(110): a periodic facet reconstruction studied by LEED and STM. *Surf. Sci.*, 301: 233, 1994.
9. R.M. Tsong, M. Schmid, C. Nagl, P. Varga, R.F. Davis and I.S.T. Tsong, Scanning tunneling microscopy studies of niobium carbide (100) and (110) surfaces. *Surf. Sci.*, 366: 85–92, 1996.
10. M. Hammer, C. Tornevik, J. Rundgren, Y. Gauthier, S.A. Flodstrom, K.L. Hakansson, L.I. Johansson and J. Haglund, Surface atomic structure of reconstructed VC_{0.8}(111) studied with scanning tunneling microscopy. *Phys. Rev. B*, 45: 6118, 1992.
11. E. Pathe and V. Sadagopan, The structure of dimolybdenum carbide by neutron diffraction technique. *Acta Crystallogr.*, 16: 202–205, 1963.
12. R.-L. Lo, K. Fukui, S. Otani, S.T. Oyama and Y. Iwasawa, C-terminated reconstruction and C-chain structure on Mo₂C(0001) surface studied by LEED and STM. *Jpn. J. Appl. Phys.*, 38: 3813–3815, 1999.
13. M.J. Ledoux, C. Pham-Huu, H. Dunlop and J. Guille, n-Hexane isomerization on high specific surface Mo₂C activated by an oxidative treatment. *Proc. 10th Int. Cong. Catal.*, pp. 955–967, 1993.
14. J. Ahn, H. Kawanowa and R. Souda, STM study of oxygen-adsorbed TiC(111) surface. *Surf. Sci.*, 429: 338–344, 1999.
15. R.-L. Lo, K. Fukui, S. Otani and Y. Iwasawa, High resolution images of Mo₂C(0001)-(√3 × √3)R30° structure by scanning tunneling microscopy. *Surf. Sci.*, 440: L857–L862, 1999.
16. K. Fukui, R.-L. Lo, S. Otani and Y. Iwasawa, Novel selective etching reaction of carbon atoms on molybdenum carbide by oxygen at room temperature visualized by scanning tunneling microscopy. *Chem. Phys. Lett.*, 325: 275–280, 2000.
17. R. Young, J. Ward and F. Scire, Metal-vacuum-metal tunneling, field emission, and the transition region. *Phys. Rev. Lett.*, 27: 922–924, 1971.
18. R. Young, J. Ward and F. Scire, The Topografiner: An instrument for measuring surface microtopography. *Rev. Sci. Instrum.*, 43: 999–1011, 1972.
19. G. Binnig, H. Rohrer, Ch. Gerber and E. Weibel, Tunneling through a controllable vacuum gap. *Appl. Phys. Lett.*, 40: 178–180, 1982.
20. G. Binnig, H. Rohrer, Ch. Gerber and E. Weibel, Surface studies by scanning tunneling mi-

- croscopy. *Phys. Rev. Lett.*, 49: 57–61, 1982.
21. S. Otani and Y. Ishizawa, Preparation of Mo₂C single crystals by the floating zone method. *J. Cryst. Growth*, 154: 202–204, 1995.
 22. T.P. St. Clair, S.T. Oyama, D.F. Cox, S. Otani, Y. Ishizawa, R.-L. Lo, K. Fukui and Y. Iwasawa, Characterization of α -Mo₂C(0001). *Surf. Sci.*, 426: 187–198, 1999.
 23. NIST Surface Structure Database, ver. 3.0.
 24. E.I. Ko and R.J. Madix, Adlayer effects on adsorption/desorption kinetics: N₂, H₂, C₂H₄, and CO on Mo(100)-C. *Surf. Sci.*, 100: L449–L453, 1980.
 25. K. Fukui, T. Aruga and Y. Iwasawa, Chemisorption of CO and H₂ on clean and oxygen-modified Mo(112). *Surf. Sci.*, 281: 241–252, 1993.
 26. G.S. Ranhotra, A.T. Bell and J.A. Reimer, Catalysis over molybdenum carbides and nitrides. *J. Catal.*, 108: 24–39, 1987.
 27. H. Brune, J. Wintterlin, R.J. Behm and G. Ertl, Surface migration of hot adatoms in the course of dissociative chemisorption of oxygen on Al(111). *Phys. Rev. Lett.*, 68: 624–626, 1992.
 28. J. Wintterlin, R. Schuster and G. Ertl, Existence of a “hot” atom mechanism for the dissociation of O₂ on Pt(111). *Phys. Rev. Lett.*, 77: 123–126, 1996.
 29. W.D. Mieber and W. Ho, Photochemistry of oriented molecules coadsorbed on solid surfaces: the formation of CO₂+O from photodissociation of O₂ coadsorbed with CO on Pt(111). *J. Chem. Phys.*, 91: 2755–2756, 1989.
 30. E. Iglesia, J.E. Baumgartner, F.H. Ribeiro and M. Boudart, Bifunctional reactions of alkanes on Tungsten carbide modified by chemisorbed oxygen. *J. Catal.*, 131: 523–544, 1991.
 31. A. Muller, V. Keller, R. Ducros and G. Maire, Catalytic activity and XPS surface determination of tungsten carbide for hydrocarbon reforming. Influence of the oxygen. *Catal. Lett.*, 35: 65–74, 1995.

Chapter 17

Infra-Red Spectra, Electron Paramagnetic Resonance, and Proton Magnetic Thermal Analysis

Osamu Ito^a, Tadaaki Ikoma^a and Richard Sakurovs^b

^a*Institute of Multidisciplinary Research for Advanced Materials, Tohoku University, Katahira, Sendai 980-8577, Japan;* ^b*CSIRO, Division of Energy Technology, North Ryde 1670, Australia.*

Abstract: This chapter describes the characterization of carbon alloys using infra-red spectroscopy (IR spectra), electron paramagnetic resonance (EPR) and proton magnetic resonance thermal analysis (PMRTA). The broad absorption bands of IR spectra observed using diffuse reflectance methods provide information about the ring size of aromatic molecules within a sample and the extent to which these are ordered. The sharp C–H stretching peaks are quantitatively compared with peaks using solid-state NMR. Two magnetic resonance methods employed pulse techniques where relative hydrogen contents are evaluated as ratios to carbon contents. PMRTA, which measures the temperature dependence of signal intensities and relaxation times of proton magnetic resonance, provides information about molecular motion in heat-treated carbons and in coals. These spectroscopic techniques give information about the composition of carbon precursors prepared at temperatures below 500–600°C.

Keywords: IR, UV, Vis, Near-IR, NMR, EPR, PMRTA.

1 Infra-Red (IR) Spectra

1.1 Diffuse Reflectance Absorption (DRA) Spectroscopy.

IR spectra of carbons from the KBr pellet transmittance method contain a broad background (from scattering of the monitoring light) that needs to be subtracted from the spectrum. With decreasing particle size these broad backgrounds are reduced and must be subtracted to obtain reliable IR spectra. An example is shown in Fig. 1a for a bituminous coal [1]. For IR spectra from the diffuse reflectance absorption (DRA) method, the absorption intensities, represented as a Kuberka–Munk function ($f(R_\infty)$ or $F(R_\infty)$) show weak broad bands in the higher wave-number region (Fig. 1b). By the DRA method, high rank coals, heat-treated organic materials and coal-tar pitches (CTP) also show broad absorptions attributable to the absorption tail of electronic transitions extending from the UV/Vis regions [2]. Such broad bands are observed by

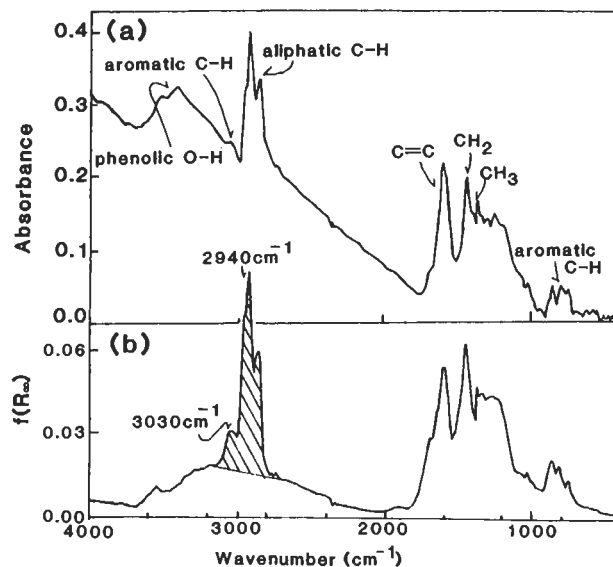


Fig. 1. IR spectra of a bituminous coal (sample/KBr = 1/150): (a) transmittance KBr pellet method; (b) diffuse reflectance absorption method [1].

DRA and increase with decreasing particle size of the sample [2]. Thus, it is not necessary to subtract these broad absorptions in the entire region measured by the DRA method.

FT-IR spectra observed by DRA for various coals are shown in Fig. 2 [2]. The baseline of a low rank coal (Morwell coal: C = 67.4 wt%) is flat in the region of 4000–6000 cm^{-1} . For bituminous coal (Oyubari coal: C = 85.4 wt%), small absorptions were observed at 4000–6000 cm^{-1} with a decrease in the IR-band intensities of hydrogen bonds at 3000–3500 cm^{-1} and carbonyl groups at 1700 cm^{-1} . With a further increase in coal rank, Moura (C = 85.6 wt%) and Hongei (C = 93.7 wt%), the absorption tails extend to lower wave-numbers with a decrease in intensity of alkyl group band at 2940 cm^{-1} . For active carbon, only the broad band was observed, the absorption edge extending to wave-numbers less than 1000 cm^{-1} , indicating a narrow band gap in the active carbon. Absorptions in the near-IR region are used as a measure of coal rank [2].

For a bituminous coal (Shin-Yubari: C = 86.9 wt%), the intensity of the broad band increases with increasing heat treatment temperature (HTT) to 400°C accompanied by a decrease in the intensities of the alkyl bands. At an HTT of 600°C, the step rise of the near-IR absorption ceases when it then resembles the absorption spectrum of activated carbon as in Fig. 2. These changes in absorption spectra in the near-IR region are used to study effects of HTT on organic materials.

On heat-treating decacyclene to 500°C, the broad band in the near-IR region appeared after 1 h increasing in intensity after 2 h, but decreased after 3 h. At an HTT

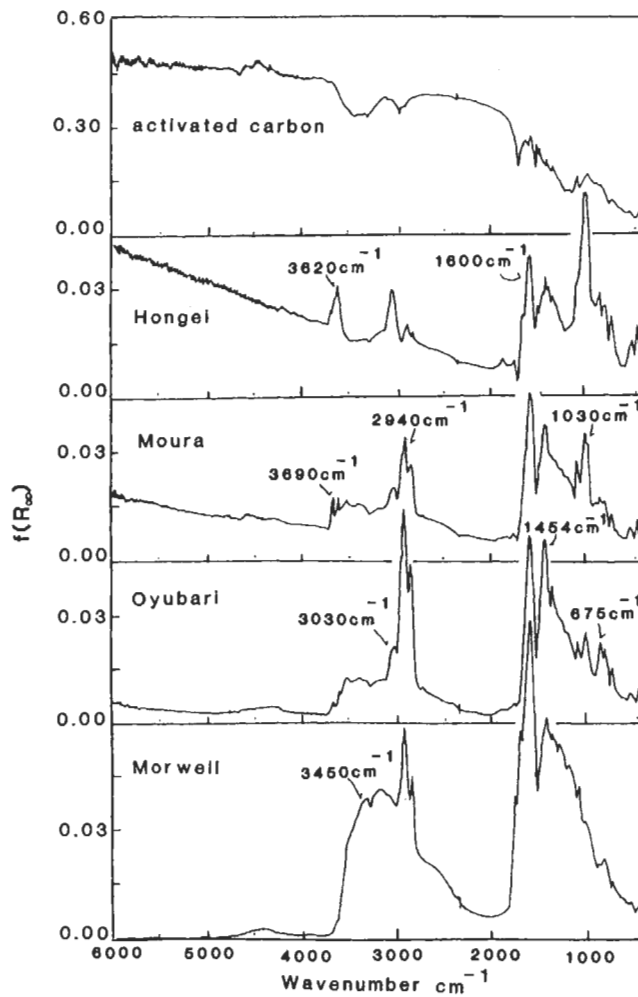


Fig. 2. IR/near-IR spectra of several coal samples [2].

of 550°C, the absorption spectrum in the near-IR region is flat showing decreases in the intensities of the C-H bands. These changes in the near-IR region relate to absorption bands in the Vis regions (see below).

1.2 Relationship of IR spectra with UV/Vis/Near-IR Spectra

On heat-treatment of aromatic hydrocarbons, polycondensation reactions occur resulting in formation of mesophase which is the precursor of graphitizable carbon fibers and carbons. Changes in the molecular structures and molecular arrangements during this process are monitored as electronic transitions in the Vis and near-IR region.

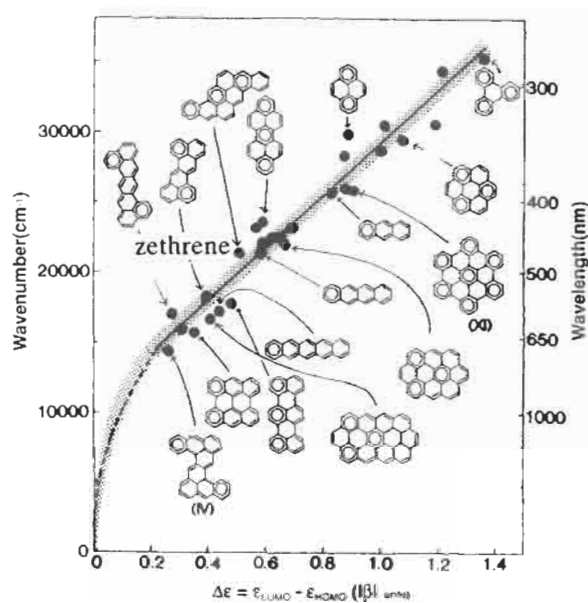


Fig. 3. Correlation of observed p-band wave-number with calculated energy gap ($\Delta\epsilon$) between LUMO and HOMO in β -unit for several hydrocarbons [3].

The absorption spectra of solid carbon precursors are measured using the KBr-CsI pellet transmittance method. At an HTT of 500°C, decacyclene first forms mesophase spheres which coalesce into anisotropic flow textures. The absorption band of parent decacyclene is only slightly broader than when in solution, because of intermolecular interactions in a concentrated solution and the solid state. With heat-treatment, the absorption bands at wavelengths longer than 500 nm increase in intensity. Intermediates of the carbonization reactions of decacyclene are zethrene derivatives, with absorption bands beyond 550 nm. The relationship between the energy gap from the highest occupied molecular orbital (HOMO) to the lowest unoccupied molecular orbital (LUMO) and the absorption maximum at longest wavelength of the aromatic hydrocarbons is shown in Fig. 3. By comparing the observed absorption bands with Fig. 3, it is seen that a zethrene dimer is a main component in pyrolyzed decacyclene [3]. For coal-tar pitch, the diffusion reflectance method gives more reliable absorption spectra in Vis/near-IR region compared with the transmittance method.

At 500°C, coal-tar pitch forms mesophase spheres [4], a process described by the absorption spectra in Vis/near-IR/IR region as measured by the DRA (Fig. 4). Here, the absorption intensities of the Vis region increase with heat-treatment time (1 h). The absorption intensity in the 300–500 nm region reaches a maximum at ~3 h and then decreases. The initial increase in absorption intensity is attributed to the aromatization of the coal-tar pitch, the later decrease in intensities being due to the broadening of absorption bands because of inter-aromatic interactions. The

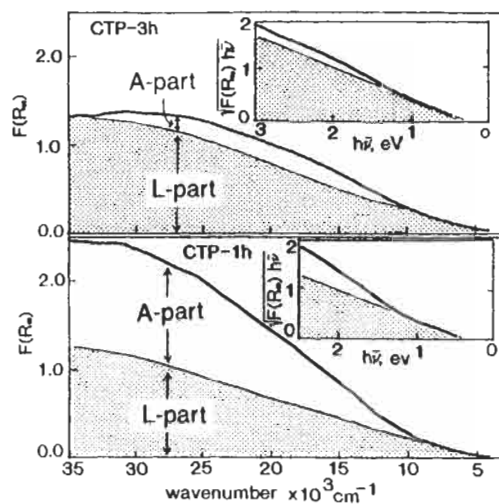


Fig. 4. Separation of the observed spectra into intensities due to lamella (L-part) and to isolated aromatic hydrocarbons (A-part). Inset: Shaded parts are plots of Eq. (1) [4].

absorption band of the lamellar aromatic hydrocarbons is described by the following equation, which has been applied to amorphous semiconductors [5]:

$$[F(R_{\infty}) hv]^{1/2} = B(hv - \Delta E) \quad (1)$$

where ΔE is the band gap energy and B to a proportional factor increasing with extents of ordering of the lamellar aromatic hydrocarbons. The straight line of the inset in Fig. 4 shows values as calculated from Eq. (1). The hatched area in Fig. 4 results from absorption by lamella (L-part), the remaining white area being due to absorption by single aromatic molecules (A-part). After heat treatment for 0.5 h, the L-part increases, but the A-part decreases, indicating increased interactions between aromatic molecules due to the improved alignment and ordering of the aromatic molecules.

1.3 Relationship with Solid-State NMR

^{13}C -NMR spectra of solid carbon samples are measured using magic-angle NMR. However, the NMR signals for carbons and coals samples that are rich in quaternary carbon atoms surrounded by other carbon atoms exhibit 'side-bands'. In the ^{13}C -NMR signals from coronene, the main signal is at 125 ppm, but with side-bands in the wings of the 125 ppm signal (Fig. 5a) [1]. The positions and relative intensities of the side-bands change with the rotation speed of the sample probe. NMR spectra of coals observed under the same conditions are composed of signals and side-bands (Fig. 5b), the principal signal, 100–150 ppm, being assigned to aromatic carbon atoms.

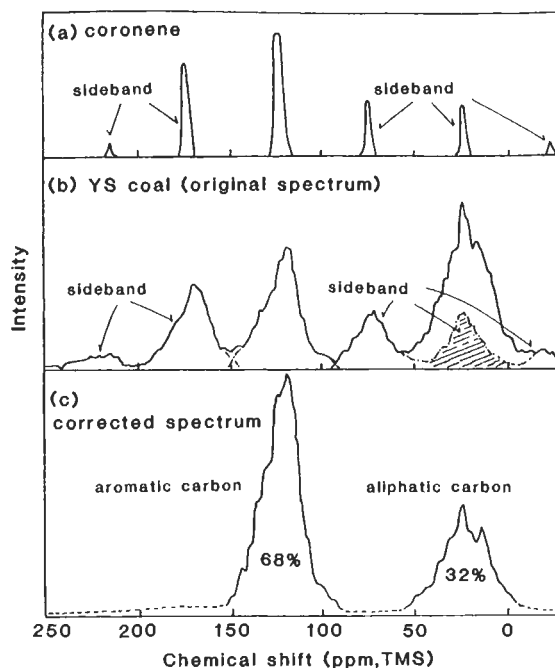


Fig. 5. ^{13}C -CP/MAS NMR spectra measured with 300 MHz spectrometer: (a) coronene; (b) original spectrum of a bituminous coal (the same coal as that in Fig. 1); (c) spectrum obtained by the correction of the aromatic side-bands [1].

Signals with higher chemical shifts (150–200 and 200–250 ppm) are attributed to side-bands, with almost all of the signal at 50–100 ppm also being attributed to side-bands. However, the signal in the region 0–50 ppm is stronger than the side band, but is expected to be of intensity equal to the side-band at 50–100 ppm. Thus, assuming that the distribution of side-band intensities for the coal is the same as for coronene, the side-band component of the 0–50 ppm signal can be subtracted from the observed signal at 0–50 ppm. The subtracted signals are shown in Fig. 5c. The aliphatic carbon is assigned to 0–50 ppm, and aromatic carbon is directly assigned to the 100–150 ppm signal (Fig. 5b).

To distinguish further aromatic carbon atoms and carbon atoms in alkyl groups, the technique of dipolar dephasing is used. Thus, from a spectrum observed at $T_{\text{dd}} = 0$, in which the signal has not decayed, signals are obtained (Fig. 6), in which side-bands have already been subtracted. At $T_{\text{dd}} = 40 \mu\text{s}$, that is the decay time of components with shorter relaxation times, carbon atoms with long relaxation times such as quaternary C, CH_3 , mobile CH_2 , and polar carbon atoms, remain. The difference between the total signal and the signal with long relaxation times is assigned to signals of short T_{dd} such as aromatic CH, aliphatic CH and rigid CH_2 .

In order to determine the absorption coefficients of the FT-IR bands corresponding to these isolated NMR signals, the IR bands need to be curve-resolved. For

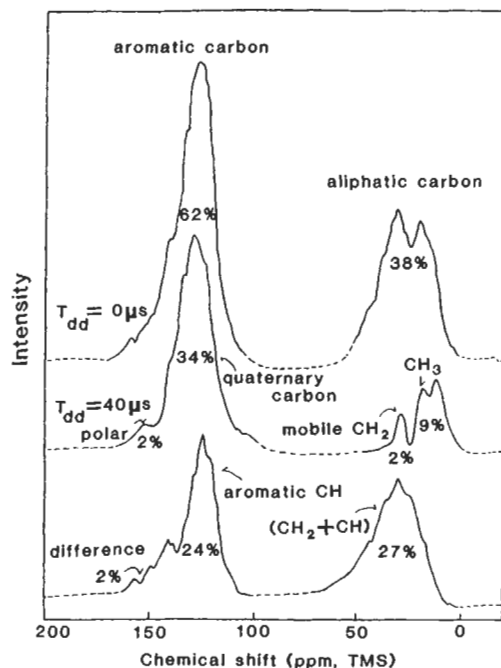


Fig. 6. NMR spectra of a bituminous coal. Top: original spectrum ($T_{dd} = 0 \mu s$); middle: dipolar dephasing spectrum ($T_{dd} = 40 \mu s$) extrapolated to 0 s; bottom: subtracted spectrum (top - middle). Numbers are the fraction of carbon per total carbon [1].

the same coal, the FT-IR spectra are shown in Fig. 1 [1]. Figure 1b, observed by the DRA method, shows the aromatic C-H band at 3030 cm^{-1} and aliphatic groups in the $2800\text{--}3000 \text{ cm}^{-1}$ region. The aromatic C-H band at 3030 cm^{-1} is hidden in the broad scattering bands of the IR spectra obtained by the KBr transmittance method (Fig. 1a). The shadowed signals in the region of $2700\text{--}3500 \text{ cm}^{-1}$ in Fig. 1b are curve-resolved as shown in Fig. 7. The aromatic C-H has two peaks at wave-numbers higher than 3000 cm^{-1} . The CH_2 group also has two peaks at 2850 cm^{-1} and 2930 cm^{-1} . The CH_3 group has two peaks at 2880 and 2960 cm^{-1} . The alkyl C-H has one band at 2870 cm^{-1} . The sum of the band areas of each group is plotted against the corresponding NMR signal areas. The same plots are made for several coals and model compounds. Then, linear relationships between the NMR signal intensity and the IR peak area were obtained. By using the gradients of these plots, IR intensities obtained by the DRA method are converted directly to a weight percentage of different carbon atoms in coals [1].

For the coal-tar pitch, it is more difficult to separate the solid NMR signals from the side-bands in the alkyl C-H region because of strong side-bands and weak alkyl C-H signals. It is also not easy to evaluate alkyl C-H bands from the IR spectra, because of quite weak alkyl C-H bands relative to the strong aromatic C-H bands. Coal-tar pitches require different treatments.

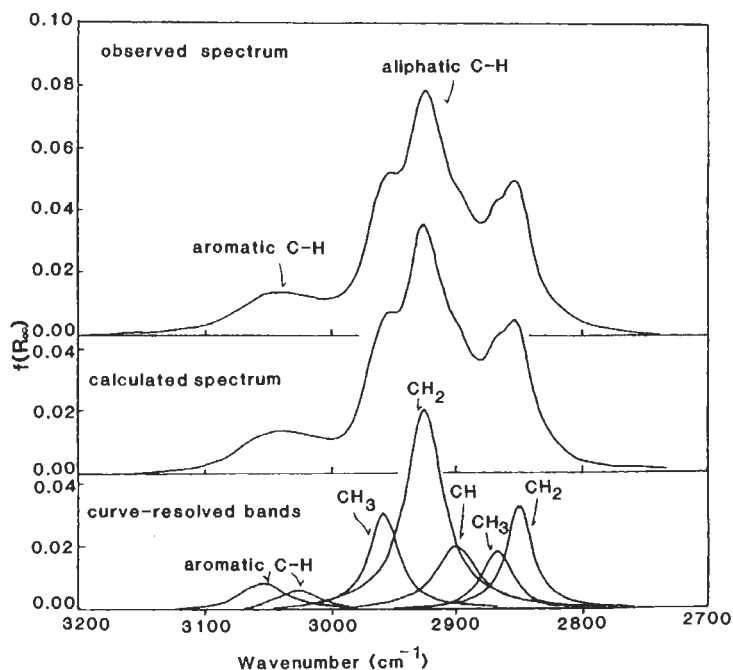


Fig. 7. Curve-resolution of the C-H stretching region of the IR spectrum of a bituminous coal [1].

2 EPR

2.1 CW-EPR

Amorphous carbons usually give single symmetric signals when using continuous wave (CW)-EPR. Spin concentrations are evaluated by comparing the signal intensity with that of a standard sample. The magnetic field position of the signal corresponds to the 'g-value' of the paramagnetic species which derives from the free electron value of 2.00023 as a result of increases in spin-orbit interactions. Because heteroatoms induce strong spin-orbit interactions, g-values measure the presence of heteroatoms included in the radical content of carbon. The line-width (ΔH_{pp}) of an EPR signal is related to the spin relaxation times (T_1 and T_2), which are strongly influenced by the presence of adsorbed oxygen. The relative relaxation time (T_2) is evaluated, quantitatively, from the dependence of signal intensity upon incident microwave power (P). Measurements of these EPR parameters for a coal-tar pitch are given in Fig. 8 [6]. The plot of the peak-peak signal height (h_{pp}) against $\log P$ is normally a parabolic curve. The microwave power at the maximum signal intensity (P_{max}) and that at half the maximum signal intensity ($P_{1/2}$) are known. The P_{max} and $P_{1/2}$ parameters closely relate to spin relaxation times.

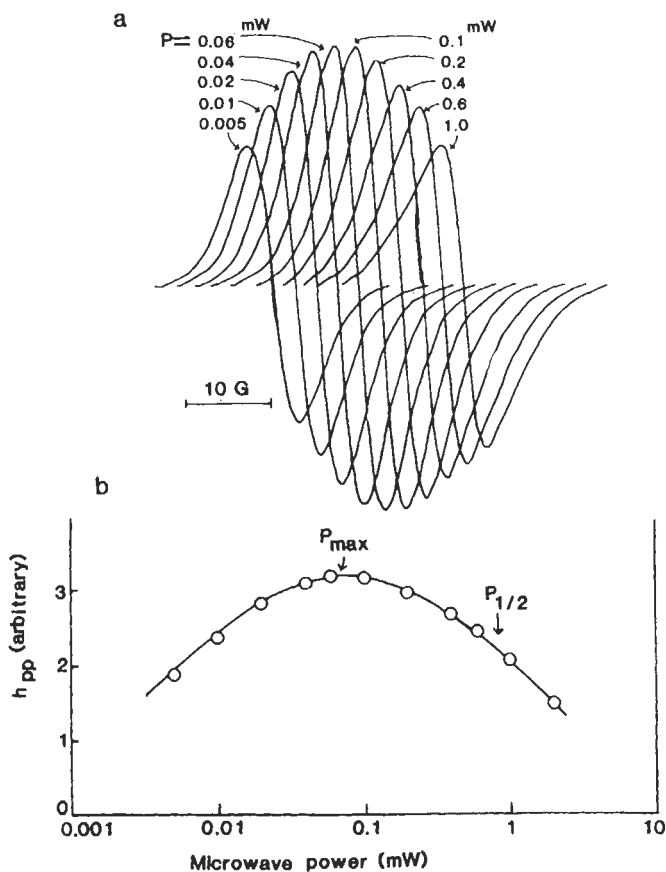


Fig. 8. (a) Dependence of EPR signal intensity on microwave power (P) for a coal-tar pitch at room temperature; EPR signals are depicted with changing central magnetic field. (b) Plot of signal intensity (h_{pp}) against $\log P$; P_{max} and $P_{1/2}$ are shown by arrow [7].

EPR parameters obtained by *in-situ* measurements of coals and a coal-tar pitch change with heat-treatment temperature [7]. On cooling immediately after heating to 500°C, the $\log (1/P_{max})$ values return to almost the same values as observed before heating the sample, indicating that the mobility of the molecules in the coal-tar pitch does not change appreciably after heat-treatment at 500°C for a short time. On the other hand, when the coal-tar pitch is kept at 500°C for 2 h, $1/P_{max}$ changes drastically, indicating a significant change in the mobilities of the constituent molecules. For ΔH_{pp} , irreversible changes were observed for a sample maintained at 500°C for 2 h, indicating that chemical changes took during the heat-treatment. The observed increase in the signal intensity with increasing temperature suggests that chemical reactions, producing free radicals, took place at relatively low temperatures. P_{max} and $P_{1/2}$ differ for coals of different rank and maceral contents [6].

2.2 Pulsed-EPR

Many microwave pulse sequences are developed for pulsed EPR, by which new EPR and electron nuclear double resonance (ENDOR) spectra are measured. This section introduces two examples of pulsed EPR applications to carbonaceous solids. The nutation spectrum for a coal sample is shown in Fig. 9a, which uses a pulse sequence due to two-pulse echo detection (Fig. 9b) [8,9]. The nutation is a rotational motion of a magnetization vector caused by the interaction with microwave pulse (B_1) in a rotation axis system. For the weak limit of B_1 compared with zero-field splitting due to interactions between spins, the nutation frequency (ν_n), for EPR allowed transitions, is analytically written as follows:

$$\nu_n = \gamma_e B_1 \sqrt{S(S+1) - M_S(M_S - 1)} \quad (2)$$

Here, γ_e is the magnetogyric ratio for electron spin; ν_n depends on the spin multiplicity (S) and the spin sublevels (M_S) resonating with the applied microwave. Therefore, this

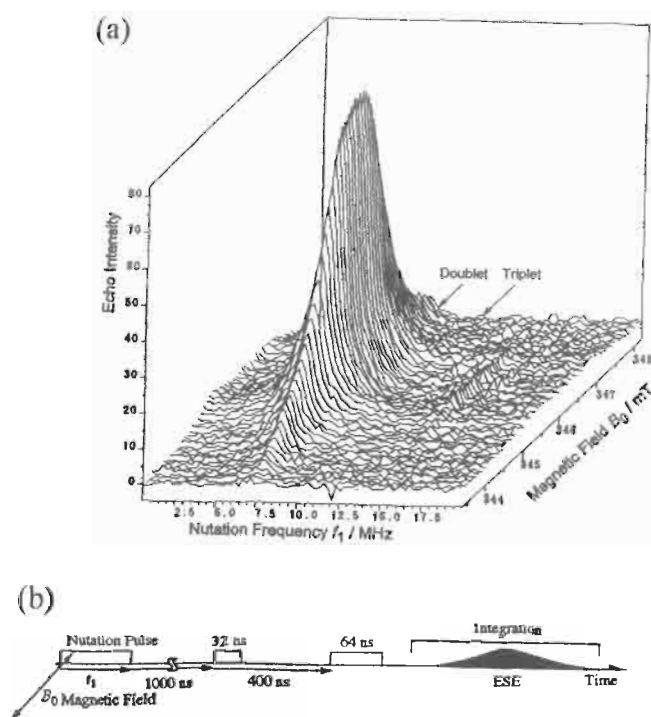


Fig. 9. (a) Field swept nutation spectrum of a bituminous coal. Time width for nutation pulse was varied from 0 to 4080 ns. Arrows indicate the nutation frequency for doublet and triplet state species ($f_1 = 7.08$ and 10.01 MHz, respectively) estimated from a comparison with DPPH (doublet species) and (b) pulse sequences for 2D-nutation in which microwave power (= 1 kW) was adequately attenuated to create 90° pulses [8].

nutations spectrum is useful to distinguish between signals from doublet (free radical) species and triplet species. As indicated by arrows in Fig. 9a, the signal detected for the coal sample is almost entirely due to the doublet species. There is little evidence for triplet species in this coal. Similar spectra, lacking in triplet states, are also observed for the coal-tar pitch.

Another pulsed EPR method is hyperfine sublevel correlation spectroscopy (HYSCORE) which is two-dimensional electron spin echo envelope modulation (ESEEM) that allows the detection of a broad hyperfine spectrum from disordered carbons. Figure 10a illustrates an electron spin (e) and a nuclear spin (n) in an external magnetic field (B_0). The e -spin is almost quantized along B_0 , but the n -spin orients to the effective field (B_{eff}) composed of B_0 and the magnetic dipole field (B_{hf}) due to the e -spin. B_{hf} reverses its direction, leading to a sudden change in B_{eff} , when the resonance with the e -spin takes place due to a strong microwave pulse (Fig. 10b). As a consequence, the n -spin starts to precess along the new B_{eff} . This periodic motion of the n -spin induces an oscillating local field ($B_{\text{local}}(t)$) that modulates the intensity of electron spin echo (ESE). This coherent interaction between the electron and nuclear spins is a basic mechanism for ESEEM and is called a nuclear modulation effect. Hence, the spectrum in the frequency domain obtained by Fourier transformation of

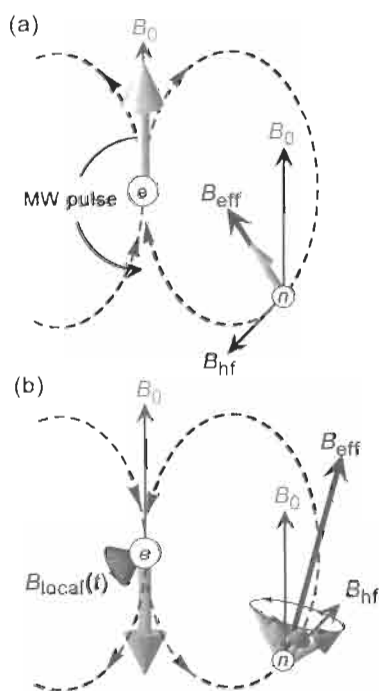


Fig. 10. Vector model of the electron- e and nuclear- n spins: (a) in thermal equilibrium; and (b) after applying microwave (MW) pulse.

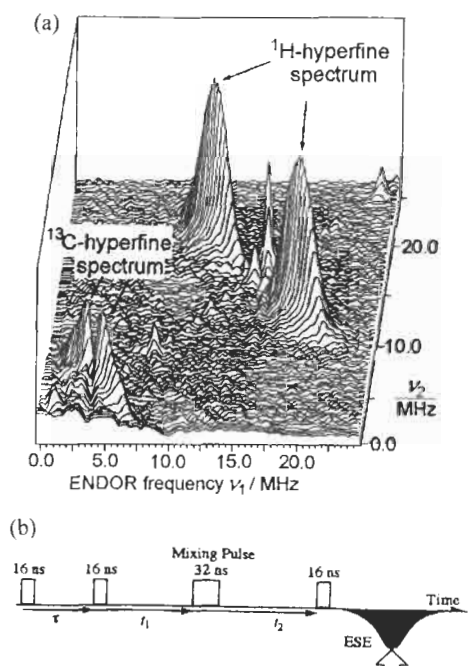


Fig. 11. (a) HYSCORE spectra of ^1H and ^{13}C for a coal-tar pitch; $\tau = 128$ ns and measurement temperature of 298 K, (b) pulse sequences for HYSCORE [10].

ESEEM is attributed to an alternative of ENDOR that enhances spectral resolution substantially.

The spectra of CTP observed by HYSCORE are shown in Fig. 11a [10] and were measured using the four pulses shown in Fig. 11b. The nuclear Zeeman frequencies (ν_{H} and ν_{C}) of ^1H and ^{13}C are 14.7 and 3.7 MHz, respectively, at the external magnetic field for the usual pulsed EPR experiment. The ENDOR frequencies of ν_1 and ν_2 in Fig. 11a indicate the energy separation among the nuclear spin sublevels, which include Zeeman and hyperfine interactions. The broad ridge-type signals crossing at the diagonal point of $(\nu_{\text{H}}, \nu_{\text{H}})$ run perpendicular to the diagonal $\nu_1 = \nu_2$. Such broad ridge-type signals are identified as the hyperfine spectrum due to ^1H . The other broad ridge around $(\nu_{\text{C}}, \nu_{\text{C}})$ is assigned to ^{13}C -hyperfine spectrum. The signals on the $\nu_1 = \nu_2$ axis are mainly due to noise. From a comparison with various model radicals, the intensity ratio of the $^{13}\text{C}/^1\text{H}$ of HYSCORE spectrum affords a good measure of the molecular size of the radical. The intensity ratio of $^{13}\text{C}/^1\text{H}$ of CTP is larger than that of the cation radical of coronene [8]. This indicates that the average size of molecules included in coal-tar pitch is larger than that of coronene. The $^{13}\text{C}/^1\text{H}$ ratio of CTP increases on heat treatment, indicating that the radical size increases on heating. On heating a coal-tar pitch with iodine, the $^{13}\text{C}/^1\text{H}$ ratio in the HYSCORE spectrum also increases, indicating an acceleration of dehydrogenation at relatively low temperatures from the charge transfer complexes formed between iodine and aromatic

hydrocarbons. The ^{13}C -hyperfine spectral width of a coal-tar pitch also becomes narrow with time of iodine treatment. This narrowing may relate to aromatization of the charge-transfer complexes. Although the HYSORE spectrum is distorted by a blind-spot effect depending on the τ -value (Fig. 11b), this advanced spectroscopy is useful to investigate the chemical shift of paramagnetic species. This is because the signals due to the composite atoms in the radicals, acting as intermediates in solid state reactions, can be detected separately.

3 Proton Magnetic Resonance Thermal Analysis (PMRTA)

The monitoring of *in-situ* amounts and locations of hydrogen atoms in carbons during heat-treatment (carbonization) experiments provides useful information about the carbonization processes. PMRTA was developed to monitor the changes in physical structures that occur on heating coals and related materials, particularly the degree and extent to which they fuse [11]. A typical solid-echo signal observed after the pulse sequence of $90_x^\circ-\tau-90_y^\circ$ is shown in Fig. 12. Usually, the ^1H -NMR signal at each temperature shows a rapid decay (within about $50\ \mu\text{s}$) followed by a slow decay. The rapid decay component corresponds to hydrogen included in the rigid (solid-like) component of materials and the slow decay component to hydrogen included in the mobile (fluid-like) component of materials. The initial intensity of the signal indicates the total hydrogen. The rapid decay and slow decay components can be separated using the following equation:

$$\text{Signal intensity } (t) = I_0^f[\exp(-1/T_2^f t)] + I_0^s[\exp(-1/T_2^s t)^n] \quad (3)$$

where I_0^f and I_0^s are the initial intensities of hydrogen included in the fluid-like and solid-like carbonaceous materials, respectively; and T_2^f and T_2^s are the relaxation

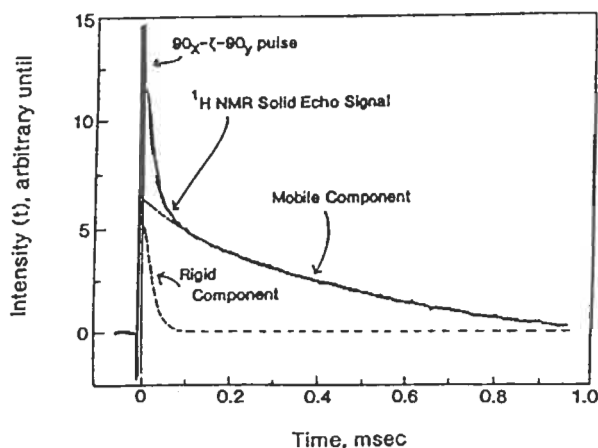


Fig. 12. Solid-spin echo signal of ^1H -NMR of a brown coal; isothermal PMRTA [11].

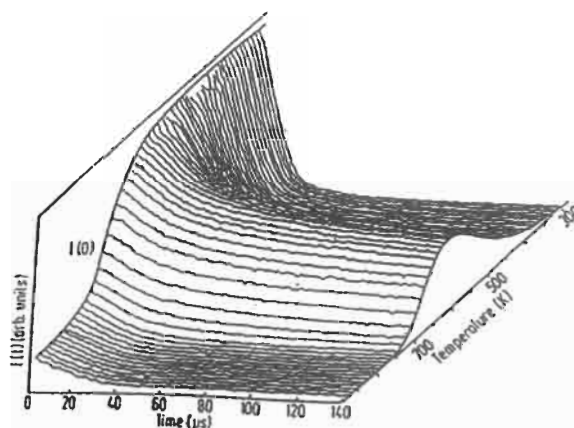


Fig. 13. Three-dimensional expression of *in-situ* ^1H -solid spin echo signals of a brown coal with increasing HTT; non-isothermal PMRTA [11].

times of fluid-like and solid-like hydrogens, respectively. The solid-like component, theoretically, takes a Gaussian form ($n = 2$), but in practice, for inhomogeneous solids such as coals and coal-tar pitches, n takes values around 1.7 [11]. The resolved curves of a solid-echo signal of a brown coal are shown in Fig. 12.

With carbonization (pyrolysis) temperature (HTT), the time-profile of the solid-echo signals for a brown coal changes as shown in Fig. 13 [11], which is a typical non-isothermal PMRTA method. At room temperature, the decay time is short, because the coal is solid-like at this temperature. At 400 K, a long-lived component appears, arising from the melting components in the coal, and this increases in intensity with increasing HTT. By 517 K, most of the signals decay slowly, indicating that most of the coal is molten. The amount of fluid component then increases, reaching about 60% of the total coal. With further rises in temperature, the T_2 begins to decrease again and the initial signal intensity decreases, indicating that some carbonization reactions occur with the loss of total hydrogens, which can be separated into mobile and rigid hydrogen using Eq. (3). The plots of total hydrogen for the coal-tar pitch and petroleum pitches show that a coal-tar pitch is more stable than petroleum pitch in the HTT range of 400–500°C. The amounts of mobile hydrogen and rigid hydrogen, which are plotted against HTT, also give a useful insight into the processes of pyrolysis of pitches [12,13].

Kinetic studies of decomposition of a brown coal were studied by isothermal PMRTA at constant HTT between 400 and 450°C, when the coal in the NMR probe decomposed in a few minutes [12]. The quantitative measurements of PMRTA also provide insights into the interactions between mixtures of materials on heating. This technique shows, for the first time, how coals can co-interact on heat treatment, resulting in increased fluidities [14]. It was also found that components of coals bind materials such as pitches and aromatic hydrocarbons [15].

References

1. O. Ito, S. Akiho, T. Nozawa, M. Hatano and M. Iino, Carbon distribution of bituminous coals studied by dipolar dephasing NMR and FT-IR. *Fuel*, 89: 335–340, 1989.
2. O. Ito, H. Seki and M. Iino, Diffuse reflectance spectra in near-IR region; a new index for degree of coalification. *Fuel*, 67: 573–578, 1988.
3. O. Ito, T. Kakuta and M. Iino, Optical absorption spectra of heat-treated decacyclene during mesophase formation. *Carbon*, 28: 553–558, 1990.
4. O. Ito, UV-visible and near-IR spectra of heat treated pitches during mesophase formation. *Carbon*, 31: 401–406, 1993.
5. J. Ozaki and Y. Nishimura, *Carbon*, 25: 267–275, 1987.
6. O. Ito, H. Seki and M. Iino, ESR and FT-IR studies for coal structures. Characteristics of Japanese coals. *Bull. Chem. Soc. Jpn*, 60: 2967–2978, 1987.
7. O. Ito, T. Kakuta and M. Iino, *In-situ* ESR measurement for heat treatment and cooling processes of pitches for mesophase formation. *Carbon*, 27: 869–875, 1989.
8. T. Ikoma, K. Akiyama, O. Ito and S. Tero, Two-Dimensional EPR spectroscopic studies on the radicals in Argonne premium coals. *Energy Fuels*, 12: 996–1000, 1998.
9. T. Ikoma, O. Ito, S. Tero and K. Akiyama, HYSCORE study on coal radicals. *Energy Fuels*, 12: 1363–1368, 1998.
10. N. Miyajima, T. Akatsu, T. Ikoma, O. Ito, B. Rand, Y. Tanabe, E. Yasuda, A role of charge-transfer complex with iodine in the modification of coal tar pitch. *Carbon*, 38: 1831–1838, 2000.
11. L.J. Lynch, R. Sakurovs, D.S. Webster and P.J. Redlich, ^1H n.m.r. evidence to support the host/guest model of brown coals. *Fuel*, 67: 1036–1041, 1988.
12. O. Ito, R. Sakurovs, T. Parks and L.J. Lynch, *In situ* proton magnetic resonance thermal for mesophase formation of pitches. *Tanso*, 186: 20–24, 1999.
13. T.J. Parks, The correspondence between loss of ^1H -NMR signal intensity and mesophase growth during the thermal maturation of a petroleum pitch. *Carbon*, 36, 1729–1737, 1998.
14. R. Sakurovs, Some factors controlling the thermoplastic behavior of coals. *Fuel*, 79: 379–389, 2000.
15. R. Sakurovs, Interactions between a bituminous coal and aromatic hydrocarbons at elevated temperatures. *Energy Fuels*, 12: 631–636, 1998.

Chapter 18

Raman Spectroscopy as a Characterization Tool for Carbon Materials

Masato Kakihana and Minoru Osada

Materials and Structures Laboratory, Tokyo Institute of Technology, 226-8503, Japan

Abstract: The application of Raman spectroscopy to the characterization of carbon materials is reviewed. General characteristics of Raman spectroscopy are compared with other spectroscopies. These include (1) the coherence length of periodicity for light scattering is relatively short, typically ~ 10 nm and (2) the Raman microprobe is capable of a high spatial resolution, typically $1 \mu\text{m}$. Representative Raman spectra are presented for allotropic forms of carbon, including diamond, graphite, disordered carbons such as glassy carbon and diamond-like carbon, C_{60} , and carbon nanotubes. Raman spectroscopy studies photo-induced structural changes in C_{60} , the one-dimensional properties of carbon nanotubes in conjunction with their resonant behavior, the detection of sp^3 -bonded carbons using high energy ultra-violet (UV) excitation, electron-phonon coupling in the superconducting K_3C_{60} , and the Raman imaging of diamond in a CVD-diamond film.

Keywords: Raman spectroscopy, Resonance effects, Raman imaging, Amorphous carbons, Fullerenes, Nanotubes.

1 Introduction

This chapter describes how Raman spectroscopy can be applied to the characterization and study of the physical properties of carbon materials.

1.1 Raman Parameters

The versatility of Raman spectroscopy as a tool in investigating carbon materials is well documented [1–5]. The parameters of Raman spectra and factors determining Raman parameters are represented as the generic diagram of Fig. 1, which explains how Raman spectroscopy provides insight into the physics of carbons. Experimental parameters include: (i) the number of vibrational modes, (ii) mode frequency, (iii) line width and (iv) intensity. These parameters are directly linked to “symmetry”, “spring constant”, “life time” and “Raman efficiency”, respectively. The latter three parameters relate to such factors as “bonding character”, “phonon density”, “Bose

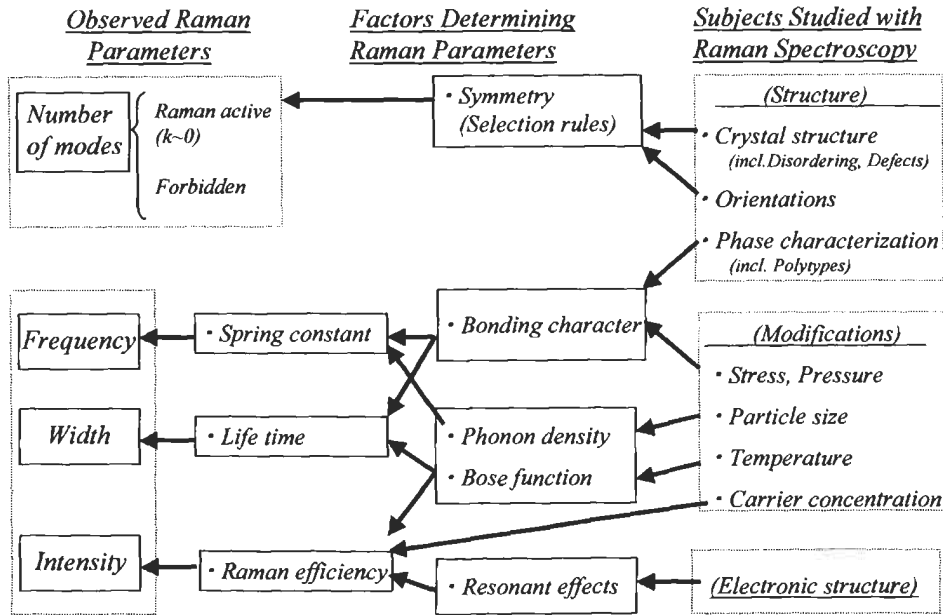


Fig. 1. Relationship between Raman parameters experimentally observed, the factors determining the Raman parameters, and the subjects studied with Raman spectroscopy and their contribution to each factor.

function” and “resonant effects”. The arrows of Fig. 1 show the relationships between Raman parameters and indicate how each factor influences the fundamental Raman parameters.

Figure 1 also lists those structural properties of materials which are studied by Raman spectroscopy and how these relate to their physical properties. Raman spectroscopy is used to study crystal structure, the orientations and phase characterization of materials. One unique use of Raman spectroscopy is the study of disordering or defects in crystals, these giving rise to additional disorder-induced Raman modes because of non-adherence to the strict selection rules. Phase transitions or changes in structures caused by temperature, pressure or stress changes are extensively studied by Raman spectroscopy. Raman spectra are influenced by particle size and carrier concentration because they influence phonon density and Raman efficiency, respectively. Electronic structures of materials are studied by Raman spectroscopy through observance of resonant Raman effects which influence intensities of Raman spectra.

1.2 Coherence Length of Periodicity

Figure 2 shows the range of coherence length of periodicity covered by the several spectroscopic techniques available as experimental tools. Extended X-ray absorption fine structure (EXAFS) selectively examines the radial distribution around a specific

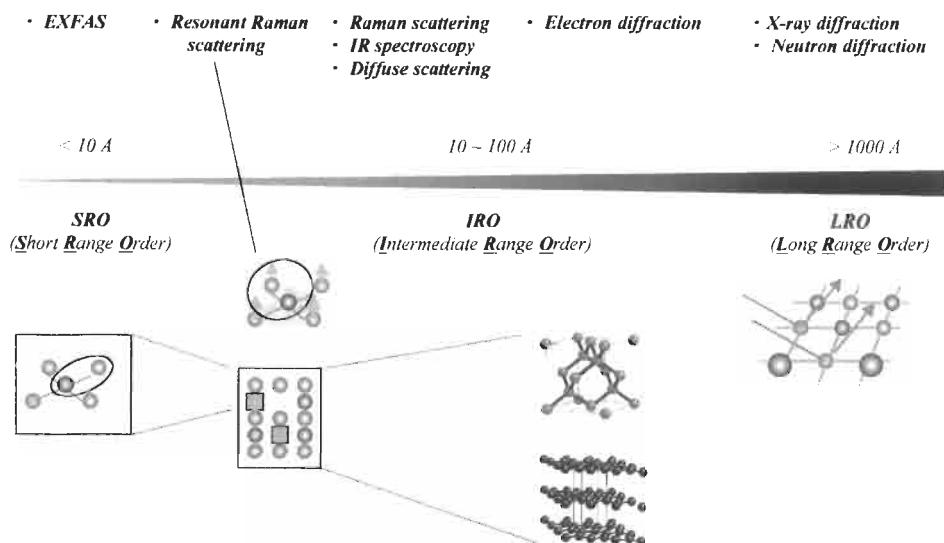


Fig. 2. Coherence lengths for different experimental techniques.

element, and can be applied to disordered systems with no long-range order. Consequently, short-range order within a domain even less than 1 nm can be studied by EXAFS. In contrast, the typical coherence length of periodicity for X-ray diffraction is in the order of 100 nm. Raman spectroscopy and IR spectroscopy have coherence lengths of periodicity of ~ 10 nm. The coherence length of periodicity for Raman scattering light can be reduced, in some favorable cases, to 1–10 nm through a ‘Resonant Raman Effect’. Hence, Raman spectra provide information of bonding in materials which are too disordered for X-ray diffraction studies.

1.3 Spatial Resolution

Figure 3 is a diagram of spatial resolutions of different Raman spectroscopies, varying from 100 μm for conventional macro Raman spectroscopy to ~ 1 μm for micro-Raman spectroscopy. The spatial resolutions of micro-IR spectroscopy are ~ 10 μm , this 10-fold increase being attributed to the fact that spatial resolution is determined by the wavelength of the light used. Ultraviolet (UV) lasers rather than visible lasers facilitate improvements in spatial resolution in the submicron regions [6]. The development of scanning near-field optical microscopy has led to the approximate 10-fold increase in spatial resolution [7].

Surface-enhanced-Raman-spectroscopy (SERS) is not a methodology that directly improves spatial resolution as can be done by methods described above. It is independent of the optical design of a Raman microprobe so enabling a laser beam to be focused onto a diffraction spot of dimension close to the wavelength of the laser light. SERS is important in the field of ultrasensitive instrumentation because the

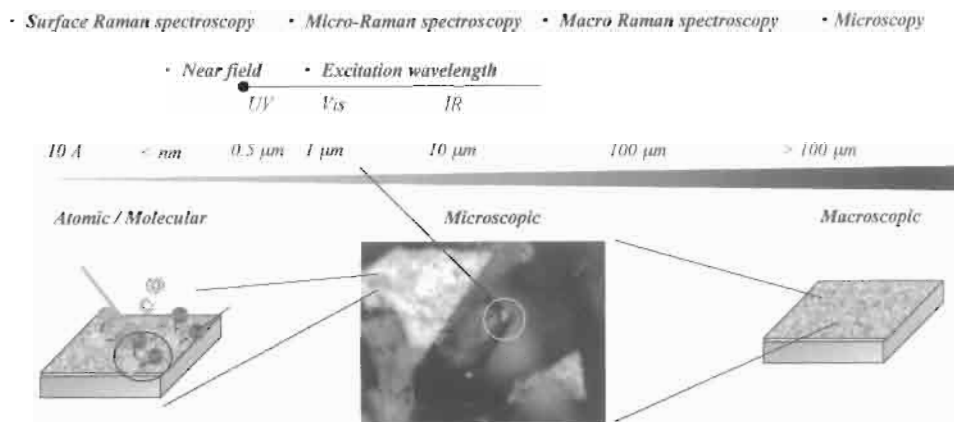


Fig. 3. Spatial resolution for various Raman scattering techniques.

Raman cross-section of a material adsorbed on a metal surface is increased by a factor of $\sim 10^7$. By combining SERS enhancement with resonant Raman enhancement, Raman cross-sections have been further increased by a factor of 10^{14} to 10^{15} , making it possible to observe a single Raman scattering molecule [8]. For carbon materials, SERS has been used to study C_{60} or C_{70} placed on noble-metal surfaces to examine silent modes and charge transfer processes between the C_{60} or C_{70} molecules and the metal surface [9–11]. The observation of the Raman peak from a thin diamond film (~ 20 nm) has been reported [12].

2 Raman Spectra of Carbon Materials

Raman spectroscopy has been successful in studies of diamond, diamond-like carbon (DLC), graphite, disordered carbons, fullerenes and carbon nanotubes. Distinctive Raman bands are observed for each of these individual forms of carbon, making it possible to distinguish one form of carbon from another.

The upper two traces of Fig. 4 correspond to Raman spectra of diamond (consisting of sp^3 -carbon) and highly oriented pyrolytic graphite (HOPG) consisting of sp^2 -carbon atoms with well-defined single peaks at 1333 and 1580 cm^{-1} , respectively. HOPG is a synthetic carbon representative of a large ‘single-crystal’ graphite. The crystal structure of graphite shows up as the 1580 cm^{-1} peak, i.e. the G (graphite) peak. A second peak at 1357 cm^{-1} , called the D (disorder) peak shows up in the Raman spectrum of polycrystalline graphite (Polycryst.G) (see the trace in the middle of Fig. 4). Its intensity relative to that of the G peak is high in the Raman spectrum of disordered glassy carbon (GC) (see the second trace from the bottom of Fig. 4). The introduction of lattice disorder or reduction in crystalline size causes a breakdown in the selection rules so creating the disorder-induced lines. The D peak, ~ 1360 cm^{-1} , in

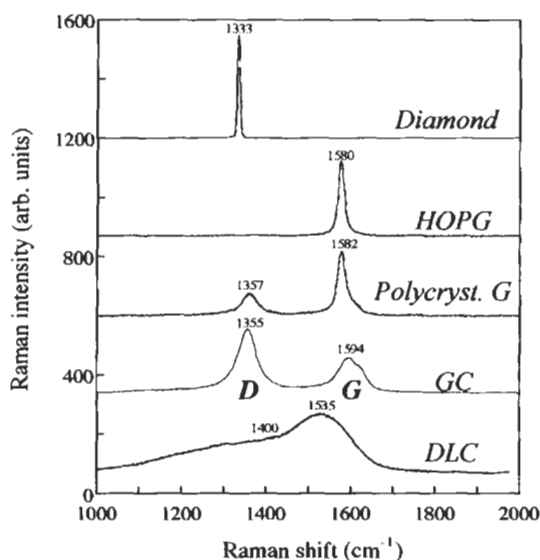


Fig. 4. Raman spectra of diamond, HOPG (highly oriented pyrolytic graphite), Polycryst. G (polycrystalline graphite), GC (glassy carbon), and DLC (diamond-like carbon, a-C:H).

the Raman spectra of disordered carbons is related to this disorder-induced process. The ratio of the integrated intensity of the D peak to the G peak, $I(D)/I(G)$, is extensively used to measure degrees of disorder in a carbon or particle sizes of disordered carbons [2]. Some caution is required, however, as the characterizations of disorder or the estimations of particle sizes, from the D-peak positions and $I(D)/I(G)$, both vary with the photon energy of the laser light used for excitation [12,13].

The lower trace of Fig. 4 is a typical Raman spectrum of a-C:H (hydrogenated amorphous carbon) film obtained using the conventional Ar-green line (514.5 nm). Hard a-C:H films, the diamond-like carbon (DLC), is an 'alloy' of sp^2 - and sp^3 -bonded carbon atoms. The Raman cross-section of the sp^2 -bonded carbon atom is more than 50 times larger than that of the sp^3 -bonded carbon atom when excited with the 514.5 nm line of an Ar-laser [14]. The resultant visible-light (514.5 nm) excitation Raman spectrum of the DLC film in Fig. 4 is, therefore, significantly dominated by scattering from sp^2 -bonded carbon atoms. Hence, visible Raman spectroscopy is an excellent tool allowing a sensitive detection of small fractions of sp^2 -bonded carbon atoms in a diamond film. The use of lasers, with photon energy above 4 eV ($\lambda < 310$ nm), is effective in observing scattering from sp^3 -bonded carbon atoms [15–18]. The resonant enhancement of the Raman cross-section of the sp^2 -bonded carbons is greatly suppressed by high energy excitation.

Figure 5 compares Raman spectra of diamond and HOPG with those of C_{60} and a single-wall carbon nanotube. Because each carbon atom in both C_{60} and a single-wall carbon nanotube is bonded to three neighbors, as are sp^2 -bonded carbon atoms in

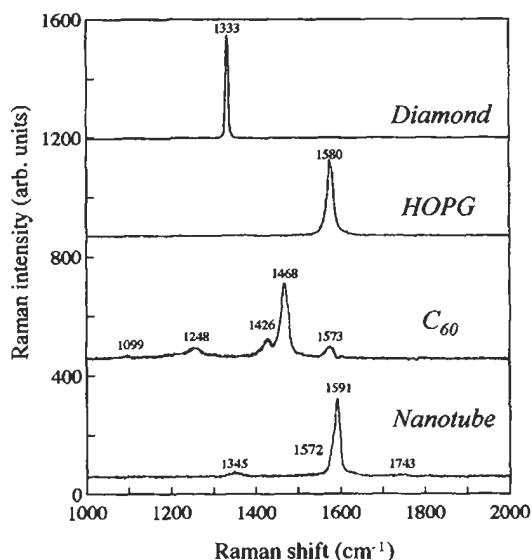


Fig. 5. Raman spectra of diamond, graphite (HOPG), C_{60} , and a single-wall nanotube.

graphite, there are similarities between these Raman spectra. The intense mode at 1591 cm^{-1} , in the Raman spectrum of a nanotube, is closely related to the graphite (G) E_{2g} mode at 1580 cm^{-1} , and is referred to the tangential C–C stretching mode. The strongest of the high frequency A_g -modes, at 1468 cm^{-1} , in the Raman spectrum of C_{60} corresponds to an in-plane tangential displacement of the five carbon atoms surrounding each of the twelve pentagons. It is therefore often called the “pentagonal pinch” mode. Raman spectra of C_{60} and related fullerene-based carbons are discussed and reviewed by Dresselhaus et al. [3] and Menéndez and Page [4].

3 Remarks about Raman Measurements

There are, however, three disadvantages to Raman spectroscopy which include intrinsically weak Raman scattering, the heating of a carbon in a focused laser beam (or photo-decomposition induced by the laser illumination) and sample fluorescence. Below, two factors are described that require attention in Raman measurements; one is related to the phenomena of phototransformation/photo-decomposition specifically in C_{60} , and the other to a fluorescence that interferes with observations of the intrinsic Raman scattering from a carbon.

3.1 Phototransformation and Photo-decomposition in C_{60}

Raman spectroscopy of photo- or heat-sensitive materials requires special care. Intrinsically weak Raman scattering needs to be processed and laser illumination of

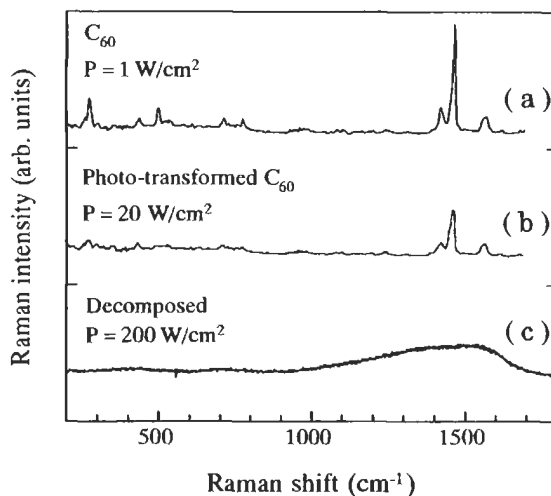


Fig. 6. Effect of phototransformation on the Raman spectrum for C_{60} . The top spectrum (a) shows the Raman spectrum for pristine C_{60} measured with an incident power level of 1 W cm^{-2} . Phototransformation was induced by 2 h irradiation with power level of $P = 20 \text{ W cm}^{-2}$ (b). As the laser power level was further increased to 200 W cm^{-2} the structure decomposed (c).

low intensity has to be used. The phototransformation of C_{60} is an example [19,20]; the effect on the Raman spectrum of C_{60} is shown in Fig. 6. Phototransformation of C_{60} is induced by 2 h of irradiation using the 514.5 nm line of an Ar-laser with an optical flux of 20 W cm^{-2} (Fig. 6b). The Ag-“pentagonal pinch” mode at 1469 cm^{-1} in pristine C_{60} , undergoes a down-shift to 1458 cm^{-1} on phototransformation. Here, several additional modes appear due to the lowering of symmetry resulting from formation of covalent bonds between adjacent C_{60} molecules. The use of a higher optical flux of 200 W cm^{-2} causes photo-decomposition in C_{60} , and this is evident from the changes in the Raman spectra from Fig. 6a to Fig. 6c, the latter Raman spectrum being that of an amorphous carbon. A similar transformation from C_{60} to amorphous carbon occurred under pressures higher than 22 GPa [21].

3.2 Fluorescence Rejection

Although Raman spectroscopy is useful for “finger-printing” the allotropic forms of carbon, relevant, weak, scattered Raman signals are often swamped by strong fluorescences from the target carbon or from its surroundings, so making interpretations obscure. Thus, it is important to avoid these fluorescence problems so that Raman spectroscopy will have a broader applicability to synthesized carbons. One effective way to do this is to use either near-infrared (IR) low energy or near- to deep-ultraviolet (UV) high energy excitations instead of the more widely used visible excitations. This is because fluorescence emissions occur in the visible-light energy region.

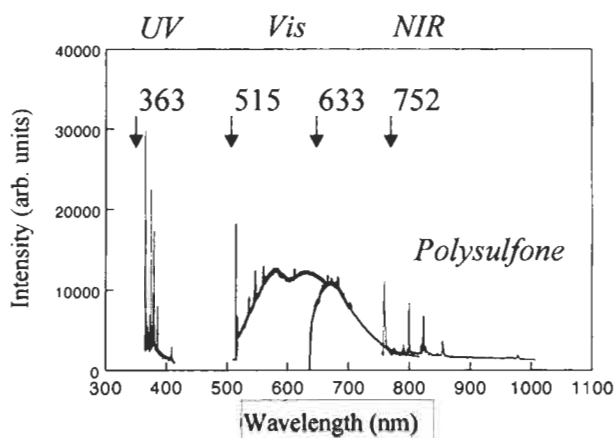


Fig. 7. Raman spectra of polysulfone measured with 363, 515, 633, and 752 nm laser excitations. The spectra are plotted as a function of wavelength.

Figure 7 shows Raman spectra of polysulfone (an industrial polymer) obtained with four laser wavelengths in the range from near-UV (363 nm) to near-IR (752 nm). The spectra are plotted as a function of wavelength rather than Raman shift. The large broad bump corresponds to unwanted fluorescence. The Raman spectra excited at either 752 nm or 363 nm indicate an almost complete elimination of broad-band fluorescence observed with visible 515/633 nm light. The use of near-UV excitation at 363 nm minimizes spectral overlap between the fluorescence and Raman emissions. The use of near-IR excitation at 752 nm prevents a carbon from being excited to the first electronic state from which fluorescence occurs.

4 Recent Raman Studies of Carbon Materials

4.1 Resonance Raman Scattering of a Single-Wall Carbon Nanotube

Resonant Raman spectroscopy is without doubt a powerful tool with which to characterize the one-dimensional (1D) properties of carbon nanotubes [22–25]. Figure 8a shows the high-frequency Raman bands of the tangential C–C stretching modes of a single-wall nanotube, using five laser excitation wavelengths in the energy range $1.65 \text{ eV} \leq E \leq 2.71 \text{ eV}$ (i.e. $752.5 \text{ nm} \geq \lambda \geq 457.9 \text{ nm}$). The striking feature of Fig. 8a is the anomalous resonant behavior of the individual tangential C–C stretching modes; that is, a strong broad feature shows up around $\sim 1540 \text{ cm}^{-1}$ at 2.18 eV ($\lambda = 568.2 \text{ nm}$), its intensity increasing further at 1.92 eV ($\lambda = 647.1 \text{ nm}$), but vanishing almost completely at 1.65 eV ($\lambda = 752.5 \text{ nm}$).

Figure 8b is a line shape analysis of the Raman band from the tangential modes for $E = 1.92 \text{ eV}$ ($\lambda = 647.1 \text{ nm}$), indicating that this specific Raman band fitted four Lorentzian peaks at $1520, 1540, 1560$ and 1590 cm^{-1} . The diameter distribution within

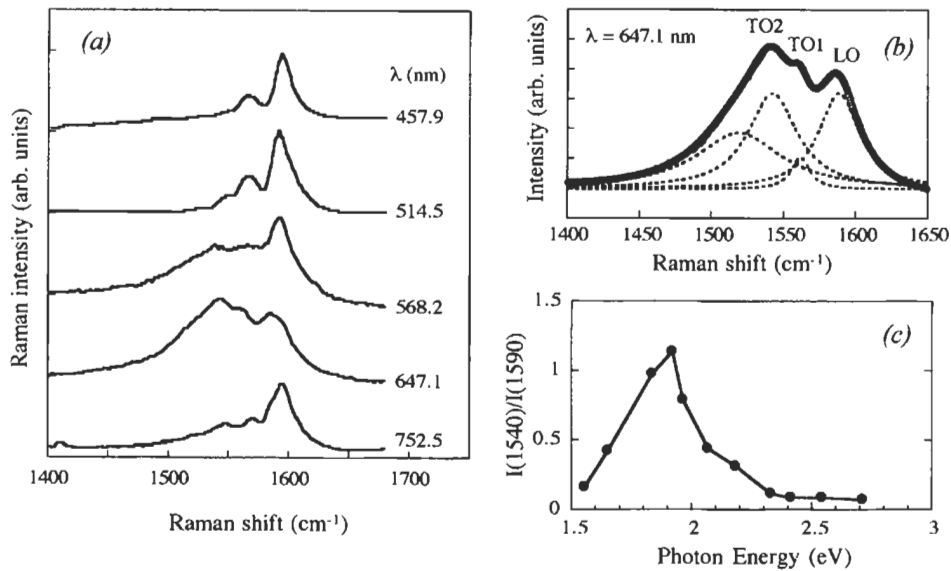


Fig. 8. (a) Raman spectra of a single-wall nanotube obtained with several different laser lines. (b) A fit of the Raman band associated with the tangential modes for $\lambda = 647.1 \text{ nm}$. (c) The intensity ratio of the Raman peaks at 1540 cm^{-1} and 1590 cm^{-1} as a function of laser energy.

the single-wall carbon nanotube is responsible for the multi-line spectral features near to 1550 cm^{-1} . Resonant enhancements of the Raman scattering intensities from carbon nanotubes occur when the laser excitation energy corresponds to electronic transitions between the first singularities in the 1D electronic density of states (DOS) in the valence (v) and conduction (C) bands $v_1 \rightarrow C_1$. Because the energy gaps for the transitions depend strongly on nanotube diameter, the laser energy at which the Raman resonance maxima are observed differ for each individual Raman band (Fig. 8b), as seen in Fig. 8. With an approximately constant intensity of the highest frequency band at 1590 cm^{-1} within the excitation range, a relatively sharp resonance maximum was observed for the 1540 cm^{-1} band at 1.92 eV ($\lambda = 647.1 \text{ nm}$) as shown in Fig. 8c. This is a plot of the ratio of the intensities of the two peaks at 1540 cm^{-1} and 1590 cm^{-1} , $I(1540)/I(1590)$, as a function of E . Single-wall carbon nanotubes exhibit either metallic or semiconducting properties depending upon the nanotube diameter and the tube symmetry. Scanning tunneling microscopy and spectroscopy (STM and STS) studies [26–28] show that metallic nanotubes exhibit an energy gap of $1.7\text{--}2.0 \text{ eV}$ for the $v_1 \rightarrow C_1$ transition, whereas for semiconducting nanotubes the gap is in the range of energy $0.5\text{--}0.65 \text{ eV}$.

These considerations permit the conclusion that the Raman mode at 1540 cm^{-1} with a strong resonance at 1.92 eV is associated with a metallic nanotube and the non-resonant Raman mode at 1590 cm^{-1} is associated with a semiconducting nanotube.

4.2 Raman Characterization of Diamond-like Carbon

Diamond-like carbon (DLC) is an amorphous carbon containing up to 80% of sp^3 -bonded carbon atoms, as determined by Raman spectroscopy. However, because sp^2 -bonded carbon atoms have an energy gap of ~ 2 eV in the region of visible light and the sp^3 -bonded carbons have a much higher energy gap of ~ 5.5 eV, the conventional visible Raman spectra of DLC are dominated by scattering from sp^2 -bonded carbons due to the resonant enhancement effect. Because of large differences between the Raman cross-sections for the sp^2 - and sp^3 -bonded carbons in the visible region, then the as-obtained visible Raman spectrum of DLC (a-C:H) sp^2 -bonded carbon atoms cannot be unambiguously separated from sp^3 -bonded carbons. The relative contribution of the sp^2 -bonded carbons to Raman spectra is then minimized by using ultra-violet (UV) excitations outside the resonance range of the sp^2 -bonded carbons.

Figure 9 shows Raman spectra of an amorphous carbon obtained at several excitation wavelengths. The intensity of the D (disorder) peak is decreased as the excitation wavelength is decreased. For the UV excitation at 244 nm (5.1 eV), the D-peak intensity is sufficiently depressed. It has been reported that the UV Raman spectra of DLC containing a large fraction of sp^3 -bonded carbon atoms, obtained with 244 nm-excitation, exhibit a new broad peak at ~ 1100 cm^{-1} , associated with the vibrational modes of an sp^3 -bonded carbon cluster [15-18]. The fact that the UV-Raman spectrum of the amorphous carbon exhibits no significant peak at ~ 1100 cm^{-1} (the upper trace of Fig. 9) suggests that this carbon contains no sp^3 -bonded carbon atoms.

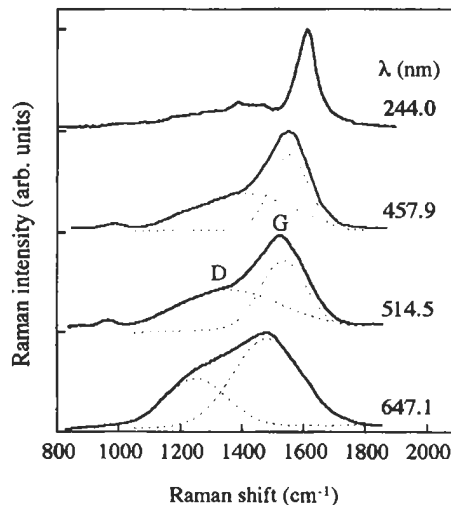


Fig. 9. Raman spectra of an amorphous carbon obtained with several different laser lines.

4.3 Raman Spectra of Doped Fullerenes

Raman spectroscopy has been extensively used as a probe to elucidate the unique properties of fullerene molecules and related materials [3]. In particular, Raman studies of fullerene-derived solids, including the superconducting K_3C_{60} and Rb_3C_{60} compounds, have played a major role in elucidating whether or not the superconducting pairing interaction is mediated by vibrational modes [3].

Figure 10 shows a typical Raman spectrum of the undoped pristine C_{60} as well as those of the doped-superconducting K_3C_{60} and non-superconducting K_6C_{60} . Two major perturbations of the Raman spectrum of C_{60} , following addition of potassium atoms, include (i) the softening of the “pentagonal pinch” mode at 1468 cm^{-1} and (ii) the broadening of several Raman lines derived from the H_g modes in the superconducting K_3C_{60} . The softening of the “pentagonal pinch” mode, following doping by potassium, is due to the elongation of the C–C bonds induced by a transfer of electrons to the p -electron orbitals on the surface of C_{60} [3]. The softening by $\sim 6\text{ cm}^{-1}$ /potassium atom has been used as a convenient method to estimate the stoichiometry x of K_xC_{60} compounds. The remarkable large broadening of H_g modes of K_3C_{60} has been interpreted in terms of strong electron–phonon coupling [3] which is absent in the nonsuperconducting C_{60} and K_6C_{60} .

4.4 Raman Imaging of Diamond in CVD-Diamond Film

Raman imaging of a significant area of a solid sample in conjunction with the use of an advanced confocal line scanning technique makes a valuable contribution to the

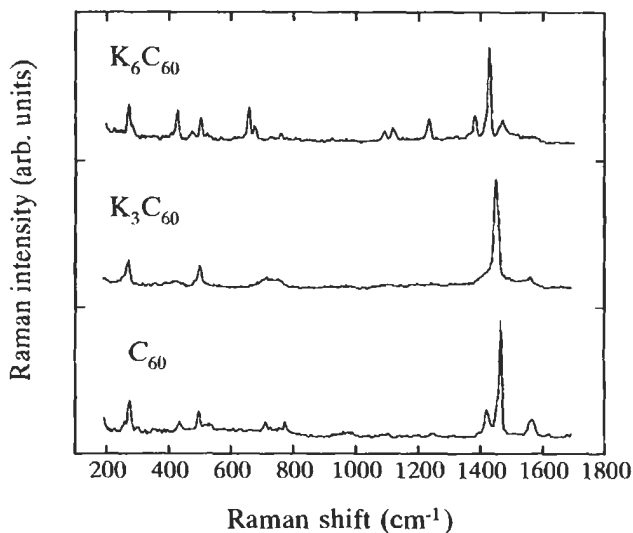


Fig. 10. Raman spectra of C_{60} and its potassium doped salts.

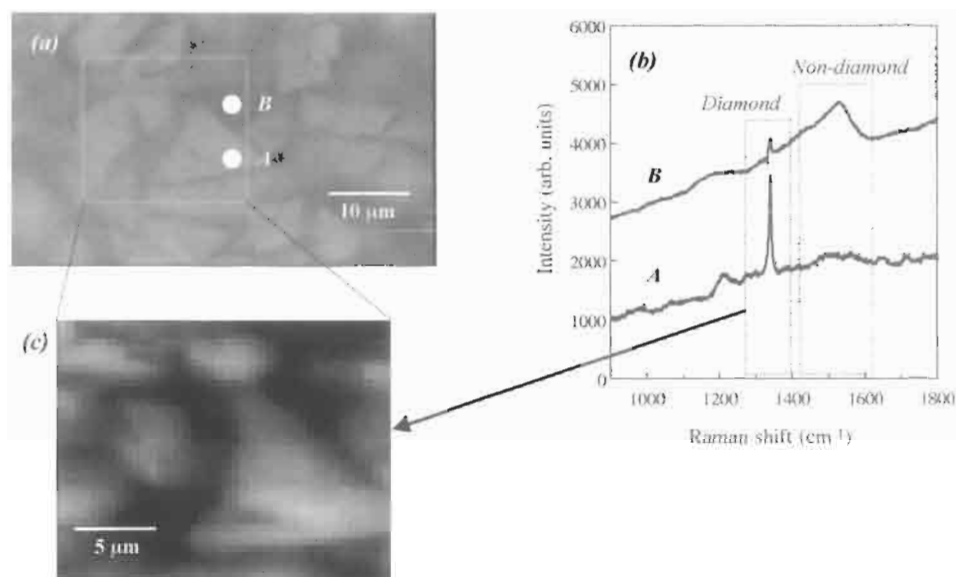


Fig. 11. Raman imaging analysis of a synthetic diamond film. (a) Optical micrograph of a diamond film prepared by a CVD method. (b) The development of a Raman spectrum during a surface scan between a large grain (A) and the grain boundary (B). The analysis was carried out using an R64000-COE microspectrometer equipped with an automated X-Y stage. The spot size of the He-Ne laser ($\lambda = 632.8$ nm) focused on to the surface is $\sim 1 \mu\text{m}$. (c) Raman-band intensity map of a first order peak for cubic diamond at 1332.5 cm^{-1} . Decreasing brightness (from white to black) indicates a decrease in the Raman band intensity. The bright area corresponds to diamond and the black area corresponds to non-diamond carbon.

understanding of structure in carbons. The Raman imaging technique is particularly useful for the characterization of CVD diamond films. This is because the various non-diamond carbon structures are deposited as part of the CVD-diamond film.

Figure 11 is a Raman imaging analysis of a synthetic diamond film prepared by the CVD method. First, the 632.8 nm line of a He-Ne laser was focused by a $100\times$ objective at positions A and B on the film surface to a spot size of $\sim 1 \mu\text{m}$ (Fig. 11a). The Raman spectrum at position A within a large grain is characteristic of pure diamond. That obtained at position B, corresponding to a grain boundary, indicates the presence of non-diamond carbon atoms (Fig. 11b). The result of the Raman imaging of diamond is shown in Fig. 11c where decreasing brightness (from white to black) means a decrease in the fraction of diamond.

References

1. M.S. Dresselhaus and G. Dresselhaus, Light scattering in graphite intercalation compounds. In: M. Cardona and G. Güntherodt (Eds.), *Light Scattering in Solids III*. Recent Results, Chapter 2, pp. 3–57. Springer-Verlag, Berlin, 1982.
2. D.S. Knight and W.B. White, Characterization of diamond films by Raman spectroscopy. *J. Materials Res.*, 4: 385–393, 1989.

3. M.S. Dresselhaus, G. Dresselhaus and P.C. Eklund, Raman scattering in fullerenes. *J. Raman Spectrosc.*, 27: 351–371, 1996.
4. J. Menéndez and J.B. Page, Vibrational spectroscopy of C_{60} . In: M. Cardona and G. Güntherodt (Eds.), *Light Scattering in Solids VIII. Fullerenes, Semiconductor Surfaces, Coherent Phonons*, Chapter 2, pp. 27–95. Springer-Verlag, Berlin, 2000.
5. R. Saito, *Physical Properties of Carbon Nanotubes*. Imperial College Press, London, 1998.
6. V. Pajcini, C.H. Munro, R.W. Bormett, R.E. Witkowski and S.A. Asher, UV Raman microspectroscopy: Spectral and spatial selectivity with sensitivity and simplicity. *Appl. Spectrosc.*, 51: 81–86, 1997.
7. M. Goetz, D. Drews, D.R.T. Zahn and R. Wannemacher, Near-field Raman spectroscopy of semiconductor heterostructures and CVD-diamond layers. *J. Luminescence*, 76&77: 306–309, 1998.
8. S. Nie and S.R. Emory, Probing single molecules and single nanoparticles by surface-enhanced Raman scattering. *Science*, 275: 1102–1106, 1997.
9. A. Rosenberg and D.P. DiLella, Anomalously enhanced Raman scattering of C_{60} on Ag and In surfaces. *Chem. Phys. Lett.*, 233: 76–81, 1994.
10. R.L. Garrell, T.M. Herns, C.A. Szafranski, F. Diederich, R. Ettl and R.L. Whetten, Surface enhanced Raman spectroscopy of C_{60} on gold: evidence for symmetry reduction and perturbation of electronic structure in the adsorbed molecule. *J. Am. Chem. Soc.*, 113: 6302–6303, 1991.
11. K.L. Akers, L.M. Cousins and M. Moskovis, Surface-enhanced vibrational Raman spectroscopy of C_{60} and C_{70} on rough silver surfaces. *Chem. Phys. Lett.*, 190: 614–620, 1992.
12. M.J. Matthews, M.A. Pimenta, G. Dresselhaus, M.S. Dresselhaus and M. Endo, Origin of dispersive effects of the Raman D band in carbon materials. *Phys. Rev. B*, 59: R6585–R6588, 1999.
13. A.C. Ferrari and J. Robertson, Interpretation of Raman spectra of disordered and amorphous carbon. *Phys. Rev. B*, 61: 14095–14107, 2000.
14. N. Wada, P.J. Gaczi and S.A. Solin, Diamond-like three-fold coordinated amorphous carbon. *J. Non-Crystall. Solids*, 35&36: 543–548, 1980.
15. K.W.R. Gilkes, H.S. Sands, D.N. Batchelder, W.I. Milne and J. Robertson, Direct observation of sp^3 bonding in tetrahedral amorphous carbon UV Raman spectroscopy. *J. Non-Crystall. Solids*, 227–230: 612–616, 1998.
16. J.R. Shi, X. Shi, Z. Sun, E. Liu, B.K. Tay and S.P. Lau, Ultraviolet and visible Raman studies of nitrogenated tetrahedral amorphous carbon films. *Thin Solid Films*, 366: 169–174, 2000.
17. V.I. Merkulov, J.S. Lannin, C.H. Munro, S.A. Asher, V.S. Veerasamy and W.I. Milne, UV studies of tetrahedral bonding in diamond-like amorphous carbon. *Phys. Rev. Lett.*, 78: 4869–4872, 1997.
18. K. Okada, H. Kanda, S. Komatsu and S. Matsumoto, Effect of the excitation wavelength on Raman scattering of microcrystalline diamond prepared in a low pressure inductively coupled plasma. *J. Appl. Phys.*, 88: 1674–1678, 2000.
19. T. Wågberg, P. Jacobsson and B. Sundqvist, Comparative Raman study of photopolymerized and pressure-polymerized C_{60} films. *Phys. Rev. B*, 60: 4535–4538, 1999.
20. G. Chambers and H.J. Byrne, Raman spectroscopic study of excited states and photopolymerization of C_{60} from solution. *Chem. Phys. Lett.*, 302: 307–311, 1999.
21. D.W. Snoko, Y.S. Raptis and K. Syassen, Vibrational modes, optical excitations, and phase transition of solid C_{60} at high pressures. *Phys. Rev. B*, 45: 14419–14422, 1992.
22. A.M. Rao, E. Richter, S. Bandow, B. Chase, P.C. Eklund, K.A. Williams, S. Fang, K.R. Subbaswamy, M. Menon, A. Thess, R.E. Smalley, G. Dresselhaus and M.S. Dresselhaus, Diameter-selective Raman scattering from vibrational modes in carbon nanotubes. *Sci-*

- ence, 275: 187–191, 1997.
23. M.A. Pimenta, A. Marucci, S.A. Empedocles, M.G. Bawendi, E.B. Hanlon, A.M. Rao, P.C. Eklund, R.E. Smalley, G. Dresselhaus and M.S. Dresselhaus, Raman modes of metallic carbon nanotubes. *Phys. Rev. B*, 58: R16016–R16019, 1998.
 24. A. Kasuya, M. Sugano, T. Maeda, Y. Saito, K. Tohji, H. Takahashi, Y. Sasaki, M. Fukushima, Y. Nishina and C. Horie, Resonant Raman scattering and the zone-folded electronic structure in single-wall nanotubes. *Phys. Rev. B*, 57: 4999–5001, 1998.
 25. P.M. Rafailov, H. Jantoljak and C. Thomsen, Electronic transition in single-walled carbon nanotubes: A resonance Raman study. *Phys. Rev. B*, 61: 16179–16182, 2000.
 26. J.W.G. Wildöer, L.C. Venema, A.G. Rinzler, R.E. Smalley and C. Dekker, Electronic structure of carbon nanotubes investigated by scanning tunneling spectroscopy. *Nature*, 391: 59–62, 1998.
 27. T.W. Odom, J.L. Huang, P. Kim and C.M. Lieber, Atomic structure and electronic properties of single-walled carbon nanotubes. *Nature*, 391: 62–64, 1998.
 28. M.S. Dresselhaus, New tricks with nanotubes. *Nature*, 391: 19–20, 1998.

Chapter 19

Basics of Nuclear Magnetic Resonance and its Application to Carbon Alloys

Takashi Nishizawa

Chemical and Environmental Tech. Lab., Kobe Steel, Ltd., Kobe, Hyogo 651-2271, Japan

Abstract: In this chapter applications of Nuclear Magnetic Resonance (NMR) spectroscopy to carbon/carbon alloys are presented. The principles of NMR and explanations of such technical terms as FID, relaxation time and spin locking are set out. A brief account is given of the preparations necessary for pitch samples and methods of determination of aromaticity from ^1H -NMR spectra. A detailed description is given of ^{13}C -NMR spectrometry, which is the most suitable method to characterize pitches. Preparation of both solid-state and fused-state samples as well as solution/liquid state samples, assignments of spectral peaks in terms of functional groups in constituent molecules of pitches, and an interpretation on a spectrum of a mesophase pitch in the liquid crystalline phase are all discussed. Finally, chemical shifts of ^7Li -NMR from systems of carbons and graphites containing lithium are listed and probable assignments made.

Keywords: ^1H -NMR, ^{13}C -NMR, ^7Li -NMR, Pitch, Carbonaceous mesophase, Graphite intercalation compound.

1 Introduction

The nuclear magnetic resonance (NMR) technique cannot be used for carbon/graphite materials as such but is a powerful tool to analyze pitches which are the parent materials of carbons, as well as lithium contained within carbons and graphites. This chapter describes: (1) the basics of ^1H - and ^{13}C -NMR spectroscopy (i.e. spin 1/2); (2) the characterization of pitches; and (3) the characterization of the several chemical states of lithium in Li-carbon and Li-graphite compounds by ^7Li -NMR. This work has relevance to the lithium battery.

2 Apparatus

An NMR spectrometer consists of a magnet, a probe, an oscillator, a spectrometer and a computer. Figure 1 is an illustration of the magnet and probe for liquid/solution

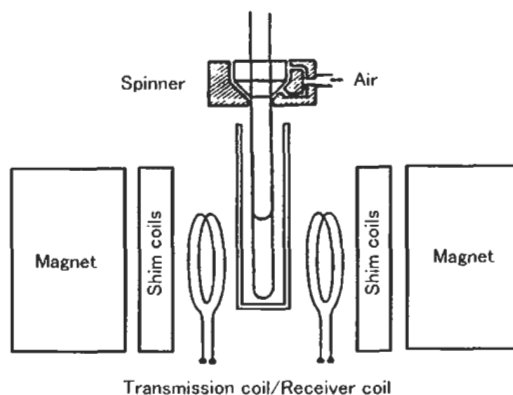


Fig. 1. Illustration of a magnet and a probe.

samples. Generally, the NMR approach to many materials, using high magnetic fields, is able to obtain high-resolution spectra, But for pitch, high resolution is impossible, even with the highest of magnetic fields, because pitch has too many constituent compounds to make possible a resolution of individual signals. A merit of the use of high magnetic fields is the ability to obtain a spectrum with a high signal to noise ratio (S/N):

$$\begin{aligned} (S/N) &\propto \nu_0^3 \\ \nu_0 &\propto B_0 \end{aligned} \quad (1)$$

where ν_0 and B_0 are the resonance frequency and the static magnetic field, respectively. However, a disadvantage associated with the use of NMR for solid samples with high magnetic fields is that large spinning side bands appear when using MAS (magic angle spinning). So, a 3–400 MHz (7–9.4 T) NMR spectrometer is suitable as a general purpose instrument to analyze pitch-like materials and also the states of lithium within carbons and graphites.

3 Basics of NMR for Spin 1/2 Nucleus

When a spin 1/2 nucleus is in a magnetic field, B_0 , conventionally along the Z-axis, the spin energy splits into two levels, such as an electron spin (Zeeman splitting), where the spin absorbs electromagnetic waves (radio frequency waves (r.f.)) of the Zeeman energy. To represent classically a magnetization of nucleus n , in a magnetic field, B_0 , aligns with respect to B_0 and precesses at an angle θ (the Larmor precession). The Larmor frequency of the spin, ν_N , is given by

$$\nu_N = \gamma_N \times B_0 / 2\pi \quad (2)$$

where γ_N is the nuclear magnetogyric ratio of spin N. Consider a small magnetic field

B_1 whose frequency is ν_N rotating around the Z-axis (the ν_N is equal to the frequency of electromagnetic wave corresponding to the Zeeman energy). When B_1 is applied to the nucleus, the angle θ becomes large accompanied with energy absorption. Basically, NMR spectroscopy observes this absorption making it possible to analyze chemical structures of a sample from the position of the signal in the spectrum. This is because the nuclei under investigation absorb at different radio frequencies (with a fixed field) depending on the chemical environment of the nuclei.

3.1 NMR Locking and Chemical Shift Standard

Usually, a magnetic field is not sufficiently stable to obtain a high-resolution spectrum of ^1H . To overcome this, an NMR signal of a different nuclear species (i.e. other than the nucleus under investigation) is monitored and the magnetic field is corrected to give the monitored signal a constant resonance frequency (field/frequency locking, NMR locking). A high-resolution spectrum, in general, requires a sample to be in a solvent. A deuterized compound is commonly used as the solvent and the D (deuterium) signal is used as the locking signal. Notwithstanding this, it is possible to obtain a high-resolution spectrum when making ^{13}C measurements within a short time period.

It is essential with NMR spectroscopy to use a reference signal in order to obtain chemical shifts, because the strength of a magnetic field cannot be determined precisely enough for the requirements of spectral analysis. For ^1H -NMR and ^{13}C -NMR, tetramethylsilane (TMS) is generally used as a reference compound, and its spectrum recorded with this signal taken as zero. Even when a signal other than that of TMS is used as a reference, the spectrum is usually expressed with respect to TMS as zero. For ^{13}C -NMR, it is possible to measure a reference compound just before the measurement of a sample and chemical shifts of the sample are determined by the signal position of the reference compound (sample exchange method). This technique is useful to measure a sample without using a locking signal. The experimental error for this method is ca. 0.01 ppm (enough for ^{13}C -NMR). Spectra are normally plotted with the magnetic field increasing (decreasing frequency) from left to right.

3.2 Pulse

It is possible to reverse the magnetization of nuclear spins in a static field by a pulse of near Larmor frequency. A pulse whose flip angle is 90° is called a 90° pulse, and a pulse reversing the magnetization vector is a 180° pulse. A pulse width of 180° is twice as long as a 90° pulse, and a flip angle of a half-width pulse is equal to that of a half-power pulse, i.e. a flip angle is proportional to pulse energy. Figure 2 suggests the relationship between a pulse shape and frequencies in the pulse. As the number of components becomes larger, the pulse shape approaches a rectangle. In other words, a pulse of steeper slope as well as a narrower width includes more frequencies, i.e. a

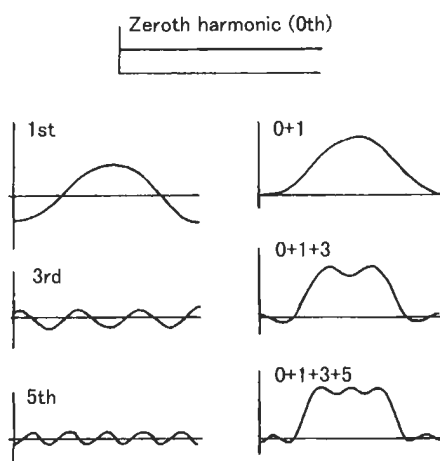


Fig. 2. Synthesis of waves.

pulse with a wide frequency range. It is necessary to satisfy the following equation which relates the spectrum range, S_w (Hz), to the pulse width, t_p (s):

$$t_p \ll 1/(4S_w) \quad (3)$$

However, as far as ^1H - and ^{13}C -NMR are concerned, all commercially based spectrometers satisfy this condition.

3.3 FID and FT-NMR Spectroscopy

After a resonance pulse has activated a spin system, transverse magnetization of the spins is observed and this decays exponentially with a time constant T_2 . This decay is called FID (free induction decay), and Fourier transformation of the FID gives the NMR spectrum. FT-NMR is a method to obtain spectra through this process and peak positions on a spectrum correspond to a frequency component of FID. For example, when a spin is subjected to a pulse whose frequency differs by 100 Hz from the precise resonance frequency, then an oscillation of 100 Hz is superimposed on the free induction decay. This relationship is illustrated in Fig. 3. For many signals existing in a spectrum, the FID is equal to the sum of the FID of individual signals and the frequencies in the FID are disclosed by FT (i.e. a spectrum is obtained).

3.4 Relaxation

There are two relaxation mechanisms in a nuclear spin system. One is longitudinal relaxation (the time constant is expressed by T_1) corresponding to spin–lattice relaxation (an energy effect) and the second is transverse (T_2) corresponding to spin–spin relaxation (an entropy effect).

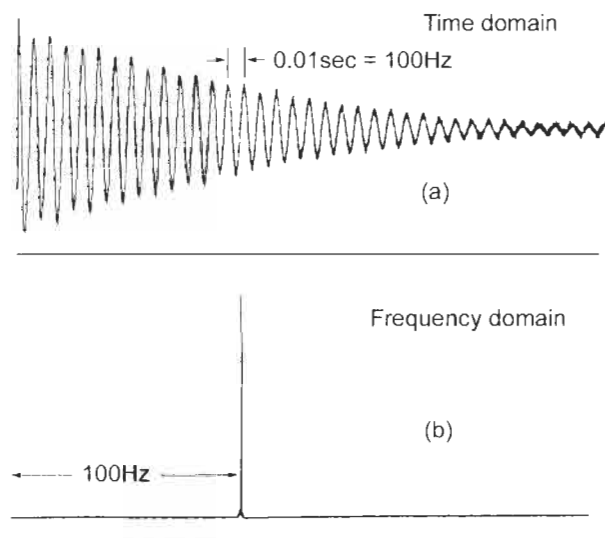


Fig. 3. Relationship between a FID and the spectrum: (a) FID, (b) spectrum.

3.4.1 Longitudinal Relaxation (T_1)

After the reversal of the magnetization (M_z) of a spin system by a 180° pulse, the magnetization gradually returns to a thermal equilibrium by transferring energy from the nuclear spin system to its surroundings (called lattice). The rate of return of the magnetization (T_1) is described by:

$$\frac{dM_z}{dt} = -\frac{1}{T_1}(M_0 - M_z) \quad (4)$$

where T_1 is the longitudinal relaxation time. This relaxation occurs through the interaction of the nuclear spin with fluctuating local magnetic fields (i.e. magnetic noise), which are generated by the motion of molecules. When the locally induced magnetic fields include the components of the resonance frequency of the spins, they can then interact with the spin energy to bring about relaxation, i.e. the energy transfer from the spin system to the lattice. The more abundant the component, the quicker the relaxation occurs. In general, the fluctuation of magnetic fields is induced by the dipole of ^1H nuclei. Because the magnitude of the local field, induced by a dipole, is proportional to $1/r^3$, only the nearest ^1H is affected. Thus, ^{13}C -NMR spectroscopy, for quaternary carbon (i.e. having no C-H bond, the nearest proton being absent) shows a long T_1 (more than 60 s). With increasing temperature, the average frequency of the magnetic noise becomes higher and with decreasing temperature it becomes lower and amounts of noise decrease. So the T_1 has a minimum value near to the melting/softening point of the sample (Fig. 4).

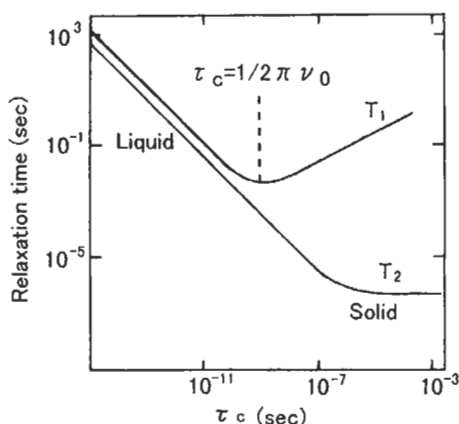


Fig. 4. Effect of molecular correlation time (τ_c) on T_1 and T_2 .

As for pulse repetition times, periods of more than five times T_1 are required to guarantee the quantifying of signals when 90° pulses are employed.

3.4.2 Transverse Relaxation (T_2)

The transverse magnetization of spins, caused by B_1 , relaxes exponentially with a time constant T_2 . This relaxation is the process of losing the coherency of the magnetization of the spin system and is caused by spin–spin interactions. The line width at half height of the NMR spectrum, w , is related to the spin–spin relaxation time T_2 ($w = 2/\pi T_2$ Hz). When molecules move vigorously, T_1 and T_2 have the same value (see Fig. 4) and decrease as the molecular motion decreases to a temperature near to the melting point of the sample. As temperatures decrease further, T_1 then increases but T_2 continues to decrease. This means that in a solid phase, T_1 is long (requires a long time for pulse repetition) and T_2 is short (the signal quickly vanishes) and so it is often very difficult to obtain a NMR spectrum from a solid-state sample.

3.5 Spin Locking

When a static magnetic field B_0 is applied to a sample, the nuclear spin has a Larmor frequency $\nu_N (= \gamma_N B_0 / 2\pi)$ around the Z -axis. This frequency can be changed to the X – Y plane as follows: first, irradiate a 90° pulse to the spin system and then rotate the longitudinal magnetization on to the X – Y plane. Thus, the magnetization rotates on the X – Y plane at the frequency of ν_N . Immediately after this pulse is irradiated, a rotational magnetic field B_1 around the Z -axis, whose frequency is ν_N , is applied to the spin system. Because the magnetic field (B_1) and the nuclear spins rotate at the same rate around the same Z -axis, the spins behave as if being subject to a static magnetic field B_1 on the X – Y plane. Thus, the spin system is quantized by the rotational magnetic field B_1 . In this case, the new Larmor frequency ν_1 (note that the rotational

axis of the B_1 rotates at the frequency of ν_N on the X - Y plane) is determined by B_1 ($\nu_1 = \gamma_N \times B_1/2\pi$). This technique is called spin locking.

Using this technique, nuclear spin energy can be transferred to other nuclear species. For example, initially the spin system of ^1H is subject to a 90° pulse, and then the nuclear spin is locked by a rotational magnetic field B_H . Next, another rotational magnetic field (B_C), which also rotates around the Z -axis, is applied and satisfies the following equation:

$$\gamma_C \times B_C = \gamma_H \times B_H \text{ (Hartmann-Hahn condition)} \quad (5)$$

This means that ^1H and ^{13}C have the same Zeeman energy on the X - Y plane. Thus, it is possible to transfer the energy from ^1H to ^{13}C . At the same time, the large magnetization of ^1H transfers to ^{13}C so that the sensitivity of ^{13}C -NMR increases to $(1 + \gamma_H/\gamma_C) \cong 3$. Moreover, the relaxation of ^{13}C is governed by T_1 of ^1H , which is much shorter than that of ^{13}C . The pulse repetition time is thus shortened considerably. This is called cross-polarization (CP) and is employed generally in solid state NMR measurements.

3.6 Nuclear Overhauser Effect

In the case of cross-polarization, the ^{13}C spins in the excited states return to their thermal equilibrium via dipole-dipole interactions between ^{13}C and ^1H . Generally, when relaxation of ^{13}C occurs via ^1H - ^{13}C dipole-dipole interactions, magnetization of ^1H transfers to ^{13}C . Proton decoupling (see later section) is the case when the sample is a liquid or in solution, because here the relaxation of a ^{13}C nucleus mainly occurs via dipole-dipole interactions to the ^1H which is chemically bonded to the nucleus. This phenomenon is known as the nuclear Overhauser effect (NOE) and the ratio of the signal enhancement is $(1 + \gamma_H/\gamma_C)$, being the same as for cross-polarization. The NOE is small or zero on quaternary carbon atoms or in a sample including a relaxation reagent (see following section). In both cases, the ^1H - ^{13}C dipole-dipole interaction is a minor factor in the total relaxation mechanism of the ^{13}C spin.

3.7 Relaxation Reagent

Because the magnetogyric ratio of an electron is 657 times that of a nucleus, small paramagnetic contamination in a sample greatly reduces the T_1 of the sample. Some paramagnetic compounds such as tris-acetylacetonatechromium ($\text{Cr}(\text{acac})_3$) reduce somewhat the T_1 of quaternary carbon atoms as well as T_1 values of other carbon atoms, but this does not lead to severe line broadening nor to changes in the signal position of the sample. Additions of such paramagnetic compounds to a sample shorten the pulse repetition-time, so they are called relaxation reagents. Such an addition has the further merit of improving a quantitative interpretation of the spectrum.

3.8 Dipole–dipole Interaction

The direct dipole–dipole interaction energy E_{μ} is represented by

$$E_{\mu} = \mu_{\alpha} \cdot \mu_{\beta} (3 \cos^2 \theta - 1) / 4r^3 \quad (6)$$

where r is the distance of the first dipole from the second and θ is the angle between the axis of the first dipole and the line joining their centers. This direct dipole–dipole interaction, due to the term r^3 , is very local and the average of E_{μ} is equal to zero due to the term $(3 \cos^2 \theta - 1)$. Molecules in a solvent are not affected by this direct dipole–dipole interaction because their rapid molecular motion averages the energy. On the contrary, in the solid state, such averaging does not occur and very broad lines result. In the case of ^{13}C and ^1H which is bonded to the carbon, the maximum energy of the dipolar interaction is about 25 kHz, corresponding to 250 ppm for 9.4 T (resonance frequency of ^{13}C : 100 MHz) and 340 ppm for 7 T (75 MHz).

On the other hand, the spin coupling constant J , which is observed in a liquid/solution sample, is an indirect dipole–dipole interaction via bonding electrons and is affected by the nature of the chemical bonding. The units of J are Hz, so J is not altered by the intensity of a static magnetic field. Some $J_{\text{C-H}}$ values are listed in Table 1.

3.9 Chemical Shift

Chemical shifts are due to the shielding of the external magnetic field by electron clouds associated with the chemical structure of the molecule. Consequently, a resonance frequency of a nucleus in a molecule basically depends on the angle between the molecule and a magnetic field (chemical shift anisotropy). For aromatic carbon atoms, the chemical shift anisotropy covers over 200 ppm. For example, benzene in the solid state (polycrystalline or powder) shows a broad signal from 10 to 220 ppm on a ^{13}C -NMR spectrum (powder pattern), this being the sum of individual signals from whole directions in space (Fig. 5). On the other hand, benzene in a solvent shows a sharp single peak at 127 ppm (as referred to TMS) and the peak position is called “the chemical shift” of benzene. The 127 ppm is the average position of the powder pattern and the averaging results from rapid and random molecular motion.

Table 1

$J_{\text{C-H}}$ values of some compounds

| Compounds | $J_{\text{C-H}}$ (Hz) | Compounds | $J_{\text{C-H}}$ (Hz) | Compounds | $J_{\text{C-H}}$ (Hz) |
|------------------------|-----------------------|---------------------------------------|-----------------------|----------------------------|-----------------------|
| C_2H_6 | 125 | CH_3OH | 141 | CHCl_3 | 209 |
| $(\text{CH}_2)_6$ | 123 | $(\text{CH}_3)_4\text{Si}$ | 118 | $\text{HC}\equiv\text{CH}$ | 249 |
| C_6H_6 | 129 | $(\text{CH}_3)\text{CO}(\text{CH}_3)$ | 127 | HCOOH | 222 |

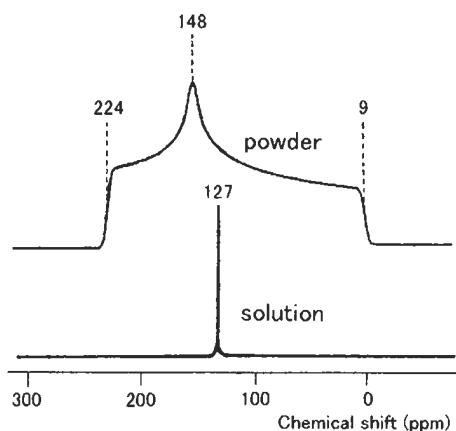


Fig. 5. ^{13}C -NMR spectra of benzene (powder and solution).

The unit of chemical shift is ppm and the anisotropy of aromatic carbon (ca. 200 ppm) corresponds to 20 kHz at 9.4 T (resonance frequency 100 MHz) and 15 kHz at 7 T (75 MHz). As “the chemical shift” is a function of chemical structure, NMR spectra have extensive applications in determinations of chemical structures of molecules.

3.10 Magic Angle Spinning

In samples in solution, rapid and random molecular motion averages the chemical shift anisotropy to “the chemical shift” and the direct dipole–dipole interaction is averaged to zero. Such averaging does not occur in the solid state and very broad lines are observed. As a result, not only does the S/N ratio of the spectrum decrease considerably but also it is impossible to analyze the spectrum because of overlapping of the broadened signals. But, it is still possible to obtain motion, equivalent to random fluctuations, by mechanical rotation about an axis. This axis has the same angle with respect to the X -, Y -, and Z -axes. This is $54^{\circ}44'$ with respect to the static magnetic field (Z -axis). The mechanical rotation around this axis averages the X -, Y - and Z -component; it is equal to the averaging over the whole space, though it requires rotational speed more than signal width. That is, to extinguish the direct dipole–dipole interaction of 25 kHz it needs the rotation speed of the sample to be ca. 25 kHz. To average the chemical shift anisotropy of 200 ppm, it is ca. 20 kHz for the 9.4 T magnet (resonance frequency 100 MHz) and 15 kHz for the 7 T magnet (75 MHz). When a rotational speed is less than this speed, then spinning side bands (SSB) are observed whose interval is equal to the rotational frequency and the center is “the chemical shift”. It is noticeable that the center signal does not always show the maximum intensity because the envelope of the side bands is the same as the signal without spinning (i.e. powder pattern). Though some magic angle spinning (MAS) equipment can rotate a sample to speeds of 20 kHz, so enabling the averaging of the dipole–dipole interactions and the chemical shift anisotropy completely, there are

some limitations, e.g., only a small amount of a sample can be used. Generally, rotational frequencies of 4–9 kHz are used as a MAS speed, so the SSB cannot be removed completely. With regard to the direct dipole–dipole coupling, it is possible to remove by high-power decoupling (see the next section), the rest of the SSB is ascribed by chemical shift anisotropy. Thus, analyses of spectra with SSB are possible.

3.11 Decoupling

A severe problem associated with the use of high-resolution solid-state ^{13}C -NMR is the direct dipole–dipole interaction between ^{13}C and ^1H which is bonded to the carbon. Though it can be removed using high-speed MAS, a more convenient method is to use a strong r.f. at the Larmor frequency of ^1H . The use of the r.f. causes nuclear spin of ^1H to inverse at high speed. As a result, the local field around the ^{13}C is averaged to zero. This technique is called decoupling. For a sample dissolved in a solvent, indirect dipole–dipole interaction is about 1/100 of that of direct coupling. The power required for decoupling is in the same ratio.

The decoupling for direct dipole–dipole coupling is called high-power decoupling in order to distinguish it from the decoupling of the indirect case which is normally used in NMR spectroscopy. High-power decoupling is severe for the instrument and an extended decoupling period (for example 2 s) may destroy the irradiation coil.

3.12 Gated Decoupling

To obtain a ^{13}C -NMR spectrum from a solution, generally ^1H decoupling is employed because indirect coupling complicates the spectrum. But, the decoupled spectrum cannot be quantified because of NOE. One method to quantify the spectrum, as shown above, is to add a relaxation reagent in the solution. Another method is to employ a gated-decoupling technique. NOE is established on the time scale of the appropriate spin–lattice relaxation time. The associated decoupling effect, effectively, is established instantaneously. Thus, a decoupled ^{13}C -NMR spectrum without NOE can be obtained when the decoupler is switched off during the period of the pulse to the ^{13}C nuclei and it is switched on during data acquisition.

4 Characterization of Pitch

Pitch is an important material in studies of carbon alloys and is a necessary raw material in the manufacture of graphitizable and graphitized carbons. A general method for material characterization is to elucidate the molecular structure of the material, but it is impossible for pitch because it is made up of so many compounds. Pitch is an intermediate material in the conversion of dominantly polycyclic aromatic compounds to carbon materials by the processes of pyrolysis and carbonization, in an inert atmosphere. Thus, it is useful to introduce the concept of average molecular structure where pitch is treated statistically.

4.1 Characterization by $^1\text{H-NMR}$

The best way to prepare a pitch for $^1\text{H-NMR}$ measurement is to dissolve it in a solvent, just like other organic compounds. To remove large signals generated by the solvent, a deuterated chemical (normally CDCl_3) is employed and the D signal of the solvent is used as a locking signal.

It is important to note that saturated solutions are not needed because a pitch often re-precipitates in the sample tube on standing. Also, it is noted that $^1\text{H-NMR}$ has enough sensitivity to provide a spectrum from dilute solutions. Further, not all of a pitch will be soluble in the selected solvent.

The most useful characterization of a pitch from a $^1\text{H-NMR}$ spectrum is the aromaticity, as determined by the Brown–Ladner equation [1]:

$$f_a = \frac{C_a}{C} = \frac{[C/H] + H_\alpha/H + H_0/H}{[C/H]} \quad (7)$$

where C_a is the quantity of aromatic carbon atoms; C is the quantity of total carbon atoms; $[C/H]$ is the atomic number ratio of carbon and hydrogen determined by ultimate analysis; H_α/H is the ratio of H_α to total hydrogen determined by $^1\text{H-NMR}$; H_0/H is $[H_\beta + H_\gamma]$ ratio by $^1\text{H-NMR}$. The definitions of H_α , H_β and H_γ are listed in Table 2, and H is defined as $[H_a + H_\alpha + H_\beta + H_\gamma]$. A $^1\text{H-NMR}$ spectrum of a coal-tar pitch is shown in Fig. 6, as an example.

Table 2
Assignment of $^1\text{H-NMR}$ spectra for pitch-like materials

| Region (ppm) | Symbol | Assignment | |
|--------------|------------|--------------------|----------------------------------|
| 6–9 | H_a | Aromatic hydrogen | |
| 2–4 | H_α | Aliphatic hydrogen | Bonding to α -carbon* |
| 1–2 | H_β | Aliphatic hydrogen | Bonding to β -carbon* |
| 0.5–1 | H_γ | Aliphatic hydrogen | Bonding to $\geq\gamma$ -carbon* |

* α -Carbon: an aliphatic carbon bonding to an aromatic carbon. β -Carbon: an aliphatic carbon next to an α -carbon.

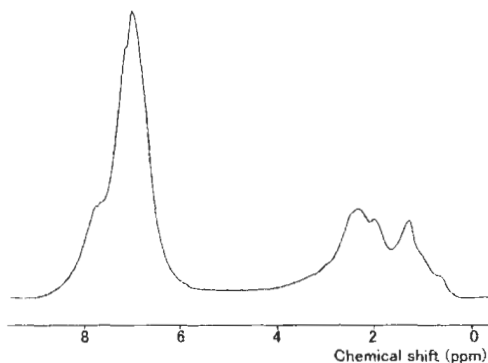


Fig. 6. $^1\text{H-NMR}$ spectrum of a coal-tar pitch.

4.2 Characterization by ^{13}C -NMR

A skeletal structure of molecules in pitch is mainly composed of carbon atoms. Thus, a pitch can be directly characterized by ^{13}C -NMR. Because pitch materials have been subject to considerable thermal polymerization and cracking only stable functional groups exist in the material. As a result, the types of functional groups found in pitches are limited in number and ^{13}C -NMR is able to identify all of them (Table 3 [2]).

4.2.1 Measurement of Liquid/Solution Sample

It is conventional to measure a pitch in a solvent, though large solvent signals are always observed. In general, a solvent is selected not to overlap with sample signals from such solvents as CHCl_3 or CS_2 whose chemical shifts are 77.2 and 192.5 ppm, respectively. CDCl_3 (77.0 ppm) is the most frequently used solvent because it has signals for locking. Because the quantitative nature of spectra is important for the characterization of the pitch, it is necessary to employ the following procedures:

1. A relaxation reagent is added to the sample at a concentration of 5–10 mmol l^{-1} . Acetylacetonatechromium(III) ($\text{Cr}(\text{acac})_3$) is generally used as a relaxation reagent.
2. Flip angle of 30 – 45° and a pulse delay time of 2 s are employed.
3. Inverse gated decoupling is used.
4. Though 4096 (4 k) data points are acceptable for the FID sampling, 16 k or 32 k points are preferred considering the speeds of modern computers and the inexpensive nature of hard disks.

As an example, a spectrum of a coal-tar pitch is shown in Fig. 7 [3], which is measured by means of the fused state method (described later).

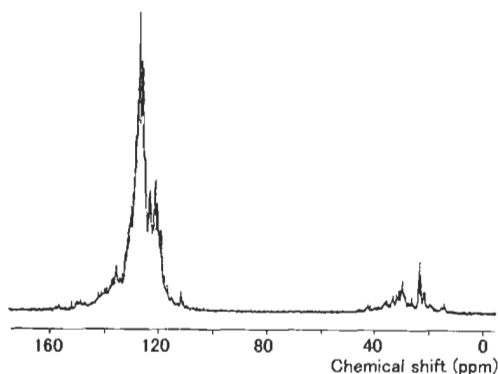


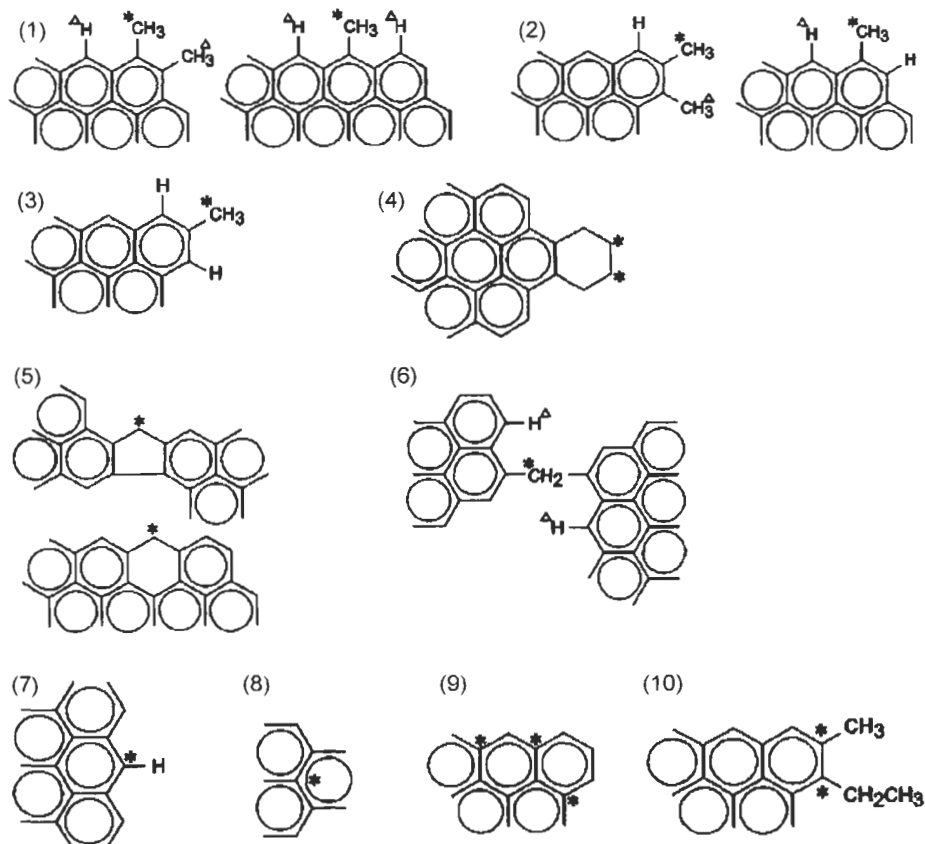
Fig. 7. ^{13}C -NMR spectrum of a coal-tar pitch.

Table 3

Assignment of ^{13}C -NMR spectra for pitch-like materials

| Chemical shift (ppm) | | Assignment |
|----------------------|-----------------------|---|
| 14–15 | (Ar)-*CH ₃ | Methyl groups suffering two steric hindrances ⁽¹⁾ |
| 18.5–20 | | Methyl groups suffering a steric hindrance ⁽²⁾ |
| 20.5–22 | | Methyl groups suffering no steric hindrances ⁽³⁾ |
| 22.5–24 | -*CH ₂ - | Naphthenes of β position ⁽⁴⁾ |
| 28–32 | | Naphthenes of α position ⁽⁵⁾ |
| 35–38 | | Bridge methylenes between two aromatic rings ⁽⁶⁾ |
| 118–129 | *Ar | (a) Tertiary aromatic carbons ⁽⁷⁾ |
| 121–125 | | (b) Inner quaternary aromatic carbons ⁽⁸⁾ |
| 129–134 | | (c) Outer quaternary aromatic carbons ⁽⁹⁾ |
| 134–146 | | (d) Aromatic carbons bonding to an aliphatic carbon ⁽¹⁰⁾ |

*: Concerned carbon. Δ : Hydrogen atoms causing steric hindrance.



4.2.2 Measurement of Solid-state Sample

A solid sample is usually measured by MAS combined with the CP (CP/MAS method). It is important to note that CP effects differ according to distances from ^1H atoms. The intensity profile of the spectrum varies greatly according to the operating time of CP (contact time). Though 2 ms is generally used as a contact time for the measurement of pitch-like materials, a quantitative analysis of the spectrum is not guaranteed. So careful attention is required when comparing samples and it is recommended to do so only between closely related pitches and their derivatives, e.g. samples prepared by different heat treatments of the same parent pitch.

As mentioned above, excessive decoupling time will burn out the decoupling coil. So the number of data points for FID has to be controlled when measuring a solid sample, because it is in proportion to the acquisition time, i.e. the decoupling period.

Solidified pitch-like material is in a glass state, not in a crystalline state, and as a result, the environments of individual molecules differ little from each other. This environment affects the chemical shift by about 6 ppm and this portion is not averaged by MAS. Thus, it is intrinsically impossible to obtain well-resolved spectra from solid pitch-like materials by the CP/MAS method (see Fig. 8 [3]).

4.2.3 Measurement of Fused State Sample and Application to Carbonaceous Mesophase

When a sample has a softening or melting point, it is possible to get a high-resolution spectrum by measuring the sample in a fused or molten state. For pitch-like materials, the best temperature for measurement is the softening point plus 100°C . A spectrum of an isotropic pitch is shown in Fig. 7. This method also allows a mesophase pitch to be studied in the liquid crystalline phase (Fig. 9 [4]). The mesophase pitch used has an anisotropic content of 100%. The mesophase pitch is mixed with a small amount of hexamethylbenzene (HMB) which has only one type of aromatic carbon having a signal at 130 ppm when in the liquid/solution phase. The sharp signal at 130 ppm is assigned to the carbon. The other signals between 100 and 140 ppm are attributed to aromatic carbon of the isotropic pitch, although these signals are not observed for the original mesophase pitch. The broad signal from 150 to 190 ppm is assigned to the

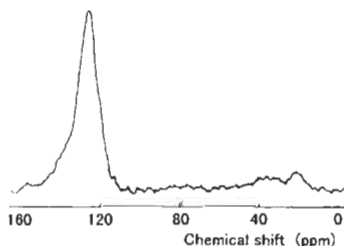


Fig. 8. CP/MAS spectrum of a coal-tar pitch.

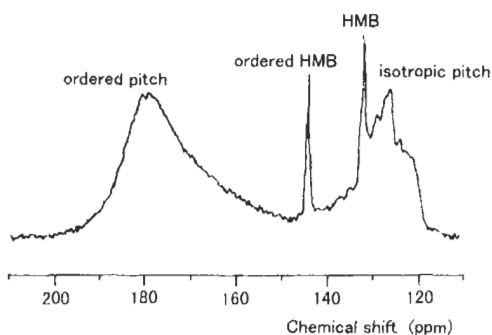


Fig. 9. ^{13}C -NMR spectrum of a HMB-including mesophase pitch in the liquid crystalline phase (HMB: Hexamethylbenzene).

mesophase pitch in the liquid crystalline phase whose constituent molecules are oriented to the magnetic field of the NMR equipment. The remaining signal at 145 ppm has to be attributed to aromatic carbon of the HMB. This means that HMB is trapped in the mesophase pitch and adopts the ordering of the mesophase pitch. Interpretations of this spectrum are as follows:

1. HMB dissolves a part of mesophase pitch and changes it to an isotropic pitch.
2. Some of HMB is trapped in a mesophase pitch and becomes ordered.

5 Solid-state ^7Li -NMR

Basically, the principle of ^7Li -NMR is the same as for the ^1H - and ^{13}C -NMR. Distinctions arise from the spin quantum number, that is, ^7Li has a spin number of 3/2, or quadrupolar moment. Here, the resonance line generally splits into three lines by the local electrical field gradient (EFG) at the nuclear site as shown in the following equation:

$$\nu_{(m \rightarrow m-1)} = \nu_0 + 1/2\nu_Q(3\cos^2\phi - 1)(m - 1/2) \quad (8)$$

where m is 3/2, 1/2 or -1/2, ν_Q is the quadrupolar coupling and ϕ is the angle between the EFG and an external magnetic field B_0 . The central peak due to the transition (1/2 \rightarrow -1/2) is not perturbed by this first order effect as seen in this equation. So investigations by ^7Li -NMR usually analyze this peak.

5.1 Measurement of Solid-state ^7Li -NMR

Chemical shifts of lithiated organic compounds are one of the smallest (ca. 10 ppm) as predicted from the periodic table. Nevertheless, Li-carbon/graphite compounds have a large range of chemical shifts due to Pauli paramagnetism, called Knight shift. Care should be taken with pulse widths to ensure that the whole spectrum is covered when studying Li-carbon/graphite compounds (see Eq. (3)).

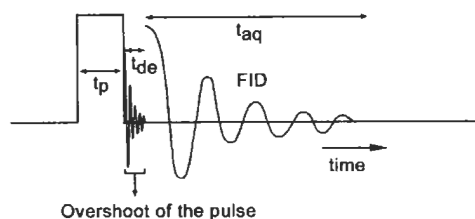


Fig. 10. Sequence of pulse-NMR measurement. t_p : pulse width, t_{de} : dead time, t_{aq} : acquisition time.

Care should also be taken with “dead time”. An irradiation pulse is not ideal, so acquisition of FID must start after the dead time to avoid the pulse influence (Fig. 10). Spin relaxation of the quadrupolar nucleus rapidly occurs through the local electrical field gradient by the quadrupolar electrical moment (self-relaxation). Too long a dead time may cut off large parts of the FID signals. Moreover, when the spectrum includes sharp signals and broad signals, then long dead times alter the relative intensity in the spectrum. The solid-state ^7Li -NMR spectra of Li-carbon/graphite compounds illustrate these aspects.

Li-carbon/graphite compounds are frequently measured without MAS because comparatively sharp signals are available and no spinning band is observed. This is acceptable in discussions of approximate chemical shifts. But, to require more detailed information then MAS should be used for the following reasons:

1. Li-carbon/graphite compounds are composed of hybrid orbitals of Li(2s) and C(2p) and this makes for anisotropy of shielding for the lithium nucleus, though it is not so large.
2. In some carbons and graphites, the lithium atom is surrounded by an anisotropic matrix. This matrix may possibly be oriented to the magnetic field in a NMR probe, then the orientation may shift the resonance frequency of the lithium nucleus somewhat.

To determine a pulse repetition period, a T_1 value of Li-carbon/graphite compound is required. Observed values for various Li-carbon/graphite compounds are listed in Table 4 [5].

Table 4

T_1 of ^7Li in various carbon materials at 77.8 MHz[5]

| Sample | Lithiation state | T_1 at 25°C (s) | T_1 at -150°C (s) |
|------------------|-------------------|-------------------|---------------------|
| Natural graphite | LiC_6 | 2.0 | 3.9 |
| | LiC_{18} | 6.9 | – |
| Carbon fiber (a) | Fully lithiated | 0.19 | 4.4 |
| Carbon fiber (b) | Fully lithiated | 0.08 | 0.71 |
| Li metal | | 0.14 | 0.30 |

Carbon fiber (a): mesophase pitch-based fiber (HTT: 1200°C).

Carbon fiber (b): isotropic pitch-based fiber (HTT: 1200°C).

5.2 Characterization of Li-carbon/Graphite Compounds

5.2.1 Defined Intercalation Compounds of Graphite

The first stage of Li-graphite intercalation shows a peak at 38–45 ppm (as referred to LiCl); the peaks at 6–13 and 38–45 ppm are observed in the second stage. On the other hand, a signal at 2–13 ppm is observed in the third or higher stages. The peaks at 38–45 ppm and 2–13 ppm are attributed to the lithium atom at the site of $\text{LiC}_{6\text{S}}$ and $\text{LiC}_{9\text{S}}$ respectively (see Fig. 11) [6,7]. The existence of two peaks in the second stage indicates that the lithium atom, at the site of 38–45 ppm, does not exchange for a lithium atom site of 2–13 ppm at room temperature. The Lorentzian shape of the two peaks suggests that lithium atoms move rapidly at room temperature. Thus, lithium atoms move only in the domains of each site. Though the rapid motion of the lithium atoms is in agreement with the behavior of the Li-ion battery, it seems curious that lithium atoms in $\text{LiC}_{6\text{S}}$ and $\text{LiC}_{9\text{S}}$ have sites in which they cannot exchange with each other despite the rapid motion of the lithium atoms (Fig. 11).

5.2.2 Graphitized Soft Carbons

A graphitizable (soft) carbon, heat treated at 2000°C, absorbs Li-ions which exhibit an NMR peak at 27 ppm. On the other hand Li-ion in the carbon heat treated at above 2400°C shows peaks at 27 and 45 ppm simultaneously. The peak at 45 ppm is assigned to a $\text{LiC}_{6\text{S}}$ site, the lithium of other peaks being trapped at sites which overlap the carbon-rings of two graphene layers stacked without regularity (Fig. 12) [8]. Again, it

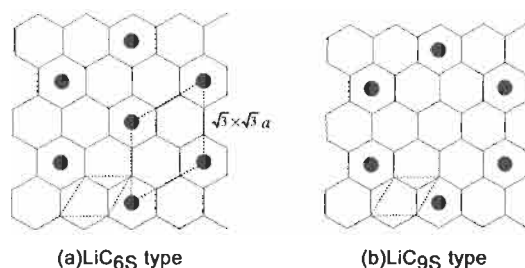


Fig. 11. Structure of Li site in Li-graphite intercalation compound [7]. (●) Li atom.

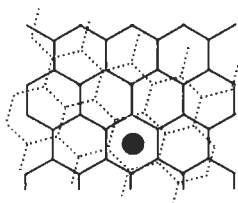


Fig. 12. Structure model for Li ion between two graphene layers stacked without regularity [7].

is worthy of note that it is impossible to transfer Li-ions between the 27 and 45 ppm sites although the ions move rapidly. Another question is why is the signal of Li-ion in Fig. 12 is observed between LiC_{65} and LiC_{95} positions. Considering the concentration of Li-ion in the graphene layers, the order of $\text{LiC}_{65} \rightarrow \text{LiC}_{95} \rightarrow \text{Li}$ in Fig. 12 seems reasonable for the ^7Li -NMR chemical shifts.

5.2.3 Hard Carbons

Hard carbons (isotropic, non-graphitizable) heat treated at 1000–1400°C also absorb Li-ions. The Li-ion in these carbons shows a broad NMR peak at 90–120 ppm (at room temperature). This peak is shifted with decreasing measurement temperature and divides into two peaks below -30°C and the chemical shifts reach 20 and 190 ppm below -100°C . Both peaks are different from the Li signals in soft carbons and graphite; the former is assigned to the lithium intercalated in the carbon though the details are not clarified, while the 190 ppm one is assigned to small clusters of lithium atoms [9]. In this case, Li-ions exchange rapidly between the two sites at room temperature.

5.2.4 Carbons Heat-treated at Low Temperature

A carbon prepared at 700°C from carbonaceous mesophase is able to store more than 650 Ah kg^{-1} , though irreversible capacity and electrical resistance are very large [10,11]. Lithium in these carbons shows the NMR signal at ca. 7 ppm and is considered that it makes a type of Li–C complex compound

In this chapter, chemical shift data of ^7Li NMR data for Li-carbon/graphite compounds are listed and current ‘best possible’ explanations are put forward. The chemical shift data of ^7Li -NMR treated in this chapter are summarized in Table 5.

Symbols Used

| | |
|---------------|---|
| B_0 : | Static magnetic field (T) |
| B_1 : | Rotational magnetic field for spin locking (Hz) |
| B_C : | Rotational magnetic field for ‘cross polarization’ (Hz) |
| B_H : | Rotational magnetic field for proton spin-locking’ (Hz) |
| C_a/C : | Ratio of aromatic carbons to the total carbons (dimensionless) |
| $[C/H]$: | Atomic number ratio of carbon to hydrogen determined by ultimate analysis (dimensionless) |
| E_{μ} : | Energy of direct dipole–dipole interaction (Hz) |
| f_a : | Coefficient to evaluate the growth of aromatic rings named aromaticity (dimensionless) |
| H : | $[H_a + H_\alpha + H_\beta + H_\gamma]$ (dimensionless) |
| H_β/H : | $[H_\beta + H_\gamma]$ ratio to total hydrogen determined by a ^1H -NMR spectrum (dimensionless) |

Table 5

Chemical shift of ^7Li NMR of Li-graphite/carbon alloys [7]

| Sample | Chemical shift (ppm) | Possible assignment | Note |
|--|-----------------------------------|--|---|
| Natural graphite HOPG | 6–13 | $\text{LiC}_{9\text{S}}^{(1)}$ | 2nd stage. Non-exchangeable for ca. 40 ppm peak |
| | 38–45 | $\text{LiC}_{6\text{S}}^{(1)}$ | 1st & 2nd stage. Non-exchangeable for ca. 10 ppm peak |
| Graphitized soft carbon ⁽²⁾ | 27 | | Non-exchangeable for 45 ppm peak |
| | 45 | A kind of $\text{LiC}_{6\text{S}}^{(1)}$ | Non-exchangeable for 27 ppm peak |
| Carbon ⁽³⁾ | 50–120 (r.t.) | – | Average of 20 and 190 ppm peaks |
| | 20 ($\leq -110^\circ\text{C}$) | Between | Exchangeable for 190 ppm peak at r.t. |
| | 190 ($\leq -110^\circ\text{C}$) | Li cluster | Exchangeable for 20 ppm peak at r.t. |
| Low HT T carbon ⁽⁴⁾ | ca. 7 | A kind of complex compound | |
| Li metal | 261–262 | | |
| $\text{LiCl}^{(5)}$ | 0 | | |

(1) See Fig. 11. (2) $\text{HTT} \leq 2000^\circ\text{C}$. (3) $1000^\circ\text{C} \leq \text{HTT} \leq 1400^\circ\text{C}$. (4) HTT : ca. 700°C . (5) Chemical shift standard.

H_α : Hydrogen bonding to an aliphatic carbon of α position from an aromatic carbon (dimensionless)

H_α/H : Ratio of H_α to total hydrogen determined by a ^1H -NMR spectrum (dimensionless)

H_β : Hydrogen bonding to an aliphatic carbon β position from an aromatic carbon (dimensionless)

H_γ : Hydrogen bonding to an aliphatic carbon more than β position from an aromatic carbon (dimensionless)

m : Eigenvalue of a nuclear spin (dimensionless)

M_0 : Equilibrium macroscopic magnetization of a spin system in (T)

M_z : Z component of macroscopic magnetization of a spin system in the presence of B_0 (T)

r : Distance between two magnetic dipoles (m)

Sw : Spectrum width (Hz)

T_1 : Longitudinal relaxation time (s)

T_2 : Transverse relaxation time (s)

t_p : Pulse width (s)

w : Line width at half height of a NMR spectrum (Hz)

γ_C : Nuclear magnetogyric ratio of carbon nucleus (Hz)

γ_H : Nuclear magnetogyric ratio of proton (Hz)

γ_N : Nuclear magnetogyric ratio of spin N (Hz)

θ : Angle of Larmor precession (dimensionless)

- μ_α : Dipole moment of spin α ($A\ m^2$)
 ν_0 : Unperturbed transition energy between spin states in a static magnetic field B_0 (Hz)
 ν_1 : Larmor frequency in a rotational magnetic field B_1 (Hz)
 $\nu_{(m \rightarrow m-1)}$: Transition energy between spin states m and $m - 1$ (Hz)
 ν_N : Larmor frequency of spin N in a static magnetic field B_0 (Hz)
 ν_Q : Quadrupolar coupling energy (Hz)
 ϕ : Angle between a local electrical field gradient and an external static magnetic field B_0 (dimensionless)

References

1. J.K. Brown, W.R. Ladner and N. Sheppard, A study of the hydrogen distribution in coal-like materials by high-resolution nuclear magnetic resonance spectroscopy, I: The measurement and interpretation of the spectra. *Fuel*, 39: 79–86, 1960; J.K. Brown and W.R. Ladner, A study of the hydrogen distribution in coal-like materials by high-resolution nuclear magnetic resonance spectroscopy, II: A comparison with infra-red measurement and the conversion to carbon. *Fuel*, 39: 87–96, 1960.
2. T. Nishizawa and M. Sakata, High temperature ^{13}C n.m.r. measurements on fused pitches and a carbonaceous mesophase. *Fuel*, 70: 124–127, 1991.
3. T. Nishizawa, Basics of nuclear magnetic resonance (NMR) and characterization of pitch. *Tanso*, 187: 109–115, 1999.
4. T. Nishizawa and M. Sakata, Fused state ^{13}C -NMR study on molecular orientation in a carbonaceous mesophase. *Carbon*, 30: 147–152, 1992.
5. K. Tatusmi, Solid state 7Li nuclear magnetic resonance analysis for lithium inserted into carbon materials. *Tanso*, 186: 54–57, 1999.
6. D. Billaud, E. McRae, J.F. Mareche and A. Herold, *Synth. Met.*, 3: 21–26, 1981).
7. P. Pjluger, V. Geiser, S. Stolz and H.J. Guntherodt, *Synth. Met.*, 3: 27, 1981.
8. K. Tatsumi, In: Carbon Society of Japan (Eds.), *New Experimental Techniques on Carbon Material*, Chapter 11. Realize Inc., 2001.
9. S. Yamazaki, T. Hashimoto, T. Iriyama, Y. Mori, H. Siroki and N. Tamura, *Proc. Soc. Solid-State NMR Mat.*, 20: 39–41, 1996.
10. A. Mabuchi, K. Tokumitsu, H. Fujimoto and T. Kasuh, Charge-discharge characteristics of the mesocarbon microbeads heat-treated at different temperatures. *J. Electrochem. Soc.*, 142: 1041–1046, 1995.
11. M. Hara, Asatoh, N. Takami and T. Ohsaki, Structural and electrochemical properties of lithiated polymerized aromatics. Anodes for lithium-ion cells. *J. Phys. Chem.*, 99: 16338–16343, 1995.

Chapter 20

Gas Adsorption

Yohko Hanzawa and Katsumi Kaneko

Department of Chemistry, Faculty of Science, Chiba University, Chiba 263-8522, Japan

Abstract: The IUPAC classification of pores such as micropores, mesopores, and macropores has particular relevance to carbon materials. Definitions of porosity are given. Volumetric and gravimetric methods of determination of adsorption isotherms are compared and recommended experimental procedures are described. The relationship between the adsorption isotherm and the pore structure of carbon materials is interpreted with direct relevance to adsorption mechanisms. Experimental adsorption isotherms of an activated carbon, a carbon aerogel, and a carbon black are used as examples.

Keywords: Adsorption isotherm, Porosity, Micropore filling, Adsorption hysteresis, Supercritical gas.

1 Adsorption, Absorption, Occlusion and Storage

Recent research into the storage of, for example, methane and hydrogen [1,2] by carbons uses terminologies which may cause confusion in terms of the nature of gas–solid interactions. Traditionally, it is believed that the concept of “absorption” includes the concept of “adsorption”. The terms “storage” and “occlusion” have been used to describe the strong interactions of gases with solids such as in the H₂-Pd system. On the other hand, the term “storage” has been widely used in practical applications to describe extents (amounts) of gases (usually) taken up by a solid. In this chapter, the use of only four terminologies (definitions) namely (i) physical adsorption, (ii) chemisorption, (iii) absorption, and (iv) occlusion are recommended [3]. The term “storage” may be used within a wider concept which includes these four terminologies. The criteria for the four terminologies are based on structural changes to an adsorbate and/or an adsorbent upon an interaction. There are two possible structural changes for an adsorbate molecule and two for the adsorbent solid, the total number of possible structural changes therefore being four. When a molecule interacts weakly with the solid surface through dispersion interactions, as in physical adsorption, then structures of the molecule and solid do not change. On the other hand, when the interaction of an admolecule with a solid surface involves charge

transfer or electron transfer, then the structure of the surface molecules changes. Thus, the adsorbate molecule changes its structure upon “chemisorption” and the bulk structure of the adsorbent solid remains unchanged. When the solid structure changes during the interaction with a gas, and the gas remains unchanged, this is called “absorption”. For the case of “occlusion”, both the structure of a molecule and a solid vary upon their interaction. As a result, these four types of the gas-solid interactions describe nicely these concepts of physical adsorption, chemisorption, absorption, and occlusion. If the term “storage” is used as a wider concept which can include these four terminologies, then there is no confusion about the nature of the gas-solid interactions. This chapter describes only physical adsorption processes on carbons, but not overlooking that chemisorption and occlusion processes are important to carbon materials.

2 Classification of Pores and Porosity

Carbon materials are classified into non-porous and porous carbons. Carbon black, glassy carbon, and graphite are representatives of non-porous carbon. In particular, the basal plane of graphite has a uniform structure and as a result the graphite surface is used as an ideal (perfect) flat surface for considerations of molecular adsorption processes. Activated carbon is a representative porous carbon. The surface structure of carbons is a key factor for interfacial characterizations. As an extreme case, flat surfaces can be regarded as the wall of a pore that is infinitely wide compared with the sizes of molecules, other pores being classified according to the IUPAC recommendations [4]. Here, pores are classified according to the pore width w (the shortest distance parameter of three-dimensional geometry). The pores are classified into three categories: macropores ($w > 50$ nm), mesopores (2 nm $< w < 50$ nm), and micropores ($w < 2$ nm). Consequently, a flat surface can be seen as a pore of infinite width. The term “nanopore” which is also used is not recommended by IUPAC [4]. However, if a nanopore is defined as a pore whose width is in the range of 1.5 to 5 nm, then it is convenient to use this definition because of the existence of some inherent special adsorption phenomena as revealed in recent progress in adsorption technology and science. The three classifications of micropores, mesopores, and macropores can be further understood from the way they adsorb nitrogen at 77 K. Nitrogen molecules are adsorbed by different mechanisms, namely by multilayer adsorption, capillary condensation, and micropore filling for the macropores, mesopores, and micropores, respectively. Thus, these three categories describe mechanisms of adsorption of nitrogen at 77 K. The critical widths of 50 nm and 2 nm are chosen for both empirical and physical reasons. The pore width of 50 nm corresponds to the relative pressure P/P_0 of 0.96 of the nitrogen adsorption isotherm at 77 K, for the Kelvin equation, as given by Eq. (3). Experimental studies of the adsorption isotherm at values of P/P_0 above 0.96 are difficult because 50 nm is the upper limit of pore width which can be evaluated from the nitrogen isotherm. The critical width of 2 nm corresponds to $P/P_0 = 0.39$, for the Kelvin equation, where unstable behavior of

the adsorbed layer of nitrogen is observed [5]. For pores having widths smaller than 2 nm capillary condensation theory cannot be applied. Accordingly, the mesopores are those pores to which the Kelvin equation can be realistically applied. Micropores have two subgroups, namely supermicropores ($0.7 \text{ nm} < w < 2 \text{ nm}$), and ultramicropores ($w < 0.7 \text{ nm}$). The statistical thickness of an adsorbed layer of nitrogen on a solid surface is 0.354 nm. The maximum size of ultramicropores corresponds to a layer of adsorbed nitrogen two molecules thick. Although the ultramicropores are very important in molecular sieving effects, evaluation of their ultramicroporosity is very difficult due to blocking processes which occur near to the pore entrance.

Pores which open up to the external surface are termed open pores and are accessible to molecules or ions in the surroundings, as described above. Pore structure in a carbon depends on many factors including the structure of the parent materials, the conditions of the carbonization and activation processes when insufficient carbonization and activation leave closed pores that cannot communicate with the surroundings. Also, excessive heat-treatment often causes collapse of open pores to produce closed pores. The closed pore is not associated with adsorption or permeability of molecules, but does influence the mechanical properties of carbons. As to a classification of pores based on considerations of accessibility to surroundings, the use of open and closed porosity is not enough to describe porosity in carbon. An open pore whose width is smaller in size than that of a probe molecular size is regarded as a closed pore. Nitrogen molecules are used as a molecular probe. Closed porosity and chemically closed pores are termed "latent" pores. Ruike et al. [6] proposed for the characterization of porosity the following methods: (i) density, (ii) nitrogen adsorption, (iii) water adsorption, and (iv) SAXS measurements, these methods determining volumes of microporosity and the size and volume of the latent pores.

The concept of porosity is directly associated with pores. The porosity is defined as the ratio of the pore volume to the total solid volume. A density value is a function of the method used to measure the density. Three density values are useful: (i) true density ρ_t , (ii) apparent density ρ_{ap} , and (iii) the He-replacement density ρ_{He} . These are used to determine the open pore porosity $\epsilon_{op} = (1 - \rho_{ap}/\rho_{He})$ and closed pore porosity $\epsilon_{cp} = (\rho_{ap} (1/\rho_{He} - 1/\rho_t))$. Nevertheless, determination of such densities is not easy, experimentally. Although a true density value is given by the unit cell structure from X-ray diffraction studies for well-crystalline materials, the true density of less-crystalline carbon materials such as activated carbon cannot be determined by such X-ray diffraction methods. Murata and Kaneko [7] proposed an accurate method for the determination of ρ_{He} of activated carbon based on high-pressure helium buoyancy measurements.

3 Selection of an Adsorbate Molecule

Molecular adsorption in pores depends on the equilibrium established between the interaction of a molecule with the pore wall and intermolecular interactions. The

selection of the probe molecule and adsorption conditions is important to elucidate the structure of porosity. The probe molecule must be of sufficiently small size, adequate stability, facilitate convenient adsorption measurements, and have applicability to an established adsorption theory. The adsorption of nitrogen at 77 K, with typical physical adsorption processes, is the most current method for the characterization of porosity. This is because, experimentally, it is very convenient to carry out and analytical theories are available. The effective size of the nitrogen molecule on a solid surface is 0.354 nm, and hence nitrogen adsorption describes the sub-nanostructure of solid surfaces without destruction of that surface. However, the nitrogen molecule is a diatomic molecule and its shape is not that of a sphere. The nitrogen molecule has a quadrupole moment which determines molecular orientation on the wall of the pore. As a result, nitrogen molecules are strongly adsorbed at the pore mouth so blocking further adsorption. Hence, nitrogen adsorption at 77 K is not appropriate for the characterization of ultramicropores. Recently, it has been shown that nitrogen adsorption at ambient temperatures is very effective to determine pore widths at the pore mouth for molecular sieve carbons [8].

Other probe molecules used in the analyses of carbon surfaces include H_2O , Ar, CO_2 and He. The molecular shape of the argon molecule is spherical and its quadrupole moment is zero. Also, its adsorption isotherm can be measured at 77 K, the temperature of liquid nitrogen. Of course, the measurement of the argon adsorption isotherm at its boiling point (87 K) is possible, but is much less convenient to do. Argon is used for characterization of micropores of activated carbons. As the quadrupole moment of carbon dioxide is greater than that of nitrogen, carbon dioxide is adsorbed in micropores at room temperature, and has been used extensively to characterize activated carbon. Rodriguez-Reinoso et al. [9] demonstrated the suitability of adsorption of carbon dioxide. H_2O is adsorbed only in micropores of carbon. Hanzawa and Kaneko [10] examined H_2O adsorption on an activated carbon aerogel possessing both micro- and meso-porosities. Extents of adsorbed H_2O correspond to micropore volumes of pores with widths of 0.7 nm. H_2O vapor is not adsorbed below $P/P_0 = 0.3$ and extents of adsorption rapidly increase above $P/P_0 = 0.5$. However, the mechanism of adsorption of water in carbon micropores may be quite different from that of nitrogen. Müller et al. [11] and McCallum et al. [12] used the GCMC approach to elucidate the mechanism, and Kaneko et al. [13,14] used *in situ* X-ray diffraction and *in situ* SAXS [15] as well as heat of adsorption measurements [16]. These approaches confirmed the cluster-promoted adsorption mechanism as originally proposed by Dubinin et al. [17]. As an H_2O molecule can be effectively adsorbed in small ultramicropores, the adsorption of H_2O is applied to characterizations of molecular sieve carbons [8]. Extents of adsorption of H_2O below $P/P_0 = 0.1$ are sensitive to concentrations of functional groups on surfaces, and hence this provides information on hydrophobicity of surfaces. For example, H_2O vapor is not adsorbed on fluorinated ACF even close to $P/P_0 = 1$ [18]. Extents of irreversible H_2O adsorption correlate with extents of nitrogen adsorption controlled by the chemical vapor deposition of pyridine [19]. Thus, H_2O adsorption can determine the concentration

Table 1

Probe molecules and adsorption conditions

| | He | H ₂ O | N ₂ | Ar | CO ₂ |
|-----------------------------------|-------|------------------|----------------|-------|-----------------|
| Molecular area (nm ²) | 0.117 | 0.125 | 0.162 | 0.138 | 0.142–0.244 |
| Molecular diameter (nm) | 0.26 | 0.27 | 0.37 | 0.34 | 0.39–0.45 |
| Adsorption temperature (K) | 4.2 | room temp. | 77 | 87 | room temp. |

and state of hydrophilic sites on activated carbons. Kuwabara et al. [20] and Setoyama et al. [21] developed a new porosimeter using helium at 4.2 K. Adsorption of helium at 4.2 K is effective to evaluate ultramicroporosity in activated carbons. A comparative study of adsorption of helium at 4.2 K and of adsorption of nitrogen at 77 K provides a detailed description of micropore structures. However, a comprehensive analytical theory for adsorption of helium still awaits development. Table 1 summarizes properties of these probe molecules and adsorption conditions.

Organic molecules are also used to study surface structures of non-porous carbon materials as well as pore-wall structures of activated carbon. A surface fractal analysis using different organic vapor molecules leads to the quantitative evaluation of surface roughness [22,23]. The surface fractal dimension D_s is given by Eq. (1) [22].

$$n_m = k \sigma^{-D_s/2} \quad (1)$$

Here n_m is the monolayer capacity, σ the cross-sectional area of an adsorbate molecule, and k is a constant. Values of σ for non-porous carbons are determined by the BET method. The BET method cannot be applied to activated carbon, but the SPE method is available, as described later. In order to have the fractal dimension D_s , adsorption isotherms of adsorbates, having different values of σ , need to be measured. Sato et al. [23,24] showed that the fractal dimension of the micropore walls of an activated carbon fiber (ACF) is close to 3. This decreases to about 2 following high temperature treatment in argon for 1 h, as shown in Table 2. For activated carbons, values of D_s can be obtained from a single adsorption isotherm using the Avnir and Jaroniec equation (Eq. (2)) [25] through the Dubinin–Stoeckli relationship:

$$\phi = k' [\ln(P_0/P)]^{D_s-3} \quad 2 < D_s < 3 \quad (2)$$

Here ϕ is the fractional filling at a relative pressure of P/P_0 and k' is a constant. However, the appropriate fractional filling range must be used to determine D_s [26].

Table 2

Change in surface fractal dimension D_s of ACF with high temperature treatment

| Treatment temperature (K) | None | 1472 | 1673 |
|---------------------------|------|------|------|
| D_s | 2.7 | 2.6 | 2.3 |

A comparative study using several organic vapor molecules can determine the pore size distribution, as shown by Carrot et al. [27].

4 Surface Structure and the Adsorption Isotherm

4.1 Determination of the Adsorption Isotherm

An adsorption isotherm describes amounts adsorbed as a function of equilibrium gas pressure, at constant temperature. The amount of adsorption can be determined either gravimetrically or volumetrically after initially degassing the carbon at temperatures above 373 K. The degassing temperature is changed according to the pore structure of carbon. A degassing temperature above 523 K is necessary for carbons having ultramicropores. When using commercial adsorption equipment, degassing at 373 K is not enough due to slow evacuation rates, although a lower degassing temperature is preferable to preserve pore structure. The equilibration time must be measured in advance. Commercial adsorption equipment is based on the volumetric method, this having several advantages such as high sensitivity with high performance at low cost. New volumetric equipment uses highly sensitive pressure gauges to measure pressures from as low as $P/P_0 = 10^{-6}$, these being necessary for analyses of microporosity. However, dead volume corrections, the maintenance of constant levels of liquid nitrogen in the bath and high vacuums are essential to obtain reliable data. The gravimetric method must incorporate a balance of high sensitivity such as a quartz spring, an electronic balance, or a magnetic suspension balance in association with high sensitive pressure gauges. The gravimetric method can determine, independently, both the amounts adsorbed and equilibrium adsorbate pressures. Weight changes must be corrected for buoyancy effects. A further difficulty is that of making sure that the temperature of the adsorbent is that of the liquid nitrogen. The fact that the carbon sample is in a vacuum associated with low thermal conductivity in the very low pressure range means that the temperature of the sample may not coincide with the bath temperature. The adsorption temperature must be checked prior to any adsorption measurement.

The amount of adsorption W_a depends on the gas equilibrium pressure P , the adsorption temperature T , the adsorptive (gas) selected, and the amount of the adsorbent in the system. Parameters other than P are pre-determined when measuring an adsorption isotherm in which W_a is expressed as a function of P . Physical adsorption is the dominant process for a gas (namely vapor), of saturated vapor pressure P_0 , below its critical temperature. The pressure of the adsorbate is usually expressed as the relative pressure P/P_0 . Amounts adsorbed, W_a , may be expressed by the mass of gas (usually mg) or the volume reduced to STP (usually $\text{cm}^3(\text{STP})$) per unit mass of the adsorbent (usually g). The W_a vs. P or W_a vs. P/P_0 is called the adsorption isotherm. IUPAC recommended the following six types of the adsorption isotherms [4] instead of the BDDT five groups, as shown in Fig. 1.

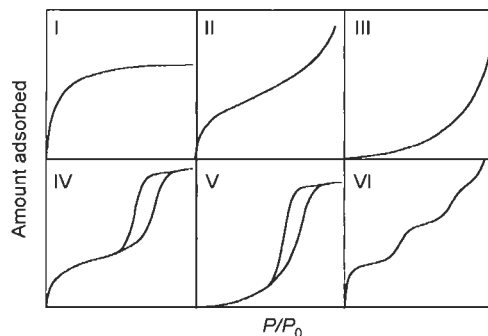


Fig. 1. The IUPAC classification of adsorption isotherms.

4.2 Type I Adsorption Isotherm

The type I isotherm corresponds to the so-called Langmuir isotherm. In physical adsorption, the type I isotherm indicates the presence of micropores where adsorbate molecules are adsorbed by micropore filling. Activated carbons have this type of adsorption isotherm of nitrogen at 77 K. Figure 2 shows high-resolution adsorption isotherms of nitrogen at 77 K for pitch-based activated carbon fibers (ACFs) as a function of average pore widths, as evaluated by the SPE-method [28,29]. Here, the abscissa of Fig. 2a is expressed by P/P_0 , whereas that of Fig. 2b is expressed by the logarithm of P/P_0 . The smaller the pore width of ACF the larger is the ratio of amounts adsorbed (below $P/P_0 = 10^{-3}$) to the total adsorption amounts. Although the W_a vs. P/P_0 graph shows no obvious differences at low values of P/P_0 , adsorption isotherms expressed using $\log(P/P_0)$ show clear differences in adsorption behavior. Atkinson et al. [28] introduced the α_s -plot idea to analyze adsorption isotherms, proposing a two-stage mechanism of primary and cooperative (or secondary) filling. However, they did not analyze, in sufficient detail, adsorption isotherms below $\alpha_s = 0.5$, which is dominantly important where micropore filling is concerned. No clear physical model for the two-stage mechanism was given. Setoyama et al. [29] and Kaneko et al. [30] introduced the concept of the high resolution α_s -plot over wide α_s ranges from 0.01 to 2.4 using adsorption isotherms in the region $P/P_0 = 10^{-5}$ – 10^{-6} . They showed the presence of two upward deviations from the linear α_s -plot below $\alpha_s = 1.0$. The upward deviations from the linearity below and above $\alpha_s = 0.5$ are called filling and cooperative swings, respectively. The filling swing is ascribed to an enhanced monolayer adsorption on micropore walls and the cooperative swing comes from filling the residual space between the monolayer on both micropore walls. This mechanism was supported by GCMC simulation studies [31].

Kuwabara et al. [20] and Setoyama et al. [21] studied micropore filling by He, SO_2 [32], and H_2O [33] with high-resolution adsorption, heat of adsorption, *in situ* X-ray diffraction [13], and *in situ* small angle X-ray scattering [15]. On the other hand, Seaton et al. [34], Nicholson [35], Bojan and Steele [36], Neimark et al. [37], and

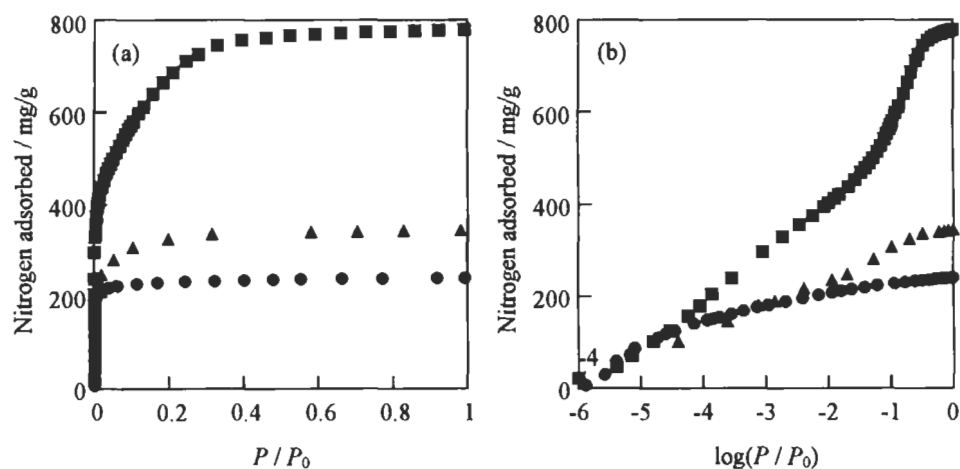


Fig. 2. The adsorption isotherms of N_2 on pitch-based activated carbon fibers having different pore widths at 77 K. Average pore width ± 0.1 nm: (●) 0.7, (▲) 0.9, (■) 1.1.

Gubbins et al. [38,39] studied micropore filling with sophisticated molecular simulations in order to model mechanisms of adsorption.

4.3 Type II and III Adsorption Isotherms

The type II isotherm is the most familiar of experimental isotherms. The multi-layer adsorption theory of Brunauer, Emmett, and Teller [40] was originally developed to explain the type-II isotherm. Hence, this isotherm is indicative of the multi-layer adsorption process, suggesting the presence of non-porous or macroporous surfaces. Non-porous carbon black has a nitrogen adsorption isotherm representative of type II isotherms, and this is used as the “standard adsorption isotherm” for comparison plots. Although the adsorption isotherm near $P/P_0 = 1$ has important information about macropores, such an analysis is not practical for accurate measurements. Figure 3 shows the nitrogen adsorption isotherm of the non-porous carbon black, and is type II. The type III isotherm originates with non-porous or macroporous surfaces which interact very weakly with adsorbate molecules. The adsorption isotherm of sulfur dioxide on non-porous carbon black is of type III [41].

4.4 Type IV Adsorption Isotherm

Classical type IV isotherms contain information about the mesopore structure of carbons making use of its hysteresis loop where there is non-overlapping of the adsorption and desorption branches of the isotherm. The adsorbate is adsorbed on the mesopore wall by a multilayer adsorption process in the low-pressure range and, later, vapor is condensed into the mesopore space at saturated vapor pressures just

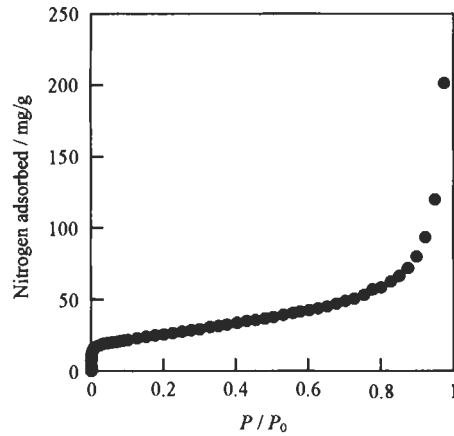


Fig. 3. The adsorption isotherms of N_2 on nonporous carbon black.

less than P_0 . This is so-called capillary condensation. Capillary condensation is explained by the Kelvin equation given by Eq. (3):

$$\ln(P/P_0) = -(2 \gamma V_m \cos\theta)/(r_m RT) \quad (3)$$

Here, the mean radius r_m of curvature of the meniscus of the condensate in pores is associated with the vapor pressure P of the condensate, γ and V_m are the surface tension and molar volume of the condensate, respectively, and θ is the contact angle (believed to be nearly zero). As P is smaller than P_0 , vapors condense in mesopores below P_0 . The Kelvin equation determines the condensation (P_c) and evaporation (P_e) pressures which are governed by r_m . When P_c and P_e are different from each other due to the different r_m values for the meniscus on condensation and evaporation, adsorption and desorption branches do not overlap so giving to the hysteresis loop. This classical capillary condensation theory predicts that an isotherm of nitrogen adsorption in cylindrical mesopores, open at both ends, will have a distinct adsorption hysteresis described as the IUPAC H1 [4]. Recently, mesoporous silica, having regular cylindrical pores, was synthesized by two research groups using different experimental methods [42,43]. Many physical adsorption studies on the regular mesoporous silica of MCM41 and FSM have been undertaken [44–52], showing the dependence of the hysteresis loop on pore width and the adsorbate molecule used. Although the Kelvin equation takes into account molecule-surface interactions with the macroscopic concept of the contact angle, a more microscopic introduction of a molecule with the mesopore wall should be included for the nanopores including larger micropores and small mesopores [51,52]. The evaluation of the pore size distribution in the nanopore range should be further improved for activated carbons.

Carbon aerogels made from the agglomerates of uniform carbon spheres have a significant content of uniform mesopores and have nitrogen adsorption isotherms of

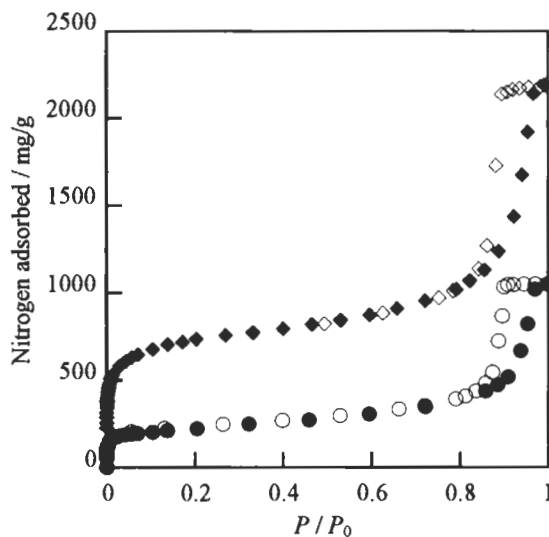


Fig. 4. The adsorption isotherms of N_2 on carbon aerogel samples at 77 K. (\bullet , \circ): carbon aerogel; (\blacklozenge , \diamond) activated carbon aerogel. Solid and open symbols denote adsorption and desorption branches, respectively.

type IV-H1, as shown in Fig. 4. The adsorption and desorption branches of the adsorption hysteresis are very steep. When a carbon aerogel is activated, the adsorption isotherm has a rectangular increase near $P/P_0 = 0$ due to the presence of micropores. The H1 type adsorption hysteresis is explained by the agglomerate structure of uniform spheres using classical Kelvin theory.

4.5 Type V Adsorption Isotherm

The type V isotherm is close to the type IV isotherm but is associated with weak molecule–solid surface interactions. Hence, almost no initial uptake is observed. The H_2O adsorption isotherm on activated carbon, with few surface functional groups, belongs to this type. Figure 5 shows H_2O adsorption isotherms of pitch-based ACFs of $w = 1.1$ nm at 303 K. The adsorption uptake at the low P/P_0 region is zero, indicating that surface functional groups are few and basically this ACF shows a hydrophobic nature. The adsorption isotherm has a steep rise at a medium P/P_0 and a clear adsorption hysteresis. The adsorption hysteresis depends on the pore width; the larger the pore width, the more marked the adsorption hysteresis loop. With increasing P/P_0 for an ACF, treated at 1273 K in hydrogen to remove surface functional groups according to a previous XPS study, adsorption shifts to higher values, but still with a noticeable hysteresis. The detailed adsorption mechanism of water on activated carbon is not elucidated sufficiently. There still remains a question of how water molecules are adsorbed into hydrophobic carbon micropores. It is well established that water molecules form dimers or clusters even in the gas phase. In

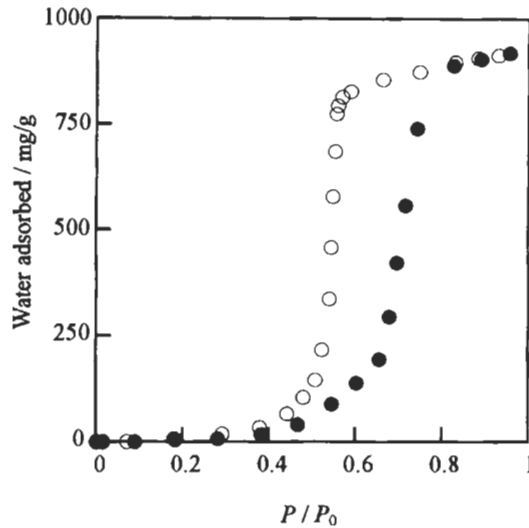


Fig. 5. The adsorption isotherms of H_2O on pitch-based activated carbon fiber of average pore width = 1.1 ± 0.1 nm at 303 K. Open and solid symbols denote adsorption and desorption branches, respectively.

micropores of activated carbon, high concentrations of water clusters such as the pentamer (H_2O)₅ or hexamer (H_2O)₆, whose size is about 0.5–0.6 nm, must be formed due to the compressed conditions [53]. Water molecules are hydrogen-bonded with each other in the cluster and thereby the electrostatic charge of the water molecule should be more compensated, inducing a strong van der Waals attractive interaction with the graphitic micropore-walls. For a single water molecule, the interaction is very weak, but the clusters in which point charges are used for the hydrogen bonding formation, have a deeper potential well through the dispersion interactions. Cluster filling for the micropore geometry has a deeper potential well. This mechanism needs further study. The adsorption hysteresis of the water adsorption isotherm is not caused by ordinary capillary condensation [10]. Water molecules are not adsorbed in mesopores, but in micropores. Iiyama et al. [15] confirmed the existence of different physical processes for the adsorption and desorption branches of the adsorption hysteresis loop with *in situ* SAXS, so supporting the above model.

The type VI isotherm is a stepped adsorption isotherm which comes from phase transitions of the adsorbed molecular layer or adsorption on the different faces of crystalline solids.

4.6 Adsorption Isotherm for a Supercritical Gas

The above-mentioned adsorption isotherms are obtained for vapors. If a supercritical gas is used as an adsorbate then the saturated vapor pressure P_0 is not defined and the relative pressure P/P_0 is not used for the adsorption isotherm. Many adsorption

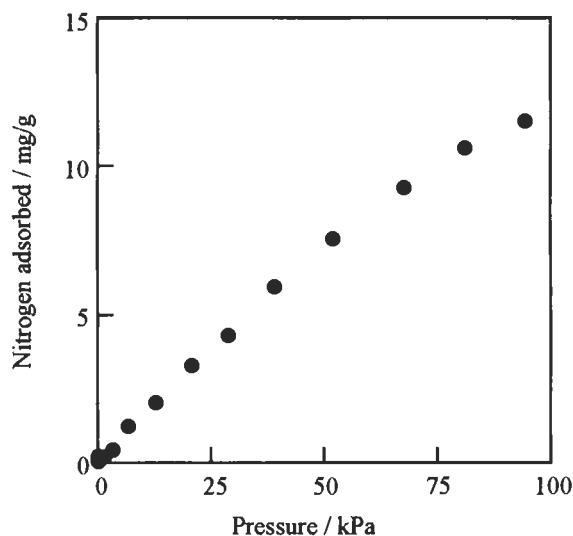


Fig. 6. Adsorption isotherm of supercritical N_2 on molecular sieve carbon at 303 K.

isotherms of supercritical gases on activated carbon belong to the Henry's Law or Langmuir type. For example, the nitrogen adsorption isotherm for a molecular sieve carbon, at 303 K, is of the Henry's Law type, as shown in Fig. 6. The amount of adsorption increases almost linearly with increasing nitrogen pressure. Although molecular sieve carbons have ultramicropores of $w = 0.6$ nm, the interaction potential of a nitrogen molecule with the pore is not strong enough to give a type I isotherm at 303 K. As supercritical gas adsorption begins with the narrowest of the micropores of activated carbon, the supercritical gas adsorption isotherm is helpful to determine the pore-mouth structure of micropores and this has relevance to the nitrogen adsorption isotherm at 77 K [8,54,55].

When there is a need to measure significant amounts of a supercritical gas, a special adsorption apparatus is needed capable of working at high pressures of up to 10–15 MPa. As the density of the bulk gas phase becomes comparable to the adsorbed density, then amounts of surface excess adsorption become smaller. Many fundamental issues still remain to be studied in the high-pressure adsorption of supercritical gases, although many researchers are now working in this area [56–60].

Adsorption isotherms must be analyzed using an appropriate theory. As to the analysis of micropores, there are progressive studies using molecular simulation and density functional theories. A need still exists to choose carefully the appropriate analytical theory for each system [37,38,61–63]. Although the Dubinin–Radushkevich analysis has been widely applied to analyses of pore structures of carbons, the recent grand canonical Monte Carlo simulation shows the limitation of the application. Therefore, the absolute pore size distribution for micropores still remains to be determined when using the gas adsorption technique.

References

1. V.C. Menon and S. Komarneni, Porous adsorbents for vehicular natural gas storage: a review. *J. Porous Mater.*, 5: 43–58, 1998.
2. M.S. Dresselhaus, K.A. Williams and P.C. Eklund, Hydrogen Adsorption in Carbon Materials. *MRS Bull.*, 11: 45–50, 1999.
3. K. Kaneko. Carbon, in preparation.
4. K.S.W. Sing, D.H. Everett, R.A.W. Haul, L. Moscou, R.A. Pierotti, J. Rouquerol and T. Siemieniewska, Reporting physisorption data for gas/solid systems with special reference to the determination of surface area and porosity. *Pure Appl. Chem.*, 57: 603–619, 1985.
5. S.J. Gregg and K.S.W. Sing, In: *Adsorption, Surface Area and Porosity*, pp. 154, Academic Press, London, 1982.
6. M. Ruike, T. Kasu, N. Setoyama and K. Kaneko, Inaccessible pore characterization of less-crystalline microporous solids. *J. Phys. Chem.*, 98: 9594–9600, 1994.
7. K. Murata and K. Kaneko, Nano-range interfacial layer upon high-pressure adsorption of supercritical gases. *Chem. Phys. Lett.*, 321: 342–348, 2000.
8. T. Suzuki, R. Kobori and K. Kaneko, Grand canonical Monte Carlo simulation-assisted pore-width determination of molecular sieve carbons by use of ambient temperature N₂ adsorption. *Carbon*, 38: 630–633, 2000.
9. F. Rodriguez-Reinoso and A. Linares-Solano, Microporous structure of activated carbons as revealed by adsorption methods. In: P.A. Thrower (ed.), *Chemistry and Physics of Carbon*, Vol. 21, pp. 1–146. Marcel Dekker, New York, 1989.
10. Y. Hanzawa and K. Kaneko, Activated carbon aerogels. *Langmuir*, 25: 6167–6169, 1996.
11. E.A. Müller, L.F. Rull, L.F. Vega, and K.E. Gubbins, Adsorption of water on activated carbons: a molecular simulation study. *J. Phys. Chem.*, 100: 1189–1196, 1996.
12. C.L. McCallum, T.J. Bandosz, S.C. McGrother, E.A. Müller and K.E. Gubbins, Molecular model for adsorption of water on activated carbon: comparison of simulation and experiment. *Langmuir*, 15: 533–544, 1999.
13. T. Iiyama, K. Nishikawa, T. Otowa and K. Kaneko, An ordered water molecular assembly in a slit-shaped carbon nanospace. *J. Phys. Chem.*, 99: 10075–10076, 1995.
14. T. Iiyama, K. Nishikawa, T. Suzuki and K. Kaneko, Study of the structure of a water molecular assembly in a hydrophobic nanospace at low temperature with *in situ* X-ray diffraction. *Chem. Phys. Lett.*, 274: 152–158, 1997.
15. T. Iiyama, M. Ruike and K. Kaneko, Structural mechanism of water adsorption in hydrophobic micropores from *in situ* small angle X-ray scattering. *Chem. Phys. Lett.*, 331: 359–364, 2001.
16. T. Kimura, Y. Hattori, T. Suzuki and K. Kaneko, Adsorption mechanism of water on activated carbon. *J. Phys. Chem.*, to be submitted.
17. M.M. Dubinin, E.D. Zaverina and V.V. Serpinsky, The sorption of water vapour by active carbon. *J. Chem. Soc.*, 1955: 1760–1766, 1955.
18. G.X. Li, K. Kaneko, S. Ozeki, F. Okino, R. Ishikawa and H. Touhara, Water rejective nature of fluorinated microporous carbon fibers. *Langmuir*, 11: 716–717, 1995.
19. C.-M. Yang and K. Kaneko, Adsorption properties of nitrogen-alloyed activated carbon fiber. *Carbon*, 39: 1075–1082, 2001.
20. H. Kuwabara, T. Suzuki and K. Kaneko, Ultramicropores in microporous carbon fibers evidenced by helium adsorption at 4.2 K. *J. Chem. Soc. Faraday Trans.*, 87, 1915–1916, 1991.
21. N. Setoyama, K. Kaneko and F. Rodriguez-Reinoso, Ultramicropore characterization of microporous carbons at low temperature helium adsorption. *J. Phys. Chem.*, 100: 10331–10336, 1996.

22. D. Avnir, *The Fractal Approach to Heterogeneous Chemistry, Surface, Colloids, Polymers*, Chap. 4, pp. 247–380. Wiley, Chichester, 1989.
23. M. Sato, T. Sukegawa, T. Suzuki, S. Hagiwara and K. Kaneko, Surface fractal dimensional change of microporous carbon fibers. *Chem. Phys. Lett.*, 186: 526–530, 1991.
24. M. Sato, S. Sukegawa, T. Suzuki and K. Kaneko, Surface fractal dimension of less-crystalline carbon micropore walls. *J. Phys. Chem.*, 101, pp.1845–1850, 1997.
25. D. Avnir and M. Jaroniec, An isotherm equation for adsorption on fractal surfaces of heterogeneous pores. *Langmuir*, 5, 1431–1433, 1989.
26. K. Kaneko, M. Sato, T. Suzuki, Y. Fujiwara, K. Nishikawa and M. Jaroniec, Surface fractal dimension of microporous carbon fibers by nitrogen adsorption. *J. Chem. Soc. Faraday Trans.*, 87, 179–184, 1991.
27. P.J.M. Carrot, R.A. Robert and K.S.W. Sing, A new method for the determination of micropore size distributions. In: K.K. Unger, J. Rouquerol, K.S.W. Sing and H. Kral (Eds.). *Characterization of Porous Solids*, pp. 89–100. Elsevier, Amsterdam, 1988.
28. D. Atkinson, A.I. McLeod and K.S.W. Sing, Adsorptive properties of microporous carbons: primary and secondary micropore filling. *J. Chim. Phys.*, 81: 791–794, 1984.
29. N. Setoyama, T. Suzuki and K. Kaneko, Simulation study on relationship between high resolution α_s -plot and pore size distribution for activated carbon. *Carbon*, 36: 1459–1467, 1998.
30. K. Kaneko and C. Ishii, Superhigh surface area determination of microporous solids. *Colloids and Surface*, 67: 203–212, 1992.
31. T. Ohba, T. Suzuki and K. Kaneko, Preformed monolayer-induced filling of molecules in micropores. *Chem. Phys. Lett.*, 326: 158–162, 2000.
32. J. Miyawaki, T. Kanda, T. Okui, M. Saito, T. Suzuki and K. Kaneko, Macroscopic evidence of enhanced formation of methane nanohydrates in hydrophobic nanospaces. *J. Phys. Chem.*, 102: 2187–2192, 1998.
33. Z.M. Wang and K. Kaneko, Effect of pore width on micropore filling mechanism of SO_2 in carbon micropores. *J. Phys. Chem.*, 102: 2863–2868, 1998.
34. N.A. Seaton, J.P.R.B. Walton and N. Quirk, A new analysis method for the determination of the pore size distribution of porous carbons from nitrogen adsorption measurements. *Carbon*, 27: 853–861, 1991.
35. D. Nicholson, Using computer simulation to study the properties of molecules in micropores. *J. Chem. Soc. Faraday Trans.*, 92: 1–10, 1996.
36. M.J. Bojan and W.A. Steele, Computer simulation of sorption in pores with rectangular cross sections. *Carbon*, 36: 1417–1423, 1998.
37. V. Neimark and P.I. Ravikovitch, Calibration of pore volume in adsorption experiments and theoretical models. *Langmuir*, 13: 5148–5160, 1997.
38. C. Lastoskie, K.E. Gubbins and N. Quirke, Pore size distribution analysis of microporous carbons: a density functional theory approach. *J. Phys. Chem.*, 97: 4785–4796, 1993.
39. C. Lastoskie, K.E. Gubbins and N. Quirke, Pore size heterogeneity and the carbon slit pore: a density functional theory model. *Langmuir*, 9: 2693–2702, 1993.
40. S. Brunauer, P.H. Emmett and E. Teller, Adsorption of gases in multimolecular layers. *J. Am. Chem. Soc.*, vol. 60: 309–319, 1938.
41. Z. M. Wang and K. Kaneko, Dipole oriented states of SO_2 confined in a slit-shaped graphitic subnanospace from calorimetry. *J. Phys. Chem.*, 99: 16714–16721, 1995.
42. S. Inagaki, Y. Fukushima and K. Kuroda, Synthesis of highly ordered mesoporous materials from a layered polysilicate. *J. Chem. Soc. Chem. Commun.*, 1993: 680–682, 1993.
43. C.T. Kresge, M.E. Leonowicz, W.J. Roth, J.C. Vartuli and J.S. Beck, Ordered mesoporous molecular sieves synthesized by a liquid-crystal template mechanism. *Nature*, 359: 710–712, 1992.

44. P.J. Branton, P.G. Hall and K.S.W. Sing, Physisorption of nitrogen and oxygen by MCM-41, a model mesoporous adsorbent. *J. Chem. Soc. Chem. Commun.*, 1993: 1257–1258, 1993.
45. P.L. Llewellyn, Y. Grillet, F. Schütthe, H. Reichert and K.K. Unger, Effect of pore size on adsorbate condensation and hysteresis within a potential model adsorbent: M41S. *Microporous Mater.*, 3: 345–349, 1994.
46. R. Schmidt, M. Stöcker, E. Hansen, D. Akporiaye and O.H. Ellestad, MCM-41: a model system for adsorption studies on mesoporous materials. *Microporous Mater.*, 3: 443–448, 1995.
47. P.I. Ravikovitch, S.C.O. Domhnaill, A.V. Neimark, F. Schüth and K.K. Unger, Capillary hysteresis in nanopores: theoretical and experimental studies of nitrogen adsorption on MCM-41. *Langmuir*, 11: 4765–4772, 1995.
48. P.J. Branton, K. Kaneko and K.S.W. Sing, Physisorption of oxygen in narrow mesopores. *J. Chem. Soc. Chem. Commun.*, 1999: 575–576, 1999.
49. K. Morishige, H. Fujii, M. Uga and D. Kinukawa, Capillary critical point of argon, nitrogen, oxygen, ethylene, and carbon dioxide in MCM-41. *Langmuir*, 13: 3494–5184, 1997.
50. M. Kruk and M. Jaroniec, Adsorption study of surface and structural properties of MCM-41 materials of different pore sizes. *J. Phys. Chem.*, 101: 583–589, 1997.
51. C.G. Sonwane, S.K. Bhatia and N. Calos, Experimental and theoretical investigations of adsorption hysteresis and criticality in MCM-41: studies with O₂, Ar, and CO₂. *Ind. Eng. Chem. Res.*, 37: 2271–2283, 1998.
52. S. Inoue, Y. Hanzawa and K. Kaneko, Prediction of hysteresis disappearance in the adsorption isotherm of N₂ on regular mesoporous silica. *Langmuir*, 14: 3079–3081, 1998.
53. K. Liu, M.G. Brown, C. Carter, R.J. Saykally, J.K. Gregory and D.C. Clary, Characterization of a cage form of the eater hexamer. *Nature*, 381: 501–503, 1996.
54. M.V. López-Ramón, J. Jagiello, T.J. Bandosz, and N.A. Seaton, Characterization of microporous carbons by using molecular simulation to analysis the adsorption of molecules of different sizes. In: B. McEnaney, T.J. Mays, J. Rouquerol, F. Rouquerol, F. Rodriguez-Reinoso, K.S.W. Sing and K.K. Unger (Eds.). *Characterization of Porous Solids IV*, pp. 73–80. Royal Society of Chemistry, London, 1997.
55. M. Aoshima, K. Fukasawa and K. Kaneko, Micropore filling of supercritical Xe in micropores of activated carbon fibers. *J. Colloid Interface Sci.*, 222: 179–183, 2000.
56. K. Murata, K. Kaneko, F. Kobori, K. Takahashi, M. Yudasaka and S. Iijima, Pore structure of single-wall carbon nanohorn aggregates. *Chem. Phys. Lett.*, 331: 14–20, 2000.
57. K. Murata, M. El-Merraoui and K. Kaneko, A new determination method of absolute adsorption isotherms of supercritical gases under high pressure with a special relevance to DTF study. *J. Phys. Chem.*, 114: 4196–4205, 2001.
58. S. Sircar, Gibbsian surface excess for gas adsorption-revisited. *Ind. Eng. Chem. Res.*, 38: 3670–3682, 1999.
59. C. Nguyen and D.D. Do, Adsorption of supercritical gases in porous media: determination of micropore size distribution. *J. Phys. Chem. B*, 103: 6900–6908, 1999.
60. G.L. Aranovich and M.D. Donohue, Adsorption of supercritical fluids. *J. Colloid Interface Sci.*, 180: 537–541, 1996.
61. K. Kaneko, Determination of pore size and pore size distribution. *J. Membrane Sci.*, 96: 59–89, 1994.
62. N.A. Seaton, J.P.R.B. Walton and N. Quirke, A new analysis method for the determination of the pore size distribution of porous carbons from nitrogen adsorption measurements. *Carbon*, 27: 853–858, 1991.

63. M.E. Merraoui, M. Aoshima and K. Kaneko, Micropore size distribution of activated carbon fiber using the density functional theory and other methods. *Langmuir* 16: 4300–4304, 2000.
64. T. Ohba, T. Suzuki and K. Kaneko, Relationship between DR-plot and micropore width distribution from GCMC simulation. *Carbon*, 30: 1879–1902, 2000.

Chapter 21

Electrochemical Characterization of Carbons and Carbon Alloys

Tsuyoshi Nakajima

Department of Applied Chemistry, Aichi Institute of Technology, Toyota-shi, 470-0392, Japan

Abstract: Fundamental techniques of electrochemistry, i.e. cyclic voltammetry and galvanostatic methods for characterizing carbon materials are described. Examples of cyclic voltammograms and charge/discharge curves are shown for carbon, graphite and the carbon alloys BC_x and C_xN . The capacities are increased by boron and nitrogen substitution in graphene layers. The increase in the capacities of BC_x and C_xN result from formation of low SOMO and LUMO levels in graphene layers which enhance the chemical interaction of lithium with BC_x and C_xN .

Keywords: Cyclic voltammetry, Galvanostatic method, Carbon alloy, C_xN , BC_x , Graphite intercalation compound.

1 Introduction

One of the important uses of carbon materials is the application to battery materials, i.e. primary and secondary batteries, fuel cells, etc. Various types of powdery, fibrous or sintered carbon materials, which are prepared from natural and synthetic graphites, and graphitizable and non-graphitizable carbons, are currently employed in batteries as electrode and electroconductive materials. Among many applications of carbon materials to batteries, graphite intercalation compounds occupy a very important place in primary and secondary batteries. A typical example is the lithium/graphite fluoride ($Li/(CF)_n$) battery which was developed at the beginning of 1970s by Matsushita Ind. Co., Ltd. in Japan [1–3]. This battery was the first to use metallic lithium as anode and to use organic solvents. After the development of $Li/(CF)_n$ battery, the Li/MnO_2 battery was commercialized in the mid-1970s. These batteries are not rechargeable, i.e., they are primary lithium batteries, as used for watches, cameras and many kinds of electronic instruments. After these primary lithium batteries were in commercial production, research efforts were devoted to the development of secondary batteries using the metallic lithium anode. The use of metallic lithium as anodes was unsuccessful due to the formation of lithium dendrites

following repeated charge/discharge cycling. To avoid this dendrite formation, several types of metallic alloys were applied to anode materials. However, this attempt was also unsuccessful. After these efforts to develop new lithium anodes, the graphite intercalation compound of lithium was found to be an excellent material as anodes for secondary batteries. The Sony Company in Japan commercialized Lithium-ion secondary batteries using non-graphitizable carbon as anodes and LiCoO_2 as cathodes [4]. Lithium ions were intercalated into carbon in the charge process and de-intercalated from carbon in the discharge process. Lithium is safely accommodated in carbon without dendrite formation. Today, graphite is mainly used as an anode host for lithium in commercial lithium-ion secondary batteries. Considering the importance in applications of carbon materials to batteries, their electrochemical properties need to be correlated with their structural parameters. Electrochemical behavior of carbon materials is governed by surface area, crystallinity, surface functional groups such as oxygen, hydrogen or nitrogen and by heteroatom content of such elements as boron and nitrogen atoms substituted into the graphene layers. Several electrochemical methods are usually employed for characterizing carbon materials. Typical ones are cyclic voltammetry and the galvanostatic method. In this chapter, fundamental aspects of these electrochemical techniques and some examples of analytical results on carbon materials are presented.

2 Characterization Techniques

2.1 Cyclic Voltammetry

Cyclic voltammetry is a convenient method to study redox reactions which occur in a specified range of potential. Three types of electrode cell consisting of working, counter and reference electrodes are normally used, as shown in Fig. 1. The working electrode is a carbon material. When the carbon material is in sheet or block form, it is easy to use as an electrode. For powder carbons, it is bound onto a foamed nickel surface using a binder such as polyvinylidene fluoride (PVDF) [5] or pressed onto nickel mesh. In order to characterize a carbon for use as an anode of the lithium ion secondary battery, metallic lithium is employed as the counter and reference electrodes in organic solvents. They are prepared by pressing metallic lithium onto a nickel mesh. When highly crystalline graphite is used as an electrode material, a mixture of ethylene carbonate (EC) with either diethyl carbonate (DEC) or dimethyl carbonate (DMC) (1:1 in volume) containing $1 \text{ mol dm}^{-3} \text{ LiClO}_4$ or LiPF_6 should be employed. Of these, EC is an essential component in the solvents because EC decomposes electrochemically to form a thin protective film on the graphite surface so preventing degradation of the graphite during charge/discharge cycling [6]. On the other hand, when a non-graphitic carbon is used, propylene carbonate (PC) containing solvents is preferable for the formation of this surface film. In commercial batteries, LiPF_6 is used as an electrolyte to avoid explosions. However, LiClO_4 is used

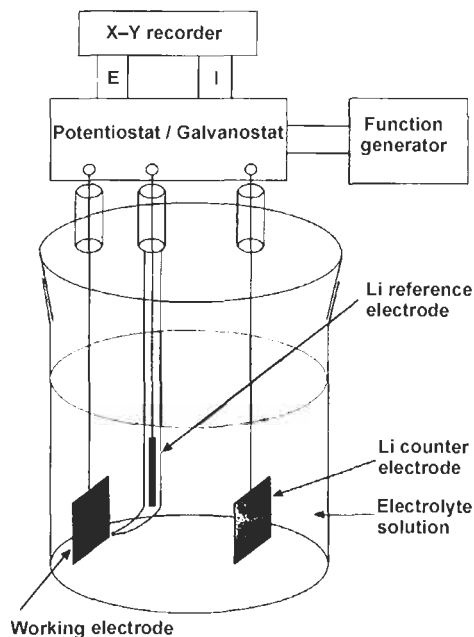


Fig. 1. Schematic illustration of an electrochemical cell.

in laboratory experiments because of its relatively high solubility in organic solvents. The electrochemical cell is placed in a glove box filled with dry argon gas. The glove box is thermostatted to about 25°C.

The electrode potential of the working electrode is measured relative to that of a lithium reference electrode, vs Li/Li^+ , through a Luggin capillary used to reduce errors (usually several tens mV) caused by an IR drop in solution. If the error is not important, then the Luggin capillary is not used. Three electrodes are connected to a potentiostat/galvanostat. In cyclic voltammetry experiments, the electrode potential is scanned in a negative direction from the rest potential (≈ 3 V for a carbon material) and reversed at 0 V vs Li/Li^+ by a function generator and potentiostat/galvanostat. After the potential reverse, the potential is scanned in a positive direction and again reversed at a desired positive potential. Potential scans are usually repeated between 0 and 1–3 V vs Li/Li^+ depending on the kind of experiment or carbon material used. The scan speed is changed in the range of 0.1 mV s^{-1} – 100 V s^{-1} . Slow scan speeds of 0.1 – 1 mV s^{-1} are close to a steady-state method. Current flow during a potential scan is recorded on a chart of an X–Y recorder as a function of the potential of the working electrode. In cyclic voltammetry experiments, a cyclic voltammogram, as shown in Fig. 2, is obtained. The horizontal and vertical axes show the potential of the working electrode and current flow during a potential scan, respectively. Two cathodic peaks and the corresponding anodic peaks are usually observed. Peak current, i_p , increases as the reaction rate increases. When the rate of charge transfer is much faster than

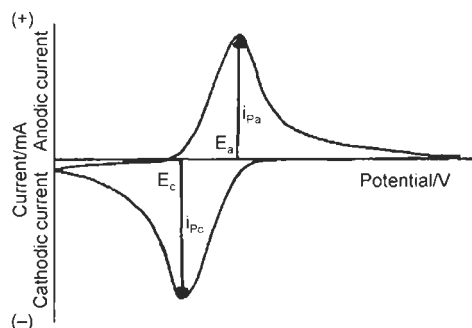
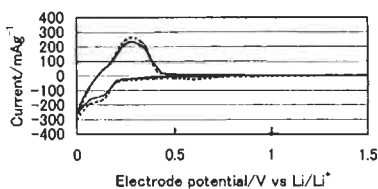


Fig. 2. A cyclic voltammogram.

rates of diffusion of a reactant or a product, then the peak current i_p is proportional to $\nu^{1/2}$ (ν : scan speed). When the rate of charge transfer is comparable to or slower than rates of diffusion, the rate of charge transfer becomes faster as the scan speed decreases. When the scan speed is sufficiently high, the rate of charge transfer, relatively, is much slower than rates of diffusion. In this case, values of i_p are also proportional to $\nu^{1/2}$, but are not proportional to $\nu^{1/2}$ in an intermediate condition. It is also found that the potential difference between anodic and cathodic peaks, ΔE_p ($= E_a - E_c$) decreases as the rate of charge transfer increases. When several reactions occur at different potentials, the same number of corresponding peaks is usually observed. Figure 3 shows an example of a cyclic voltammogram for graphite powder (average particle diameter $7 \mu\text{m}$) obtained at 0°C in 1 mol dm^{-3} of $\text{LiClO}_4\text{-EC/DEC}$. On the first scan in the cathodic direction, a small peak is observed at $0.6\text{--}0.7 \text{ V}$, indicating the electrochemical reduction of EC. Further reduction of graphite yields two peaks at ca. 0.15 V and nearly 0.0 V , which are regarded as the formation of stage 2 and 1 lithium-intercalated graphite, respectively [7]. With anodic oxidation, two peaks corresponding to those observed on the cathodic side appear at ca. 0.12 and 0.28 V . The two cathodic and anodic peaks show the reversible intercalation and de-intercalation of lithium. From the second cycle, only anodic and cathodic currents for lithium intercalation/de-intercalation are observed.

Recently, a new compact apparatus for cyclic voltammetry experimentation was developed. The three parts of the experimental system are accommodated in one apparatus which is conveniently operated by a computer system. It is now commercially available.

Fig. 3. Cyclic voltammogram for a graphite powder ($\approx 7 \mu\text{m}$) obtained in 1 mol dm^{-3} $\text{LiClO}_4\text{-EC/DEC}$ at 0°C . Dashed line: 1st cycle; solid line: 6th cycle.

2.2 Galvanostatic Method

Electrochemical characteristics of carbon materials are examined by the galvanostatic method, i.e., a constant current method. In this constant current method, the electrode potential is monitored and recorded as a function of time, i.e., capacity (mAh g^{-1} or Ah kg^{-1}). The galvanostatic method is a more standard technique than cyclic voltammetry because potential is the only variable. In cyclic voltammetry, both the current and potential are changed. The same cell with its three electrodes, as shown in Fig. 1, is used in galvanostatic experiments. The cell is placed in a thermostatted glove box with dry argon. A constant current of $10\text{--}300 \text{ mA g}^{-1}$ (usually $30\text{--}60 \text{ mA g}^{-1}$ less than 100 mA g^{-1}) is supplied to the electrochemical cell from an electric source. Currently, an apparatus for the experiment of charge/discharge cycling is commercially available. The potential range in which charge/discharge cycling is done is set between 0 and $1\text{--}3 \text{ V}$ vs Li/Li^+ . An example of charge/discharge potential curves for natural graphite powder (average particle diameter $7 \mu\text{m}$) is shown in Fig. 4 [5,8]. The potential of a carbon material is initially about 3 V vs Li/Li^+ , which is reduced in the direction of negative potential by application of a constant current to the cell. For graphite electrodes, the electrode potential sharply decreases and approaches 0.0 V . Lithium ion is electrochemically intercalated into graphite in this process. A small plateau indicating the electrochemical decomposition of EC with thin film formation usually appears at $0.6\text{--}0.7 \text{ V}$ vs Li/Li^+ , and this is observed only in the first reduction process. From the second cycle, a smooth potential curve is obtained. When the electrode potential reaches 0.0 V , the electric current is automatically changed to the opposite direction, that is, lithium ion is de-intercalated from graphite accompanied by a slight increase in the electrode potential. The potential, however, sharply increases at the final stage of lithium ion de-intercalation from graphite. When the electrode potential reaches a pre-fixed value (usually $1\text{--}3 \text{ V}$ vs Li/Li^+), the current flow is again changed to the opposite direction so that lithium ions may again be intercalated into the graphite. This operation is usually repeated ten to one hundred times in a fixed potential range. For commercial lithium-ion secondary batteries, a carbon material is used as anode. Lithium ion intercalation into carbon material is then the charge process and de-intercalation of lithium ion is the discharge process. However, in a test cell in which metallic lithium is used as a counter electrode, a

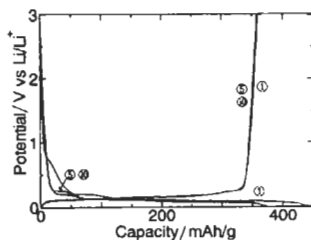


Fig. 4. Charge/discharge curves for natural graphite powder ($\approx 7 \mu\text{m}$). 1st, 5th and 10th cycles at 30 mA g^{-1} [5].

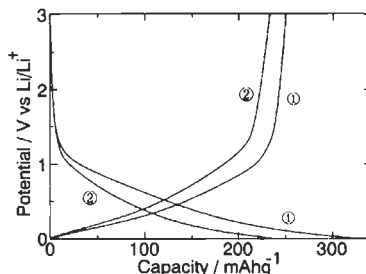


Fig. 5. Charge/discharge curves for carbon prepared at 1000°C without nickel [9]. (1): 1st cycle, (2): 10th cycle, current density: 60 mA g⁻¹.

carbonaceous electrode is the cathode, i.e., the positive electrode. Therefore, lithium ion intercalation is the discharge process and de-intercalation of lithium ion is the charge process.

Profiles of potential curves for charge/discharge reactions differ depending on the kind of carbon material used. When highly crystalline graphite is used, flat and low potentials are obtained in both charge and discharge processes, and the electrode potential sharply increases at the end of lithium ion de-intercalation reactions. However, the electrode potential has a slope for non-graphitic carbon materials, as shown in Fig. 5 [9]. The theoretical capacity of graphite is 372 mAh g⁻¹, calculated on the basis that the stage 1 of lithium-intercalated graphite is LiC₆. The capacity of a non-graphitic carbon is sometimes larger than 372 mAh g⁻¹. But often they have larger irreversible capacities and lower cycleabilities than graphite. The first coulombic efficiency of graphite is usually 80–90% while that of non-graphitic carbon is often less.

To evaluate electrochemical properties of carbons as anodes in lithium secondary batteries, such properties as discharge capacity, first coulombic efficiency and cycleability are examined. High values are of course desirable for discharge capacity and coulombic efficiency. Low first coulombic efficiencies mean that some of the intercalated lithium is not released from the anode during the first discharge or that some of the organic solvent is electrochemically decomposed at the surface of anode. If degradation of carbon materials by charge/discharge cycling is quite small, a high capacity may be kept for many cycles. Another important property for secondary batteries is whether or not a large current can be taken out. Lithium ion batteries using carbon materials as anodes are usually operated at low current densities.

3 Electrochemical Characterization of Carbon Alloys

3.1 Modification of Electronic Structures of Carbon Materials by Boron and Nitrogen Substitution

As understood from the periodic table of elements, those similar to carbon are neighboring boron and nitrogen in terms of their sizes, although boron has one

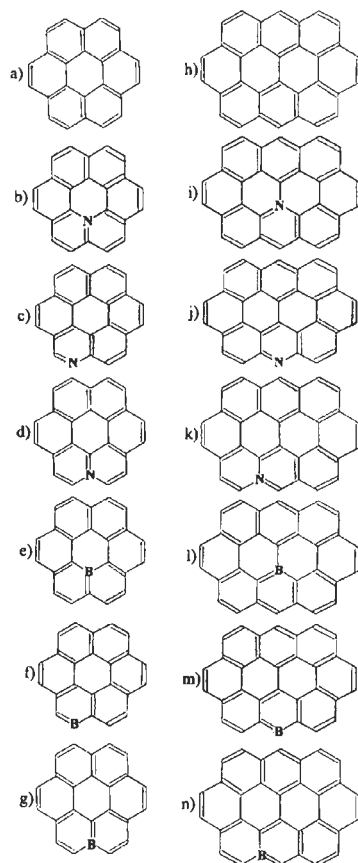


Fig. 6. The cluster models representing carbon, C,N and BC_x . (a) Coronene; (b) N-substituted coronene (center-N); (c) N-substituted coronene (edge-N); (d) N-substituted coronene (valley-N); (e) B-substituted coronene (center-B); (f) B-substituted coronene (edge-B); (g) B-substituted coronene (valley-B); (h) Ovalene; (i) N-substituted ovalene (center-N); (j) N-substituted ovalene (edge-N); (k) N-substituted ovalene (valley-N); (l) B-substituted ovalene (center-B); (m) B-substituted ovalene (edge-B); (n) B-substituted ovalene (valley-B).

electron less and nitrogen has one electron more than carbon. Boron or nitrogen atoms can be partially substituted for carbon atoms in the graphene layers by chemical vapor deposition (CVD), by ion implantation and by heat-treatment with a boron compound such as B_4C , etc. Because boron or nitrogen substitution modifies the electronic structure of graphite, electron acceptance or donation properties are changed on introduction of heteroatoms into the graphene layers.

Boron is easily incorporated into graphene layers because of planar BC_3 bonds (see Figs. 6e and l). BC_x is prepared by CVD using BCl_3 , a hydrocarbon such as benzene or cyclohexane, and hydrogen gas at 800–1100°C [10–12]. The composition of BC_x is in the range of BC_4 – BC_{60} [11] in which boron contents decrease with increasing reaction temperature. Because the boron–carbon bond length is slightly longer than

carbon-carbon bond length in graphene layer, boron, at higher temperatures, is removed from the graphene layer in order to reduce the structural strain. Only 3 at% of boron is contained in graphite heat-treated at 3000°C [7,13]. X-ray photoelectron spectra of BC_x show the existence of C_2B-BC_2 and BC_3 bonds in graphene layers with B-O bonds also present [11]. The use of nickel catalyst enables the formation of crystallized BC_x filaments [11]. Boron-substituted graphite is prepared by heat-treatment of a carbon material with ca. 4 wt% of B_4C at 3000°C [7,13].

Nitrogen substituted carbons are prepared by thermal decomposition of such nitrogen-containing organic compounds as acetonitrile, pyridine or acrylonitrile at 800–1100°C [5,10,14,15]. Compositions of C_xN are in the range of $C_{14}N-C_{60}N$, the highest nitrogen content ($C_{14}N-C_{21}N$) being obtained between 900 and 1000°C. The crystallinity of C_xN is improved by the use of nickel or cobalt catalysts [5,15]. Nitrogen atoms, substituted in graphene layers, exist mainly in two forms: a nitrogen atom bonded to three carbon atoms (trigonal nitrogen: Figs. 6b, d, i and k) and a nitrogen atom bonded to two carbon atoms situated at the edge of a graphene layer (edge-N: Figs. 6c and j) [5,15,16]. Trigonal nitrogen is classified into two types: nitrogen substitutionally incorporated inside of a graphene layer (center-N: Figs. 6b and i) and that existing at the edge of a graphene layer (valley-N: Figs. 6d and k). Nitrogen atoms bonded to two carbon atoms are of the pyridinic type (edge-N: Figs. 6c and j).

Semi-empirical molecular orbital calculations using MOPAC ver. 6.00, AM1 were made to elucidate changes in electronic structures following boron or nitrogen incorporation into graphene layers [16]. Figure 6 shows BC_x and C_xN cluster models used for the calculation in which different types of boron or nitrogen atoms are incorporated in graphene layers [16]. Coronene, $C_{24}H_{12}$ and ovalene, $C_{32}H_{14}$ are adopted as host carbon clusters. Figure 7 also indicates BC_x and C_xN cluster models in which one to four heteroatoms are substitutionally incorporated into ovalene [16]. The calculated results are given in Tables 1 and 2. In boron-substituted carbon clusters, edge-B (Figs. 6f and m) has a higher charge than center-B (Figs. 6e and l) and valley-B (Figs. 6g and n) bonded to three carbon atoms. HOMO levels of boron-substituted carbon clusters are lower than those of original carbon clusters for center-B and valley-B, but higher for edge-B. On the other hand, LUMO energy levels are higher than those of coronene and ovalene except coronene with edge-B. These differences in HOMO and LUMO energy levels by boron incorporation are rather small. An interesting point is that low SOMO (Singly Occupied Molecular Orbital) levels are created in the carbon clusters with center-B and valley-B, as given in Table 1. These SOMO levels are significantly lower than LUMO levels. When one to four boron atoms are substituted for carbon atoms in ovalene as shown in Fig. 7, low SOMO levels appear for ovalenes with odd numbers of boron atoms as given in Table 2. LUMO levels also decrease in ovalenes with two to four boron atoms (center-2B, center-3B and center-4B: Figs. 7f, g and h, respectively). For nitrogen-substituted carbon clusters, the charges of the trigonal nitrogen atoms (center-N and valley-N) are higher than those of pyridine-type nitrogen (edge-N). Electrons are localized at edge-N positions. HOMO energy levels of nitrogen-substituted carbon

Table 1

HOMO, SOMO and LUMO energies and charges of boron and nitrogen atoms in the C_xN and the BC_x cluster models calculated by AM1

| Model | HOMO (eV) | SOMO (eV) | LUMO (eV) | Charge |
|---------------------|-----------|-----------|-----------|--------|
| Coronene | -8.187 | — | -0.980 | — |
| Coronene (center-N) | -8.362 | -3.541 | -0.957 | -0.035 |
| Coronene (edge-N) | -8.317 | — | -1.159 | -0.129 |
| Coronene (valley-N) | -8.331 | -3.640 | -0.904 | -0.086 |
| Coronene (center-B) | -8.208 | -5.216 | -0.799 | 0.233 |
| Coronene (edge-B) | -7.636 | — | -1.007 | 0.412 |
| Coronene (valley-B) | -8.314 | -5.067 | -0.793 | 0.249 |
| Ovalene | -7.629 | — | -1.556 | — |
| Ovalene (center-N) | -7.834 | -3.926 | -1.022 | -0.028 |
| Ovalene (edge-N) | -7.923 | — | -1.726 | -0.129 |
| Ovalene (valley-N) | -7.755 | -3.775 | -1.333 | -0.002 |
| Ovalene (center-B) | -8.302 | -5.008 | -1.263 | 0.233 |
| Ovalene (edge-B) | -7.088 | — | -1.124 | 0.475 |
| Ovalene (valley-B) | -7.778 | -5.154 | -1.373 | 0.219 |

Table 2

HOMO, SOMO and LUMO energy levels of the C_xN and the BC_x cluster models calculated by AM1

| | HOMO (eV) | SOMO (eV) | LUMO (eV) |
|-----------|-----------|-----------|-----------|
| Center-1N | -7.834 | -3.926 | -1.022 |
| Center-2N | -6.223 | — | -1.213 |
| Center-3N | -6.400 | -3.930 | -0.987 |
| Center-4N | -6.262 | — | -1.054 |
| Center-1B | -8.302 | -5.008 | -1.263 |
| Center-2B | -7.458 | — | -2.887 |
| Center-3B | -7.916 | -4.694 | -2.725 |
| Center-4B | -7.349 | — | -2.726 |

clusters are slightly lower than those of coronene and ovalene while LUMO levels become higher except for both coronene and ovalene with edge-N. Low SOMO levels are also observed in the carbon clusters with center-N and valley-N (Table 1), and center-1N (Fig. 7a) and center-3N (Fig. 7c) (Table 2). An electron would be delocalized in such carbon clusters having SOMO. The delocalized charges contribute to the

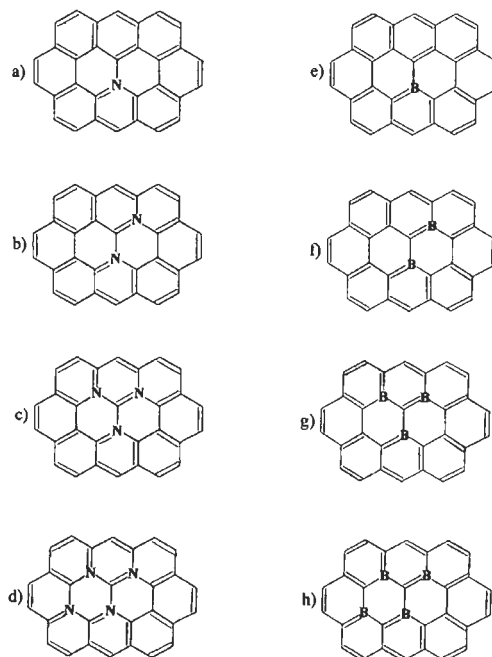


Fig. 7. The cluster models representing carbon, C_xN and BC_x ($x = 1-4$). (a) N-substituted ovalene (center-1N); (b) N-substituted ovalene (center-2N); (c) N-substituted ovalene (center-3N); (d) N-substituted ovalene (center-4N); (e) B-substituted ovalene (center-1B); (f) B-substituted ovalene (center-2B); (g) B-substituted ovalene (center-3B); (h) B-substituted ovalene (center-4B).

low SOMO energy levels in the clusters. Boron- and nitrogen-substituted carbons with such low SOMO and LUMO levels are better electron acceptors than non-substituted carbon materials, i.e., they may be electrochemically reduced at higher potentials.

3.2 Electrochemical Behavior of Boron and Nitrogen Substituted Carbon Materials

Boron-substituted graphite is prepared by heat-treatment of a carbon with 4 wt% of B_4C at $3000^\circ C$ for 1 h [7,13]. Electrochemical intercalation and de-intercalation of lithium were examined using boron-substituted graphite by cyclic voltammetry [7,13]. Figure 8 shows cyclic voltammograms for graphitized carbon and boron-substituted graphite, obtained at $25^\circ C$ in $1 \text{ mol dm}^{-3} \text{ LiClO}_4$ -ethylene carbonate (EC)/dimethyl carbonate (DMC) (1:1 by volume). The voltammograms were obtained at a scan speed of $5 \mu\text{V s}^{-1}$ between 0 and 0.3 V vs Li/Li^+ . For graphitized carbon without boron, two cathodic peaks indicating the formation of stages 2 and 1 lithium-intercalated phases are observed at 100 and 80 mV vs Li/Li^+ . On the anodic scan, three peaks appear at 90, 140 and 190 mV corresponding to the decomposition of first, second and

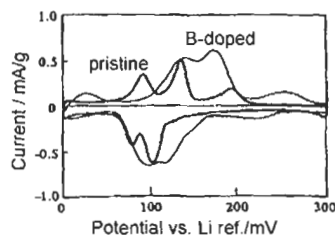


Fig. 8. Cyclic voltammograms for pristine and B-doped graphites [7,13]. Thick line: pristine graphite; thin line: B-doped graphite.

higher stage phases. For boron-substituted graphite, the potential indicating the intercalation of lithium into boron-substituted graphite shifts to a higher potential by 20 mV as shown in Fig. 8. The potential for de-intercalation of lithium from boron-substituted graphite also shifts to a higher potential by 40 mV. These potential shifts to higher values indicate an increase in the interaction of lithium with boron-substituted graphite. Galvanostatic charge/discharge experiments for boron-substituted graphite revealed that capacity increased by 40 mAh g^{-1} and reached 340 mAh g^{-1} as shown in Fig. 9 [7,13]. Coulombic efficiencies are also increased by boron substitution. The increases in the capacity and coulombic efficiency observed for boron-substituted graphite are due to the improvement of crystallinity and formation of low LUMO and SOMO levels by boron substitution. Formation of new acceptor levels enhances the chemical interaction of lithium with graphite.

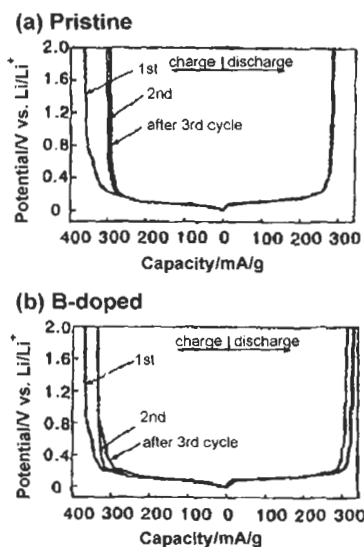


Fig. 9. Charge/discharge curves for pristine and B-doped graphites [7,13]. (a) pristine graphite, (b) B-doped graphite.

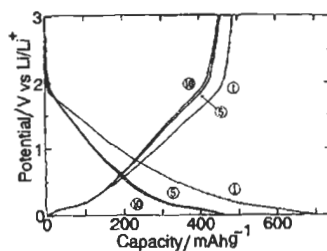


Fig. 10. Charge/discharge curves for $BC_{6,8}$ prepared by 2 h deposition at 900°C with nickel catalyst [17].

Boron-substituted carbon is prepared by CVD using BCl_3 , a hydrocarbon and hydrogen at $800\text{--}1100^{\circ}\text{C}$ [10–12]. $BC_{3,8}$ prepared at 900°C , without a catalyst, shows a low capacity with a high irreversible capacity. However, $BC_{6,8}$ prepared with a nickel catalyst for graphitization at 900°C shows a higher capacity with a lower irreversible capacity, and better cycleability, as shown in Fig. 10, because of its higher crystallinity than that of $BC_{3,8}$ prepared without a catalyst [17]. The electrochemical characteristics of BC_x prepared at $800\text{--}1100^{\circ}\text{C}$ are significantly influenced not only by the electronic structure but also by crystallinity and surface chemical species such as oxygen and hydrogen. This is because the crystallinity of BC_x is lower than that of graphite and oxygen is easily introduced into BC_x because of a strong B–O bond. As shown in Fig. 10, electrode potentials linearly increase in lithium de-intercalation processes. This may be due to the interaction of lithium ion with oxygen. For boron-substituted graphite, the crystallinity is high and effects of oxygen may be much smaller because oxygen is almost totally removed in the graphitization process.

Nitrogen-substituted carbon is prepared by thermal decomposition of a nitrogen-containing organic compound such as acetonitrile, pyridine or acrylonitrile at $800\text{--}1100^{\circ}\text{C}$ [5,10,14,15]. The composition of C_xN is in the range of $C_{14}N$ to $C_{60}N$. The optimum temperature range to prepare $C_{14}N\text{--}C_{21}N$ is between 900 and 1000°C . Nitrogen substitution for carbon atoms in the graphene layer is more difficult than boron substitution because NC_3 bonds (see Figs. 6b and i) are not planar while BC_3 bonds (see Figs. 6e and l) have a planar structure. Nitrogen substitution becomes difficult above 1100°C . Substituted nitrogen atoms are eliminated from graphene layers by heat-treatment at high temperatures in order to reduce structural strain. Nitrogen-substituted graphite is therefore difficult to prepare. However, the crystallinity of C_xN can be increased by use of nickel or cobalt catalysts [5,15]. The crystallinity of carbon prepared from benzene is also improved by the catalytic action of nickel. Figures 11, 12 and 13 show charge/discharge curves obtained for carbon prepared from benzene at 900°C and C_xN samples prepared at 900 and 1000°C in the presence of nickel catalyst [5]. The graphitization effect of nickel is distinct when the potential curves in Fig. 11 are compared with those for carbon prepared without a catalyst, shown in Fig. 5. The carbon prepared with nickel catalyst has low and flat potentials, and higher capacity. Cycleability is also much better. The use of a nickel catalyst not only improves the crystallinity of a carbon material but also increases the

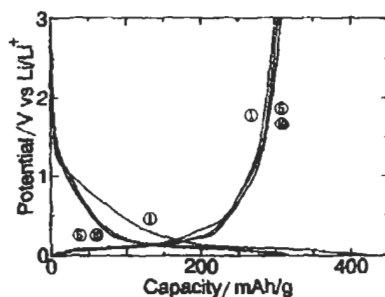


Fig. 11. Charge/discharge curves for benzene-derived carbon prepared at 900°C in the presence of nickel [5]; 1st, 5th and 10th cycles at 30 mA g⁻¹.

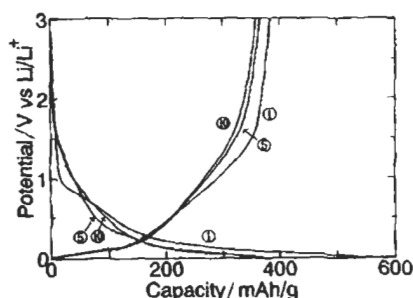


Fig. 12. Charge/discharge curves for C₂₁N prepared from acetonitrile at 900°C with nickel catalyst [5]; 1st, 5th and 10th cycles at 30 mA g⁻¹.

trigonal nitrogen NC₃ in C_xN layers [5,15]. The effect of nitrogen substitution in graphene layers can be understood from the comparison of potential curves for C_xN shown in Figs. 12 and 13 with those for carbon in Fig. 11. During the lithium ion de-intercalation process, the potentials gradually increase until ca. 150 mAh g⁻¹ in both C_xN and carbon samples. However, the potential increase differs among three samples after 150–200 mAh g⁻¹. The potential of the carbon quickly increases and shows a charge capacity of 306 mAh g⁻¹ between 0 and 3 V. On the other hand, the C_xN, samples prepared at 900 and 1000°C, show a slower increase in potential and exhibit the higher capacities of 390–362 and 408–391 mAh g⁻¹, respectively. The higher charge capacities obtained on C_xN samples are due to the interaction of lithium with SOMO created in graphene layers by nitrogen substitution. Slow increases of electrode potential at the end of the lithium de-intercalation process are desirable because this larger capacity is available for commercial batteries.

A new type of composite electrode was developed by a CVD treatment using natural graphite powder as a substrate [9,17]. BC_x or C_xN layers were coated onto natural graphite powder by CVD at 1000°C. The concept of a composite electrode takes advantage of both the graphite and the boron- or nitrogen-substituted carbon. Graphite shows a low and flat potential, but the potential quickly increases at the end

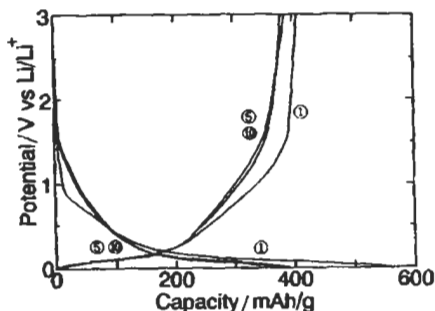


Fig. 13. Charge/discharge curves for $C_{20}N$ prepared from acetonitrile at $1000^{\circ}C$ with nickel catalyst [5]; 1st, 5th and 10th cycles at 30 mA g^{-1} .

of the lithium de-intercalation reaction. This phenomenon limits the use of the full capacity of graphite. On the other hand, boron- or nitrogen-substituted carbons show gradual increases in potential during the latter half of the lithium de-intercalation reaction. The CVD technique combines these two different behaviors. Until the last stage of lithium ion de-intercalation is reached, the new composite electrode keeps a low and flat potential to be followed by a gradually increasing potential. Figure 14 shows the charge/discharge curves of C_xN -coated graphite and C_xN itself prepared without a nickel catalyst [9]. The C_xN -coated graphite exhibits a higher charge capacity than graphite and has good cycleability. The charge capacities of C_xN -coated

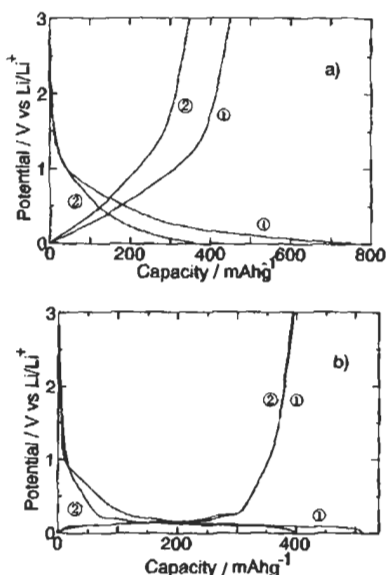


Fig. 14. Charge/discharge curves for $C_{14}N$ and C_xN -coated graphite prepared at $1000^{\circ}C$ [9]. (a) $C_{14}N$; (b) C_xN -coated graphite prepared by 2 h deposition. (1): 1st cycle, (2): 10th cycle, current density: 60 mA g^{-1} .

graphite are also higher than those of carbon-coated graphite [9]. With deposition of C_xN onto graphite powder, the chemical interaction between the substrate graphite powder and deposited C_xN layers could be improved. For this purpose, C_xN layers are deposited onto graphite powder which is oxidized in advance using 94% HNO_3 . This procedure is expected to cause carbon-carbon bond breakage with release of oxygen as CO and/or CO_2 at high temperatures. New carbon-carbon bonds could be formed between graphite powder and deposited C_xN layers during CVD. In fact, C_xN -coated graphite prepared by this procedure has a better cycleability than that prepared without pre-treatment by the 94% HNO_3 .

4 Conclusions

The electrochemical behavior of carbon materials is essentially governed by their crystallinity, surface area, and surface functional groups. In addition, carbon alloys such as boron- and nitrogen-substituted carbons have modified electronic structures. Boron substitution creates low LUMO and SOMO in graphene layers, and nitrogen substitution also yields low SOMO. The formation of new acceptor levels enhances the electron accepting ability of boron- and nitrogen-substituted carbons. This gives rise to an increase in the charge capacities of BC_x and C_xN . The redox reactions of BC_x and C_xN occur at potentials more positive than those of non-substituted carbon materials, i.e., lithium intercalation and de-intercalation reactions take place at higher potentials.

References

1. T. Nakajima and N. Watanabe, Graphite Fluorides and Carbon-Fluorine Compounds. CRC Press, Boca Raton, 1991.
2. M. Fukuda and T. Iijima, Lithium/poly-carbonmonofluoride cylindrical type batteries, Proc. the 9th Int. Power Sources Symp., Academic Press, London, pp. 713-728, 1974.
3. T. Nakajima, Carbon-fluorine compounds as battery materials. J. Fluorine Chem., 100: 57-61, 2000.
4. K. Kanamura, Fluorine compounds in battery applications. In: T. Nakajima, B. Zemva and A. Tressaud (Eds.), Advanced Inorganic Fluorides, Chapter 16. Elsevier Science, Amsterdam, 2000.
5. T. Nakajima, M. Koh and M. Takashima, Electrochemical behavior of carbon alloy C_xN prepared by CVD using a nickel catalyst. Electrochim. Acta, 43, 883-891, 1998.
6. R. Fong, U. v. Sacken and J.R. Dahn, Studies of lithium intercalation into carbons using nonaqueous electrochemical cells. J. Electrochem. Soc., 137: 2009-2013, 1990.
7. Y. Nishimura, T. Takahashi, T. Tamaki, M. Endo and M.S. Dresselhaus, Anode performance of B-doped mesophase pitch-based carbon fibers in lithium ion secondary batteries. Tanso, 172: 89-94, 1996.
8. T. Nakajima, M. Koh, R.N. Singh and M. Shimada, Electrochemical behavior of surface-fluorinated graphite. Electrochim. Acta, 44: 2879, 1999.
9. T. Nakajima, M. Koh and T. Katsube, Structure, chemical bonding and electrochemical behavior of heteroatom-substituted carbons prepared by arc discharge and chemical vapor deposition. Solid State Sci., 2: 17-29, 2000.

10. M. Kawaguchi and N. Bartlett, Synthesis, structures, and intercalation chemistry of B/C/N materials based on the graphite network. In: T. Nakajima (Ed.), *Fluorine–Carbon and Fluoride–Carbon Materials: Chemistry, Physics and Applications*, Chapter 5. Marcell Dekker, New York, 1995.
11. M. Koh and T. Nakajima, Synthesis of well-crystallized boron-carbon filament by chemical vapor deposition using a nickel catalyst. *Carbon*, 36: 913–920, 1998.
12. B.M. Way and J.R. Dahn, The effect of boron substitution in carbon on the intercalation of lithium in $\text{Li}_x(\text{B}_z\text{C}_{1-z})_6$. *J. Electrochem. Soc.*, 141: 907–911, 1994.
13. M. Endo, Y. Nishimura, T. Takahashi, A. Takamuku and T. Tamaki, Evaluation of carbon fibers as an anode material of lithium ion secondary battery and their performances. *Tanso*, 172: 121–129, 1996.
14. W.J. Weydanz, B.M. Way, T. van Buuren and J.R. Dahn, Behavior of nitrogen-substituted carbon (N_zC_{1-z}) in $\text{Li}/\text{Li}(\text{N}_z\text{C}_{1-z})_6$ cells. *J. Electrochem. Soc.*, 141: 900–906, 1994.
15. T. Nakajima and M. Koh, Synthesis of high crystalline carbon–nitrogen layered compounds by CVD using nickel and cobalt catalysts. *Carbon*, 35: 203–208, 1997.
16. M. Koh and T. Nakajima, Adsorption of aromatic compounds on C_xN -coated activated carbon. *Carbon*, 38: 1947–1954, 2000.
17. M. Koh and T. Nakajima, Electrochemical behaviors of carbon alloy BC_x and of BC_x -coated graphite prepared by chemical vapor deposition. *Electrochim. Acta*, 44: 1713–1722, 1999.

Chapter 22

Mechanical Probe for Micro-/Nano-characterization

Mototsugu Sakai

Department of Materials Science, Toyohashi University of Technology, Toyohashi 441-8580, Japan

Abstract: Theoretical considerations and experimental examinations are made of pyramidal indentation as an efficient mechanical test for micro-/nano-characterization of engineering materials. Mathematically formulated are the constitutive relations for elastoplastic indentation in time-independent regime, as well as for viscoelastic indentation in time-dependent regime. A critical review for indentation test systems and the details for designing test apparatuses are also given. The application of indentation tests to carbon-related materials is demonstrated where elastic/plastic parameters as well as viscoelastic functions are examined in terms of their microscopic characteristics.

Keywords: Pyramidal indentation, Elasticity, Plasticity, Viscoelastic deformation, Mechanical probe.

1 Introduction

The relationship of indentation load (P) with depth (h) (that is the curve (P - h curve)) during loading/unloading cycles gives all the information on the microscopic processes and mechanisms of surface deformation and failure [1,2]. In brittle ceramics, the loading curve yields elastic/plastic deformation parameters, and the unloading curve has been utilized for estimating elastic parameters [3–18]. The total area of the hysteresis loop enclosed by a P - h curve for an indentation loading/unloading cycle, that is the external work consumed to create an indentation impression, has also been used to provide energy-derived elastic/plastic parameters [1,6,10,12–14,17].

The relationship between the load P and the size d (chordal diameter) of a remaining impression, for spherical indenters, has been expressed by several empirical relationships. The first, referred to as Meyer's law, states $P = kd^n$, where k and n are constants for the material under examination [19]. The value of n generally lies between 2.0 and 2.5. For fully work-hardened metals, it is close to 2.0, and has a value near 2.5 for fully annealed metals. Meyer found, for an extensive series of spherical indenters with various diameters D that the index n was almost independent of D , but that k decreases with increasing D . He finally derived a simple empirical

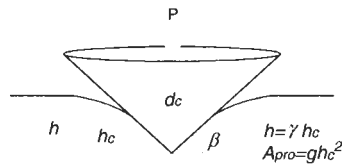


Fig. 1. In-surface profile and geometrical parameters for conical indentation at the load of P .

relation of $P/d^2 = f(d/D)$, where $f(d/D)$ is a characteristic material function, and then concluded that P/d^2 must be constant for “geometrically similar” impressions with a constant of d/D (the principle of geometrical similarity). This principle, then, leads to a universal expression that the Meyer hardness H_M (the “apparent” mean contact pressure defined by the ratio of the load P to the projected area $A_{\text{pro}} (\equiv \pi d^2/4)$ of residual “impression”, i.e., $H_M = P/A_{\text{pro}} = 4P/\pi d^2$) is a constant for geometrically similar impressions, being independent of indentation loads applied [19].

Because of the geometrical similitude of an indenter, the apparent mean pressure (i.e. the Meyer hardness) expressed in terms of the in-surface diameter d of the conical “impression”, $H_M = 4P/\pi d^2$, will also be a constant, independent of indentation loads. The contact depth $h_c(P)$ and the diameter $d_c(P)$ of the contact circle of the indenter (see Fig. 1) at the load P is related to $d_c = 2h_c \cot\beta$ using the inclined face angle β of the conical indenter. This consideration on the depth/diameter relationship combined with the principle of geometrical similarity suggests the quadratic P - h relation of $P = (\pi \cot^2\beta/\gamma^2)h^2 \cdot \langle p \rangle$, where the “true” mean pressure $\langle p \rangle$ is defined by $\langle p \rangle = 4P/\pi d_c^2$. The geometrical factor γ for surface deformation is defined by $h = \gamma h_c$, as shown in Fig. 1 [5,12].

The diamond pyramidal indenters with geometrical similitude include Vickers-, Berkovich-, and Knoop-indenters. Because of the geometrical similitude, the projected area $A_{\text{pro}}(h_c)$ at the contact depth h_c of the respective indenters is easily related to h_c by $A_{\text{pro}}(h_c) = g \cdot h_c^2$, where g is the geometrical factor of the indenter, details of which are in Section 3.1. Accordingly, the P - h relationship for geometrically similar indentations is formulated in terms of the true mean pressure $\langle p \rangle (\equiv P/A_{\text{pro}}(h_c))$, as $P = \langle p \rangle (g/\gamma^2)h^2$. The conical indenter addressed above, by way of example, has a g -factor of $\pi \cot^2\beta$.

The preceding considerations of the P - h curve suggest a simple quadratic relation between P and h , i.e. $P \propto h^2$, provided that Meyer’s principle for geometrical similarity universally dictates the indented surface deformation. In other words, whenever the true mean pressure $\langle p \rangle$ is independent of h , there exists a quadratic P - h relationship during indentation loading. The well-known quadratic P - h relation of the Sneddon theory [20] for conical indentation on a perfectly elastic body encourages the application of the quadratic P - h relationship to materials ranging from being perfectly elastic to being perfectly plastic. Loubet et al. [6] first reviewed the experimental studies of P - h curves of elastic/plastic materials, and concluded that the quadratic experimental relation of $P \propto h^2$, during loading for point indenters, applied to various metallic

materials. Stilwell and Tabor [3] experimentally and theoretically examined the (load P vs. elastic recovery h_c)-relationships of metals during unloading for conical indenters with the semi-apical angles of 68° and 45° (i.e., the inclined face angle β of 22° and 45° , respectively, in Fig. 1). Sakai [12] also found the quadratic proportionality of $P \propto h_c^2$, and successfully applied it to the Vickers indentation unloading curves of various types of brittle to ductile materials.

The time-dependent indentation tests have exclusively been conducted using a constant indentation load, referred to as the “indentation creep test”. Douglas et al. [21] conducted indentation creep tests of viscous materials (molten inorganic glasses) using of a spherical indenter. They used the linear relation between the time t and the indentation depth $h^{2/3}$ to estimate the shear viscosity of the glasses indented. General theories for the viscoelastic constitutive equation of a spherical indenter are accredited to Radok et al. [22] and Lee and Radok [23]. They used the fact that the Laplace transform of a linear viscoelastic constitutive equation results in an elastic formula, and then made the Laplace transform inversion of the elastic Hertz solution for spherical indentation to gain a viscoelastic solution.

This chapter systematically addresses the elastic, plastic, elastoplastic, and viscoelastic surface deformations for pyramidal indenters. The contact mechanics for pyramidal indentation provides a sound basis of efficient mechanical probes for micro-/nano-characterization, in particular, of extremely small-size test materials and thin films coated onto a substrate. Applications of the contact mechanics to carbon-related materials will also be demonstrated.

2 Theoretical Considerations

2.1 Representative Stress and Strain

A conical/pyramidal rigid contact is accommodated over the contact in elastic, plastic, elastoplastic, viscous, and/or viscoelastic manner(s) to avert a stress singularity. The contact stresses are highly concentrated close to the contact, and decrease rapidly in intensity with distance from the contact region. In spite of such a complicated stress/strain field around the impression, Meyer’s principle of geometrical similarity suggests the presence of the representative stress $\bar{\sigma}$ and the strain $\bar{\epsilon}$ which express properly the mechanical field at the representative region of indented subsurface, meaning that geometrically similar indentations produce similar stress/strain distributions around the impression. The mean contact pressure, which is defined by the ratio of indentation load P to the projected area $A_{\text{pro}}(h_c)$ at the contact depth h_c , has been utilized as the representative stress $\bar{\sigma}$:

$$\bar{\sigma} = \frac{P}{A_{\text{pro}}(h_c)} \quad (1)$$

The representative strain in its infinitesimal formula for conical/pyramid indentation may be defined by:

$$d\bar{\epsilon} = c \cdot \frac{dh}{h} \quad (2)$$

in terms of the infinitesimal penetration depth dh . In Eq. (2), the front factor c is a constant dependent on the geometry of the indenter.

Consider a cone/pyramid indentation on a surface of ideally elastic body with the Hookean constitutive equation of

$$\bar{\sigma} = E' \bar{\epsilon} \quad (3)$$

where E' is the elastic modulus defined by $E/(1 - \nu^2)$ using Young's modulus E and Poisson's ratio ν . Substituting Eqs. (1) and (2) into Eq. (3) leads to a simple and straightforward derivation of Sneddon's elastic solution [20] for a conical indenter with the inclined face angle β (see Fig. 1):

$$P = \frac{E'}{2} \tan \beta \frac{g}{\gamma_c^2} h^2 \quad (4)$$

In Eq. (4), use has been made of the relation of $c = \tan \beta$ for the frontal factor c of Eq. (2) to conform the present derived relation to Sneddon's solution. The geometrical factor for "elastic" surface deformation γ_c (the γ -factor defined as $h = \gamma h_c$ in Fig. 1) is $\pi/2$ (Love's solution) [2].

In contrast to elastic indentation, a perfectly plastic contact in conical/pyramidal indentation defines the "true" indentation hardness H as a size- and geometry-invariant material parameter for plasticity [12,16,17];

$$\bar{\sigma} = H \quad (5)$$

being similar to the yield stress Y for uniaxial loading of a perfectly plastic material. Accordingly, Eq. (1) combined with Eq. (5) results in the following quadratic P - h relation for a perfectly plastic body [12,16,17];

$$P = \frac{gH}{\gamma_p^2} h^2 \quad (6)$$

where the geometrical factor γ for ideally plastic surface deformation is denoted by γ_p .

2.2 Time-Independent Regime

2.2.1 Elastic, Plastic, and Elastoplastic Indentations

According to the preceding arguments, the P - h relationships of elastic and plastic contacts are, respectively, recast into the following quadratic formulae:

$$P_e = k_e h_e^2 \quad (7a)$$

for elastic contact with the relation of

$$k_e = \frac{E'}{2} \tan \beta \cdot \frac{g}{\gamma_c^2} \quad (7b)$$

and

$$P_p = k_p h_p^2 \quad (8a)$$

for the plastic contact with the relation of

$$k_p = \frac{gH}{\gamma_p^2} \quad (8b)$$

In Eqs. (7a) and (8a), P_e and h_e , and P_p and h_p are the indentation load and its adjoin depth for elastic or plastic contact, respectively.

Consider a simple model for an elastoplastic body in which a purely elastic component is connected to a purely plastic component in series in a sense of the Maxwell combination [12,16,17]. The elastic component is characterized by the elastic modulus E' and the plastic component by the “true hardness” H . The nominal indentation load P and the depth h of this elastoplastic model material then are expressed by $P = P_e = P_p$ and $h = h_e + h_p$ due to the Maxwell combination of the elastic and plastic components. The resultant constitutive relationship for a conical/pyramidal indentation along the loading path is again given by the following quadratic expression:

$$P = k_1 h^2 \quad (9)$$

with the frontal factor k_1 in terms of the elastic measure of E' and the plastic measure of H , being as follows:

$$k_1 = \frac{gH}{(1 + \sqrt{2/\tan \beta} \sqrt{H/E'})^2} \quad (10)$$

where the subscript “1” of k_1 indicates “loading”. In Eq. (10), use has been made of the compatibility relation of $\gamma_c \equiv \gamma_p \approx 1.0$ between the elastic and plastic geometrical factors γ_c and γ_p , for both the elastic and the plastic model components combine in a serial manner to produce a “single” elastoplastic surface profile of impression.

2.2.2 Meyer Hardness

The Meyer hardness H_M may be considered to be an efficient and practical parameter for mechanical characterization of engineering materials including polymers, metals

and ceramics. Hardness measurements quickly yield quantitative information on the elastic, plastic, viscous, and fracture properties of isotropic/anisotropic materials. However, because of the multitude of relationships between the Meyer hardness and these mechanical properties, some of which result from completely independent physical processes and mechanisms, hardness testing has been considered among the most maligned of physical measurements. Besides the simple definition of Meyer hardness as a “mean contact pressure”, it has no sound physical basis.

The Meyer principle of geometrical similarity combined with the definition of the Meyer hardness H_M provides the following formula which expresses the Meyer hardness in terms of the loading parameter k_1 of Eq. (9) [16];

$$H_M = \frac{\gamma_1^2}{g} \cdot k_1 \quad (11)$$

The geometrical factor for indentation surface deformation γ , as depicted in Fig. 1, is defined by $h = \gamma_1 h_c$, where the subscript 1 specifies “loading”. The empirical correlation between the observed H_M and k_1 in our previous work resulted in $\gamma_1 = 0.89 \pm 0.08$ averaged over several brittle materials and three different types of the indenter’s geometry (Vickers, Berkovich and Knoop) [16]. A similar result of $\gamma_1 = 0.91 \pm 0.08$ was reported in the literature [5]. Combining Eq. (10) with Eq. (11) enables the Meyer hardness to be expressed in terms of E' , H , and the inclined face angle β of indenter:

$$H_M = \frac{H}{[1 + \sqrt{2/\tan\beta} \cdot \sqrt{H/E'}]^2} \quad (12)$$

where an approximation of $\gamma_1 \approx 1.0$ is used for simplicity. This approximation does not cause difficulties in the following considerations of the physical insight into the Meyer hardness. As seen in Eq. (12), the Meyer hardness, even for the present simple model, exhibits somewhat complicated dependence on the plastic parameter H , elastic parameter E , and the indenter’s geometry β , meaning that H_M is by no means a geometry-invariant material characteristic parameter.

2.2.3 Energy-derived Hardness Parameters

A schematic for the hysteresis loops associated with an indentation loading/unloading cycle is shown in Fig. 2 for (a) purely elastic, (b) purely plastic, and (c) elastoplastic materials. The total energy U_t required for indenting a material to the peak load P_{\max} , i.e., the externally applied work to create an indentation impression at P_{\max} , is given by the integral of the indentation load P with respect to the adjoind penetration depth h along the loading path, i.e., $U_t = \int_0^{h_{\max}} Pdh$, and then [17]:

$$U_t = \frac{1}{3} k_1 h_{\max}^3 \quad (13)$$

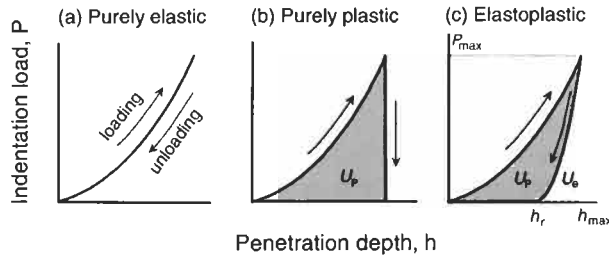


Fig. 2. Conical or pyramidal indentation load P vs. penetration depth h hystereses during a loading and unloading cycle for (a) purely elastic, (b) purely plastic, and (c) elastoplastic materials.

The elastic energy U_c (see Fig. 2c) released during unloading is expressed by the integral of P with respect to h along the unloading path, i.e., $U_c = \int_{h_r}^{h_{\max}} P dh$, resulting in

$$U_c = \frac{1}{3} k_2 h_{\max}^3 (1 - \xi_r)^3 \quad (14)$$

where h_r stands for the residual depth of penetration after complete unloading (see Fig. 2c). The empirical expression of $P = k_2(h - h_r)^2$ is *a priori* assumed in Eq. (14). The relative residual depth ξ_r is defined by $\xi_r = h_r/h_{\max}$. Accordingly, the hysteresis loop energy U_p (see Figs. 2b and 2c) defined as the area enclosed with the loading/unloading paths is given by

$$U_p (\equiv U_t - U_c) = \frac{1}{3} k_1 h_{\max}^3 \cdot \xi_r \quad (15)$$

where use has been made of the compatibility relation of $\xi_r = 1 - \sqrt{k_1/k_2}$. This loop energy U_p is consumed as an energy dissipation for creating a residual impression. These energy-based considerations lead to several important physical insights into the indentation hardness parameters [12,13,17], as demonstrated below.

A. Indentation ductility index, D

The present author has defined the indentation ductility index D in terms of U_p and U_t , as follows:

$$D = \frac{U_p}{U_t} \quad (16)$$

namely, as the ratio of the consumed energy for creating the residual impression to the total work at P_{\max} . It has been confirmed experimentally that D is independent of P_{\max} and h_{\max} [13]. D must be 1.0 for a purely plastic (purely ductile) body without

elastic recovery during unloading (see Fig. 2b), and 0.0 for a purely elastic body exhibiting a complete unloading recovery in an elastic manner along its preceding “loading path” (see Fig. 2a). The author has successfully used the index D combined with the energy fracture toughness, K_{Ic}^2/E' (K_{Ic} : fracture toughness in mode I failure), in order to examine the machinability and the machining induced damage of engineering materials [13].

Combining Eqs. (13) and (15) results in a simple relation of $D = \xi_r$, namely D simply expresses the relative residual depth ξ_r . Detailed considerations of the dependence of D on E' , H , and the geometry of the indenter were made in the literature [17].

B. Work-of-indentation, W_1

The ‘work-of-indentation’, W_1 , is defined by the present author as the work required to create a unit volume of residual impression [12,13,17]:

$$W_1 = \frac{U_p}{V_r} \quad (17)$$

where V_r is the total volume of residual impression after complete unloading, and is approximated by

$$V_r \approx \frac{1}{3} \frac{g}{\gamma_i^2} h_{\max}^3 \cdot \xi_r \quad (18)$$

In the derivation of Eq. (18), the surfaces and edges of pyramidal impressions are assumed to be straight, and the elastic recovery of the in-surface chordal dimensions is ignored [3,5,12]. It is worthy of note that the unit of W_1 [$J m^{-3}$] is equivalent to the unit of Meyer hardness [$N m^{-2}$], implying an intimate relation between W_1 and H_M , and actually resulting in

$$W_1 \approx H_M \quad (19)$$

Accordingly, it can be concluded that *the Meyer hardness is the elastic/plastic work for creating a unit volume of residual indentation impression.*

C. True hardness, H

Upon rewriting Eq. (15) in terms of P_{\max} instead of h_{\max} , the relation between the hysteresis loop energy U_p and P_{\max} is as follows:

$$U_p = \frac{1}{3\sqrt{g}} \cdot \frac{1}{\sqrt{H}} P_{\max}^{3/2} \quad (20)$$

for the present elastoplastic model material. Equation (20) was first derived by the present author to estimate the true hardness H from the loop energy U_p by the use of an observed linear relationship between U_p and $P_{\max}^{3/2}$ [12].

The true hardness H is a characteristic material property, used as a measure of plasticity, and defined as the consumed energy to create a unit volume of purely “plastic” impression. As a matter of fact, in the extreme of plastic (ductile) indentation, i.e., the extreme of H/E' to 0 or the indentation ductility D to 1.0, the work-of-indentation affords the true hardness:

$$\lim_{H/E' \rightarrow 0} W_I \text{ (or } \lim_{D \rightarrow 1} W_I) = H \quad (21)$$

2.3 Time-Dependent Regime – Viscoelastic indentation [18]

Consider now the case where a given strain $\bar{\epsilon}(t)$ as a function of time t is applied to a linear viscoelastic material. Good use can be made of the relaxation modulus $E(t)$ for this viscoelastic material instead of using the Young’s modulus E for elastic material, if the applied strain $\bar{\epsilon}(t)$ is a succession of infinitesimal steps $d\bar{\epsilon}(t)$. Consider one such step at time t' indicated as $d\bar{\epsilon}(t')$. The stress increment $d\bar{\sigma}(t)$ is, thus, obtained by using the relaxation modulus with the time duration $(t-t')$:

$$d\bar{\sigma}(t) = \frac{1}{1-\nu^2} E(t-t') d\bar{\epsilon}(t') \quad (22)$$

Substituting the representative stress (Eq. (1)) and the representative strain (Eq. (2)) with $c = \tan\beta$ into Eq. (22), and integrating the resultant equation with respect to t' in hereditary manner from $t' = 0$ to $t' = t$, the induced indentation load $P(t)$ at time t for an arbitrary applied indentation depth history $h(t')$ is given as [18]

$$P(t) = \frac{gc}{2\gamma^2} \frac{1}{1-\nu^2} \int_0^t E(t-t') \left[\frac{dh^2(t')}{dt'} \right] dt' \quad (23)$$

There is an *a priori* assumption in Eqs. (22) and (23) that the Poisson ratio ν of this viscoelastic material is independent of time t' . Equation (23) is also straightforwardly derived by simply replacing E with $E(t-t')$ in the elastic solution (Eq. (4)), and making a hereditary integral. The complementary expression for Eq. (23) is given in terms of the creep compliance function $D(t)$, as follows [18]:

$$h^2(t) = \frac{2\gamma^2(1-\nu^2)}{gc} \int_0^t D(t-t') \left[\frac{dP(t')}{dt'} \right] dt' \quad (24)$$

Upon using Eq. (23), the indentation made with a constant rate of penetration ν_0 , i.e., $h(t') = \nu_0 t'$, results in the following viscoelastic constitutive equation [18]:

$$P(t) = \frac{gc}{\gamma^2} \frac{v_0^2}{1-v^2} \int_0^t E(t-t')t' dt' \quad (25)$$

The indentation load $P(t)$ is proportional to the square of the penetration rate v_0 . A very important corollary of Eq. (25), enabling the determination of the relaxation modulus $E(t)$ from the observed $P(t)$, is derived by differentiating Eq. (25) two times with respect to t [18]:

$$E(t) = \frac{\gamma^2}{gc} \frac{1-v^2}{v_0^2} \frac{d^2 P(t)}{dt^2} \quad (26)$$

Accordingly, the indentation with a constant rate of penetration will provide an efficient rheological microprobe to the study of viscoelastic surface deformation, as actually seen in the following sections.

The indentation creep test with a constant load of indentation P_0 , i.e., the loading history of $P(t) = P_0 H(t)$ ($H(t)$: Heaviside step function) applied to Eq. (24) leads to the following creep formula [18]:

$$h^2(t) = \frac{2\gamma^2(1-v^2)}{gc} P_0 \cdot D(t) \quad (27)$$

The experimental measurement of the indentation depth $h^2(t)$ as a function of time, therefore, easily provides the creep function $D(t)$, that is, the complement of the relaxation modulus $E(t)$ in linear viscoelastic regime. Instead of applying a constant load to a conical/pyramidal indenter, the application of a fixed indentation depth h_0 , i.e., $h(t) = h_0 H(t)$ to Eq. (23) results in the following load relaxation [18]:

$$P(t) = \frac{gc}{2\gamma^2} \frac{h_0^2}{1-v^2} E(t) \quad (28)$$

leading to an easy estimate of the relaxation modulus $E(t)$ in terms of the load relaxation $P(t)$ observed in a fixed depth indentation test.

3 Experimental Details

3.1 Pyramidal Indenters [16]

3.1.1 Vickers Indenter

The Vickers indenter with its geometrical parameters is depicted in Fig. 3(a). The apex (the diagonal face-to-face angle, $2\alpha_v$) was designed to be 136° because this is the angle subtended by the tangents of a Brinell sphere when $d/D = 0.375$, the most

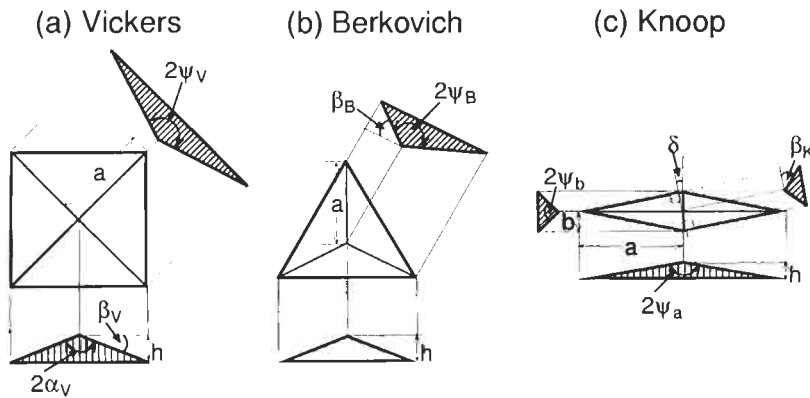


Fig. 3. Geometrical parameters for (a) Vickers, (b) Berkovich, and (c) Knoop indenters.

recommended ratio for Brinell hardness testing [1]. The inclined face angle $\beta_v (\equiv (180^\circ - 2\alpha_v)/2)$ (see Fig. 3a), therefore, is 22.0° . The diagonal edge-to-edge angle $2\psi_v$, which is related to β_v through $\tan\beta_v = \sqrt{2}\cot\psi_v$, is 148.1° . The semi-diagonal length a is given by $(\sqrt{2}/\tan\beta_v)h$, and the projected area $A_{\text{pro}}(h)$ is expressed by $A_{\text{pro}}(h) = (4/\tan^2\beta_v)h^2$. Accordingly, from the definition of the geometrical factor g made in Section 1, $g = 4/\tan^2\beta_v = 24.5$ for the Vickers indenter.

3.1.2 Berkovich Indenter

The geometry of this indenter is illustrated in Fig. 3b. The Berkovich geometry is easier to fabricate with a sharp tip than that for the Vickers indenter. This is the main reason why the Berkovich indenter is more widely utilized in depth-sensing “nano”-indentation systems than is the Vickers indenter. The Berkovich indenter was designed to provide the same area to depth relationship, i.e., the same g -factor as has the Vickers indenter. Subsequently, the following relationships appear: the inclined face angle $\beta_B = 24.7^\circ$ (see Fig. 3b), the apex angle $\psi_B = 77.1^\circ$, the projected edge length $a = (2/\tan\beta_B)h$, and $g = 3\sqrt{3}/\tan^2\beta_B = 24.5$.

3.1.3 Knoop Indenter

This indenter, as shown in Fig. 3c, has the apical angles $2\psi_a (= 172.5^\circ)$ and $2\psi_b (= 130^\circ)$ subtended by the longer and shorter edges $2a$ and $2b$, respectively. The impression has the shape of a lozenge, in which the longer diagonal ($2a (= 2\tan\psi_a \cdot h)$) is about seven times ($a/b = 7.11$) as large as the shorter diagonal ($2b (= 2\tan\psi_b \cdot h)$), while the Vickers and Berkovich indenters form regular pyramidal impressions, where all the lateral edges are of equal length. The angle $\delta = 8.00^\circ$, inclined face angle $\beta_k = 25.2^\circ$, and the g -factor is given by $g = 2\tan\psi_a \cdot \tan\psi_b (= 2[(1 + \tan^2\delta) / \tan\delta](1/\tan^2\beta_k)) = 65.4$. This g -value, about 2.7 times larger than those of Vickers and

Berkovich, means that the Knoop indenter is more blunt than the other indenters. Hence, the Knoop indenter not only gives a shallower impression for the same load, but also induces minor indentation surface cracks, a characteristic of importance in the microhardness testing of brittle materials and thin films.

3.2 Instrumented Test System

3.2.1 Elastic Compliance of Test System

The depth of indentation h_{\max} at the peak indentation load P_{\max} ordinarily ranges from 5 to 100 μm for micro-indentation systems, while the h_{\max} -values for nano-indentation testing are ordinarily from 10 to 1000 nm. The elastic recovery of the depth at the tip of impression during unloading is, roughly speaking, about a half of h_{\max} for brittle ceramics [10,12–16]. The displacement gauge for sensing the indentation depth, therefore, must be operated with extremely high resolution within 0.1 μm for the former and 1 nm for the latter.

In such indentation tests, which require the displacement detection on a micro- or nano-scale, the displacement and deformation of elastic surroundings, such as the load frame, load train, load cell, test specimen holder/stage, etc., in addition to irreversible contact clearances at mechanical joints of the load frame and those between the test specimen and its holder/stage, even if these undesirable deformations and clearances are extremely small, all lead to crucial difficulties in determining reliable indentation depth and then to unacceptable uncertainties in the measurements.

Figures 4a and 4b typify the indentation test systems with different depth-sensing configurations: (a) the displacement gauge is mounted on the test frame, and senses the motion of the load train attached to the diamond indenter (see Fig. 4a). Systems of this type include most of the commercially available indentation test systems [Nano-indenter (Nano Instruments Inc., Knoxville, TN, USA), UMIS-2000 (CSIRO,

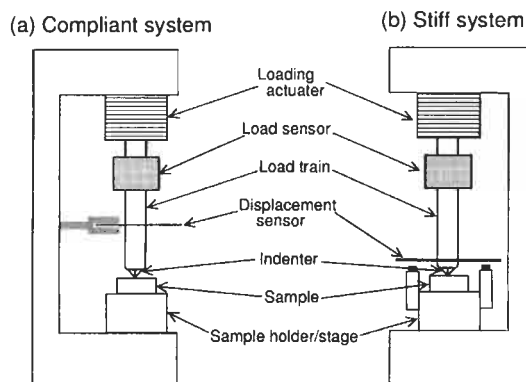


Fig. 4. Schematics of instrumented indentation test setup for (a) a compliant, and (b) a stiff system.

Lindfield, Australia), DUH-200, DUH-50 (Shimazu Inc., Kyoto, Japan), MHA-400 (NEC Inc., Tokyo, Japan), Nano Test 200 (Micro Materials, Clywd, UK)]. (b) The displacement gauge is mounted on the holder/stage of test specimen and senses the “relative” displacement of load train immediately above the indenter tip (see Fig. 4b). The present author has developed indentation systems of this type [12–18].

The observed indentation depth, h_{obs} , in the former system (Fig. 4a), and referred to as a “compliant system”, inevitably and significantly includes undesirable contributions from elastic compliance of the surroundings as well as contact clearances. However, this system has the advantage of easily monitoring indentation behavior at elevated temperatures, in hostile environments, etc. The observed depth h_{obs} is related to the penetration depth h by $h_{\text{obs}} = h + \Delta h$, where Δh is the elastic and/or irreversible depth (displacement) which mainly stems from undesirable load frame compliance and mechanical contact clearances. A precise calibration for Δh must be made prior to indentation testing.

In contrast, the latter system given in Fig. 4b, referred to as the “stiff system” minimizes or eliminates the contribution of Δh . Note that the displacement measured by this system includes only the depth of penetration and the elastic deformation of diamond indenter/its mount, provided that the contact clearance between the specimen and its holder is carefully negated.

3.2.2 Indentation Test [12–18]

Two different types of indentation tests are recommended: (1) indentation loading/unloading tests with constant rate of penetration both in time-dependent and time-independent regimes, and (2) indentation creep tests with constant indentation load for time-dependent indentation. In the former test system as shown in Fig. 5a, a constant rate of penetration is applied on an indenter through a very stiff load train by the use of a conventional displacement-controlled test machine. The load of

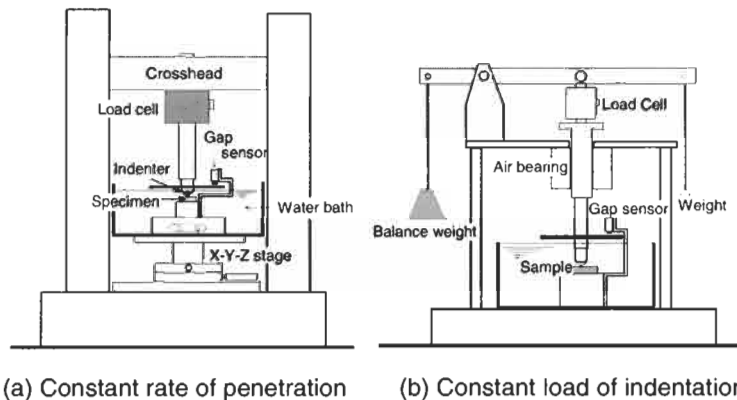


Fig. 5. Instrumented indentation test systems for (a) constant rate of penetration, and (b) constant load of indentation.

indentation was monitored by a load cell, and the adjoined penetration depth by a gap detector. The latter test system of constant loading (indentation creep) is depicted in Fig. 5b. A constant external load was applied to the indenter by an appropriate weight via a mechanical lever. The apparatus must be furnished with an air bearing which controls the applied load with the accuracy of ± 0.01 N. A load cell connected in series to the load train is utilized to confirm that the applied load is kept constant during a creep test.

The temperature control system used both for the constant penetration rate and for the constant load tests comprises a water bath, circulator, and a temperature-controlling unit. The temperature of circulating water is controlled within $\pm 0.05^\circ\text{C}$. This temperature controlling system is very essential in the “time-dependent” regime of indentation. In the “time-independent” regime, however, due to the indentation behavior that is insensitive to temperature, indentation tests can always be conducted at ambient temperatures without a temperature controlling system.

4 Application to Carbon-related Materials

4.1 *Elastoplastic Deformation of Heat-Treated Carbons [24]*

The form of the stress vs. strain curves (S–S curves) of various types of carbon materials has been studied in tensile, compressive, and flexural fields. Most of these S–S curves are nonlinear (inelastic), and have a permanent residual strain after complete unloading [25]. The apparent elastic moduli defined by the tangent of loading S–S curves at respective strain values are always greater at small strains than those at large strains, demonstrating “work-hardening”. However, the unloading S–S relationship is rather linear, resulting in a hysteresis loop during a loading/unloading cycle. In addition, the subsequent reloading curve does not coincide with the foregoing unloading curve, yielding another hysteresis loop. It has also been noted that pre-stressing alters the apparent elastic modulus at small strains; pre-stressing in compression reduces the elastic modulus [25]. Increased heat-treatment temperatures of carbon materials, in general, enhance these complicated nonlinear and inelastic behaviors [24].

In this section, a pyramidal (tetragonal Vickers) indentation technique is applied to examine the elastoplastic surface deformation of carbon materials heat-treated at various temperatures ranging from 880 to 2600°C. The elasticity and the plasticity of carbon materials will, then, be related to the degree of graphitization in a quantitative manner.

4.1.1 *Test Materials*

The degree of graphitization is controlled by the heat-treatment temperature (HTT) of an isotropic carbon. This starting carbon material was treated at 880°C by baking a molded green body (about 100 mm in diameter and 100 mm in thickness) made by

Table 1
Structural parameters of heat-treated carbons

| Heat-treated carbon | HTT (°C) | Bulk density (g/cm ³) | $d_{(002)}$ (nm) | $L_c(002)$ (nm) | $L_a(110)$ (nm) | P_1 |
|---------------------|-------------|--------------------------------------|---------------------|--------------------|--------------------|-------|
| S-880 | 880 | 1.67 | 0.3497 | 3.3 | – | – |
| S-1000 | 1000 | 1.69 | 0.3493 | 3.4 | – | – |
| S-1550 | 1550 | 1.75 | 0.3446 | 7.7 | – | – |
| S-1800 | 1800 | 1.75 | 0.3431 | 18.2 | – | 0.10 |
| S-2300 | 2300 | 1.77 | 0.3376 | 41.9 | 55.1 | 0.45 |
| S-2600 | 2600 | 1.78 | 0.3371 | 49.5 | 67.4 | 0.53 |

cold-isostatic pressing fine-grained coal-tar cokes (average grain size of about 5 μm) with coal-tar pitch binder. A carbon rod (about 30 mm in diameter and 100 mm in length) was machined out of 15 mm thickness. Each carbon disk was then heat-treated in an electric furnace with argon gas at temperatures of 1000, 1550, 1800, 2300, and 2600°C; heated to the required temperature during 1.0 h, held at the final temperature for 1.0 h, and then cooled to room temperature. These carbon specimens are named S-880, S-1000, S-1550, S-1800, S-2300, and S-2600. Some of the structural parameters of these heat-treated carbons are listed in Table 1. The graphitic inter-layer spacing $d_{(002)}$ was determined from the 002 and 004 X-ray diffraction lines. The mean thickness $L_c(002)$ and the diameter $L_a(110)$ of graphitic crystallites are, respectively, estimated from the 002 and 110 diffraction lines. The Warren's probability P_1 for finding the AB-stacking of graphitic layers was determined from the Fourier analysis of the asymmetric 10 and 11 diffraction lines.

One flat face of each disk specimen was finished to a mirror surface using alumina abrasives (mean grain size of about 1 μm) prior to indentation tests.

4.1.2. Indentation Test

The test setup of instrumented indentation apparatus is depicted in Fig. 5a without using the water bath. Indentation loads were monitored with a precision of ± 0.01 N by a load cell (TCLZ-100KA, Tokyo Sokki Co., Ltd.) mounted in a very stiff load train. The relative displacement between the Vickers indenter and the specimen surface was measured with the precision of ± 0.1 μm by an eddy-current extensometer (VS-011, Ono Sokki, Co., Ltd.) mounted on the test specimen holder. The extensometer monitors the relative displacement of a thin stainless steel disk attached to the stiff load train immediately above the indenter. This instrumental setup, to detect the depth of indentation penetration via measuring the “relative” displacement, is mandatory to eliminate undesirable deformations/clearances of surrounding fixtures and the load frame of the test system. Details of the reproducibility and the reliability of the instrumented indentation apparatus used in this study are reported in the literature [16].

All of the indentation loading/unloading tests were conducted using a conventional displacement-controlled test machine (Sanwa Kiki Co., Ltd) with a constant crosshead speed of 0.01 mm min^{-1} . The applied peak load of indentation was 19.6 N (20.0 kgf) for all the test specimens. Five separate indentation loading/unloading tests were performed for each specimen at different locations of the polished surface to ensure the reproducibility/reliability of measurement and consistent indentation behavior. The outputs from the load cell and the extensometer were recorded in a digital data logger (Memory Hi-Corder 8851, Hioki Co., Ltd.), as well as an analogue X-Y recorder (WX4000, Graphtec Co. Ltd.) connected in parallel to the digital logger.

4.1.3 Test Results and Discussion [24]

A. Crystallographic structures of the heat-treated carbons

None of the characteristic diffraction peaks or the extremely weak and diffused peaks of 004 and 110 were observed for the carbons of low HTT (S-880, S-1000, and S-1550) typifying the X-ray diffraction spectra of disordered carbons. The $L_c(002)$ -, P_1 -values (see Table 1) and the existence of a 101 diffraction peak for carbons with HTT exceeding 1800°C (S-1800, S-2300, and S-2600) confirms the presence of a transition at temperatures between 1550 and 1800°C from the disordered turbostratic to graphitic stacking of carbon layers. In contrast to these crystallographic characteristics, the bulk density and the interlayer spacing d_{102} vary rather monotonously with HTT, followed by saturation at temperatures above 2300°C .

B. Indentation P - h relationship

Examples of the Vickers indentation P - h hysteresis loops during loading to $P_{\text{max}} = 19.6 \text{ N}$ and subsequent unloading are shown in Fig. 6 for the carbon materials (S-880, S-1550, and S-2600) heat-treated at 880 , 1550 and 2600°C , respectively. The maximum penetration depth h_{max} at $P_{\text{max}} (= 19.6 \text{ N})$ progressively increases with increase in the heat-treatment temperature (HTT), indicating easier penetration, i.e., enhanced "softening" caused by an increase in HTT. The area U_p of hysteresis loop (the area enclosed with the loading and unloading P - h curves; refer to Fig. 2c), that is the external work required for the elastoplastic indentation process in a loading/unloading cycle, also progressively increases with increasing HTT.

A significant elastic recovery of impression was observed during unloading for all the carbon materials. The residual depth h_r (defined in Fig. 2) was well recognized for the test materials heat-treated at temperatures below 1550°C . However, the residual depth of impression of tested materials with HTT exceeding 1800°C was so small that the residual impression after unloading is hardly visible on the indented surface, meaning a nearly complete elastic recovery of indented surface. The elastic energy U_c released along the unloading P - h curve, i.e., the area enclosed with the unloading P - h

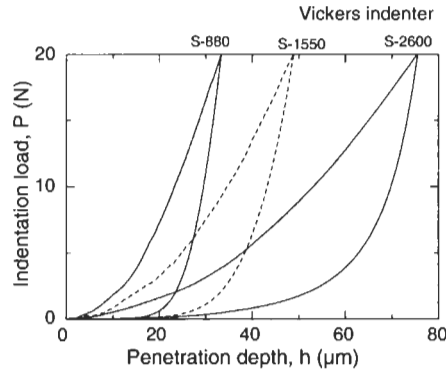


Fig. 6. Load vs. depth hystereses of Vickers indentation on carbons; S-880, S-1550, and S-2600 heat-treated, respectively, at 880°C, 1550°C, and 2600°C.

Table 2

Indentation parameters at $P_{\max} = 19.6$ N

| | h_{\max} (μm) | h_r (μm) | U_p (mJ) | U_c (mJ) | h_c (μm) | h_p (μm) | ξ_r (-) | ξ_c (-) | ξ_p (-) |
|--------|---------------------------------|----------------------------|---------------|---------------|----------------------------|----------------------------|----------------|----------------|----------------|
| S-880 | 33.3 | 10.4 | 0.135 | 0.092 | 14.2 | 19.1 | 0.31 | 0.43 | 0.57 |
| S-1000 | 40.5 | 15.1 | 0.167 | 0.122 | 13.5 | 25.0 | 0.37 | 0.33 | 0.67 |
| S-1550 | 49.2 | 10.7 | 0.187 | 0.146 | 16.5 | 32.7 | 0.22 | 0.34 | 0.66 |
| S-1800 | 52.9 | 4.3 | 0.171 | 0.192 | 17.5 | 35.4 | 0.082 | 0.33 | 0.67 |
| S-2300 | 61.6 | 5.2 | 0.248 | 0.175 | 18.4 | 43.2 | 0.085 | 0.30 | 0.70 |
| S-2600 | 75.4 | 8.9 | 0.322 | 0.172 | 19.4 | 56.0 | 0.12 | 0.26 | 0.74 |

Vickers indentation.

line and the abscissa (i.e., h -axis) of P - h diagram (see Fig. 6, and refer to Fig. 2c) is also strongly dependent on HTT. The indentation parameters, h_{\max} , h_r , ξ_r ($\equiv h_r/h_{\max}$), U_p , and U_c in Vickers indentation tests conducted at $P_{\max} = 19.6$ N are listed in Table 2.

In most of the brittle ceramics, their loading as well as unloading behaviors for pyramidal indentations (Vickers, Berkovich, and Knoop indentations) are characterized by the quadratic P - h relations; $P = k_1 h^2$ for loading and $P = k_2 (h - h_r)^2$ for unloading, as addressed in Sec. 2.2 [12-18]. The loading parameter k_1 , as defined in Eq. (10), is related to the elastic modulus E' and the true hardness h . In contrast, the unloading parameter k_2 that reflects the elastic recovery associated with unloading process is, therefore, exclusively dominated by the elastic modulus E' [17].

The P - h loading curves of all the carbon materials of different HTT conform to P vs. h^2 linear or \sqrt{P} vs. h linear relationships, as illustrated in Fig. 7. In order to confirm the reproducibility of observations, Fig. 7 plots the superposition of test results in several separate indentation tests for each carbon material. The slope of the \sqrt{P} vs. h linear line affords $\sqrt{k_1}$. The loading parameter k_1 , thus determined from the slope of

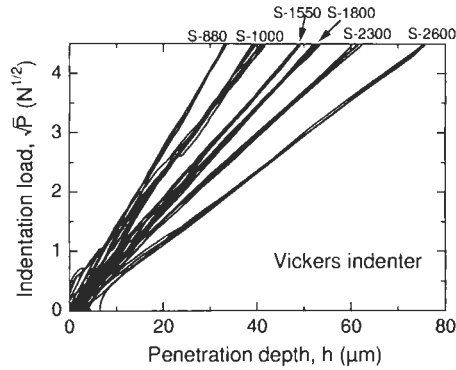


Fig. 7. \sqrt{P} vs h linear relations of Vickers indentation loading for the heat-treated carbons; S-880, S-1000, S-1550, S-1800, S-2300, and S-2600. The slope of the respective linear lines gives the loading parameter $\sqrt{k_1}$ (see Eq. (9)).

Table 3

Elastic moduli and hardness parameters (Vickers indenter)

| | Young's modulus E (GPa) | Poisson's ratio ν (-) | Loading parameter k_1 (GPa) | Meyer hardness H_M (GPa) | True hardness H (GPa) |
|--------|------------------------------|------------------------------|-------------------------------------|-------------------------------|----------------------------|
| S-880 | 19.2 | 0.17 | 17.8 | 0.73 | 2.21 |
| S-1000 | 19.1 | 0.24 | 11.1 | 0.45 | 1.02 |
| S-1550 | 13.5 | 0.25 | 8.01 | 0.33 | 0.74 |
| S-1800 | 12.0 | 0.29 | 7.03 | 0.29 | 0.64 |
| S-2300 | 11.5 | 0.23 | 5.28 | 0.22 | 0.44 |
| S-2600 | 10.8 | 0.16 | 3.65 | 0.15 | 0.27 |

the linear plot in Fig. 7, is listed in Table 3 along with Young's modulus E and Poisson's ratio ν determined with a conventional ultrasonic method.

In comparison to the loading P vs. h^2 quadratic relation, or \sqrt{P} vs. h linear relation in Fig. 7, the unloading P - h relations for all the carbon materials are by no means subject to the quadratic $P \propto (h-h_r)^2$ relationships, unlike the unloading behavior of most brittle ceramics. Partially or fully "reversible" slip of dislocations in graphitic layers may lead to such a unique unloading curve, resulting in a sizable deviation from the quadratic P vs $(h-h_r)^2$ relation, the details of which are given in the literature [24].

C. Hardness Parameters

The Meyer hardness H_M is the mean pressure defined by the ratio of indentation load P to the "projected" residual area A_{pro} of indentation impression, i.e., $H_M = P/A_{\text{pro}}$. The carbon materials examined in this work as well as those in the literature, leave

hardly visible impressions after complete unloading, due to the significant elastic recovery of penetration depth during unloading, so leading to a difficulty in determining the projected area A_{proj} , and then H_M . In order to circumvent this difficulty, an alternative expression (Eq. (11)) for H_M in terms of the loading parameter k_1 is utilized to estimate H_M . The geometrical factor g of the Vickers indenter is 24.5 ($\equiv 4/\tan^3\beta$ with the inclined face angle $\beta = 22.0^\circ$). The geometrical γ_1 -value of the surface profile of elastoplastic impression ranges from 0.9 to 1.1, being ordinarily approximated to 1.0 without any crucial ambiguities. The Meyer hardness H_M of the carbon materials for Vickers' indentation, thus estimated in Eq. (11), is listed in Table 3. The Meyer hardness is not a measure for "plasticity". It depends not only on plastic properties but also on elastic properties, as readily inferred from the E' - and H -dependent k_1 -parameter (see Eqs. (11) and (12)); the Meyer hardness decreases with the decrease in H , as well as the decrease in E' [17]. Accordingly, H_M cannot be utilized simply as a measure for plasticity.

The true hardness H , the parameter proposed by the present author, is one measure to quantitatively characterize the plasticity of materials, and is singled out by using Eq. (10) with the k_1 - and E' -values determined experimentally. The true hardness values, H , thus obtained for the present carbon materials, are listed in Table 3.

Both the elastic parameter E and the plastic parameter H monotonously decrease with the increase in HTT. It must be noted that the decrease in H -values with increasing HTT at $880^\circ\text{C} \leq \text{HTT} \leq 1000^\circ\text{C}$ is significant. Values of H at $\text{HTT} = 880^\circ\text{C}$ decrease by more than a half at $\text{HTT} = 1000^\circ\text{C}$. In contrast to the HTT-dependence of H -values at $\text{HTT} \approx 900^\circ\text{C}$, no significant change was observed for the elastic modulus E in the same range of HTT. This is then followed by a rather significant reduction of E -value in $1000^\circ\text{C} < \text{HTT} \leq 1800^\circ\text{C}$. The E -values are reduced to 3/5 in this range of HTT.

The "indentation softening" induced by decreases both in the E - and H -values with increasing HTT directly reflects on the Meyer hardness H_M , for it is prescribed by the combined deformation in elastic and plastic penetration processes. H_M experiences a sharp decrease from the value of 0.73 GPa to 0.45 GPa in $880^\circ\text{C} \leq \text{HTT} \leq 1000^\circ\text{C}$, and it then exhibits a linear decrease for $\text{HTT} > 1000^\circ\text{C}$ with increasing HTT.

D. Elastic and Plastic Deformations in Indentation Loading

In the elastoplastic regime, the total penetration depth h is represented by the sum of elastic and plastic penetration depths, h_c and h_p , i.e., $h = h_c + h_p$. Combining this additivity with the basic constitutive equations (Eqs. (7) to (10)), the normalized expressions of the relative elastic and plastic depths $\xi_c (\equiv h_c/h)$ and $\xi_p (\equiv h_p/h)$ are given in terms of E' and H , as follows [2]:

$$\xi_c \left(\equiv \frac{h_c}{h} \right) = \frac{\sqrt{2(H/E')/\tan\beta}}{1 + \sqrt{2(H/E')/\tan\beta}} \quad (29a)$$

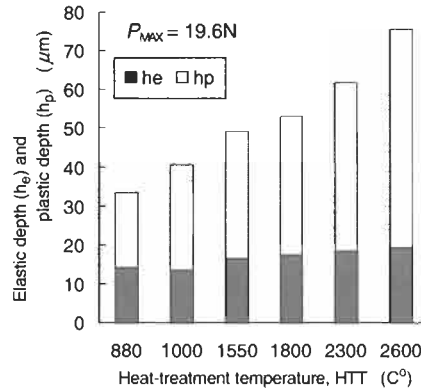


Fig. 8. Contribution of the elastic penetration h_e and the plastic penetration h_p to the total penetration of $h(= h_e + h_p)$ at the indentation load $P_{\max} = 19.6$ N on the carbon materials heat-treated at temperatures ranging from 880°C to 2600°C.

and

$$\xi_p \left(\equiv \frac{h_p}{h} \right) = \frac{1}{1 + \sqrt{2(H/E')/\tan\beta}} \quad (29b)$$

The relative depths ξ_c and ξ_p are independent of the total depth h , and so of the applied indentation load P . They are described using the characteristic material parameters E' and H , as well as the indenter's geometry β . These relative depths estimated for the carbon materials with different HTTs are listed in Table 2 where the absolute values, h_e and h_p , at an indentation load $P = 19.6$ N are also listed. Due to the "softening" enhanced by increasing HTT, both h_e and h_p significantly increase with increasing HTT. However, the contribution of the elastic penetration to the total depth h (the ratio of h_e to h , i.e., ξ_c) becomes less important with increasing in HTT, and vice versa in the plastic contribution (ξ_p), as clearly seen in Fig. 8. The plastic contribution becomes progressively significant with increasing HTT. The development of graphitic structures with increasing HTT (see Table 1) makes easier the movements (slippages) of dislocations that lie in the graphitic basal planes, and resulting in an increased importance of plastic contributions to indentation loading processes.

4.2 Viscoelastic Deformation of Coal-Tar Pitch [26]

Pitches are typical glass-forming organic materials. No crystalline phases appear even when molten pitches are cooled as slowly as possible. They form amorphous (glassy) solids below their glass transition temperature T_g . The Brownian motion of constituent molecules in pitch is largely depressed below T_g . In general, these glass-forming materials exhibit viscoelastic deformation and flow at temperatures exceeding T_g .

Their viscoelastic parameters, such as the steady-state shear viscosity η_s , creep compliance function $D(t)$, and the stress relaxation modulus $E(t)$, are intimately related to the molecular weight and its distribution, shape/configuration of constituent molecules, etc. An increase in molecular weight results in increases in the glass transition temperature, steady-state viscosity, and creep resistance [27].

It is recognized, empirically, that rheological behaviors of coal-tar pitches and crude oil residues are highly modified by halogen/halide-treatments such as adding halides or by exposure to halogen gases, etc. These chemical treatments significantly raise the glass transition temperature, softening point, and the shear viscosity of pitches, which on carbonization produce various types of hard carbons (non-graphitizable) [28].

The major objectives in this section are to demonstrate the efficiency of the indentation approach to viscoelastic studies of pitches and to examine the effect of iodine-treatment on the viscoelastic behavior of a coal-tar pitch through the quantitative analysis of Vickers indentation load-depth curves measured under various test conditions. The indentation test technique is superb as an efficient microprobe for mechanical characterizations in a hostile environment as found in the present study for iodine-treated materials. Conventional viscoelastic test apparatus face crucial difficulties at elevated temperatures in such a corrosive test environment.

4.2.1 Test Materials

Some of the properties of the initial coal-tar pitch include softening point (ring and ball method) of 101°C, toluene- and quinoline-insoluble components of 14.6 wt% and 0.6 wt% respectively, and a carbon yield of 53.3 wt% during carbonization. A molded coal-tar pitch disk (12 mm in diameter, 5 mm in height, and about 0.5 g in weight) was set in the reactor and exposed to saturated iodine vapor at 373 K (100°C). Extents of reaction with iodine were controlled by changing the soak time. Thus six different iodine-treated pitch samples (CTP-00, CTP-12, CTP-24, CTP-48, CTP-72, and CTP-96) were prepared for viscoelastic indentation testing; “CTP” indicates the coal-tar pitch used as the starting material, and the two digits after CTP represent the soaking time in hours. Accordingly, CTP-00 is the original coal-tar pitch without iodine treatment, and CTP-96 means the pitch sample was iodine-treated for 96 h. Amounts of iodine absorbed in the pitch samples were estimated from changes in weight before and after the iodine treatment. Iodine contents progressively increased with increasing soaking time. An electron probe microanalysis confirmed a uniform distribution of iodine within the respective disk-shaped samples. The microstructural details of the iodine-treated pitches are reported in the literature [28].

4.2.2 Time-dependent Indentation Tests

These disk-shaped CTP samples were mounted in an epoxide resin and cured at room temperature. The mounted specimen disks were then polished flat for the indentation

tests. The test specimen was glued onto a steel-made specimen holder using a cyanoacrylate adhesive and the holder fixed on a magnetic chuck in the indentation test apparatus.

Conducted were (1) tests for a constant rate of penetration during indentation loading/unloading, and (2) creep tests with a constant indentation load. A constant rate of penetration of $0.83 \mu\text{m/s}$ was applied on a Vickers indenter through a load train using a conventional displacement-controlled test machine, as illustrated in Fig. 5a. In the creep test, a constant load of 0.98 N was applied on a Vickers indenter via a mechanical lever furnished with an air bearing, as depicted in Fig. 5b.

The viscoelastic indentation tests included temperatures of measurement from 282.9 K (9.7°C) to 338.3 K (65.1°C) in constant rate of penetration tests, and from 312.7 K (39.5°C) to 362.4 K (89.2°C) in constant load indentation creep tests. Details of the temperature controlling system are given in Section 3.2.

4.2.3 Results

The test results of penetration depth h under a constant indentation load (P_0) of 0.98 N are shown in Fig. 9 for increasing temperature scanning at a rate of 2 K min^{-1} . The indentation load P_0 was applied to a test specimen at room temperature which is well below the glass transition temperatures of the pitches, so creating a time-independent elastoplastic impression with the penetration depth h_{cp} . This time-independent elastoplastic penetration depth h_{cp} is offset to zero in Fig. 9 in order to single out the time-dependent viscoelastic penetration which appears in the subsequent softening process along with scanning using increasing temperatures. Softening of the non-treated coal-tar pitch, CTP-00, starts at about 324 K (51°C). The temperature of softening increases with increasing in soaking time in the iodine vapor. Another important rheological feature in this temperature-scanning diagram is that the iodine

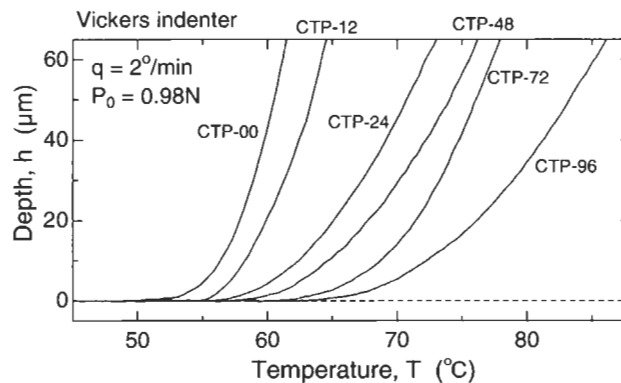


Fig. 9. Softening curves of as received and iodine-treated pitches under a constant indentation load of 0.98 N for rising temperature scanning with the rate of $q = 2^\circ/\text{min}$.

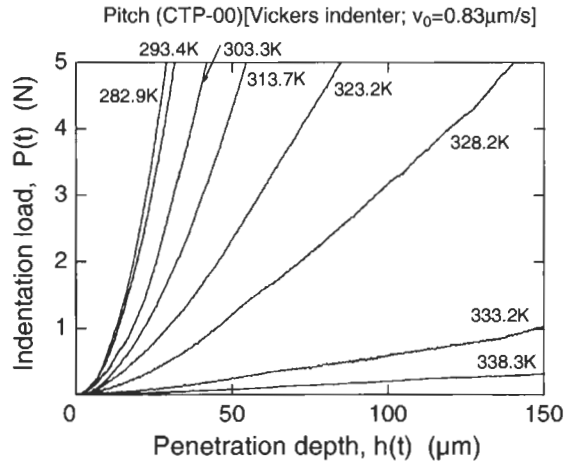


Fig. 10. Vickers indentation test results at various temperatures of measurement for a constant rate of penetration ($0.83 \mu\text{m/s}$) of the pitch as received (CTP-00).

non-treated pitch sample (CTP-00) exhibits a sharply increasing depth curve with respect to temperature scanning, whereas this increasing behavior tends to become progressively sluggish with increasing in soak time. As a matter of fact, a temperature scanning of only 5° is enough to cause a viscoelastic penetration depth of $60 \mu\text{m}$ for CTP-00, while CTP-96 requires about 20°C of temperature scanning to attain the same penetration depth.

The time (t)-dependent indentation load $P(t)$ vs. penetration depth $h(t)$ relations of CTP-00 during indentation loading in constant rate of penetration tests ($v_0 = 0.83 \mu\text{m/s}$) are shown in Fig. 10 for the temperatures of measurement. The loading P - h curve changes its functional form from quadratic ($P(t) \propto [h(t)]^2$) in the lower temperature regime to linear ($P(t) \propto h(t)$) in the higher temperature regime, indicating the transition from more elastic to more viscous behaviors with increasing temperature [18].

Some examples of the test results in constant load ($P_0 = 0.98 \text{ N}$) indentation creep tests are shown in Figs. 11a–c for CTP-00, CTP-12, and CTP-24, respectively. The penetration depth of $[h(t)]^2$ is plotted against time t on the basis of the linear viscoelastic expression (see Eq. (27)). Accordingly, these penetration depth curves in Fig. 11 straightforwardly express the creep compliance function $D(t)$. In Fig. 11, the intercept of the ordinate [the axis of penetration depth $h^2(t)$] represents an instantaneous elastoplastic penetration depth $h(0)$ immediately after the stepwise creep loading. It is seen in Fig. 11 that the iodine treatment of coal-tar pitch significantly modifies the viscoelastic behavior. However, it has no important influence on the instantaneous penetration depth $h(0)$ and hence on the instantaneous compliance $D(0)$. This fact means an insignificant effect of iodine treatment on Young's modulus E , for $D(0)$ as related to E by $E = 1/D(0)$.

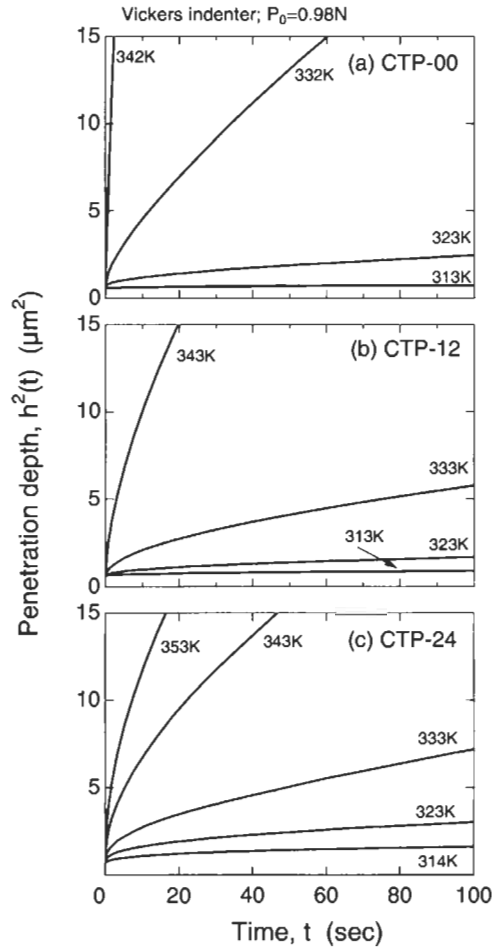


Fig. 11. Vickers indentation creeps ($P_0 = 0.98$ N) at various temperatures of measurement for (a) CTP-00, (b) CTP-12, and (c) CTP-24 pitches.

4.2.4 Discussion

A. Time-Temperature Superposition

The time (t)–temperature (T) superposition procedure for rheological functions such as creep compliance function and stress relaxation modulus is well established and accepted in simple thermorheologically materials [29,30]. These functions at different temperatures of measurement are sufficiently accurate to be superimposed and compose a master curve at an arbitrary reference temperature T_0 when shifted parallel to the $\log t$ axis. Sakai et al. [27] demonstrated in creep tests that coal-tar

itches and petroleum oil residues are thermo-rheologically simple [27]. The time-temperature superposition means that time t always appears in these rheological functions coupled with a temperature dependent characteristic relaxation (or retardation) time, say $\tau(T)$, in the dimensionless form $t/\tau(T)$. Then the shift factor a_T for superposition is defined by $\tau(T)/\tau(T_0)$ using the relaxation times $\tau(T)$ and $\tau(T_0)$ at temperature T and the reference temperature T_0 . As a familiar example, the temperature dependence of a_T has been characterized by the WLF-equation in glass-forming materials [29,30].

In thermo-rheologically simple materials, Eq. (25) allows the following superposition rule in a constant rate penetration test [18,26];

$$[P(t)/a_T^2]_T = [P(t/a_T)]_{T_0} \quad (30)$$

or

$$[P(h)/a_T^2]_T = [P(h/a_T)]_{T_0} \quad (30')$$

in which $[...]_T$ and $[...]_{T_0}$ represent the load P with respect to time t or to penetration depth h at temperature T , and at the reference temperature T_0 , respectively. Accordingly, Eqs. (30) and (30') conform to the superposition rules of time-temperature and also of penetration depth-temperature in double logarithmic plots of $\log P$ vs. $\log t$ and $\log P$ vs. $\log h$, respectively. The P - t or P - h curve measured at a temperature T in a constant rate penetration test is superposed on the curve at the reference temperature T_0 upon shifting the curve by $\log a_T$ along the $\log t$ or the $\log h$ axis due to the term of t/a_T or h/a_T , as well as adjoint shifting by $2\log a_T$ along the $\log P$ axis due to the term of $P(t)/a_T^2$ or $P(h)/a_T^2$. This procedure is, therefore, referred to as "one-two" superposition [18].

An example of "one-two" superposition applied to the P - h curves in Fig. 10 (CTP-00) is shown in Fig. 12. The respective P - h curves at different temperatures of measurement were superposed on the curve at the reference temperature of $T_0 = 323.2$ K ($\equiv 50.0^\circ\text{C}$). This process composes a single master P - h curve by shifting along the $\log h$ axis with $\log a_T$ and along the $\log P$ axis with $2\log a_T$. As seen in Fig. 12, the superposition procedure is sufficiently accurate to yield a well-defined master curve. The slope of the master curve is 2.0 for the extreme case of small penetration depth, which corresponds to a purely elastic deformation, and is 1.0 in the extreme case of large penetration depth corresponding to a purely viscous flow.

The shift factor used for the superposition in Fig. 12 is shown in Fig. 13 (open circles) as an Arrhenius plot of $\log a_T$ vs. $1/T$ relation. Because the shift factor a_T has been defined by $\tau(T)/\tau(T_0)$ in terms of the characteristic relaxation times at T and T_0 , it is also alternatively expressed as $\eta_s(T)/\eta_s(T_0)$ by use of the steady-state shear viscosity $\eta_s(T)$ at T and $\eta_s(T_0)$ at the reference temperature T_0 . Accordingly, the slope of the $\log a_T$ vs. $1/T$ linear approximation gives the activation energy ΔH_η for viscous flow of CTP-00 (open circles in Fig. 13), resulting in $\Delta H_\eta = 340$ kJ mol $^{-1}$, being similar to the reported values which were evaluated at temperatures near to the softening point [27].

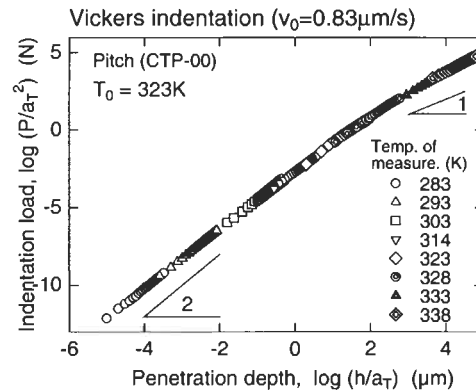


Fig. 12. P - h master curve of CTP-00 for the Vickers indentation with a constant rate of penetration ($v_0 = 0.83 \mu\text{m/s}$). The temperature dependence of shift factor a_T used in time-temperature superposition procedure (the reference temperature $T_0 = 323.2 \text{ K}$) is plotted in Fig. 13.

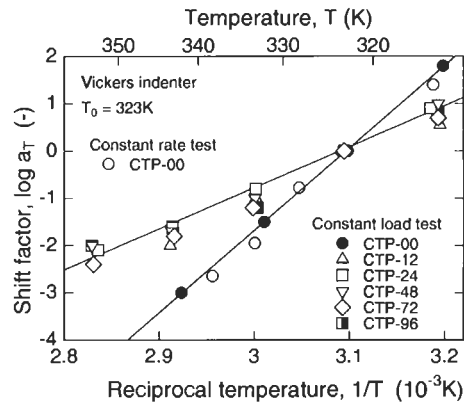


Fig. 13. Dependence of the shift factor a_T on temperature with the reference temperature T_0 of 323.2 K. The circles mark the data of CTP-00, and the noncircular symbols are for the iodine-treated pitches.

The time-temperature superposition procedure in creep curves is straightforward, and is well established [29]. An example of the superposition applied to the creep curves in Fig. 11(a) for CTP-00 is illustrated in Fig. 14 as the master creep curve at the reference temperature T_0 of 323.2 K. The master creep compliance function $D(t)$ in Fig. 14 was composed from the observed penetration depths along the $\log t$ axis using the shift factor a_T to superpose on the reference curve at $T_0 = 323.2 \text{ K}$. The superposition was satisfactorily conducted, as shown in Fig. 14. The shift factor a_T of CTP-00 used for superposition is given in Fig. 13 (closed circles) as an Arrhenius plot, demonstrating an excellent agreement between the shift factors in the indentation tests for constant rate of penetration (open circles) and for constant load creep

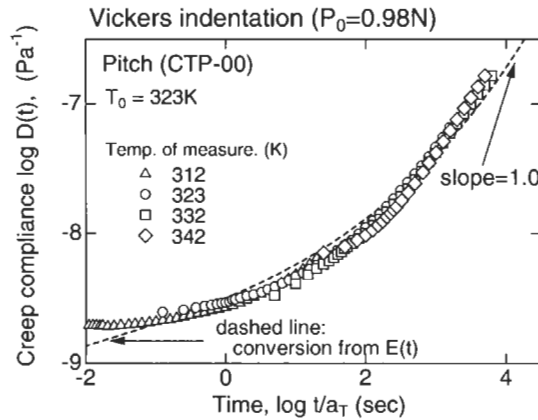


Fig. 14. Creep compliance master curve of CTP-00 composed at $T_0 = 323.2$ K. The broken line indicates the creep curve numerically converted from the stress relaxation modulus $E(t)$ shown in Fig. 15.

(closed circles). This excellent agreement confirms the self-consistency in the present theoretical as well as experimental analyses for viscoelastic indentations.

B. Dual Correlation Between $E(t)$ and $D(t)$

The stress relaxation modulus $E(t)$ is estimated in constant rate of penetration tests from the second derivative of indentation load $P(t)$ with respect to time t (see Eq. (26)), or with respect to penetration depth h in the following alternative expression [18]:

$$E(t) = \frac{\gamma^2 (1 - \nu^2)}{gc} \frac{d^2 [P(h)]}{dh^2} \quad (26')$$

The application of Eq. (26') to the master curve of CTP-00 (Fig. 12) results in the relaxation modulus $E(t)$ at 323.2 K, as shown in Fig. 15, where the extrapolated relaxation modulus to short times reaches 4.1 GPa, that is, the Young's modulus E of CTP-00 at 323.2 K, showing a satisfactory agreement with the E -value determined by the conventional ultrasonic method in a separate measurement. The relaxation modulus of CTP-00 at 323.2 K (50.0°C) exhibits a sharp fall in the terminal zone in a time of 10^4 s, this being the time required for a complete relaxation of all possible viscoelastic processes and mechanisms, and for the onset of purely viscous steady-state flow.

The application of a Laplace transform to $E(t)$ facilitate the computation of the creep compliance function $D(t)$ [18]. The Laplace-converted $D(t)$ thus estimated from $E(t)$ observed is illustrated in Fig. 14 by the broken line. An excellent coincidence of the numerically converted $D(t)$ with that observed experimentally again confirms the

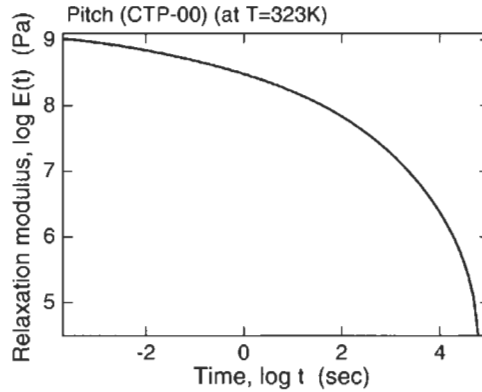


Fig. 15. Stress relaxation modulus of CTP-00 at 323.2 K.

self-consistency of the present theoretical/experimental framework for viscoelastic indentation.

C. Effect of Iodine Treatment

Figures 9 and 11 indicate that the iodine treatment significantly alters the viscoelastic behavior of the original coal-tar pitch CTP-00. Softening as well as creeping are progressively suppressed by the iodine treatment.

The master creep curves of the iodine-treated coal-tar pitches, which were superposed at the reference temperature $T_0 = 323.2$ K (50.0°C), are shown in Fig. 16, the shift factors a_T used in these superposition procedures being plotted in Fig. 13. The following specific rheological features are worthy of note: The iodine treatment (1) has an insignificant effect on the instantaneous creep compliance $D(0)$, meaning no effects on the instantaneous elastic behavior, (2) significantly and progressively retards creep deformation and flow, and (3) alters the temperature dependence of the

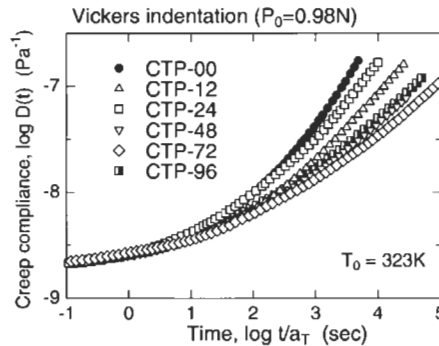


Fig. 16. Creep compliance master curves of the pitches as received, and iodine-treated.

shift factor a_T and thus, varies the temperature dependence of the steady-state viscosity η_s , once the coal-tar pitch is iodine-treated. However, the soaking time, i.e., the content of iodine within pitch, has an insignificant effect on this temperature dependence, as clearly seen in Fig. 13. The activation energy ΔH_η , which was estimated from the slope of the Arrhenius linear approximation in Fig. 13, was reduced from 340 kJ mol^{-1} (open and closed circles) to 172 kJ mol^{-1} (non-circular marks) by the iodine treatment.

Further rheological information on the effect of iodine treatment is given by introducing the spectrum of retardation times, $L(\tau)$. The creep compliance function $D(t)$ is written in terms of the retardation time spectrum $L(\tau)$, as follows [29]:

$$D(t) = D(0) + \int_{-\infty}^{\infty} L(\tau)(1 - e^{-t/\tau}) d \ln \tau + t / [2(1 + \nu)\eta_s] \quad (31)$$

where the continuous retardation spectrum is defined as $L(\tau)d \ln \tau$, the contribution to compliance (inverse of rigidity) associated with retardation times whose logarithms lie in the range between $\ln \tau$ and $\ln \tau + d \ln \tau$. The second approximation method of Schwarzl and Starverman [29] gives the retardation time spectrum $L(\tau)$ in terms of the time-derivatives of creep compliance function $D(t)$;

$$L(\tau) = \left[\frac{d[D(t)]}{d(\ln t)} - \frac{d^2[D(t)]}{d(\ln t)^2} \right]_{t=2\tau} \quad (32)$$

The numerical results of $L(\tau)$ for the iodine-treated pitch samples are illustrated in Fig. 17, demonstrating a significant effect of iodine treatment on the retardation time spectrum. The longest retardation time τ_M of the iodine non-treated CTP-00 is of the order of 10^3 s , and that of CTP-96, by way of example, is of 10^5 s . At the longest retardation time τ_M , the respective pitches reach a state of steady flow, and hence $L(\tau)$ vanishes. The τ_M -value as well as the peak value of each spectrum which appears at long retardation times are increased with the increase in the soaking time in the iodine vapor. It is to be noted, however, that with increasing soaking time the contributions to $L(\tau)$ from short-time retardation mechanisms change the spectrum very little.

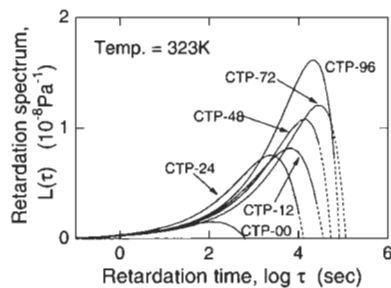


Fig. 17. Retardation time spectra at 323 K.

The magnitude of the retardation time spectrum $L(\tau)$, at each retardation time τ , represents the elastic compliance (the inverse of elastic stiffness) for the molecular processes and mechanisms with the characteristic retardation time of τ . In the region of shorter retardation times, the Brownian motions of small-size molecules and ions or the very localized small segments within larger molecules and molecular/ionic complexes dominate the retardation processes. In contrast, the microscopic mechanisms associated with the Brownian motions of large-size molecules and ionic complexes as their global and cooperative movements contribute to the longer retardation processes. Accordingly, as clearly seen in Fig. 17, the small-size components and the localized small segments of coal-tar pitch and iodine-treated charge-transfer complexes, which exclusively contribute to short-time retardation processes, behave less compliant (more stiff). On the other hand, the large-size pitch molecules and charge-transfer complexes that were created by iodine treatment behave more compliant (less stiff) in long-time retardation processes.

The steady-state compliance D_s is a measure of the elastic deformation during “steady flow” of viscoelastic liquids [29]. In other words, D_s expresses how compliant in an elastic manner the material tested is against a long-time mechanical response, that is in contrast to the compliance $D(0)$ for instantaneous mechanical response. The steady-state compliance D_s is given by the following formula using $L(\tau)$ [29],

$$D_s = D(0) + \int_{-\infty}^{\infty} L(\tau) d \ln \tau \quad (33)$$

where instantaneous compliance $D(0)$ is ordinarily negligible in comparison with the integral. Accordingly, the area enclosed with each retardation time spectrum curve in Fig. 17 approximately yields D_s as a measure of the elastic deformation, indicating that the iodine treatment progressively makes the coal-tar pitch more compliant. This may be reflected from the presence of charge-transfer complexes larger in their sizes and bulkier in their configurations. The D_s -values of iodine-treated pitches thus obtained by applying Eq. (33) to Fig. 17 are plotted in Fig. 18. The steady-state shear viscosity η_s is approximated by $\eta_s = \tau_M/[2(1 + \nu)D_s]$, and then calculated using the observed D_s and τ_M . The η_s -values thus calculated at 323.2 K (50.0°C) are also shown in Fig. 18 along with τ_M -values. These rheological parameters (η_s , D_s , and τ_M) significantly increase with iodine treatment.

5 Concluding Remarks

A pyramidal indenter, as an efficient mechanical probe for micro-/nano-characterization, has been applied to engineering materials with time-dependent/-independent mechanical responses. The constitutive relationships of (a) purely elastic, (b) purely plastic, (c) purely viscous, (d) elastoplastic, and (e) viscoelastic deformations were formulated for pyramidal indentations. The present mathematical analyses for pyramidal indenters may also be extended to flat-ended and spherical indenters [31].

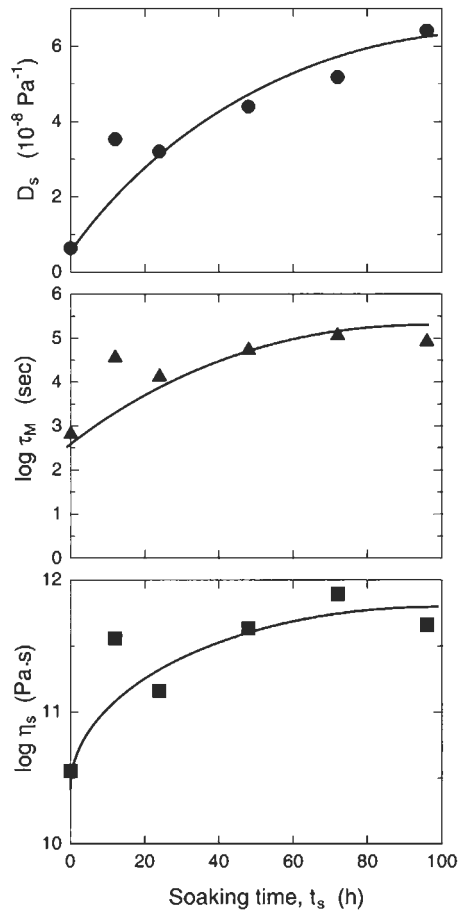


Fig. 18. Dependence of long-term rheological parameters (steady-state compliance D_s , maximum retardation time τ_M , and steady-state shear viscosity η_s) on the soaking time in saturated iodine vapor.

The following conclusions are made from the theoretical considerations.

1. It is possible to quantitatively separate the plastic (true hardness H) and the elastic (Young's modulus E) measurements in the elastoplastic regime.
2. Meyer hardness H_M is the indenter's geometry-dependent elastoplastic parameter, increasing with H , as well as with E .
3. The Meyer hardness H_M , being defined as a mean pressure against elastoplastic penetration, is recognized as the elastoplastic energy consumed to create a unit volume of pyramidal impression.
4. Energy-based considerations are efficient to understand the microscopic processes and mechanisms associated with the complicated elastoplastic penetration of indentation.

5. The Boltzmann hereditary integral combined with the concept of representative stress/strain easily extends the elastic solutions to viscoelastic ones.
6. Rheological functions (stress relaxation modulus, creep compliance function, etc.) can be estimated directly from the time-dependent indentation load $P(t)$ and penetration depth $h(t)$ observed in experimental.
7. The conventional rule of “time-temperature superposition” is also applicable to pyramidal indentation.

Details for designing test apparatus and a critical review for test systems are addressed. Applications of the indentation test technique were made to the elasto-plastic behavior of heat-treated carbons, and to the viscoelastic deformation and flow of iodine-treated coal-tar pitches. The elastoplastic parameters of carbons and the viscoelastic functions of pitches are, respectively, related to their microstructural parameters. Through these applications and test results, it is emphasized that indentation tests afford an efficient micro-/nano-probe for mechanical characterization of materials with extremely small dimensions and thin films coated onto substrates.

References

1. D. Tabor, *Hardness of Metals*. Clarendon Press, Oxford, 1951.
2. K.L. Johnson, *Contact Mechanics*. Cambridge University Press, Cambridge, 1985.
3. N.A. Stilwell and D. Tabor, Elastic recovery of conical indentation. *Proc. Phys. Soc. Lond.*, 78: 169–179, 1961.
4. M.Kh. Shorshorov, S.I. Bulychev and V.P. Alekhin, Work of plastic and elastic deformation during indenter indentation. *Sov. Phys. Dokl.*, 26: 769–771, 1975.
5. B.R. Lawn and V.R. Howes, Elastic recovery at hardness indentations. *J. Mater. Sci.*, 16: 2745–2752, 1981.
6. J.L. Loubet, J.M. Georges and G. Meille, Vickers indentation curves of elastoplastic materials. In: P.J. Blay and B.R. Lawn (Eds.), *Microindentation Techniques in Materials Science and Engineering*, pp. 72–89. ASTM STP 889, Philadelphia, 1986.
7. M.F. Doerner and W.D. Nix, A method for interpreting the data from depth-sensing indentation instruments. *J. Mater. Res.*, 1: 601–609, 1986.
8. E. Söderlund and D.J. Rowcliffe, Analysis of penetration curves produced by depth-sensing indentation systems. *J. Hard Mater.*, 5: 149–177, 1994.
9. W.C. Oliver and G.M. Pharr, An improved technique for determining hardness and elastic modulus using load and displacement sensing indentation experiments. *J. Mater. Res.*, 7: 1564–1583, 1992.
10. G.M. Pharr and R.F. Cook, Instrumentation of a conventional hardness tester for load-displacement measurement during indentation. *J. Mater. Res.*, 5: 848–851, 1990.
11. J.S. Field and M.V. Swain, A simple predictive model for spherical indentation. *J. Mater. Res.*, 8: 297–306, 1993.
12. M. Sakai, Energy principle of the indentation-induced inelastic surface deformation and hardness of brittle materials. *Acta Metall. Mater.*, 41: 1751–1758, 1993.
13. M. Sakai and R. Nowak, Fracture toughness and brittleness of ceramic materials. In: M.J. Bannister (Ed.), *Ceramics-Adding The Value (Proceedings of Austceram 92)*, Vol. 2, pp. 922–931. The Australian Ceramic Society, Melbourne, 1992.

14. R. Nowak and M. Sakai, Energy principle of indentation contact: the application to sapphire. *J. Mater. Res.*, 8: 1068–1078, 1993.
15. M. Sakai, H. Hanyu and M. Inagaki, Indentation-induced contact deformation and damage of glass-like carbons. *J. Am. Ceram. Soc.*, 78: 1006–1012, 1995.
16. M. Sakai, S. Shimizu and T. Ishikawa, The indentation load-depth curve of ceramics. *J. Mater. Res.*, 14: 1471–1484, 1999.
17. M. Sakai, The Meyer hardness, a measure of plasticity? *J. Mater. Res.*, 14: 3630–3639, 1999.
18. S. Shimizu, Y. Yanagimoto and M. Sakai, The pyramidal indentation load–depth curve of viscoelastic materials. *J. Mater. Res.*, 14: 4075–4086, 1999.
19. E. Meyer, Untersuchungen über Härteprüfung und Härte. *Zeits. d. Vereines Deutsch. Ingenieure*, 52: 645–654, 1908.
20. I.N. Sneddon, The relation between load and penetration in the axisymmetric Boussinesq problem for a punch of arbitrary profile. *Int. J. Eng. Sci.*, 3: 47–57, 1965.
21. R.W. Douglas, W.L. Armstrong, J.P. Edward and D. Hill, A Penetration Viscometer. *Glass Tech.*, 6: 52–55, 1973.
22. J.R.M. Radok, Visco-elastic stress analysis. *Q. App. Math.*, 15: 198–202, 1957.
23. E.H. Lee and J.R.M. Radok, The contact problem for viscoelastic bodies. *J. Appl. Mech.*, 27: 438–444, 1960.
24. M. Sakai, Y. Nakano and S. Shimizu, Elastoplastic Indentation on heat-treated carbons. *J. Am. Ceram. Soc.*, 85: 1522–1528, 2002.
25. B.T. Kelly. *Physics of Graphite*, Chap. 3, Applied Science, London, 1981.
26. M. Sakai, S. Shimizu, N. Miyajima, Y. Tanabe and E. Yasuda, Viscoelastic indentation on iodine-treated coal-tar pitch. *Carbon*, 38: 605–614, 2000.
27. M. Sakai, T. Kida and M. Inagaki, Creep and glass transition behavior of fractionated petroleum pitches: the influence of molecular weight and its distribution. *J. Mater. Sci.*, 19: 2651–2663, 1984.
28. N. Miyajima, T. Akatsu, T. Ikoma, O. Ito, B. Rand, Y. Tanabe and E. Yasuda, A role of charge-transfer complex with iodine in the modification of coal-tar pitch. *Carbon*, 38: 1931–1938, 2000.
29. J.D. Ferry. *Viscoelastic Properties of Polymers*, 2nd Edn., Chap. 11. Wiley, New York, 1970.
30. M.L. Williams, R.F. Landel and J.D. Ferry, Temperature dependence of relaxation mechanisms in amorphous polymers and other glass-forming liquids. *J. Am. Chem. Soc.*, 77: 3701–3707, 1955.
31. M. Sakai and S. Shimizu, Indentation rheometry for glass-forming materials. *J. Non-Crystal. Solids*, 282: 236–247, 2001.

Chapter 23

Magnetism of Nano-graphite

**Toshiaki Enoki, Bhagvatula L.V. Prasad, Yoshiyuki Shibayama, Kazuyuki Takai
and Hirohiko Sato**

Department of Chemistry, Tokyo Institute of Technology, Ookayama, Tokyo, 152-8551 Japan

Abstract: The magnetism of nano-sized graphite using activated carbon fibers (ACFs) and heat-treated nano-diamond particles has been investigated. ACFs are considered to be a disordered network of nano-graphites, for which non-bonding π -electron spins of edge origin (edge-state) are responsible for the observed magnetism (as suggested theoretically). Near to a heat-induced insulator–metal transition, spin-glass-like disordered magnetism appears and is related to the random strengths of inter-nano-graphite antiferromagnetic interactions mediated by π -conduction carriers. Fluorination of ACFs generates localized spins of sp^3 -defects at the expense of edge-state spins. The isolated feature of the former is entirely different from that of the latter. Heat-treatment of diamond nano-particles converts the diamond nano-particles to carbon nano-particles with complete graphitization taking place around 1600°C. The itinerant π -electron system of graphite is gradually developed with heat-treatment and completely graphitized samples clearly reveal the presence of edge-state spins.

Keywords: Nano-graphite, Edge state, Disordered magnetism, Metal–insulator transition, Fluorination, Diamond/graphite conversion.

1 Introduction

Nano-sized particles are intriguing systems due to their novel electronic features depending on their size, topology, etc. Recently, a nano-sized graphene sheet with open edges has been studied intensively because of relevance to the fullerenes and carbon nanotubes with their closed-shape π -electron systems. For the nano-graphene, recent theoretical studies [1,2] predict that edge states, consisting of the non-bonding π -orbitals, appear around the Fermi level and give unique features to the electronic state. Therefore, it is expected that the interplay between edge-state spins and conduction π -electrons produces unconventional magnetism of the nano-graphite-based mesoscopic systems. These developments have provided an impetus to investigations of magnetism of nano-graphite using activated carbon fibers (ACFs) and heat-treated nano-diamond particles as model materials.

The structure of ACFs can be described by a 3D disorder network of nano-graphites where each nano-graphite domain consists of stacked 3–4 graphene sheets having a mean size of 3 nm [3]. As-prepared ACFs exhibit Coulomb gap variable-range hopping conduction [4,5], revealing the essential role of charging effects of the nano-graphite domains, where the magnetism is associated with edge-state spins. Moreover, heat treatment above 1300°C causes an insulator–metal (I-M) transition due to the development of an infinite percolative carrier conduction path network in the nano-graphite assembly. The heat treatment also affects the magnetism of the ACFs resulting in the disappearance of the localized edge-state spins observed in the as-prepared ACFs [5]. Fluorination is an interesting chemical tool to modify the electronic structure of a graphitic system because it can easily generate sp^3 -defects at any location in the π -electron network. Therefore, the fluorination effect on nano-graphite systems is expected to give a clue in the characterization of the magnetism in relation to the edge-state.

Nano-diamond is another source of nano-graphite obtained by heat-treatment of diamond above 1600°C [6]. Diamond-derived graphite nano-particles have a polyhedral shape with an internal hollow. The facets of the polyhedron comprise a stacking of 3–7 graphene sheets with an in-plane size of 3–4 nm and an inter-sheet distance of 0.353 nm. The larger inter-sheet distance, when compared with bulk-graphite (0.3354 nm) and the disordered stacking features, suggests that the graphite nano-particles are an assembly of weakly bonded nano-graphene sheets and so are good model systems of nano-graphites. The diamond nano-particles are prepared under explosion induced conditions leading to the presence of a large number of defects in this sp^3 carbon dominated system. Following heat-treatment, the sp^3 carbon dominated diamond is gradually converted to sp^2 carbon dominated graphite from the surface inwards with the nucleation of graphitization probably taking place at defect sites.

In this chapter, the following issues are discussed relative to the magnetism of nano-graphite systems; disordered magnetism in ACFs around the I-M threshold, modification of magnetism by fluorine-induced sp^3 -defects, and change in magnetism upon the conversion from diamond to graphite.

2 Conversion from Diamond to Graphite in Nano-scale Dimension

The as-prepared nano-diamond particles (~5 nm) were boiled in HCl prior to heat treatment so as to remove such magnetic impurities as transition metals. Several heat-treatment temperatures (HTTs), namely, 900, 1200, 1400 and 1600°C were used to investigate the gradual development of a π -electron network during the diamond to graphite transition in these nano-sized systems. The susceptibility is described by orbital, Curie, Pauli and core terms. In Fig. 1 are plotted the observed localized spin density and the orbital susceptibility χ_{orb} as a function of HTT. The same figure also provides the g -value and line-widths from the ESR studies. The localized spin density is obtained from the Curie contribution at low temperatures. The χ_{orb} is estimated

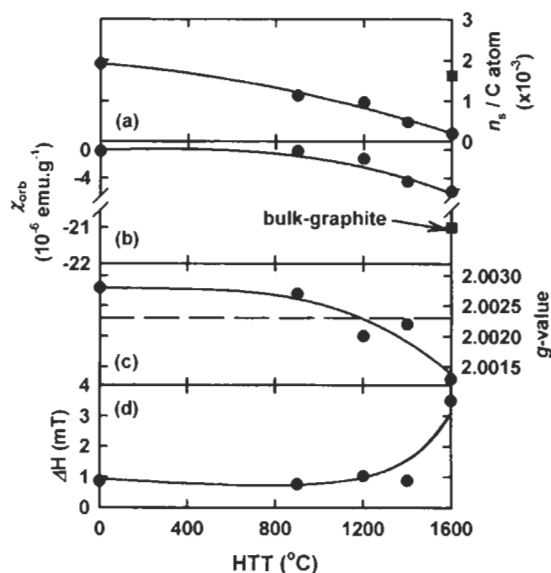


Fig. 1. The localized spin concentration per carbon atom (a), orbital susceptibility term, χ_{orb} (see text for the details of calculation of χ_{orb}) (b), ESR g -values (c), and line widths (d), as a function of HTT. The solid squares are of the 1600°C graphite: (a) is the estimate of the π -electron concentration obtained from the Pauli susceptibility using the value $k_B T \chi_p / \mu_B^2$, where χ_p is the Pauli susceptibility. The dashed line in (c) represents the g -value of free electron spin. The solid lines are a guide for the eye.

from the following equation, $\chi_{\text{orb}} = 3\chi_{\parallel} - 2\chi_{\perp}$, where χ_{\parallel} is the susceptibility at infinite temperature with contributions from the orbital term, χ_{orb} , the Pauli paramagnetic term χ_p , and the core diamagnetic term χ_{core} . It is assumed that χ_{\perp} is equal to the core diamagnetism and is calculated from Pascal rules. It is also assumed that the χ_p makes a negligible contribution to the observed susceptibility. This is justified by the fact that the χ_p from the edge π -electrons is at most 10% even in the carbon of HTT 1600°C which has the largest π -electron contribution [7]. A comparison of the χ_{orb} of condensed polycyclic aromatic systems having N benzene rings, with the χ_{orb} observed for the present samples, as plotted in Fig. 2, may give important clues to understanding the development of π -electronic structures in these materials. The χ_{orb} for condensed polycyclic aromatic compounds is taken from the literature [8] after doing the necessary corrections for the anisotropy, as described above. Diamagnetic susceptibilities have been considered of highly symmetrical molecules only (e.g., ovalene, 10 benzene rings), because they show the maximum diamagnetic susceptibility when compared with less symmetrical molecules with the same number of benzene rings. This plot also depicts the χ_{orb} values of bulk-graphite along with the χ_{orb} values of the present samples. The number of benzene rings in the present samples is determined from the graphene in-plane sizes obtained from Raman experiments [7].

The diamond nano-particles are prepared by explosion induced techniques in closed containers resulting in the generation of a high pressure over short time

periods ($\sim\mu\text{s}$) [9]. Due to this non-equilibrium condition in the formation of diamond, a large number of defects are produced as evident from the observed large spin concentrations (Fig. 1a). The observed χ_{orb} in Fig. 1b is negligible indicating that the itinerant π -electron system, giving rise to the orbital diamagnetic susceptibility, is not developed in these samples. The observed g -values (Fig. 1c) of nano-diamond particles are also quite close to the g -values of micro-crystalline diamond where the spins are attributed to the paramagnetic centers created by defects in the sp^3 bonded network [10]. As the HTT is increased to 900°C , a lattice distortion, in equilibrium in the whole diamond particle, becomes relaxed. This is in addition to the formation of a disordered sp^2 carbon phase on the surface of the particle at the expense of localized defect spins. This explains the large change in the spin concentration (Fig. 1a) from the as-prepared sample to the sample of HTT 900°C . On the other hand, similar χ_{orb} values and the negligible change in the g -value at 900°C suggest that the extent of the itinerant π -electron network is insignificant and that the localized spins are of the same origin as those of the as-prepared sample. Increasing the HTT to 1200°C increases the graphite fraction of the sample when the ESR signal can be credited to the graphite π -electrons as the g -value is less than that of the free electron spin value (g_0). As shown in Fig. 1a, the localized spin density in this sample is considerably lower than the as-prepared and the 900°C samples so demonstrating that most of the localized spins are already part of the extended π -electron network. However, the magnitude of the $|\chi_{\text{orb}}|$ is less than expected on the basis of the number of benzene rings present, as shown in Fig. 2. This suggests that this sample is still dominated by defects (vacancies in the sp^2 network or remnant corrugated features from the diamond lattice) which effectively lead to a shrinkage in the graphite π -electron network. For the more graphitized 1400 and 1600°C samples, the $|\chi_{\text{orb}}|$ is more than that expected for polycyclic aromatic molecules with the same number of benzene rings. In bulk graphite, the large enhancement of χ_{orb} compared to the value in large polycyclic aromatic molecules is attributed to inter-band transitions [11], because the π and π^* bands in bulk-graphite are degenerate at the Fermi energy whereas the

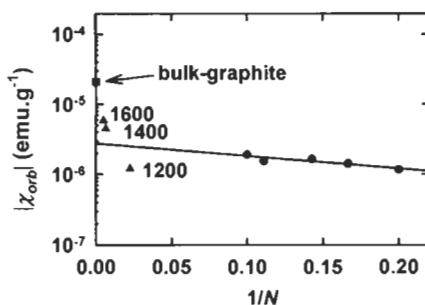


Fig. 2. The orbital susceptibility χ_{orb} of polycyclic aromatic molecules (solid circles) compared with χ_{orb} of the present samples (solid triangles) and the χ_{orb} of bulk-graphite (solid squares) plotted on the logarithmic scale vs $1/\text{number of benzene rings } (N)$. The numbers 1200, 1400 and 1600 denote the heat-treatment temperatures. The straight line is a linear regression for the data of aromatic molecules which are taken from the literature [8] after appropriate corrections.

aromatic molecules are characterized by an energy gap. Thus, the increase in the χ_{orb} value from that expected, on the basis of number of benzene rings, clearly depicts the extended nature of the π -electron network. However, this value is still smaller than that of bulk graphite. This can be attributed to finite crystallite sizes and the presence of sp^3 -like defects for the 1400°C sample. Although the in-plane domain sizes are larger than in the 1200°C sample, the g -value remains in the vicinity of g_0 and the ESR line widths are small in the 1400°C sample (Figs. 1c and d). This is indicative of the localized nature of the π -electron network to small regions due to the defects. Hence, it is concluded that at the intermediate heat-treatments of 1200 and 1400°C, the itinerant π -electrons from the graphite phase and the sp^3 defects from the diamond phase are homogeneously distributed, and that there is a possibility that these two spin species are strongly interacting with each other. For the completely graphitized 1600°C sample, the effect of the localized spins due to defects on the itinerant π -network is quite insignificant because their absolute number is very low, as shown in Fig. 1a. These localized spins are also associated with very few inhomogeneously distributed sp^3 -like defects, making them quite independent of itinerant π -electrons. Hence, at 1600°C, two different ESR signals are observed unlike the 1200 and 1400°C samples where there is only one signal. Figure 1a provides the π -electron spin density obtained from the Pauli susceptibility [7] in the 1600°C sample using the value of $k_B T \chi_p / \mu_B^2$, where k_B and μ_B are the Boltzmann constant and Bohr magneton, respectively. Here, it should be noted that χ_p is governed mainly by the density of states of the non-bonding edge states [7]. It is clear from the figure that the localized spin density from defect origins is quite small ($\sim 10\%$) compared to the edge state π -electron spin density. This implies that the presence of non-bonding edge states plays an important role in determining the electronic properties of the completely graphitized 1600°C sample. More clearly, for the 1600°C carbon, it is concluded that the edge spins are due to the zig-zag edge sites as predicted from theoretical studies. The Fermi energy obtained from the susceptibility studies is ~ 0.1 eV for this carbon [7]. The g -value observed in the 1600°C carbon is less than g_0 , while in bulk-graphite, it is higher than g_0 . However, it is established that the g -value in bulk graphite is critically controlled by the location of the Fermi level and also by the ratio of holes and electrons present in the vicinity of the contact point of π and π^* bands. It is also reported that, for boronated pyrocarbons, a drastic drop in g -value is observed, depending on the boron admixture in the pyrocarbons which makes the Fermi level shift deeper into the valence band [12]. Thus, the presence of the Fermi level away from the contact point in the 1600°C sample explains the g -value deviation, even though getting a quantitative estimation of the deviation will be quite difficult.

3 Nano-graphite Network

Pitch-based ACFs having specific surface areas of $1500 \text{ m}^2 \text{ g}^{-1}$ were used as samples. These were heat-treated progressively to 1500°C, where the samples had a soak time at the required heat treatment temperature (HTT) for 15 min [13]. Moreover, heat

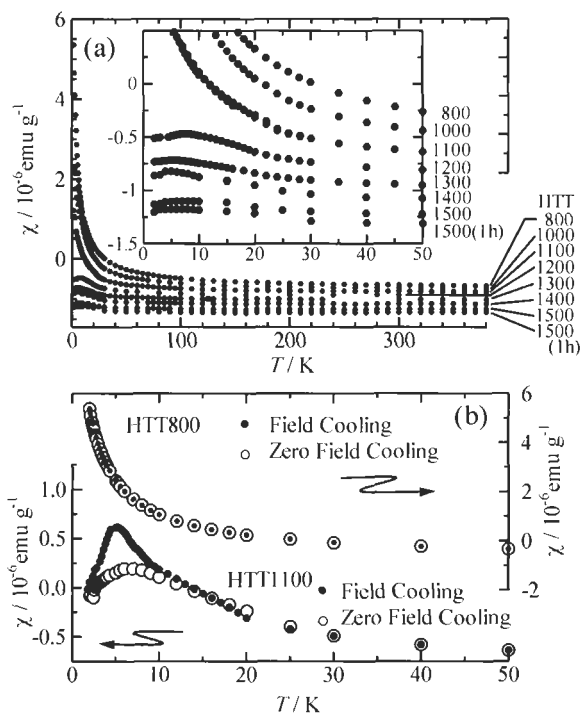


Fig. 3. (a) χ - T plots for the ACFs heat-treated to 1500°C. The inset shows the detailed behavior. (b) Field-cooling effects on χ for HTT 800 and 1100 samples, where the open and solid symbols correspond to the data on zero-field and field (1T) cooling runs, respectively.

treatment at 1500°C for 1 h (1500 (1 h)) was carried out as the most intensive condition. The susceptibility vs. temperature (χ - T) plots under 1T is given in Fig. 3a. As shown in Fig. 3a, the present samples form two groups. The susceptibility of ACFs heat-treated below 1100°C (low HTT ACFs) obeys the Curie-Weiss law in the whole temperature range investigated. The susceptibility of ACFs heated above 1200°C (high HTT ACFs) deviates from the Curie-Weiss law below 20 K and shows a cusp around 4–7 K. In addition, only the high HTT ACFs exhibit the field cooling effects as shown in Fig. 3b, where the samples are prepared independently of those in Fig. 3a. The measurements were carried out under $H = 1T$ in heating runs after cooling processes from room temperature to 2 K with fields of $H = 0$ and $1T$. The 800°C sample, where χ obeys the Curie-Weiss law, shows no field cooling effect, while the 1100°C sample, having a cusp, shows a difference below 15 K between the zero field and the field cooling runs, i.e., the field cooling enhances the cusp. Figure 4 shows the Weiss temperature θ and the number of localized spins per nano-graphite n for the samples in Fig. 3a. θ is around -3 K irrespective of HTT, proving the presence of antiferromagnetic interactions. The spin density exhibits a considerable reduction caused by the heat treatment [13]. However, n shows a more moderate decrease, because of the growth of the nano-graphite size. Namely, each nano-graphite has

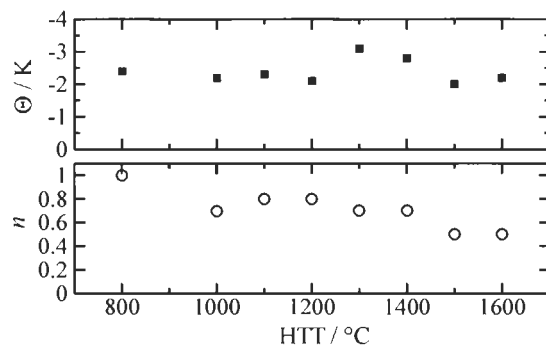


Fig. 4. HTT dependence of the Weiss temperature θ and the number of localized spins per nano-graphite n in ACFs. The data for the carbon of HTT 1500°C (1 h) is positioned at HTT = 1600°C for clarity.

about one spin irrespective of the nano-graphite size, suggesting an important role of nano-graphene edges in the origin of the spins. In general, the localized spins of disordered carbons have been considered to originate from σ -dangling bonds [14]. The origin of the spins, however, remains unverified because the σ -dangling bonds of carbon atoms are too chemically active to be stabilized in the atmosphere. In addition, the nano-graphite in the ACFs is composed of well-characterized condensed aromatic rings with few sp^3 bonds forming nano-graphite bridges [3]. Moreover, in relation to the novel magnetism in a nano-graphene, theoretical studies predict the presence of non-bonding π -electron edge states. These are localized on peripheral carbon atoms composing zig-zag edges even if these carbon atoms are terminated by foreign atoms [2]. These predictions have been reinforced by recent experiments confirming that the novel magnetism is due to edge states [6]. Eventually, judging from the theoretical and experimental studies, the spins observed in the present work are considered to originate from the non-bonding edge states of π -electron.

Heat treatment above 1300°C causes the development of percolative carrier conduction paths in the nano-graphite network, leading to the I-M transition [5]. The threshold between the low HTT and high HTT samples is in good agreement with HTT dominating the I-M transition, suggesting the essential correlation between transport and magnetic properties. Taking into account the presence of an infinite conduction-electron path network and the number of spins per nano-graphite domain being ca. 1, the itinerant π -electrons are considered to connect antiferromagnetic interactions between the localized edge-state spins, similar to the s - d interaction in transition metal magnets. The appearance of a cuspy peak in χ in the vicinity of the I-M transition is suggestive of a cooperative phenomenon of the spin system, in which field-cooling effects observed are characteristic features of a spin glass state. In addition to the field-cooling effects, the magnetization curves suggest the presence of a large randomness in the strengths of the exchange interactions [13], being favorable for disordered magnetism. The observed field-cooling effects, however, deviate from those of typical spin glass behavior [15]. In the present case, it is considered that a

competition between antiferromagnetic ordering and disordered magnetism interferes with the formation of a prototypical spin-glass transition. In addition, taking into account that the exchange interaction between the spins is brought about by the percolating conduction π -electron, the dimensionality of the present spin system becomes considerably lowered in the vicinity of the I-M threshold [16], at which point the novel magnetism appears. Eventually, the low-dimensionality of the exchange interaction path network might remove a true spin glass feature from the present spin system.

4 Fluorinated Nano-graphite

Fluorine is the most chemically active element, so that the reaction of fluorine with carbons breaks the strong graphite π -bonds resulting in the formation of sp^3 bonds that corrugate the graphene planes. The reaction with a nano-graphite, having a large contribution of edge carbon atoms is expected to be different from bulk graphite. Below, fluorine-induced changes in the magnetism of nano-graphites using a phenol-based ACF (Kurare FR20) having specific surface areas of $2000 \text{ m}^2 \text{ g}^{-1}$ are discussed.

Figure 5 shows the spin concentration of the fluorine-treated ACFs as a function of fluorine concentration. The samples, whose fluorine concentrations are lower than $F/C \sim 0.5$, were prepared by a thermal defluorination of the fluorinated samples having $F/C \sim 0.5$. This is because it is difficult to prepare carbons with low fluorine concentrations. Carbons with $F/C > 0.5$ were obtained by direct fluorination of ACFs. The present treatment of the samples with the low fluorine concentrations is verified to be effective because the fluorine atoms so attached to the samples are easily removed with no change in the graphite moiety [17]. The spin concentration, which is $2 \times 10^{19} \text{ g}^{-1}$ in the non-fluorine-treated ACFs, decreases monotonically as the fluorine concentration increases to about $F/C = 0.4$. Above $F/C \sim 0.4$, it shows an increase with a maximum around $F/C = 0.8$, and then approaches zero around $F/C = 1.2$. In bulk graphite, fluorination is completed at $F/C = 1$ because each carbon atom accepts

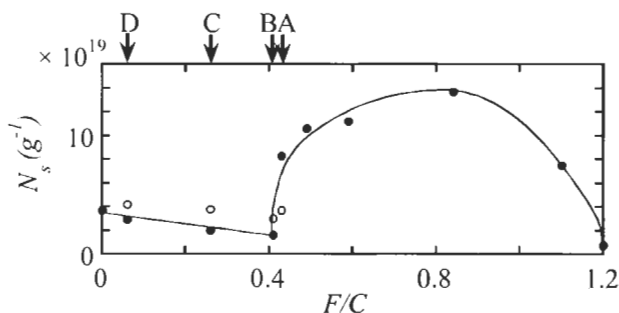


Fig. 5. The localized spin concentration N_s for fluorinated ACFs with $F/C = 0-1.2$. Closed circles placed at fluorine concentrations A, B, C, and D represent samples prepared by defluorination of weakly fluorinated samples ($F/C = 0.49$) at 200, 400, 500, 600°C, respectively. Open circles at the same concentrations are non-fluorinated samples heat-treated to the same temperatures. Solid lines are a guide for the eye.

one fluorine atom for the formation of an sp^3 bond. In contrast, in nano-graphites that have a large contribution of edge carbon atoms, these interact with fluorine atoms differently from non-edge carbon atoms. The number of the edge carbon atoms is estimated at about 20% of that of internal carbon atoms for the nano-graphite domains with a size of 3 nm, which make up the structure of the ACFs. The decrease in spin concentration, at low fluorine concentrations below $F/C \sim 0.4$, is explained by the reaction of fluorine atoms mainly with edge carbon atoms, so reducing the concentration of spins after formation of fluorine-induced sp^3 bonds. Edge carbon atoms are more reactive than internal (in-plane) carbon atoms. The concentration at which this decreasing trend ends is consistent with the concentration ratio of edge carbon atoms to the total carbon atoms in a nano-graphite, taking into account that some of the interior carbon atoms also react with the fluorine. A different mechanism causes the increase in the spin concentration above $F/C \sim 0.4$ when all the edge carbon atoms are bonded to fluorine atoms. The reaction of a fluorine atom with an interior carbon atom converts a graphite sp^2 bond into an sp^3 bond at the expense of a π -bond. This results in the generation of a dangling bond having a localized magnetic moment at the carbon site which is adjacent to the site attacked by the fluorine atom. The maximum in the spin concentration emerging at around $F/C \sim 0.8$ is explained by the fact that about half of the interior carbon atoms have reacted with fluorine atoms resulting in the formation of a maximum number of dangling bond spins. The disappearance of spins around $F/C \sim 1.2$ is caused by the completion of the reaction with all the carbon atoms in nano-graphites. The ESR line width of the fluorine-treated ACFs above $F/C \sim 0.4$ increases steeply as the fluorine concentration is raised. Actually, the line width reaches about 12 mT at $F/C \sim 1.2$, which is more than two times larger than that for the non-fluorinated ACFs. This suggests a line width broadening mechanism associated with the large hyperfine interaction of fluorine atoms. From the analysis of the hyperfine broadening, the electronic state of the dangling bond is found to extend to the surrounding fluorine atoms, consistent with a recent calculation by Saito et al. [18].

References

1. M. Fujita, K. Wakabayashi, K. Nakada and K. Kusakabe, *J. Phys. Soc. Jpn.*, 65: 1920–1923, 1996.
2. K. Wakabayashi, M. Fujita, H. Ajiki and M. Sigrist, *Phys. Rev.*, B59: 8271–8282, 1999.
3. M.S. Dresselhaus, A.W.P. Fung, A.M. Rao, S.L. di Vittorio, K. Kuriyama, G. Dresselhaus and M. Endo, *Carbon*, 30: 1065–1073, 1992.
4. A. W. P. Fung, Z. H. Wang, M. S. Dresselhaus, G. Dresselhaus, R. W. Pekala and M. Endo, *Phys. Rev.*, B49: 17325–17335, 1994.
5. Y. Shibayama, H. Sato, T. Enoki, X.X. Bi, M.S. Dresselhaus and M. Endo, *J. Phys. Soc. Jpn.*, 69: 754–767, 2000.
6. O.E. Anderson, B.L.V. Prasad, H. Sato, T. Enoki, Y. Hishiyama, Y. Kaburagi, M. Yoshikawa and S. Bandow, *Phys. Rev.*, B58: 16387–16395, 1998.
7. B.L.V. Prasad, H. Sato, T. Enoki, Y. Hishiyama, Y. Kaburagi, A.M. Rao, P.C. Eklund, K. Oshida and M. Endo, *Phys. Rev.*, B62: 11209–11218, 2000.

8. H. Akamatsu and Y. Matsunaga, *Bull. Chem. Soc. Jpn.*, 26: 364–372, 1953.
9. V.L. Kuznetsov, A.L. Chuvilin, E.M. Moroz, V.N. Kolomiichuk, Sh.K. Shaikhutdinov and Yu.V. Butenko, *Carbon*, 32: 873–882, 1994.
10. G.K. Walters and T.L. Estle, *J. Appl. Phys.*, 32: 1854–1859, 1961.
11. B.T. Kelly, *Physics of Graphite*. Applied Science, London, 1981.
12. A.S. Kotosonov, *Carbon*, 26: 735–741, 1988.
13. Y. Shibayama, H. Sato, T. Enoki and M. Endo, *Phys. Rev. Lett.*, 84: 1744–1747, 2000.
14. C. Lewis and L.S. Singer, In: P.L. Walker, Jr. and P.A. Thrower (Eds.), *Chemistry and Physics of Carbon*. Marcel Dekker, New York, 17, p. 1, 1981.
15. M. Mezard, G. Raris and M.A. Virasoro, *Spin Glass Theory and Beyond*. World Scientific, New Jersey, 1987.
16. R.J. Birgeneau, R.A. Cowley, G. Shirane, J.A. Tarvin and H.J. Guggenheim, *Phys. Rev.*, B21: 317–332, 1980.
17. V. Gupta, R.B. Mathur, O.P. Bahl, A. Tressaud and S. Flandrois, *Synth. Metals*, 73: 69–75, 1995.
18. R. Saito, M. Yagi, T. Kimura, G. Dresselhaus and M.S. Dresselhaus, *J. Phys. Chem. Solids*, 60: 715–721, 1999.

Chapter 24

Magnetoresistance and its Application to Carbon and Carbon Alloys

Yoshihiro Hishiyama

Musashi Institute of Technology, Tokyo 158-8557, Japan

Abstract: The measurement of magnetoresistance on carbon materials yields useful information about the structure and microtexture of carbon materials. The magnetoresistance is positive for graphite materials, while it is negative for carbon materials with turbostratic structures. Initially, the background of the measurement of magnetoresistance of carbon materials is described. As an application of this technique, the graphitization behavior of a PPT-derived carbon film, which is very graphitizable, is shown. Finally, the negative magnetoresistance observed in boron-doped graphite materials is given as a recent example of negative magnetoresistance.

Keywords: Magnetoresistance, Microtexture, X-ray diffraction, Graphite film, Boron-doped graphite

1 Introduction

The measurement of magnetoresistance on carbon materials gives useful information about the structure and microtexture of carbon materials [1], although subsidiary to X-ray diffraction and electron microscopy. Magnetoresistance values are sensitive to imperfections within a graphite structure and are valuable with which to characterize structures within a carbon. The dependence of the magnetoresistance on the direction of the magnetic field of the equipment describes preferred orientation of hexagonal carbon (graphene) layers. Values of magnetoresistance are used as indices of extents of graphitization within a carbon.

2 Background for the Magnetoresistance Measurement

A magnetoresistance measurement describes the change in the electrical resistivity of a conductor when a magnetic field is applied. The magnetoresistance $\Delta\rho/\rho_0$ is defined by

$$\Delta\rho/\rho_0 = \{\rho(B) - \rho(0)\}/\rho(0) \quad (1)$$

where $\rho(B)$ and $\rho(0)$ are the resistivities in a magnetic field B and in a zero magnetic field, respectively. Unlike most materials, the magnetoresistance of carbons and graphites is sensitive to their structure and microtexture. Experimentally, magnetoresistance is measured for both rod-shaped and bridge-shaped specimens. For such carbons as porous cokes, the magnetoresistance is measured with high reproducibility with specimens cut directly from a coke piece. Turbostratic carbons (non-graphitic), where only holes exist, have a negative magnetoresistance, i.e. the magnetoresistance decreases in a magnetic field. Graphitic carbons possess a positive magnetoresistance. To understand magnetoresistance phenomena in carbons and graphites, it is assumed that carbons consist of hexagonal carbon (graphene) layers stacked parallel to each other, irrespective of stacking order. In this chapter, positive magnetoresistance is discussed assuming that a transport system exists consisting of two types of carriers, namely co-existing electrons and holes, there being no magnetoresistance in a single hole.

2.1 Positive Magnetoresistance in a Simple Two-carrier System

With graphites, carriers move principally within the hexagonal carbon (graphene) layers. These layer planes are two-dimensionally homogeneous electrons and holes flowing freely in each plane with the majority of carriers being electrons and holes. Their densities and mobilities describe such transport properties as electrical resistivity, Hall coefficient and magnetoresistance. The densities of electrons and holes in a perfect graphite crystal are equal, being smaller than those in, e.g. alkali metals and noble metals. Mobilities only differ slightly between electrons and holes and are much larger than the mobilities of carriers in metals. The simple two-band (STB) model approximates the transport properties of graphite.

Consider a band of electrons and one of the holes with carrier densities n_e and n_h , and mobilities μ_e and μ_h , respectively. For such a system, when a magnetic field B is applied perpendicular to the carbon layer planes and an electrical current flows along the x -axis defined parallel to the layer planes, then the transverse magnetoresistance $\Delta\rho/\rho_0$ is given by

$$\Delta\rho/\rho_0 = \frac{\rho_{xx}(B) - \rho_{xx}(0)}{\rho_{xx}(0)} = \frac{\rho_{xx}(B)}{\rho_{xx}(0)} - 1 \quad (2)$$

where $\rho_{xx}(B)$ is the in-plane magnetoresistivity written as

$$\rho_{xx} = \frac{\sigma_{xx}}{(\sigma_{xx})^2 + (\sigma_{yy})^2} \quad (3)$$

In Eq. (3) $\sigma_{xx}(B)$ and $\sigma_{yy}(B)$, the in-plane magnetoconductivity tensor components, are expressed using n_e , n_h , μ_e and μ_h as

$$\sigma_{xy} = \frac{n_e e \mu_e}{1 + (\mu_e B)^2} + \frac{n_h e \mu_h}{1 + (\mu_h B)^2}, \quad \sigma_{yx} = \frac{n_e e \mu_e^2 B}{(1 + (\mu_e B)^2)^2} + \frac{n_h e \mu_h^2 B}{(1 + (\mu_h B)^2)^2} \quad (4)$$

where e is the proton charge. The transverse magnetoresistance can be obtained thus

$$\Delta\rho / \rho_0 = \frac{n_e n_h \mu_e \mu_h (\mu_e + \mu_h)^2 B^2}{(n_e \mu_e + n_h \mu_h)^2 + \mu_e^2 \mu_h^2 (n_e - n_h)^2 B^2} \quad (5)$$

Using the notations $b = \mu_e / \mu_h$ and $\bar{\mu}^2 = \mu_e \mu_h$, Eq. (5) is written as

$$\Delta\rho / \rho_0 = \bar{\mu}^2 B^2 \frac{n_e n_h (1+b)^2}{(n_h n_e b)^2 + (\bar{\mu} B)^2 b (n_e - n_h)^2} \quad (6)$$

For the case of perfect graphite, Eq. (6) reduces to:

$$(\Delta\rho / \rho_0)_G = (\bar{\mu}_G B)^2 = \mu_{Ge} \mu_{Gh} B^2 \quad (7)$$

because of $n_e = n_h \equiv n$, where suffix "G" indicates a perfect graphite crystal.

Apart from good single crystals, all other graphite materials are defective, the crystal defects disturbing the scattering centers and electron traps (they depress the Fermi level) which are the transport carriers. When the energy band structure of a single crystal is retained for defective graphitic carbons, then the dependence of n_e and n_h on the density X of trapped electrons in the material can be written as

$$n_e = n(1 - X/n), \quad n_h = n(1 + X/n) \quad (8)$$

where n is the density of electrons or holes in perfect single crystals. Using Eq. (8), then Eq. (6) can be rewritten as:

$$\Delta\rho / \rho_0 = \bar{\mu}^2 B^2 C(X/n), \quad (9)$$

$$C(x/n) = \frac{\{1 - (x/n)^2\}(1+b)^2}{\{1 - X/n + (1 + X/n)b\}^2 + 4(X/n)^2 b(\bar{\mu}B)^2}$$

The function $C(X/n)$ is zero when $X = n$. The function $C(X/n)$ is a decreasing function of X/n in any applied field, as shown in Fig. 1 which also shows that $C(X/n)$ is a function of b for the two fixed values of $(\bar{\mu}B)^2$ of 0.05 and 1.0, respectively, as examples. Values of b obtained by Soule [2] for a single crystal of graphite at various temperatures, decrease from 1.1 to 0.79 with decreasing temperature from room temperature to that of liquid helium temperature. The term $(\bar{\mu}B)^2$ is the square of the mean cyclotron frequency multiplied by the mean relaxation time of the carriers. It

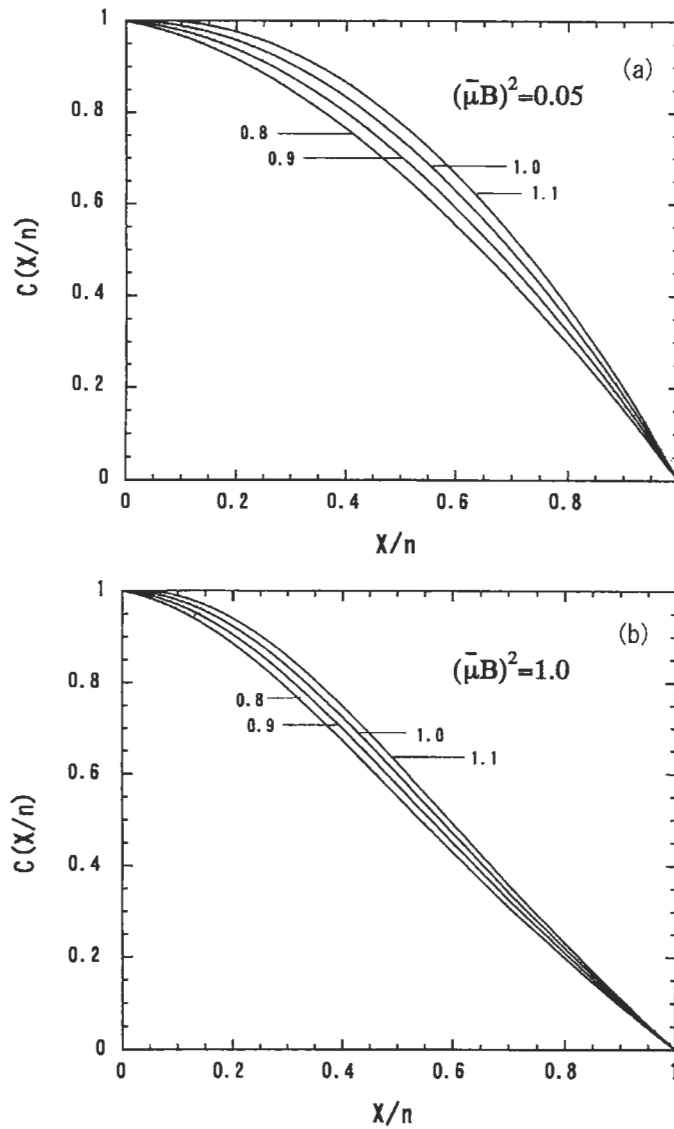


Fig. 1. Function $C(X/n)$ with a parameter of b for a fixed value of $(\bar{\mu}B)^2$ of 0.05 (a) and 1.0 (b), respectively. Numbers are the values of b .

approximates to the value of the transverse magnetoresistance in the field of 1 T. The transverse magnetoresistance ratio of polycrystalline graphite materials to the perfect single-crystal graphite, MRR , is written as:

$$MRR = \frac{\Delta\rho/\rho_0}{(\Delta\rho/\rho_0)_G} = \frac{\bar{\mu}^2}{\bar{\mu}_G^2} C(X/n) \quad (10)$$

where $\bar{\mu}$ decreases with increasing defect density and cooperates with the function $C(X/n)$ to decrease $\Delta\rho/\rho_0$. In other words, $\bar{\mu}$ is a function of effects caused by the scattering centers and $C(X/n)$ relates to the depression of the Fermi level. Hence, values of transverse magnetoresistance $\Delta\rho/\rho_0$ of the perfect crystal of graphite decrease with increasing density of defects in a constant field. Values of $\Delta\rho/\rho_0$ change inversely as the degree of crystallinity (degree of graphitization) increases within a carbon material. Because of this, values of $\Delta\rho/\rho_0$ are used as parameters to characterize graphite materials. For graphitic carbons, as values of X/n are smaller than 0.1, then $C(X/n) \sim 1$ and values of $\Delta\rho/\rho_0 B^2$ approximate to $\bar{\mu}^2$.

The above considerations relate to carbons when a magnetic field is applied transverse to the current. However, when a magnetic field is applied parallel to the current, i.e. along the carbon (graphene) layers, work done by the magnetic force on electrons and holes is zero, i.e. the longitudinal magnetoresistance is zero.

2.2 Magnetoresistance of Single-hole System

For the single-hole system, in the scheme of STB model, the upper band is completely vacant with the lower band of the Fermi level being located near the top of the lower band. For a band of holes with carrier density n_h and mobility μ_h , with an electrical current flowing in x direction and the applied magnetic field B being transverse to the current, then the magnetoresistivity tensor components are written as:

$$\sigma_{xx} = n_h e \mu_h / \{1 + (\mu_h B)^2\}, \quad \sigma_{xy} = n_h e \mu_h^2 B / \{1 + (\mu_h B)^2\} \quad (11)$$

It can be shown that for the single-hole system $\Delta\rho/\rho_0 = 0$.

2.3 Negative Magnetoresistance of Turbostratic Carbon

Because a positive Hall coefficient is observed with turbostratic carbons, then the conduction carriers must be holes. However, turbostratic carbons do have negative values of magnetoresistance and these can be measured at room temperature [3]. For pyrolytic carbons, the absolute value of negative magnetoresistance, as a function of the magnetic field direction in a constant magnetic field, is the maximum value when the magnetic field is perpendicular to the carbon layers, i.e. the magnetic field is transverse to the current. The negative magnetoresistance becomes significant when measured at temperatures below that of liquid nitrogen. At such a temperature, the absolute value of the negative magnetoresistance in a given magnetic field increases with increasing degree of graphitization (increasing crystallite sizes) [4]. Several theoretical studies have been published explaining negative magnetoresistance [2–6]. Of these, the theories proposed by Bright [5] and by Bayot et al. [6] discuss observed magnetoresistance behavior.

The Bright theory [5] considers increases in carrier density with magnetic field from the point-of-view of the unusual Landau level structure of two-dimensional

carbon layer planes. Increasing carrier density leads to a decrease in electric resistance, i.e. negative magnetoresistance. Bayot et al. [6] paid special attention to a weak localization effect in order to explain negative magnetoresistance. This is, generally, a low-temperature effect occurring in disorganized materials when the probability of elastic scattering of carriers by static defects is much larger than temperature-dependent inelastic scattering due to carrier-phonon and carrier-carrier interactions. The constructive interference of the elastically scattered partial electron waves occurs in the backward direction so leading to an enhanced back-scattering probability. This effect gives rise to a slight increase in the electrical resistivity with decreasing temperature, which is the prominent feature of weak localization phenomena. Because the magnetic field tends to suppress the phase coherence of back-scattered waves, it destroys the localization effect. The observed magnetoresistance for the turbostratic carbons is negative and its absolute value increases as the temperature of measurement decreases.

3 Measurement of Magnetoresistance

A successful scheme of the classification of the microtextures of various carbon materials has been proposed by Inagaki [7,8] as shown in Fig. 2. This classification is based on the preferred orientation of carbon layers, referring to a plane, an axis and a point.

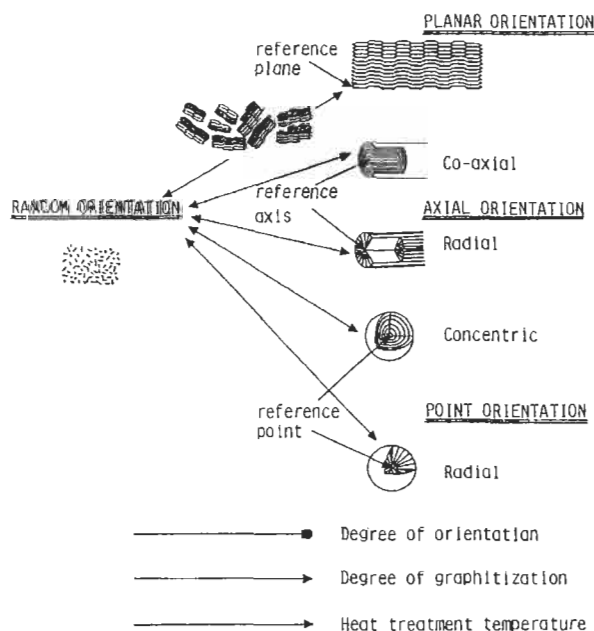


Fig. 2. Scheme of classification of microtexture for various carbon materials proposed by Inagaki [7].

The first scheme is the orientation of the layers along a reference plane. The extreme case of this orientation scheme is single crystal graphite. Highly oriented pyrolytic graphite (HOPG), together with highly oriented graphite films prepared from aromatic polyimides, and Grafoil have microtextures in this scheme.

The second scheme is the axial orientation of the layers where the orientations of the layers along and normal to the fiber axis (reference axis), are considered. The extreme case of co-axial orientation is the graphite whisker. The vapor-grown carbon whiskers (fibers) have microtextures of an extreme nature. The extreme of the perfect orientation, radial to the reference axis, is not known in other carbons. Such radial orientations, with an open crack, are also seen in mesophase pitch-based carbon fibers. With increasing heat treatment temperature (HTT) graphene layers grow with improved orientation, the opening of the wedge-shaped crack being widened. In PAN-based carbon fibers, the carbon layers are oriented along the fiber axis, but in their cross-sections the layers are arranged randomly or have radial and co-axial schemes.

The third scheme of Inagaki [7,8] is orientation around a reference point as found in spherical particles. There are two cases to consider: concentric and radial but without perfect orientation. Concentric orientations can be found in Gilsonite coke and carbon black particles, and the radial arrangement in the spheres are formed from a mixture of polyethylene and polyvinyl chloride by carbonization under pressure.

Random orientation of the layers is common to the three schemes. As an example of this microtexture, glass-like carbons prepared from the various starting materials can be mentioned.

Because in carbon materials an electrical current flows mainly along the carbon layers, the magnetoresistance depends strongly on the preferred orientation of carbon layers. In other words, the magnetoresistance anisotropy on a specimen gives information regarding the preferred orientation of the carbon layers along the main current direction. Therefore, magnetoresistance measurements, in one experiment, provide information about crystallinity and preferred orientation in carbon materials.

For polycrystalline graphite, the maximum magnetoresistance is almost an averaged transverse magnetoresistance of the graphene layers with the current perpendicular and the magnetic field parallel to the *c*-axis. As a consequence of strong anisotropy of the electrical resistivity and the influence of the magnetic field, this graphene layer magnetoresistance can be detected even when the magnetic field is parallel to the current direction if the layer planes are orientated. The situation is the same for turbostratic carbons, though the sign of the magnetoresistance is negative.

For carbon materials, the magnetoresistance must be measured for the three principal directions of the magnetic field vector \mathbf{B} as shown in Fig. 3. The T_{\max} is the direction of \mathbf{B} in which the largest absolute value of the magnetoresistance is observed. The other two directions correspond to the highest and lowest magnetoresistance values (absolute values) when the magnetic field is rotated in the plane perpendicular to the T_{\max} direction. The direction making the smallest angle with the

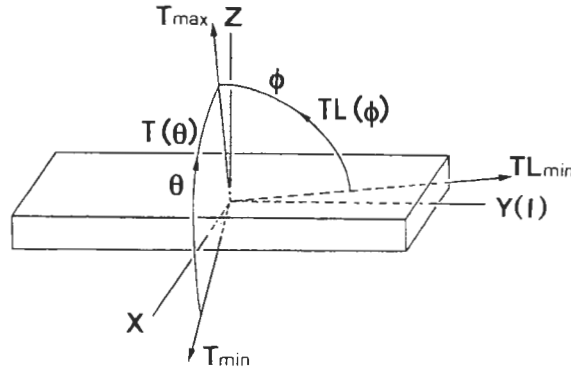


Fig. 3. Three principal directions of the magnetic field vector B and magnetic field rotation schemes (reprinted with the permission of Marcel Dekker Inc. from Ref. [1]).

current direction I is denoted by TL_{\min} and the other T_{\min} , the direction TL_{\min} being coincident with the current direction. These three directions are mutually perpendicular. The T_{\max} direction is recorded against the flat surface of the sample mount for each measurement. The values of the magnetoresistances along the three principal directions are denoted by $(\Delta\rho/\rho_0)_{\max}$, $(\Delta\rho/\rho_0)_{TL_{\min}}$ and $(\Delta\rho/\rho_0)_{T_{\min}}$, respectively. These values are determined by measurements on the magnetic field rotation schemes, $TL(\phi)$ and $T(\theta)$, as shown in Fig. 3 [9]. The average crystallite layer plane transverse magnetoresistance $(\Delta\rho/\rho_0)_{cr}$ is defined by the sum of these three components.

$$(\Delta\rho/\rho_0)_{cr} = (\Delta\rho/\rho_0)_{\max} + (\Delta\rho/\rho_0)_{TL_{\min}} + (\Delta\rho/\rho_0)_{T_{\min}} \quad (13)$$

This value of $(\Delta\rho/\rho_0)_{cr}$ corresponds to the transverse magnetoresistance of graphite with parallel stacking of layers and is used as a structural parameter for characterizing carbon materials.

Anisotropy ratios, r_{TL} and r_T , corresponding to the layer planer orientation texture of the specimen can be defined as follows:

$$r_{TL} = (\Delta\rho/\rho_0)_{TL_{\min}} / (\Delta\rho/\rho_0)_{\max} \quad (14)$$

and

$$r_T = (\Delta\rho/\rho_0)_{T_{\min}} / (\Delta\rho/\rho_0)_{\max} \quad (15)$$

where r_{TL} is a measure of the degree of orientation and r_T an indicator of the orientation mode. The values of r_{TL} and r_T for three limiting extreme cases of microtexture in carbon materials are as follows:

1. for perfect planar orientation, $(\Delta\rho/\rho_0)_{TL_{\min}} = (\Delta\rho/\rho_0)_{T_{\min}} = 0$, $(\Delta\rho/\rho_0)_{\max} \neq 0$ and $r_{TL} = r_T = 0$.

2. for perfect axial orientation, $(\Delta\rho/\rho_0)_{TL\min} = 0$, $(\Delta\rho/\rho_0)_{T\min} = (\Delta\rho/\rho_0)_{\max} = (\Delta\rho/\rho_0)_{cr}/2$, and $r_{TL} = 0$, $r_T = 1$.
3. for point and random orientation, $(\Delta\rho/\rho_0)_{TL\min} = (\Delta\rho/\rho_0)_{T\min} = (\Delta\rho/\rho_0)_{\max} = (\Delta\rho/\rho_0)_{cr}/3$, and $r_{TL} = r_T = 1$.

In a carbon sample, the lower is the value of r_{TL} , then the closer is the degree of orientation of carbon (graphene) layers to a perfect orientation of carbon. Values of r_T indicate how perfect are the orientations of the graphene layers. It is impossible to clarify from the anisotropy ratios r_{TL} and r_T if the orientation is the point orientation or is random orientation or if the co-axial or radial arrangements are in the axial orientation.

To make magnetoresistance measurements, the carbon sample is fixed onto a sample mount. Four gold wires, two for current and two for voltage, are cemented to the specimen with gold paint. The diameter of the gold wire depends on the size of the specimen. For $10\ \mu\text{m}$ graphite films or carbon fibers, the diameter of the wire must be about $25\ \mu\text{m}$. When negative magnetoresistance is measured, its value is so small that the current must be stabilized within an accuracy below 10 ppm, and to measure the voltages associated with the magnetoresistance a precise detector must fitted.

Magnetic field rotation by the rotation schemes $TL(\phi)$ and $T(\theta)$ can be made by rotation of a pair of the electromagnet poles or by sample rotation. A super-conducting solenoid is convenient to generate a very high field but, if used, special care must be taken with the location of the sample holder, because the field is generated along the axis of the solenoid.

4 Application of Magnetoresistance Technique for Synthesis of High-Quality Graphite Film from Aromatic Polyimide Film

As explained above, magnetoresistance measurements are useful in the characterization of carbon materials [1]. This section, as an example, discusses the application of magnetoresistance to the graphitization of a carbonized aromatic polyimide film from pyromellitic dianhydride/p-phenylenediamine (PMDA/PPD) [10] (see Fig. 4) and preparation of the graphite film from its carbonized films [11].

The aromatic polyimide film carbonizes in an inert gas atmosphere without development of cracks and pores. There are three reasons why these various polyimide-based carbon films exhibit graphitizability: (1) the parent organic molecules are planar, (2) there is a high degree of orientation, and (3) during carbonization non-carbon-containing molecules are lost as volatile compounds. Of these aromatic

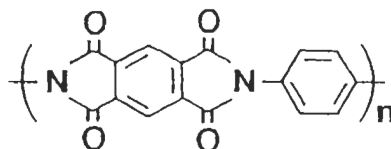


Fig. 4. Molecular structure of PMDA/PPD.

polyimide molecules, PMDA/PPD is the most flat, as shown in Fig. 4. This molecule does not contain ether oxygen but its film is very brittle. A PMDA/PPD film, named PPT, was prepared at the Research Laboratory of Toho Rayon Co. Ltd. with a small amount of additive to keep the film flexible (Fig. 4).

Rectangular specimens, approximately 26 mm long and 10 mm wide, were cut from a 45 μm thick PPT film, sandwiched between polished artificial graphite plates and heated by infrared radiation to 900°C at a rate of 2°C min⁻¹ in a flow of nitrogen for 1 h. These carbonized films were then stepwise heat-treated, 1800–3200°C in flowing argon. The residence times at final temperatures were 30 min between 1800 and 3000°C, and 10 min at 3200°C.

Figure 5 shows changes in the X-ray 006 diffraction profiles (using Cu K α radiation) of the specimen films with increasing HTT. For each film specimen, in the

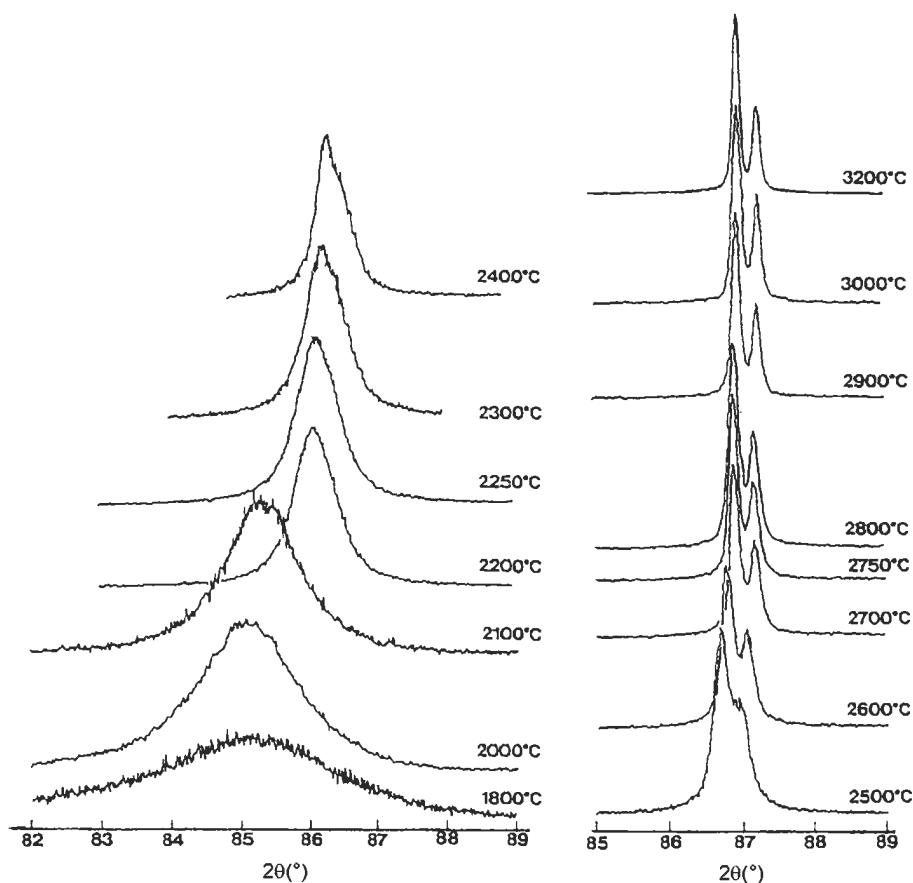


Fig. 5. '006' Diffraction profiles of PPT-derived carbon films heat-treated at various temperatures (reprinted with the permission of Elsevier Science from Ref. [10]).

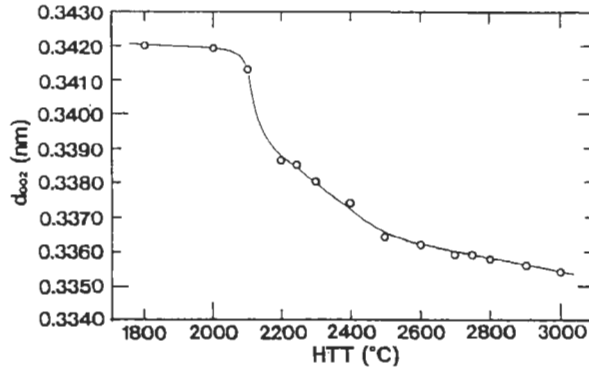


Fig. 6. d_{002} for PPT-derived carbon films heat-treated at temperatures between 1800 and 3000°C (reprinted with the permission of Elsevier Science from Ref. [10]).

2θ range from 82 to 89°, only the 006 line was observed with no trace of the 112 line, implying a high degree of orientation of graphene planes parallel to the film surface. After heat treatment above 2600°C each 006 line had clearly separated into the two lines of the $K\alpha_1$ and $K\alpha_2$ radiation. The d_{002} values obtained are plotted as a function of HTT in Fig. 6. The d_{002} values for the specimens of HTT 3000°C and 3200°C are 0.3354 nm, namely that of natural graphite. The parameter “mosaic spread” measures the orientations of graphene layers and by the width at half the maximum height of the 002 diffraction, when plotted against the rotation angle ϕ of the film. ϕ is referred to the normal of the film surface at the diffraction angle which gives maximum intensity. The mosaic spread of the carbon film is plotted against HTT in Fig. 7. It is worth noting that the value of ϕ of the specimen of HTT 1800°C is as narrow as 13°, indicating relatively good orientation of the graphene layers.

Figure 8 shows $(\Delta\rho/\rho_0)_{\max}$ in a magnetic field of 1 T for the PPT-derived carbon films, HTT 1800–3000°C. The $(\Delta\rho/\rho_0)_{\max}$ values are negative for specimens heat-treated below 2100°C and become positive at HTT \geq 2250°C.

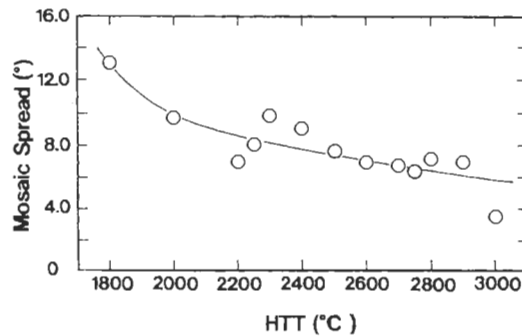


Fig. 7. Mosaic spread for PPT-derived carbon films heat-treated at temperatures between 1800 and 3000°C (reprinted with the permission of Elsevier Science from Ref. [10]).

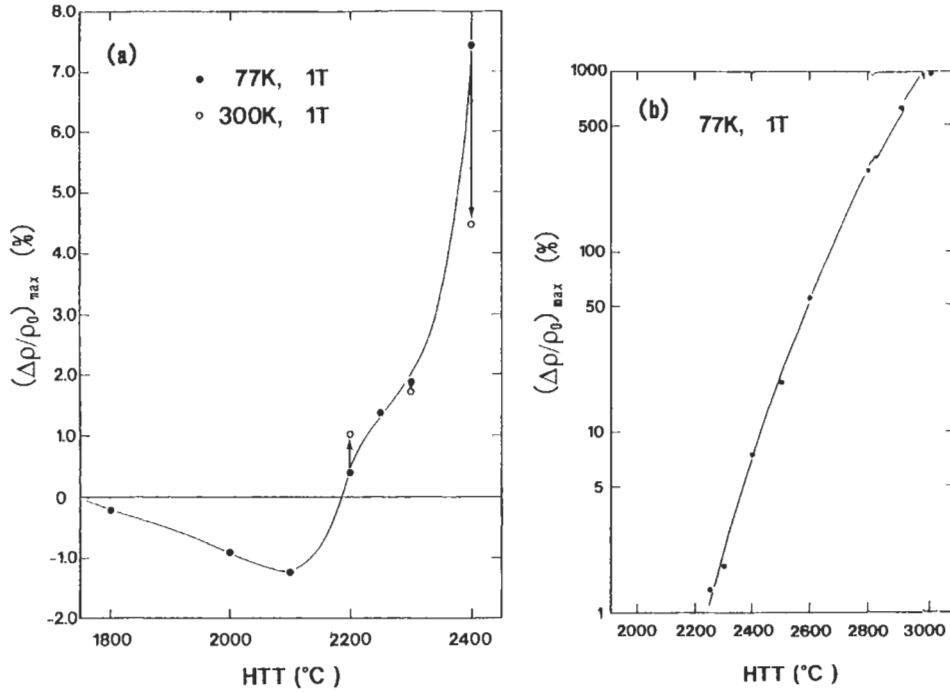


Fig. 8. $(\Delta\rho/\rho_0)_{\max}$ measured in a field of 1 T for PPT-derived carbon films heat-treated at temperatures between 1800 and 3000°C (reprinted with the permission of Elsevier Science from Ref. [10]).

The values of $(\Delta\rho/\rho_0)_{\max}$ for the 2200°C specimen, at 77 K, are positive at all magnetic fields up to 1 T, but are slightly negative for $(\Delta\rho/\rho_0)_{T_{\min}}$ and $(\Delta\rho/\rho_0)_{TL_{\min}}$, -0.01% and -0.009% , respectively. This dependence of magnetic field orientation at 1 T results from the superposition of two magnetoresistance components, one component with positive magnetoresistance and the other with negative magnetoresistance. Because the negative magnetoresistance relates to the turbostratic structures and the positive to graphite, the 2200°C specimen consists, electrically, of two phases. But no direct evidence for such a composite structure has been found in X-ray diffraction studies. The negative magnetoresistance decreases its absolute value more rapidly with increasing temperature of measurement than the positive magnetoresistance [12]. Hence, the value of $(\Delta\rho/\rho_0)_{\max}$ of the 2200°C specimen, when measured at room temperature, should be larger than that at 77 K. Results in a field of 1 T confirm this as being 1.03% at room temperature and 0.400% at 77 K, as indicated by open circles in Fig. 8a. Also, the 2250°C specimen gives nearly the same values, 1.33 and 1.37%, respectively. Further increases of HTT up to 2300 and 2400°C cause reversal of the relative magnitudes as indicated by changes to arrows from solid to open circles in Fig. 8a. With a decreasing contribution of the negative component, the net magnetoresistance is reduced with increasing temperature. This is the case for the specimen of HTT 2400°C (Fig. 8a), and less markedly for the specimens of HTT 2250 and 2300°C.

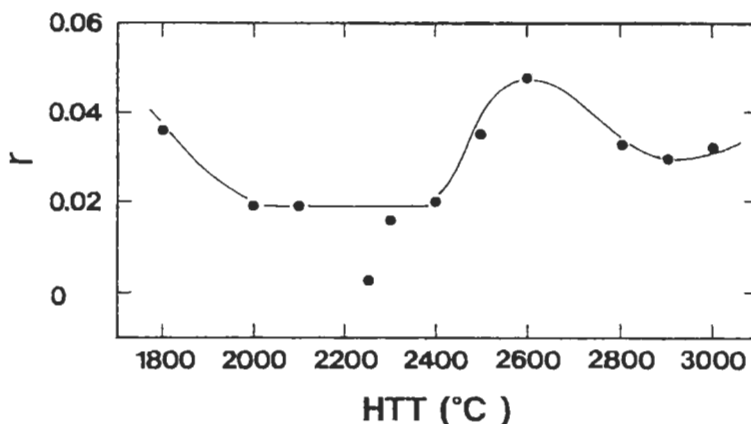


Fig. 9. r for PPT-derived carbon films heat-treated at temperatures between 1800 and 3000°C (reprinted with the permission of Elsevier Science from Ref. [10]).

Figure 8b shows the dependence of $(\Delta\rho/\rho_0)_{\max}$ on HTT between 2250 and 3000°C. $(\Delta\rho/\rho_0)_{\max}$ exceeds 900% for the specimen of HTT 3000°C and reaches 1206% for the specimen of HTT 3200°C (held for 10 min). It must be noted that values of $(\Delta\rho/\rho_0)_{\max}$ observed in regular quality HOPG, are in the range of 1100–1300% [8].

The textures of the carbon films are similar to that of ideal graphite but are less perfect. The values of r_T and r_{TL} of each heat-treated film are close to zero, but are not identical with each other, because of a small inhomogeneity (heterogeneity) in texture. Therefore, the mean value of r_T and r_{TL} , $r = (r_T + r_{TL})/2$, was used as a parameter for the degree of orientation. In Fig. 9, r is plotted as a function of HTT. The trend in Fig. 9 can be interpreted as follows.

The orientation of the specimen of HTT 1800°C is turbostratic and with a relatively high degree of orientation of the graphene layers along the film surface. The degree of orientation was improved by successive heat treatment up to 2000°C even though the transformation from turbostratic structure to graphite was initiated. A further increase in HTT caused slight deformation of the film, probably due to the growth of the graphite crystallites. At higher values of HTT, the crystallites continue to grow and, as a consequence, r increased gradually. It seems that at a certain HTT an annealing effect of lattice imperfections takes place in addition to the crystal growth. A critical HTT appears at $\sim 2600^\circ\text{C}$ when the maximum value of r was obtained. However, the annealing effect might granulate graphite crystallites, so that r begins to level off changing little on heating to 2900°C. The r value at 3200°C is 0.0333 (not shown in Fig. 9). The resistivity ratio $\rho_{RT}/\rho_{4.2K}$ of this carbon specimen is 3.45, ρ_{RT} and $\rho_{4.2K}$ being the resistivities at room and liquid helium temperatures with the crystallinity corresponding to that of an HOPG.

Kaburagi et al. [11] obtained highly graphitic films from PPT-derived carbon films by heat treatment at 3200°C. Rectangular strips of film, 3 mm wide and 20 mm in length, were cut from the PPT film and carbonized by infrared heating. The

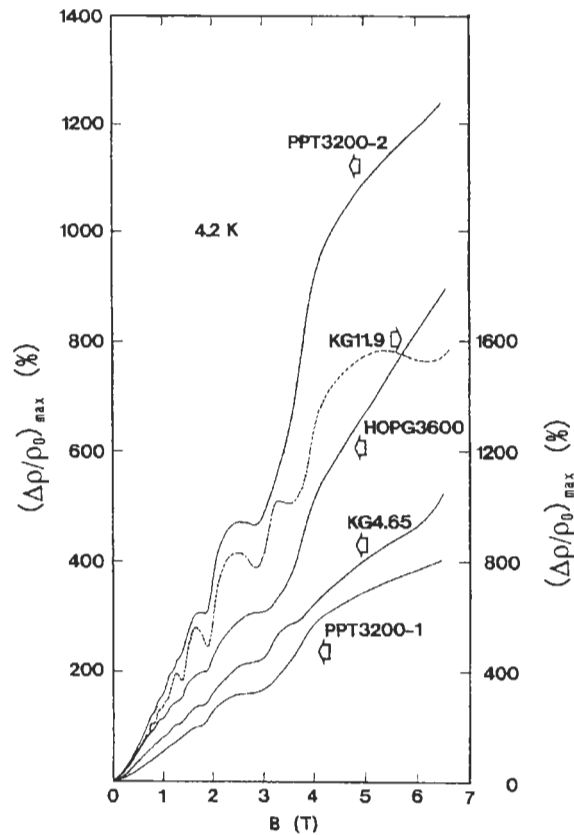


Fig. 10. $(\Delta\rho/\rho_0)_{\max}$ at liquid helium temperature for PPT3200-2, together with those KG4.65, KG11.9, HOPG3600 and PPT3200-1 (reprinted with the permission of Material Research Society from Ref. [11]).

carbonized film-strips were then heat treated using two different procedures. Each of the carbonized films was sandwiched between two polished artificial graphite plates. One, called PPT3200-1, was heated up 3200°C in a graphite resistance furnace in a flow of argon (soak time 10 min). The second strip, called PPT3200-2, was heated to 3100°C (soak time 40 min) and then at 3200°C (soak time 23 min). The $d_{(002)}$ values for these specimens were identical, i.e. 0.3354 nm.

The resistivity ratio $\rho_{RT}/\rho_{4.2K}$ was 3.45 for PPT3200-1 and 4.90 for PPT3200-2, while $(\Delta\rho/\rho_0)_{\max}$ in a field of 1 T at 77 K was 1206% for PPT3200-1 and 1621 % for PPT3200-2, indicating higher crystallinity of PP3200-2. This is supported by a measurement of the Shubnikov–de Haas oscillation observed of $(\Delta\rho/\rho_0)_{\max}$ at 4.2 K for PPT3200-2, as shown in Fig. 10. Here, the results for KG4.65, KG11.9, HOPG3600 and PPT3200-1 are shown for comparison (KG is kish graphite) followed by its resistivity ratio $\rho_{RT}/\rho_{4.2K}$, the number after HOPG is the annealing temperature. The r values for PPT3200-1 and PPT-3200-2 are 0.0170 and 0.0051, and that of HOPG3600 is 0.0051. These results indicate the extensive graphitization of PPT3200-2.

5 Negative Magnetoresistance in Boron-doped Graphites

Boron substitutes carbon atoms in graphene layers, the maximum solid solubility being 2.35 at% at 2350°C [13]. Hishiyama et al. [14–16] and Sugihara et al. [17] found a weak negative transverse magnetoresistance for three kinds of boron-doped graphites with the field perpendicular to the specimen surface, and characterized by a field dependence proportional to $B^{1/2}$ at temperatures below 4.2 K. The boron-doped natural graphite compacts, boron-doped Grafoil materials and boron-doped graphite films were studied, the boron-doped graphite films being Kapton-derived highly graphitic graphite films (HOGF). All of the boron-doped carbons have interlayer spacing, d_{002} , lower than for single crystal graphite, 0.3345 nm, and electrical resistivities which exhibit weak temperature dependence but which, at substantially lower temperatures, increase with decreasing temperature expressed as $T^{1/2}$. This type of negative magnetoresistance is not due to increases in carrier density, as for turbostratic carbons [4], nor to two-dimensional weak localization which was used by Bayot et al. to explain the negative magnetoresistance of turbostratic carbons, because of the different type of field dependence of the negative magnetoresistance and the different type of dependence of the resistivity on temperature [6]. It is probably explained by a three-dimensional weak localization in graphites as proposed by Hishiyama et al. [16,17]. Hishiyama et al. [16] related the negative magnetoresistance of boron-doped graphite to a disordered structure created by the substitution by boron atoms. An X-ray study of the boron-doped HOGFs (B-HOGFs) was carried out as well as a cross-sectional study by scanning electron microscopy (SEM) and Raman scattering.

Hishiyama et al. [16] used HOGF, about 11 μm in thickness, for boron doping. The high level of orientation of the graphene layers is slightly disturbed by boron doping. The disturbance is seen in cross-sectional SEM micrographs of HOGF and B-HOGF. The lattice constant c_0 was determined from the 002, 004 and 006 diffraction lines measured in the reflection mode with a_0 being measured from the 100 and 110 diffraction lines in the transmission mode. The atomic fraction of dissolved boron x_B for B-HOGFs was estimated from X-ray diffraction measurements from relationships of the lattice constants a_0 and c_0 vs x_B given by Lowel [13]. The values of a_0 and c_0 , x_B and the full width at half maximum of the peak intensity of the 002 diffraction $\phi_{1/2}$ for the samples are listed in Table 1.

The X-ray diffraction results for the B-HOGF indicated well-crystallized materials, but appear to be rather disordered as indicated by the Raman spectra. Figure 11 shows the first and second order Raman spectra of HOPG, HOGF, B-HOGFs and glass-like carbon heat-treated at 1600°C (GC-1600). The Raman spectra of HOPG and HOGF are those of well-crystallized graphite materials and show a G band at 1585 cm^{-1} , an overtone band at 2441 cm^{-1} , a doublet at 2680 cm^{-1} (G_1' band) and 2725 cm^{-1} (G_2' band) and an overtone band at 3249 cm^{-1} . The spectra of B-HOGF-0.4 and B-HOGF-2.2 are similar to those of carbons with small crystallites [18,19]. The spectra show the relatively strong D band (1367 cm^{-1}), the D' band (1623

Table 1

The lattice constants a_0 and c_0 , atomic fraction of boron dissolved into lattice x_B , the full width at the half-maximum of the peak intensity recording of the 002 diffraction $\phi_{1/2}$, room temperature resistivity ρ_{300K} , resistivity ratio ρ_{300K}/ρ_{3K} and transverse magnetoresistance measured at 3 K in a field of 1 T $(\Delta\rho/\rho_0)_{3K,1T}$ for HOGF and B-HOGFs [16]

| Sample code | a_0 (nm) | c_0 (nm) | x_B (at%) | $\phi_{1/2}$ (°) | $\rho_{300K} \times 10^7$ (Ωm) | ρ_{300K}/ρ_{3K} | $\Delta\rho/\rho_0)_{3K,1T}$ (%) |
|-------------|---------------|---------------|----------------|---------------------|---|-------------------------|-------------------------------------|
| HOGF | 0.24612 | 0.67076 | 0 | 4.04 | 6.33 | 1.13 | 901 |
| B-HOGF-0.4 | 0.24623 | 0.67054 | 0.4 | 4.62 | 13.0 | 1.0391 | 0.137 |
| B-HOGF-0.5 | — | 0.67046 | 0.5 | — | 14.2 | 0.9911 | 0.003 |
| B-HOGF-0.9 | — | 0.67022 | 0.9 | — | 19.5 | 0.9735 | -0.183 |
| B-HOGF-1.4 | — | 0.66992 | 1.4 | — | 24.8 | 0.9645 | -0.179 |
| B-HOGF-2.2 | 0.24682 | 0.66944 | 2.2 | 10.23 | 26.4 | 0.9785 | -0.169 |

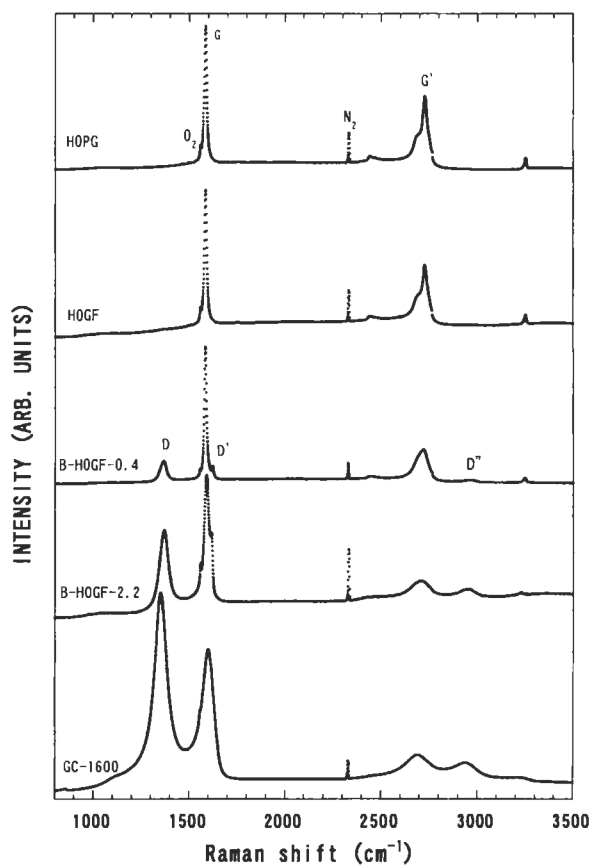


Fig. 11. Raman spectra of HOPG, HOGF, B-HOGF-0.4, B-HOGF-2.2, and GC-1600 with 514.5-nm excitation [16].

cm^{-1}) at the high frequency side of the G band (1584 cm^{-1}), the weak 2441 cm^{-1} band, and the single unsymmetrical G' band (2720 cm^{-1}) which is a merged band of G' and G'' bands observed in HOPG and HOGF, the D'' band (2962 cm^{-1}), and the band at 3246 cm^{-1} . The occurrence of D , D' and D'' bands is a characteristic of a disordered graphite structure and is related to the substituted boron atoms in the graphene layers. With increasing x_B , the relative intensities of the D and D' bands to the G band increase and that of the G' band to the G band decreases. The Raman spectrum of GC-1600 is similar to that of B-HOGF-2.2, showing a higher disorder.

The room temperature electrical resistivity, $\rho_{300\text{K}}$, the resistivity ratio $\rho_{300\text{K}}/\rho_{3\text{K}}$, where $\rho_{3\text{K}}$ is the resistivity at 3.0 K and transverse magnetoresistance at 3.0 K in a magnetic field of 1 T $(\Delta\rho/\rho_0)_{3\text{K},1\text{T}}$ for HOGF and B-HOGFs are listed in Table 1.

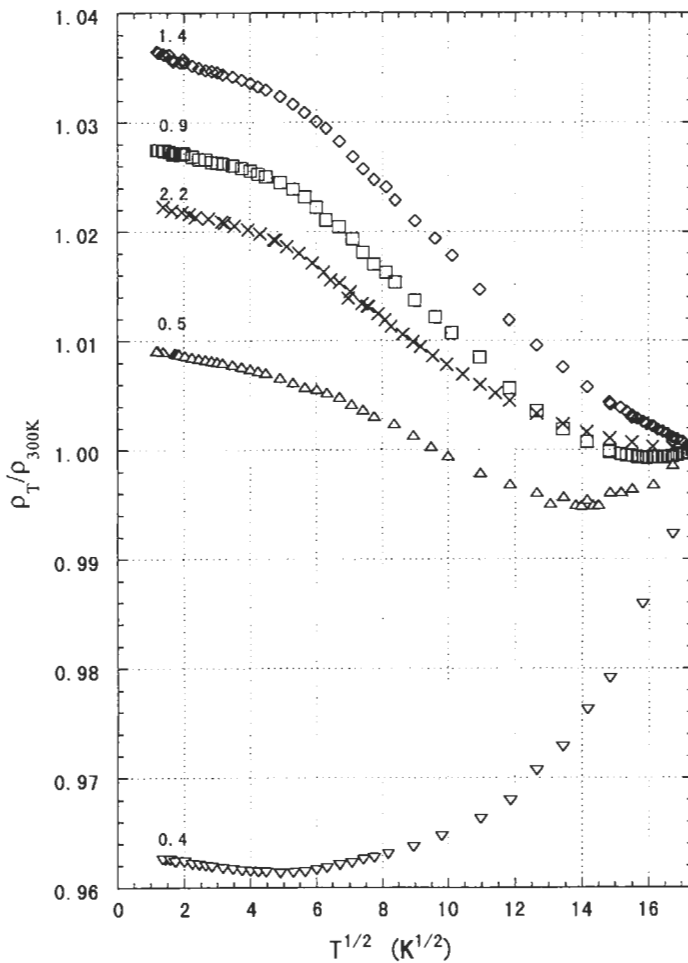


Fig. 12. Relative resistivity $\rho_T/\rho_{300\text{K}}$ for B-HOGFs plotted as a function of $T^{1/2}$ [16].

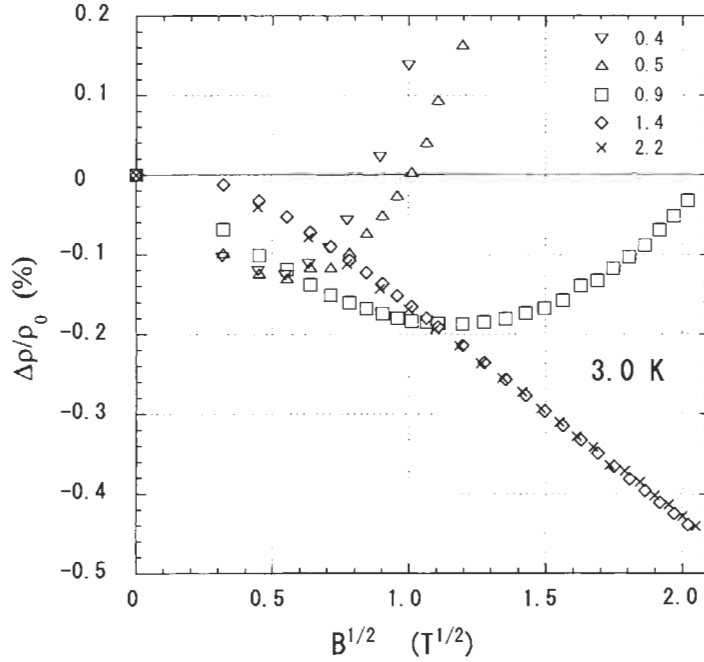


Fig. 13. Transverse magnetoresistance $\Delta\rho/\rho_0$ measured at 3.0 K for B-HOGFs, plotted as a function of $B^{1/2}$ [16].

HOGF is characterized by a large value of $(\Delta\rho/\rho_0)_{3K,17}$, while each of the B-HOGFs is differentiated by a small positive or a small negative value of $(\Delta\rho/\rho_0)_{3K,17}$. The dependence of the resistivity ρ_T on temperature for HOGF is weakened at the lowest x_B value, while keeping the weak dependence for all of the B-HOGF carbons. This fact indicates that scattering from the substituted boron atoms dominates over the lattice scattering [20]. Values of ρ_T/ρ_{300K} for B-HOGF carbons are plotted as a function of $T^{1/2}$ in Fig. 12 where the number represents the value of x_B . With increasing $T^{1/2}$, starting from the lowest temperature, the resistivity decreases gradually and linearly with $T^{1/2}$ to about 20 K, then decreases a little gradually to pass through a shallow minimum and then finally increases. The temperature of minimum resistivity increases with increasing x_B , exceeding 300 K for B-HOGF-1.4 and -2.2. Because the temperature dependence of the resistivity for B-HOGF-1.4 and -2.2 is very weak, the linear $T^{1/2}$ dependence at low temperature is related to an additional resistivity superimposed onto the Boltzmann contribution. The additional resistivity could be attributed to the quantum correction of the resistivity due to the 3-D weak localization $\delta\rho$ which is obtained by extending the Kawabata's theory to the SWMcC band [16,17].

Figure 13 shows the transverse magnetoresistance $\Delta\rho/\rho_0$ measured at 3.0 K for B-HOGF-1.4 and -2.2 plotted as a function of $B^{1/2}$ and indicating that $\Delta\rho/\rho_0$ is negative

and decreases with increasing $B^{1/2}$. For B-HOGF-0.9, $\Delta\rho/\rho_0$ is negative in low fields, decreases linearly with $B^{1/2}$ in fields below 0.41 T, passes through a minimum and then increases with a change in sign with a further increase of B . Similarities among the curves of the field dependence of $\Delta\rho/\rho_0$ for B-HOGF-0.4, 0.5, and 0.9, and the linear $B^{1/2}$ dependence of $\Delta\rho/\rho_0$ in low fields for these samples is qualitatively explained by Hishiyama et al. [16] and Sugihara et al. [17]. For B-HOGF-1.4 and -2.2, $\Delta\rho/\rho_0$ decreases linearly with $B^{1/2}$ in fields above about 0.8 T.

References

1. Y. Hishiyama, Y. Kaburagi and M. Inagaki, Characterization of structure and microtexture of carbon materials by magnetoresistance technique. In: P.A. Throver (Ed.), Chemistry and Physics of Carbon, Vol. 23, pp. 1–68. Marcel Dekker, New York, 1991.
2. D.E. Soule, Magnetic field dependence of the Hall effect and magnetoresistance in graphite single crystals. *Phys. Rev.*, 112: 698–707, 1958.
3. Y. Hishiyama, Negative magnetoresistance in soft carbons and graphite. *Carbon*, 8: 259–259, 1970.
4. P. Delhaes, P. de Kepper and M. Uhlich, A study of the negative magnetoresistance in pyrolytic carbons. *Phil. Mag.*, 29: 1301–1330, 1974.
5. A.A. Bright, Negative magnetoresistance of pregraphitic carbons. *Phys. Rev.*, B20: 5142–5149, 1979.
6. V. Bayot, L. Piraux, J.-P. Michenaud, J.-P. Issi, M. Lelaurain and A. Moore, Two-dimensional weak localization in partially graphitic carbons. *Phys. Rev.*, B41: 11770–11779, 1989.
7. M. Inagaki, Microtextures of carbon materials. *Tanso* (No. 122): 114–121, 1985.
8. M. Inagaki, *New Carbons*. Elsevier Science, Oxford, 2000.
9. Y. Hishiyama, Y. Kaburagi, M. Inagaki, T. Imamura and H. Honda, Graphitization of oriented coke made from coal tar pitch in magnetic field. *Carbon*, 13: 540–542, 1975.
10. Y. Hishiyama, M. Nakamura, Y. Nagata and M. Inagaki, Graphitization behavior of carbon film prepared from high modulus polyimide film: synthesis of high-quality graphite film. *Carbon*, 32: 645–650, 1994.
11. Y. Kaburagi, A. Yoshida and Y. Hishiyama, Microtexture of highly crystallized graphite as studied by galvanomagnetic properties and electron channeling contrast effect. *J. Mater. Res.*, 11: 769–778, 1996.
12. Y. Kaburagi, R.H. Bragg and Y. Hishiyama, Electrical resistivity, transverse magnetoresistance and Hall coefficient in pyrolytic carbon: correlation with interlayer spacing $d_{(10)2}$. *Phil. Mag. B.*, 63: 417–436, 1991.
13. C.E. Lowell, Solid solution of boron in graphite. *Am. Ceram. Soc.*, 50: 142–144, 1967.
14. Y. Hishiyama, Y. Kaburagi, K. Kobayashi and M. Inagaki, Structure and properties of boronated graphite. *Molec. Cryst. Liquid Cryst.*, 310: 279–284, 1998.
15. Y. Hishiyama, Y. Kaburagi and K. Sugihara, Negative magnetoresistance and of magnetic susceptibility of boronated graphite. *Molec. Cryst. Liquid Cryst.*, 340: 337–342, 2000.
16. Y. Hishiyama, H. Irumano, Y. Kaburagi and Y. Soneda, Structure, Raman scattering and transport properties of boron-doped graphite. *Phys. Rev. B*, 63: 245406-1–24506-11, 2001.
17. K. Sugihara, Y. Hishiyama and Y. Kaburagi, Electronic and transport properties of boronated graphite: 3D-weak localization effect. *Molec. Cryst. Liquid Cryst.*, 340: 367–371, 2000.

18. R.J. Nemanich and S.A. Solin, First and second-order Raman scattering from finite-size crystals of graphite. *Phys. Rev. B*, 20: 392–401, 1979.
19. R.P. Vidano, D.B. Fischbach, L.J. Wills and T.M. Loehr, Observation of Raman band shifting with excitation wavelength for carbons and graphites. *Solid State Commun.*, 39: 341–344, 1981.
20. D.E. Soule, The effect of boron on the electronic properties of graphite. In: *Proceedings of the Fifth Conference on Carbon*, Vol. 1, pp. 13–21. Pergamon Press, Elmsford, N.Y., 1962.

Part 5

Function Developments and Application Potentials

Chapter 25

Applications of Advanced Carbon Materials to the Lithium Ion Secondary Battery

Morinobu Endo and Yoong Ahm Kim

Faculty of Engineering, Shinshu University, Nagano-shi 380-8553, Japan

Abstract: Lithium ion secondary batteries are currently the best portable energy storage device for the consumer electronics market. Recent developments of the lithium ion secondary batteries have been achieved by the use of selected carbon and graphite materials as anodes. The performance of lithium ion secondary batteries depends significantly on the microstructure of the anode materials made from carbon and graphite. Due to the contribution of the carbon materials used in the anode for last ten years, the capacity of the typical Li-ion battery has been improved almost double. However, active investigations continue to identify the key parameters of carbons that provide improved anode properties. Carbon and graphite materials have a wide variety of microstructure, texture, crystallinity and morphology, depending on their preparation processes and precursor materials, as well as various forms such as powders, fibers and spherules. This chapter describes correlations between microstructural parameters and electrochemical properties of conventional and novel types of carbon materials for Li-ion batteries. Anode carbons include graphitizable carbons such as milled mesophase pitch-based carbon fibers, non-graphitizable carbon such as polyparaphenylene-based carbon heat-treated at low temperatures. Market demand and the trends in lithium-ion secondary batteries are commented upon.

Keywords: Carbon, Microstructure, Anode material, Lithium ion battery.

1 Introduction

This chapter discusses recent achievements of carbon anode materials and their structural design for better performances of Li-ion secondary batteries. Metallic lithium is very promising as an electrode material of batteries that can bring the lightest weight with high voltage and high energy density. Because lithium possesses the lowest electronegativity of the standard cell potential -3.045 V in existing metals, it is the anode material which gives electrons most easily to form positive ions [1]. However, the negative electrode of lithium metal has serious problems in secondary battery use, because its cyclic life is too short and there are safety factors caused by dendrite formation on surfaces of lithium metal electrode during charge/discharge

cycles [2–5]. To solve these problems a locking-chair concept was established in which intercalation phenomena were used for the anode reaction of lithium ion secondary batteries [6–10]. The intercalation of lithium into graphite through vapor transport was first synthesized as a graphite intercalation compound (GIC) with stage structure [11]. Since then, extensive studies have investigated both staging and charge transfer phenomena of the Li-GICs, of composition Li_xC_6 , with $0 \leq x \leq 1$, and $x = 3$ under high pressure, in carbon materials having a wide range of structures [12–15].

In the rechargeable Li-ion batteries, based on the rocking chair or shuttle cock concept, lithium ions shift back and forth easily between the intercalation hosts of cathode and anode. Thus, lithium ion secondary batteries consist of a carbonaceous anode and a lithium transition metal oxide such as LiCoO_2 , LiNiO_2 and LiMn_2O_4 as the cathode, as shown in Fig. 1a. The anode on Cu foil and cathode on Al foil are formed into spiral or plate-folded shapes which give a US18650 cylindrical type (18

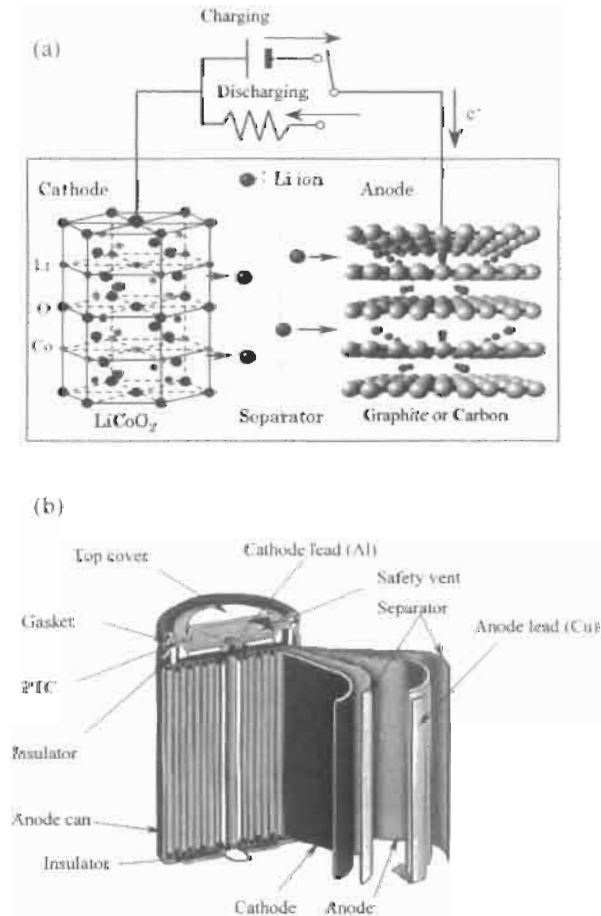


Fig. 1. (a) Charging/discharging mechanism of Li-ion secondary battery; (b) cylindrical cell.

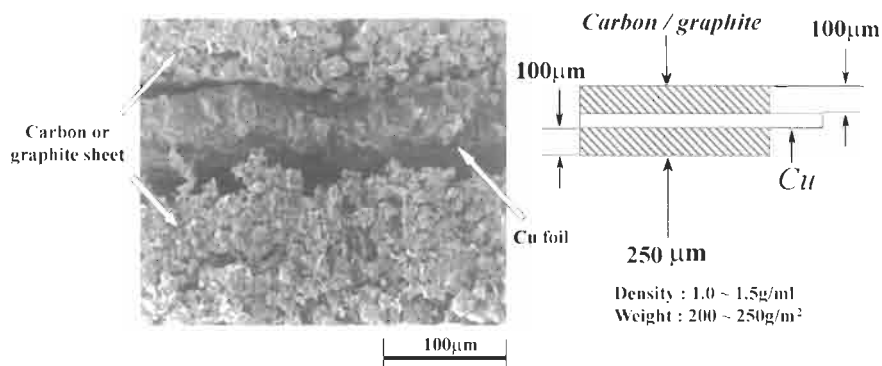
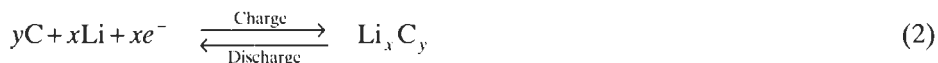
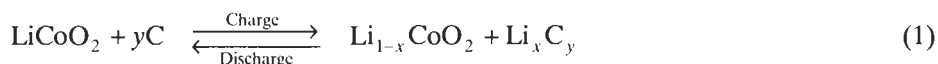


Fig. 2. SEM photographs of the carbon anode sheets formed on both sides of a Cu foil lead.

mm diameter and 650 mm height, Fig. 1b), and prismatic cells. Between these two electrodes, a porous polymer separator of polyolefin with about 25 μm thickness, made by polyethylene (PE) and polypropylene (PP) is placed (Fig. 1b) [16,17]. Figure 2 shows SEM photographs of anodes in which carbon sheets are formed on both sides of a copper-foil lead. The electrolyte is an organic liquid such as PC, EC+DEC or a recently developed gel type polymer stable under high voltages. A lithium salt such as LiClO₄, LiBF₄ and LiPF₆ is dissolved in the electrolyte.

A theoretical lithium storage capacity of a graphite anode for a Li ion secondary battery could be 372 mAh g⁻¹ and corresponding to the 1st stage GIC LiC₆. The charge/discharge total reactions and anode reaction based on Li⁺ intercalation and de-intercalation are as follows [18]:



On the other hand, disordered carbons with lithium storage capacities exceeding the theoretical capacity have been reported. This phenomenon is still difficult to explain by the GIC formation mechanism mentioned above, and new explanations are required.

Several carbon types from highly ordered graphite to disordered carbons have been investigated experimentally and theoretically for applications as anode materials with an emphasis on specific capacity, cyclic efficiency and cyclic lifetime. As anodes in lithium-ion batteries, carbon microstructure and morphology must be controlled. It is already established that the performance of lithium-ion batteries depends strongly on the thermal history and morphology of carbon and graphite materials used [19]. As carbon and graphite materials vary widely in their

microstructure, texture, crystallinity and morphology, it has been important to choose an anode material to give the best battery performance [20–22]. Two types of carbon material have been used, that is highly ordered graphites heat-treated to 3000°C and non-graphitizable carbon heat-treated only to 1100°C. Precursor materials include cokes, polymers and fibers. The insertion behavior and mechanism of lithium ions into carbon and graphite hosts have been extensively studied [23–28]. In particular, lithium insertion and resultant electrochemical properties of low temperature carbons are not yet fully understood. Low temperature carbons are promising for the Li-ion battery because of their superior capacity. Also, low temperature forms of carbons could save production energy because graphites need to be heated to ~3000°C with a production level of ~ 200 ton month⁻¹.

2 Characteristics of Li-ion Secondary Battery

The basic features of Li-ion secondary batteries are summarized as follows [16]:

1. High energy density: 135 Wh kg⁻¹ and 300 Wh L⁻¹.
2. High operating output voltage: the operating output voltage is 3.6 V, three times higher than that of Ni-Cd or Ni-MH cells.
3. High charging characteristics: there is no memory effect as may occur with Ni-Cd batteries with repeated weak discharges.
4. Long cycle life: superb recharging properties allow more than 500 repeated charge/discharged cycles.
5. Minimal self-discharge: self-discharge is less than 10% per month.
6. Remaining capacity display: use of a discharge curve easily shows remaining capacity.

Therefore, Li-ion secondary batteries, currently, are the best of available energy storage devices for portable consumer electronics. They were first developed and commercialized in 1992 and are used in computer notebooks, cellular phones, digital video cameras, personal computers with color liquid crystal device (LCD) and high speed CPU [22,29,30]. As shown in Fig. 3, lithium-ion secondary batteries are superior to Ni-Cd batteries (1.2 V). They have the advantages of 1.5 times in volume and 1.5–2 times in energy density (on a weight basis), and have ~3 times the voltage (~3.6V) [29]. There exists a strong consumer demand from the electronics market for further improvements in energy density, out-put current, safety and cost. High performance batteries in personal computers and cellular phones may eliminate battery charging. Li-ion polymer type batteries, described later, may be the next challenge in this market.

3 Carbon and Graphite Host Materials

Carbon materials exhibit many relevant and diverse characteristics including their crystallinity, morphology and texture. Structure is the most important characteristic in terms of electrochemical performance. Structure in a carbon is a function of the

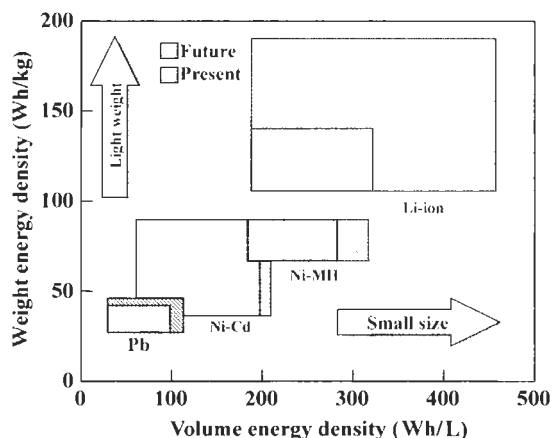


Fig. 3. Energy density of various kinds of secondary batteries; present (shaded area) and future (cross-hatched area) based on electrodes.

chemical composition of the parent material and of its preparation history (pyrolysis and carbonization) [22]. Carbons are classified into two types, i.e., graphitizable (soft carbons) and non-graphitizable (hard carbons) according to the parent material and heat treatment temperature (HTT). Graphitizable carbons have an HTT > 2300°C. Non-graphitizable carbons do not graphitize even at temperature >2800°C. Non-graphitizable carbons are mostly prepared by solid-phase pyrolysis of organic polymer precursors.

Anisotropic single crystal graphite is hexagonal, with the graphene layers stacked in an AB sequence or is the less common rhombohedral structure with an ABC sequence. The anisotropy relates directly to strong intralayer interactions and very weak Van der Waals interplanar interactions. In addition, non-graphitic carbons contain defective carbon layers characterized by misfits and misorientation angles (turbostratic disorder) leading to higher average layer plane spacing [31–34].

4 Lithium/Graphite Intercalation Compounds

Lithium graphite intercalation compounds (Li-GICs) were synthesized by vapor transport and exhibit a “staged” structure [10]. At 0.1 MPa a maximum lithium uptake of LiC_6 was obtained in highly crystalline graphite. Intercalation proceeded via the edges, arm-chair and zigzag faces of the graphite because of the low concentration of defects in the graphene layer surfaces [35]. Figure 4 shows the several stage structures of Li-graphite intercalation compounds (Li-GICs). However, lithium-ion secondary batteries using graphitic carbons as anode, did not provide the capacity (372 mAh g^{-1}) of the first stage of Li-GIC. Lithium inserted electrochemically between the graphene layers exists as ions and shielding effects of electrons in the graphene layers may prohibit entry of further lithium ions. Also, it is thought that stacking faults in the graphite layers may contribute.

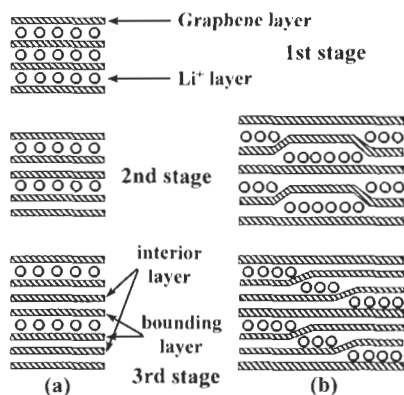


Fig. 4. The various stage structures of Li-graphite intercalation compounds (Li-GICs).

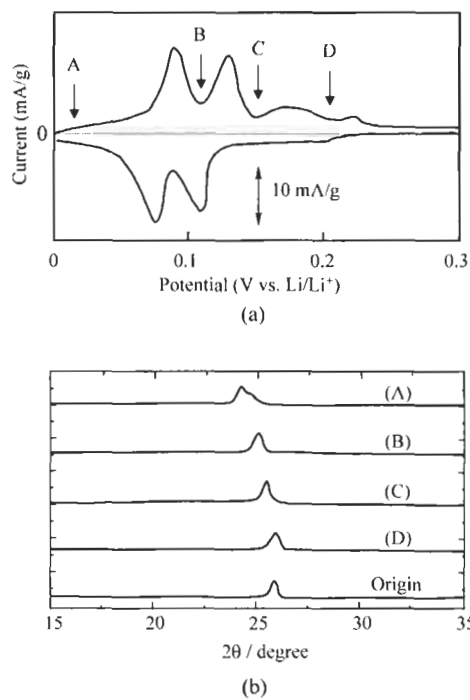


Fig. 5. (a) Voltammogram of graphitized MCMBs (mesocarbon microbeads); (b) X-ray diffraction patterns of the intermediate compounds obtained by charging to the potentials of (A) 0.01, (B) 0.11, (C) 0.14, and (D) 0.20 V [36].

Figure 5 shows (a) a voltammogram of graphitized MCMBs (mesocarbon microbeads) and (b) X-ray diffraction patterns of the intermediate compounds obtained at potentials of (A) 0.01, (B) 0.11, (C) 0.14 and (D) 0.20 V. Interlayer spacings, d_{002} of

Table 1

Structural parameters of intermediate compounds of MCMBs formed at potentials between reversible peaks [40]

| Inter- mediate compounds | $I_{c(\text{obs})}/\text{\AA}$ | $I_{c(\text{theoret.})}/\text{\AA}$ | | | | | | | Assign- ment |
|--------------------------------|--------------------------------|-------------------------------------|---------|---------|---------|---------|---------|---------|-----------------|
| | | Stage 1 | Stage 2 | Stage 3 | Stage 4 | Stage 5 | Stage 6 | Stage 7 | |
| A | 3.69 ± 0.001 | 3.70 | 3.54 | | | | | | Stage 1 |
| B | 3.53 ± 0.001 | 3.70 | 3.54 | 3.48 | | | | | Stage 3 |
| C | 3.49 ± 0.001 | | 3.54 | 3.48 | 3.46 | | | | Stage 3 |
| D | 3.43 ± 0.001 | | | | | 3.44 | 3.43 | 3.42 | Stage 5–7 |

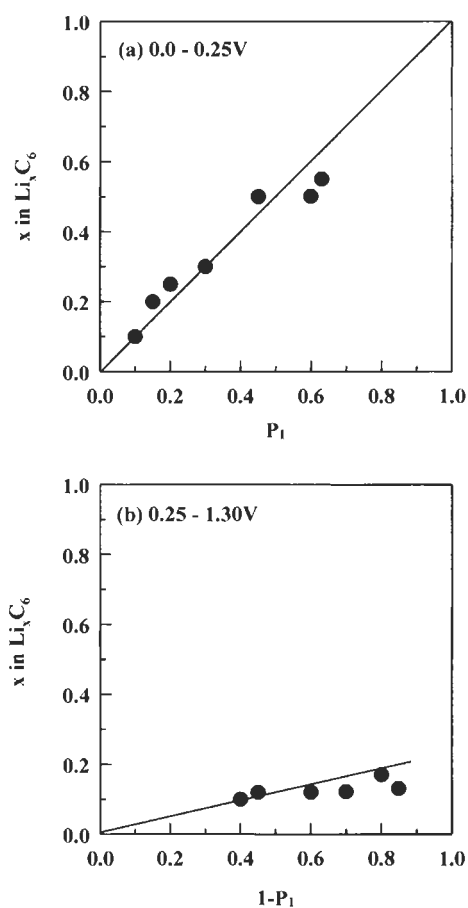


Fig. 6. The relationship linking the charge capacity of MCMBs during the first cycle and the volume ratio of the structures: (a) the charge capacity in the potential range 0–0.25 V vs. P_1 plots; (b) the charge capacity in the potential range 0.25–1.3 V vs. $(1-P_1)$ plots, from Tatsumi et al. [40].

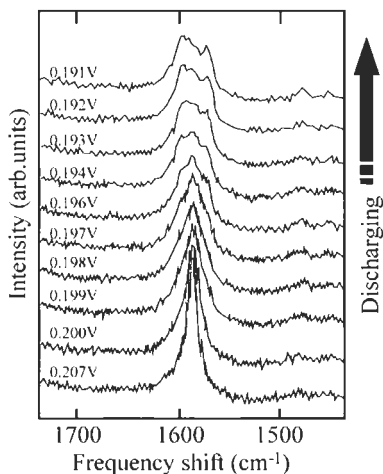


Fig. 7. *In-situ* Raman spectra of HOPG [40].

each compound, from X-ray diffraction data are in Table 1 [36] and show the different stages of Li-GICs. The Li^+ de-intercalation capacity was 282 mAh g^{-1} in the voltammogram equivalent to a decomposed lithium content $\text{LiC}_{7.9}$. The capacity of B compound is equivalent to LiC_{15} . Those values are close to theoretical values of LiC_6 and LiC_{12} suggesting that A and B compounds are first and second stages. Well-defined voltammogram peaks were not found for non-graphitic (non-graphitizable) carbons.

Factors to explain capacities of less than 372 mAh g^{-1} include effects of a - b axis crystallite size [37], stacking defects [25,38] and defects within graphene layers [39]. Tatsumi et al. [38] divided the discharge curve of graphitized MCMB at the threshold potential of 0.25 V, and evaluated the corresponding charge capacity as functions of graphitization and turbostratic components, as shown in Fig. 6. The capacity below 0.25 V related well to amounts of the graphitic component P_1 with the 0.25–1.3 V capacity, $1-P_1$, being dependent upon the turbostratic component.

Lithium insertion processes into anodes have been studied by *in-situ* Raman spectroscopy. In Figure 7, for an HOPG, the peak at 1580 cm^{-1} divides into two peaks at about 0.193 V on discharging. The 1580 cm^{-1} peak is attributable to a bonding layer mode surrounding a lithium ion [40] indicating that a high stage compound was formed via the first stage. Therefore, the change to a lower stage GIC occurs during the discharge (Li^+ intercalation) process. That is, it is clear that charge/discharge reactions occur via exact changes of the stages.

5 Voltage Profiles of Carbon Electrodes

Figure 8 shows voltage profiles during second discharge and charge cycles for lithium/carbon electrochemical cells made from representative carbon and graphite

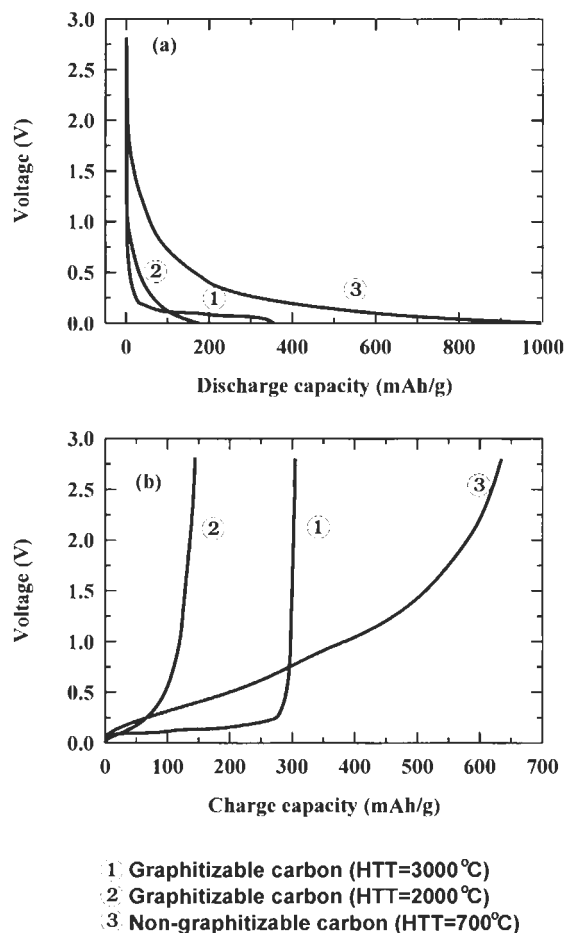


Fig. 8. Plots of voltage vs. reversible capacity for (a) the second discharge and (b) charge cycle of representative carbon and graphite samples; (1) graphitizable carbons HTT 3000°C, (2) graphitizable carbon HTT 2000°C, (3) non-graphitizable carbon HTT 700°C.

materials [25]. In the electrochemical cell, the electrodes of carbon materials are positive electrodes, the counter electrode being lithium metal. Here, lithium intercalation into carbon is the discharge process with the de-intercalation of lithium ions being the charge process. The graphite electrode cell gives a reversible capacity of 280–330 mAh g⁻¹. The lithium discharge/charge plateau, at about 0.2 V, was reproducible [15,21]. In the first cycle, all carbon materials show an irreversible capacity at about 0.8 V due to electrolyte decomposition and formation of a solid electrolyte interphase [41]. Then, after the 2nd cycle, the irreversible capacity is much reduced, and the electrode exhibits relatively stable cyclic properties. Of the many types of carbon electrode, well-ordered graphite is considered to be representative as an industrial standard because of its long voltage profile plateau and low electrode

potential relative to lithium metal. However, a major disadvantage of graphite is the limited capacity of $\sim 310 \text{ mAh g}^{-1}$ compared with 372 mAh g^{-1} for LiC_6 . On the other hand, non-graphitizable carbons, of HTT of $\sim 1100^\circ\text{C}$, have a reversible capacity of 600 mAh g^{-1} , but exhibit an irreversible capacity and hysteresis between charge and discharge in the voltage profile [25,42,43].

In commercial cells, highly ordered graphite such as from mesocarbon microbeads (MCMB) heat-treated at 3000°C , natural graphite, and non-graphitizable carbons have been mainly used and have charge capacities of 310 and 600 mAh g^{-1} , respectively [44]. Non-graphitizable carbons show different output properties with constant and slightly inclined discharge potentials the commercial cells, and which are suitable for cellular phones and EV battery applications, respectively [16].

6 Effect of Microstructure of Carbon Anode on the Capacity

Figure 9 shows the second cycle charge capacity as a function of crystallite thickness, $L_{c(002)}$, for several carbon fibers and PPP-based carbon electrodes [19]. Well-ordered graphites ($L_{c(002)} > 20 \text{ nm}$) and low crystalline materials ($L_{c(002)} < 3 \text{ nm}$) have larger capacities. However, intermediate carbons ($L_{c(002)} \sim 10 \text{ nm}$) possess minimum capacities. Dahn et al. [25] reported similar dependencies of charge capacity, as a function of HTT, and placed carbon materials suitable for commercial lithium-ion

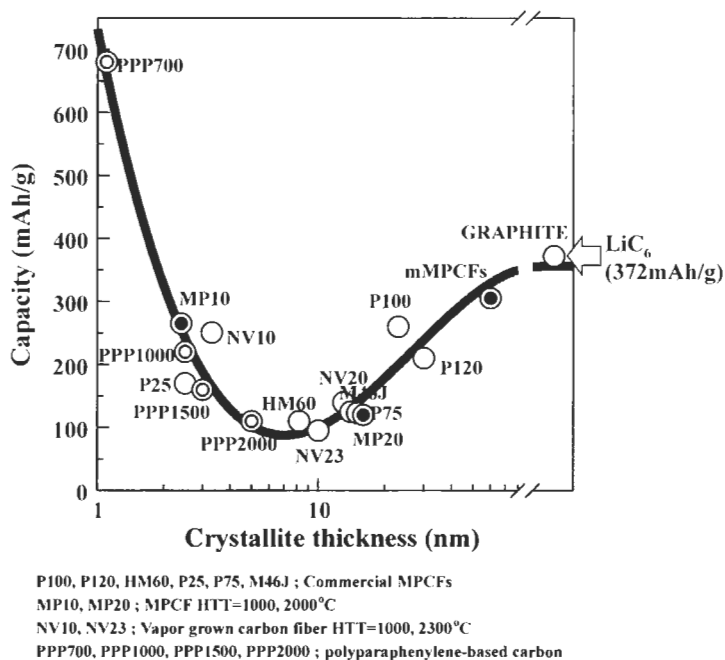


Fig. 9. Charge capacities of several kinds of carbon fiber and PPP-based carbon electrodes at the second cycle as a function of crystallite thickness, $L_{c(002)}$, determined by X-ray diffraction analysis.

batteries into three regions. The highly disordered PPP-700 carbon (HTT 700°C) has a large charge capacity of 680 mAh g⁻¹. Based on Li⁺ intercalation into turbostratic carbons, as $Lc_{(002)}$ becomes smaller the charge capacity decreases monotonically to $Lc_{(002)}$ values of about 10 nm. On the other hand, for $Lc_{(002)} < 10$ nm, a different process of charge and discharge of Li-ions occurs, a process largely enhanced by decreasing $Lc_{(002)}$ values. For $Lc_{(002)}$ of ~10 nm, both reaction processes occur incompletely and may cause a minimum in capacity.

The high charge capacity of PPP-700 has been studied by high-resolution transmission electron microscopy (HR-TEM), NMR [24] and by Raman spectroscopy [45–47]. Lattice images of HR-TEM of pristine PPP-based carbon (Fig. 10a) and Li-charged PPP-based carbon (Fig. 10b) do not show a layered structure. Short graphene layers are seen to be randomly located. An interlayer spacing of ~0.3440 nm compared with 0.3354 nm for pristine PPP-based carbon increases by ~10% (~0.4. nm) by Li doping suggesting that Li ions are located among the defective layers.

The ⁷Li NMR spectrum of Li-doped PPP-based carbon (Fig. 11a) reveals no metallic band. A main band with fine structure is observed at around 0 ppm.

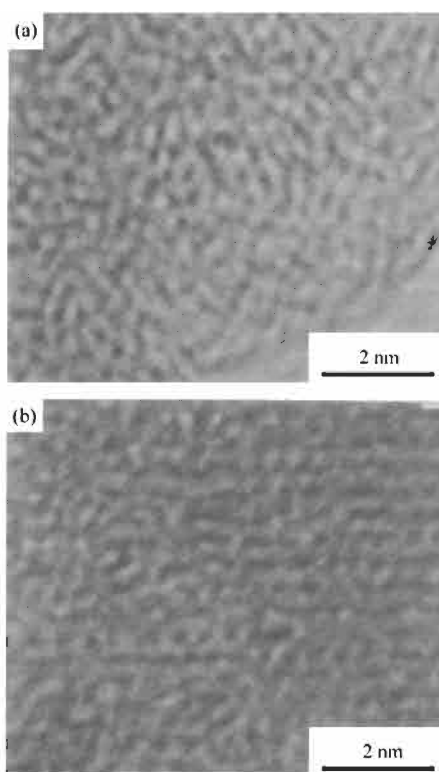


Fig. 10. High-resolution lattice images, obtained by transmission electron microscopy at a 400-kV acceleration voltage, of (a) pristine and (b) Li-doped (LiC₆) PPP-based carbon.

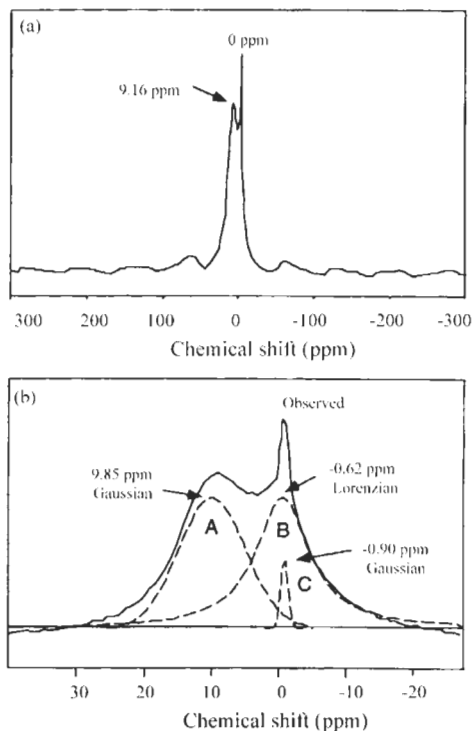


Fig. 11. (a) Nuclear magnetic resonance spectra of ${}^7\text{Li}$ in heat-treated PPP for a specific charge of capacity of 1000 mAh g^{-1} ; (b) Nuclear magnetic resonance line shape simulation for the main band around 0 ppm in (a).

Superposition of the three bands A, B, and C reproduce well the observed line shape of the main band (Fig. 11b). The lithium in Li-doped PPP-based carbon must occupy two different sites corresponding to bands A and B. Band C can be assigned to the by-product lithium carbonate. Band A has a Gaussian line shape with a chemical shift of 9.85 ppm and a half width of 11.6 ppm . Band B has a Lorentzian line shape with a chemical shift of -0.62 ppm and a half width of 8.9 ppm . The origin of band A must be associated with electron occupation in the lowest unoccupied molecular orbital (LUMO) giving rise to radical formation. The Gaussian line shape of band A is consistent with the ionic mechanism, where ${}^7\text{Li}$ nuclei are fixed and inhomogeneous broadening determines the line shape. That is, site A can be considered as an ionic or GIC site. On the other hand, band B may be caused by molecular Li_2 in the PPP-based carbon. A small chemical shift for band B is consistent with a Li_2 molecule model. This model is also consistent with a Lorentzian line shape. Site B may be called a “covalent” site.

Raman spectra were obtained for carbon samples heat treated at $650\text{--}750^\circ\text{C}$ in increments of 25°C . Figure 12 shows the development of a peak profile over this temperature range. The lines at 1240 and 1330 cm^{-1} suggest regions in the sample with a quinoid-like structure produced by the introduction of defects by the heat

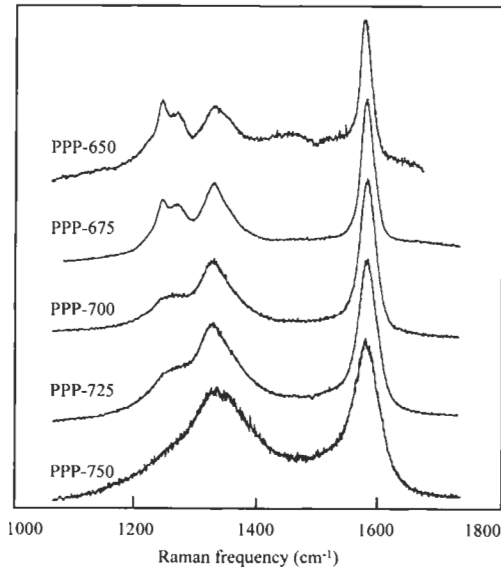


Fig. 12. Raman spectra for PPP heat-treated to between 650 and 750°C showing several PPP-derived A_g modes.

treatment. The lines near 1218 and 1270 cm^{-1} could be due to benzenoid PPP peak remnants which appear slightly downshifted. Therefore, these Raman spectra suggest that the PPP-700 carbons are only partially carbonized showing the signature of a residual disordered quinoid-like PPP structure.

A line-shape analysis of the peak near to 1600 cm^{-1} , from the *in-situ* Raman spectra (Fig. 13), provides information about Raman frequency shifts in a Li/PC/PPP-700 battery system during discharging and charging. The high frequency peak position, as

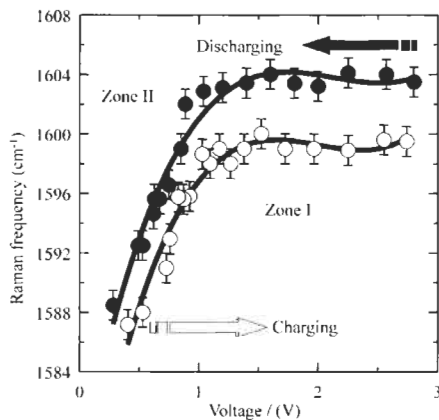


Fig. 13. The voltage dependence for the high frequency Raman modes of the PPP-700 electrode obtained by fits to Lorentzian line shape.

a function of electrode voltage in the range between about 2.8 V and 0.0 V for both of the discharging and charging processes, reflects Li^+ uptake and release in PPP-700. It is to be noted that the curves have thresholds at ~ 1.0 V and are divided into two zones by the threshold voltages. In Zone I (2.8–1.0 V) the Raman peak shows no change with decreasing voltage up to 1.0 V. Zone II (1.0–0.3 V) corresponds to a downshift of wave number with decreasing discharge voltage. During charging, the change in peak position is almost reversible with some hysteresis indicating some residual lithium. These results suggest that in Zones I and II the Li^+ ions have different insertion behaviors. The change in Zone II could be due to a charge transfer effect, as in GIC, occurring in the PPP-700 electrode, which would modify the localized electron density and electrical conductivity resulting in the final diminishing of the peaks. It is to be noted that with the disordered PPP-700 carbon, the same charge transfer behavior as in GIC takes place to store Li^+ ions between the defective carbon layers, and is relatively consistent with the formation of Li_2 molecules [24]. On the other hand, lithium storage in Zone I might be different from lithium storage in Zone II. Though it is still difficult to clarify the lithium storage mechanisms, it can be suggested that lithium in Zone I may be at preferred sites when charge transfer, affecting the peak wave number, does not occur. Inaba et al. [46] reported the *in-situ* Raman study on MCMB heat treated at $\sim 1000^\circ\text{C}$, and showed no change in the 1580 cm^{-1} Raman peak [46]. These different results indicate that charge and discharge mechanisms taking place in low temperature carbons with super-high lithium storage capacities vary carbon to carbon.

7 Li Storage Model

Figure 14 shows a theoretical model of LiC_6 in graphite. The insertion of lithium into graphite is described as follows: (1) the first stage by insertion of lithium ions electrochemically; (2) formation of high stage GICs; and (3) transformation to lower stages.

Three lithium insertion mechanisms for low crystalline carbon materials are as in Fig. 15 showing (a) formation of Li_2 molecules between layers, (b) cluster formation

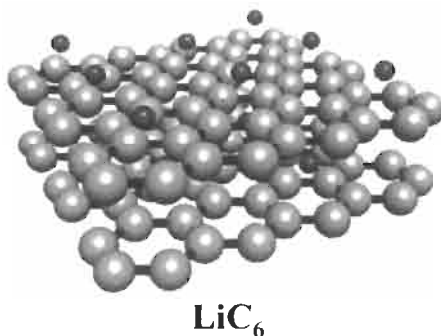


Fig. 14. Schematic representation of LiC_6 model based on graphite anode material.

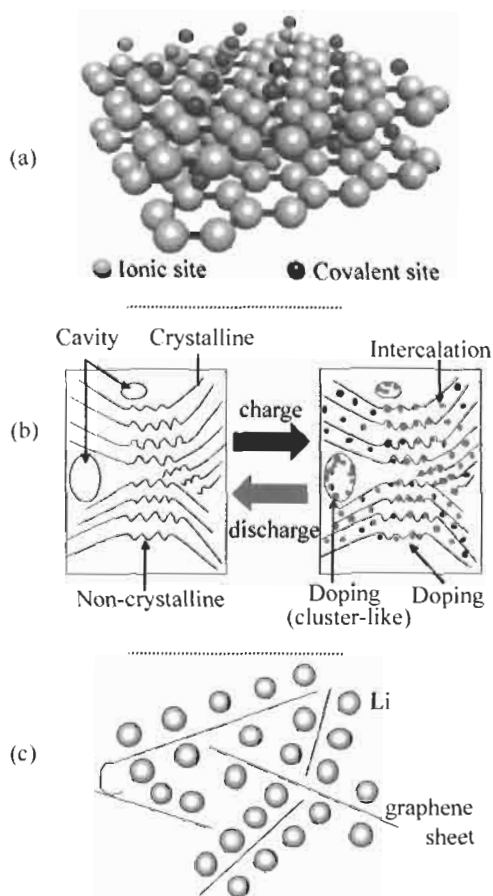


Fig. 15. Schematic representations of (a) Li_2 model [24], (b) cavity model [26], and (c) single-layer model [25].

of lithium ions in nano-cavities, and (c) single graphene layers in relation to hydrogen content of carbon materials of low HTT. It is not yet known which mechanism is correct. It is thought that those phenomena have a close relationship with nano-structures of carbon materials.

8 Conclusions

It is not an overstatement that the success of the Li^+ -ion batteries is linked to the GIC and carbon sciences since the beginning of the 1990s by providing designed anode materials for the batteries. Enhancement of battery performance and cost reduction have been achieved over the past ten years, with further improvements in battery performance being demanded for the future. Structural characterization of

non-graphitizable carbons with high capacities, elucidation of lithium storage mechanisms and the need to reduce irreversible capacities will be important aspects. Further research into carbonization and graphitization conditions of new starting materials and of, e.g., B, N and P including mechanical treatments will need to be extensive. A remarkable improvement in the Li⁺-ion battery will be made in the future corresponding to lithium metal itself. Of the many types of carbons studied, it is the low crystalline carbon-based Li⁺-ion battery, of higher capacities, which will feature in the further development of Li⁺-ion batteries for the second generation of the battery. High performance Li⁺-ion batteries will advance carbons into the 21st century of multimedia and portable computers, etc.

References

1. J.P. Gabano, *Lithium Batteries*. Academic Press, New York, 1983.
2. E. Peled, *J. Electrochem. Soc.*, 126: 2047, 1979.
3. V.R. Koch, J.L. Goldman, C.J. Mattor and M. Mulvaney, *J. Electrochem. Soc.*, 129: 1, 1982.
4. M. Arakawa, S. Tobishima, Y. Nemoto and M. Ichimura, *J. Power Sources*, 43: 27, 1993.
5. T. Hirai, I. Yoshimatsu and J. Yamaki, *J. Electrochem. Soc.*, 141: 2300, 1994.
6. M.B. Armand, In: W. van Gool (Ed.), *Fast Ion Transport in Solids*. Elsevier, Amsterdam, p. 665, 1973.
7. D.W. Murphy and J.N. Carides, *J. Electrochem. Soc.*, 126: 349, 1979.
8. M. Lazzari and B. Scrosati, *J. Electrochem. Soc.*, 127: 773, 1980.
9. J.J. Auborn and Y.L. Barberio, *J. Electrochem. Soc.*, 134: 638, 1987.
10. S. Megahed and B. Scrosati, *J. Power Sources*, 51: 79, 1994.
11. A. Herold, *Bull. Soc. Chim. France*, 187: 999, 1955.
12. R. Juza and V. Wehle, *Nature*, 52: 560, 1965.
13. D. Guerard and A. Herold, *Acad CR, Sci. Ser. C*, 275: 571, 1972.
14. M.S. Dresselhaus and G. Dresselhaus, *Adv. Phys.*, 30: 139, 1981.
15. J.R. Dahn, R. Fong and J.J. Spoon, *Phys. Rev. B*, 42: 6424, 1990.
16. Sony's Catalog, *Lithium ion rechargeable battery*, ACG-4012-N-9707-P3-002, 1997.
17. M. Endo, T. Karaki and T. Fujino, *New Ceramics*, 4: 46, 1998 (in Japanese).
18. S. Yata, H. Kinoshita, M. Komori, N. Ando, A. Anekawa and T. Hashimoto, *Extended Abstract of 60th Annual Meeting of the Electrochemical Society of Japan*, Tokyo, 2G09, 1993.
19. M. Endo, Y. Nishimura, T. Takahashi, K. Takeuchi and M.S. Dresselhaus, *J. Phys. Chem. Solids*, 57: 725, 1996.
20. M.S. Dresselhaus, G. Dresselhaus, K. Sugihara, I.L. Spain and H.A. Goldberg, In: M. Cardona (Ed.), *Graphite Fibers and Filaments*. Springer-Verlag, New York, 1988.
21. A. Oberlin, In: P.A. Thrower (Ed.), *Chemistry and Physics of Carbon Vol. 22*. Marcel Dekker, New York, 1989.
22. N. Imanishi, Y. Takeda and O. Yamamoto, *Lithium Ion Batteries Fundamentals and Performance*. Wiley-VCH, p. 98, 1997.
23. J.R. Dahn, *Phys. Rev. B*, 44: 9170, 1991.
24. K. Sato, M. Noguchi, A. Demachi, N. Oki and M. Endo, *Science*, 264: 556, 1994.
25. J.R. Dahn, T. Zheng, Y. Liu and J.S. Xue, *Science*, 270: 590, 1995.
26. A. Mabuchi, K. Tokumitsu, H. Fujimoto and T. Kasuh, *J. Electrochem. Soc.*, 142: 1041, 1995a.
27. A. Funabiki, M. Inaba, Z. Ogumi, S. Yuasa, J. Otsuji and A. Tasaka, *J. Electrochem. Soc.*, 145: 172, 1998.

28. S. Flandrois and B. Simon, *Carbon*, 37: 165, 1999.
29. T. Nagaura and K. Tozawa, *Prog. Batt. Solar Cells*, 9: 209, 1990.
30. CMC, Development of Li-ion Rechargeable Battery Materials. Tokyo, p. 149, 1998 (in Japanese).
31. B.E. Warren, *Phys. Rev.*, 59: 693, 1941.
32. R.E. Franklin, *Acta Crystallogr.*, 4: 253, 1951.
33. H.O. Pierson, *Handbook of Carbon, Graphite, Diamond and Fullerenes*. Noyes Publications, p. 43, 1993.
34. M. Winter and J.O. Besenhard, *Lithium Ion Batteries Fundamentals and Performance*. Wiley-VCH, p. 127, 1997.
35. T. Tran and K. Kinoshita, *J. Electroanal. Chem.*, 386: 221, 1995.
36. A. Mabuchi, PhD Thesis, Kyoto University, 1995.
37. H. Fujimoto, A. Mabuchi, K. Tokumitsu, T. Kasuh and N. Akuzawa, *Carbon*, 32: 193, 1994.
38. K. Tatsumi, N. Iwashita, H. Sakaebe, H. Shioyama, S. Higuchi, A. Mabuchi and H. Fujimoto, *J. Electrochem. Soc.*, 142: 716, 1995.
39. M. Endo, J. Nakayama, Y. Sasabe, T. Takahashi and M. Inagaki, *Tanso*, 165: 282, 1994 (in Japanese).
40. M. Inaba, H. Yoshida, Z. Ogumi, T. Abe, Y. Mizutani and M. Asana, *J. Electrochem. Soc.*, 42: 75, 1995.
41. F. Fong, K. Sacken and J.R. Dahn, *J. Electrochem. Soc.*, 137: 2009, 1990.
42. E. Buiel, A.E. George and J.R. Dahn, *J. Electrochem. Soc.*, 145: 2252, 1998.
43. J.R. Dahn, A.K. Sleight, H. Shi, B.M. Way, W.J. Weycanz, J.N. Reimers, Q. Zhong and U. von Sacken. In: G. Pistoia (Ed.), *Lithium Batteries, New Materials and Perspectives*. Elsevier, Amsterdam, 1993.
44. A. Yoshino, *Tanso*, 186: 45, 1999 (in Japanese).
45. M. Endo, C. Kim, T. Karaki, T. Fujino, M.J. Matthews, S.D.M. Brown, and M.S. Dresselhaus, *Synth. Metals*, 98: 17, 1998.
46. M. Inaba, H. Yoshida and Z. Ogumi, *J. Electrochem. Soc.*, 143: 2572, 1996
47. M.J. Matthews, M.S. Dresselhaus, M. Endo, Y. Sasabe, T. Takahashi and K. Takeuchi, *J. Mater. Res.*, 11: 3099, 1996.

Chapter 26

Electrochemical Functions

Mikio Miyake

*School of Materials Science, Japan Advanced Institute of Science and Technology, Ishikawa,
923-1292, Japan*

Abstract: Carbon has a high electrical conductivity and is a semi-metal with similar values in ionization potential and electron affinity. Such unique electronic properties suggest that carbon can both donate and accept electrons and is a promising material for electrodes. Various carbons with different shapes and properties are available as electrodes, such as highly ordered pyrolytic graphite (HOPG), glassy carbon (GC), carbon fiber (CF), and activated carbons, etc. Carbon surfaces, such as pore size, electronic states, and presence of functional groups, can be modified and controlled by various chemical and physical treatments. Therefore, development of carbon electrodes with superior functions is the subject of the Carbon Alloys project. Electrode materials in new industries are also briefly described, e.g., lithium rechargeable batteries, electric double layer capacitors, and sensors.

Keywords: Electrode, Electrochemistry, Lithium rechargeable battery, Capacitor, Sensor.

1 Features of Carbon Materials as Electrodes

Carbon materials, consisting of sp^2 carbon atoms, show high electrical conductivity and several other prominent characteristics such as high chemical and thermal stability, catalytic properties, light weight, etc. Furthermore, carbon materials with widely different properties and shapes are available at reasonable prices. Therefore, carbon has been used as electrodes for a wide variety of electrochemical applications. Examples are electrodes for batteries (e.g. MnO_2 , lithium ion), for metal smelting (e.g. Fe, Al, Mg), for electrolytic production of chemicals (e.g. Li, Na, NaOH, F_2 , Cl_2), and for microsensors *in vivo* measurements, etc.

The following characteristics of carbons show them to be superior to typical metals, such as Pt and Hg as electrode materials [1–3]. Firstly, a variety of carbons with different properties are obtained by controlling sizes and orientations of crystallites consisting of hexagonal planes. Examples include highly oriented pyrolytic graphite (HOPG), glassy carbon (GC), carbon fibers (CF), and activated carbon fibers (ACF). Secondly, highly crystalline carbon (e.g. HOPG) is a semi-metal with similar values of ionization potential (I_p) and electron affinity (E_a) [4]. Thus, carbon is expected to work both as an electron donor and as an acceptor. Thirdly, carbon is relatively stable

because of slow kinetics of oxidation. Fourthly, properties of carbon surfaces can be modified and controlled by various physical and chemical treatments.

Electrochemical reactions are initiated by adsorption of chemical species on electrodes. Such a process is essentially controlled by the chemical and physical states of the electrode surface. Carbon surfaces are modified easily by various chemical and physical treatments. One of the objectives of the Carbon Alloys project is to modify carbon surfaces to derive new functionalities. Thus, studies of electrochemical functions of carbon electrodes are of major interest to carbon alloys.

The objective of this chapter is to understand the electrochemical characteristics of carbon materials in relation to carbon alloys. Applications of carbon electrodes, including future uses such as lithium rechargeable batteries, capacitors and sensors are described.

2 Electrochemical Reactions on Carbon

HOPG, a synthetic, highly graphitic carbon, is a semi-metal, with a small overlap (0.04 eV) between the conduction and valence bands [4]. Thus, HOPG has the same values of 4.4 eV for its ionization potential (I_p) its electron affinity (E_a) [4]. This means that HOPG can simultaneously donate and accept electrons. Carbons can catalyze both oxidative and reductive reactions. In fact, the reducing power of solid carbon is well recognized and it is known that solid carbons behave as oxygen electrodes to produce H_2O_2 by the reduction of molecular oxygen in acidic solutions [2]. Therefore, carbon electrodes may accommodate a wide variety of reactions including both oxidative and reductive reactions.

HOPG has a highly anisotropic structure. The basal planes of HOPG consists of condensed aromatic rings with π electrons (graphene layers), with edges bonding aromatic hydrogen and oxygen functional groups with σ bonds. Thus, the electrochemical behavior of HOPG electrodes should differ depending on exposed surfaces.

From an electrochemical perspective, solid carbons undergo two types of reactions associated with their anisotropic structure, namely, surface reactions and intercalation reactions. Such entirely different reactions are discussed in this chapter as oxidation reactions.

2.1 Surface Oxidation Reactions

Several types of oxygen functional groups, in different amounts, are present on carbon surfaces depending on preparation and pretreatment conditions. The surface oxides exist principally as a submonolayer on edge sites of hexagonal planes (Fig. 1) [1,2]. When carbon is oxidized extensively, multilayer oxides may be formed consisting of oxidized layers of planes (Fig. 2) [1]. Variations in surface oxide properties are a major source of variability in electrochemical performance. Electrochemical reactions of surface oxides produce background currents over a region of wide potential associated with their different redox potentials [1,2].

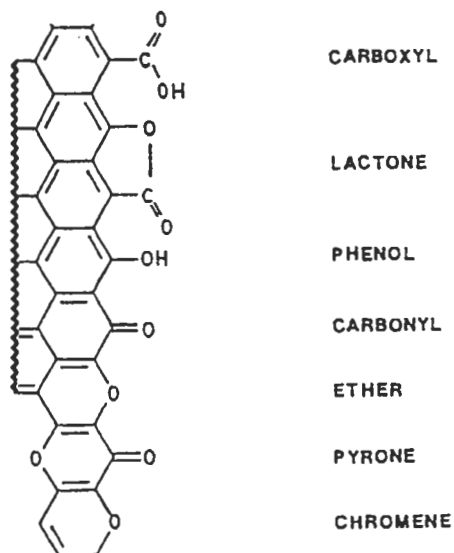


Fig. 1. Oxygen functional groups exist on edge plane sites of carbon surfaces [1,2].

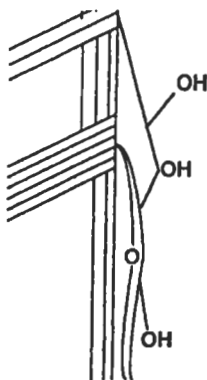


Fig. 2. Schematic illustration of multilayer oxide films formed on carbon surfaces [1].

Electrochemical reactions for various oxygen functional groups on carbon are proposed as follows. A sequence of reactions for the quinoid complex, usually called quinone, is shown in Fig. 3 [2,5]. Quinone (I) and the radical (II) are in equilibrium. The radical (II) accepts an electron to form the anion (III), which can accept a proton to form phenol or hydroquinone (IV). The processes between (II) and (III) and (III) and (IV) are reversible. It is suggested that an ether-type oxygen cation (oxonium ion) is in resonance with a carbonium ion as shown in Fig. 4 [2,6]. Two types of cyclic esters called lactones, with five and six member rings respectively, may be formed on aromatic rings (Fig. 5) [2,7]. Both lactones undergo reversible one-electron transfer

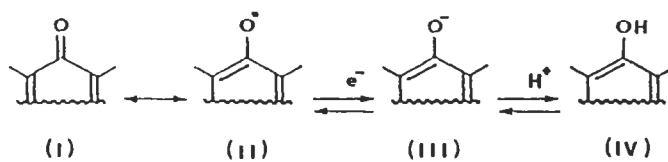


Fig. 3. A sequence of reactions proposed for quinoid complex [2,5].

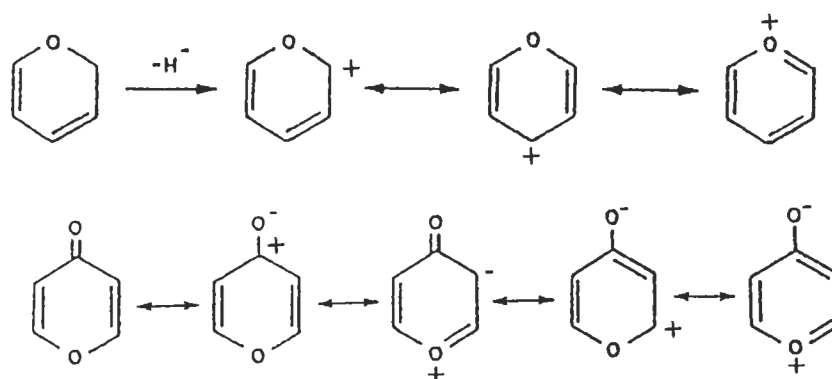
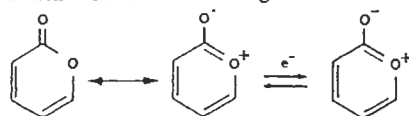


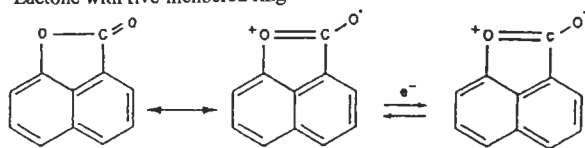
Fig. 4. A sequence of resonance structures proposed for ether-type oxygen cations [2,6].

In acidic solution (pH < 7)

Lactone with six-membered ring



Lactone with five-membered ring

**In basic solution (pH > 7)**

Lactone with dissociated form (carboxylic acid)

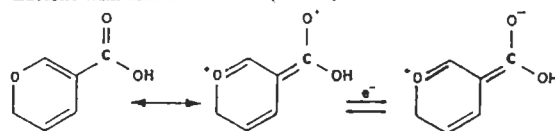


Fig. 5. A sequence of one electron-transfer reactions proposed for cyclic esters [2,7].

processes without dissociation in acidic solutions ($\text{pH} < 7$). In basic solutions, lactones dissociate to form carboxylic groups which also may undergo reversible one-electron transfer reactions.

2.2 Oxidative Intercalation Reactions

Graphite forms intercalation compounds with various atoms, ions, and molecules. Graphite intercalation compounds of H_2SO_4 are a typical example produced by anodic oxidation of graphite [8]. When the intercalation compound of graphite thus formed is reduced, the original graphite is reformed via reversible redox processes [1,8]. When graphite intercalation compounds of H_2SO_4 are further oxidized by using a higher anodic potential in concentrated H_2SO_4 solution, the oxidation processes are irreversible and the reduced product is quite different from the original graphite [1,9]. Breakage of structure is suggested by a noted decrease in the La crystallite size as measured by Raman spectroscopy. Such reversible intercalation and irreversible oxidation mechanisms are schematically shown in Fig. 6 [1]. Extensive oxidation of graphite removes electrons from the aromatic π system, resulting in the formation of aliphatic bonds in the graphite plane [1]. As a result, such an oxidized graphite has a significantly lower electrical conductivity than the original graphite [1].

3 Electrochemical Behavior of Various Carbons

Many types of carbons have been used as electrodes, such as HOPG, GC, CF, etc. The properties of the carbon electrode vary greatly because of differences in size and orientation of crystallites, which are characterized by L_a , L_c , or $d_{(002)}$ calculated from X-ray diffraction and Raman scattering measurements. In this section the electrochemical behavior of several carbon materials are described in terms of their structures [1–3]. Such a discussion is useful to select or control variables of carbon materials when using them as electrodes for special purposes.

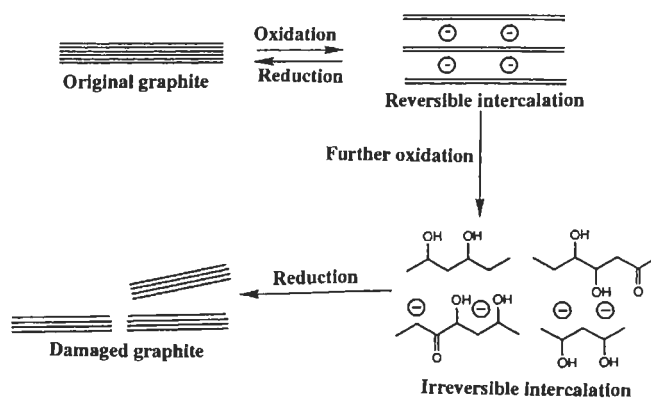


Fig. 6. Schematic structural image of reversible and irreversible oxidative intercalation of graphite [1,9].

3.1 Highly Ordered Pyrolytic Graphite

Highly ordered pyrolytic graphite (HOPG) has a highly developed crystal structure and shows extensive anisotropy. The well-defined ordered structure of HOPG is suitable to estimate electrochemical behavior of ideal basal or edge planes. A clean basal plane (graphene layer), with a low defect concentration, is easily prepared by cleavage, laser activation, or electrochemical activation [1]. The basal plane is extremely inert as an electrode (for electron transfer) in contrast to the edges of the planes (edge planes) as reported by cyclic voltammetry measured over cleaved basal and edge planes of HOPG in aqueous solution containing $\text{Fe}(\text{CN})_6^{-3/-4}$ [1,10]. The observed electric double layer capacitance of a basal plane is only 5% of that of an edge plane [1,10]. Therefore, the main conclusion derived from comparison of edge and basal planes of HOPG is the extreme anisotropy of such electrochemical behavior as electron transfer and capacitance [1,10].

HOPG forms intercalation compounds with various elements, molecules, and ions by electrochemical methods as well as chemical methods. Recently, intercalation compounds with lithium have been extensively studied as anode materials for the lithium-ion secondary battery.

3.2 Glassy Carbon

Glassy carbon (GC) is a vitreous carbon with isotropic properties. GC is impermeable to gases and liquids. In addition, it may be polished, exposed to high vacuum, heated, and chemically modified. Thus, GC can be conveniently made into electrodes with such shapes as disks and rods. A highly porous reticulated vitreous carbon (RVC) has also been used in a variety of electrochemical measurements [1].

3.3 Carbon Fiber

Some pitch-based carbon fibers (CF) have an anisotropic structure because hexagonal planes (graphene layers) prefer to orientate along the fiber axis. There are different types of orientation as seen (by SEM) in cross-sections of fibers such as onion, radial, and/or random [1]. Different electrochemical responses can be expected from fiber ends vs. fiber sides because of different anisotropic presentations. A wide range of carbon fibers are available, from different sources and with different values of HTT and hence with different properties producing different electrochemical behaviors.

Carbon fibers are especially applied as microelectrodes for *in vivo* analysis of bio-related materials.

3.4 Carbon Paste

Carbon paste is a mixture of graphite with an organic liquid of low volatility. A major

advantage of carbon paste is the ease of renewal of a surface so providing a fresh surface unaffected by electrode history. An electrode prepared from carbon paste has an extremely low oxidative background current when compared with those of platinum and graphite [1]. The development of carbon paste has led to the widespread use of voltammetry for studying organic reaction mechanisms and the development of electrochemical detectors for liquid chromatography [1].

4 Application of Carbon Electrodes

Carbon materials have unique characteristics superior to those of metals. Thus, various carbon electrodes are used extensively in industry and are available commercially. This section describes recent applications of carbon electrodes, especially the lithium rechargeable battery, the electric double layer capacitor and sensors.

4.1 Lithium Rechargeable Battery

The success of lithium rechargeable batteries arises from the use of carbon materials as a lithium reservoir at the negative electrode [11–14]. Reversible intercalation of lithium into a carbon host lattice avoids the problem of lithium dendrite formation coming from the decomposition of electrolyte organic solvent. An objective of the Carbon Alloys project is to control the “atomic” spaces of carbon to form a heteroatomic alloy. The development of high performance anodes for lithium rechargeable batteries with a controlled carbon microstructure is a research target for the Carbon Alloys project. Several research groups are actively engaged in this Carbon Alloys project. Of these, Endo and Kim have studied correlations between the microstructural parameters and electrochemical properties of various carbon materials; their results are described in Chapter 25.

Another important objective of Carbon Alloys is control of electronic states of carbon by introduction of heteroatoms (doping). Such modification by doping has been investigated recently for carbon anodes of lithium rechargeable batteries. The doping methods include: (i) co-deposition by CVD of carbon and foreign atoms, (ii) pyrolysis of organic molecules containing foreign atoms, and (iii) chemical treatment of the carbon [14]. Boron is known to enter into the carbon lattice by substitution. For example, by CVD from benzene and boron trichloride, carbons containing up to 25 at% boron can be prepared [14]. Carbon doped with boron is reported to show greater reversible capacity for lithium than pure carbon [14]. In addition, an increase in a cell voltage of about 0.5 V is reported [14]. The effect of boron doping in carbon can be interpreted qualitatively as follows [14]: Boron has three valence electrons and an acceptor character. In a rigid-band model, the Fermi level is lowered by the addition of boron which allows more lithium (electron donor) to be intercalated. In addition, the presence of boron strengthens the chemical bond between the lithium and boron-carbon host. As a result, the potential of the lithium in boron-substituted carbon increases compared with pure carbon. Nitrogen is another element which can

be incorporated, by substitution, into carbon, either alone or together with boron [14]. Unfortunately, results reported for nitrogen-containing carbons differ from each other at the moment.

New approaches have been proposed in order to improve performance of carbon anodes for lithium rechargeable batteries. For example, carbons with controlled porosity were prepared from polymeric precursors by using inorganic templates [15]. Control of surface states of carbon is very important to enhance lithium insertion from solvents. A composite electrode made up of ultrafine silver particles supported on graphite has been reported to provide a higher volumetric specific capacity and longer cycle life than conventional graphite electrodes [16,17]. The formation of thin, passivating surface films is clarified to prevent co-intercalation of solvent molecules together with lithium ions, which causes exfoliation of the graphite [11–14]. The search for new solvents, salts, and additives, in which graphites behave reversibly due to unique surface chemistry, has been extensively studied [11–14].

4.2 *Electrochemical Double-Layer Capacitor*

Another objective of the Carbon Alloys project is to control surface space of carbon to form new functional interface. The storage of electrical energy based on the separation of charged species (supporting electrolyte) by adsorption on electrode surfaces in electrolytic double layers is simple compared with rechargeable batteries. Such devices are called electrochemical double-layer capacitors (EDLCs). The EDLC has been considered as one of the most attractive rechargeable power devices because of its excellent high-rate charge/discharge ability with high energy density and with long cycle life compared with the common rechargeable battery [18]. Essentially all electrode/electrolyte interfaces form electric double-layer (i.e., capacitance); however, EDLCs work as devices when no Faradaic reactions proceed over the potential range of operation. Because capacitance is proportional to amount of adsorbed ions on electrodes, electrochemically inert materials of high specific surface area can be utilized as electrodes in EDLC. Thus, the electrode must be designed to have (1) high specific surface areas; (2) good intra- and inter-particle conductivity in porous materials; and (3) good electrolyte accessibility to intra-pore surface area [18–20].

Carbon materials, such as activated carbons and ACF cloths, are promising electrode materials for EDLC, since they can be produced inexpensively with high surface areas. However, carbon materials are far from being electrochemically inert and surface chemical reactions may occur during polarization to introduce functional groups. Various types of oxygen functional groups are present on carbon surface (see Figs. 1 and 2) and may be further introduced by the application of voltage during operation of EDLCs devices, especially overcharging. Such oxygen functional groups on carbon cause some electrochemical reactivity and affect polarization, point of zero charge, and wettability with electrolyte solution (hydrophilic) [20]. The wettability, estimated by the contact angle measurements, increases by an increase in oxygen content and determines accessible porosity of aqueous electrolyte solutions, which

might influence capacitance values [20]. Electrochemical oxidation of an active carbon fiber (ACF) electrode showed an enhancement of electrode capacitance presumably by improved wettability [20]. Many powder carbon materials inherently have dangling bonds, which are associated with free-radical behavior. It can also influence the self-discharge characteristics [20]. In order to remove such oxygen functional groups, heat-treatments at elevated temperatures in a vacuum, nitrogen, or hydrogen and sometimes in water vapor are known to be effective [20]. These heat-treatments are expected to open pore structures and increase the degree of crystallization to decrease inter-particle contact resistance. Various surface treatments of carbon materials are reported recently. For example, a cold plasma generated at low temperature has been used to modify the chemical and physical properties of surfaces of carbon materials, such as pore size and functionality distribution, without changing bulk properties [20].

In the case of the graphite electrode, certain intercalation processes occur on charging in which various species or ions in the electrolyte become injected into the interlayer space. Although such intercalation processes are essentially reversible at defined voltages, application of highly excessive voltage may cause carbon electrodes to physically fail (Fig. 6).

The use of organic electrolytes in capacitors has been of interest due to high operating voltages [18–20]. A disadvantage of organic electrolyte system is their low power densities due to higher resistivity than that of an aqueous system. Unlike lithium rechargeable batteries, where the electrode passivation occurs due to electrolyte decomposition, the use of organic electrolytes in the EDLC is potentially less restricted. Next generation EDLCs should supply higher energy and power densities than those achieved previously. Recently, the transition between supercapacitors and batteries has been discussed, which is called “pseudo-capacitances” (i.e., two-dimensional reversible Faradaic surface reactions) [20].

Applications of new types of carbons with unique pore structures are proposed; polyacenic semiconductor (PAS) materials prepared from pyrolytic treatment of phenol-formaldehyde resin [21], open-cell aerogel [22] and xerogel [23], foam carbon materials, and carbon nanotubes which have narrow distributions of pore sizes, highly accessible surface area, low resistivity, and high stability [24].

4.3 Sensor

An electrochemical sensor is a device that quantitatively detects a particular chemical species as an oxidation or reduction current [3,25,26]. An electrochemical sensor has advantages such as simple measurement procedure, short response time, and sufficient sensitivity and selectivity. Although chemical sensor systems, utilizing chemical reactions to convert target species to detectable ones (e.g., by UV-vis spectroscopy), have attained quite high sensitivity, they are not feasible to *in situ* measurements because of indirect detection of target species. On the other hand, an electrochemical sensor system can easily monitor changes in concentration with time. In order to

establish high performance electrochemical sensors, modifications to electrode surface should be carried out. For example, modification by electrocatalytic materials has been proposed to attain high sensitivity [27]. In order to attain high selectivity, an electrode surface is coated with films as well as modified with enzyme or mediator, which show specific affinity to target chemicals [27]. Carbon is the preferred electrode material for such modifications because it has reactive functional groups on the surface available for chemical modification. Clearly, preparation and pretreatment history of carbon electrodes strongly affect the performance as a sensor, such as electron transfer kinetics, background current, reproducibility, and adsorption properties. Among various carbon materials, carbon fibers (CF) or activated carbon fibers (ACF) are used extensively as microelectrodes which can be used in very small spaces and to establish chemical events occurring inside single biological cells, such as neurotransmitter in living brain tissue [1–3,25,26]. A microelectrode used *in vivo* is typically made by placing a single carbon fiber in the lumen of a small glass tube. The entire electrode, including the surrounding insulator, must be of micrometer dimensions in order to minimize disruption of the biological environment in which the electrodes are employed. The use of microelectrodes mounted on piezoelectric micropositioners allows the local concentration of electroactive substances to be mapped in two dimensions, referred to as scanning electrochemical microscopy.

New candidates of carbon materials used in electroanalytical chemistry have been proposed. Chemically modified carbon paste electrodes incorporated with zeolite molecular sieves were constructed as sensor electrodes for voltammetric determination of trace copper in aqueous solution [28]. An amperometric biosensor for the detection of ethanol vapor was fabricated on a flexible polyester substrate where conventional screen-printing technology was employed to fix alcohol dehydrogenase to the carbon working electrode [29]. Ultra-thin porous carbon films are employed as transducers for amperometric biosensors [30]. Such foam-like nanoscopic films combine the advantage of high enzyme loadings within the micropore hosts and large microscopic area with a small geometric area [30]. Conductive boron-doped diamond thin films have been reported to have superior properties for electrochemical sensors, such as low background current, a wide potential window, high resistance to deactivation, and insensitivity to dissolved oxygen [31].

There seems to be no limit to the diversity and versatility of carbon materials, and it is certain that electroanalytical performance will improve as the nature and preparation of such materials continues to be better understood.

References

1. R.L.M. McCreery, Carbon Electrodes: Structural Effects on Electron Transfer Kinetics. In: A.J. Bard (Ed.), *Electroanalytical Chemistry*, Vol. 17, pp. 221–374. Marcel Dekker, New York, 1991.
2. C.A. Leon and L.R. Radovic, Interfacial Chemistry and Electrochemistry of Carbon Surfaces. In: P.A. Thrower (Ed.), *Chemistry and Physics of Carbon*, Vol. 24, pp. 213–310. Marcel Dekker, New York, 1994.

3. R.L.M. McCreery and K.K. Cline, Carbon Electrodes. In: P.T. Kissinger and W.R. Heineman (Eds.), *Laboratory Techniques in Electroanalytical Chemistry*, pp. 293–332. Marcel Dekker, New York, 1996.
4. H. Tohara, *Electrochemistry*, 66: 368, 1998.
5. S.E. Slein and D.M. Golden, *J. Org. Chem.*, 42: 839, 1977.
6. M. Voll and H.P. Boehm, *Carbon*, 9: 481, 1971.
7. H.P. Boehm, *Angew. Chem. Int. Ed. Engl.*, 5: 537, 1966.
8. J.O. Besenhard and H.P. Fritz, *Angew. Chem. Int. Ed. Engl.*, 22: 950, 1983.
9. Y. Maeda, Y. Okamoto and M. Inagaki, *J. Electrochem. Soc.*, 132: 2369, 1985.
10. R. Rice and R.L. McCreery, *Anal. Chem.*, 61: 1637, 1989.
11. M. Noel and R. Santhanam, *J. Power Sources*, 72: 53, 1998.
12. M. Broussely, P. Biensan and B. Simon, *Electrochim. Acta*, 45: 3, 1999.
13. D. Aurbach, B. Mavkovsky, I. Weissman, E. Levi and Y. Ein-Eli, *Electrochim. Acta*, 45: 67, 1999.
14. S. Flandrois and B. Simon, *Carbon*, 37: 165, 1999.
15. R.E. Winans and K.A. Carrado, *J. Power Sources*, 54: 11, 1995.
16. H. Momose, H. Honbo, S. Takeuchi, K. Nishimura, T. Horiba, Y. Muranaka, Y. Kozono and H. Miyadera, *J. Power Sources*, 68: 208, 1997.
17. J. Aragane, K. Matsui, H. Andoh, S. Suzuki, H. Fukuda, H. Ikeya, K. Kitaba and R. Ishikawa, *J. Power Sources*, 68: 13, 1997.
18. A. Nishino, *J. Power Sources*, 60: 137–147, 1996.
19. A. Yoshida, *Electrochemistry*, 66: 884–891, 1998.
20. B.E. Conway, *Electrochemical Super Capacitors: Scientific Fundamentals and Technological Applications*. Kluwer Academic/Plenum Publishers, New York, pp. 183–229, 1999.
21. S. Yata, E. Okamoto, H. Satake, H. Kubota, M. Fujii, T. Taguchi and H. Kinoshita, *J. Power Sources*, 60: 207, 1996.
22. S.T. Mayer, R.W. Pekala and J.L. Kaschmitter, *J. Electrochem. Soc.*, 140: 446, 1993.
23. C. Lin, J.A. Ritter and B.N. Popov, *J. Electrochem. Soc.*, 146: 3639, 1999.
24. C. Niv, E.K. Sichel, R. Hoch, D. Moy and H. Tennent, *Appl. Phys. Lett.*, 70: 1480, 1997.
25. G.A. Evtugyn, H.C. Budnikov and E.B. Nikolskaya, *Talanta*, 46: 465, 1998.
26. J. Anderson, L.A. Coury, Jr. and J. Leddy, *Anal. Chem.*, 70: 519R, 1998.
27. A. Kitajima, T. Teranishi and M. Miyake, *Electrochemistry*, 69: 16, 2001.
28. B. Chen, N-K. Guh, and L-S. Chia, *Electrochim. Acta*, 42: 595, 1997.
29. J-K. Park, H-J. Yee, and S-T. Kim, *Biosensors & Bioelectronics*, 10: 587, 1995.
30. J. Wang and Q. Chen, *Anal. Chem.*, 66: 1988, 1994.
31. T.N. Rau, I. Yagi, T. Miwa, D.A. Tryk and A. Fujishima, *Anal. Chem.*, 71: 2506, 1999.

Chapter 27

Electric Double Layer Capacitors

Soshi Shiraishi

Department of Chemistry, Faculty of Engineering, Gunma University, Kiryu, Gunma 376-8515, Japan

Abstract: The electric double layer capacitance of porous carbon electrodes strongly depends on its pore size distribution. Mesoporous activated carbon fibers (ACFs), prepared by the carbonization and steam-activation of a phenolic resin fiber containing a small amount of activation catalyst, have many mesopores in addition to well-developed micropore structure. The double layer capacitance in propylene carbonate electrolytes was not proportional to the BET specific surface area for mesoporous ACFs. This is due to the low mobility of the ions in the narrow micropores. However, mesoporous ACFs showed higher double layer capacitance than conventional ACFs consisting of mainly micropores, especially, in the case of high current density measurements. This result suggests that the presence of mesopores promotes the formation of an effective double layer or the fast transfer of ions to the micropores. The property of the double layer capacitance for single walled carbon nanotubes (SWCNT) is also discussed from the viewpoint of a comparison with ACFs.

Keywords: Capacitor, Electric double layer, Activated carbon fiber, Pore size distribution, Capacitance, Carbon nanotubes.

1 Introduction

Electric double layer capacitor (EDLC) [1,2] is the electric energy storage system based on charge–discharge process (electrosorption) in an electric double layer on porous electrodes, which are used as memory back-up devices because of their high cycle efficiencies and their long life-cycles. A schematic illustration of EDLC is shown in Fig. 1.

Recently, EDLCs have been proposed as the sub-power source for the hybrid electric vehicle because of its higher power density (larger than 1000 W kg⁻¹ or 1000 W l⁻¹) and fast charge–discharge ability. Because the energy density of EDLC is only several Wh kg⁻¹ or Wh l⁻¹, much lower than that of rechargeable batteries, an improvement in the capacitance of EDLC is required. The energy density of EDLC can be expressed as follows:

$$E = \frac{CV^2}{2} \quad (1)$$

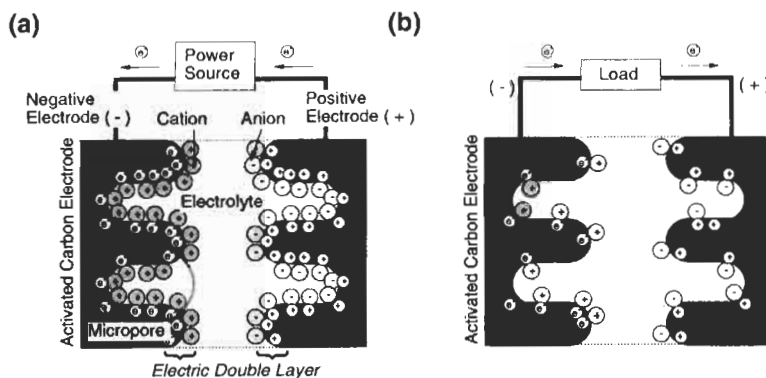


Fig. 1. Schematic illustration of electric double layer capacitor: (a) charge state, (b) discharge state.

where E is electric energy stored in the capacitor, C is capacitance, and V is applied voltage. The above correlation suggests that stability to electrochemical decomposition of the electrolyte, that is the electrochemical window of the electrolyte, is a key factor in energy storage, because the energy of EDLC varies as the square of applied voltage. Therefore, EDLC with a non-aqueous electrolyte has essentially a higher energy density than the aqueous type EDLC because non-aqueous electrolytes have wider electrochemical windows (≈ 3 V) compared with aqueous electrolytes (≈ 1 V).

The practical electrode materials for EDLC are porous carbons, such as activated carbons. The high capacitance ($100\text{--}200$ F g^{-1}) is derived from the high specific surface area (>1000 m^2 g^{-1}) in microporosity (pore width < 2 nm [3]). In general, it is believed that there is a proportional correlation between specific surface area and the electric double layer capacitance of activated carbons as based on the following equation [1,4,5]:

$$C = \int \frac{\epsilon_0 \epsilon_r}{\delta} dS \quad (2)$$

where C is specific capacitance, ϵ_0 is permittivity in vacuum, ϵ_r is relative permittivity of the double layer, δ is thickness of the double layer, and S is specific surface area. This equation (2) is derived from an ideal capacitor consisting of a solid dielectric layer between two parallel plate electrodes such as practical ceramic or film capacitors (condensers). However, some researchers have reported non-linearity of the double layer capacitance with surface area of carbon [6–14]. This may be due to the dimensions of the ion or solvent in the electrolyte and the pore size distribution (PSD) of activated carbons. The PSD depends on the structure and type of carbon precursor and the preparation method of the porous carbon. Thus, the dependence of the double layer capacitance on PSD for activated carbon electrodes has to be investigated using various porous carbons with different pore size distribution.

2 Influence of Pore Size Distribution of ACFs on Double Layer Capacitance

2.1 Mesoporous Activated Carbon Fibers

Mesopores (pore width of 2–50 nm [3]) or macropores (pore width > 50 nm [3]) influence the permeation of electrolyte into micropores and the mobility of ions in pores. Activated carbon fibers (ACF) have a narrow pore size distribution of micropores without, e.g., mesopores [15,16]. However, ACFs with mesopores have been prepared by blending an activation catalyst into a phenolic resin [17] or an isotropic pitch [18]. The blending method by which catalyst metal particles with nanometer size are uniformly dispersed in the carbon matrix is a topic for Carbon Alloys. These ACFs with mesopores and macropores are suitable to investigate their influence on double layer capacitances. In this chapter, double layer capacitances of ACFs with mesopores (mesoporous ACF) are comparatively discussed with conventional ACFs without mesopores or macropores (microporous ACF).

2.2 Pore Size Distributions (PSD) of ACFs

Mesoporous ACFs were prepared by carbonization and steam-activation of a phenolic resin fiber containing a small amount (0.1 wt%) of an organic nickel complex [19–21]. The nickel species in ACFs were present as metallic nickel particles (~50 nm diameter). Microporous ACFs, as the reference samples, were also prepared from the phenolic resin fiber but without catalyst. The PSD in of mesopores for mesoporous ACFs and microporous ACFs, as calculated by the Dolimore–Heal (DH) method, are shown in Fig. 2. The former has only a few mesopores except for small pore size (~2 nm), close to those of micropores, while the latter has larger volume of mesopores in

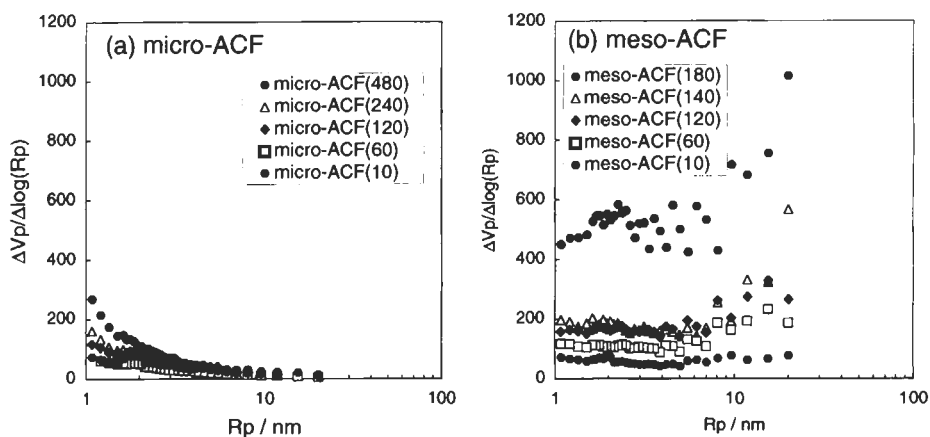


Fig. 2. Pore size distributions (PSDs) for the mesopore region of (a) microporous ACFs and (b) mesoporous ACFs, calculated by the DH method. Numbers in parenthesis mean the time of activation (min). R_p : pore radius; V_p : pore volume.

the whole mesopore region. Especially, the amount of mesopore volume in the range of 10–40 nm width became much larger in the mesoporous ACFs prepared with longer activation. This indicates that the nickel catalyst is effective in the formation of mesopores with relatively large pore sizes.

BET specific surface areas (corresponding to total specific surface area of ACFs) [22] and mesopore volumes (V_{meso} , estimated by DH method) [23] are summarized in Table 1. In both microporous ACFs and mesoporous ACFs, BET specific surface areas were higher with longer times of activation indicating that porosity in ACFs develops further with longer activation times. Mesopore volumes in microporous ACFs increased slightly with activation, but more so for the mesoporous ACFs. Mesoporous ACFs have larger mesopore volumes than microporous ACFs for comparable BET specific surface areas. Micropore volume (V_{micro}) and average micropore width (2χ) estimated by the Dubinin–Radushevich (DR) equation [24,25] are also summarized in Table 1. The micropore volume and average micropore width for microporous and mesoporous ACFs and BET surface area are almost identical (micro-ACF (120) vs. meso-ACF (120)), and micro-ACF (480) vs. meso-ACF (180)). These results suggest that surface area in mesopores contributes little to total surface areas although mesopore volumes are significant in the total pore volume ($V_{\text{meso}} +$

Table 1

BET specific surface area, mesopore volume, average micropore width, and micropore volume of microporous ACF (micro-ACF) and mesoporous ACF (meso-ACF)

| Sample* | BET-SSA ($\text{m}^2 \text{g}^{-1}$) | V_{meso} (ml g^{-1}) | V_{micro} (ml g^{-1}) | 2χ (nm) |
|-----------------------------------|---|---|--|-----------------|
| Micro-ACF (10) | 650 | 0.06 | 0.28 | 0.64 |
| Micro-ACF (60) | 930 | 0.03 | 0.37 | 0.73 |
| Micro-ACF (120) | 1150 | 0.08 | 0.47 | 0.85 |
| Micro-ACF (240) | 1480 | 0.09 | 0.60 | 0.94 |
| Micro-ACF (480) | 1780 | 0.16 | 0.73 | 1.07 |
| Meso-ACF (10) | 710 | 0.10 | 0.28 | 0.69 |
| Meso-ACF (60) | 960 | 0.21 | 0.38 | 0.74 |
| Meso-ACF (60) _{acid} ** | 920 | 0.23 | 0.36 | 0.72 |
| Meso-ACF (120) | 1050 | 0.30 | 0.42 | 0.83 |
| Meso-ACF (120) _{acid} ** | 1000 | 0.32 | 0.39 | 0.79 |
| Meso-ACF (140) | 1290 | 0.35 | 0.52 | 0.88 |
| Meso-ACF (180) | 1660 | 0.86 | 0.69 | 1.06 |

*Numbers in parentheses means the activation duration (min).

**Meso-ACFs after immersion in 1.0 M H_2SO_4 aq for 12 h.

BET-SSA: Specific surface area calculated by BET plot in the region of 0–0.05 P/Ps [22].

V_{meso} : Pore volume of mesopore calculated from DH method of adsorption branch [23].

V_{micro} : Pore volume of micropore calculated from DR method [24,25].

2χ : Average micropore width calculated from DR method [24,25].

Table 2

Yield of various ACFs, bulk density of composite electrode, and surface oxygen/carbon atomic ratio of various ACFs

| Sample | Yield (%) | d^* (g cm ⁻³) | O/C** |
|----------------|-----------|-----------------------------|-------|
| Micro-ACF (10) | 52 | 1.00 | 0.07 |
| Micro-ACF (10) | 45 | 0.87 | 0.08 |
| Micro-ACF (10) | 41 | 0.85 | 0.06 |
| Micro-ACF (10) | 35 | 0.74 | 0.06 |
| Micro-ACF (10) | 23 | 0.68 | 0.06 |
| Meso-ACF (10) | 47 | 0.85 | 0.07 |
| Meso-ACF (10) | 29 | 0.62 | 0.05 |
| Meso-ACF (10) | 16 | 0.54 | 0.04 |
| Meso-ACF (10) | 15 | 0.42 | 0.04 |
| Meso-ACF (10) | 5 | 0.38 | 0.05 |

* d : Bulk density of the composite electrode composed of ACF, acetylene black, and binder (86:10:4 wt%).

**O/C: Surface oxygen/carbon atomic ratio estimated by XPS.

V_{micro}). Consequently, mesoporous ACFs contain both mesopores and micropores in significant amounts, but with specific surface areas being contained in the micropores. The metallic particles of nickel, dispersed in mesoporous ACFs, can be removed by acid treatment using 1 M H₂SO₄aq. BET surface area, pore volumes and micropore widths of acid-treated mesoporous ACFs are shown in Table 1. The removal of nickel particles from mesoporous ACFs has little influence on pore structures.

Yields of microporous and mesoporous ACFs are shown in Table 2, with yields becoming smaller with activation time. Yields of mesoporous ACFs were lower than for microporous ACFs with comparable surface areas. The lower yields result from the presence of mesopores formed by catalytic activation. Densities of electrodes made from these ACFs are also shown in Table 2, the densities using mesoporous ACF being smaller than for microporous ACFs at comparable surface areas and yields, resulting from the larger pore volumes of mesoporous ACF.

The surface oxygen/carbon atomic ratios of the ACFs, estimated by the XPS analysis, are also shown in Table 2 indicating little difference in oxygen contents between them. The XPS O1s and the C1s spectra of both ACFs are similar indicating little difference in their surface functionalities so suggesting that surface functionality and double layer capacitance need not be considered further.

2.3 Electric Double Layer Capacitance of ACFs

The gravimetric electric double layer capacitances of both ACFs were measured in the galvanostatic condition using a standard three-electrode cell [19–21]. In general, the capacitance for a single electrode, obtained with the three electrode system, is

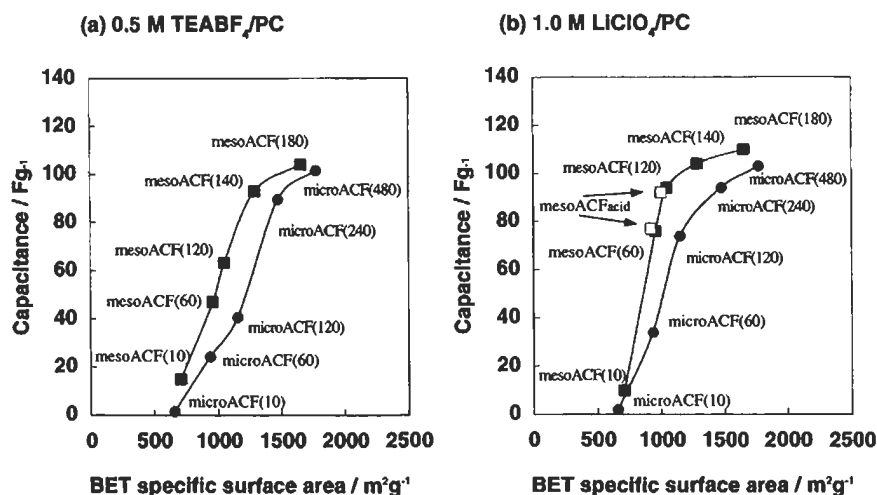


Fig. 3. Correlations between BET specific surface area and electric double layer capacitance during a positive process for microporous and mesoporous ACFs in (a) 0.5 mol dm⁻³ (C₂H₅)₄NBF₄/propylene carbonate and (b) 1.0 mol dm⁻³ LiClO₄/propylene carbonate. The capacitances were estimated by chronopotentiograms (40 mA g⁻¹) of positive process ((a) -2 V → 0 V vs Ag/Ag⁺, (b) 2 V → 4 V vs Li/Li⁺).

four times greater than when using the two electrode system or the coin cell [7]. Figures 3 (a) and (b) show the correlations between BET specific surface area and gravimetric double layer capacitance in a propylene carbonate solution containing 0.5 mol dm⁻³ of tetraethyl ammonium tetrafluoroborate (TEABF₄/PC) or 1.0 mol dm⁻³ LiClO₄ (LiClO₄/PC), respectively. The initial potential of the ACF electrodes was ~3 V vs Li/Li⁺, corresponding to the center between the upper limit potential (4 V vs Li/Li⁺) and the lower potential (2 V vs Li/Li⁺). Therefore, the capacitances reflect an average capacitance of cation desorption and anion adsorption. The correlation for the mesoporous ACFs_{acid} without nickel, is also plotted in these figures confirming that nickel particles in the mesoporous ACFs do not influence the double layer capacitance.

Figure 3 shows the limits to capacitance for the ACFs with high BET surface areas. Neither of the correlation lines for both ACFs pass through the axis origins indicating that the double layer capacitance is not linearly proportional to BET surface area. The small capacitance of the non-activated ACFs, such as micro-ACF (10) or meso-ACF (10), is due to the difficulty of forming an effective double layer (or low mobility of the ion) in the initial narrow micropores of < 0.7 nm pore width. The ion sizes of Li⁺, ClO₄⁻, TEA⁺, and BF₄⁻ are summarized in Table 3. The solvated ion sizes are estimated as being twice the Stokes radius [26,27] suggesting that the sizes of the solvated anions and cations are close to micropore widths. Therefore, an “ion-sieving effect” by these micropores, (as in “molecular sieving”) is an explanation of the non-linearity of capacitance of the non-activated ACFs. Soffer et al. [14] also reported an ion-sieving phenomenon of micropores in ACFs prepared from cotton cloth

Table 3

Solvated and unsolvated sizes of various cations or anions used in propylene carbonate electrolyte

| Ions | Solvated size* (nm) | Unsolvated size** (nm) |
|-------------------------------|------------------------|---------------------------|
| TEA ⁺ | 0.72 | 0.68 |
| Li ⁺ | 0.82 | 0.16 |
| BF ₄ ⁻ | 0.48 | 0.46 |
| ClO ₄ ⁻ | 0.52 | 0.48 |

*Twice value of Stokes radius [26].

**Twice value of ionic radius estimated from the crystallographic data [26].

with steam activation. The critical pore diameter was estimated to be 0.8 nm using a density functional theory calculation for the PSD [9]. These suggest a limitation to pore sizes available to EDLC.

Table 3 also shows that the sizes of unsolvated and solvated ion sizes are almost the same except for the Li⁺ cation, the latter being due to the large solvation shell of the Li⁺ cation arising from the high charge density of the Li⁺ cation. However, small capacitances for both ACFs with small micropore widths were measured in LiClO₄/PC electrolyte as well as in TEABF₄/PC suggesting that the Li⁺ cation is always associated with its solvent cage.

For both ACFs, with micropores ≤ 0.8 nm, the double layer capacitances of the mesoporous ACFs were higher than those of microporous ACFs at comparable surface areas. This is attributable to the mesopores which facilitate transfer of ions or permeation of solvated ions to form an electric double layer on the pore surface. Figure 3 also indicates that the advantage of the mesopores for the capacitance was not so effective in ACFs with large micropore width (ex. micro-ACF (480) and meso-ACF (180)) confirms the above “ion-sieving” of micropores and the mesopore effect.

2.4 Rate Phenomena of Double Layer Capacitance of ACFs

As mentioned above, one merit of EDLC is its fast charge-discharge so rates of the double layer capacitance are significant. Figure 4 shows the dependence of the double layer capacitance on the current density for ACFs. The double layer capacitance of mesoporous ACFs decreased slightly at high current densities, with that of microporous ACFs being reduced markedly at higher current density except for micro-ACF (240). These results suggest that the mesopores contribute to high rates under such conditions as high current density. According to Morita et al. [28], a mesoporous ACF prepared with a yttrium activation catalyst also showed high rates in a mixed solution of ethylene carbonate with dimethyl carbonate containing LiBF₄. A mesoporous ACF (1409 m² g⁻¹ and 4 nm pore size) showed little change in capacitance in the range of 0.2–5 mA cm⁻², but a conventional ACF (1990 m² g⁻¹ with 2 nm pore

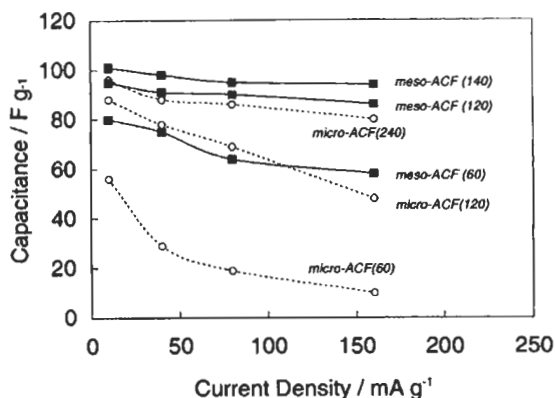


Fig. 4. Dependence of electric double layer capacitance (negative process) on current density for various ACFs in $1.0 \text{ mol dm}^{-3} \text{ LiClO}_4/\text{propylene carbonate}$. The capacitances were estimated by chronopotentiograms ($10, 40, 80, 160 \text{ mA g}^{-1}$) of negative process ($4 \text{ V} \rightarrow 2 \text{ V}$ vs Li/Li^+). Each capacitance was calculated from each chronopotentiogram in the region of $2.25\text{--}3.75 \text{ V}$ vs Li/Li^+ to eliminate the influence of resistance for electrode and bulk electrolyte.

size) showed capacitance loss at high current density [28]. Thus, mesoporous ACFs can be considered as a promising material for ultra high power EDLC.

3 Double Layer Capacitance of Other Carbon Materials

3.1 Other Porous Carbons

Double layer capacitances have been studied of other mesoporous carbons such as carbon aerogel [29], carbon xerogel [9], porous carbon prepared with metal oxide template [12] and highly porous carbons derived from defluorination of perfluoropolymer [13]. Higher capacitance of mesoporous carbons and enhancements at high rates are also reported. This characteristic results from the high wettability of pore walls by the electrolyte and the high mobility of ions in pores. Especially, it is surprising that the EDLC from a carbon aerogel has a gravimetric power density of 7.5 kW kg^{-1} [29]. On the other hand, mesoporous carbons such as carbon aerogels generally have low bulk densities, so the electrodes composed of mesoporous carbons as well as the mesoporous ACFs all have low bulk densities. The lower electrode density usually causes low volumetric specific capacitance. Because volumetric capacitance is more important for energy storage than gravimetric capacitance, there are few merits with mesoporous carbons for practical use. Therefore, a more rigorous control of pore size distributions is required for improvements in the volumetric energy density of EDLC. Recently, an interesting result was reported for a porous carbon electrode prepared by carbonizing polyvinylidene chloride (PVDC) [30]. An EDLC with the PVDC carbon showed high volumetric capacitance in aqueous electrolyte regardless of its relatively low specific surface area ($600\text{--}700 \text{ m}^2 \text{ g}^{-1}$) [30].

Porous carbons with high densities such as the PVDC carbons will contribute practically to improvements in energy densities for EDLC if they also show higher volumetric capacitance in organic electrolytes.

3.2 Carbon Nanotubes

The EDLC performance of carbon nanotubes (CNTs) has attracted much attention since their discovery [31–38]. In particular, single-walled carbon nanotubes (SWCNT) are expected as new carbon electrodes for EDLC. This is because SWCNTs have the theoretical surface area of $2630 \text{ m}^2 \text{ g}^{-1}$ (the total surface area of the outside of the plane and of the inside plane). The inner tube has a very uniform pore structure of nanometer size. Reported values for the gravimetric double layer capacitance of SWCNT electrodes are in a wide range between 20 and 300 F g^{-1} [34–38]. This dispersion may result from differences in the electrolytes used and a low purity of SWCNT. Therefore, it is still difficult to understand the capacitance of SWCNTs accurately. However, recently, highly pure SWCNTs have been prepared by the thermal decomposition of carbon monoxide under high pressure using an iron catalyst [39]. Figure 5 shows the dependence of the double layer capacitance on current density for these highly pure SWCNT electrodes and the ACF electrode. The SWCNT electrode maintained the capacitance even at high current density although the double layer capacitance value is lower than that of ACFs with high specific surface area. The BET area of the SWCNT electrode was only $444 \text{ m}^2 \text{ g}^{-1}$ (nitrogen adsorption at 77 K) and the α_s plot [22] indicated that the external surface area was $\sim 90\%$ of the total area. These results suggest that the high rates of SWCNTs are due to the high external surface area on which ions can be adsorbed or desorbed fast [40]. Thus, CNT electrodes may exhibit a better performance than the present EDLC with conventional activated carbons if high surface areas, close to the theoretical areas can be achieved by detailed structure control such as the opening of tube ends, etc.

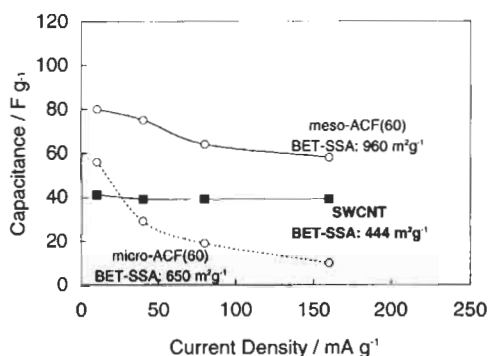


Fig. 5. Dependence of electric double layer capacitance (negative process) on current density for SWCNT and various ACFs in 1.0 mol dm^{-3} $\text{LiClO}_4/\text{propylene carbonate}$. The electrochemical conditions are the same as those in Fig. 4. The electrode consisted of the SWCNT bundles (tube diameter is around 0.9 nm, and tube bundle width is around 50 nm). The main impurities were metallic Fe particles ($\approx 20 \text{ wt}\%$) with several nanometers size. Few amorphous carbons and no graphite flakes were contained. SWCNT electrode was treated with 6 M HCl to remove Fe catalysts exposed on the surface.

4 Conclusion

Mesoporous ACFs that contain many mesopores in addition of micropores were prepared from carbonization and steam-activation of a phenolic resin fiber blended with a nickel activation catalyst. The gravimetric electric double layer capacitance of mesoporous ACFs and conventional microporous ACFs were measured in non-aqueous electrolytes. The following correlations between double layer capacitance and pore structure were established.

1. For both mesoporous and microporous ACFs, the double layer capacitance did not depend linearly on specific surface area. The reason for this is the ion-sieving effect of the narrow micropores of ACFs.
2. Mesoporous ACFs showed a higher double layer capacitance than microporous ACFs, especially for high current density measurements. This result suggests that the presence of many mesopores promotes the formation of an effective double layer or the fast transfer of ions to micropores.

The above results indicate the importance of pore size distributions in activated carbons and of ion sizes in electrolytes to bring about improvements of double layer capacitance. In the future, pore size distributions of porous carbon electrodes must be carefully controlled to increase both high gravimetric capacitance ($F g^{-1}$) and volumetric capacitance ($F cm^{-3}$). Additionally, the double layer capacitance of new porous carbons such as carbon nanotubes, carbon nanofibers, etc. must be examined in more detail.

References

1. B.E. Conway, *Electrochemical Super Capacitors*. Kluwer Academic/Plenum Publishers, New York, 1999.
2. Nishino, J. *Power Sources*, 60: 137–147, 1996.
3. S.J. Gregg and K.S.W. Sing, *Adsorption, Surface Area and Porosity*. Academic Press, London, 1982.
4. Takahashi, A. Yoshida and A. Nishino, *Denki Kagaku (presently Electrochemistry)*, 56: 892–897, 1988.
5. T. Morimoto, K. Hiratsuka, Y. Sanada and K. Kurihara, *J. Power Sources*, 60: 239–247, 1996.
6. H. Shi, *Electrochim. Acta*, 41: 1633–1639, 1996.
7. D. Qu and H. Shi, *J. Power Sources*, 74: 99–107, 1998.
8. S. Iwasaki, Y. Okusako, M. Miyahara and M. Okazaki, *Kagaku Kogaku Ronbunshu*, 23: 512–518, 1997 (in Japanese).
9. C. Lin, J.A. Ritter and B.N. Popov, *J. Electrochem. Soc.*, 146: 3639–3643, 1999.
10. H. Nakagawa, A. Shudo and K. Miura, *J. Electrochem. Soc.*, 147: 38–42, 2000.
11. Y. Sakata, A. Muto, M.A. Uddin, N. Yamada, C. Marumo, S. Ibaraki and K. Kojima, *Electrochem. Solid-State Lett.*, 3: 1–3, 2000.
12. S. Yoon, J. Lee, T. Hyeon and S.M. Oh, *J. Electrochem. Soc.*, 147: 2507–2512, 2000.
13. S. Shiraishi, H. Kurihara, H. Tsubota, A. Oya, S. Soneda, and Y. Yamada, *Electrochem. Solid-State Lett.*, 4, A5–A8, 2001.

14. G. Salitra, A. Soffer, L. Eliad, Y. Cohen and D. Aurbach, *J. Electrochem. Soc.*, 147: 2486–2493, 2000.
15. M. Suzuki, *Carbon*, 32: 577–586, 1994.
16. S.K. Ryu, *High Temperature-High Pressures*, 22: 345–354, 1990.
17. A. Oya, S. Yoshida, J. Alcaniz-Monge and A. Linares-Solano, *Carbon*, 33: 1085–1090, 1995.
18. H. Tamai, K. Kakii, Y. Hirota, T. Kumamoto, and H. Yasuda, *Chem. Mater.*, 8: 454–462, 1996.
19. S. Shiraishi, H. Kurihara and A. Oya, *Carbon Science*, 1: 133–137, 2001.
20. S. Shiraishi, H. Kurihara and A. Oya, *Electrochemistry*, 69: 440–443, 2001.
21. S. Shiraishi, H. Kurihara and A. Oya, *Proceedings of Carbon '01*, 24.3, 2001.
22. K. Kaneko, C. Ishii, M. Ruike and H. Kuwabara, *Carbon*, 30: 1075–1088, 1992.
23. D. Dollimore and G.R. Heal, *J. Applied Chem.*, 14: 109–114, 1964.
24. M.M. Dubinin and H.F. Stoeckli, *J. Colloid Interface Sci.*, 75: 34–42, 1980.
25. M.E. Merraoui, H. Tamai, H. Yasuda, T. Kanata, J. Mondori, K. Nadai and K. Kaneko, *Carbon*, 36: 1769–1776, 1998.
26. Y. Matsuda, H. Nakashima, M. Morita and Y. Takasu, *J. Electrochem. Soc.*, 128: 2552–2556, 1981.
27. M. Ue, *J. Electrochem. Soc.*, 141: 3336–3342, 1994.
28. M. Morita, S. Watanabe, M. Ishikawa, H. Tamai and H. Yasuda, *Electrochemistry*, 69: 462–466, 2001.
29. S.T. Mayer, R.W. Pekala and J.L. Kaschmitter, *J. Electrochem. Soc.*, 140: 446–451, 1993.
30. M. Endo, Y.J. Kim, T. Takeda, T. Maeda, T. Hayashi, K. Koshiba, H. Hara and M.S. Dresselhaus, *J. Electrochem. Soc.*, 148: A1135–1140, 2001.
31. C. Niu, E.K. Sichel, R. Hoch, D. Moy and H. Tennent, *Appl. Phys. Lett.*, 70: 1480–1482, 1997.
32. R.Z. Ma, J. Liang, B.Q. Wei, B. Zhang, C.L. Xu and D.H. Wu, *J. Power Sources*, 84, 126–129, 1999.
33. Ch. Emmenegger, P. Mauron, A. Zuttel, Ch. Nutzenadel, A. Schneuwly, R. Gallay and L. Schlapbach, *Appl. Surf. Sci.*, 162–163: 452–456, 2000.
34. C. Liu, A.J. Bard, F. Wudl, I. Weitz and J.R. Heath, *Electrochem. Solid-State Lett.*, 2: 577–578, 1999.
35. J.N. Barisci, G.G. Wallace and R.H. Baughman, *Electrochim. Acta*, 46: 509–517, 2000.
36. E. Frackowiak, K. Jurewicz, S. Delpeux and F. Beguin, *J. Power Sources*, 97–98: 822–825, 2001.
37. K.A. An, W.S. Kim, Y.S. Park, Y.C. Choi, S.M. Lee, D.C. Chung, D.J. Bae, S.C. Lim and Y.H. Lee, *Adv. Mater.*, 13: 497–500, 2001.
38. L. Duclaux, Y. Soneda and M. Makino, *Tanso*, 196: 9–13, 2001.
39. P. Nikolaev, M.J. Bronikowski, R.K. Bradley, F. Rohmund, D.T. Colbert, K.A. Smith and R.E. Smalley, *Chem. Phys. Lett.*, 313: 91–97, 1999.
40. S. Shiraishi, H. Kurihara, K. Okabe, D. Hulicova and A. Oya, *Electrochem. Commun.*, 4: 593–598, 2002.

Chapter 28

Field Electron Emissions from Carbon Nanotubes

Yahachi Saito^a, Koichi Hata^a and Sashiro Uemura^b

^a*Department of Electrical and Electronic Engineering, Mie University, Tsu 514-8507, Japan*

^b*Ise Electronics Corp., Ise 516-1103, Japan*

Abstract: Field emission microscopy (FEM) has been used to investigate the field emission of electrons from carbon nanotubes (CNTs) and related fibers, viz., multi-wall nanotubes (MWNTs), single-wall nanotubes (SWNTs), nanofibers (named “nanografibers”) grown in hydrogen gas, and vapor grown carbon fibers (VGCFs). Recent observations of pentagonal rings located on the capped tip of a clean MWNT, and adsorption and desorption phenomena of residual gas molecules on the tip, are presented. Developments of CNT-based field emission displays are briefly reviewed.

Keywords: Carbon nanotube, Field emission, Electron source, Display.

1 Introduction

When a high electric field of the order of 10^7 V cm⁻¹ is applied to a solid surface with a negative electrical potential, electrons inside the solid are emitted into vacuum by the quantum mechanical tunneling effect. This phenomenon is called field emission of electrons. Such extremely high fields are obtained on the sharp tip of a very thin needle because electric fields concentrate at the sharp tip. Carbon nanotubes (CNTs) possess the following properties which are favorable for field emitters: (1) needle-like shape with a sharp tip, (2) high chemical stability, (3) high mechanical strength, (4) low carbon atom mobility, and (5) good electrical conductivity. In 1995, field emissions (FE) from an isolated single multi-wall nanotube (MWNT) was first reported by Rinzler et al. [1], and field emissions from a MWNT film by de Heer et al. [2]. Saito et al. [3,4] studied the field emission microscopy (FEM) of CNTs in 1997 and experimentally manufactured CRT-type lighting elements with CNT cold cathodes. It was in 1998 that the first CNT-based field emission display (FED) was reported [5,6]. In 1999, Samsung SDI [7] reported the experimental fabrication of a 4.5 inch color FED panel with CNT cold cathodes.

In this chapter, emission characteristics of various CNTs are described followed by recent observations of pentagonal rings within a CNT cap. Finally, the present state of the development of CNT-based FEDs is briefly described.

2 FEM Study of Nanotubes

Six kinds of carbon nanotubes and fibers, with and without processes, were used as field emitters: (1) as-grown MWNTs prepared in a helium arc (“pristine MWNTs”), (2) MWNTs as-grown in hydrogen (“nanografibers”) [8], (3) purified MWNTs with open ends, (4) purified single-wall nanotubes (SWNTs), (5) vapor grown carbon fibers (VGCFs of Showa Denko) and (6) oxidized VGCFs [9]. Tips of the respective nanofibers are shown in Figs. 1 and 2. Tips of pristine MWNTs are capped by graphitic layers (Fig. 1a). Purified MWNTs, obtained after oxidation, have open ends (Fig. 1c). Nanografibers have an extremely narrow central channel. The smallest diameter of the innermost layer is about 1 nm or less. This is the reason why they are called “nanografibers” (the name coming from graphitic nanofibers) instead of multi-wall nanotubes. A TEM image in Fig. 1b shows that the tip of a nanografiber is partially broken or etched. Purified SWNTs form bundles each bundle consisting of about 100 nanotubes (Fig. 1d).

VGCFs are graphitic fibers with diameters of 100–500 nm as shown in Fig. 2a and the length exceeds 10 μm . Their structure and morphologies are similar to those of MWNTs grown by arc-discharge though the diameter of VGCFs is about five times larger than that of the MWNTs. The thick diameter and blunt tips of VGCFs are disadvantages to their use as field emitters. The morphology of VGCFs can be modified to have a sharp tip and a slender body by partial oxidation, as shown in Fig. 2b.

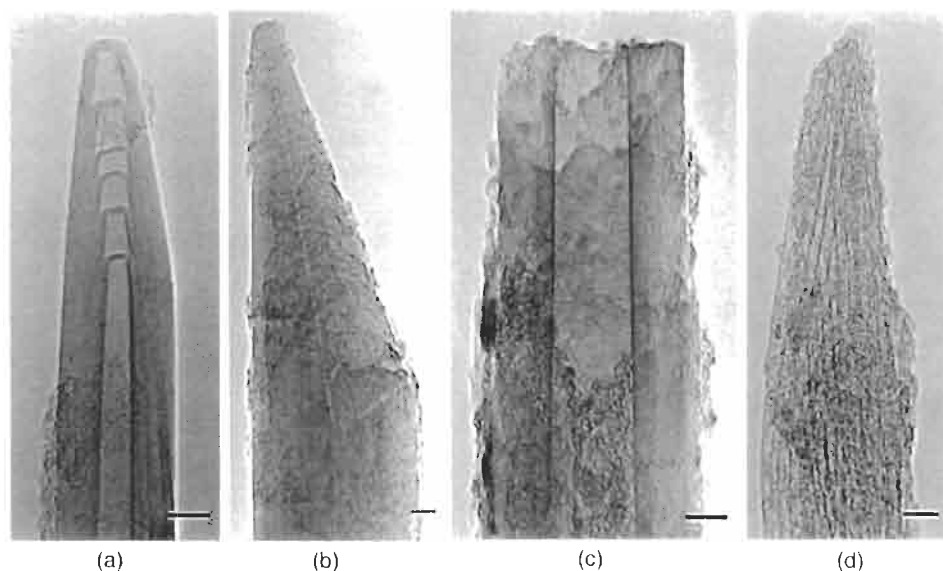


Fig. 1. TEM images of tips of four types of carbon nanotubes used for FEM studies [15]: (a) pristine MWNT with a capped end; (b) pristine nanografiber formed in a hydrogen arc; (c) MWNT with an open end; and (d) bundle of purified SWNTs. Scale bars: 5 nm.

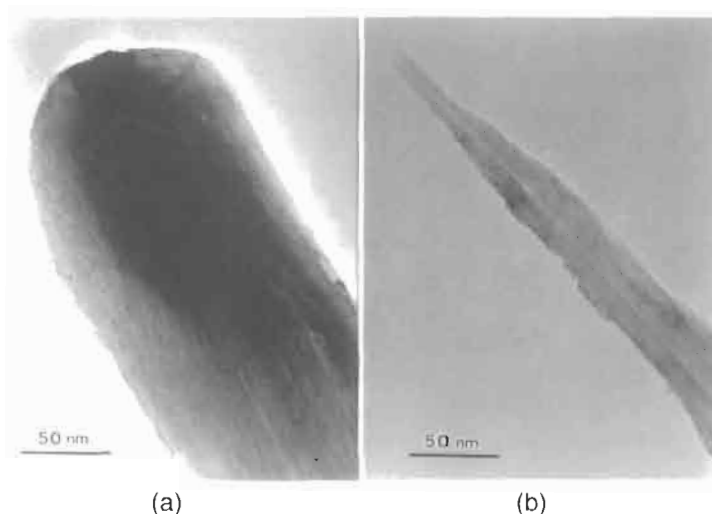


Fig. 2. TEM images of tips of VGCFs (vapor grown carbon fibers): (a) as-obtained VGCF; and (b) oxidized VGCF after a heat treatment (750°C) in air (mass reduction of 70–87%).

Experimentally, a bundle of respective nanotubes for an FEM study was fixed on the apex of a hairpin-shaped tungsten wire (0.15 mm in diameter) using conductive paste. Two types of FEM apparatus were used. In one apparatus, whose structure is schematically shown in Fig. 3, a probe hole for accepting electron current emitted from a restricted region of an emitter tip was placed on an observation screen and the base vacuum pressure was 1.3×10^{-6} to 1.3×10^{-7} Pa (10^{-8} – 10^{-9} Torr). The emitter tip of the nanotube was positioned 60 mm in front of an anode screen with a 1 mm probe hole. Field emission patterns could be observed on the anode screen that was coated with phosphor. Behind the probe hole a Faraday cup was placed and the electron

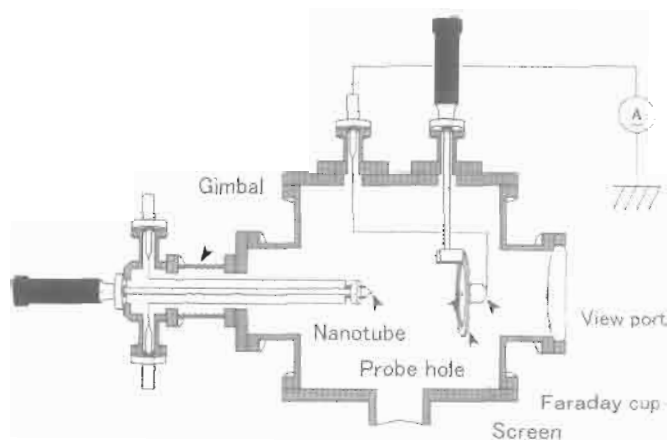


Fig. 3. Schematic drawing of an FEM apparatus with a probe hole [8].

current emitted from a restricted region of an emitter was measured. The acceptance half angle of the probe hole was 17 mrad. In the other apparatus, an emission experiment was made under an ultrahigh vacuum of 1.3×10^{-8} Pa (10^{-10} Torr), though no probe hole was fitted. Details of the tip preparation and FEM apparatus are described [3,8,10,11].

2.1 Current vs. Voltage Characteristics of Various CNTs

In FEM, regions where electrons are emitted from CNTs are imaged at high magnification (of the order of one million) as bright spots on the anode screen. Therefore, by placing the probe hole of the screen within one of bright spots, emission currents from a single nanotube were measured. Emission current accepted by the probe hole, I_p , was measured as a function of voltage applied to the tip (V). The $I_p - V$ characteristics for all the nanofibers are shown in Fig. 4.

Threshold voltages and maximum current densities are summarized in Table 1. Open-ended MWNTs begin to emit electrons at the lowest tip voltage and sustain the highest current density. Nanografibers grown in hydrogen give higher currents than ordinary MWNTs (i.e., pristine MWNTs grown in helium). This is caused mainly by the cleanliness of nanografiber samples (i.e., very small quantities of carbon debris) and partially by the structural defects on nanografiber tips which have a lower work function. The VGCFs showed poor emission properties though some improvement was obtained by sharpening their tips (oxidized VGCFs).

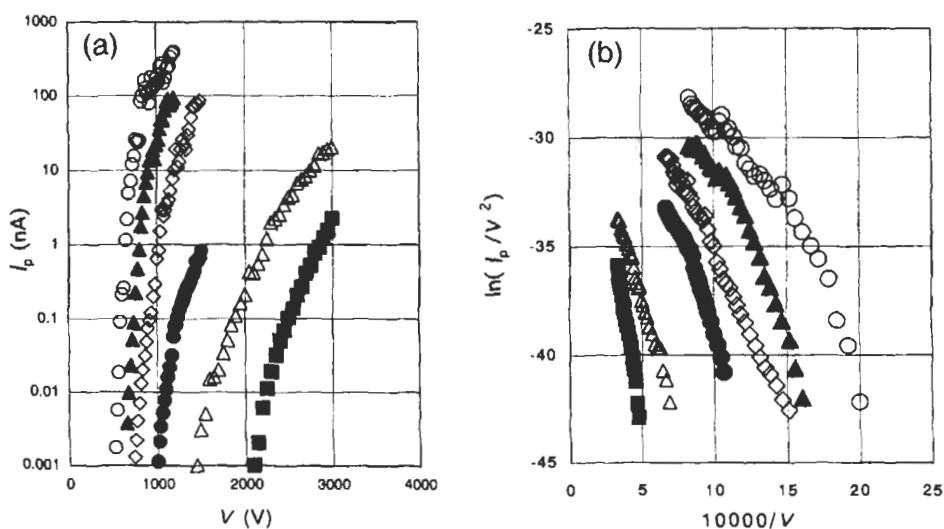


Fig. 4. (a) Current vs. voltage characteristics; (b) F-N plots for a pristine MWNT (●), a nanografiber (◇), an open MWNT (○), a bundle of SWNTs (▲), as-obtained VGCF (■), and oxidized VGCF (△). Current (I_p) was measured with the 1 mm probe hole.

Table 1

Field emission properties of the four kinds of carbon nanotubes. Since emission current was measured by the 1-mm probe hole, the properties come from a single tube for MWNT and nanografiber, and from one bundle for SWNTs.

| Carbon nanotubes | Threshold voltage* (V) | Maximum current density ($\times 10^6$ A/cm ²) |
|------------------|---------------------------|--|
| Capped MWNT | 900–1000 | 0.1–1 |
| Nanografiber | 700–800 | ~1 |
| Open MWNT | 500–600 | 10–100 |
| SWNTs | 600–700 | ~10 |
| As-obtained VGCF | ~2000 | ~0.01 |
| Oxidized VGCF | ~1500 | ~0.1 |

*Threshold voltages represent tip voltages at which currents measured by the probe hole exceed 0.1 pA.

The emission data shown in this chapter were obtained using the first apparatus which was not an ultrahigh vacuum and could not keep the emitter surfaces clean. Therefore, emissions probably did not come from clean surfaces but from molecules adsorbed on to CNT surfaces.

2.2 Field Emission Patterns Exhibiting Pentagons

In an earlier FEM study, in a vacuum of 1.3×10^{-6} to 1.3×10^{-7} Pa (10^{-8} – 10^{-9} Torr), all of the nanofibers studied, except the purified MWNTs, gave emission patterns consisting of a number of bright spots with no inner structure [3,10]. On the other hand, emission patterns from open MWNTs showed “doughnut-like” annular bright rings [4,11]. A black spot in the central region (i.e., the absence of electrons in the core of an electron beam) corresponds to the cavity of a nanotube.

Recently, FEM experiments of CNTs (MWNTs produced by arc discharge) in ultra-high vacuum with a base pressure of about 1.3×10^{-8} (10^{-10} Torr) have been carried out [12]. The nanotube emitters were heated to ~1300 K before the FEM study in order to clean their surfaces. A phosphor screen was placed at 30–40 mm from the emitter. The electrical potential applied to the emitter relative to the screen was typically from –0.9 to –1.6 kV.

Figure 5 shows FEM patterns obtained from a capped MWNT with clean surfaces. Six pentagonal rings arranged in five-fold (Fig. 5a) and six-fold symmetry (Fig. 5b) were observed. Each pentagonal region contains a small dark spot in its center. It should also be noted that interference fringes are observed between the neighboring pentagonal rings. Structural models of CNT tips which give the FEM patterns of Figs. 5a and 5b are shown in Figs. 6a and 6b, respectively.

When the electrical potential is applied to a nanotube, the electric field around the pentagonal rings will be stronger than that on other flat regions because the pentagonal rings are point-like vertices of a polyhedron. Furthermore, it is theoretically

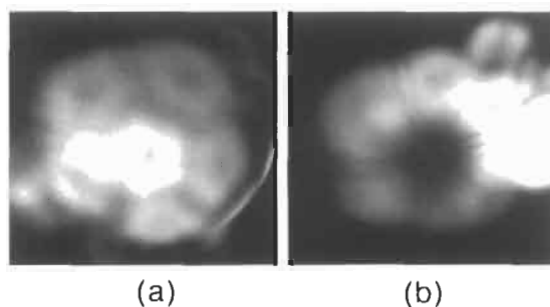


Fig. 5. FEM patterns from capped MWNTs showing (a) five-fold and (b) six-fold symmetry [12].

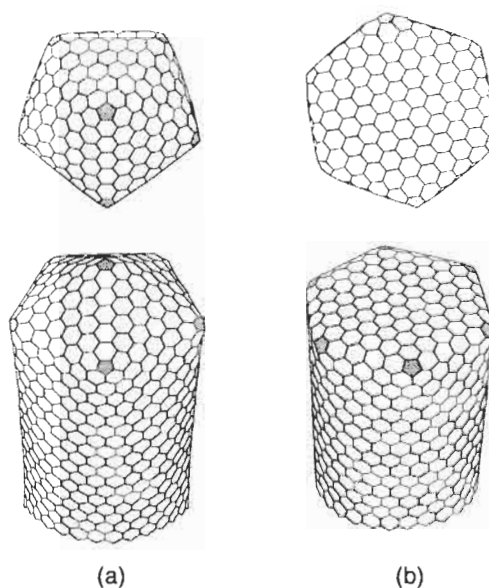


Fig. 6. Geometries of nanotube caps exhibiting (a) five-fold and (b) six-fold symmetry [12].

suggested that the pentagonal sites have a higher density of states near the Fermi level than the other hexagonal sites [13]. Therefore, electron tunneling through the pentagonal rings will occur preferentially.

2.3 Adsorption and Desorption of Residual Gas Molecules on a CNT Tip

Even in the ultra-high vacuum, residual gas molecules adsorb on the nanotube tip through field-enhanced surface migration. The adsorbed molecules reside preferentially on the pentagonal sites, giving bright spots in FEM patterns. These adsorbed molecules could be easily removed by heating CNTs at about 1300 K for 3

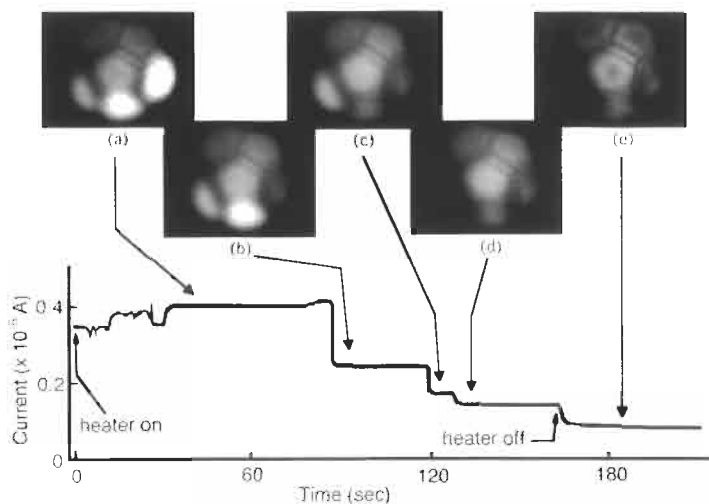


Fig. 7. Field emission patterns showing a desorption sequence of gas molecules and the corresponding changes in the emission current from a MWNT [14].

min. The desorption process during the heat cleaning is shown in Fig. 7, together with the corresponding time trace of the emission current [14]. Bright spots on the pentagons disappear one by one with time, and the stepwise decreases in the emission current at about 90 s, 120 s and 130 s occur concurrently with the disappearance of bright spots (i.e., desorption of molecules). The final step at 160 s is due to stopping heating (i.e., temperature decrease of the tip). Here, it is recognized that the contrast (or visibility) of the pentagonal rings and the interference fringes is high at a low temperature (room temperature) while it is low at a high temperature (1300 K). The decrease of the visibility at the high temperature results from additional incoherent thermal emission of electrons.

Molecular species adsorbed on the nanotubes are not yet identified. Possible gaseous molecules are hydrogen, carbon monoxide (or nitrogen) and carbon dioxide, which are major residual gas species in the ultra-high vacuum chamber.

A few years ago we reported stepwise fluctuations of the emission current from carbon nanotubes [3,15]. Similar current fluctuations were observed for field emissions from glassy carbon tips [16]. The origin of the stepwise changes so far is not clear, but it could be due to the adsorption and desorption of molecules on the surface of the carbon emitter in the experiment.

3 Nanotube-based Display Devices

Developing the field emission study, we experimentally fabricated field emission display (FED) elements. FEDs that we employed for examining the performance of nanotube field emitters are CRT (cathode-ray tube)-type lighting bulbs and VFD (vacuum fluorescent display)-like panels.

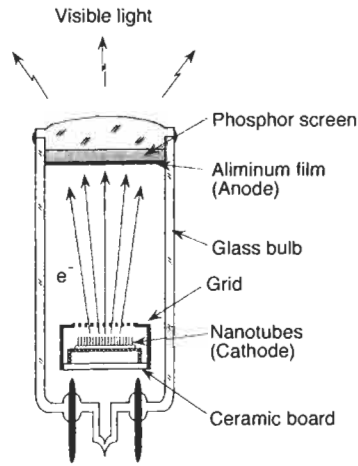


Fig. 8. Longitudinal cross-section of a CRT fluorescent display with a field emission cathode made of carbon nanotubes [5]. The size of the element is 20 mm in diameter and 74 mm in length.

3.1 Light Sources

The first CNT-based FED elements are CRT-type light bulbs. Figure 8 shows a longitudinal cross-section of the CRT lighting bulb that consists of three electrodes; CNT cold cathode, grid, and anode (phosphor screen). CNTs we used were MWNTs produced by an arc-discharge. In our first trial fabrication, fibrous materials containing abundant MWNTs were directly glued on to a stainless steel plate by using conductive paste [5]. Subsequently, several methods were examined to fix nanotubes on the cathode surface. The screen printing technique was found to be the most effective for industrial application [17].

The nanotube cathode is covered with a grid electrode; the spacing between the cathode and the grid (d_{T-G}) is 0.2–1.0 mm. The phosphor screen is printed on the inner surface of a front glass and backed by a thin aluminum film. After sealing the vacuum tube, getter material was flashed to attain high vacuum on the order of 10^{-6} Pa.

The cathode was grounded (0 V), and the grid was biased to a positive voltage. For $d_{T-G} = 0.2$ mm, current density on the cathode was ca. 25 mA cm^{-2} at an average field strength of $2 \text{ V } \mu\text{m}^{-1}$.

A high voltage (typically 10 kV) was applied to the anode to accelerate electrons, which excite the phosphor screen. Luminance of the phosphor screens was intense enough for practical use: e.g., $6.3 \times 10^4 \text{ cd m}^{-2}$ for green light (ZnS:Cu, Al for green phosphor) at an anode current of $200 \mu\text{A}$, which is two times more intense than that of commercially available conventional thermionic CRT lighting elements which are operated at $100 \mu\text{A}$. A lifetime test revealed that the nanotube cathode had a life of over 15,000 hours.

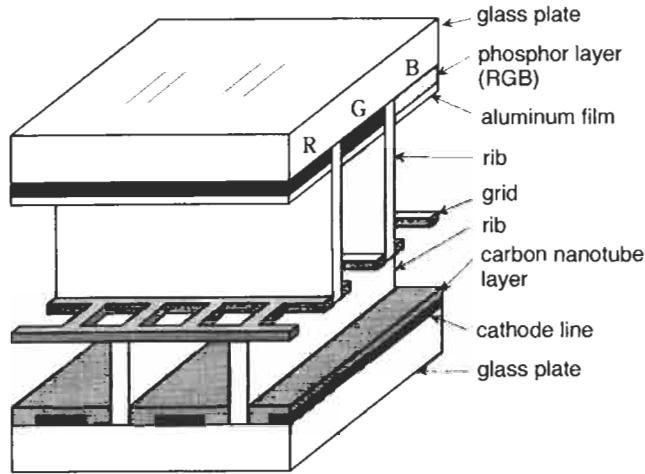


Fig. 9. Structure of a triode-type vacuum fluorescent display (VFD)-like flat panel display with carbon nanotube cathodes [17].

3.2 FED Panels

Field emission display (FED) flat panels were also experimentally fabricated in 1998. Figure 9 shows the structure of a triode type panel display [17]. One set of anodes, operated at a high-positive potential, consists of lines of RGB (red, green, blue)-color-phosphor (1 mm width) with metal-back film. The phosphor screen is just like a CRT-screen, with the many ribs formed on black matrix area between each phosphor line. These ribs (ca. 0.15 mm width) prevent mis-addressing of color phosphor by stray electrons. The second electrode is one set of cold-cathodes, which consists of carbon nanotube layers printed on a glass substrate equipped with silver electrodes. The cathode is covered with a grid electrode, which is placed on the cathode ribs and is parallel with a phosphor line. The grid controls emissions of electrons from nanotubes. The distance between the anode and the grid is 2.0–4.0 mm, and the distance between the top of nanotube tips and the grid (d_{T-G}) is 0.3–0.6 mm. After evacuating and sealing the panel, getter material was flashed to attain a high vacuum of the order of 10^{-5} Pa.

The screen size is 66×66 mm and a pixel size is 3 (RGB) × 2.54 mm. Displayed colors depend on phosphors printed on the anode, viz., ZnS:Cu, Al for green, $Y_2O_3:Eu$ for red, and ZnS:Ag for blue. A high voltage of typically 6 kV is applied to the anode. A luminance of the phosphor screens is $\sim 7 \times 10^5$ cd m⁻² for green, $\sim 1.8 \times 10^5$ cd m⁻² for red, and $\sim 1 \times 10^5$ cd m⁻² for blue under a dc-driving condition of 6 kV and ca. 1 mA cm⁻².

Samsung SDI of Korea has experimentally manufactured a 4.5-inch color FED in 1999, and a 9-inch color FED in 1999 [7], both of which are diode-type (i.e., consisting of CNT-cathode and phosphor anode) and employ SWNTs as field emitters. For full

gray scales and high brightness of FEDs, a triode structure is required. Recently, Samsung also began the development of triode-type FED panels using CNT emitters [18].

References

1. A.G. Rinzler, J.H. Hafner, P. Nikolaev, L. Lou, S.G. Kim, D. Tomanek, P. Nordlander, D.T. Colbert and R.E. Smalley, *Science*, 269: 1550–1553, 1995.
2. W.A. de Heer, A. Chatelain and D. Ugarte, *Science*, 270: 1179–1180, 1995.
3. Y. Saito, K. Hamaguchi, T. Nishino, K. Hata, K. Tohji, A. Kasuya and Y. Nishina, *Jpn. J. Appl. Phys.*, 36: L1340–L1342, 1997.
4. Y. Saito, K. Hamaguchi, K. Hata, K. Uchida, Y. Tasaka, F. Ikazaki, M. Yumura, A. Kasuya and Y. Nishina, *Nature*, 389: 554–555, 1997.
5. Y. Saito, S. Uemura and K. Hamaguchi, *Jpn. J. Appl. Phys.*, 37: L346–L348, 1998.
6. S. Uemura, T. Nagasako, J. Yotani, T. Shimojo and Y. Saito, *SID '98 Digest*, pp. 1052–1055, 1998.
7. W.B. Choi, D.S. Chung, J.H. Kang, H.Y. Kim, Y.W. Jin, I.T. Han, Y.H. Lee, J.E. Jun, N.S. Lee, G.S. Park and J.M. Kim, *Appl. Phys. Lett.*, 75: 3129–3131, 1999.
8. Y. Saito, R. Mizushima, S. Kondo and M. Maida, *Jpn. J. Appl. Phys.*, 39: 1468–1473, 2000.
9. Y. Tanaka and Y. Saito, In: *Abstracts of the 17th Fullerene General Symposium*, pp. 262–263, Gifu, Japan, August 9–10, 1999.
10. Y. Saito, K. Hamaguchi, K. Hata, K. Tohji, A. Kasuya, Y. Nishina, K. Uchida, Y. Tasaka, F. Ikazaki and M. Yumura, *Ultramicroscopy*, 73: 1–6, 1998.
11. Y. Saito, K. Hamaguchi, S. Uemura, K. Uchida, Y. Tasaka, F. Ikazaki, M. Yumura, A. Kasuya and Y. Nishina, *Appl. Phys. A*, 67: 95–100, 1998.
12. Y. Saito, K. Hata and T. Murata, *Jpn. J. Appl. Phys.*, 39: L271–L272, 2000.
13. R. Tamura and M. Tsukada, *Phys. Rev. B*, 52: 6015–6026, 1995.
14. K. Hata, A. Takakura and Y. Saito, *Surface Sci.*, 490: 296–300, 2001.
15. Y. Saito and S. Uemura, *Carbon*, 38: 169–182, 2000.
16. S. Yamamoto, S. Hosoki, S. Fukuhara and M. Futamoto, *Surface Sci.*, 86: 734–742, 1979.
17. S. Uemura, J. Yotani, T. Nagasako, Y. Saito and M. Yumura, *Proc. Euro Display '99 (19th IDRC)*, pp. 93–96, 1999.
18. J.M. Kim, N.S. Lee, J.H. You, J.E. Jun, C.G. Lee, S.H. Jo, C.J. Lee, D.S. Chung, S.H. Park, J.H. Kang, Y.S. Choi and H.Y. Kim, *Proc. 1st Int. Display Manufacturing Conf.*, pp. 39–43, 2000.

Chapter 29

Gas Separations with Carbon Membranes

Katsuki Kusakabe and Shigeharu Morooka

Department of Applied Chemistry, Kyushu University, Fukuoka 812-8581, Japan

Abstract: This chapter describes recent developments of carbon membranes for gas separations. Carbon membranes are prepared by carbonizing various polymeric materials. The molecular sieving carbon membranes produced under optimized conditions possess several advantages over polymer membranes including high selectivity as well as thermal and chemical stabilities. Controlled oxidation of the membranes at elevated temperature improved permeation properties. Carbon membranes with 0.4–1.5 nm diameter pores were used to separate hydrocarbons or hydrogen sulfide from hydrogen by surface diffusion mechanisms.

Keywords: Membrane, Gas separation, Micropore, Permeation, Carbonization.

1 Properties of Carbon Membranes

Carbon membranes, prepared by the carbonization of polymeric membranes under optimized conditions, show appreciable permeation rates with high selectivities for a variety of gas mixtures. From the viewpoint of designing a separation process for gases, it is necessary to compare the separation properties of such membranes with other types of molecule-selective membranes. As shown in Fig. 1, inorganic membranes, including carbon membranes, are classified as being either dense or microporous. Examples of dense membranes include palladium membranes, used exclusively for the separation of hydrogen, and perovskite membranes, used only for oxygen separation. Microporous membranes are further classified into amorphous and crystalline membranes. Amorphous membranes include silica and carbon membranes, and crystalline membranes include a variety of zeolite membranes, such as MFI-, FAU- and LTA-type zeolites. The size of the micropores in amorphous materials is controlled by an appropriate selection of precursor materials and preparation conditions. The size of micropores of zeolites is dependent on their crystal structures. In general, permeation rates and selectivities are higher for inorganic membranes than for polymeric membranes because inorganic membranes are designed for specific separation systems with a wider degree of freedom than polymeric membranes. However, polymeric membranes are normally produced in the

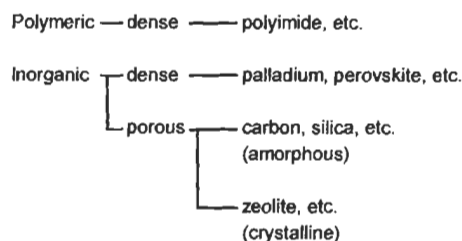


Fig. 1. Classification of membranes for gas separation [13].

shape of hollow fibers (100–300 μm in diameter), having a wide membrane area per unit volume of the module composed of a bundle of hollow fibers [1]. Thus, the permeation rate of a polymeric membrane module is often higher than that of an inorganic membrane module. Koros and coworkers [2,3] reviewed strategies for applying membrane processes to large-scale gas separations.

In a round micropore, molecules may move by single file diffusion. Masuda et al. [4] determined diffusivities within crystals of a highly siliceous MFI-type zeolite for binary component systems. The diffusivities of the more rapidly diffusing molecules were strongly affected by the co-existence of slower diffusing molecules. The diffusion of the former decreased as the number of the latter increased and the intrinsic diffusivity of the latter also decreased. In contrast, the diffusivities of the slower molecules were not affected by the co-existence of the faster molecules.

Micropores of carbon membranes, on the other hand, are usually assumed to be slit-like. As a result, this shape enables the more rapid molecules to pass the slower molecules, even if the size of molecules approaches the narrow width of the slits. Furukawa et al. [5,6] performed computer simulations to study the effects of surface heterogeneity on the permeation of CH_4 and C_2H_6 for single- and binary-component systems through carbon membranes. A small heterogeneity on the pore surface results in a large decrease in permeation fluxes due to an increase in the frequency of molecular collisions at the heterogeneous sites. Furukawa et al. [7] further simulated the permeation of CH_4 and C_2H_6 across carbon membranes the pores of which were modeled as diamond path (DP), zigzag path (ZP) and straight path (SP). The permeation resistance through the DP and ZP membranes was diffusion inside the pores, while that through the SP membrane resistance was shown to exist at the pore exits. The $\text{C}_2\text{H}_6/\text{CH}_4$ separation factor for binary mixtures was larger than that for the single-component systems but smaller than that calculated from the adsorption equilibria of the two components. This was explained by the slower diffusivity of C_2H_6 , compared with CH_4 .

MacElroy and Boyle [8] also simulated the permeation of H_2 and CH_4 through a slit-like pore in carbon membranes of various thickness. Results suggested that the adsorption of molecules at entrances and their desorption at exits need to be considered for hydrogen/hydrocarbon separations if the length of the controlling pores within the carbon membrane is $\leq 1.0 \mu\text{m}$. The cross-coefficients of diffusion play

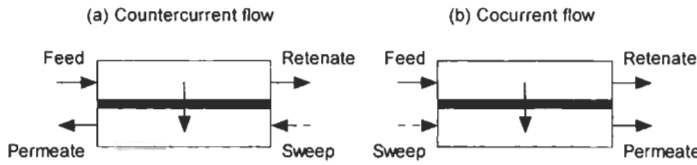


Fig. 2. Flows in membrane separators.

a relatively minor role in the pressure-driven separation of hydrogen–methane mixtures. Under isobaric conditions, however, H_2/CH_4 cross-coupling has a significant role in hindering the hydrogen counter-diffusion flux within carbon membranes which contain long narrow pores.

In order to evaluate permeation rates through carbon membranes, macroscopic models based on adsorptivity and diffusivity are convenient. Figure 2 shows a schematic diagram for a separation system using a carbon membrane. The partial pressure of the permeants on the permeate side can be reduced by pressurizing the feed side, evacuating the permeate side, or introducing a sweep gas into the permeate side. The permeance, $\Pi(i)$, is defined based on the difference in partial pressures on the feed and permeate sides, $p(i)_f - p(i)_p$.

$$\Pi(i) = \frac{J(i)}{p(i)_f - p(i)_p} \tag{1}$$

where $J(i)$ is the flux of component i through the membrane. Permeance is usually expressed in units of $\text{mol m}^{-2} \text{s}^{-1} \text{Pa}^{-1}$ and sometimes in units of GPU ($= 3.4 \times 10^{-10} \text{ mol m}^{-2} \text{ s}^{-1} \text{Pa}^{-1}$). In order to express the permeation rate through a membrane, a term of permeability, which is defined as $\Pi(i)\delta$, is frequently used. Permeability can be calculated only when the membrane thickness, δ , is known, and is often described in units of Barrer, which is equal to $3.4 \times 10^{-16} \text{ mol m}^{-1} \text{ s}^{-1} \text{Pa}^{-1}$. It should be noted that the thickness of asymmetric membranes is difficult to determine. The separation factor for a binary gas mixture of i and j components is defined as $\Pi(i)/\Pi(j)$.

The Maxwell–Stefan diffusivity, $D_{MS}(i)$, is defined by the following equation [9–12]:

$$J(i) = -\rho D_{MS}(i) \Gamma(i) \frac{dq(i)}{dz} \tag{2}$$

where ρ is the density of the membrane, and $q(i)$ is the sorptivity of component i on the membrane. $\Gamma(i)$ is the Darken factor and is usually described as

$$\Gamma(i) = \frac{d \ln p(i)}{d \ln q(i)} = \frac{1}{1 - \theta(i)} \tag{3}$$

where $\theta(i)$ is the occupancy of component i and is dependent on the sorption equilibrium for a gas mixture.

Table 1
Regimes for gas separation through micropores [13]

| Regime | Molecular size | | Size exclusion | | Surface concentration | | Pore concentration | |
|--------|----------------|-------|----------------|-----|-----------------------|------|--------------------|------|
| I | Small | Small | No | No | Low | Low | Low | Low |
| II | Small | Large | No | No | Low | High | Low | High |
| III | Large | Large | No | No | High | High | High | High |
| IV | Large | Large | No | Yes | High | High | High | Low |
| V | Small | Large | No | Yes | Low | High | Low | Low |
| VI | Large | Large | Yes | Yes | High | High | Low | Low |

Separation factors for binary component systems have been intensively investigated for MFI-type zeolite membranes. Keizer et al. [13] classified molecules into large and small ones.

“Small” molecules have: (a) low concentrations on the external surface and in the pores; and (b) high mobilities on the external surface and in the pores. “Large” molecules have: (a) high concentrations on the external surface; (b) high or low concentrations in the pores, depending on the relative size of the molecules and the pores; and (c) low mobilities on the external surfaces and in the pores.

Table 1 shows the regimes classified into four parameters. Gases corresponding to regime II are separated based on differences in their adsorptivities. The adsorptivity of the more adsorptive component is not substantially altered in the presence of the less adsorptive component. Adsorption of the less adsorptive component is decreased as a result of competitive adsorption. Thus, the separation factor is increased in the case of a binary system. Gases corresponding to regime IV are separated based on size exclusion, and gases corresponding to regime V are separated on differences in adsorptivities as well as size exclusion. The concepts of these regimes can be applied to carbon membranes.

2 Preparation of Carbon Membranes

Carbon membranes have been prepared from a variety of precursors including polyimides [14–38], polyfurfuryl alcohol [39–43], (polyvinylidene chloride)–acrylate terpolymer [44–46], phenolic resin [47–50], polypyrrolone [51], polyetherimide [52–53], poly(vinylidene chloride-co-vinyl chloride) [54], polyaromatic resins [55], and coal-tar pitch [56].

Of these, the carbonization of polyimides has been the most intensively investigated (Fig. 3). Typically, a solution of polyamic acid is prepared from a combination of dianhydride and diamine and then coated as a film on the outer surface of a porous support by dip-coating. The resulting film is imidized in an inert atmosphere or in vacuum, and carbonized in an inert atmosphere at temperatures of 773–1173 K. The carbonization temperature strongly affects the permeation

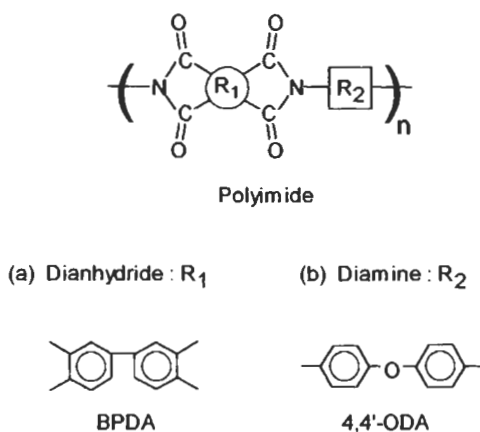


Fig. 3. The chemical structure of polyimide.

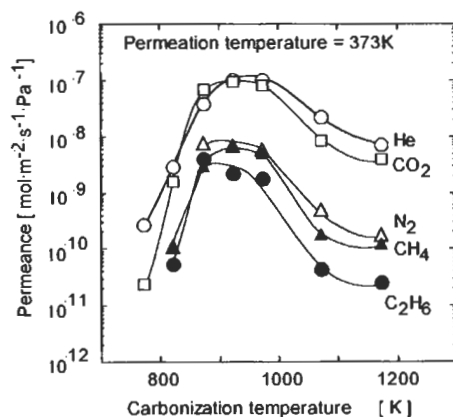


Fig. 4. Effect of carbonization temperature on permeances at 373 K [17].

properties of the resulting carbon membranes. Generally, permeances reach maximum levels at heat treatment temperatures (HTT) of 873–973 K, as shown in Fig. 4 [17], and decrease with higher HTT due to shrinkage of the membrane. The permeances and permselectivities are dependent on pore volume and pore size distribution both being determined by the carbonization conditions.

Because carbon membranes are not mechanically strong, they are typically formed on porous supports. When a supporting substrate is used for a carbon membrane, the substrate must be chemically and physically stable and possess a diffusion resistance which is lower than that of the carbon membrane. Tubular substrates are mechanically stronger against a compressing pressure than flat substrates. The membrane area, per unit module volume, is increased by decreasing the diameter of the support.

However, solid porous supports are not always necessary for asymmetric hollow carbon fibers [14,23,24,30,31,33,34,47]. The precursor hollow fiber developed by Kusuki et al. [23] was spun from polyimide and had an O.D. of 0.40 mm and an I.D. of 0.12 mm. It was then heat-treated in air at 673 K for 30 min and pyrolyzed at 873–1273 K for 3.6 min. The hollow fiber shrunk to 0.35–0.28 mm O.D. and 0.11–0.09 mm I.D. depending on the carbonization temperature. The fractured face of the membrane was composed of a skin layer and a macroporous bulk layer. Such a structure confers flexibility on the carbon fiber.

3 Permeances of Molecular Sieving Carbon Membranes

3.1 Unary Gases

The permeation through membranes is governed by the sorptivity and diffusivity of permeates, as shown in Eq. (2). Figure 5 [18] shows that permeances do not decrease simply with increasing molecular size of the permeants [57]. Larger and more polar molecules are more strongly sorbed to the membranes, but their diffusivities are often lower than smaller molecules. For molecules with similar sizes, diffusivities do not differ greatly when selectivity becomes dependent on sorptivity. The permeance to carbon dioxide is high compared to other gases [29,30,33] and often higher than those of helium and hydrogen (Fig. 6). However, the effective size of carbon dioxide molecules in micropores is disputed. Acharya and Foley [40] prepared a membrane via spray coating of an acetone solution of polyfurfuryl alcohol on a porous stainless steel disk. The disk was dried and pyrolyzed in an inert atmosphere to a final

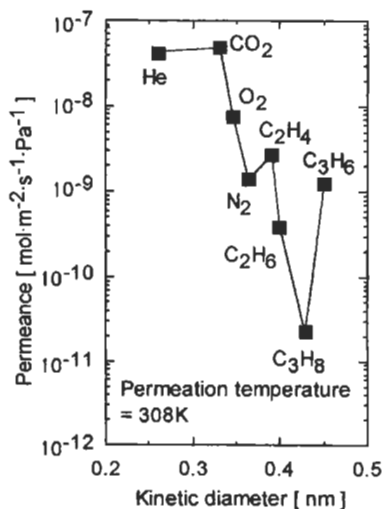


Fig. 5. Effect of kinetic diameters of permeates on their permeances at 308 K for a membrane prepared by carbonization at 973 K [18].

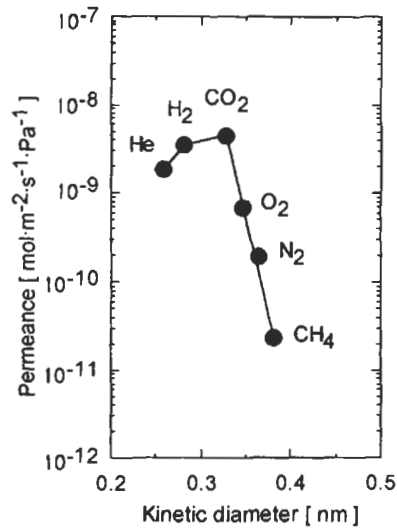


Fig. 6. Effect of kinetic diameters of permeates on their permeances at 298 K [33].

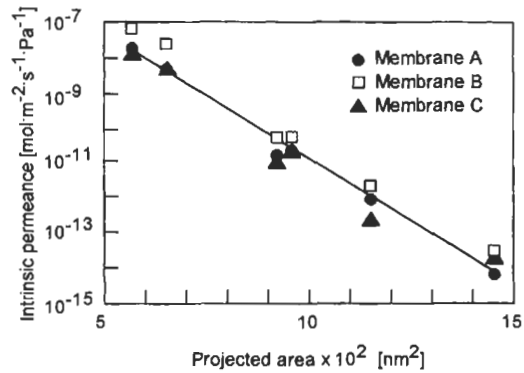


Fig. 7. Relationship between intrinsic permeances at 294 K and minimum projection area of permeating molecules [40].

temperature of 873 K. After correction for the adsorption effect, intrinsic permeances to single-component gases was correlated with the projected areas of the molecules. As shown in Fig. 7 [40], the intrinsic permeance to carbon dioxide was much lower than that to hydrogen.

3.2 Binary and Ternary Mixtures

Based on the permeation modes shown in Table 1, mixtures of carbon dioxide and nitrogen fall into regime II. The permeance to the less adsorptive component

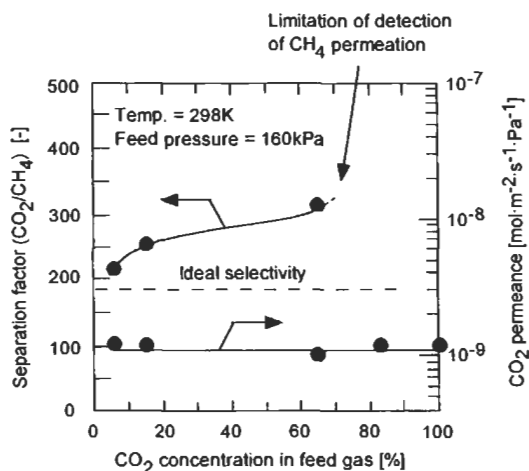


Fig. 8. Effect of carbon dioxide concentration in the feed on CO₂/CH₄ separation factor and permeance of carbon dioxide [34].

(nitrogen) decreases with increasing fraction of the more adsorptive component (carbon dioxide) on the feed side. Figure 8 [34] shows typical data for this category. The total pressure is not a major factor in the separation of dry gases [30]. When gases are condensed in pores, however, a different permeation mode appears. As shown in Fig. 9, the permeance to carbon dioxide reached a maximum near its critical pressure and then decreases at higher pressures [47]. The maximum was not observed at a permeation temperature of 333 K which is higher than the critical temperature.

Carbon membranes are effective for the separation of alkanes and alkenes. Hayashi et al. [18] found that a carbonized membrane prepared using a BPDA-pp'ODA polyimide procedure gave higher C₃H₆/C₃H₈ and C₂H₄/C₂H₆ permselectivities than those of the corresponding polyimide membrane. The C₃H₆/C₃H₈ selectivity was approximately 30 at a permeability coefficient of 50 Barrer, which is

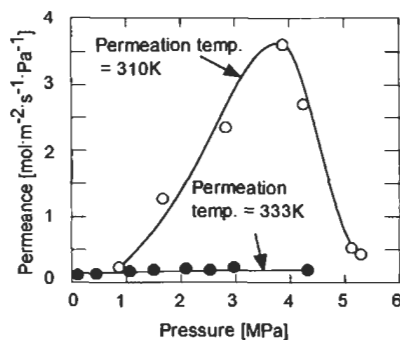


Fig. 9. Effect of total pressure on permeances [47].

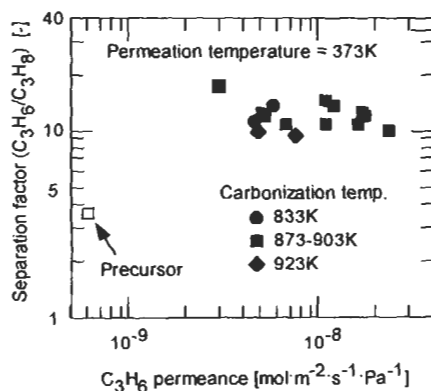


Fig. 10. Relationship between C_3H_6/C_3H_8 separation factor and C_3H_6 permeance for single-component systems [31].

equivalent to a permeance of $3 \times 10^{-9} \text{ mol m}^{-2} \text{ s}^{-1} \text{ Pa}^{-1}$, when the membrane thickness, δ , is $6 \mu\text{m}$. This suggests that the carbonized membranes possess a micropore structure which is capable of differentiating between alkane and alkene molecules. These high separation factors are explained in terms of the minimum size of the molecules. The minimum size of C_3H_6 is 0.40 nm , which is smaller than that of C_3H_8 , 0.43 nm [18]. Okamoto et al. [31] reported similar results, as shown in Fig. 10. The C_3H_6/C_3H_8 separation factor was 10–20, while the C_3H_6 permeance was larger than $10^{-8} \text{ mol m}^{-2} \text{ s}^{-1} \text{ Pa}^{-1}$.

The separation factor for ternary component systems is complicated. Figure 11 shows the separation factors for $\text{CO}_2\text{-CH}_4\text{-H}_2$ systems [53]. The mole fractions of carbon dioxide and hydrogen were kept equal with a varying mole fraction of CH_4 . The H_2/CH_4 separation factor decreased with an increase in the mole fraction of CH_4 . This is in accord with the findings relative to a binary $\text{H}_2\text{-CH}_4$ system. However, the CO_2/CH_4 separation factor increased at higher CH_4 mole fractions.

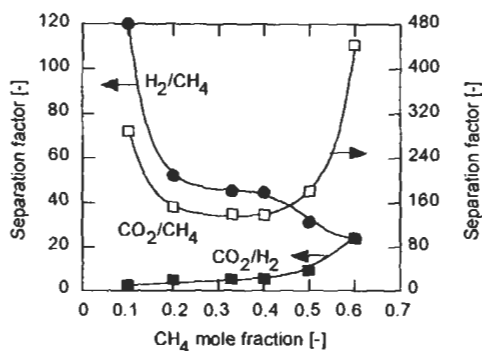


Fig. 11. Effect of feed composition on separation factor for $\text{CO}_2\text{-CH}_4\text{-H}_2$ systems. Permeation temperature = 293 K , pressure = 207 kPa [53].

4 Oxidation of Molecular Sieving Carbon Membranes

Heat-treatment in an oxidizing atmosphere improves permeances [21,22,28]. Kusakabe et al. [28] carbonized BPDA-pp'ODA membranes in an inert atmosphere at 973 K, followed by oxidization using a mixture of O_2 - N_2 (O_2 fraction = 0.1) at 573 K for 3 h. The oxidation decreased the H/C ratio and increased the O/C ratio, suggesting that peripheral alkyl groups had undergone decomposition and that oxygen had been incorporated into the membrane. Figure 12 shows permeances for carbon membranes at permeation temperatures of 338 K and 373 K [21]. The oxidation resulted in an increase in permeance without greatly altering the permselectivities. Thus, oxidation at 573 K for 3 h significantly increased the micropore volume while the pore size distribution remained relatively unchanged. However, treatments in an oxidative atmosphere need to be more extensively studied because results often are not reproducible.

In order to examine the long-term stability, Hayashi et al. [21] exposed BPDA-pp'ODA-based carbon membranes, which had been carbonized at 973 K, to air at 373 K for one month. As shown in Fig. 13, this exposure caused no change to the O/C ratio and only a limited decrease in the H/C ratio following decomposition of peripheral alkyl groups. The N/C and O/C ratios remained constant during the exposure. After the long-term oxidation, the membrane was heat-treated in nitrogen at 873 K for 4 h. Figure 13 also shows that the mass of the membrane decreased to 84% of its original value as a result of the long-term oxidation. After the heat treatment, it further decreased to 76% of its original value, while the H/C, O/C and N/C ratios remained unchanged within experimental error. Figure 14 shows data on

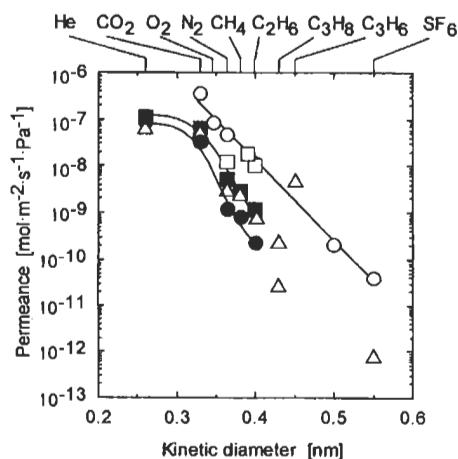


Fig. 12. Effect of oxidation at 673 K for 3 h on permeances of membranes carbonized at 973 K. Permeation temperature = 338 K; (●) = as-formed, (○) = oxidized in O_2 . Permeation temperature = 373 K, (■) = as-formed, (△) = oxidized in O_2 - N_2 mixture (O_2 fraction = 0.1), (□) = oxidized in O_2 [28].

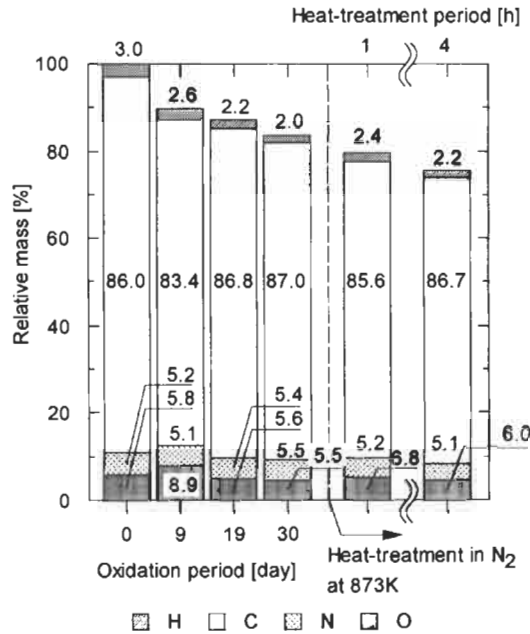


Fig. 13. Changes in mass and elemental distribution in membranes during the stability test at 373 K in air. The mass of the initial membrane is assumed to be unity [21].

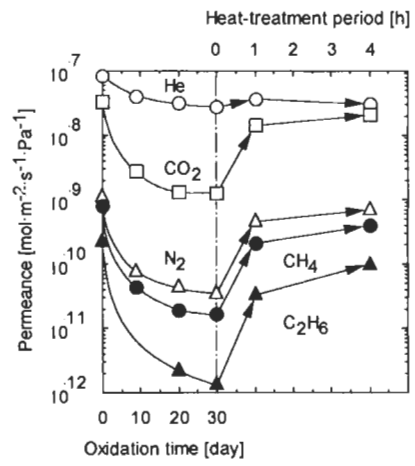


Fig. 14. Effect of long-term exposure to air at 373 K and post heat-treatment in nitrogen at 873 K for 4 h on permeances at 338 K [21].

permeances, for the long-term oxidized and heat-treated carbon membrane, to a single-component gas at the permeation temperature of 338 K. The permeances of the membrane decreased with increasing exposure time and recovered approximately to original values after heat-treatment. The membrane showed a CO_2/CH_4 perm-

selectivity of 80 at 338 K. Thus, oxidation in air at 373 K does not appear to have a great effect on the chemical structure of the membranes. Surface oxides, introduced by oxidation at 373 K, may reduce the aperture of the micropores and decrease permeances. Most of the surface oxides are decomposed by post heat-treatment at 873 K.

The separation properties of carbon membranes are sensitive to steam, which is strongly adsorptive. Jones and Koros [15] reported that permeances to oxygen and nitrogen for an asymmetric hollow fiber carbon membrane, carbonized at 773–823 K, decreased to 0.4–0.5 of the initial value after the membrane was exposed to air at relative humidities of 23–85% at ambient temperature. The stability of the carbon membrane was improved by coating the membrane with perfluoro-2,2'-dimethyl-1,3-dioxole or tetrafluoroethylene [16]. The oxygen flux, after exposure to humidity, decreased to 11% as a result of the coating procedure.

5 Separation Based on Surface Flow

Fuertes [50] prepared carbon membranes by carbonizing cured phenolic resin films at 973 K in vacuum, followed by oxidizing the membranes with air at 537–673 K for 30 min. The oxidation decreased the separation factors for single component gases. For combinations of adsorptive hydrocarbon and nonadsorptive nitrogen, however, the permeance to nitrogen decreased as shown in Figure 15, and, as a result, the separation factor for hydrocarbon increased. This effect is pronounced for hydrocarbons, which have high adsorptivity and small molecular size.

Carbon membranes with 0.4–1.5 nm diameter pores were also developed and applied to separation of hydrocarbons from hydrogen [44,46,58,59]. An enriched hydrogen stream was produced on the high-pressure side (i.e., the feed side) of the membrane. Carbon membranes of this type have also been applied to the separation of hydrogen sulfide from hydrogen [60] and methane [61].

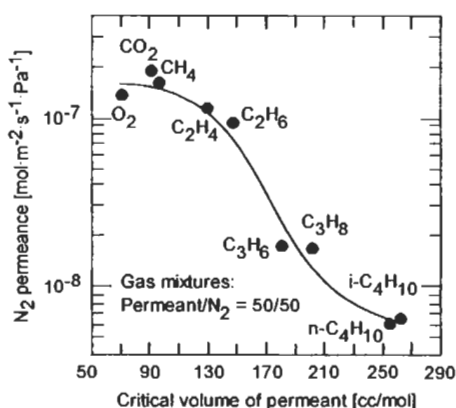


Fig. 15. Relationship of nitrogen permeances at 293 K and critical volumes of co-existing gas [50].

6 Conclusions

Molecular sieving carbon membranes, from a variety of polymeric precursors, are made by carbonizing precursor membranes. When carbonization conditions, such as temperature and time, are properly selected, the permeation properties and stabilities of the carbon membranes are greatly improved. Permeation through carbon membranes is dependent on molecular size relative to pore size, adsorptivity, diffusivity and pore size distribution. Controlled oxidation at elevated temperatures increases permeances of the carbon membranes. However, permeances may be decreased by exposing the membranes to an oxidative or humidified atmosphere as the result of formation or the adsorption of oxygen-containing functionalities in the pores. Permeances can be recovered by heat-treating the membranes in an inert atmosphere without damage to selectivity. Carbon membranes with pores of 0.4–1.5 nm are useful for producing hydrogen at the exit of the feed side by transferring hydrocarbons or hydrogen sulfide to the permeate side via surface flow through the pores.

References

1. S.A. McKelvey, D.T. Clausi and W.J. Koros, A guide to establishing hollow fiber macroscopic properties for membrane allocations. *J. Memb. Sci.*, 124: 223–232, 1997.
2. C.M. Zimmerman, A. Singh and W.J. Koros, Tailoring mixed matrix composite membranes for gas separations. *J. Memb. Sci.*, 137: 145–154, 1997.
3. W.J. Koros and R. Mahajan, Pushing the limits on possibilities for large scale gas separation: which strategies? *J. Memb. Sci.*, 175: 181–196, 2000.
4. T. Masuda, Y. Fujikata, H. Ikeda and K. Hashimoto, Diffusivities in the binary components system within MFI-type zeolite crystals. *Microporous Mesoporous Mater.*, 38: 323–332, 2000.
5. S. Furukawa, T. Sugahara and T. Nitta, Non-equilibrium MD studies on gas permeation through carbon membranes with belt-like heterogeneous surfaces. *J. Chem. Eng. Japan*, 32: 223–228, 1999.
6. S. Furukawa and T. Nitta, Non-equilibrium molecular dynamics simulation studies on gas permeation across carbon membranes with different pore shape composed of micro-graphite crystallites. *J. Memb. Sci.*, 178: 107–119, 2000.
7. S. Furukawa, K. Hayashi and T. Nitta, Effects of surface heterogeneity on gas permeation through slit-like carbon membranes by non-equilibrium molecular dynamics simulations. *J. Chem. Eng. Japan*, 30: 1107–1112, 1997.
8. J.M.D. MacElroy and M.J. Boyle, Nonequilibrium molecular dynamics simulation of a model carbon membrane separation of CH_4/H_2 mixtures. *Chem. Eng. J.*, 74: 85–97, 1999.
9. W.J.W. Bakker, L.J.P. van den Broeke, F. Kapteijn, J.A. Moulijn, Temperature dependence of one-component permeation through a silicalite-1 membrane. *AIChE J.*, 43: 2203–2214, 1997.
10. R. Krishna and J.A. Wesselingh, The Maxwell–Stefan approach to mass transfer. *Chem. Eng. Sci.*, 52: 861–911, 1997.
11. C.M. Zimmerman, A. Singh and W.J. Koros, Diffusion in gas separation membrane materials—A comparison and analysis of experimental characterization techniques. *J. Polym. Sci. Part B-Polymer Phys.*, 36: 1747–1755, 1998.

12. I.A. Karimi and S. Farooq, Effect of sorbate–sorbate interaction on micropore diffusion in steady-state adsorption processes. *Chem. Eng. Sci.*, 55: 3529–3541, 2000.
13. K. Keizer, A.J. Burggraaf, Z.A.E.P. Vroon and H. Verweij, Two component permeation through thin zeolite MFI membranes. *J. Memb. Sci.*, 147: 159–172, 1998.
14. K. Haraya, H. Suda, H. Yanagishita and S. Matsuda, Asymmetric capillary membrane of a carbon molecular sieve. *J. Chem. Soc., Chem. Commun.*: 1781–1782, 1995.
15. C.W. Jones and W.J. Koros, Characterization of ultramicroporous carbon membranes with humidified feeds. *Ind. Eng. Chem. Res.*, 34: 158–163, 1995.
16. C.W. Jones and W.J. Koros, Carbon composite membranes: A solution to adverse humidity effects. *Ind. Eng. Chem. Res.*, 34: 164–167, 1995.
17. J.-I. Hayashi, M. Yamamoto, K. Kusakabe and S. Morooka, Simultaneous improvement of permeance and permselectivity of 3,3',4,4'-biphenyltetracarboxylic dianhydride-4,4'-oxydianiline polyimide membrane by carbonization. *Ind. Eng. Chem. Res.*, 34: 4364–4370, 1995.
18. J.-I. Hayashi, H. Mizuta, M. Yamamoto, K. Kusakabe, S. Morooka and S.-H. Suh, Separation of ethane/ethylene and propane/propylene systems with a carbonized BPDA-pp'ODA polyimide membrane. *Ind. Eng. Chem. Res.*, 35: 4176–4181, 1996.
19. V.C. Geiszler and W.J. Koros, Effects of polyimide pyrolysis conditions on carbon molecular sieve membrane properties. *Ind. Eng. Chem. Res.*, 35: 2999–3003, 1996.
20. J.-I. Hayashi, H. Mizuta, M. Yamamoto, K. Kusakabe and S. Morooka, Pore size control of carbonized BPDA-pp'ODA polyimide membrane by chemical vapor deposition of carbon. *J. Memb. Sci.*, 124: 243–251, 1997.
21. J.-I. Hayashi, M. Yamamoto, K. Kusakabe and S. Morooka, Effect of oxidation on gas permeation of carbon molecular sieving membranes based on BPDA-pp'ODA polyimide. *Ind. Eng. Chem. Res.*, 36: 2134–2140, 1997.
22. M. Yamamoto, K. Kusakabe, J.-i. Hayashi and S. Morooka, Carbon molecular sieve membrane formed by oxidative carbonization of a copolyimide film coated on a porous support tube. *J. Memb. Sci.*, 133: 195–205, 1997.
23. Y. Kusuki, H. Shimazaki, N. Tanihara, S. Nakanishi and T. Yoshinaga, Gas permeation properties and characterization of asymmetric carbon membranes prepared by pyrolyzing asymmetric polyimide hollow fiber membrane. *J. Memb. Sci.*, 134: 245–253, 1997.
24. J. Petersen, M. Matsuda and K. Haraya, Capillary carbon molecular sieve membranes derived from Kapton for high temperature gas separation. *J. Memb. Sci.*, 131: 85–94, 1997.
25. H. Suda and K. Haraya, Alkene/alkane permselectivities of a carbon molecular sieve membrane. *Chem. Commun.*: 93–94, 1997.
26. H. Suda and K. Haraya, Gas permeation through micropores of carbon molecular sieve membranes derived from Kapton polyimide. *J. Phys. Chem., B*, 101: 3988–3994, 1997.
27. A.B. Fuertes and T.A. Centeno, Preparation of supported asymmetric carbon molecular sieve membranes. *J. Memb. Sci.*, 144: 105–111, 1998.
28. K. Kusakabe, M. Yamamoto and S. Morooka, Gas permeation and micropore structure of carbon molecular sieving membranes modified by oxidation. *J. Memb. Sci.*, 149: 59–67, 1998.
29. A.B. Fuertes, D.M. Nevskaja and T.A. Centeno, Carbon composite membranes from Matrimid and Kapton polyimides for gas separation. *Microporous Mesoporous Mater.*, 33: 115–125, 1999.
30. N. Tanihara, H. Shimazaki, Y. Hirayama, S. Nakanishi, T. Yoshinaga and Y. Kusuki, Gas permeation properties of asymmetric carbon hollow fiber membranes prepared from asymmetric polyimide hollow fiber. *J. Memb. Sci.*, 160: 179–186, 1999.
31. K. Okamoto, S. Kawamura, M. Yoshino, H. Kita, Y. Hirayama, N. Tanihara and Y. Kusuki, Olefin/paraffin separation through carbonized membranes derived from an asymmetric

- polyimide hollow fiber membrane. *Ind. Eng. Chem. Res.*, 38: 4424–4432 1999.
32. A.B. Fuertes and T.A. Centeno, Preparation of supported carbon molecular sieve membranes. *Carbon*, 37: 679–684 1999.
 33. M. Ogawa and Y. Nakano, Gas permeation through carbonized hollow fiber membranes prepared by gel modification of polyamic acid. *J. Memb. Sci.*, 162: 189–198, 1999.
 34. M. Ogawa and Y. Nakano, Separation of CO₂/CH₄ mixture through carbonized membrane prepared by gel modification. *J. Memb. Sci.*, 173: 123–132, 2000.
 35. A. Singh-Ghosal and W.J. Koros, Air separation properties of flat sheet homogeneous pyrolytic carbon membranes. *J. Memb. Sci.*, 174: 177–188, 2000.
 36. H. Suda, A. Wenzel, H. Yanagishita and K. Haraya, Gas permeation properties of carbon molecular sieve, membranes prepared in alkali metal-organic solvent systems. *Molec. Cryst. & Liq. Cryst.*, 341: 567–572, 2000.
 37. N. Itoh and K. Haraya, A carbon membrane reactor. *Catal. Today*, 56: 103–111, 2000.
 38. M.-B. Hägg, Membrane purification of Cl₂ gas II. Permeabilities as function of temperature for Cl₂, O₂, N₂, H₂ and HCl in perfluorinated glass and carbon molecular sieve membranes. *J. Memb. Sci.*, 177: 109–128, 2000.
 39. M. Acharya and H.C. Foley, Spray-coating of nanoporous carbon membranes for air separation. *J. Memb. Sci.*, 161: 1–5, 1999.
 40. M. Acharya and H.C. Foley, Transport in nanoporous carbon membranes: Experiments and analysis. *AIChE J.*, 46: 911–922, 2000.
 41. M.B. Shiflett and H.C. Foley, On the preparation of supported nanoporous carbon membranes. *J. Memb. Sci.*, 179: 275–282, 2000
 42. M.S. Strano and H.C. Foley, Deconvolution of permeance in supported nanoporous membranes, *AIChE J.*, 46: 651–658, 2000.
 43. H. Wang, L. Zhang and G.R. Gavalas, Preparation of supported carbon membranes from furfuryl alcohol by vapor deposition polymerization. *J. Memb. Sci.*, 177: 25–31, 2000.
 44. M.B. Rao and S. Sircar, Performance and pore characterization of nanoporous carbon membranes for gas separation. *J. Memb. Sci.*, 110: 109–118, 1996.
 45. M. Anand, M. Langsam, M.B. Rao and S. Sircar, Multicomponent gas separation by selective surface flow (SSF) and poly-trimethylsilylpropyne (PTMSP) membranes. *J. Memb. Sci.*, 123: 17–25, 1997.
 46. T. Naheiri, K.A. Ludwig, M. Anand, M.B. Rao and S. Sircar, Scale-up of selective surface flow membrane for gas separation, *Sep. Sci. Technol.*, 32: 1589–1602, 1997.
 47. F.K. Katsaros, T.A. Steriotis, A.K. Stubos, A. Mitropoulos, N.K. Kanellopoulos and S. Tension, High pressure gas permeability of microporous carbon membranes. *Microporous Mater.*, 8: 171–176, 1997.
 48. H. Kita, H. Maeda, K. Tanaka and K. Okamoto, Carbon molecular sieve membrane prepared from phenolic resin. *Chem. Lett.*: 179–180, 1997.
 49. T.A. Centeno and A.B. Fuertes, Supported carbon molecular sieve membranes based on a phenolic resin. *J. Memb. Sci.*, 160: 201–211, 1999.
 50. A.B. Fuertes, Adsorption-selective carbon membrane for gas separation. *J. Memb. Sci.*, 177: 9–16, 2000.
 51. H. Kita, M. Yoshino, K. Tanaka and K. Okamoto, Gas permselectivity of carbonized polypyrrolone membrane. *Chem. Commun.*: 1051–1052, 1997.
 52. A.B. Fuertes and T.A. Centeno, Carbon molecular sieve membranes from polyetherimide. *Microporous Mesoporous Mater.*, 26: 23–26, 1998.
 53. M.G. Sedigh, L. Xu, T.T. Tsotsis and M. Sahimi, Transport and morphological characteristics of polyetherimide-based carbon molecular sieve membranes. *Ind. Eng. Chem. Res.*, 38: 3367–3380, 1999.

54. T.A. Centeno and A.B. Fuertes, Carbon molecular sieve gas separation membranes based on poly(vinylidene chloride-co-vinyl chloride). *Carbon*, 38: 1067–1073, 2000.
55. K. Kusakabe, S. Gohgi and S. Morooka, Carbon molecular sieving membranes derived from condensed polynuclear aromatics (COPNA) resins for gas separation. *Ind. Eng. Chem. Res.*, 37: 4262–4266, 1998.
56. C. Liang, G. Sha and S. Guo, Carbon membrane for gas separation derived from coal tar pitch. *Carbon*, 37: 1391–1397, 1999.
57. D.W. Breck, *Zeolite Molecular Sieves*, Wiley, New York, 1974.
58. S. Sircar, T.C. Golden and M.B. Rao, Activated carbon for gas separation and storage. *Carbon*, 34: 1–12, 1996.
59. S. Sircar, M.B. Rao and C.M.A. Thaeron, Selective surface flow membrane for gas separation. *Sep. Sci. Technol.*, 34: 2081–2093, 1999.
60. D.J. Parrillo, C. Thaeron and S. Sircar, Separation of bulk hydrogen sulfide hydrogen mixtures by selective surface flow membrane. *AIChE J.*, 43: 2239–2245, 1997.
61. C. Thaeron, D.J. Parrillo, S. Sircar, P.F. Clarke, M. Paranjape and B.B. Pruden, Separation of hydrogen sulfide–methane mixtures by selective surface flow membrane. *Sep. Purif. Technol.*, 15: 121–129, 1999.

Chapter 30

Property Control of Carbon Materials by Fluorination

Hidekazu Touhara

Department of Materials Chemistry, Faculty of Textile Science and Technology, Shinshu University, Ueda 386-8567, Japan

Abstract: Fluorination is effective in chemically modifying and controlling physicochemical properties of carbon materials over a wide range so creating opportunities to prepare carbon alloys with new functionalities. Carbon alloyed nanotubes were prepared by selective fluorination of hidden surfaces of multi-wall carbon nanotubes using a template carbonization technique. Carbon–fluorine bonds are formed on the hidden surfaces of the tubes while internal surfaces retained their sp^2 -hybridization. Fluorination (as a form of carbon-alloying) significantly affects such properties of hidden surface extents of nitrogen adsorption, hysteresis loops and pore size distributions. Fluorination enhanced the coulomb efficiency of Li/carbon nanotube rechargeable cells in an aprotic medium (with reversible lithium insertion in hidden surfaces) as studied by galvanostatic discharge-charge experiments.

Keywords: Carbon nanotubes, Activated carbon fibers, Fluorination, Hidden surface, Electrochemical lithium insertion, Adsorption properties.

1 Introduction

The interaction of fluorine with carbon materials provides fluorine–carbon materials with diverse structural and physical properties [1]. The nature of bonding between carbon and fluorine varies from covalent, through semi-ionic, to ionic, with van der Waals interactions also having a role. To understand the wide range of interactions between carbon and fluorine, the diversity of structure of carbon materials has to be taken into account. There are three allotropes of carbon, viz., graphite, diamond, and fullerenes, and other structural forms of carbons such as activated carbon, carbon fibers, and carbon nanotubes. Of these, extents of carbon s - p hybridization vary resulting in diverse electronic structures affecting their electrical conductivity, electron ionization potential, electron affinity, etc. Physical properties are affected with, for example, electrical conductivity of fluorine–carbon materials changing widely from $2 \times 10^5 \text{ S cm}^{-1}$ (fluorine intercalated HOPG C_6F) to $1 \times 10^{-20} \text{ S cm}^{-1}$ (graphite fluoride $(\text{CF})_n$). These suggest that fluorination is an effective way to prepare carbon alloys with new functionalities.

Of the many types of carbon materials, the chemistry of carbon nanotubes is of considerable interest in terms of alloying by heteroatom-doping or intercalation and of side-wall chemical functionality. Both single-wall carbon nanotubes (SWNTs) and multi-wall carbon nanotubes (MWNTs) are amphoteric and form donor and acceptor compounds such as graphite intercalation compounds (GICs) [2–6]. These properties together with their 1D type host lattice structure, with a central tube (canal), suggest energy-related applications such as the secondary lithium battery, electric double layer capacitors and fuel cells. In this chapter, control over carbon properties by fluorination is presented with an emphasis on the alloying of carbon nanotubes by selective fluorination of their hidden surfaces of MWNTs [7–10].

2 Control of Carbon Properties by Fluorination

Binding energies of C1s and F1s bonds of fluorinated carbon materials including MWNT, as measured by XPS, are given in Fig. 1. These energies show how effectively fluorination and fluorine/fluoride intercalation procedures modify carbon materials [1,9]. Figure 1 shows the progressive change in the C–F bonding from ionic, through to semi-ionic, to covalent as fluorination temperatures increase from room temperature to 600°C. The C1s and F1s binding energies of the graphite fluorides, $(CF)_n$ and $(C_2F)_n$, prepared at temperatures $> 400^\circ\text{C}$ are 290 and 688.5 eV, respectively, indicating the binding energy for a completely covalent C–F bond. In these fluorinated compounds the graphene (graphite) layers change to arrays of trans-

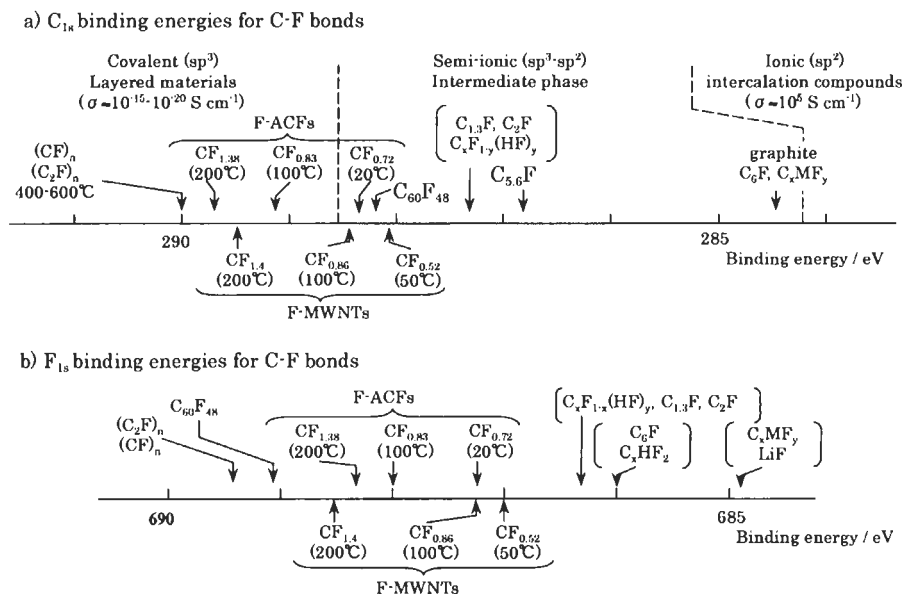


Fig. 1. XPS binding energies (eV) of fluorinated activated carbon fibers (F-ACFs), hidden surface fluorinated multi-wall carbon nanotubes (F-MWNTs) and other fluorinated carbon materials.

linked cyclohexane-type chairs with sp^3 -hybridized carbons, and are, consequently, electrical insulators. Films of $(CF)_n$ and $(C_2F)_n$ from the fluorination of HOPG are transparent. On the other hand, graphite intercalated by fluorine at room temperature (graphite C_6F) is ionic and metallic blue in color. In this graphite intercalation compound (GIC), graphene layers with sp^2 -hybridized carbons are maintained. The bonds between fluorine and carbon atoms are not covalent but are ionic. The C1s binding energy 284.5 eV is that of graphite with the F1s binding energy approximating to that of LiF. For activated carbon fibers (ACFs), the C1s binding energy increases from 288.5 to 289.7 eV as the fluorination temperature increases from room temperature to 200°C with the C1s binding energy being between that of $(CF)_n$ and C_6F . The color of fluorinated ACFs (F-ACFs) changes from black, through brown and yellow, to white following fluorination in the temperature range 20–200°C. The F/C atomic ratio ($CF_{0.72}$ – $CF_{1.28}$) and color are strongly dependent on fluorination conditions. The characteristic variations in color of the F-ACFs can be explained in terms of the nature of the C–F bond, hence the electronic structure of F-ACFs. The carbon nanotubes, MWNTs, synthesized by the template carbonization technique, behave as ACFs in regard to fluorination.

3 The Chemistry of Carbon Nanotubes with Fluorine and Carbon Alloying by Fluorination

3.1 Side Wall Fluorination of Single-wall Carbon Nanotubes

Nanometer-sized carbon tubes (nanotubes), a novel form of carbon, have currently attracted considerable scientific interest and nanotechnological interest as applications to electronic devices and energy-related technologies. Progress in bulk syntheses and purification of SWNTs has been developed and high-quality materials in sufficient quantities are now available for research into the chemical reactivity of SWNTs and MWNTs.

Mickelson et al. [11] were the first to report the fluorination of purified and end-closed SWNTs, the subject being of interest for carbon alloying of external surfaces of nanotubes and side-wall chemical functionality. The fluorination used purified SWNTs prepared by the dual-pulsed laser vaporization of Co/Ni doped graphite rods in the temperature range 150–600°C for 5 h using fluorine gas diluted with helium. Compositions of the products, fluorinated at 150, 250, 325, and 400°C were $CF_{0.114}$, $CF_{0.521}$, $CF_{0.495}$, and $CF_{0.565}$ respectively. The tube-like morphology of the fluorinated SWNTs was maintained to a limiting composition of C_2F . Further fluorination at 350°C led to the breaking of C–C bonds and, hence, the destruction of the tube.

Fluorination changed the electronic properties of the SWNTs drastically. The pristine SWNTs were good conductors (10–15 Ω for two-probe resistance across the length of the ca. 10 mm \times 3 mm \times 30 μ m bucky paper samples). Tubes fluorinated at temperatures of 250°C and above were insulators (two-probe resistance > 20 M Ω).

TEM studies showed that with fluorination at 325°C, the majority of the nanotubes maintained their tube-like morphology.

These results indicate that the formation of carbon alloyed SWNTs by fluorination, and the information of chemical state in terms of the surface element distribution/concentration and chemical structures of these materials are of interest in connection with possible applications.

3.2 *Multiwall Carbon Nanotubes*

The fluorination of commercially available powdered cylinder core (MER Corp.) was reported by Nakajima et al. [6]. These samples were a mixture of MWNTs (964 nm in average length, 18.4 nm and 3.6 nm in average external and internal diameters, respectively) with small carbon particles (45 nm in average diameter). A TEM study selectively examined the fluorinated MWNTs. Fluorine intercalation at room temperature into MWNTs was confirmed to be “stage 1 C_{5,3}F”. Fluorine was intercalated into the outer part of the nanotube wall where the graphene layers are planar. The interlayer distance of 0.53 nm (by X-ray diffraction) was nearly equal to that of fluorine intercalated graphite with semi-ionic C–F bonds. In contrast, the inner part of the wall of MWNTs was not intercalated. When the MWNTs were fluorinated at 300–400°C, fluorinated buckled layers were observed at the surfaces with distances of 0.65 nm, indicating the formation of graphite fluoride layers (2–3 nm in thickness) with covalent C–F bonds. TEM images showed that the tubular morphology was retained after fluorination at room temperature to 400°C and that the ends of the tubes were closed. These results suggest the carbon alloying of external surfaces of MWNTs.

Fluorination is also reported for MWNTs (10 μm in length and 20–40 nm in outer diameter), free from amorphous carbon particles, and prepared by thermal decomposition of acetylene over silica-supported cobalt catalysts [12]. Reaction at room temperature using a mixture of F₂, HF, and IF₅ with the MWNTs yielded intercalation-type compounds. For all samples, XRD diffractions indicated the persistence of the main reflection at interlayer spacings $d(002)$ of 0.340 nm, with diffractions corresponding to two fluorine-intercalated phases with repeat distances of $I_c = 0.63$ and 0.746 nm. TEM images of graphitized MWNTs showed that the tubular morphology had been preserved but that the outer layers of the walls were perturbed.

3.3 *Template-synthesized Carbon Nanotubes*

Initial preparation methods for SWNTs or MWNTs include carbon-arc synthesis, laser vaporization of graphite and catalytic decomposition of hydrocarbons. Synthesis of carbon nanotubes by a new template method has recently been developed [13–15].

Kyotani et al. [13,14] developed the template carbonization technique based on anodic aluminum oxide (alumina) films of uniform and straight channels with nanometer-sized diameters. Aligned and monodispersed carbon nanotubes *with open*

ends were successfully synthesized using chemical vapor deposition (CVD) of carbon within the pores of the alumina films. Such open-ended nanotubes embedded in the alumina template can be filled with selected compounds, and chemical functionality of the internal surfaces (the hidden surfaces), after of the nanotubes are separated from the template, can be changed by chemical reaction. As fluorination effectively perturbs the π -electron systems of carbon then carbon-alloying of the hidden surfaces of nanotubes in the Al_2O_3 template via fluorination was attempted experimentally.

3.3.1 Hidden Surface Fluorination

Hattori et al. [7] prepared pristine MWNTs to be used for hidden surface fluorination experiments. Aluminum oxide films used as the template were ca. $75\ \mu\text{m}$ in thickness with ca. 30 nm diameter straight channels. The reaction cell was initially evacuated to a pressure of 0.1 Pa (ca. 1×10^{-3} Torr) overnight at 200°C . Thermal decomposition of propylene in the alumina channels deposited carbon on the channel walls giving carbon-coated Al_2O_3 composite ($\text{C-Al}_2\text{O}_3$) films [14]. Fluorination was by the direct reaction of elemental fluorine with the $\text{C-Al}_2\text{O}_3$ films, at 0.1 MPa pressure of fluorine, $50\text{--}200^\circ\text{C}$ for 5 days. The resulting compounds were washed with an excess of 46% HF solution at room temperature to dissolve the Al_2O_3 template. In this way, the nanotubes, the hidden surfaces of which were selectively fluorinated, were obtained in the form of an insoluble fraction (see Fig. 2) [9].

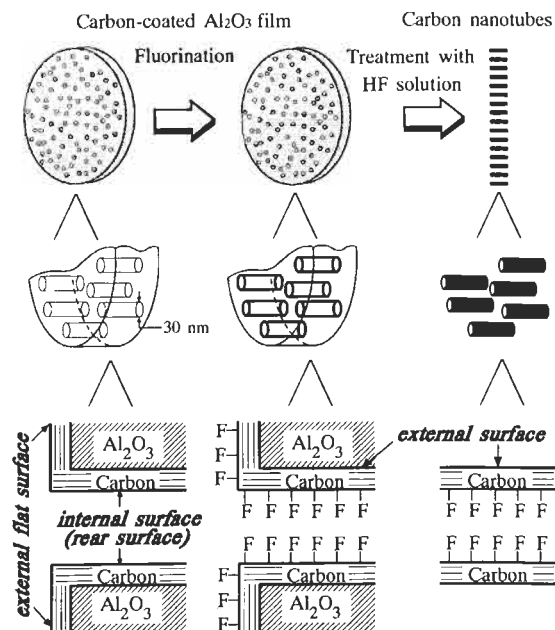


Fig. 2. Schematic drawing of the fluorination process of carbon nanotubes (reproduced with permission from Ref. [7]).

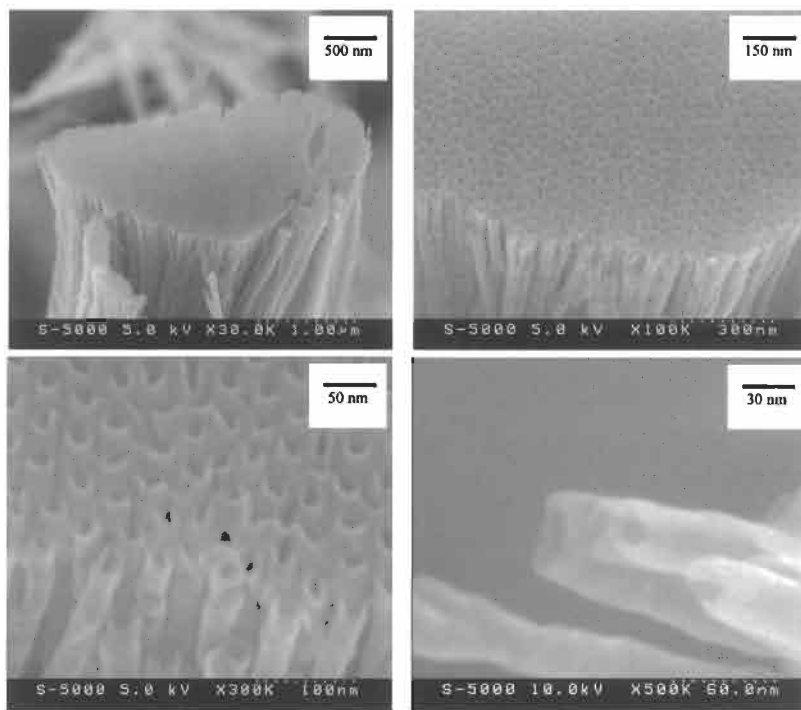


Fig. 3. SEM images of the template-synthesized carbon nanotubes fluorinated at 200°C (reproduced with permission from Ref. [9]).

3.3.2 SEM and TEM Observations

Figure 3 shows SEM images of the template-synthesized carbon nanotubes fluorinated at 200°C and essentially are a free-standing nanoporous carbon membranes. In addition, Fig. 4 shows high-resolution TEM images of the carbon nanotubes and the nanotubes fluorinated at 200°C. These images show that the nanotubes have a wall thickness of ~ 4 nm and a diameter of ~ 30 nm, the outer diameters remaining unchanged after fluorination.

Figures 4a–c, show short and wavy 002 lattice fringes in the cross-section of the tube walls, the lines lying parallel to the tube axis. The lattice images of the fluorinated tubes (Figs. 4d–f) show that tubular morphology is preserved and that the hidden surfaces of the tubes may be slightly perturbed. The 002-lattice fringe image suggests slight modifications to the hidden surface of the tubes after fluorination, such as buckled fluorinated carbon layers.

3.3.3 Characterization by EDX, XPS, and Raman Spectroscopy

The selective fluorination of the hidden surfaces of nanotubes is supported further by EDX and EELS. Figure 5 shows the EDX spectrum for a single tube selected from

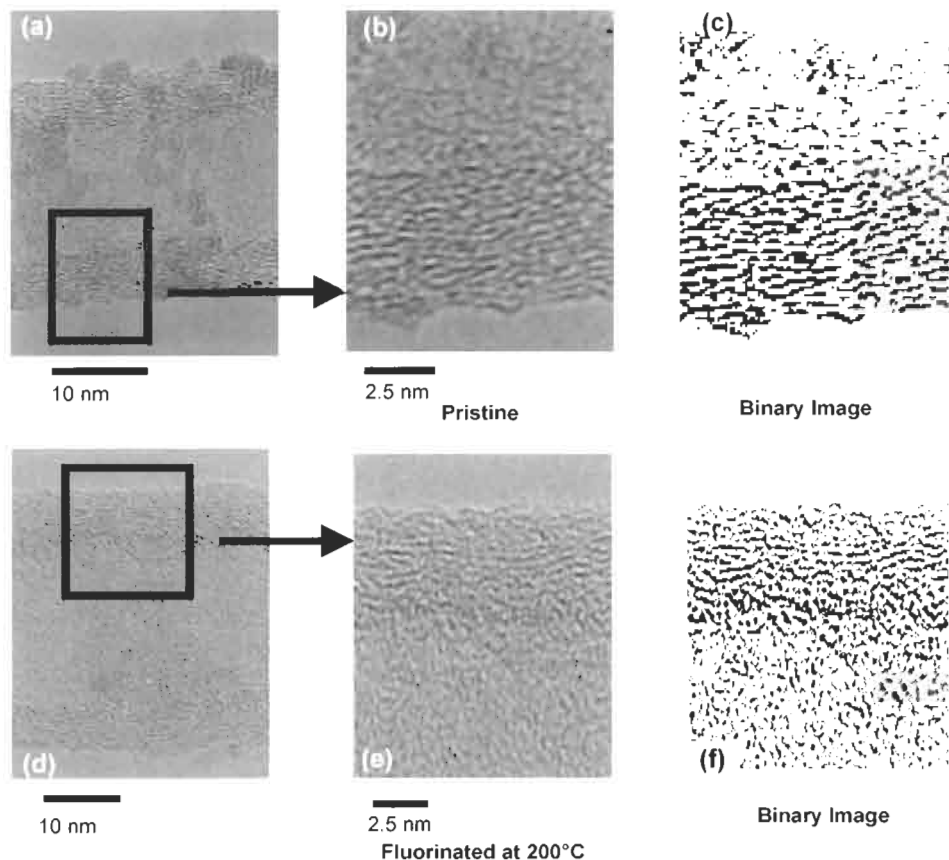


Fig. 4. High-resolution TEM images of template-synthesized carbon nanotubes: (a), (b) and (c) pristine; (d), (e) and (f) fluorinated at 200°C.

fluorinated carbon nanotube membranes by STEM observations. The intense peak ascribed to fluorine atoms in the spectrum clearly indicates hidden surface fluorination because the external surfaces of the nanotubes are covered with the alumina template during fluorination. Fluorinated hidden surfaces were investigated by XPS. Figure 6 shows the C1s and F1s XPS spectra of the C-Al₂O₃ films fluorinated in the temperature range 50 to 200°C. The peaks observed at 288.2–289.4 eV (Fig. 6A) are from *sp*³-hybridized carbon atoms with covalent C–F bonds, similar to those in the covalent graphite fluorides, (CF)_{*n*} and (C₂F)_{*n*}. In contrast to the C1s spectra, the F1s spectra (Fig. 6B) have a symmetrical shape, F1s electron binding energy of 686.8–688.5 eV being close to that of C–F covalent bond. With increasing temperature of fluorination, the C1s and F1s peaks assigned to fluorine functional groups shift to higher binding energies and increasing intensities. The surface compositions (F/C) determined by the peak area ratio of C1s and F1s XPS spectra are 0.52, 0.86 and 1.42

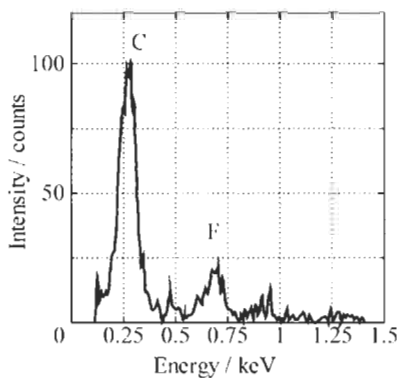


Fig. 5. EDX spectrum of a single carbon nanotube fluorinated at 200°C.

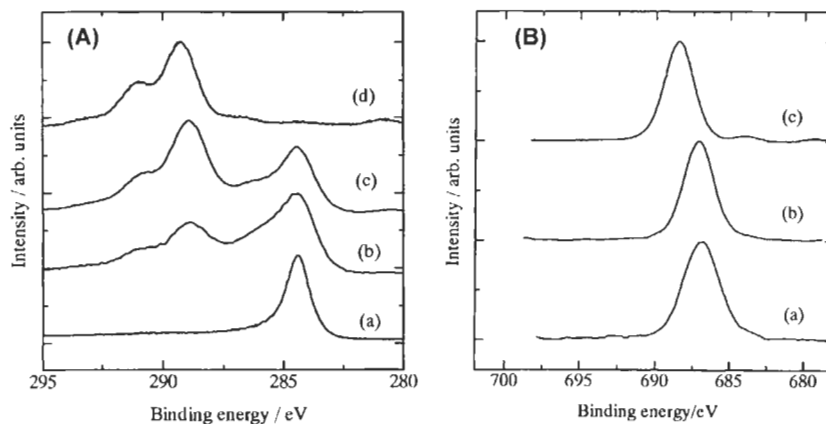


Fig. 6. C1s (A) and F1s (B) XPS spectra of the carbon coated Al_2O_3 films: (a) pristine; fluorinated at (b) 50°C, (c) 100°C, and (d) 200°C (reproduced with permission from Ref. [7]).

at fluorination temperatures of 50, 100 and 200°C, respectively. The material obtained at 200°C (Fig. 6A(d)) shows a barely observable peak at 284.4 eV, with two intense peaks at 289.3 and 291.1 eV, indicating surface coverage by covalent C–F bonds. The peaks assigned to the fluorine groups almost disappeared after 30 s of etching by argon ions, the C1s peak becoming narrower and more symmetrical. These depth profiles indicate the fluorination is limited only to the outermost layers of surfaces.

The Raman study also characterized the microstructures of the carbon material deposited on the $\text{C-Al}_2\text{O}_3$ films [7]. In the Raman spectra of fluorinated samples, two bands was observed at ~ 1340 and ~ 1590 cm^{-1} being features of Raman peaks of less-ordered carbon materials. The spectra confirm that internal carbon atoms, below the outermost layer, still retain their sp^2 -hybridization after fluorination.

3.4 Properties and Potential Applications

The chemistry of fluorination of SWNTs and MWNTs is just beginning to be understood. Consequently, research into the physical and chemical properties related to potential applications are at an early stage. However, these ensembles of aligned and mono-dispersed carbon nanotubes indicate promising prospects such as gas storage and energy-related applications. Such membranes as shown in Fig. 3 could be optimum materials for electrochemical cells or capacitors based on the electric double-layer. The selective fluorination either of the hidden surfaces or of the outer surfaces of tubes could bring about other improved applications including selective gas permeation, lithium batteries and conductive materials.

3.4.1 Adsorption Properties

The adsorption and desorption isotherms of nitrogen at 77 K on pristine and fluorinated carbon nanotube membranes, where open-ended nanotubes are embedded in the Al_2O_3 templates, were measured using an automatic volumetric sorption analyzer [7] as shown in Fig. 7. The amount of nitrogen adsorbed by the pristine sample at $P/P_0 = 0.96$ decreased from 84.9 to 52.5 and 35.0 $\text{cm}^3 \text{g}^{-1}$ (gas volume at STP) by fluorination at temperatures of 50 and 100°C, respectively. The adsorption and desorption branches for the pristine sample do not coincide, that is hysteresis is observed. The isotherm is nearly of type IV, indicating that both samples are mesoporous materials.

The BET analysis of isotherms leads to surface areas and c -values. The fluorination temperature dependence of c -values, BET surface areas and amounts adsorbed

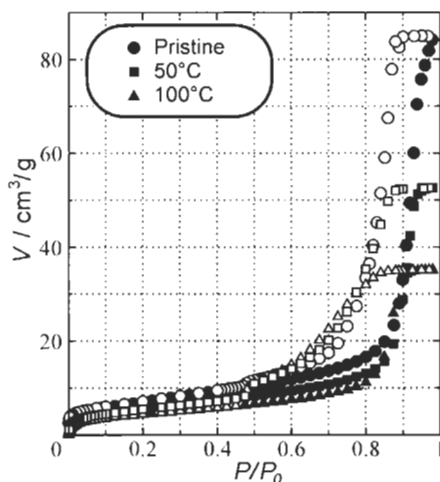


Fig. 7. Adsorption and desorption isotherms of nitrogen at 77 K for pristine and fluorinated carbon nanotubes membranes. Closed and opened symbols indicate adsorption and desorption, respectively (reproduced with permission from Ref. [9]).

Table 1

Fluorination temperature dependence of c -value, BET surface area and amounts of adsorbed nitrogen of carbon nanotube membranes (reproduced with permission from Ref. [10])

| Fluorination temperature | c -value | S_{BET} (m^2/g) | $V_{P/P_0=0.96}$ (cm^3/g) |
|--------------------------|------------|--|---|
| Pristine | 104 | 26.4 | 84.9 |
| 50°C | 72 | 20.5 | 52.5 |
| 100°C | 60 | 15.5 | 35.0 |

at $P/P_0 = 0.96$ are in Table 1 [10]. The BET surface areas and the amounts of nitrogen adsorption by the fluorinated nanotubes are smaller than for the pristine sample. The c -values from the BET analysis of the fluorinated sample were 72 and 60 at fluorination temperatures of 323 K and 373 K, respectively. The c -values for the fluorinated sample are much smaller than that for the pristine sample (104). As the c -value is associated with the enthalpy of adsorption, the decrease in the c -value indicating the formation of surfaces of lower energy by fluorination.

The α_s -plots for pristine carbon nanotube membranes and fluorinated membranes at 100°C using reference data of nonporous carbon black are shown in Fig. 8. In the α_s -plot for the pristine sample (Fig. 8a), two deviations are observed at a low α_s -region

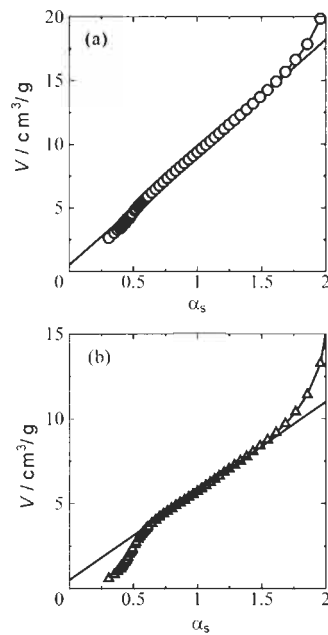


Fig. 8. The α_s plots for carbon nanotube membranes: (a) pristine and (b) fluorinated at 100°C (reproduced with permission from Ref. [10]).

and at $\alpha_s > 1.5$. The former is due to differences in surface free energy between the reference and pristine membranes, the latter to capillary condensation in the hollow cores of the nanotubes. As for the α_s -plot of the fluorinated sample shown in Fig. 8b, the deviation at $\alpha_s > 1.5$ was also observed, indicating the presence of capillary condensation. Although these α_s -plots have a good linearity at $0.6 < \alpha_s < 1.5$, a downward deviation from linearity is clearly observed below $\alpha_s = 0.6$. The downward deviation of the α_s -plot for the fluorinated membranes indicates that the fluorinated membranes have a lower surface free energy than carbon black [16–18]. The downward deviation for the sample fluorinated at 373 K is larger than that for the sample fluorinated at 323 K, indicating a decrease in the surface free energy with an increase in fluorine content of the internal surfaces of nanotubes embedded in the Al_2O_3 templates.

The surface area and the pore size distribution were determined using the BET equation and the BJH method, respectively. The surface area ($26.2 \text{ m}^2 \text{ g}^{-1}$) of the pristine membranes decreased to 20.5 and $15.5 \text{ m}^2 \text{ g}^{-1}$ by fluorination at temperatures of 50 and 100°C , respectively. The decreases in surface area and in amounts adsorbed following an increase in fluorination temperature suggest that the interaction between the hidden surfaces of fluorinated nanotubes and the nitrogen adsorbate becomes weaker. Therefore, the surface free energy of the fluorinated sample is smaller than that of pristine sample.

The pore size distribution curve for pristine membranes had a peak at about 25 nm pore diameter which was consistent with the hollow core diameter of nanotubes embedded in Al_2O_3 templates. The pore distribution curves for fluorinated films shifted to smaller diameters with increasing fluorination temperature. Because the TEM images show that nanotubes retain their structural properties in the bulk after fluorination, the change in adsorption behavior is due to a change in the surface properties of the fluorinated membranes. After fluorination, the contact angle of a water droplet on the carbon-coated Al_2O_3 film increased from 86.6° to 104.2° . This result also supports the concept that the surface free energy of the hidden surfaces of nanotubes decreases on fluorination.

3.4.2 Electrochemical Properties

A primary battery based on fluorine and lithium is theoretically an optimum redox system for a high energy density power source. Such a battery has been developed commercially using graphite fluoride (CF_n) as a cathode material for a lithium battery with an electrolyte-organic solvent system. In this context, the use of fluorinated MWNTs as high-density energy conversion materials may make worthwhile an investigation into lithium cells with fluorinated MWNTs cathodes.

Electrochemical properties of fluorinated MWNTs, as cathode materials for primary lithium cells, have been studied using the $\text{Li}/1\text{M LiClO}_4\text{-PC/F-MWNTs}$ cell (PC: propylene carbonate, F-MWNTs: fluorinated MWNTs) [19]. The F-MWNT cathode (fluorinated MWNTs at 480°C) showed a flat and stable discharge potential

at ca. 2.4 V with a capacity of 620 Ah kg⁻¹. Discharge performances of conventional cathode materials are dependent on the structure of pristine carbons, fluorine contents and C-F bonding nature. Nevertheless, cathode behavior for F-MWNTs, similar to those of fluorinated activated carbon fibers [20], indicate that further detailed investigations of structural properties and discharge reactions could bring improvements to F-MWNTs as cathode materials.

Electrochemical energy storage has been investigated using template-synthesized tubule membranes [21] and MWNTs produced by catalytic decomposition of acetylene [22] using lithium test cells with non-aqueous electrolyte solutions. Early work by Martin et al. [21] indicated that highly ordered carbon nanotubule membrane are good candidates as anodes for lithium ion secondary batteries [21].

Electrochemical insertion of lithium into template-synthesized MWNTs, heat-treated MWNTs to 1000°C (HT1000-MWNTs) has been studied. Hidden surfaces of F-MWNTs fluorinated at 50°C (F-MWNTs) were examined by cyclic voltammetry (CV) and discharge-charge experiments on Li/1M LiClO₄-PC/WE (WE (working electrode) = pristine MWNTs, HT1000-MWNTs, and F-MWNTs) cells [8,23-25]. Effects of degree of crystallinity and hidden surface fluorination on the electrochemical properties were studied. In the test cells, lithium was inserted into MWNTs in the cathodic (discharge) process and extracted in the anodic (charge) process.

The hidden surface fluorination resulted in significant changes in electrochemical properties of MWNTs. The OCV value of 2.98 V of pristine MWNTs increased to 3.64 V by fluorination. This value of OCV was comparable to that of (C₂F)_n prepared by fluorination of activated carbon fibers [20]. The first discharge sweep in the CV of F-MWNTs started with a reduction of C-F bond at 3.0 V. The current peak due to reduction of oxygenated groups and electrolyte observed in the CV of the pristine MWNTs almost disappeared. Replacement of oxygenated groups by fluorine species during fluorination probably occurred. The potential hysteresis of insertion/extraction processes disappeared for both heat-treated and fluorinated samples compared to pristine MMNTs. Partial organization of the surface micro-texture and enhanced crystallinity of MWNTs by heat treatment could account for the disappearance of the potential hysteresis. For the F-MWNTs, fluorination removed the amorphous carbon on the hidden surface of pristine MWNTs [20] and created a relatively ordered micro-texture so accounting for the disappearance of the potential hysteresis.

The galvanostatic discharge-charge curves of pristine MWNTs are shown in Fig. 9a for 2nd-5th cycles. The large irreversible capacity in the reduction processes was observed for the first cycle. This was attributed to a relatively high BET surface area of 28 m² g⁻¹ about 5-20 times that of powder graphite and the occurrence of oxygen functional groups on the MWNTs. The reversibility of the insertion and extraction process enhanced considerably the second and consecutive cycles. For example, it was observed from galvanostatic discharge-charge experiments that the first cycle coulomb efficiency of 22% increased to about 80% with a reversible capacity of 460 mAh g⁻¹ at the sixth cycle. The effect of fluorination of MWNTs on their discharge-

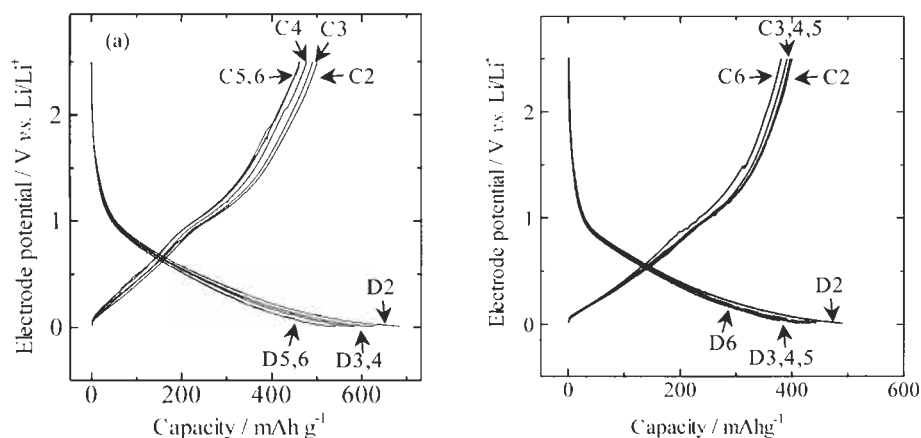


Fig. 9. Discharge-charge characteristics of lithium insertion into (a) carbon nanotube membranes and (b) hidden surface fluorinated carbon nanotube membranes at 50°C, under a current density of 50 mA/g. D2–D6: 2nd–6th discharge curves; C2–C6: 2nd–6th charge curves (reproduced with permission from Ref. [25]).

charge properties is shown in Fig. 9b. The irreversible capacity at the first cycle occurs for both pristine and fluorinated MWNTs. Also, there is a significant increase in coulombic efficiency from ca. 23% to ca. 90% with a reversible capacity of ca. 400 mAh g⁻¹ after the second cycle. Surface lithiation and formation of SEI may explain irreversible charge losses in the first discharge sweep, reduced in the second and consecutive sweeps. The change in hidden surface properties by fluorination reduced the formation of SEI and resulted in an increase in coulomb efficiency of more than 10% after the second cycle.

References

1. F. Okino and H. Touhara, Solid state supramolecular chemistry: two- and three dimensional inorganic networks. In: G. Alberti and T. Bein (Eds.), *Comprehensive Supramolecular Chemistry*, Vol. 7, Chapter 2. Pergamon, Oxford, 1996.
2. O. Zhou, R.M. Fleming, D.W. Murphy, C.H. Chen, R.C. Haddon, A.P. Ramirez and S.H. Glarum, Defects in carbon nanotubes. *Science*, 263: 1744–1747, 1994.
3. R.S. Lee, H.J. Kim, J.E. Fisher, A. Thess and R.E. Smalley, Conductivity enhancement in single-walled carbon nanotubes bundles doped with K and Br. *Nature*, 388: 255–257, 1997.
4. A.M. Rao, P.C. Eklund, S. Bandow, A. Thess and R.E. Smalley, Evidence for charge transfer in doped carbon nanotube bundles from Raman scattering. *Nature*, 388: 257–259, 1997.
5. V.A. Nalimova, D.E. Sklovsky, G.N. Bondarenko, H. Alvergnat-Gaucher, S. Bonnamy and F. Beguin, Lithium interaction with carbon nanotubes. *Synth. Met.*, 88: 89–93, 1997.
6. T. Nakajima, S. Kasamatsu and Y. Matsuno, Synthesis and characterization of fluorinated carbon nanotube. *Eur. J. Solid State Inorg. Chem.*, 33: 831–840, 1996.
7. Y. Hattori, Y. Watanabe, S. Kawasaki, F. Okino, B.K. Pradham, T. Kyotani, A. Tomita and H. Touhara, Carbon-alloying of the rear surfaces of nanotubes by direct fluorination. *Carbon*, 37: 1033–1038, 1999.

8. H. Touhara, Potential use of carbon nanotube as anode materials for lithium batteries. *Ouyou Butsuri (Applied Physics)*, 69: 33–37, 2000.
9. H. Touhara and F. Okino, Property control of carbon materials by fluorination. *Carbon*, 38: 241–267, 1999.
10. Y. Hattroi, K. Kaneko, F. Okino, H. Touhara, T. Kyotani, and A. Tomita, Adsorptive properties of designed fluorinated carbon nanotubes. *Proceedings of the 2nd Pacific Basin Conference on Adsorption Science and Technology, Australia*, pp. 14–18, 2000.
11. E.T. Mickelson, C.B. Huffman, A.G. Rinzler, R.E. Smalley, R.H. Hauge and J.L. Margrave, Fluorination of single-wall carbon nanotubes. *Chem. Phys. Lett.*, 296: 188–194, 1998.
12. A. Hamwi, H. Alvergnat, S. Bonnamy and F. Beguin, Fluorination of carbon nanotubes. *Carbon*, 35: 723–728, 1997.
13. T. Kyotani, L. Tsai and A. Tomita, Formation of ultra-fine carbon tubes by using an anodic aluminum oxide film as a template. *Chem. Mater.*, 7: 1427–1428, 1995
14. T. Kyotani, L. Tsai and A. Tomita, Preparation of ultrafine carbon tubes in nanochannels of anodic aluminum oxide film. *Chem. Mater.*, 8: 2109–2113, 1996.
15. G. Che, B.B. Lakshmi, C.R. Martin, E.R. Fisher and R.S. Ruoff, Chemical vapor deposition based synthesis of carbon nanotubes and nanofibers using template method. *Chem. Mater.*, 10: 260–267, 1998.
16. M. Jaroniec and K. Kaneko, Physicochemical foundations for characterization of adsorbents by using high-resolution comparative plots. *Langmuir*, 13: 6589–6596, 1997.
17. N. Setoyama, G. Li, K. Kaneko, F. Okino, R. Ishikawa, M. Kanda and H. Touhara, Nitrogen adsorption on fluorinated activated carbon fiber. *Adsorption*, 2: 293–297, 1996.
18. K. Kaneko, N. Setoyama, G. Li, F. Okino, R. Ishikawa, M. Kanda and H. Touhara, Pore structure and adsorption properties of fluorinated activated carbon fiber. *Tanso*, pp. 71–76, 1999.
19. A. Hamwi, P. Gendraud, H. Gaucher, S. Bonnamy and F. Beguin, Electrochemical properties of carbon nanotube fluorides in a lithium cell system. *Mol. Cryst. Liq. Cryst.*, 310: 185–190, 1998.
20. H. Touhara, K. Kadono, N. Watanabe and J.-J. Braconnier, Electrochemical characteristics of fluorinated activated carbon fiber-lithium cells. *J. Electrochem. Soc.*, 134: 1071–1075, 1987.
21. G. Che, B.B. Lakshmi, E.R. Fisher and C.R. Martin, Carbon nanotubule membranes for electrochemical energy storage and production. *Nature*, 393: 346–349, 1998.
22. E. Frackowiak, S. Gautier, H. Gaucher, S. Bonnamy and F. Beguin, Electrochemical storage of lithium multiwalled carbon nanotubes. *Carbon*, 37: 61–69, 1999
23. H. Touhara, I. Mulopadhyay, F. Okino, S. Kawasaki, T. Kyotani, A. Tomita and W.K. Hsu, Electrochemical lithium insertion of heat treated and chemically modified multi-wall carbon nanotubes. *Int. Symp. Nanonetwork Materials: Fullerenes, Nanotubes, and Related Systems, AIP Conference Proc.*, Vol. 590, pp. 249–252, 2001.
24. I. Mukopadhyay, J. Inahara, N. Hoshino, F. Okino, S. Kawasaki, H. Touhara, T. Kyotani and A. Tomita, Electrochemical Li insertion in template synthesized highly aligned multi-wall carbon nanotubes. *Electrochem. Soc. Proc.*, *Reactive Intermediates in Organic and Biological Electrochemistry*, pp. 37–40, 2001.
25. H. Touhara, J. Inahara, T. Mizuno, Y. Yokoyama, S. Okano, K. Yanagiuchi, I. Mukopadhyay, S. Kawasaki, F. Okino and H. Shirai, Property control of new forms of carbon materials by fluorination. *J. Fluorine Chem.*, 114: 181–188, 2002.

Chapter 31

Preparation of Metal-loaded Porous Carbons and Their Use as a Highly Active Catalyst for Reduction of Nitric Oxide (NO)

Kouichi Miura and Hiroyuki Nakagawa

Department of Chemical Engineering, Kyoto University, Kyoto 606-8501, Japan

Abstract: A new method to produce porous carbons containing metal compounds in a highly dispersed state is outlined and has been applied to the formation of a catalyst for nitric oxide reduction. An ion-exchange resin with carboxylic acid groups as ion-exchange sites was exchanged with various cations and then carbonized to prepare metal-loaded porous carbons. Ni²⁺ type resins carbonized at 500°C had a high activity to convert nitric oxide (NO) to nitrogen in the absence of gaseous reducing agents at 300°C. However, their activity decreased when the nickel was oxidized to NiO. The deactivated catalyst was regenerated by reducing agents such as carbon monoxide without loss of catalytic activity so suggesting the use of this catalyst in practical applications. In the presence of carbon monoxide in the feed stream, the high activity of the catalyst was maintained for quite some time because *in situ* regeneration reactions occurred simultaneously without loss of carbon from the catalyst. The metal-loaded carbons were of high catalytic activity because of relatively large amounts of metal in a highly dispersed state.

Keywords: Metal-loaded porous carbon, Catalytic decomposition of nitric oxide, Ion-exchange resin.

1 Introduction

Porous carbons such as activated carbons have been used as catalysts and catalyst supports in many reactions [1]. The catalytic reduction of nitric oxide with reducing reagents such as ammonia is an example. Nozaki et al. [2] found that copper oxide supported on an activated carbon showed a high activity for nitric oxide removal in the presence of ammonia even at 130°C. Kasaoka et al. [3] simultaneously removed NO_x and SO_x using V₂O_x/TiO₂/AC (activated carbon) with the catalyst at 130°C. Nishijima et al. [4] compared the activities of metal halides (supported differently) for nitric oxide reduction and found that the metal halides supported on a carbon were more active than those supported on silica or alumina at low temperatures [4]. Singoredjo

et al. [5] found that copper salts supported on carbon exhibited high activity for the reduction of nitric oxide. Mehandjiev and Bekyarova [6] reported on the effectiveness of a carbon supporting cobalt oxide for the reduction of nitric oxide by carbon monoxide. Imai et al. [7] found that nitrogen was formed from nitric oxide over α -FeOOH-dispersed ACF without using gaseous reducing reagents such as ammonia or carbon monoxide. In these reaction systems it is important to support large amounts of a metal compound on carbon, in a highly dispersed state, for the carbon catalyst to be active.

A new method is available to produce carbons which have different micropore volume distributions by carbonizing ion-exchange resins having different cations [8]. The cations are highly dispersed in the ion-exchange resin, and hence the cations become highly dispersed metals or metal oxides in the porous carbons. In this chapter, porous carbonized resins, prepared from a weak-acid ion-exchange resin, catalytically reduced nitric oxide to nitrogen at low temperatures.

2 Sample Preparation

2.1 Starting Materials

A metacrylic acid type resin was used as a starting material. Resin particles were spherical in shape the average diameter being ~ 0.5 mm. The basic structure of the resin is shown in Fig. 1 and contains divinylbenzene as a cross-linking reagent. The total content of ion-exchange groups, determined from amounts of sodium in the Na^+ type resin, was 10.2 mol kg^{-1} of dried H^+ type resin.

2.2 Procedure

Figure 2 shows the procedure for preparing the metal-loaded porous carbons as developed by Nakagawa et al. [8]. The ion-exchange resin, as received, was treated with aqueous ammonium-complex ion solutions (basic) of sulfates (CuSO_4 , NiSO_4 , ZnSO_4) to exchange with the different cations. Basic conditions were necessary for the ion-exchange because the ion-exchange resin was a weak acid. Amounts of cation

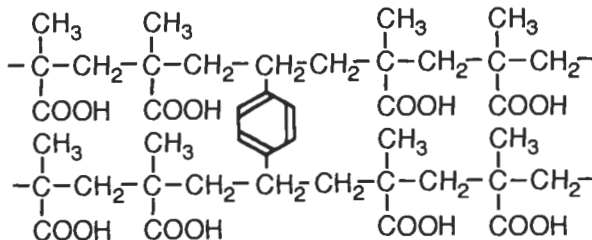


Fig. 1. Basic structure of the ion-exchange resin used.

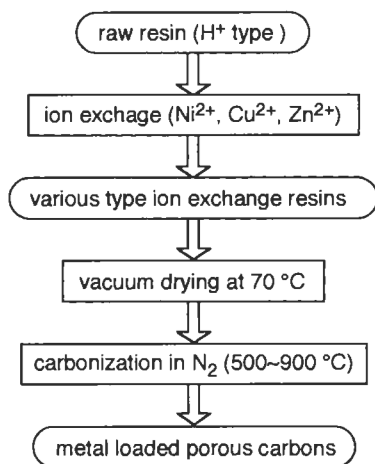


Fig. 2. Procedure for preparing metal-loaded porous carbons.

exchanged were controlled by the concentration of cation in the aqueous solution. Each exchanged resin was washed with de-ionized water followed by vacuum drying at 70°C for 24 h. A part of each resin sample was then oxidized to remove all carbon, in a digestion apparatus, and the resultant solution analyzed by atomic absorption spectrometry for amounts of cation exchanged.

The ion-exchange resins were carbonized in nitrogen at 10 K min⁻¹ to a heat treatment temperature (HTT) T_i , with a soak time of 20 min. T_i ranged from 500 to 900°C. The carbonized samples are labelled as Ni-500-32.6, where nickel is the cation, 500 is the HTT and 32.6 is wt% content of nickel.

3 Carbonization Behavior of the Resins

To follow the carbonization behavior of the cation-exchanged resins, weight changes of the resin and formation rates of H₂O, CO, CO₂, and CH₄ were continuously monitored with a thermogravimetric analyzer and a mass spectrometer [9]. Figure 3 shows the weight loss curves of the resins and the formation rates of water and carbon dioxide during carbonization of the cation-free (H⁺-type resin) basis. The weight of the H⁺-type resin decreased by ~10 wt% below 230°C (dehydration reactions), then decreased rapidly to ~420°C. One water molecule is formed from two carboxylic acid groups in the dehydration reaction. Part of the weight loss at ~420°C was due to the decomposition of acid anhydrides formed at ~230°C, by the loss of water and carbon dioxide, at ~420°C. The weight of water and carbon dioxide was 15 wt% of the total weight loss, suggesting that the decomposition of metacrylic chains is the main reaction at this temperature.

The weight loss profiles were sensitive to the cations which were exchanged. The weights of Ni²⁺- and Zn²⁺-type resins decreased rapidly at ~350 and 450°C,

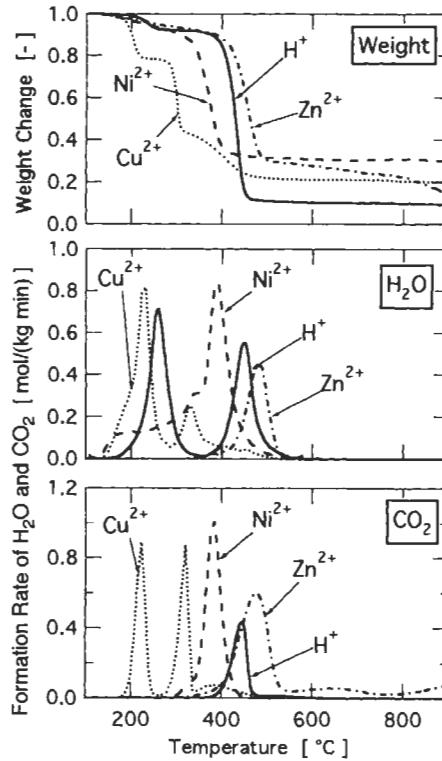


Fig. 3. Weight loss curves and rates of formation of H₂O and CO₂ during the carbonization of the resins on a cation-free basis.

respectively, whereas the weight of the Cu²⁺-type resin decreased rapidly at 200 and 300°C. The ratio of water formation rates to carbon dioxide formation rates was also dependent on the cations exchanged although water and carbon dioxide were both formed in the temperature range where the weights decreased rapidly. The solid yields at 900°C were also dependent on the cations exchanged. Hence, carbonization behavior of the resin is affected significantly by the kind of cations exchanged. Differences in carbonization behavior may well affect the pore development within the carbonized resins.

4 Characterization of Metal Loaded Porous Carbons

4.1 Appearance

Figure 4 shows the SEM images of H-500 and Ni-500-32.6 samples. The Ni-500-32.6 sample maintained the original spherical form, unlike the H-500 sample which melted. Original macropores, of 0.1–1 μm in diameter, were maintained in Ni-500-32.6. Ionic cross-linking occurs when the resin is ion-exchanged by Ni²⁺ and

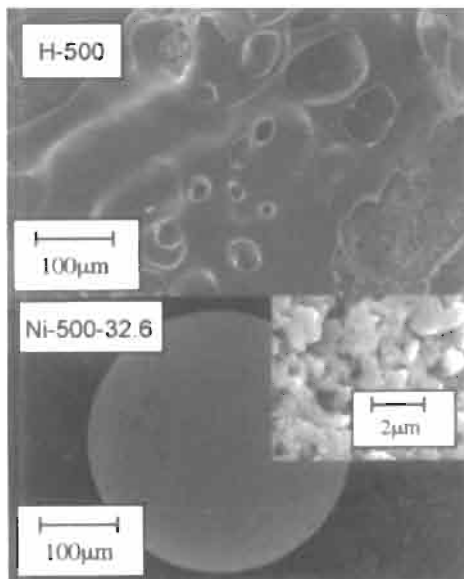


Fig. 4. SEM images of H-500 and Ni-500-32.6.

this prevents melting and the retention of original shapes. Cu^{2+} and Zn^{2+} type resins also did not melt and maintained their original spherical shapes. Di- and trivalent cations prevent the resin from melting [8].

4.2 Pore Structure

Figure 5 shows the pore volume distributions of the resins carbonized at 700°C as determined from their nitrogen isotherms (77 K) using the Dollimore and Heal analysis method [10]. The distributions depended on the kind of cation exchanged. The micropores of Ni-700-33.1 had a distribution from 0.9 to 5 nm in diameter, whereas the micropores of Cu-700-62.4 were < 2 nm in diameter.

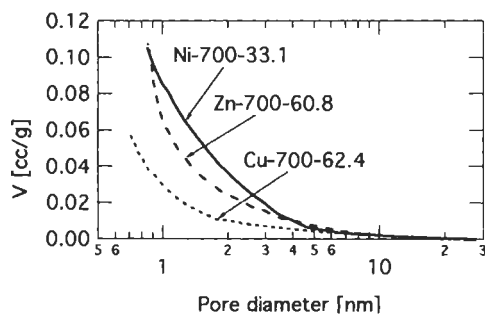


Fig. 5. Accumulated pore volume distributions of the resins carbonized at 700°C .

4.3 Forms of Metal Compounds

To examine the structure of metal compounds in the carbonized resins, X-ray diffraction studies were made. Figure 6 shows diffraction patterns from resins carbonized at 700°C indicating that structures of metal compounds were also dependent on the cation exchanged. Distinct peaks of ZnO appeared for Zn-700-60.8 and peaks of both crystalline copper metal and Cu_2O appeared for Cu-700-62.4. For Ni-700-33.1, peaks of crystalline nickel metal were rather broad, indicating that the crystallinity of the nickel was smaller than that of ZnO, Cu, or Cu_2O . Cations existing as carboxylates in the parent resin probably form metal oxides initially and then these are reduced by the carbon to metals during the carbonization. The reason why nickel exists as the metal Ni is that NiO is reduced easily by carbon at 700°C. For the Cu^{2+} type resin, peaks of crystalline copper metal appeared when the resin was carbonized at 900°C (X-ray pattern not shown), indicating that a higher temperature is needed to completely reduce Cu_2O to Cu.

5 Nitric Oxide Decomposition on Metal Loaded Porous Carbons

5.1 Nitric Oxide Removal

Figure 7 shows the apparatus used for the removal of nitric oxide. About 0.2 g of carbonized resin, $< 150 \mu\text{m}$ in particle diameter, was packed into a quartz tube reactor, 8.0 mm inner diameter, and heated at 500°C for 30 min in a stream of helium to remove adsorbed water. On cooling the sample to 300 or 400°C, nitric oxide diluted

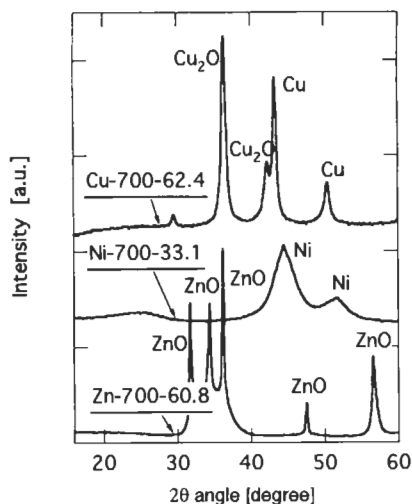


Fig. 6. X-ray diffraction patterns of resins carbonized at 700°C.

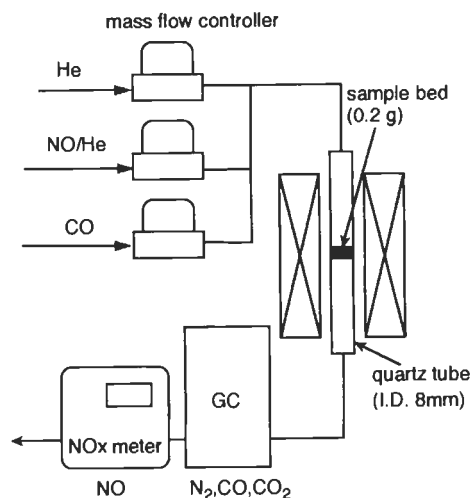


Fig. 7. Experimental apparatus for nitric oxide removal.

by helium (NO: 500 ppm) was introduced at a flow rate of 100 ml min^{-1} ($S_v = 24000 \text{ h}^{-1}$). Concentrations of nitric oxide and nitrogen, in the effluent stream, were measured by a NO_x meter and a gas chromatograph with an MS-5A column. Non-isothermal experiments heating the carbonized resin from room temperature to 300°C at 5 K min^{-1} examined the mechanism of the nitric oxide reduction reaction using continuous measurements with a mass spectrometer.

5.2 Nitric oxide conversion and yields of nitrogen

The reaction for the conversion (reduction) of nitric oxide is stoichiometrically written as



However, undesired reactions forming other oxides of nitrogen (NO₂ or N₂O) may also occur but none were detected. Nitric oxide may be adsorbed on the samples contributing to the removal of nitric oxide.

Figure 8 shows the change of total conversion of nitric oxide at the exit with time at 300°C . Reducing reagents such as ammonia or carbon monoxide were not used in this experiment. Of the several resins studied, it was Ni²⁺-type resins which showed the highest activity for nitric oxide conversion. Ni-500-47.0 maintained a high catalytic activity for 2 h, removing the nitric oxide completely. The activity of Ni-500-32.6(HCl), prepared by demineralizing Ni-500-32.6 with aqueous HCl, was low. The activity of Ni²⁺-type resin, HTT 500°C , increased with increasing nickel contents. These results indicate that nickel is essential for removal of nitric oxide. As

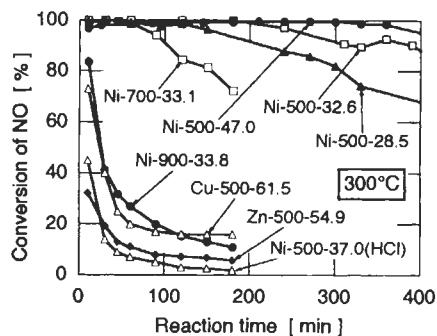


Fig. 8. Conversion of nitric oxide at 300°C for metal-loaded porous carbons. ($S_v = 24000 \text{ h}^{-1}$) [11].

for effects HTT, Ni-700-33.1 completely decomposed nitric oxide initially, but its activity gradually decreased after 60 min. The activity of Ni-900-33.8 rapidly decreased during the initial stages. Thus, catalytic activity decreased with increasing HTT.

The conversion of nitric oxide on Cu-500-61.5 rapidly decreased within 30 min and reached less than 20% at 100 min. The activity of Zn-500-54.9 was even lower than that of Cu-500-61.5.

Next, the yields of nitrogen were measured for the nickel supported samples as shown in Fig. 9 [11]. The nitrogen yields for the samples, HTT 500°C, were rather small initially but increased gradually to ~80% after 100 min. The high yields were maintained for 300 min. Because even a highly active nitric oxide decomposition catalyst, Cu-ZSM-5, converts nitric oxide to nitrogen by only 60% at 400°C [12] and because the nitric oxide to nitrogen conversion generally increases with increasing reaction temperature, the Ni^{2+} -type resins, HTT 500°C, were judged to be active in the conversion of nitric oxide to nitrogen. Comparing Figs. 8 and 9, it is seen that total nitric oxide conversions are larger than the nitrogen yields for these samples. This indicated that part of nitric oxide was retained in the sample. This retention may lower the activity of the catalyst.

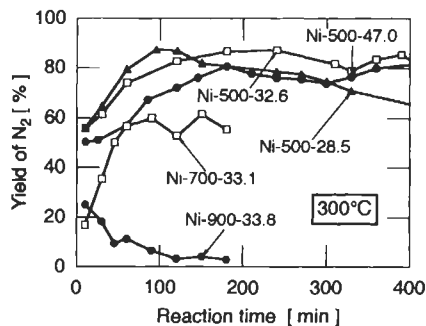


Fig. 9. Yield of nitrogen at 300°C for nickel-loaded porous carbons. ($S_v = 24000 \text{ h}^{-1}$) [11].

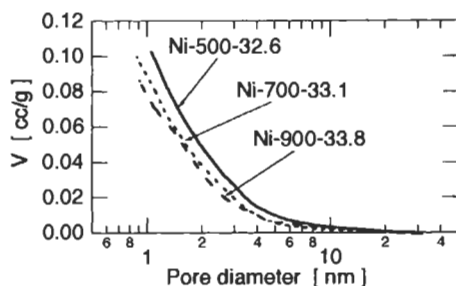


Fig. 10. Accumulated pore volume distributions of nickel-loaded porous carbons prepared at different temperatures [11].

The activity of Ni^{2+} -type resin carbonized at 500°C was higher than that of Ni^{2+} -type resin carbonized at 700 or 900°C . This difference comes from variations in pore structure or degree of dispersion of nickel in the carbon because amounts of nickel in the samples are almost identical. Figures 10 and 11 show accumulated pore volume distributions and the X-ray diffraction patterns of these samples [11]. The pore volume distributions of Ni-700-33.1 and Ni-900-33.8 are similar to that of Ni-500-32.6 with pores sizes being between 1 to 10 nm in diameter for all samples. Other samples were different. The intensity and the sharpness of Ni (111) and (200) peaks increased with increasing HTT indicating that the crystallinity of the nickel particles increased significantly with increasing HTT. Thus, differences in nitric oxide reduction rates between samples are associated with degrees of dispersion of nickel in the carbonized resins.

5.3 Durability of Removal of Nitric Oxide

Ni^{2+} -type resins carbonized at 500°C have a high activity in the conversion of nitric oxide to nitrogen. The durability (stability) of Ni-500-47.0 for extended times was tested at 300 and 400°C , as shown in Fig. 12. At 300°C the conversion of nitric oxide gradually decreased after 5 h and fell to 60% at 10 h. The sample was then

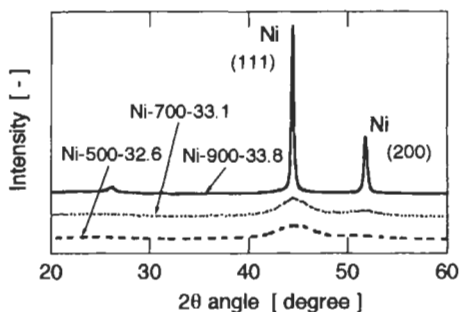


Fig. 11. X-ray diffraction patterns of nickel-loaded porous carbons prepared at different temperatures [11].

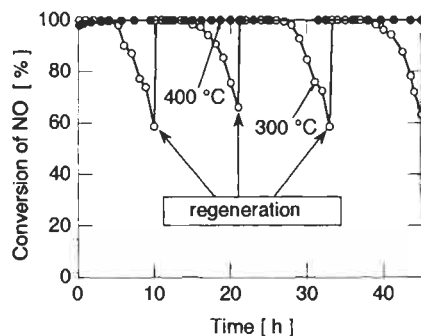


Fig. 12. Durability test of Ni-500-47.0 for the removal of nitric oxide at 300 and 400°C. ($S_g = 24000 \text{ h}^{-1}$) [11].

regenerated by heating at 500°C for 30 min in helium. After this regeneration treatment, the activity for nitric oxide removal recovered completely. The activity did not decrease after a further three cycles of reaction and regeneration. The formation of nitrogen, carbon monoxide and carbon dioxide was detected during regeneration. Nitrogen came from nitric oxide trapped in the sample during the reaction. The summation of amounts of recovered nitrogen during reaction and regeneration equaled amounts of nitric oxide removed during the reaction. Therefore, the nitric oxide removed was completely converted to nitrogen during reaction and regeneration. The formation of carbon monoxide and carbon dioxide indicated that the carbon consumed during regeneration amounted to 0.039 kg-C/kg-sample. Therefore, the number of possible reaction-regeneration cycles is limited when thermal regeneration is necessary.

At 400°C, the activity of Ni-500-47.0 was constant for more than 40 h without regeneration and with complete conversion of nitric oxide to nitrogen. However, carbon monoxide and dioxide were detected in the product stream indicating that some of the carbon was being consumed during the reaction. The results shown in Fig. 12 indicate that the carbon acts as a reducing agent and that the catalyst activity would be lost when carbon is consumed. This means that Ni^{2+} -type resin, HTT 500°C, cannot be used for long periods of time under these operating conditions despite its high conversion activity.

To suppress carbon loss during regeneration, other reducing agents were studied (reducing regeneration). Figure 13 shows the conversion of nitric oxide versus reaction time through reaction-regeneration cycles for Ni-500-47.0. In this figure, regeneration was carried out for 5 h at 300°C using 2000 ppm of carbon monoxide as the reducing agent. The catalyst activity completely recovered ever after two or three reaction-regeneration cycles with nitric oxide conversion at 100% for ~2 h. Amounts of carbon dioxide formed during the regeneration equaled amounts of carbon monoxide consumed. The deactivated catalyst was thus regenerated only by carbon monoxide so minimizing carbon loss during regeneration. Therefore, the Ni^{2+} catalyst may be used for extended periods through repeated reaction-regeneration cycles

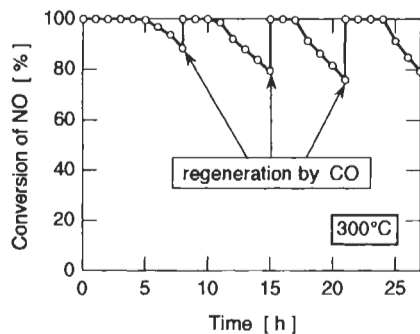


Fig. 13. Conversion of nitric oxide versus reaction time for reaction-regeneration cycles using carbon monoxide during regeneration of Ni-500-47.0. ($S_v = 24000 \text{ h}^{-1}$) [11].

when employing this regeneration method. The lifetime of the catalyst after the first regeneration was less than the lifetime of the fresh catalyst. This is because the catalyst was not completely regenerated during the first regeneration. It is necessary and important to find optimum regeneration conditions. Results so far indicate that a reducing regeneration method is effective to utilize the Ni^{2+} catalyst in practical applications.

Next, carbon monoxide was intentionally added in the feed stream during the reaction, because this gas may act as an *in situ* reducing agent. Figure 14 shows the changes in conversions of nitric oxide, the yields of nitrogen and the concentrations of oxides of carbon in the exit stream for Ni-500-47.0. In the presence of carbon monoxide, nitric oxide was completely removed for more than 20 h without regeneration even at 300°C. The concentration of carbon monoxide was smaller than its feed concentration by ca. 500 ppm, and carbon dioxide, which was not detected in the absence of carbon monoxide, was formed in ca. 500 ppm. These results show that amounts of carbon monoxide consumed were almost the same as amounts of carbon dioxide formed or amounts of nitric oxide removed. This means that almost no carbon

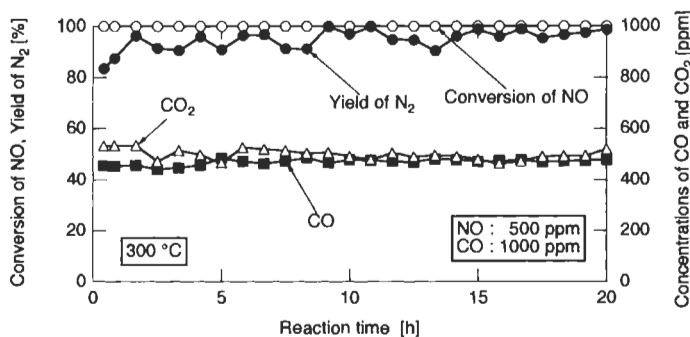


Fig. 14. Conversion of nitric oxide, yield of nitrogen, and concentrations of carbon monoxide and carbon dioxide in the effluent stream for the nitric oxide removal experiment with Ni-500-47.0 in the presence of carbon monoxide at 300°C. ($S_v = 24000 \text{ h}^{-1}$) [11].

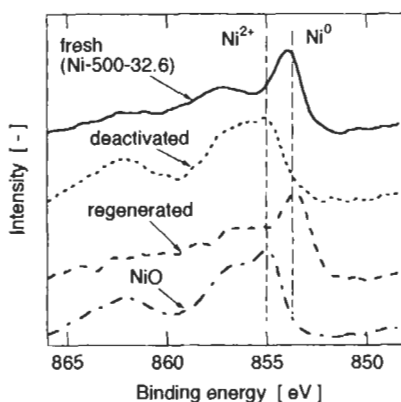


Fig. 15. Comparison of the XPS spectra of fresh catalyst (Ni-500-32.6), deactivated catalyst, and regenerated catalyst and the spectrum of NiO powders [11].

in the sample was lost during the reaction in the presence of carbon monoxide, maintaining the high catalytic activity for a long time. The yield of nitrogen was kept at more than 90%, indicating that the decomposition of nitric oxide to nitrogen was enhanced in the presence of carbon monoxide. Then, the overall reaction can approximately be written as



Thus, it is clear that the Ni²⁺ catalyst can be utilized for an extended time without loss of carbon when a reducing agent is contained within the feed stream.

5.4 Changes in the Chemical State of Nickel During Reaction

XPS studied changes in nickel forms in the Ni-500-32.6 during reactions. Figure 15 compares the XPS spectra of the fresh, deactivated (used for 10 h at 300°C), and thermally regenerated samples with the spectrum of NiO powders. The spectra of nickel in the fresh and the regenerated samples were similar to those of nickel, and were of metallic nickel. On the other hand, the nickel in the deactivated sample was NiO. These results indicate that metallic nickel is the active form of the catalyst, and that it is oxidized to NiO through the removal of nitric oxide and accordingly loses its activity. NiO is reduced to nickel by carbon through the thermal regeneration reaction at 500°C as indicated by the formation of oxides of carbon during the regeneration.

5.5 Reaction Mechanisms

Non-isothermal experiments, so-called temperature-programmed-reaction (TPR) experiments, were made to examine the mechanisms of the decomposition reaction of nitric oxide. The sample was heated at 5 K min⁻¹, from room temperature to 300°C, in

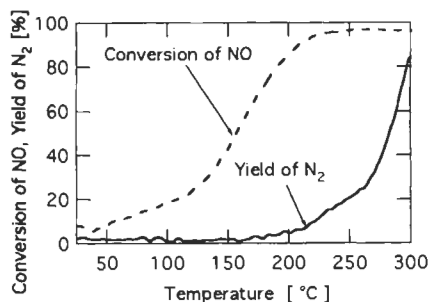


Fig. 16. Change of conversion of nitric oxide and yield of nitrogen against the temperature during the TPR experiment for Ni-500-47.0 ($S_v = 24000 \text{ h}^{-1}$) [11].

a stream of 500 ppm of nitric oxide. Figure 16 shows the concentrations of nitric oxide and nitrogen versus increasing reaction temperature. The concentration of nitric oxide decreased gradually with increasing temperature and fell to ~ 50 ppm even at 200°C . On the other hand, the concentrations of nitrogen was less than 25 ppm at temperatures $< 200^\circ\text{C}$, and then gradually increased to reach about 210 ppm at 300°C . These results indicate that nitric oxide is chemisorbed on the sample and then decomposes to form nitrogen.

Based on the above results the following reaction mechanism was proposed for nitric oxide decomposition reaction at 300°C on the Ni-loaded porous carbons in the absence of reducing agents



Nitric oxide is first chemisorbed on nickel (Reaction (3)). The chemisorbed nitric oxide decomposes to form nitrogen and oxidizing nickel to NiO (Reaction (4)). At 300°C , about 20% of the nitric oxide removed remains in the sample. As NiO is not active for the nitric oxide decomposition reaction, the activity gradually decreases with the progress of reaction. However, the initial activity of the catalyst was high because a large amount of metallic nickel ($\sim 50 \text{ wt}\%$) was highly dispersed within the porous carbon.

The regeneration reaction is the reduction of NiO to Ni. Carbon in the sample reduces NiO to Ni forming carbon monoxide at 500°C (Reaction (5)). Carbon monoxide formed through the reduction by carbon also reduces NiO (Reaction (6)).



At 400°C the activity of Ni-500-47.0 remained for more than 40 h without regeneration, because the regeneration Reactions (5) and (6) occur simultaneously.

Thus, carbon itself was found to act as a reducing agent when no reducing agents were added meaning that carbon is lost during the reaction and/or during thermal regeneration.

The reducing regeneration method and the *in situ* regeneration method were proposed (Figs. 13 and 14) based on the reaction mechanisms. Both methods used carbon monoxide as a reducing agent which reduced NiO to Ni through Reaction (6). The methods established the regeneration of the Ni²⁺ catalyst by minimizing loss of carbon.

6 Conclusions

A novel method for preparing porous carbons with highly dispersed metals is presented. The method carbonizes ion-exchange resins exchanged by different cations. Of the various carbons prepared, the proposed method uses a nickel-loaded porous carbon which shows high catalytic activity for the decomposition of nitric oxide to nitrogen. The following results were obtained.

1. A nickel-loaded porous carbon, Ni-500-47.0, removed nitric oxide completely for 5 h ($S_v = 24000 \text{ h}^{-1}$) at 300°C without any gaseous reducing reagent. The high activity of Ni-500-47.0 resulted from the large amounts of highly dispersed nickel loaded into the porous carbon.
2. The activity of deactivated sample could be completely recovered by heat treatment at 500°C in a helium atmosphere, but the regeneration method consumed carbon by reducing nickel oxide (NiO) to nickel.
3. To overcome this limitation to thermal regeneration, regeneration using carbon monoxide as a reducing agent was examined. This regeneration method minimized carbon loss suggesting the possibility to use the Ni²⁺ catalyst in practical applications.
4. In the presence of the reducing agent carbon monoxide, Ni-500-47.0 completely removed nitric oxide for more than 20 h at 300°C without regeneration. This was because carbon monoxide regenerated nickel oxide (NiO) to nickel during the reaction. This regeneration consumes little carbon and so the supported catalyst can be used for an extended.
5. Nitric oxide is first chemisorbed onto active sites of the metallic nickel, and subsequently decomposes to produce nitrogen and nickel oxide (NiO). The activity is gradually lost with the formation of nickel oxide (NiO) which can be removed by reducing agents such as carbon monoxide or carbon to recover the catalytic activity.

References

1. L.R. Radovic and F.R. Reinoso, In: P.A. Thrower (Ed.), Chemistry and Physics of Carbon, Vol. 25, pp. 243–358. Marcel Decker, New York, 1997.
2. F. Nozaki, K. Yamazaki and T. Inomata, Low temperature activity of the copper oxide catalyst supported on activated carbon for reduction of nitric oxide with ammonia. Chem.

- Lett.: 521–524, 1977.
3. S. Kasaoka, E. Sasaoka and H. Iwasaki, Vanadium oxides (V_2O_5) catalysts for dry-type and simultaneously removal of sulfur oxides and nitrogen oxides with ammonia at low temperature. *Bull Chem. Soc. Jpn.*, 62: 1226–1232, 1989.
 4. A. Nishijima, Y. Kiyozumi, A. Ueno, M. Kurita, H. Hagiwara, S. Toshio and N. Todo, Metal halide catalyst for reduction of nitric oxide with ammonia. *Bull Chem. Soc. Jpn.*, 52: 3724–3727, 1979.
 5. L. Singoredjo, M. Slagt, J. van Weers, F. Kapteijn and J.A. Moulijn, Selective catalytic reduction of nitric oxide with ammonia over carbon supported copper catalysts. *Catal. Today*, 7: 157–165, 1990.
 6. D. Mehandjiev and E. Bekyarova, Catalytic neutralization of NO on carbon-supported cobalt oxide catalyst. *J. Colloid Interf. Sci.*, 166: 476–480, 1994.
 7. J. Imai, T. Suzuki and K. Kaneko, N_2 formation from NO over metal oxide-dispersed microporous carbon fiber. *Catal. Lett.*, 20: 133–139, 1993.
 8. H. Nakagawa, K. Watanabe, Y. Harada and K. Miura, Control of micropore formation in the carbonized ion-exchange resin by utilizing pillar effect. *Carbon*, 37: 1455–1461, 1999
 9. K. Miura, H. Nakagawa and K. Hashimoto, *Carbon*, 33: 275–282, 1995
 10. D. Dollimore and G.R. Heal, An improved method for the calculation of pore size distribution from adsorption data. *J. Appl. Chem.*, 56: 109–113, 1964.
 11. K. Miura, H. Nakagawa, Ryo Kitaura and T. Satoh, Low-temperature conversion of NO to N_2 by use of a novel Ni loaded porous carbon. *Chem. Eng. Sci.*, 56: 1623–1629, 2001
 12. M. Iwamoto, H. Yahiro, Y. Mine and S. Kagawa, Excessively copper ion-exchanged ZSM-5 zeolites as highly active catalysts for direct decomposition of nitrogen monoxide. *Chem. Lett.*: 213–216, 1989.

Chapter 32

Formation of a Seaweed Bed Using Carbon Fibers

Minoru Shiraishi

Tokai University, School of High-technology for Human Welfare, Department of Material Science and Technology, Numazu, Shizuoka, 410-0395 Japan

Abstract: Micro-organisms rapidly fix onto carbon fiber surfaces when the fibers are placed in the sea. The objective is to create an artificial bed of seaweed so establishing a food chain of bacteria, algae, zoo-plankton, small animals, and fish. Initial studies in fresh water indicated that this approach had considerable potential and should therefore be extended to seawater.

Keywords: Carbon fiber, Sea, Seaweed bed, Algae, Micro-organisms.

1 Introduction

The fixation of micro-organisms onto carbon fibers has recently been undertaken in freshwater systems, one application being the purification of sewage [1,2]. On the other hand, there is no basic information on the fixation of micro-organisms onto carbon fibers in seawater systems. Therefore, carbon fibers were placed (anchored) in the sea to observe fixation phenomena of marine micro-organisms. Basic data on the utilization of this artificial bed of seaweed, in terms of fish population, were collected [3].

2 Rapid Fixation of Marine Organisms

To gain basic information on the fixation of marine organisms, field experiments were undertaken at the Marine Laboratory of Tokai University and also at the seawater intake of the Shinsihmizu thermal power station of Chubu Electric Power Co. Inc. in the Shimizu harbor basin, Shizuoka. The Marine Laboratory is in a stagnant location beyond the intake, located at the back in the bay and near to a timber yard.

Polyacrylonitrile (PAN)-based carbon fibers with a tensile strength of 3.4 GPa, tensile modulus of 230 GPa, diameter of 7 μm , density of 1.77 g cm^{-3} and 12,000 filaments per strand were used. A simple apparatus, as shown in Fig. 1, was sunk about 1 m under the surface of the sea and, during the first experiments, was withdrawn from the seawater at intervals of a few days. A plastic float of 30 cm



Fig. 1. Carbon fiber bundles attached to the experimental apparatus.

diameter was attached to the upper part of the rope which installs the apparatus, and a 3 kg weight was tied to the lower end of the rope to keep the fibers on the sea floor. Observations were made directly through the naked eye, an underwater camera and an optical microscope.

Small organisms (algae) were almost not observed on carbon fiber surfaces after the first day of the experiment. However, a weak adhesive property appeared on the fiber surfaces to provide an adhesive membrane and so the fiber surfaces adopted a membrane-like feature, as shown in Fig. 2. This phenomenon was observed in the sea at the two locations throughout the year. To facilitate access to the interior fibers of the strand for this membrane formation, it was found necessary to separate the strands into filaments. A colony grew homogeneously from these fibers on the agar medium in one or two days. There are differences between the colonies proliferated by carbon fibers picked up and the seawater without carbon fibers from the same place. The results indicate that the adhesive material was preferentially fixed to carbon fibers in the sea and was made up of micro-organisms such as *Bacillus carboniphilus*, discovered by Matsushashi [4].



Fig. 2. Adhesive material spread to the membrane on carbon fiber surface.

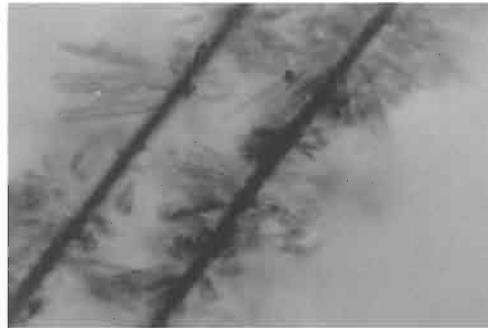


Fig. 3. Minute algae (*Navicula*) fixed on carbon fibers.

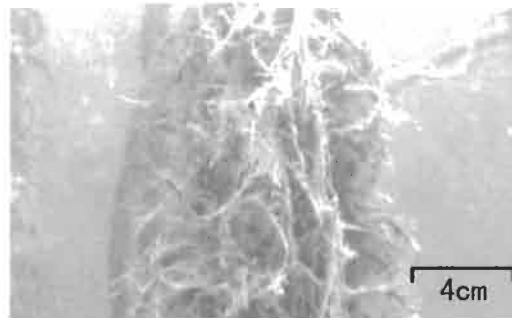


Fig. 4. Diatoms grown on the periphery of carbon fiber bundles.

Within a week after dipping, the carbon fibers had adopted the appearance of brown bio-mud, as observed macroscopically or through the camera. Minute algae, as shown in Fig. 3, were fixed to the carbon fibers as observed by optical microscopy. These algae were diatoms to be seen in seawater at depths of about 2 m. These algae were initially attached to the outside of the carbon fiber bundle, and then penetrated gradually to the inside of bundle. They grew as a slender string as shown in Fig. 4 at the

Table 1

Changes with dipping time of varieties marine organisms fixed or living on carbon fibers in the sea

| After dipping | Marine organism |
|---------------|--|
| 1 day | adhesive material |
| 5 day | diatom, zooplankton |
| 7 day | diatom, zooplankton, <i>Caprella</i> , small shrimp (<i>Maera serratipalma</i> etc.) |
| 14 day | small shrimp (<i>Maera serratipalma</i> etc.), <i>Protohydroides elegans</i> , <i>Caprella</i> , ascidian |
| 1 month | small shrimp (<i>Maera serratipalma</i> etc.), ascidian, <i>Protohydroides elegans</i> , <i>Hydrozoa</i> |
| 2 month | small shrimp (<i>Maera serratipalma</i> etc.), <i>Hydrozoa</i> , barnacle, fish |
| 3 month | small shrimp (<i>Maera serratipalma</i> etc.), barnacle, sponges, fish |



Fig. 5. Small shrimp (*Maera serratipalma*) observed in carbon fiber bundles.

periphery of the fiber bundle. Also, organisms of a size larger than several centimeters soon became associated with the bundles as well as zooplankton, as seen by optical microscopy.

Small animals, several millimeters in size, seen after 10 days and shown in Fig. 5, were confirmed as small shrimp (*Maera serratipalma* and *Photis reinhardi*). The development and growth rates of these animals were more rapid in the summer than in the winter. Large colonies of *Maera serratipalma* and *Prehotis reinhardi*, etc. lived in the apparatus in the sea during an autumn and winter.

3 Food Chain Through a Carbon Fiber Seaweed Bed

The carbon fibers were pulled out of the sea and sampled to measure the population of algae using the microscope. The results show the growth rate of these minute algae with increasing number of days in the seawater (Fig. 6). A maximum number of algae appeared after about 30 days. It is suggested that the zooplankton and small animals grow in numbers during this 30-day period and feed off these algae. Other fish, such as filefish (*Stephanolepis cirrhifer*) and globefish (*Ostracion immaculatus*) which swim

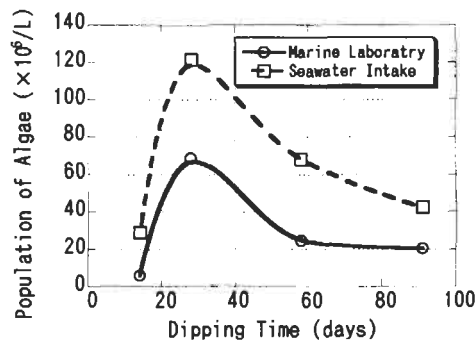


Fig. 6. Variation of quantities of algae with time of dipping (submergence).



Fig. 7. The sea-jungle appearance of the fibers after four months of dipping.

externally to the carbon fiber bed, live off these smaller animals and algae. Lugworms (*Polychaeta*) inhabited the fiber bundle and algae apparently grew on the outside of the carbon fiber bundle. A feature of this apparatus is that it forms a sea jungle in three or four months, as shown in Fig. 7.

Later, comparatively larger animals such as ascidian (*Ascidacea*), bivalve (*Bivalvia*), barnacle (*Balanomorpha*) and hydroid (*Hydrozoa*) etc., several centimeters in size, lived in the apparatus and became abundant after several months. At this time, and after the fixation and growth of the larger animals, the carbon fibers, which had originally been dispersed in the water, were apt to fasciculate (form bundles) and these included the lugworms, etc.

A conclusion is that this carbon fiber system, acting as an artificial seaweed, established a marine food chain.

4 Formation of an Artificial Bed of Seaweed Using Carbon Fibers [5]

Seaweed bed formation was developed further by sinking two larger experimental apparatus to the sea floor at a depth of 5–10 m in Suruga Bay near Numazu City. One method was to fix a carbon fiber rope in the sea floor. Carbon fibers were woven as a rope, 6 mm diameter and made into a grating-like net of 6 cm intervals. The nets of $2 \times 2 \text{ m}^2$ in size were fixed to the sea floor. The other method was designed to lift the carbon fiber up from the sea floor. Bases of $30 \times 30 \text{ cm}$ size made with ceramics, natural stone, colored coral gravel and concrete and placed on the sea floor with carbon fibers attached. The other ends of the fibers were tied to floats. Some 100 bases and carbon fibers of 1600 strands in the area of $5 \times 5 \text{ m}^2$ were used, as shown in Fig. 8. Before this equipment was installed, pisces (fish) seldom stayed though they sometimes swam through this area. Diatoms fixed themselves onto the carbon fibers immediately after installation. The small animals that lived off the fixed diatoms appeared near to the carbon fibers in one month after installation. Small fish such as *Apogon semilineatus* and filefish gathered in the circumference of this apparatus, as

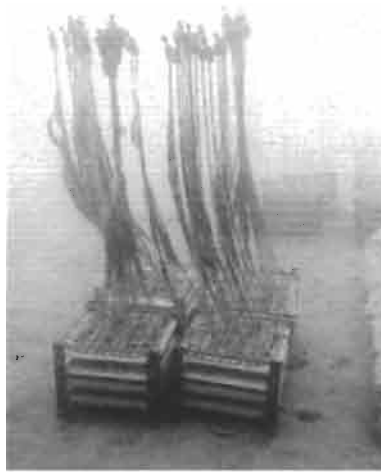


Fig. 8. Apparatus as placed on the sea floor.



Fig. 9. Small fish (*Apogon semilineatus*) grouped together.

shown in Fig. 9, and the food chain described in the preceding section was established again. The fish colony contained 21 varieties including *Apogon semilineatus* and file-fish, the number increasing to over 1000 some two months after the installation. Comparatively, many types of fish gathered and the communities of the pisces (fish) are complicated. In addition, scorpion fish appeared, including *ichthyovorous* which do not live usually in such a sand base, and *ichthyovorous horse mackerel* have been observed.

However, there are also some problems which have to be solved. For example, one is the durability of carbon fibers. Accumulation of silicon was observed on the surface of carbon fibers in some places when the carbon fibers had been in the sea for a while, and the carbon fibers may become brittle. Also, the quantity of the carbon fibers

considerably decreased in about three months after the dipping. Fish appear to tear the carbon fibers when they eat their food (bait) which is fixed to the carbon fibers. The carbon fibers are apt to gather in bundles after *ascidian* and *shellfish* become attached. The appearance of the fiber bundles changes greatly after some time in the seawater. Though these organisms will be metabolized some day, regeneration in a one-year cycle, as recognized in nature, will be difficult with this system.

References

1. A. Kojima and S. Otani, Environmental Conservation of Hydrosphere with Carbon Fiber. Proc. Int. Workshop on Advanced Materials for Functional Manifestation of Frontier and Environmental Consciousness, pp. 145–152, 1997.
2. S. Otani, Application of carbon fiber to aquatic environmental protection. Tanso, 2000: 276–287 (in Japanese).
3. M. Ooishi, M. Shiraishi and S. Otani, Fixation of marine micro-organisms on carbon fiber. The Bulletin of School of High-Technology for Human Welfare, Tokai University, 8: 79–88, 1998 (in Japanese).
4. M. Matsuhashi, A.N. Pankrushina, K. Endoh, H. Watanabe, H. Ohshima, M. Tobi, S. Endo, Y. Mano, M. Hyodo, T. Kaneko, S. Otani, S. Yoshimura, *Bacillus carboniphilus* cells respond to growth-promoting physical signals from cells of homologous and heterologous bacteria. J. Gen. Appl. Microbiol., 42: 315–323, 1996.
5. S. Ueno, T. Kosaka, Y. Sato and M. Shiraishi, Biological Functions of Artificial Seaweed Bed using Carbon Fiber. Abst. 27th Annual Meeting of the Carbon Society of Japan, pp. 180–181, 2000 (in Japanese).

Chapter 33

Carbon/Carbon Composites and Their Properties

Tatsuo Oku

Ibaraki Study Center, The University of the Air, Bunkyo, Mito, Ibaraki 310-0056, Japan

Abstract: The results of research into carbon/carbon composites and related materials are reviewed and form part of the Carbon Alloys project. The results are in five categories: (1) the development of high quality carbon fibers and new carbon coils, property evaluation, and applications; (2) novel material development and control of micro-structures; (3) improvements in properties of materials and correlations between properties and micro-structures; (4) fracture phenomena and mechanism; and (5) assessments of micro-structures. Achievements of research into carbon/carbon composites are described. Novel carbon materials, carbon fibers, carbon matrices, high quality carbon alloys and new material evaluation methods were developed within this project. New processing methods for carbon/carbon composites and carbon related composites were explored. Improvements to the following properties of carbon/carbon composites were made: oxidation resistance, mechanical properties, thermal conduction, electronic properties, and electro-magnetic wave absorption.

Keywords: Carbon fiber, Carbon matrix, Interface, Composite, Microstructure, Properties.

1 Introduction

Carbon/carbon composites, carbon fiber-reinforced carbon matrix composites, under the Carbon Alloys project have been investigated to develop new starting (parent) materials and new functionalities. Carbon/carbon composites consist of carbon fibers and carbon matrices. However, despite an abundance of research papers, there is a need for high performance carbon fibers to develop high performance carbon/carbon composites. The term 'carbon fibers' includes carbon fibers, carbon nanotubes and micro-carbon coils. Carbon matrices can contain fullerenes such as C_{60} , graphite, and composites of carbon with metals. Selected combinations of carbon fibers with carbon matrices produce high performance carbon/carbon composites. Reviews and books on carbon/carbon composites, including applications to nuclear fission and fusion fields, are available [1–4].

First we discuss fundamental research on carbon fibers with high compressive strengths. Carbon coils with new functions have been developed with applications to carbon/carbon composites being investigated. Novel composites containing carbon

nanotubes instead of carbon fibers with the C_{60} fullerene as carbon matrix have been developed and their properties examined.

The mechanical properties and oxidation resistance of carbon/carbon composites which control the microstructures of the interfaces between carbon fiber and carbon matrix have received attention. The additions of copper and small amounts of titanium to carbon/carbon composites are effective in increasing thermal conductivities compared with conventional carbon/carbon composites. Fracture mechanisms in carbon/carbon composites have been examined theoretically making use of various material parameters. Microstructures of interfaces between carbon fibers, carbon matrices and impregnated metals have been studied by transmission electron microscopy.

2 Carbon Fibers and Carbon Coils

2.1 Improvement in Compressive Strength of Carbon Fibers

Carbon fibers with high compressive strength were investigated. Korai et al. [5] successfully prepared anisotropic pitches of high spinnability by heat treatment of isotropic pitches synthesized from naphthalene and methyl-naphthalene using BF_3/BF_3 as a catalyst. As-spun and graphitized fibers made from these pitches were studied by X-ray diffraction (Table 1). Crystallite sizes in the isotropic pitch spun fibers increased with increasing soak time. Carbon fibers of high compressive strength could be made from this naphthalene pitch. Figure 1 shows the relationship between Young's modulus and compressive strength for such carbon fibers the compressive strength increasing with heat-treatment. The compressive strength varies inversely with the Young's modulus. The relationship was improved by heat treatment.

Table 1

The degree of preferred orientation of fibers [5]

| Heat-treated time (h) | Degree of preferred orientation (%) | |
|-----------------------|-------------------------------------|-------------|
| | As-spun | Graphitized |
| Isotropic pitch | 56.7 | 62.5 |
| 15 | 63.5 | 90.9 |
| 18 | 64.2 | 91.8 |
| 24 | 65.6 | 92.6 |
| 30 | 69.2 | 93.1 |
| 40 | 69.4 | 95.1 |
| 72 | 72.2 | 95.3 |
| Mesophase pitch | 78.0 | 95.5 |

Heat-treatment temperature is 360°C. Graphitization temperature is 2500°C.

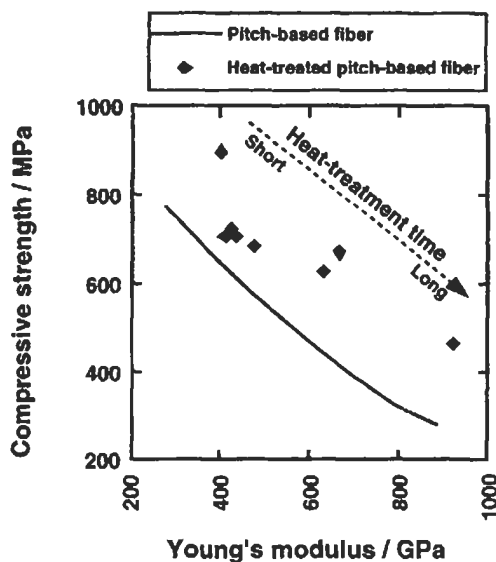


Fig. 1. Compressive strength and Young's modulus of heat-treated pitch-based fibers [5].

These heat-treated pitch carbon fibers showed high compressive strengths. However, the whole fiber does not have uniform structure because the pitches contain both isotropic and anisotropic components. The central isotropic domain was larger than peripheral regions of the fiber. It is considered that as the components are non-Newtonian fluids their viscosity decreases when large shear stresses are applied and that they will tend to gather in the central part of the fiber because the flow speed increases.

2.2 Development of Carbon Coils

Motojima et al. [6–8] and Chen et al. [9] prepared carbon micro-coils and micro-pipes by the Ni-catalyzed pyrolysis of acetylene containing a small amount of thiophene at 750–800°C. The carbon coils were coated with pyrolytic carbon layers using a gas mixture of $\text{CH}_4 + \text{Ar}$ at 900–1200°C. They were usually double helicals and regularly coiled with a coil diameter of 3–6 μm and coil length of 0.05–5 μm . Typical carbon micro-coils are shown in Fig. 2. Coil gaps were hardly seen and the micro-coils were densely packed. The electromagnetic reflection loss was measured using a Field Analyzer (ADVANTEST, U4342) and indicated that the coated coils have an excellent reflection loss of electro-magnetic waves. Figure 3 shows the reflection loss for the coated coils obtained at different reaction times for long carbon coils, 1–10 mm, when used as source coils. As-grown carbon coils hardly absorb electromagnetic waves; however, carbon micro-coils coated with pyrolytic carbon films absorb 90–99% of electromagnetic waves of 400–900 MHz. The reason for this is not clear at present.

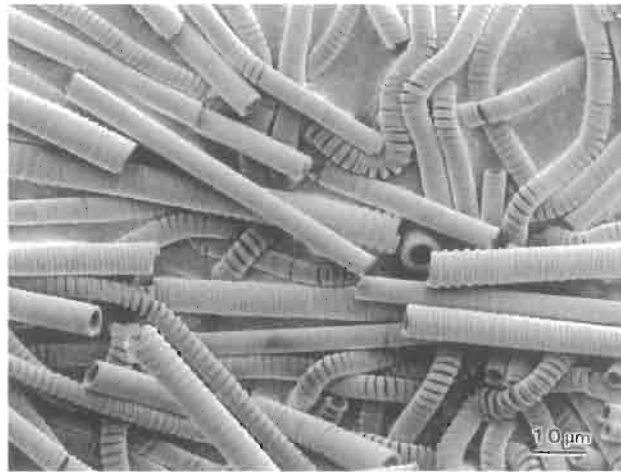


Fig. 2. Typical carbon micro-coil [6].

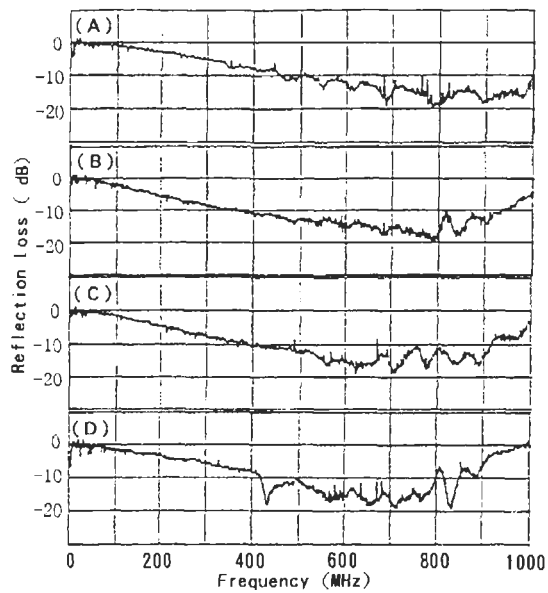


Fig. 3. Electromagnetic wave attenuation rate of carbon coil coated by PyC film [7]. Coating time: 2 h, Addition: 20 wt%.

Carbon coils or carbon pipes with metal carbide/metal nitride have been successfully manufactured by maintaining the original pipe shape of the parent material. The bulk electrical resistivity of the coated coils is about 1–0.1 Ω cm which depends on bulk density, decreasing with increasing bulk density.

3 Novel Materials and Control of Micro-structures

3.1 Novel Composites and Their Characterization

Ichinose et al. [10–11] developed and characterized new composite materials which had large plastic deformability made by controlling the microstructure at the nanometer level during production so increasing interface fractions. The research requirements included: (1) mass production of high purity C_{60} crystals and carbon nanotubes; (2) an understanding of the phase transformations caused by heat treatment of C_{60} matrix and the influence on mechanical properties; (3) structural features of C_{60} crystals and carbon nanotubes; and (4) production and characterization of novel materials using the electrical properties of nanotubes.

The C_{60} matrix and carbon nanotubes as a fiber have been produced by the arc-discharging method using a carbon rod (99.99% purity) at 25V, 300A, and He at 5.3 kPa pressure. The C_{60} powder, to be used as the matrix, was crystallized into nano-crystals by the gas evaporation method. The average diameter of these nano-crystals made at 1.3 kPa of helium was ~ 50 nm. The nano-crystals of C_{60} were mixed with 40 wt% of nanotubes using a wet mixing method with supersonic energy in ethanol solution. The density of C_{60} and nanotube were assumed to be 1.68 Mg m^{-3} and 2.0 Mg m^{-3} , respectively. After drying the mixed powder in a vacuum furnace the powder filled a silver tube and was drawn at room temperature in air.

The C_{60} matrix material tended to lose the intrinsic mechanical properties of a molecular crystal by heat treatment. Tensile test results of the composite show more than about 10% elongation at room temperature and a fracture strength of 18 MPa corresponding to about 20 times that of the C_{60} poly-crystal (Fig. 4). The elastic deformation area in the stress-strain curve was not seen clearly and the yield point was not found. The necking phenomenon was not seen and all the nanotubes were pulled from the C_{60} matrix in a fracture surface. In the single fiber carbon composite drawing deformation occurs in which interfacial slip is a main mechanism and may contribute to elongation of the composite.

Measurements of the field emission (FE) properties were made of extruded composite wire materials which included carbon nanotubes. The I-V (current-voltage) characteristics indicated that the first emission property differed from the second electron emission (Fig. 5). The reason for this could be a change in the microstructures before and after electron emission at the tip of a carbon nanotube. A plastic deformation structure was found at the tip of the nanotube after electron emission (Fig. 6). It was considered that the microstructure, associated with the plastic deformation, was produced by mechanical loading associated with the high electric field.

TEM showed that some surface relief developed at the tip of nanotubes after the field emission measurements. On the other hand, on compacting at high pressures, the X-ray diffraction (XRD) profile from the surface of the formed compact indicated that the C_{60} matrix changes into a polymerized phase indexed as a face-centered

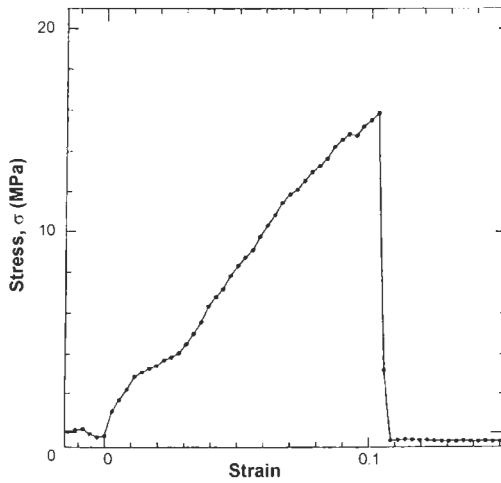


Fig. 4. Stress-strain curve of the heat-treated composite [10].

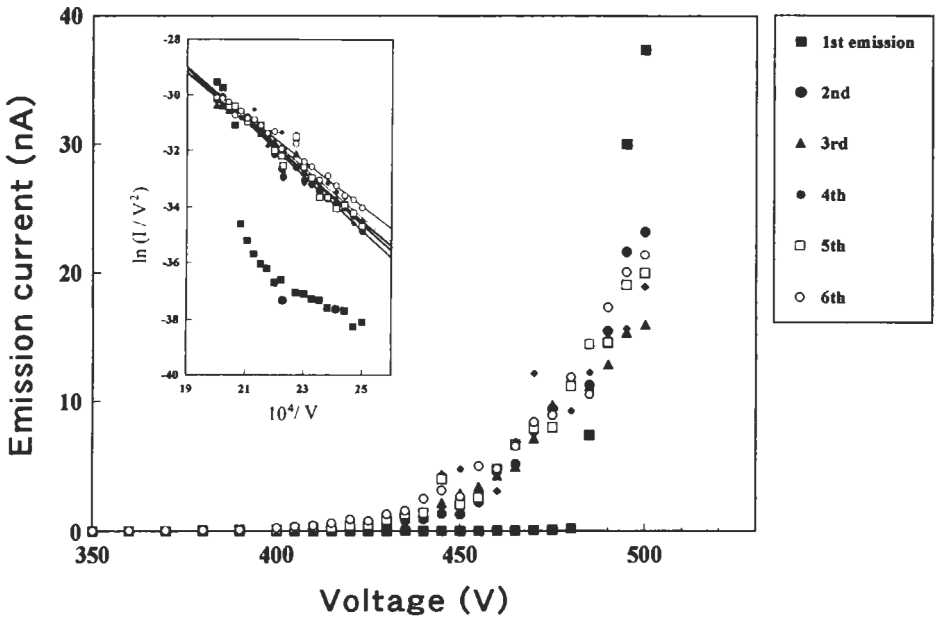


Fig. 5. Emission current versus voltage characteristic of an oriented nanotube cathode [11].

cubic (fcc) structure ($a = 1.31$ nm). In a cross-sectional surface of the specimen, the XRD profiles and TEM observations suggested that the polymerized structure approximated to a rhombohedral structure. The anisotropic structure of the bulk specimen and the handling of the specimen (bulk or powder) should be taken into account when characterizing structures of high-pressure-polymerized fullerene (C_{60}).

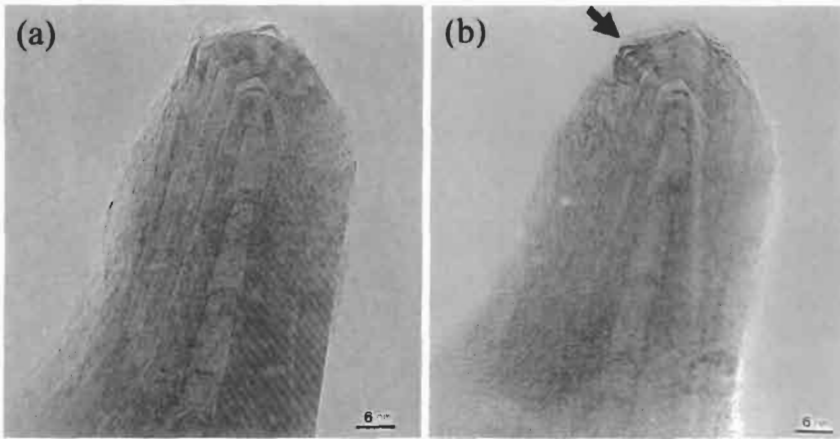


Fig. 6. High-resolution transmission electron microscope image (TEM) of structure of a nanotube tip (a) before emission and (b) after emission [11].



Fig. 7. Cross-sectional view of the drawn composite wire [10].

Novel carbon composite materials may possibly be produced based on this unique structure and the excellent properties of the C_{60} matrix and nanotubes.

Carbon nanotubes with added C_{60} polymers were successfully compressed by an ultra high-pressure method without change to the microstructure of the nanotubes. This composite was used in a lithium-ion cell. Results from the charge-discharge characteristics indicate that lithium atoms are located in the micropores and not as interstitial atoms and precipitate as micro-crystals from the charge-discharge capacity and the cycle characteristics after electrical charge-discharge. This is why the cycle characteristics deteriorate. Figure 7 shows a scanning electron micrograph (SEM) of the cross-section of the composite material. The top of the material shows

the microstructure, and has an orientation less than 30° in the direction of drawing of the nanotube.

3.2 Control of Microstructures in Carbon/Carbon Composites

Yasuda et al. [12] attempted to control the microstructures of interfaces between carbon fiber and matrix for carbon/carbon composites. Thermosetting resin (furan resin) and a thermoplastic coal-tar pitch (CTP) were selected as carbon matrix precursors. In the furan resins, stress-induced graphitization of carbon was observed. The effects of oxygen functional groups on surfaces of carbon beads on interfacial microstructures were examined. The addition of iodine to the coal-tar pitch improved carbon yield the resultant carbon becoming isotropic. A supersonic wave, 20 kHz, 5 W cm^{-2} , irradiated the resin in order to facilitate the hardening of the furan resin.

Generally, the condensation polymerization reactions of a furan resin are promoted by an acid catalyst. Hardening rates are accelerated by a factor of six by the supersonic wave treatment. An optical microscopic study of the non-irradiated and irradiated resins indicated many more pores in the non-irradiated specimens but with the larger pores being completely removed by the supersonic wave treatment. Furthermore, supersonic wave irradiation enhanced a uniform dispersion of fine carbon particles after addition to the composite.

For a carbonized furan resin, irradiation by supersonic waves brought about the removal of large bubbles, enhanced the hardening rate but was without influence on the composition of the hardened material and its crystallinity.

Effects of fine carbon particle additions on the graphitization of the furan resin have been examined. Crystallite size of the added carbon particles increased with increase in their particle size. More significant changes to the crystallinity of microstructures in particle composite materials were brought about by additions of the larger carbon particles (Fig. 8). The curvature of the interface was important for

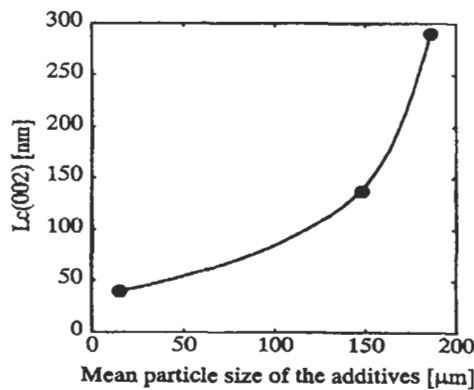


Fig. 8. Crystallite size along c-axis as a function of mean particle size of the carbon (HTT 3000°C) [12].

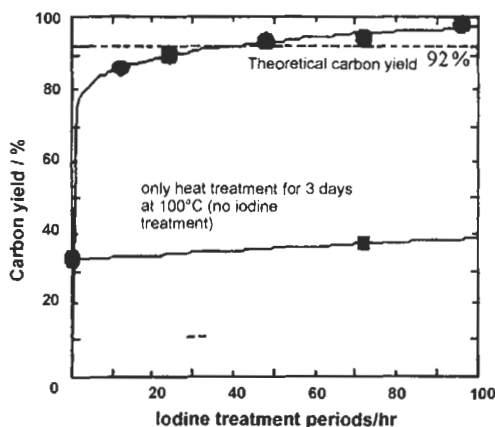


Fig. 9. Carbon yield of a coal-tar pitch (CTP) at 800°C as a function of iodine treatment [12].

graphitization at the interface and it was noted that graphitization took place only at the particle interface, not over all of the particle dispersion system.

From measurements of extents of polymerization of the resin following additions of fine carbon particles, it was found that increasing the specific surface area of the particles promoted hardening and introduced surface functional groups.

Additions of iodine to a coal-tar pitch (CTP) increased carbon yield (Fig. 9). Reaction mechanisms to explain this effect may be as follows: (1) iodine forms an electric charge transfer complex by weak interactions with aromatic compounds of the CTP; (2) a cation radical is formed from the aromatic molecule by removal of a π -electron from the aromatic molecule; (3) partial polarization is then induced in the complex and as an edge hydrogen atom is easy to desorb, then polymerization of the aromatic molecules of CTP should be facilitated.

4 Improvement of Properties and Correlation Between Properties and Microstructures

4.1 High Thermal Conductivity at High Temperatures

Oku et al. [13] investigated those factors which may have an influence on the high thermal conductivity of carbon alloys. Copper was impregnated into an isotropic fine-grained graphite and a carbon/carbon composite. Resultant thermal conductivities did not improve, probably as a result of very poor continuity at the interfaces of the copper and carbon particles caused by differences in thermal expansion coefficients. To overcome this effect small additions of titanium or zirconium were made to the copper impregnated carbons. Tested materials are listed in Table 2.

Thermal conductivities were measured, 293–1200 K, using a laser flash device to obtain thermal diffusivity and specific heat values. Temperature dependencies of

Table 2

Tested materials for thermal conductivity and microstructure [13]

| Base materials | Tested materials | wt% | vol.% | Bulk density (g/cm ³) | Electrical resistivity ($\mu\Omega$ m) |
|-------------------|------------------|-----------|-----------|-----------------------------------|---|
| Graphite | IG-430U | — | — | 1.83 | 9.0 |
| | IG-430U + Cu | 33.1 (Cu) | 10.2 (Cu) | 2.74 | 2.9 |
| | IG-430U + Cu(Ti) | 36.0 (Cu) | 11.4 (Cu) | 2.84 | — |
| | | 0.8 (Ti) | 0.5 (Ti) | — | — |
| C/C composite | CX-2002U | — | — | — | 1.7 (XX) |
| | (XX, YY, ZZ) | — | — | 1.67 | 3.4 (YY) |
| | | — | — | — | 5.1 (ZZ) |
| | | — | — | — | — |
| | CX-2002U + Cu | 44.3 (Cu) | 14.0 (Cu) | 2.83, 1.4 (XX) | — |
| CX-2002U + Cu(Ti) | 48.1 (Cu) | 17.7 (Cu) | 3.29 | — | |
| | 1.1 (Ti) | 0.8 (Ti) | — | — | |

thermal conductivity for the carbon/carbon composite, CX-2002U, C/C with Cu, C/C with Cu(Ti) and metal copper (OFHC) are shown in Fig. 10. The thermal conductivity of copper at high temperatures is larger than that of the parent carbons. The thermal conductivity of the carbon/carbon composite with copper only was smaller than that of parent carbon/carbon composite. Additions of titanium (sample number CX-2002U+Cu(Ti)) increased the thermal conductivity by about 30% and also

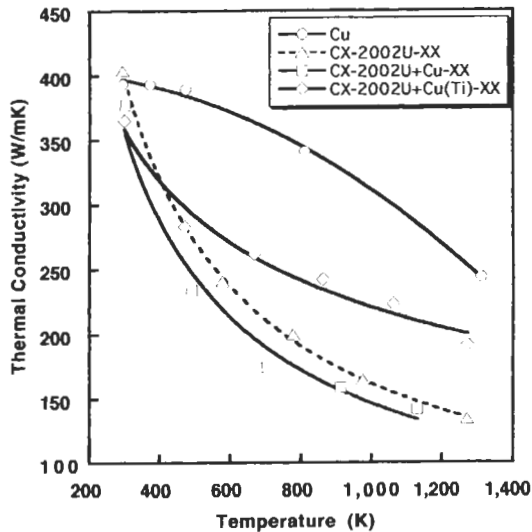


Fig. 10. Temperature dependence of thermal conductivity for Cu, CX-2002U, CX-2002U + Cu and CX-2002U + Cu(Ti) [13].

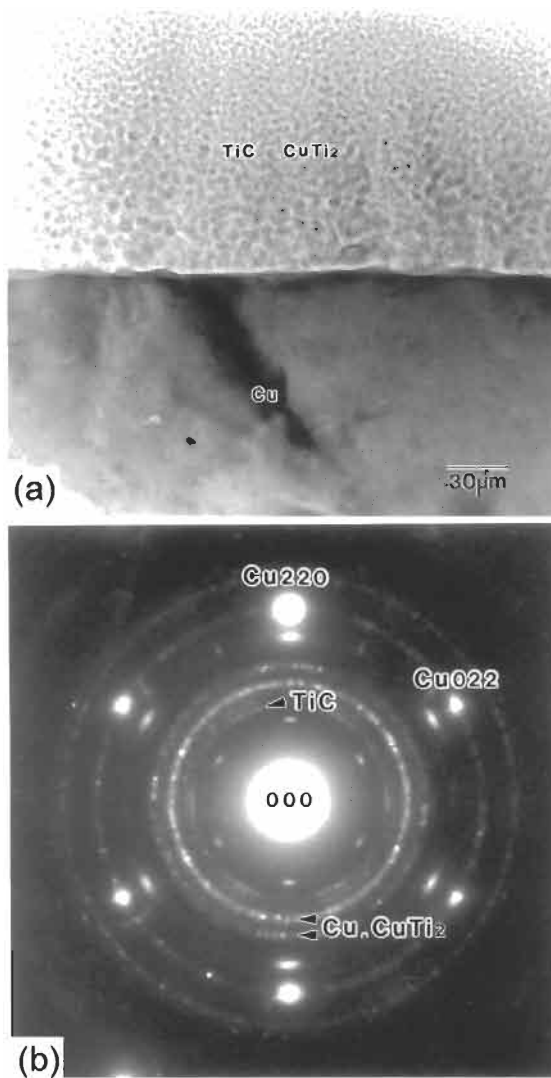


Fig. 11. TEM image (a) and ED pattern (b) of the interface between carbon and copper [13].

decreased the temperature dependence of conductivity. CX-2002U is a felt type carbon/carbon composite, the thermal conductivity being along the high thermal conductivity (graphene) planes within the felt layer.

The microstructure of the CX-2002U+Cu(Ti) was investigated by transmission electron microscopy (TEM) and electron diffraction (ED), see Figs. 11a and 11b, respectively. Microcrystals of TiC and CuTi₂ are distributed at the C/Cu interface as shown in Fig. 11a. In the ED pattern ($\{111\}$ plane of Cu) of Fig. 11(b) Debye-Scherrer rings corresponding to TiC and CuTi₂ are also observed. Grain sizes of the

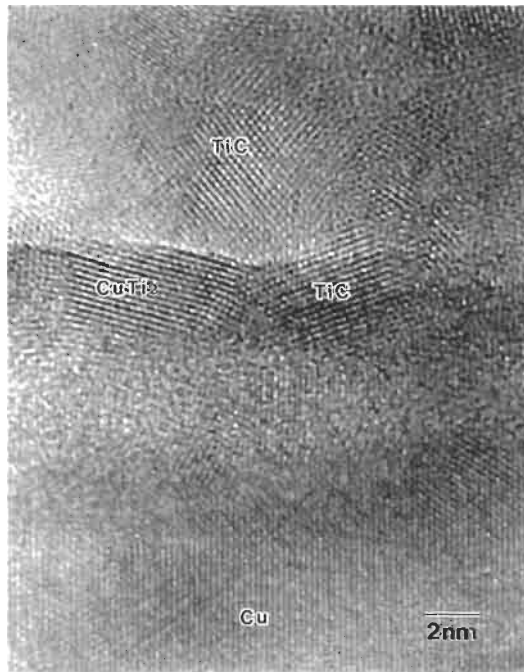


Fig. 12. HREM image at the interface between carbon and copper [13].

compounds are ~ 5 nm, as shown in Fig. 12 which is a high-resolution electron-micrograph (HREM) at the C/Cu interface of Fig. 11a. The enhanced thermal conductivity caused by addition of titanium results from the formation of TiC and Ti-Cu at the interface so promoting cohesion at the interface at high temperatures. It was also noted that additions of titanium promote graphitization within the carbon/carbon composite [14–16]. This may also contribute to the observed increase in thermal conductivity. This study therefore indicates that additions of small amounts of a third element with a low enthalpy of alloy formation of carbon and copper increases thermal conductivity and stability at high temperatures. Additions of zirconium are expected to provide positive results.

4.2 Oxidation-resistant Properties

Aoki et al. [17] and Hatta et al. [18], with two programmes, studied oxidation-resistant SiC/C multi-layer coatings on carbon/carbon composites by using a SiC/C multi-layered coating method and a sinusoidal silicon carbide (SiC) coating method. Overall, it is a prerequisite that oxygen of the atmosphere must be prevented from gaining access to the carbon/carbon composite. Their first approach was to improve oxidation resistance by preventing cracking of the SiC/C layer by (a) reducing the thickness of each silicon carbide layer and using thin multilayers and (b) by deflecting

cracks at the SiC/C interface. Their second approach was to suppress thickness cracking by reducing thermal stresses in the silicon carbide layers using bend deformation of thin wavy coatings. Their first approach had three specific objectives, the first being to develop a carbon that will not initiate cracking even if the carbon film is deposited on the surface of the C/C composite between SiC layers. The second objective was to create long diffusion paths by deviating cracks locally in the carbon layers or in the interface between silicon carbide and carbon layers introduced between thin films of SiC. The third objective was to decrease the crack width even if cracking occurs in the thin films of each layer. Further, it is known that when silicon carbide is oxidized to silica (SiO₂) there is a volume expansion. Cracks in the multilayers created thermally may then be closed up by volume expansion during formation of SiO₂.

It is reported [19] that tensile thermal stresses in layers decrease if the surface of the carbon/carbon composite is coated in a sin-curved shape. The thickness of a silicon carbide single layer was varied 0.2–170 μm using UD-C/C (Across Co.). An initiating crack spacing was measured in the coating layer. The crack spacing decreased with decreasing thickness to 0.2 μm when cracks were not seen in the fibers of the surface of the carbon/carbon composite but a small number were seen on the matrix. The SiC film thickness at which no cracks are initiated is defined as the “critical film thickness”, h_c . In addition to this, a method for making use of anisotropy of carbon/carbon composite has been examined.

The energy release rate, G_p , during initiation of cracks in the coating layer is a function of the thickness of the silicon carbide layer, using the finite element method. As a result, if $G_{IC} = 30 \text{ J m}^{-2}$ ($K_{IC} = 3.7 \text{ MPa m}^{1/2}$) is assumed, the critical film thickness, h_c , obtained by experiment was nearly equal to the calculated result. This suggests that a layer thickness of 0.2 μm, in a multilayer system, would reduce significantly any oxidation loss. To verify this experimentally, a flat plate made of UD-C/C (Advanced Materials Corp.) was cut out at an angle, θ , as shown in Fig. 13 and a multi-layered coating was applied. The reason for this is that the in-plane coefficient of thermal expansion (CTE) of the plate cut-out is then nearly equal to that of the CVD-SiC by using the large out-of-plane CTE of the UD-C/C. The critical film thickness, h_c , can then be easily deposited. The critical film thickness, h_c , in which a tensile stress, σ is induced in the coated layer, was calculated using Eq. (1) which includes the elastic modulus of the coated layer, E_{SiC} , the energy release rate, G_{IC} , and $g(\alpha, \beta)$, a function of the elastic modulus ratio of the base plate to the coated layer.

$$h_c = \frac{2E_{SiC}G_{IC}}{\sigma^2 \pi g(\alpha, \beta)} \quad (1)$$

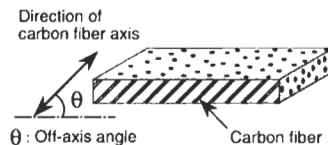


Fig. 13. Carbon/carbon specimen prepared for SiC/C multi-layered coating [17].

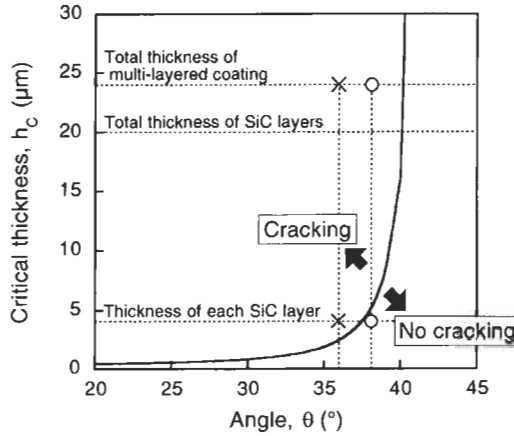


Fig. 14. Critical thickness, h_c , as a function of angle, θ [17].

Figure 14 shows the critical thickness, h_c , estimated by Eq. (1) as a function of angle cut-out. The predicted critical thickness was considered to be between the cracking and no cracking zone in the figure.

A cross-sectional photograph of the multi-layered coated specimen is indicated for $\theta = 36^\circ$ and $\theta = 38^\circ$ in Fig. 15. Each SiC layer was about $4 \mu\text{m}$ thick, that of carbon layer was about $0.8 \mu\text{m}$, giving a total thickness of $24 \mu\text{m}$ for 10 layers. In the case of $\theta = 36^\circ$, several “through-the-thickness” cracks initiated at a constant spacing as shown in Fig. 15. On the contrary, when $\theta = 38^\circ$, there were no “through-the-thickness”

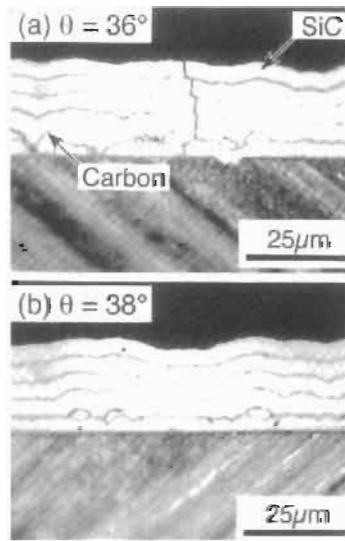


Fig. 15. Cross-sectional view of SiC/C multi-layered coatings [17].

cracks but exfoliation was seen on the interface of SiC/C. The result suggests that the use of a material with a small CTE for inter-layers is effective for oxidation resistance of carbon/carbon composites if each thickness of SiC layer is $< h_c$.

4.3 Effect of Compressive Pre-stress on the Thermal Conductivity of Carbon Materials

When carbon materials are subject to compressive pre-stresses greater than 60% of the compressive strength, cracks initiate and crystallites rotate in the materials [20]. Young's modulus decreases in directions both parallel and perpendicular to the applied compressive stress. It is also probable that thermal conductivity decreases due to compressive pre-stresses. Oku et al. [21] examined the effects of compressive pre-stress on the thermal conductivity of a carbon/carbon composite and correlations of Young's modulus with thermal conductivity [21].

A felt-type carbon/carbon composite, CX-2002U, was used as a test material. The compressive pre-stress, 90% of the average compressive strength of the material, was applied in the parallel direction to the felt plane (XX). Table 3 indicates changes in Young's modulus, density and electrical resistivity of CX-2002U, the density decreasing slightly by compressive pre-stress. The thermal conductivity decreased 5.8% in the direction of applied compressive pre-stresses and was 3.3% in the perpendicular direction. The decreasing rate of thermal conductivity was not temperature dependent.

Thermal conductivity is related to Young's modulus, apparent density, heat capacity and the mean-free-path of phonons by Eq. (2):

$$\lambda = \frac{1}{3} c \rho l \sqrt{\frac{E}{\rho}} = \frac{1}{3} c l \sqrt{\rho E} \quad (2)$$

Then, the changing rate of thermal conductivity, $\Delta\lambda/\lambda$, is expressed by Eq. (3)

$$\frac{\Delta\lambda}{\lambda} = \frac{\Delta c}{c} + \frac{\Delta l}{l} + \frac{1}{2} \left(\frac{\Delta\rho}{\rho} + \frac{\Delta E}{E_0} \right) \quad (3)$$

Table 3

Changes in Young's modulus of CX-2002U XX-direction (parallel to the stress axis) [21]

| Specimen | E_0 (GPa) | Changes in density (%) | Changes in E (%) $\Delta E/E_0$ | Changes in electrical resistivity $\Delta R/R$ (%) |
|----------|----------------|---------------------------|--------------------------------------|---|
| XX-dir. | 7.6 | 0.1 | -13.4 | -12.9 |
| ZZ-dir. | 1.9 | | -4.3 | -4.9 |

*The values were determined by the mechanical test with strain gages.
Average compressive strength of CX-2002U(XX), $\sigma_c = 54$ MPa.

Table 4

Correlation of changes in thermal conductivity with Young's modulus for IG-430U and CX-2002U materials [21]

| Material | $\Delta E/E_0$ (%) | $\Delta\lambda/\lambda$ (%) |
|---------------|--------------------|-----------------------------|
| IG-430U (L) | -12.0 | -7.3 |
| IG-430U (T) | -3.6 | -2.1 |
| CX-2002U (XX) | -13.4 | -5.8 |
| CX-2002U (ZZ) | -4.3 | -3.3 |

Decreasing rates of thermal conductivity were correlated with Young's modulus for the pre-stressed material. Table 4 shows the correlation of changes in Young's modulus with thermal conductivity for a fine-grained graphite, IG-430U, and a carbon/carbon composite, CX-2002U. Young's modulus of carbon materials has a relationship with thermal conductivity through the sound velocity.

Almost all of the changes in thermal conductivity could be due to changes in Young's modulus. However, a possibility exists that the mean free path of phonons and specific heats may have an influence.

5 Fracture and its Mechanism

5.1 The Properties and Mechanisms of the Matrix/Fiber Interface and De-bonding in Carbon/Carbon Composites

Sakai et al. [22] investigated the properties of the matrix/fiber interface and its exfoliation in carbon fiber/carbon composites. The purpose of the research was the development of interface control technology for the high performance, long carbon fiber/carbon matrix. Novel mechanical testing methods were developed to evaluate exfoliation and exfoliation fracture of fiber bundles. The results from the tensile tests on pull-out of a fiber bundle, in a unidirectional carbon/carbon composite, enabled exfoliation strengths to be evaluated, exfoliation fracture toughness values to be calculated and explained in terms of interlayer and intralayer shear strengths, exfoliation crack lengths and slip stress between exfoliated crack surfaces.

The testing method, using a unidirectional carbon/carbon composite, evaluated the tensile strength (σ_{fs}) of a reinforced fiber in the carbon/carbon composite, the pull-out stress of a fiber bundle (τ_{po}), the interface exfoliation strength (σ_a) and the mode II interface exfoliation fracture toughness value. The load-displacement diagram is indicated in Fig. 16. The value of (σ_{fs}) is evaluated by Eq. (4)

$$P_{\max} = a(f\sigma_{fs})b \quad (4)$$

where a and b are the sizes of the test section; $a = 1.0$ mm, $b = 0.04$ – 2.5 mm.

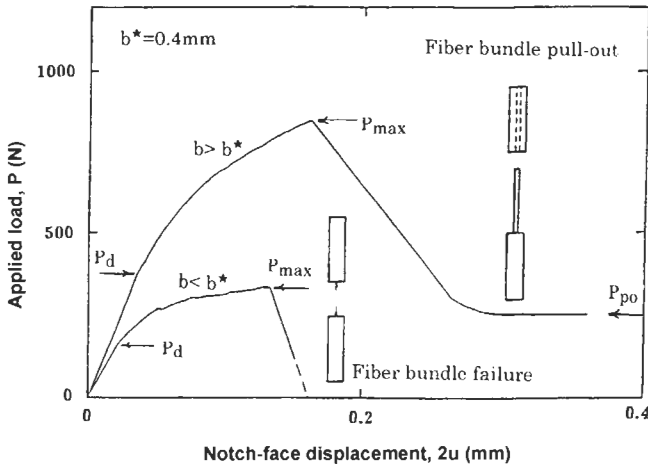


Fig. 16. Load-displacement diagram for bundle pull-out and bundle failure [22].

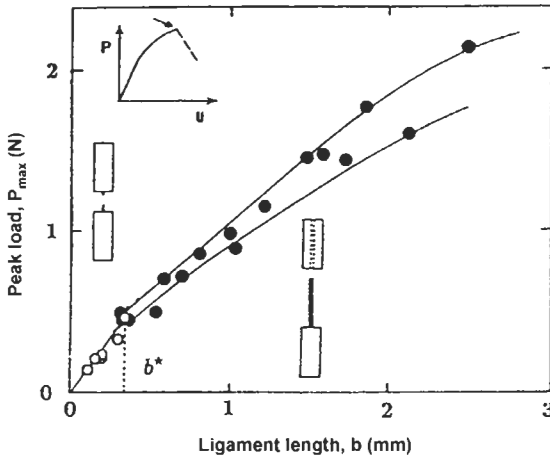


Fig. 17. Dependence of peak load on the ligament length [22].

The value of $a(f\sigma_{fs})$ is given by the slope of the line in $b \leq b^*$ in Fig. 17. The interface exfoliation strength (σ_d) was defined as Eq. (5):

$$\sigma_d = P_d/ab \tag{5}$$

The exfoliation shear stress (τ_{p0}) is defined by Eq. (6) using the steady state exfoliation load, P_{p0} (Fig. 16):

$$\tau_{p0} = P_{p0}/[2(a + b)L] \tag{6}$$

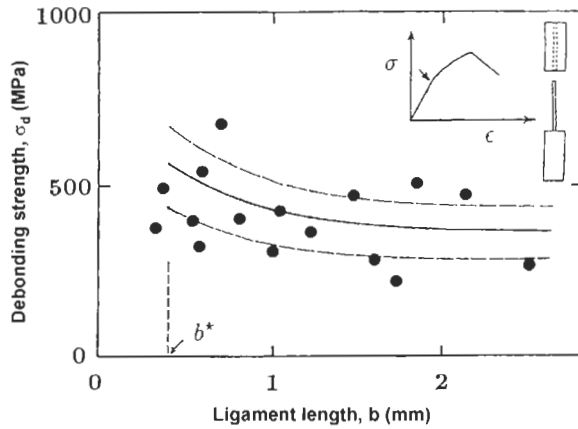


Fig. 18. Critical stress for de-bonding in terms of the ligament length [22].

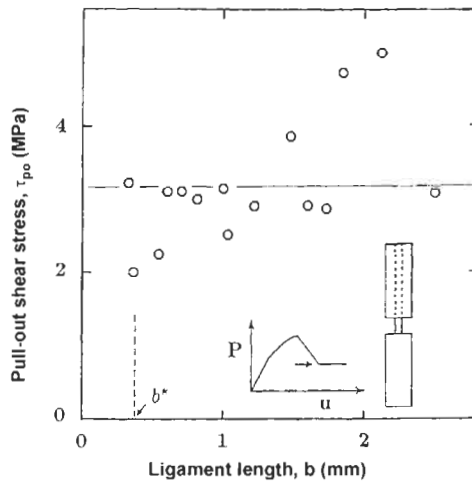


Fig. 19. Dependence of the pull-out shear stress on the ligament length [22].

σ_d and τ_{po} are shown in Figs. 18 and 19. The σ_d value, defined as the critical stress for the initiation for the exfoliation fracture, is related to the mode II exfoliation fracture toughness value, G_{IIc} , in Eq. (7):

$$\sigma_d = \sqrt{\frac{4EG_{IIc}}{ab/(a+b)}} \quad (7)$$

The relationship between σ_d and b obtained from Eq. (7) is indicated in Fig. 18 assuming $G_{IIc} = 123 \pm 50 \text{ J m}^{-2}$. The solid curve gives the relation obtained from Eq. (7) and the two dotted curves show the upper and lower limits of σ_d .

5.2 The Alloy Interface and Fracture Mechanism

Yatomi and Hojo et al. [23] examined effects on strength and fracture mechanism of carbon/carbon composites on fiber/matrix interfaces and matrix microstructures by changing the heat-treatment temperature (HTT) and by coating the surface of the carbon fiber with bismaleimide-triazine co-polymer (BT resin). For a carbon/carbon composite, HTT 1600°C, the notched strength of the wider specimens was < 8 mm, and correlated well with the net section stress criterion as shown in Fig. 20. On the other hand, Fig. 21 indicates that the notched strength of the carbon/carbon composite, HTT 2500°C, was well estimated using net section stress criterion without respect to the ligament length. For the carbon/carbon composites, without BT resin coating, the notched strength of wider specimens was smaller than the net section stress failure criterion that showed the notch effect. On the other hand, the notched strength of the carbon/carbon composite, with a BT resin coating, was well estimated by the net section stress criterion.

Changes in fracture mechanism on a macroscopic and a microscopic scale correlated well with the fracture criterion. Inter-laminar fracture toughness was also investigated to clarify effects of BT resin coating. Mode I inter-laminar fracture toughness of carbon/carbon composites was insensitive to the BT resin coating. Mode II inter-laminar fracture toughness of the carbon/carbon composite with BT resin coating was smaller than that without coating. For the satin-woven carbon/carbon composites using a high modulus yarn, effects of interface micro-structure on the in-plane strength and the out-of-plane strength, by coating with BT resin, were the formation of an isotropic matrix at the interface and a decrease in notched strength.

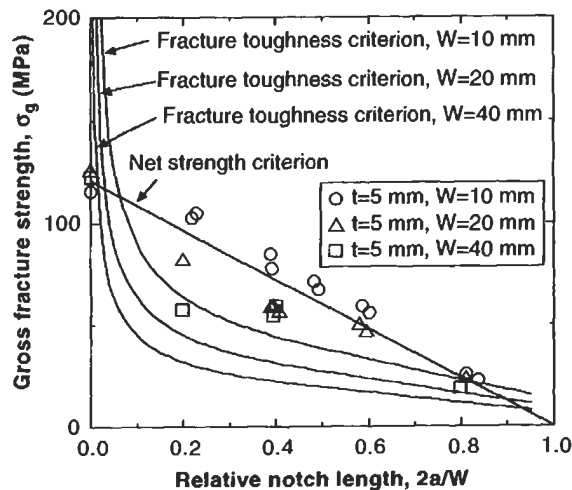


Fig. 20. Effect of relative notch length on fracture strength (HTT 1600°C, $t = 5$ mm) [23].

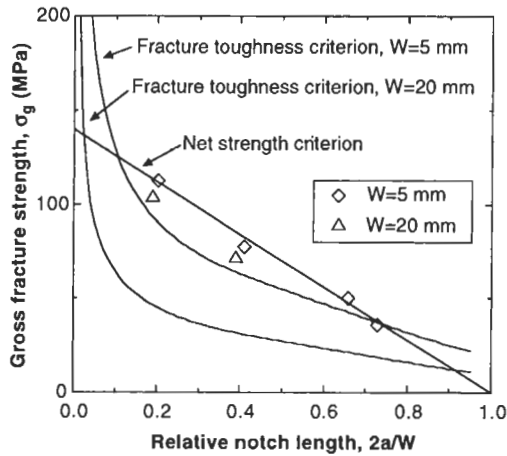


Fig. 21. Effect of relative notch length on fracture strength (HTT 2500°C, $t = 3$ mm) [23].

6 Microstructure Observation

Tsukimoto and Saka et al. [24] examined the alloying processes for Cr-C, Ti-C, and Cu-C systems by transmission electron microscopy. In the Cr-C system it was found that $Cr_{23}C_6$ were produced and a graphite layer of about 5 nm was formed between the chromium carbide and the carbon. There are defects in the graphite layer and the $\{002\}$ plane of graphite layer is formed in the direction parallel to the basal plane of the carbide. The Ti-C system was studied by *in-situ* experiments at temperatures between room temperature and 1200°C. Pure titanium underwent a $\alpha \rightarrow \beta$ phase transformation at about 900°C creating an uneven shape on the surface. No reaction with graphite was detected. On heating to about 1200°C, a contrasting liquid-like material was generated at the titanium interface, as shown in Fig. 22. The graphite structure completely disappeared. It is that the titanium diffuses into the graphite and the graphite then completely disappears, as shown in Fig. 22(d).

7 Concluding Remarks

Carbon/carbon composites have been extensively used as nose cones for space vehicles and are plasma-facing components in nuclear fusion reactors. Carbon/carbon composites have excellent thermal and mechanical properties which make them so suitable for such applications. Moreover, research continues for better oxidation-resistance and higher strengths in carbon/carbon composites. One way of doing this is to improve the properties of interfaces between carbon fibers and carbon matrices. In order to do this it is necessary to control microstructures at the interface. The Carbon Alloys project has supported research into the microstructures of

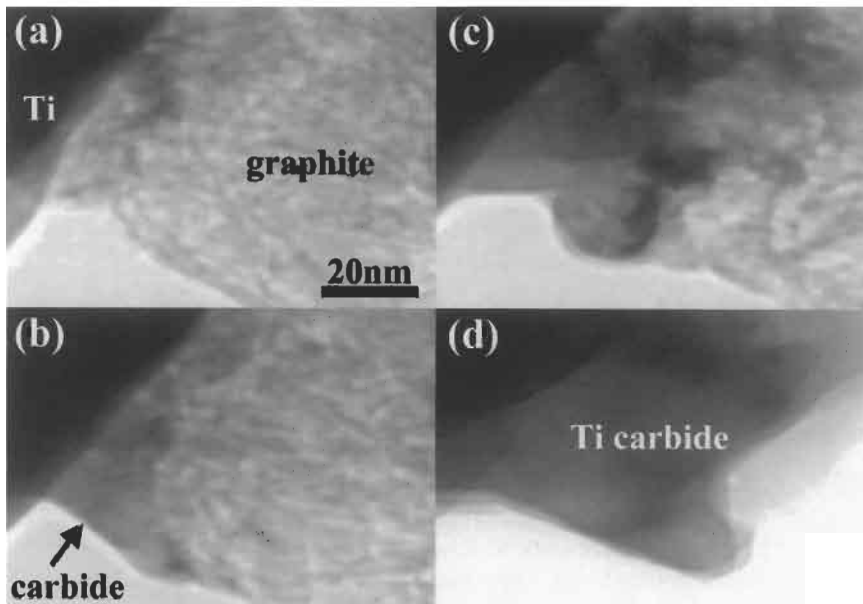


Fig. 22. Reaction process between titanium particle and graphite at 1200°C [24].

interfaces. The concept of the Carbon Alloys project has changed ways of thinking about how to improve properties of carbon/carbon composites.

A carbon/carbon composite material that consists of carbon nanotubes and C_{60} is a new composite material developed in the Carbon Alloys project. Progress in the production technology of carbon fibers, carbon nanotubes, carbon coils and fullerenes, including control of their microstructures, is expected to produce new composite materials that have novel and excellent properties.

References

1. T.D. Burchell (Ed.), *Carbon Materials for Advanced Technologies*, Pergamon Press, 1999.
2. T.D. Burchell and T. Oku, *Atomic and Plasma-Material Interaction Data for Fusion*, Vol. 5, IAEA, pp. 77–128, 1994.
3. H. Kosuda, *Introduction to Carbon Materials*, Revised Edn. The Carbon Society of Japan, pp. 215–227, 1984.
4. Y. Tanabe, *Introduction to Carbon Materials*, New Edn. The Carbon Society of Japan (Editor), Realize Inc., pp. 99–104, 1996.
5. Y. Korai, S.H. Yoon, H. Oka, I. Mochida, T. Nakajima, I. Kato and Y. Sakai, *Carbon*, 36(4): 369–375, 1998.
6. S. Motojima and Q. Chen, *J. Appl. Phys.*, 85(7): 3919–3921, 1999.
7. S. Motojima, T. Hamamoto, N. Ueshima, Y. Kojima and H. Iwanaga, *Electrochemical Society Proceedings*, Vol. 97-25, pp. 433–440, 1997.
8. S. Motojima and H. Iwanaga, *Kino Zairyo (Function Material)*, 17 (7): 37–44, 1997.
9. X. Chen, S. Motojima and H. Iwanaga, *Carbon*, 37: 1825–1831, 1999.

10. H. Ichinose et al., *Mater. Trans., JIM*, 39: 574, 1998.
11. T. Kuzumaki, Y. Horiike and H. Ichinose, *Tanso*, 195: 353–359, 2000.
12. E. Yasuda, T. Akatsu, K. Hoshi and N. Miyajima, *Matrix Microstructure and Boundary Design of C/C Composite by Alloying Technology. Summary Report of Research Project “Carbon-Alloys” in a Grant-in-Aid for Scientific Research on Priority Areas from the Ministry of Education, Science, Sports and Culture, 1997–1999*, pp. 173–180, 2001.
13. T. Oku, A. Kurumada, T. Sogabe, T. Oku, T. Hiraoka and K. Kuroda, *J. Nucl. Mater.*, 257: 59–66, 1998.
14. T.A. Burtseva et al., *J. Nucl. Mater.*, 191–194: 309, 1992.
15. L. Mazul et al., *Proc. Sixth Int. Carbon Material Workshop, Juelich*, p. 43, 1993.
16. V.N. Chernikov et al., *J. Nucl. Mater.*, 209: 148, 1994.
17. T. Aoki, H. Hatta, T. Hitomi, H. Fukuda and I. Shiota, *Carbon*, 39: 1477–1483, 2001.
18. H. Hatta, T. Aoki, T. Hitomi, H. Fukuda and I. Shiota, *Composite Interfaces*, 7 (5,6): 425–442, 2001.
19. T. Shioya, K. Uenishi, *Proc. of the 1995 Yokohama Int. Gas Turbine Congress, Yokohama, III*, pp. 93–98, 1995.
20. T. Oku, A. Kurumada, Y. Imamura, K. Kawamata and M. Shiraishi, *J. Nucl. Mater.*, 258–263: 814–820, 1998.
21. T. Oku, M. Nakata, A. Kurumada, K. Kawamata, *Tanso*, 195: 332–335, 2000.
22. M. Sakai, R. Matsuyama and T. Miyajima, *Carbon*, 38: 2123–2131, 2000.
23. M. Yatomi, M. Hojo, M. Tanaka, S. Ochiai, Y. Sawada and J. Takahashi, *J. Soc. Mat. Sci. Jpn.*, 47 (9) 939–945, 1998.
24. S. Tsukimoto and H. Saka, private communication.

Chapter 34

Super-hard Materials

Osamu Takai

Department of Materials Processing Engineering, Graduate School of Engineering, Nagoya University, Nagoya 464-8603, Japan

Abstract: Super-hard materials based on carbon alloys with a hardness exceeding 40 GPa attract attention due to possible industrial applications. Of the super-hard materials based on carbon alloys, the preparation and properties of diamond-like carbon (DLC), carbon nitride and boron carbonitride are described and compared with diamond.

Keywords: Super-hard materials, Diamond, Diamond-like carbon (DLC), Carbon nitride, Boron carbonitride (BCN).

1 Super-hard Materials

Hard materials are necessary for such industrial applications as abrasives, cutting tools, molds, automobile parts, electronic components, and optical parts. Industry uses hard materials to coat and modify surfaces of industrial materials [1]. Based on their chemical bonding character, conventional hard materials, with a hardness >15 GPa, are divided into three groups: metallic hard materials (e.g., TiN, TiC, CrN, WC), covalent hard materials (e.g., diamond, SiC, B₄C, Si₃N₄) and ionic hard materials (e.g., Al₂O₃, ZrO₂, TiO₂). Carbon also has a role as a component in hard materials. Materials with a hardness >40 GPa, the so-called “super-hard (or ultra-hard) materials” include diamond (C) (hardness: 80–100 GPa, Knoop hardness: Hk: 8000–10000), zinblende-type cubic boron nitride (c-BN) (40–60 GPa, Hk: 4000–6000) and carbon boride (B₄C) (30–45 GPa, Hk: 3000–4500) [2]. Recently, diamond-like carbon (DLC), carbon nitride, silicon carbon nitride, boron carbonitride, and ceramic nanocomposites are described as super-hard materials. Most of these super-hard materials are composed of the three elements carbon, boron and nitrogen, as shown in Fig. 1.

This chapter describes preparation methods and properties of thin films of such super-hard carbon alloys as diamond-like carbon (DLC), carbon nitride (e.g. β-C₃N₄) and boron carbonitride (B_xC_yN_z). These materials are carbon alloys and have the mixed bonding states of sp^1 , sp^2 and sp^3 , and are bonded to the alloying elements hydrogen, nitrogen and boron.

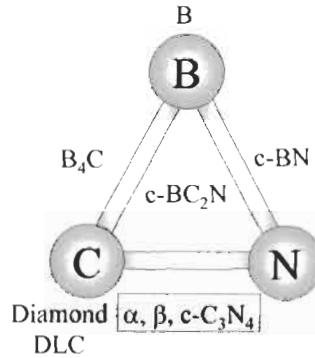


Fig. 1. Super-hard materials composed of the elements boron, carbon and nitrogen.

2 Diamond-like Carbon

Diamond-like carbon (DLC) is defined as an amorphous carbon (a-C) having structural, mechanical, electrical, optical, chemical, and acoustic properties similar to those of diamond. The name “diamond-like carbon” is currently used widely when at least one property is similar to diamond. Table 1 shows the comparison of typical properties between diamond-like carbon and diamond. Diamond-like carbon has properties similar to diamond (Table 1), and potential applications in various industrial fields, as indicated in Fig. 2. Diamond-like carbon will be used more extensively in industry in the 21st century.

Diamond has the cubic structure of zincblende with sp^3 hybridization of tetrahedrally coordinated carbon atoms, whereas graphite has a hexagonal layered structure with sp^2 hybridization of trigonally coordinated carbon atoms. According to

Table 1

Comparison of properties of diamond-like carbon films with diamond films

| | Diamond-like Carbon Films | Diamond |
|--|---------------------------|-----------------------|
| Crystal structure | amorphous | cubic lattice |
| Chemical bonding state | mainly sp^3 | sp^3 |
| Density (g cm^{-3}) | ~3 | 3.52 |
| Electrical resistivity ($\Omega \text{ cm}$) | 10^7 – 10^{14} | 10^{13} – 10^{16} |
| Dielectric constant | 8–12 | 5.6 |
| Optical transparency | infrared | ultraviolet–infrared |
| Optical band-gap (eV) | 1–2 | 5.5 |
| Refractive index | 2.0–2.8 | 2.41–2.44 |
| Hardness (GPa) | 10–90 | 90–100 |
| Hydrogen content (at%) | 0–40 | 0 |
| Morphology | very smooth | rough |

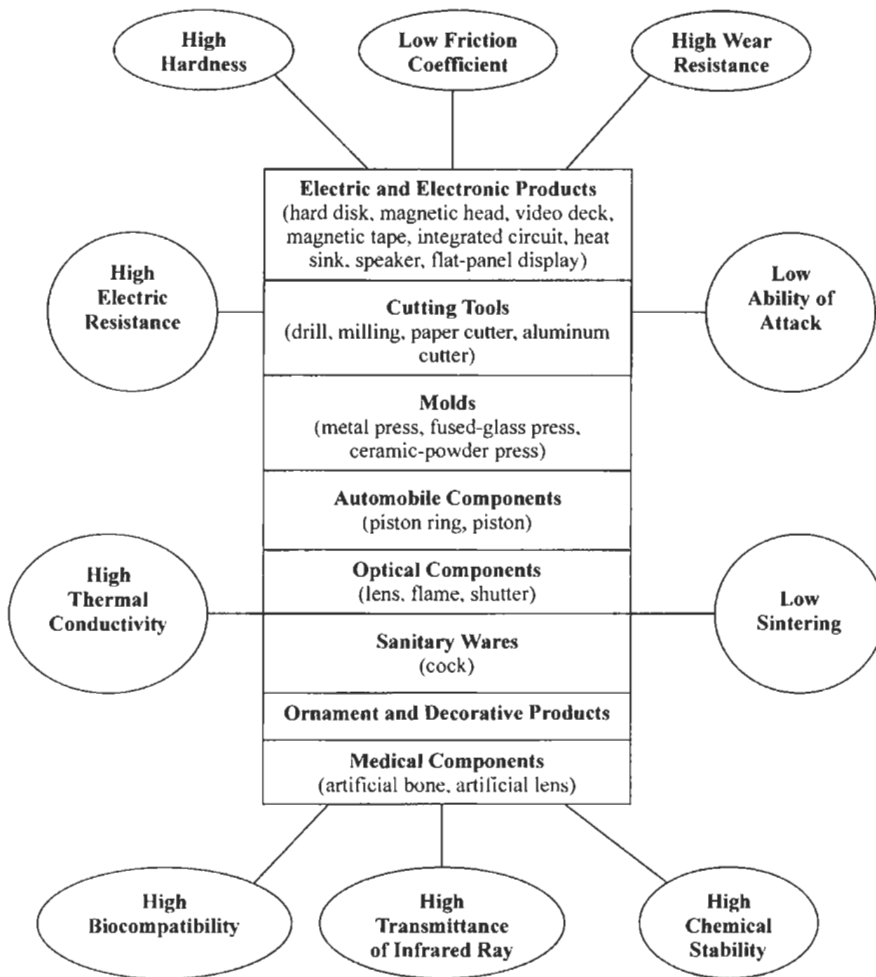


Fig. 2. Properties of diamond-like carbon films and their potential applications.

the ratio of these two carbon bonding fractions, sp^3/sp^2 , two types of amorphous carbon, diamond-like carbon and graphite-like carbon (GLC) exist. The diamond-like carbon has a higher fraction of sp^3 bonding, and the graphite-like carbon has a higher fraction of sp^2 bonding. Soft amorphous carbons are termed 'polymer-like carbon' (PLC). The boundaries between these three forms of carbon are not clearly defined. Figure 3 illustrates the regions of the three amorphous carbons (named) according to their sp^3/sp^2 ratios and hydrogen contents.

The preparation of diamond-like carbon was first reported by Aisenberg and Chabot in 1971 [3]. They used an ion beam evaporation technique. Other researchers reported the preparation of diamond-like carbon using different experimentations

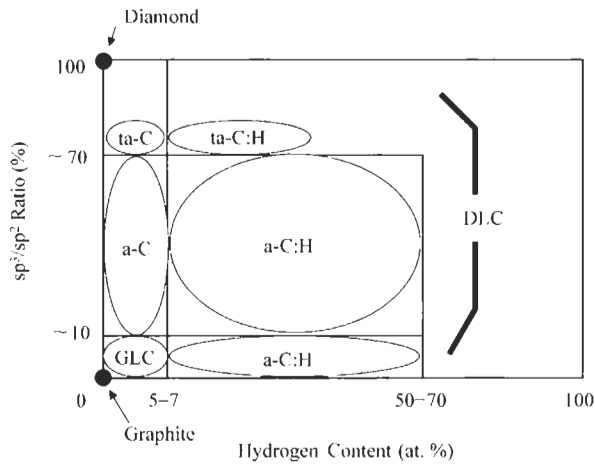


Fig. 3. Region of various amorphous carbons and their notations according to their ratios sp^3/sp^2 and hydrogen contents. a: amorphous; ta: tetrahedral.

Table 2

Methods of preparation of diamond-like carbon films

| Preparation method | Type | Carbon source |
|---------------------------------|---|------------------------|
| PVD (Physical Vapor Deposition) | | |
| Electron beam deposition | — | graphite |
| Ion beam deposition | — | graphite |
| Laser ablation | — | graphite |
| Ion plating | arc, electron-assisted | graphite, CxHy |
| Sputtering | dc, rf, electron cyclotron resonance | graphite |
| Plasma-based ion implantation | — | CxHy |
| CVD (Chemical Vapor Deposition) | | |
| Plasma-enhanced CVD | dc, rf, microwave, electron cyclotron resonance | CxHy, carbon compounds |
| Hot-filament CVD | — | CxHy, carbon compounds |

[4–6]. During the three years 1996–1998, more than 1000 papers were published describing the preparation of many types of diamond-like carbon.

There are many methods to prepare diamond-like carbon films, as shown in Table 2. Plasma-enhanced chemical vapor deposition (CVD), arc ion plating and magnetron sputtering are used in industry. The schematic diagram of a parallel-plate rf (radio frequency) plasma-enhanced chemical vapor deposition system, widely used, is shown in Fig. 4.

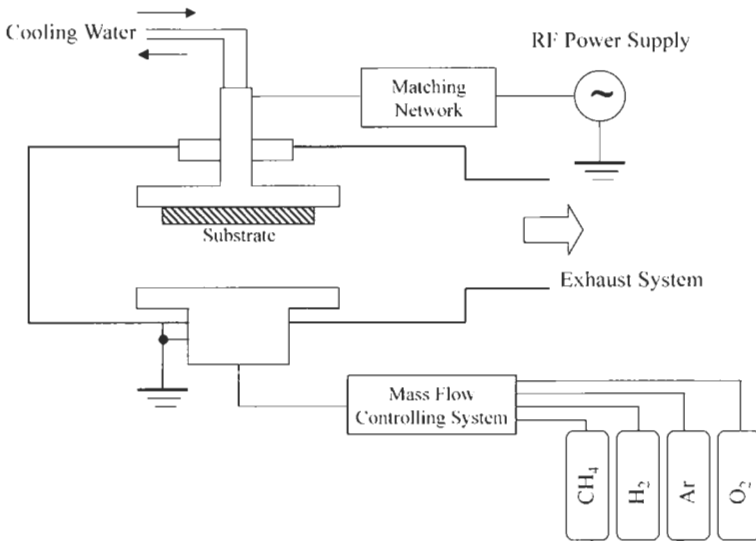


Fig. 4. Parallel-plate rf plasma-enhanced chemical vapor deposition system.

The crystal structure of diamond-like carbon is amorphous according to X-ray and electron diffraction studies. The sp^3 bonding locations and the sp^2 bonding locations constitute nano-size domains with structures too small to be determined by X-ray diffraction. These micro- and nano-structures are best investigated using Raman spectroscopy, electron loss energy spectroscopy (EELS) and Fourier-transform infrared spectroscopy (FTIR).

Conventional Raman spectroscopy uses a visible light laser as an exciting source, the energy of this visible light laser corresponding to $\pi \rightarrow \pi^*$ transitions. Due to a resonant Raman effect the strength of the sp^2 location is approximately 60 times that of the sp^3 locations. Therefore, it is relatively more difficult to determine the fraction of sp^3 location within an amorphous carbon made up of random networks of sp^2 and sp^3 bonding. However it is possible to know the existence of sp^3 parts in the carbon samples.

Typical Raman spectra using an Ar-laser of 514.5 nm excitation energy are shown in Fig. 5 [7]. The Raman spectrum of the powder after breaking of diamond-like carbon by the high internal stresses is also shown for comparison (Fig. 5b). Diamond composed of sp^3 bonding shows a sharp peak at 1333 cm^{-1} and graphite composed of sp^2 bonding shows a sharp peak at 1580 cm^{-1} . However, the spectrum of diamond-like carbon is composed of two broad peaks (Fig. 5a). The height, area ratio, position, width at half-maximum and the tangent of base lines of these two peaks vary according to the preparation method and conditions, thickness and hydrogen content, and relate to the properties of the diamond-like carbon films.

The peak at about 1500 cm^{-1} is the G-peak (or G-band; G means graphite) and relates to sp^2 bonding. The Raman spectrum for the powder shown in Fig. 5b is similar

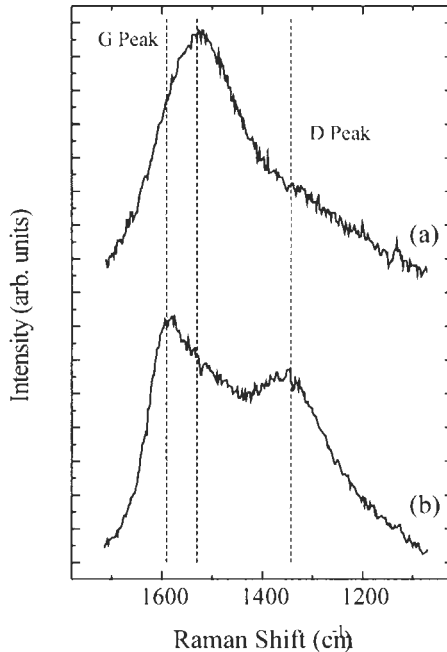


Fig. 5. Visible Raman spectra taken at 514.5 nm for diamond-like carbon films and their potential applications: (a) carbon film, and (b) carbon powder after the breakage of a diamond-like carbon film.

to the spectrum of the graphite-like carbon films, the G-peak of the graphite-like carbon spectrum being similar to that of the powder. On the other hand, the G-peak of the diamond-like carbon film is broad and shifts to lower frequencies due to the sp^3 bonding in the film so indicating the existence of sp^3 bonding. The peak at about 1350 cm^{-1} is the D-peak (or D-band; D means disordered) and is attributed to bond-angle disorder in the graphite structure induced by linking with sp^3 carbon atoms, as well as to the lack of long distance order in graphite-like microdomains. It is difficult to evaluate sp^3/sp^2 ratios from visible Raman spectroscopy.

Recently, UV Raman spectroscopy, that uses ultra violet light as an exciting source, has become available. By using UV Raman spectroscopy the portion of sp^3 bonding in carbons can be evaluated. The reason why the UV light is used is as follows: A photon $>5\text{ eV}$ is necessary to excite $\sigma \rightarrow \sigma^*$ transitions necessary to provide information on sp^3 bonding. A typical UV Raman spectrum of a diamond-like carbon film is shown in Fig. 6 [8]. There are two broad peaks at 1650 cm^{-1} and 1150 cm^{-1} , the former being due to the sp^2 bonding parts and the latter due to the sp^3 bonding. By analyzing the peak height ratios and positions of these two peaks, information on sp^3 bonding is obtained directly.

The hardness of a diamond-like carbon is dependent on sp^3/sp^2 ratios and on hydrogen contents. 'Hardness' has not yet been defined precisely as a physical

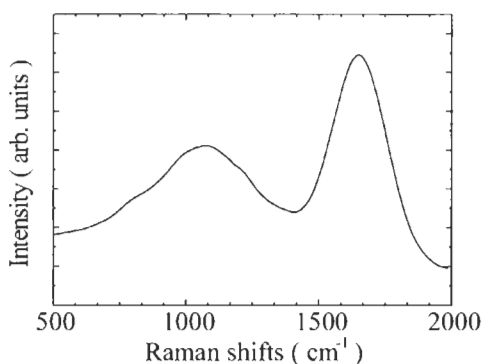


Fig. 6. UV Raman spectrum taken at 244 nm for a diamond-like carbon film [8].

parameter and values of hardness vary according to the testing method used. Hardness is a measure of resistance of a solid against deformation and, microscopically, indicates how interatomic distances vary with force when applied externally. Hardness has a close relationship to bulk modulus which is a physical parameter describing volume changes with compression of a solid. A material with a larger bulk modulus has a larger hardness. For measuring hardness, relative testing methods are used conventionally. Generally, hardness is defined in terms of the size of an indentation made by a diamond tip, that is Vickers hardness (H_V) and Knoop hardness (H_K), according to the shape of a diamond tip. H_V is usually 10–15% smaller than H_K . To measure the hardness of thin films correctly the indentation depth of a diamond tip has to be less than one tenth of the film thickness, in order to avoid the effect of substrates. Hence, the indentation load needs to be small and as a result the size of the trace becomes very small. The measurement of the size by conventional optical microscopy then becomes difficult. Therefore, a nano-indentation method has been developed to measure the indentation depth automatically under loads of less than 1 N for thin films of thickness of less than 1 μm [9].

Using the nano-indentation method, the hardness of diamond-like carbon films varies between ~ 5 GPa and ~ 90 GPa dependent on preparation methods and conditions. The hardness of diamond is 90–100 GPa and the hardness of graphite ~ 4 GPa. The hardness of manufactured films vary from that of diamond to that of graphite. A negative biasing of substrates is important to have high hardness for ion plating, sputtering and plasma-enhanced chemical vapor deposition. Bombardment by Ar-ions effectively increases the fraction of sp^3 bonding. Figure 7 shows one example of the dependence of hardness on negative bias voltage [10].

When hydrocarbon compounds are used as starting materials, hydrogenated diamond-like carbon (a-C:H) is formed, depending on the starting hydrocarbon, and so providing many types of hydrogenated diamond-like carbons. The properties of hydrogenated diamond-like carbons, therefore, can be studied precisely. The relationship between hydrogen content and properties of hydrogenated diamond-like

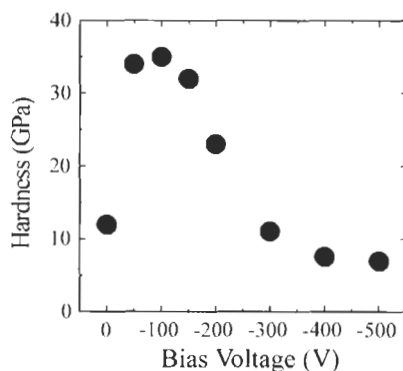


Fig. 7. Dependence of the hardness of diamond-like carbon films as a function of the substrate bias voltage. The films were prepared by shielded ion plating.

carbons is understood. The hydrogen content is determined by using elastic recoil detection analysis (ERDA), secondary ion mass spectroscopy (SIMS), glow-discharge spectroscopy (GDS), and Fourier transform infrared spectroscopy (FTIR). Hydrogen atoms in diamond-like carbon films terminate the sites of double bonding of carbon. Hence, increasing hydrogen contents decrease extents of double bonding and hardness. After considerable termination by hydrogen, the films become soft organic films. To form the harder diamond-like carbon, a lower hydrogen content is crucial.

3 Carbon Nitride

Carbon nitride is another new material that shows interesting properties. After the calculations by Liu and Cohen [11], researchers are now trying to prepare β - C_3N_4 , which may be harder than diamond, the hardest material known so far. Structures of carbon nitride have been proposed and their properties have been studied theoretically. Figure 8 shows four, theoretically predicted, crystal structures for carbon nitride [11–14]. Such preparation techniques as sputtering, ion plating, plasma-enhanced chemical vapor deposition, ion implantation, laser ablation and dynamical mixing, as listed in Table 2, have been used to synthesize carbon nitride [15–20]. Currently, almost all carbon nitride thin films which have been synthesized are amorphous and the N/C ratios in the films are usually <0.5 . The existence of microcrystallites of β - C_3N_4 was detected in an amorphous carbon matrix by transmission electron microscopy. Amorphous carbon nitride thin films have been prepared at relatively high rates by arc ion plating and their mechanical properties investigated [21–23].

Amorphous carbon nitride (a-C:N) films have been prepared in a nitrogen plasma by the shielded arc ion plating (SAIP) method in which a shielding plate is inserted

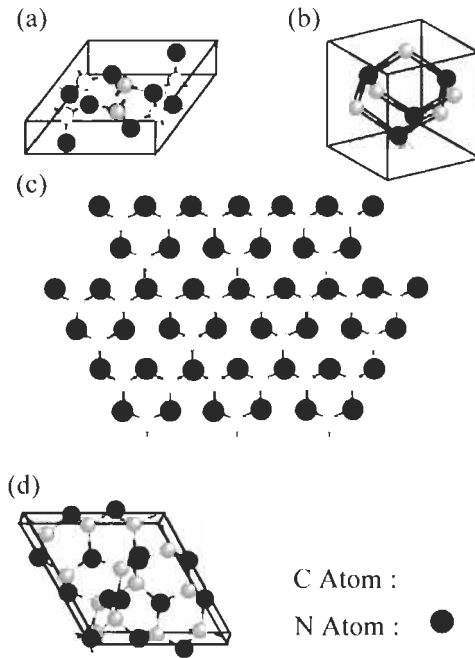


Fig. 8. Four types of crystal structures of carbon nitride predicted theoretically: (a) hexagonal β - C_3N_4 [11]; (b) zincblende-like c - C_3N_4 [12]; (c) rhombohedral C_3N_4 [13]; and (d) trigonal a - C_3N_4 [14].

between a target and a substrate in order to reduce macroparticle deposition onto the substrate. Based on the nano-indentation method, the hardness and wear resistance of these films have been measured and compared with those of hydrogen-free amorphous carbon (a-C:Ar) thin films similarly prepared by SAIP using an argon plasma [22,23]. They were further compared with those of a-C:N:Ar thin films prepared by SAIP using a N_2 -Ar plasma.

A sintered graphite target (Toyo Tanso IG510, ash 10 ppm), 64 mm in diameter and 32 mm in thickness, was mounted on a target holder and served as a cathode in an SAIP apparatus. An arc discharge was generated in N_2 , Ar or N_2 -Ar mixture gas, at a pressure of 1 Pa to synthesize the films and called a-C:N, a-C:Ar or a-C:N:Ar respectively. In the synthesis of a-C:N:Ar, 50% N_2 and 50% Ar mixture gas was used. A cathodic direct current at the target was maintained at 60 A. Si(100) wafers of 10 mm \times 30 mm with 0.5 mm thickness were used as substrates. Films, 150 nm in thickness, were prepared on these substrates. A dc bias voltage of 0 to -500 V was applied during deposition. In general, macro-particles generated at arc-discharge points on the target frequently arrive at the substrate surface. Accordingly, such particles significantly degrade a deposited film. In order to reduce the number of macro-particles arriving on the substrate, a shielding plate of stainless steel was inserted between the target and the substrate.

The chemical compositions of the a-C:N and a-C:N:Ar films and chemical bonding states of a-C:N, a-C:Ar and a-C:N:Ar films were analyzed by X-ray photoelectron spectroscopy (XPS, Shimadzu-Kratos, AXIS) using Mg K α radiation. The hardness of the films was measured by a nano-indenter (Hysitron, TriboScope) interfaced with an atomic force microscope (AFM, Park Scientific Instruments, Autoprobe-LS). A Berkovich-type diamond tip whose radius was < 100 nm was used for the measurement. A force-displacement curve of each sample was measured at a peak load of 250 μ N. Loading, holding and unloading times for each indentation were 2.5, 0 and 2.5 s, respectively. An average hardness of each film was determined from five measurements.

The wear resistance of the film was analyzed with the same indentation system. First, each film surface was scanned with the Berkovich-type diamond tip at a constant load force of 20 μ N. The tip-scanning was repeated 30 times in a 1 μ m-square region with 512 lines at a scanning rate of 2 μ m s⁻¹. After this tip-scanning, the wear profile of the film was acquired using the indenter in the AFM mode at a contact force < 5 μ N using the same identical tip. Its wear depth was determined from this wear profile. Wear depth on a sub-nm scale could be detected. Wear depths of control substrates, that is, silicon and silica, were both \sim 15 nm.

The hardness of a-C:Ar, a-C:N:Ar and a-C:N films depended on the substrate bias voltage, V_s , used in their manufacture, particularly for the a-C:Ar films, becoming >30 GPa at V_s in the range -50 to -150 V. By biasing the substrate negative, the bombardment of Ar⁺ ions on the growing film surface increased the diamond-like (sp^3) components in the film and hardened the film. The hardness showed a maximum of more than 35 GPa at $V_s = -100$ V, which corresponded to the maximum for diamond-like components. When the substrate was biased more negatively than -100 V, the hardness decreased to 7 GPa at a bias voltage less than -400 V. This value was smaller than the hardness of the silicon substrate of \sim 10 GPa, but larger than that of graphite, \sim 4 GPa. An excessive ion bombardment increased the surface temperature and enhanced the formation of graphite-like (sp^2) components in the film which became soft.

The hardness of a-C:N films prepared at $V_s = 0$ V was 10 GPa and almost equal to that of silicon. When biased at $V_s = -100$ to -500 V, the hardness slightly increased to 13–15 GPa. The maximum hardness of 15 GPa was obtained at $V_s = -250$ and -300 V. The hardness of a-C:N films was much lower than the maximum hardness of a-C:Ar films and less dependent on V_s . The main ionic species in the nitrogen plasma were N₂⁺ ions, which were found using the optical emission spectroscopy. The mass of the N₂⁺ ion is less than that of the Ar⁺ ion. The bombardment effect of N₂⁺ ions was expected, therefore, to be less than the effects of Ar⁺ ions. Hence, a bias voltage as high as -300 V was needed to increase the amounts of the diamond-like components in the film. As a result, the N₂⁺ ion bombardment did not reduce the amounts of diamond-like components significantly at V_s values of < -300 V. This leads to the small decrease in hardness with V_s .

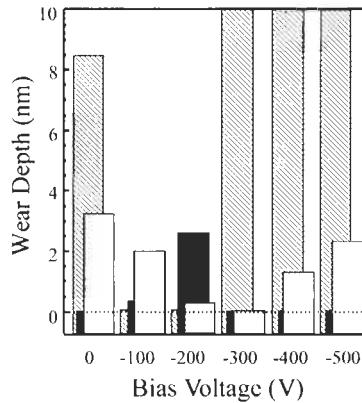


Fig. 9. Wear depth of a-C:Ar (grey bar), a-C:N:Ar (black bar) and a-C:N (white bar) films as a function of the substrate bias voltage.

The hardness of a-C:N:Ar films was intermediate between those of a-C:Ar and a-C:N films at the same V_s . The hardness showed a maximum of 20 GPa at $V_s = -100$ V, which was the same bias voltage to give the maximum hardness for a-C:Ar films. The mixing effect of argon is effective in increasing the hardness at $V_s < -300$ V.

The nitrogen to carbon atomic ratios (N/C) in a-C:N and a-C:N:Ar films were determined by XPS as a function of V_s . For a-C:N films the N/C ratio was about 0.29 at $V_s = 0$ V and increased slightly to 0.33 at $V_s = -100$ V. The reason why the N/C ratio increased could be due to the N_2^+ ions being attracted to the negatively biased substrate during deposition. However, the N/C ratio decreased at $V_s < -100$ V and approached 0.11 at $V_s = -500$ V. At highly negative values of V_s , N_2^+ ions bombarded the film surface more heavily and nitrogen atoms were selectively sputtered from the growing film surface. This reduced the N/C ratio of the deposited film. The N/C ratio for a-C:N:Ar films showed a similar behavior of decreasing V_s . Because the content of nitrogen in the N_2 -Ar plasma was less than the content in the N_2 plasma, at the same total pressure, the N/C ratios of a-C:N:Ar films were less than the ratios of a-C:N films.

Figure 9 shows wear depths of a-C:Ar, a-C:N:Ar and a-C:N films as a function of V_s . The wear depth of a-C:Ar films decreases drastically from 8.5 nm at $V_s = 0$ V to 0.7 nm at $V_s = -100$ and -200 V. The wear depth of a-C:Ar films prepared at further negative V_s (-300 , -400 and -500 V) were, however, more than 50 nm. These a-C:Ar films were much less wear resistant than silicon (Si) and silica (SiO_2). Both the wear resistance and the hardness of a-C:Ar films showed similar trends with V_s . Harder a-C:Ar films showed higher wear resistance.

The a-C:N film prepared at $V_s = 0$ V was the least wear resistant of the deposited a-C:N films, with the lowest hardness of 10 GPa. The biased a-C:N films became more wear resistant. In particular, the a-C:N films prepared at -300 V were markedly more wear resistant so that its wear depth was too shallow to be measured in spite of the fact

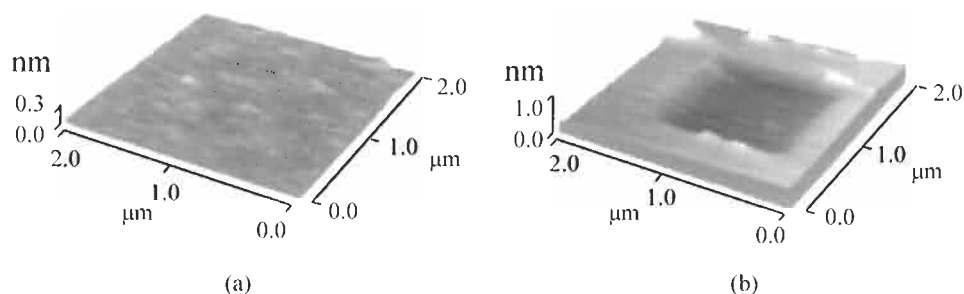


Fig. 10. AFM images of wear profiles of an a-C:N film (a) prepared at -300 V, and (b) of an a-C:Ar film prepared at -100 V.

that the much harder a-C:Ar films, i.e., the films prepared at $V_s = -100$ and -200 V, were obviously worn under the same wear test conditions. Figure 10 indicates AFM images of the wear profiles of an a-C:N film prepared at -300 V and an a-C:Ar film prepared at $V_s = -100$ V, which has the best wear resistance of the a-C:Ar films prepared. A wear depth of 0.7 nm is detected for the a-C:Ar film, but no wear depth is detected for the a-C:N film. The N1s XPS spectra of a-C:N films showed dual peaks centered at around 398.0 and 400.5 eV. With applying more negative V_s , the intensity of the first peak decreased and that of the second peak increased. Intensities of these two peaks were almost equal at around $V_s = -300$ V where the most wear-resistant film was obtained. This second peak probably relates to C–N networks that may be the origin of the excellent wear resistance.

The a-C:N:Ar films display an interesting wear-resistance behavior. Wear depths of the films prepared at $V_s = -100$ and 200 V are < 3 nm, these films having good wear resistance. Particularly, the wear depths of the films prepared at $V_s = 0, -300, -400$ and -500 V are almost zero. These films show excellent wear resistance similar to the a-C:N film prepared at $V_s = -300$ V. In these films, C–N networks similar to those in a-C:N film prepared at $V_s = -300$ V are formed. These wear resistant films are applicable as coatings on hard disks, magnetic heads, cutting tools, molds, etc.

4 Boron Carbonitride (B_xC_yN_z)

Ternary compounds containing boron, carbon and nitrogen are potential candidates as super-hard materials. These compounds are essentially carbon alloys. Hexagonal (BN)_xC_y has the properties of a high temperature semiconductor, whereas cubic (BN)_xC_y is a super-hard material finding an applicable in cutting tools for steel. The cubic boron carbonitride also has a significant resistance to high-temperature oxidation. This makes cubic boron carbonitride an excellent material for high-speed cutting and polishing of steels because it is more thermally and chemically stable than diamond and harder than c-BN.

Recently, cubic BC_2N (c- BC_2N) was synthesized from the graphite-like BC_2N at pressures >18 GPa and temperatures >2200 K [24]. As graphite can be converted into diamond, similarly, graphite-like BC_2N can be converted into c- BC_2N . The lattice parameter of c- BC_2N determined at ambient temperature and pressure is 0.3654 nm and is larger than the lattice parameters of diamond and c-BN. The nano-indentation hardness of c- BC_2N is 75 GPa and harder than that of c-BN single crystal material (55 GPa). Cubic BC_2N is a super-hard material.

5 Conclusion

Super-hard materials have important applications as tools for cutting, grinding and drilling, and as wear-resistant coatings. Super-hard materials, based on carbon alloys, possess a wide range of properties and industrial applications. The preparation and properties of such super-hard materials as diamond-like carbon, carbon nitride and boron carbonitride are presented. The development of new super-hard materials, some having new crystal structures by alloying carbon with other elements is a major research project. Theoretical approaches to predict the formulation of new super-hard materials are available [25].

References

1. J. Musil, J. Vyskčil and S. Kadlec, In: M.H. Francombe and J.L. Vossen (Eds.), *Physics of Thin Films*, Vol. 17. Academic Press, pp. 79–144, 1993.
2. R. Riedel (Ed.), *Handbook of Ceramic Hard Materials*, Vols. I and II. Wiley-VCH, 2000.
3. S. Aisenberg and R. Chabot, *J. Appl. Phys.*, 42: 2953–2961, 1971.
4. C. Weissmantel, In: K.J. Klabunde (Ed.), *Thin Films from Free Atoms and Particles* Academic Press, pp. 153–201, 1985.
5. J. Robertson, *Prog. Solid Chem.*, 21: 199–333, 1991.
6. D.R. McKenzie, *Rep. Prog. Phys.*, 59: 1611–1664, 1996.
7. Y. Taki and O. Takai, *Thin Solid Films*, 316: 45–50, 1998.
8. K.W.R. Gilkes, H.S. Sands, D.N. Batchelder, J. Robertson and W.I. Milne, *Appl. Phys. Lett.*, 70: 1980–1982, 1997.
9. W.C. Oliver and G.M. Pharr, *J. Mater. Res.*, 7: 1564–1583, 1992.
10. N. Tajima, H. Saze, H. Sugimura and O. Takai, *Vacuum*, 59: 567–573, 2000.
11. A.Y. Liu and M.L. Cohen, *Science*, 245: 841–842, 1989.
12. A.Y. Liu and R.M. Wentzcovitch, *Phys. Rev. B*, 50: 10362–10365, 1994.
13. J. Ortega and O.F. Sankey, *Phys. Rev. B*, 51: 2624–2627, 1995.
14. Y. Guo and W.A. Goddard III, *Chem. Phys. Lett.*, 237: 72–76, 1995.
15. K. Ogata, J.F.D. Chubaci and F. Fujimoto, *J. Appl. Phys.*, 76: 3791–3796, 1994.
16. Y. Taki, T. Kitagawa and O. Takai, *Thin Solid Films*, 304: 183–190, 1997.
17. N. Hellgen, M.P. Johansson, B. Hjörvarsson, E. Brotman, L. Hultman and J.-E. Sundgren, *Phys. Rev. B*, 59: 5162–5169, 1999.
18. T.W. Scarf, R.D. Ott, D. Yang and J.A. Barnard, *J. App. Phys.*, 85: 3142–3154, 1999.
19. N. Hellgen, M.P. Johansson, B. Hjörvarsson, E. Brotman, M. Östbom, B. Liedberg, L. Hultman and J.-E. Sundgren, *J. Vac. Sci. Technol. A*, 18: 2349–2357, 2000.

20. M.A. Monclus, A.K.M.S. Chowdhury, D.C. Cameron, R. Barklie and M. Collins, *Surf. Coat. Technol.*, 131: 488–492, 2000.
21. Y. Taki, N. Tajima and O. Takai, *Thin Solid Films*, 334: 165–172, 1998.
22. N. Tajima, H. Saze, H. Sugimura and O. Takai, *Jpn. J. Appl. Phys.*, 38: L1131–L1133, 1999.
23. O. Takai, N. Tajima, H. Saze and H. Sugimura, *Surf. Coat. Technol.*, 142–144: 719–723, 2001.
24. V.L. Solozhenko, D. Andrault, G. Fiquet, M. Mezouar and D.C. Ruble, *Appl. Phys. Lett.*, 78: 1385–1387, 2001.
25. J.E. Lowther, *Phys. Stat. Sol. (B)*, 217: 533–543, 2000.

Contributing Authors

Noboru Akuzawa

Tokyo National College of Technology, 1220-2 Kunugida, Hachioi-shi, Tokyo 193-0997, Japan. E-mail: noboru@tokyo-ct.ac.jp

Morinobu Endo

Faculty of Engineering, Shinshu University, 4-17-1 Wakasato, Nagano-shi 380-8553, Japan. E-mail: endo@endomoribu.shinshu-u.ac.jp

Toshiaki Enoki

Department of Chemistry, Tokyo Institute of Technology, Ookayama, Meguro-ku, Tokyo 152-8551, Japan. E-mail: tenoki@chem.titech.ac.jp

Ken-ichi Fukui

Department of Chemistry, Graduate School of Science, The University of Tokyo, Hongo, Bunkyo-ku, Tokyo 113-0033, Japan

Yohko Hanzawa

Department of Chemistry, Faculty of Science, Chiba University, 1-33 Yayoi, Inage, Chiba 263-8522, Japan

Koichi Hata

Department of Electrical and Electronic Engineering, Mie University, 1515 Kamihama, Tsu 514-8507, Japan

Takuya Hayashi

Faculty of Engineering, Shinshu University, 4-17-1 Wakasato, Nagano-shi 380-8553, Japan

Hisako Hirai

Institute of Geoscience, University of Tsukuba, Tsukuba, Ibaraki 305-8571, Japan. E-mail: hhirai@sakura.cc.tsukuba.ac.jp

Yoshihiro Hishiyama

Musashi Institute of Technology, 1-28-1 Tamazutsumi, Setagaya-ku, Tokyo 158-8557, Japan. E-mail: hishiyama@ep.ese.Musashi-tech.ac.jp

Sung Wha Hong

Faculty of Engineering, Shinshu University, 4-17-1 Wakasato, Nagano-shi 380-8553, Japan

Tadaaki Ikoma

Institute of Multidisciplinary Research for Advanced Materials, Tohoku University, Katahira, Aoba-ku, Sendai, 980-8577, Japan

Michio Inagaki

Aichi Institute of Technology, Yakusa, Toyota 470-0392, Japan. E-mail: ina@ac.aitech.ac.jp

Osamu Ito

Institute of Multidisciplinary Research for Advanced Materials, Tohoku University, Katahira, Aoba-ku, Sendai, 980-8577, Japan. E-mail: ito@tagen.tohoku.ac.jp

Yasuhiro Iwasawa

Department of Chemistry, Graduate School of Science, The University of Tokyo, Hongo, Bunkyo-ku, Tokyo 113-0033, Japan. E-mail: iwasawa@chem.s.u-tokyo.ac.jp

Masato Kakihana

Materials and Structures Laboratory, Tokyo Institute of Technology, Nagatsuta 4259, Midori-ku, Yokohama 226-8503, Japan. E-mail: kakihana@rlem.titech.ac.jp

Katsumi Kaneko

Department of Chemistry, Faculty of Science, Chiba University, 1-33 Yayoi, Inage, Chiba 263-8522, Japan. E-mail: kaneko@pchem2.s.chiba-u.ac.jp

Yoong Ahm Kim

Faculty of Engineering, Shinshu University, 4-17-1 Wakasato, Nagano-shi 380-8553, Japan

Katsuki Kusakabe

Department of Applied Chemistry, Kyushu University, Fukuoka 812-8581, Japan. E-mail: kusaktcf@mbbox.nc.kyuhau-u.ac.jp

Takashi Kyotani

Institute of Multidisciplinary Research for Advanced Materials, Tohoku University, 2-1-1, Katahira, Sendai 980-8577, Japan. E-mail: kyotani@tagen.tohoku.ac.jp

Rong-Li Lo

Department of Chemistry, Graduate School of Science, The University of Tokyo, Hongo, Bunkyo-ku, Tokyo 113-0033, Japan

Kouichi Miura

Department of Chemical Engineering, Kyoto University, Kyoto 606-8501, Japan. E-mail: miura@cheme.kyoto-u.ac.jp

Mikio Miyake

School of Materials Science, Japan Advanced Institute of Science and Technology 1-1, Asahidai, Tatsunokuchi, Nomi, Ishikawa 923-1292, Japan. E-mail: miyake@jaist.ac.jp

Shigeharu Morooka

Department of Applied Chemistry, Kyushu University, Fukuoka 812-8581, Japan

Hiroyuki Nakagawa

Department of Chemical Engineering, Kyoto University, Kyoto 606-8501, Japan

Tsuyoshi Nakajima

Department of Applied Chemistry, Aichi Institute of Technology, Yakusa-cho, Toyota-shi, 470-0392, Japan. E-mail: nakajima@ac.aitech.ac.jp

Keiko Nishikawa

Division of Diversity Science, Graduate School of Science and Technology, Chiba University, Yayoi, Inage-ku, Chiba 263-8522, Japan. E-mail: nisikawa@cuphd.nd.chiba-u.ac.jp

Takashi Nishizawa

*Chemical & Environmental Tech. Lab., Kobe Steel, Ltd., 5-5, Takatsukadai
1-chome, Nishi-ku, Kobe, Hyogo 651-2271, Japan. E-mail: t-nishizawa@
rd.kcr.l.kobelco.co.jp*

Hiroaki Ohta

*Faculty of Engineering, Shinshu University, 4-17-1 Wakasato, Nagano-shi
380-8553, Japan*

Tatsuo Oku

*Ibaraki Study Center, The University of the Air, 2-1-1 Bunkyo, Mito, Ibaraki
310-0056. E-mail: oku@u-air.ac.jp*

Minoru Osada

*Materials and Structures Laboratory, Tokyo Institute of Technology, Nagatsuta
4259, Midori-ku, Yokohama 226-8503, Japan*

Asao Oya

*Faculty of Engineering, Gunma University, Kiryu, Gunma 376-8515, Japan.
E-mail: oya@chem.gunma-u.ac.jp*

Bhagavatula L.V. Prasad

*Department of Chemistry, Tokyo Institute of Technology, Ookayama, Meguro-ku,
Tokyo 152-8551, Japan*

Riichiro Saito

*Department of Electronic-Engineering, University of Electro-Communications,
1-5-1 Chofugaoka, Chofu, Tokyo 182-8585, Japan. E-mail: rsaito@ee.uec.ac.jp.
Address from March 2003: Department of Physics, Tohoku University, Sendai,
780-8578, and CREST, JST, Japan*

Yahachi Saito

*Department of Electrical and Electronic Engineering, Mie University, 1515
Kamihama, Tsu 514-8507, Japan. E-mail: saito@is.elec.mie-u.ac.jp*

Hiroyasu Saka

*Department of Quantum Engineering, Nagoya University, Nagoya 464-8603, Japan.
E-mail: saka@numse.nagoya-u.ac.jp*

Mototsugu Sakai

*Department of Materials Science, Toyohashi University of Technology
Tempaku-cho, Toyohashi, 441-8580 Japan. E-mail: msakai@tutms.tut.ac.jp*

Richard Sakurovs

CSIRO, Division of Energy Technology, P.O. Box 136, North Ryde 1670, Australia

Hirohiko Sato

*Department of Chemistry, Tokyo Institute of Technology, Ookayama, Meguro-ku,
Tokyo 152-8551, Japan*

Yoshiyuki Shibayama

*Department of Chemistry, Tokyo Institute of Technology, Ookayama, Meguro-ku,
Tokyo, 152-8551, Japan*

Minoru Shiraishi

Tokai University, School of High-technology for Human Welfare, Dept. Material

Science and Technology, Nishino 317, Numazu, Shizuoka 410-0395, Japan.

E-mail: siraisi@wing.ncc.u-tokai.ac.jp

Soshi Shiraishi

Department of Chemistry, Faculty of Engineering, Gunma University, Tenjin-cho

1-5-1, Kiryu, Gunma 376-8515, Japan. E-mail: ssiraisi@chem.gunma-u.ac.jp

Noboru Suzuki

Utsunomiya University, Yoto 7-1-2, Utsunomiya 321-8585, Japan. E-mail:

suzukin@cc.utsunomiya-u.ac.jp

Kazuyuki Takai

Department of Chemistry, Tokyo Institute of Technology, Ookayama, Meguro-ku,

Tokyo 152-8551, Japan

Osamu Takai

Department of Materials Processing Engineering, Graduate School of Engineering,

Nagoya University, Furo-cho, Chikusa-ku, Nagoya 464-8603, Japan. E-mail:

takai@otakai.numse.nagoya-u.ac.jp

Yasuhiro Tanabe

Materials and Structures Laboratory, Tokyo Institute of Technology, 4259

Nagatsuta, Midori, Yokohama 226-8503, Japan. E-mail: y.tanabe@

rlem.titech.ac.jp

Hidekazu Touhara

Department of Materials Chemistry, Faculty of Textile Science and Technology

Shinshu University, Ueda 386-8567, Japan. E-mail: htouhara@giptc.shinshu-u.ac.jp

Shinji Tsuneyuki

Department of Physics, Graduate School of Science, The University of Tokyo,

Hongo 7-3-1, Bunkyo-ku, Tokyo 113-0033, Japan. E-mail:

stsune@phys.s.u-tokyo.ac.jp

Sashiro Uemura

Ise Electronics Corp., 728-23 Tsumura, Ise 516-1103, Japan

Hiromi Yamashita

Department of Applied Chemistry, Osaka Prefecture University, Gakuen-cho 1-1,

Sakai, Osaka 599-8531, Japan. E-mail: yamashita@chem.osakafu-u.ac.jp

Ei-ichi Yasuda

Materials and Structures Laboratory, Tokyo Institute of Technology, 4259

Nagatsuta, Midori, Yokohama 226-8503, Japan. E-mail: e.yasuda@

rlem.titech.ac.jp

Subject Index

- absorption, 319
- absorption factors, 162
- acetylene, 19
- activated carbon fibers, 61, 103, 385, 485
 - fluorination of, 392
- activated carbons, 58, 448
- adhesive material, 516
- adsorbed species, 263
- adsorption, 265, 442
 - and desorption of residual gas molecules, 464
- adsorption isotherm, 324
 - standard, 326
 - Type I, 325
 - Type II, 326
 - Type III, 326
 - Type IV, 326
 - Type V, 328
- adsorption processes, 118
- adsorption properties, 485, 493
- algae, 517
- alumina/carbon composite, 105
- amorphous carbons, 239, 285
- amorphous diamond, 239
- analysis procedures, 162
- angular resolved XPS, 213
- anisotropy ratios, 402
- anodic aluminum oxide film, 117
- apparent crystallite size, 167
- arc ion plating, 548
- atomic distances, 190
- atomic-scale visualization, 260
- Auger process, 212
- average crystallite layer plane transverse magnetoresistance, 402
- Babinet theorem, 178
- Bacillus carboniphilus*, 516
- band gap, 239
- BCN heterodiamonds, 151
- Berkovich indenter, 361
- BET specific surface areas, 450
- β -SiC, 236
- binding energy, 212
- bond-counting rule, 152
- boron, 441
- boron carbonitride, 545
- boron doping, 46
- boron-substituted carbon, 346
- boron-substituted graphite, 342, 344
- Bragg condition, 226
- Breit–Wigner–Fano lines, 34
- bright field image, 225
- Bright theory, 399
- Brown–Ladner equation, 309
- bulk modulus, 551
- C K-edge XANES, 200
- C/C composites, 85
- C₆₀ fullerenes, 249
- camera length, 228
- capillary condensation, 320
- carbon aerogels, 71, 112, 454
- carbon alloys, 9
 - definition, 9
- carbon coils, 525
- carbon family, 5
- carbon fibers, 4
 - improvement in compressive strength, 524
 - high quality, 523

- thinner, 133
- carbon matrices, 523
- carbon matrix precursors, 530
- carbon membranes, 119, 469
- carbon nanotubes, 15, 26, 41, 103, 117, 135, 201, 285, 292, 447, 455, 459, 485
 - electrical properties of, 527
- carbon nitride, 545
- ^{13}C -NMR, 273
- carbon paste, 440
- carbonization, 501
- carbyne, 8
- Car–Parrinello method, 150
- catalysts, 200
 - supports, 120
- catalytic activation, 111
- catalytic activity, 265
- cathode-ray-tube-type light bulbs, 465, 466
- charge transfer, 103
 - rate of, 337
- charge/discharge cycling, 339
- charge/discharge behavior, 101
- chemical shift, 212
 - anisotropy, 306
- chemical states, 212
- chemisorption, 319
- classic carbons, 3
- clean surfaces, 463
- coal, 202, 204, 282
- coal-tar pitch, 370
- cohesion at the interface, 534
- complementary system, 178
- composite electrode, 347
- confinement effect, 64
- confocal micro Raman spectroscopy, 35
- constant current method, 339
- contact time, 312
- continuous wave EPR, 276
- coordination numbers, 190
- core/shell particles, 135
- corrected profile, 166
- CP/MAS method, 312
- crack, 233
- cross-polarization, 305
- crystallite sizes, 162
 - distribution of, 172
- CsC_{24} , 105
- current densities, 462
- current vs. voltage characteristics of various carbon nanotubes, 462
- cyclic voltammetry, 335, 336
- dark field image, 225
- Debye rings, 228
- density functional theory, 145, 147
- density of state, 239
- dependence of the resistivity ρ_T on temperature, 412
- diamond, 7, 545
 - coating, 234
 - converting to graphite, 386
- diamond-like carbon, 294, 545, 546
 - hardness, 550
 - hydrogenated, 551
- diatoms, 517, 519
- dielectric function, 239
- differential charging, 213
- diffraction patterns, 228
- diffuse reflectance absorption, 269
- dipolar dephasing, 274
- direct dipole–dipole interaction, 306
- disordered carbons, 419
- distance distribution function, 182
- Dollimore–Heal method, 449, 503
- domain sizes, 87
- doping, 41, 441
- double resonance Raman, 33
- doubletting of $K\alpha$ radiation, 162
- Dubin–Radushevich equation, 450
- edge states, 385
- elastic modulus, 355
- elastoplastic indentation, 351
- electric double layer capacitor, 447
- electrical properties of nanotubes, 527

- electrochemical double-layer capacitors, 442
- electrochemical lithium insertion, 485, 496
- electrochemical properties, 495
- electrochemical reactions, 436
- electrochemical sensors, 443
- electrochemical techniques, 336
- electron energy-loss spectroscopy, 36, 239
- electron nuclear double resonance, 278
- electron spectroscopy for chemical analysis, 211
- electron tunneling, 464
- electronic density of states, 257
- electronic structure, 145
- elemental analysis, 230
- emission patterns, 463
- enhanced molecule–pore wall interaction, 65
- enthalpy of alloy formation, 534
- EPR, 276
- exfoliated graphite, 100
- exfoliation fracture toughness, 538
- extended X-ray absorption fine structure, 189

- field cooling effects, 390
- field emission display, 465, 467
- field emission microscopy, 459
- field emission properties, 527
- first-principles molecular dynamics method, 150
- fish, 518, 520
- fluorescence mode, 195
- fluorescence rejection, 291
- fluorinated nano-graphite, 392
- fluorinated nanotubes and nanofibers, 51
- fluorination, 103, 392, 485, 487
 - control of carbon properties by, 486
- fluorine atom on nanographite, 28
- fluorine-induced sp^3 bonds, 393

- focused ion beam, 223
- food chain, 518, 519
- fracture criterion, 541
- full width at half maximum, 162, 216
- fullerenes, 15, 26, 34, 41, 201, 285, 295
 - metal, 207
- functional groups, 212

- galvanostatic discharge-charge curves, 496
- galvanostatic method, 335, 339
- gas separations, 469
- G-band, 33
- generalized gradient approximation, 149
- glass-forming materials, 375
- glass-like carbon, 4
- glassy carbon, 91, 289, 440
- grand canonical Monte Carlo simulation, 62
- graphite, 7, 236
 - boron-substituted, 342, 344
 - converting diamond to, 386
 - C_xN-coated, 348
 - first coulombic efficiency of, 340
 - highly ordered, 419
 - theoretical capacity of, 340
- graphite intercalation compounds, 28, 42, 99, 154, 418
- graphite–diamond transformation, 150
- graphite-like carbon, 547
- graphite-slit pore model, 58
- graphitizable (soft) carbons, 43, 421
- Guinier Plot, 180
- Guinier region, 179
- gyration radius, 179, 180

- hard carbons, 16
- Hartmann–Hahn condition, 305
- Hartree–Fock self-consistent-field method, 147
- heat treatment temperature, 34
- heating experiments, *in situ*, 223
- heat-treated carbons, 364

- hetero-atomic alloys, 10
- hidden surface fluorination, 489
- hidden surfaces, 10, 57
- high resolution α_s -plot, 325
- highly active catalyst, 499
- highly ordered pyrolytic graphite, 288, 440
- high-power decoupling, 308
- high-pressure adsorption, 330
- homo-atomic alloys, 10
- host effect, 99, 104
- host-guest reaction, 99
- hybridization, 16
- hydrocarbon compounds, 200
- hydrogen content of diamond-like carbon, 550
- hydrophobicity, 70
- hyperfine sublevel correlation spectroscopy, 279
- hysteresis loop, 326

- indentation ductility index, 357
- indirect dipole-dipole interaction, 306
- infra-red spectra, 269
- in-situ* measurements, 194
- instrumental broadening, 163
- insulator-metal transition, 386
- interatomic potential, 146
- inter-band transition, 239
- intercalation, 41, 99
 - compounds, 439
- interface control, 85
- interference fringes, 463
- interlayer spacing d_{002} , 405
- internal standard, 162
- iodine treatment, 90
- ion implantation, 34
- ion-exchange resin, 110, 499
- ion-sieving effect, 452

- JSPS method, 162, 166

- K_3C_{60} , 295

- Kelvin equation, 327
- Kikuchi lines, 228
- Knight shift, 313
- Knoop indenter, 361

- laboratory XAFS, 196
- Larmor precession, 300
- lattice constants, 167
- lattice fringes, 227
- layered metal carbon alloy, 257
- lithium
 - cavity model, 46
 - electrochemical insertion of, 496
 - insertion in disordered carbon, 44
 - LiC₂ model, 44
 - rechargeable batteries, 441
 - reference electrode, 337
 - storage model, 430
- Lithium-ion battery, 99
- Li-encapsulated diamond, 154
- Li-GICs, 418
- Li NMR, 427
- local density approximation, 149
- local structures, 189
- longitudinal magnetoresistance, 399
- Lorenz-polarization factors, 162
- low energy electron diffraction, 258
- lugworms, 519

- macropores, 502
- magnetoresistance, 395
- mapping of electronic states, 265
- marine organisms, fixation of, 515
- Maxwell-Stefan diffusivity, 471
- MCl₂-GICs, 105
- mesocarbon microbeads, 5
- mesopores, 57, 111, 449
- mesoporous activated carbon fibers, 449
- mesoporous silica, 116
- metal carbides, 258
- metal-doped carbon nanotubes, 50
- metal-doped fullerenes, 49
- metallic lithium, 417

- metal-loaded porous carbons, 499
- Meyer hardness, 352, 355, 358
- microcapsules, 139
- microelectrodes, 444
- micro-organisms, 516
- micropore filling, 325
- micropores, 57, 110, 469, 503
- microstructure control, 89, 530
- microstructure effect in LIB, 426
- microstructure observation, 542
- microstructures of interfaces, 524
- microtextures, classification of, 400
- minerals, 202
- mobile hydrogen, 282
- molecular dynamics, 145
- molecular orbital methods, 147
- molecular sieving carbons, 110
- molecular simulations, 326
- molybdenum carbide, 257
- mosaic spread, 405
- multilayer adsorption, 320
- multiwall carbon nanotubes, 141, 459, 486, 488

- nano-composites, 545
- nano-diamond, 386
- nanofibers, 134, 459
- nanografibers, 459
- nanographite, 16, 99, 385
 - fluorinated, 392
- nano-indentation method, 551
- nanopores, 327
- nanorods, 75
- near-IR absorption, 270
- negative magnetoresistance, 399
- new carbons, 3
- Ni²⁺ type resins, 499
- nickel catalyst, 346
- nitric oxide
 - decomposition catalyst, 506
 - durability of removal of, 507
 - reducing reagents, 505
 - reduction of, 499

- nitrogen substituted carbons, 342
- nitrogen yields, 506
- nitrogen-doped nanotube, 51
- nitrogen-substituted carbon, 346
- non-graphitizable (hard) carbons, 43, 421
- novel composites, 523, 527

- occlusion, 319, 320
- old but new materials, 4
- optimum fitting, 171
- orbital susceptibility, 386
- organic electrolytes, 443
- oxidation resistance, 534
- oxidation, effect of alloying on, 91
- oxygen functional groups, 436

- partial density of states, 30
- Pauli susceptibility, 389
- pentagonal pinch mode, 34
- pentagonal rings, 21, 463
- permeability, 471
- permeance, 471
- permeation, 469, 474
- photoelectric effect, 211
- photo-electron spectroscopy, 36
- photoemission process, 211
- phototransformation and
 - photo-decomposition in C60, 290
- physical adsorption, 319
- π bond, 20
- π - π^* transition, 218
- plasma-enhanced chemical vapor
 - deposition, 548
- polycrystalline graphite, 401
- polymer blend carbonizations, 113
- polymer blend technique, 129
- polymer precursors, 41
- polymer-like carbon, 547
- pore development, 502
- pore size distribution, 448
- pore structures, 175
- pore volume distributions, 503

- pores
 - latent, 321
 - open, 321
- Porod region, 179
- porosity, 175
- porous carbons, 109, 129, 499
- porous glass, 114
- powder pattern, 307
- preferential etching, 213
- preferential support, 131
- primary lithium cells, 495
- proton magnetic resonance thermal analysis, 281
- pseudo-capacitances, 443
- pulsed EPR, 278
- pyramidal indentation, 351
- pyrolytic carbons, 4
- pyromellitic dianhydride/*p*-phenylene-diamine, 403

- quadrupolar moment, 313
- quasi-high pressure effect, 68

- radical content, 276
- Raman characterization of diamond-like carbon, 294
- Raman imaging, 285
- Raman spectra, 33, 409
 - doped fullerenes, 295
- Raman spectroscopy, 285, 549
- real space, 177
- reciprocal space, 177
- reducing regeneration, 508
- reflection loss of electro-magnetic waves, 525
- regeneration, *in situ*, 499, 512
- resistivity of doped single-wall carbon nanotube, 50
- resonance effects, 285
- resonance Raman scattering of a single-wall carbon nanotube, 292
- retardation time spectrum, 379
- rigid hydrogen, 282

- sample exchange method, 301
- sample thickness, 164
- scanning probe microscope, 36
- scanning tunneling microscopy, 47, 257
- scattering parameter, 176
- scattering vector, 176
- sea, 515
- seaweed bed, 518
 - artificial, 515
 - formation, 519
- self-relaxation, 314
- self-similarity, 180
- semi-empirical molecular orbital calculations, 342
- separation factor, 471
- separation processes, 118
- shear strengths, 92
- shielded arc ion plating, 552
- σ bonds, 15, 20
- Si_3N_4 , 234
- SiC/C multi-layered coating method, 534
- silica gel, 114
- simple two-band (STB) model, 396
- single file diffusion, 470
- single-hole system, 399
- single-wall carbon nanotubes, 60, 459, 486, 487
- singly occupied molecular orbital levels, 342
- slit-like pore, 470
- small-angle X-ray scattering, 175
- solid-echo signal, 282
- solid-state NMR, 273
- sp*, 5
- sp*², 5, 549
- sp*³, 5, 549
- sp*³ fraction, 239
- space alloying, 57
- SPE surface area, 65
- spectrum imaging, 247
- spin glass, 391
- spin hybridization, 15
- spin–lattice relaxation, 302

- spin magnetism, 33
- spin relaxation, 276
- spin-spin relaxation, 302
- spinning, 130
- spinning side bands, 307
- Steele potential, 59
- Stokes radius, 452
- structure image, 227
- supercritical gas, 329
- super-hard materials, 545
- surface areas, 58
- surface carbon atoms, 257
- surface enhanced Raman spectroscopy, 35
- surface fractal, 180, 183
 - dimension, 323
- surface functionalities, 212
- surface oxide, 436
- surface structure, 258
- surface-treated fibers, 85
- Suzuki effect, 230
- synchrotron radiation, 194

- temperature-programmed-reaction experiments, 510
- template carbonization, 114
- template-synthesized carbon nanotubes, 488
- thermal conductivity, 531, 532, 537
 - of graphitic materials, 89
- time-temperature superposition, 374
- topological defect in the electronic structure, 16
- transmission electron microscopy, 223

- transmission mode, 195
- trans*-polyacetylene, 20
- transverse magnetoresistance, 397
- true hardness, 355
- tunneling resistance, 257

- ultraviolet photoelectron spectroscopy, 220

- valence band spectra, 220
- vapor grown carbon fibers, 459
- Vickers indenter, 360
- viscoelastic indentation, 351

- weak-beam technique, 226
- weak localization effect, 400
- wettability, 442
- working electrode, 337
- work-of-indentation, 358

- X-ray absorption fine structure, 189
- X-ray absorption near edge structure, 190
- X-ray diffraction, 161
 - *in situ*, 61
- X-ray photoelectron diffraction, 213
- X-ray photoelectron spectroscopy, 35, 211, 260

- Zeeman splitting, 300
- zeolites, 115
- zig-zag edge, 389
- zooplankton, 518

This book is a major reference source for those working with carbon alloys. Eiichi Yasuda and his team analyse results in terms of controlling the locations of other alloying elements; describe typical carbon alloys and their preparations; discuss recent techniques for their characterization; and finally, illustrate potential applications and future developments for carbon alloy science.

Coined in 1992, the phrase “Carbon Alloys” can be applied to those materials “mainly composed of carbon materials in multi-component systems, the carbon atoms of each component having physical and/or chemical interactive relationships with other atoms or compounds. The carbon atoms of the components may have different hybrid bonding orbitals to create quite different carbon components”.

